



Development of a Continuous for Live Load Prefabricated Steel Accelerated Bridge Construction (ABC) Unit for Texas Bridges

Technical Report 0-7112-R1

Cooperative Research Program

TEXAS A&M TRANSPORTATION INSTITUTE
COLLEGE STATION, TEXAS

sponsored by the
Federal Highway Administration and the
Texas Department of Transportation
<https://tti.tamu.edu/documents/0-7112-R1.pdf>

1. Report No. FHWA/TX-25/0-7112-R1		2. Government Accession No.		3. Recipient's Catalog No.	
4. Title and Subtitle DEVELOPMENT OF A CONTINUOUS FOR LIVE LOAD PREFABRICATED STEEL ACCELERATED BRIDGE CONSTRUCTION (ABC) UNIT FOR TEXAS BRIDGES				5. Report Date Published: July 2025	
				6. Performing Organization Code	
7. Author(s) Stefan Hurlbaas, Matthew Yarnold, Jiakai Guo, Joren Falcon, John Mander, Petros Sideris, Kinsey Skillen, Jeffrey Weidner, and Gibran Cano				8. Performing Organization Report No. Report 0-7112-R1	
9. Performing Organization Name and Address Texas A&M Transportation Institute The Texas A&M University System College Station, Texas 77843-3135				10. Work Unit No. (TRIS)	
				11. Contract or Grant No. Project 0-7112	
12. Sponsoring Agency Name and Address Texas Department of Transportation Research and Technology Implementation Office 125 E. 11 th Street Austin, Texas 78701-2483				13. Type of Report and Period Covered Technical Report: September 2021–February 2025	
				14. Sponsoring Agency Code	
15. Supplementary Notes Project sponsored by the Texas Department of Transportation and the Federal Highway Administration. Project Title: Development of a Continuous for Live Load Prefabricated Steel Accelerated Bridge Construction (ABC) Unit for Texas Bridges URL: https://tti.tamu.edu/documents/0-7112-R1.pdf					
16. Abstract This research study developed and evaluated prefabricated steel bridges made continuous for live load utilizing accelerated bridge construction (ABC). The project created a steel ABC transverse connection detail at the bridge piers that allows the structure to behave as simply supported for dead load and continuous for live load. This detail is relatively easy to fabricate, fast to assemble, safe to construct, cost-effective, and it provides long-term durability. The study began with a comprehensive literature review to capture the state of the art and the state of the practice relevant to the topics addressed in this project. A field assessment on the recent Texas Department of Transportation steel girder ABC project in Dallas was performed to understand the current construction method utilized, observe performance issues, and identify the baseline performance of the transverse connection between adjacent spans. An array of preliminary connection concepts was developed and evaluated by an industry panel. Four concepts were selected for detailed evaluation. Each was studied through a full-scale laboratory test program that included service-level testing, cyclic tests, and an ultimate strength test. The purpose was to demonstrate and validate the anticipated future performance along an in-service bridge. Numerical finite element models were created for the experimental test setups to validate the modeling techniques by comparing them with experimental results. Parametric studies were then carried out to investigate an array of various bridge geometries. Finally, a recommended steel ABC transverse connection detail was selected. This selection was supplemented with design guidance, a design example, and standard details.					
17. Key Words Accelerated Bridge Construction (ABC), Continuous for Live Load, Transverse Joint, Prefabricated Steel ABC Unit			18. Distribution Statement No restrictions. This document is available to the public through NTIS: National Technical Information Service Alexandria, Virginia https://www.ntis.gov		
19. Security Classif. (of this report) Unclassified		20. Security Classif. (of this page) Unclassified		21. No. of Pages 556	
				22. Price	

DEVELOPMENT OF A CONTINUOUS FOR LIVE LOAD PREFABRICATED STEEL ACCELERATED BRIDGE CONSTRUCTION (ABC) UNIT FOR TEXAS BRIDGES

by

Stefan Hurlebaus, Ph.D.
Professor, Zachry Department
of Civil Engineering
Research Scientist,
Texas A&M Transportation
Institute

Matthew Yarnold, Ph.D.
Associated Professor,
Department of Civil
Engineering, Auburn
University

Jiacai Guo
Graduate Assistant
Researcher, Texas A&M
Transportation Institute

Joren Falcon
Graduate Assistant
Researcher, Texas A&M
Transportation Institute

John Mander, Ph.D.
Professor, Zachry Department
of Civil Engineering
Research Scientist, Texas
A&M Transportation Institute

Petros Sideris, Ph.D.
Associate Professor, Zachry
Department of Civil
Engineering
Research Scientist, Texas
A&M Transportation Institute

Kinsey Skillen, Ph.D.
Assistant Professor, Zachry
Department of Civil
Engineering
Assistant Research Scientist,
Texas A&M Transportation
Institute

Jeffrey Weidner, Ph.D.
Assistant Professor,
Department of Civil
Engineering, The University
of Texas at El Paso

Gibran Cano
Graduate Assistant
Researcher, Department of
Civil Engineering, The
University of Texas at
El Paso

Report 0-7112-R1

Project 0-7112

Project Title: Development of a Continuous for Live Load Prefabricated Steel
Accelerated Bridge Construction (ABC) Unit for Texas Bridges

Sponsored by the
Texas Department of Transportation
and the
Federal Highway Administration

Published: July 2025

TEXAS A&M TRANSPORTATION INSTITUTE
College Station, Texas 77843-3135

DISCLAIMER

This research was sponsored by the Texas Department of Transportation (TxDOT) and the Federal Highway Administration (FHWA). The contents of this report reflect the views of the authors, who are responsible for the facts and the accuracy of the data presented herein. The contents do not necessarily reflect the official view or policies of FHWA or TxDOT. This report does not constitute a standard, specification, or regulation.

This report is not intended for construction, bidding, or permit purposes. The engineer (researcher) in charge of the project was Matthew Yarnold, Ph.D., P.E. #15462 (DE).

The United States Government and the State of Texas do not endorse products or manufacturers. Trade or manufacturers' names appear herein solely because they are considered essential to the object of this report.

ACKNOWLEDGMENTS

This project was conducted at Texas A&M University and sponsored by TxDOT and FHWA. The authors are grateful to the individuals who were involved with this project and provided invaluable assistance, including Martin Dassi (TxDOT project manager) and the TxDOT Project Monitoring Committee: Addisu Tilahun, Ahmed Al-Basha, Joe Roche, Jonathan Boleware, Mei Wang, Nader Mavaddat, Remmy Cyriac, Rostam Mahbod, and Xuejian Liu.

The authors thank the American Institute of Steel Construction for donating the steel beams, Concrete Reinforcing Steel Institute for donating the steel reinforcement, NUCOR for carrying out the reinforcement fabrication, and Ken Weycker with the Euclid Chemical Company for donating the epoxy adhesive.

A number of individuals provided crucial support in ensuring the success of this project. The research team deeply appreciates their valuable contributions to the project's successful completion.

- Many students assisted with field assessment and construction of experimental specimens, including Eric Stoddard, Ryan Booth, Seung Hyun Yoon, Arash Rockey, Pushkar Shivechchhu, Zhen Zhang, Drew Krajeck, Hyeonki Hong, Mikhail Lanier, Isabel Mlo, Kaelan Lindauer, Benjamin Gonzalez, Hangil Kim, and Durga Jonnalagadda.
- The lab members at the RELLIS High Bay Lab, including Charlie Droddy, Kirk Martin, and Dr. Peter Keating, were instrumental in providing the support to achieve the laboratory testing.

TABLE OF CONTENTS

	Page
List of Figures.....	xi
List of Tables	xxiii
1. Introduction.....	1
1.1. Objective and Scope	1
1.2. Significance	1
1.3. Research Approach	2
1.3.1. Literature Review and Synthesis (Section 2).....	2
1.3.2. Field Assessment (Section 3).....	3
1.3.3. System Development (Section 4).....	3
1.3.4. Laboratory Testing (Section 5)	4
1.3.5. Analytical Modeling of Tested Specimens (Section 6)	4
1.3.6. Parametric Study (Section 7)	4
1.3.7. Recommendations and Design Guidance (Section 8).....	4
2. Literature Review and Synthesis.....	7
2.1. Overview.....	7
2.2. SDCL Steel Bridge Systems	7
2.2.1. Introduction.....	7
2.2.2. Steel Bridge SDCL Construction in Tennessee	9
2.2.3. Experimental Testing of Steel SDCL Systems in Colorado	11
2.2.4. Steel Bridge SDCL Construction in West Virginia	14
2.2.5. Experimental Testing of Steel SDCL Systems in Nebraska	16
2.3. ABC Technique	21
2.3.1. Introduction.....	21
2.3.2. Prefabricated Bridge Elements and Systems	21
2.3.3. Slide-In Bridge Construction	23
2.3.4. Self-Propelled Modular Transporters	24
2.4. SDCL Steel Bridge Systems Used in ABC Technique.....	25
2.4.1. Introduction.....	25
2.4.2. SDCL System Using ABC at the University of Nebraska-Lincoln.....	25
2.4.3. SDCL System Using ABC as Part of Strategic Highway Research Program 2	27
2.4.4. SDCL System Using ABC as Part of Little Silver Creek Bridge Project.....	30
2.4.5. SDCL System Using ABC in Seismic Regions	34
3. Field Assessment	37
3.1. Overview.....	37
3.2. Field Inspection.....	39
3.3. Field Monitoring.....	42
3.3.1. Instrumentation Design.....	42
3.3.2. Results.....	46
3.4. Field Assessment Summary	54
4. System Development.....	55
4.1. Overview.....	55
4.2. Preliminary System Concepts	55
4.2.1. Concept #1	57

4.2.2. Concept #2	58
4.2.3. Concept #3	59
4.2.4. Concept #4	60
4.2.5. Concept #5	61
4.2.6. Concept #6	62
4.3. Workshop.....	63
4.3.1. Workshop Objective	63
4.3.2. Workshop Design.....	64
4.3.3. Workshop Industry Review Panel and TxDOT Panel	66
4.3.4. Workshop Results	66
4.3.5. System Design for Testing.....	70
5. Laboratory Testing	71
5.1. General.....	71
5.2. Overview.....	73
5.3. Benchmark Bridge Design.....	73
5.3.1. Bridge Geometry and Girder Cross Section	73
5.3.2. Design Parameters and Assumptions.....	76
5.3.3. Loading	77
5.3.4. Limit States	79
5.3.5. Deflection Check	80
5.4. Experimental Testing Approach	80
5.5. Prefabricated Bridge Construction Preparations.....	83
5.6. Material Properties.....	91
5.6.1. Concrete Material Testing.....	91
5.6.2. Steel Material Testing	95
5.7. Concept A	96
5.7.1. Design, Construction, and Pretest Behavior of Concept A.....	96
5.7.2. System Experiment Testing Program, Experiment Results, and Observations	103
5.8. Concept B	149
5.8.1. Design, Construction, and Pretest Behavior of Concept B	149
5.8.2. System Experiment Testing Program, Experiment Results, and Observations	167
5.9. Concept C	214
5.9.1. Design, Construction, and Pretest Behavior of Concept C	214
5.9.2. System Experiment Testing Program, Experiment Results, and Observations	222
5.10. Concept D	266
5.10.1. Design, Construction, and Pretest Behavior of Concept D.....	266
5.10.2. System Experiment Testing Program, Experiment Results, and Observations	274
5.11. Concept Comparison.....	318
5.11.1. Precast Concrete Deck	318
5.11.2. Closure Pour.....	326
5.11.3. Tension-Resisting Elements.....	342
5.11.4. Compression-Resisting Elements	352
5.11.5. Stiffness.....	363
5.11.6. Speed of Assembly	366
5.12. Summary.....	369

6. Analytical Modeling of Tested Specimens	371
6.1. Overview.....	371
6.2. Analytic Modeling of Concept A.....	372
6.2.1. Test Setup Model Description	372
6.2.2. Model Validation with the Experimental Results	381
6.3. Analytic Modeling of Concept B.....	389
6.3.1. Test Setup Model Description	389
6.3.2. Model Validation with the Experimental Results	393
6.4. Analytic Modeling of Concept C.....	400
6.4.1. Test Setup Model Description	400
6.4.2. Model Validation with Experimental Results	403
6.5. Analytic Modeling of Concept D.....	409
6.5.1. Test Setup Model Description	409
6.5.2. Model Validation with Experimental Results	412
6.6. Analytic Modeling for Tested Specimens' Findings	417
6.7. Analytical Modeling of Refined Concepts	418
6.7.1. Introduction.....	418
6.7.2. Final System Option 1 Details	418
6.7.3. Final System Option 1 FEM—No PT.....	420
6.7.4. Final System Option 1 FEM with PT (Optional).....	424
6.7.5. Final System Option 2 Details	430
6.7.6. Final System Option 2 FEM	431
6.7.7. Discussion and Comparison.....	436
7. Parametric Study	439
7.1. Overview.....	439
7.2. Foundation Data Sources	439
7.3. Parameter Range	440
7.3.1. Bridge Configuration and Span Length	441
7.3.2. Girder Geometry	443
7.3.3. Girder Spacing	445
7.3.4. Lateral Support Spacing.....	446
7.3.5. Skew Angle	446
7.4. Full Bridge Configuration Study Framework.....	447
7.5. Parametric 3D Model Description	448
7.5.1. Area of Interest	448
7.5.2. Load Case.....	448
7.5.3. Support.....	450
7.5.4. Lateral Support Elements.....	450
7.5.5. Abaqus General Script Description.....	451
7.5.6. Concept A	451
7.5.7. Concept C.....	453
7.6. Results of Parametric Analysis—Concept A.....	455
7.6.1. Maximum Deck and Closure Pour Stress	455
7.6.2. Deck and Closure Pour Localized Stress Distribution.....	457
7.6.3. Rebar Localized Stress Distribution	457
7.7. Results of Parametric Analysis—Concept C	459

7.7.1. Maximum Deck and Closure Pour Stress	459
7.7.2. Deck and Closure Pour Localized Stress Distribution.....	461
7.8. Concept A—Results Discussion.....	463
7.9. Concept C—Results Discussion	463
7.10. Overall Discussion.....	463
8. Recommendations and Design Guidance	465
References.....	467
Appendix A: Section Properties	471
Appendix B: Instrumentation List	473
Appendix C: Value of Research.....	485
C.1. Motivation and Significance	485
C.2. Qualitative Benefits.....	486
C.2.1. Level of Knowledge	486
C.2.2. System Reliability	486
C.3. Economic Benefits	486
C.3.1. Expedited Project Delivery	487
C.3.2. Reduced Construction, Operations, and Maintenance Cost.....	487
C.3.3. Infrastructure Condition	487
C.4. Qualitative and Economic Benefits.....	487
C.4.1. Increased Service Life.....	487
C.4.2. Improved Productivity and Work Efficiency	488
C.4.3. Engineering Design Improvement	488
C.5. Quantitative Analysis of Economic Benefits	488
C.6. Summary	489
Appendix D: Design Example.....	491
Appendix E: Standard Drawing.....	531

LIST OF FIGURES

	Page
Figure 2.1. Combined Load Cases and Corresponding Bending Moment Diagrams.....	8
Figure 2.2. TDOT SDCL Initial Connection Detail (Composite Load Only) [4].....	9
Figure 2.3. TDOT SDCL Revised Connection Detail [4].	10
Figure 2.4. Colorado SDCL Connection Details [6].....	11
Figure 2.5. Steel Details for SH 36 over Box Elder Creek [6].	12
Figure 2.6. Colorado SDCL Connection Details [6].....	13
Figure 2.7. (a) Three Springs Drive Bridge, and (b) Washington Avenue Bridge [7].	14
Figure 2.8. West Virginia Steel Continuity Splice Details [7].	15
Figure 2.9. Concrete Diaphragm Detail [9].	17
Figure 2.10. Connection Details of the Three Specimens: (a) Specimen 1, (b) Specimen 2, and (c) Specimen 3 [9].	17
Figure 2.11. Test Specimen Configuration [3].	18
Figure 2.12. Cyclic Test Setup [3].	19
Figure 2.13. Specimen 3 Crack Patterns after Ultimate Testing: (a) Concrete Slab, Plan View; and (b) Face of the Diaphragm [3].	20
Figure 2.14. Concrete Deck and Joint Removed before Link Slab Installation and Forming of Link Slab [12].	22
Figure 2.15. Shake Table Test Setup [14].....	23
Figure 2.16. Replacement Superstructure Used as Temporary Runaround [16].	24
Figure 2.17. SPMT Bridge Moves in Utah [10].	24
Figure 2.18. Connection Details for Modular System [18].	25
Figure 2.19. Deck Slab Cracking [9].	26
Figure 2.20. Erection of the 262nd Street Bridge in Nebraska [18].	27
Figure 2.21. SHRP2 Module-to-Module Transverse Connection Detail [19].	28
Figure 2.22. SHRP2 Pier Elevation PT Detail [19].	29
Figure 2.23. Interface Opening and Crack Propagation [19].	30
Figure 2.24. UHPC Rupture (Top and Bottom of Deck) [19].	30
Figure 2.25. Little Silver Creek Bridge Isolated View [20].	31
Figure 2.26. Bridge Transverse Joint Details [20].	32
Figure 2.27. Strength Test Setup.....	33
Figure 2.28. Concrete Crack Patterns at the Deck Surface.	34
Figure 2.29. Concrete Crack Patterns at the Side of the Diaphragm.	34
Figure 2.30. SDCL Connection for Seismic Area Details [21].	35
Figure 3.1. Construction Sequence for the I-635 Bridge over Old Seagoville Road in Dallas [22].	37
Figure 3.2. Construction Photo from the I-635 Bridge [22].	38
Figure 3.3. Cross Section of the I-635 Bridge.	38
Figure 3.4. I-635 Bridge (a) Initial Prefabricated Unit Placement and (b) Closure Pour Detail.	39
Figure 3.5. Overall Photos of the I-635 Bridge at an Interior Bent: (a) Elevation View and (b) Underside View.	40
Figure 3.6. Underside of the Deck between the Steel End Diaphragms Obstructed by Timber Formwork.	40

Figure 3.7. Typical Condition of the Underside of the Deck Overhang at the Pier Bents.	41
Figure 3.8. Evidence of Water Leakage in the Deck Slab through Wet Areas on the Top Surface of the Pier Cap.	42
Figure 3.9. General Instrumentation Approach at the Pier Bent.....	43
Figure 3.10. Instrumentation Plan for the I-635 Bridge.....	44
Figure 3.11. Cross-Section View of the Strain Gauge Locations.	45
Figure 3.12. Photos of Installed (a) Displacement Gauges and (b) Strain Gauges near the Pier.	46
Figure 3.13. Temperature Measurements from All Sensors.	47
Figure 3.14. Midspan Strain Gauge Measurements for the Recorded Back-to-Back Truck Event Producing the Largest Response at the Pier Bent.	48
Figure 3.15. Average Girder End Rotations due to Thermal Variations (Positive Is When the Girders Are Concave Up).	49
Figure 3.16. Average Girder End Rotations due to the Controlling Live Load Event (Positive Is When the Girders Are Concave Up).	50
Figure 3.17. Relative Displacements at Girder 8 due to Thermal Variations.	51
Figure 3.18. Relative Displacements at Girder 8 due to the Controlling Live Load Event.	51
Figure 3.19. Projected Top of Slab Strains at Girders 8, 9, and 10 due to Thermal Variations.	52
Figure 3.20. Projected Top of Slab Strains at Girders 8, 9, and 10 due to the Controlling Live Load Event.	52
Figure 3.21. Girder 8 Strains at the Pier (Span 1 Side) due to Thermal Variations.	53
Figure 3.22. Girder 8 Strains at the Pier (Span 1 Side) due to the Controlling Live Load Event.	54
Figure 4.1. Areas of Focus for the Steel ABC Connection.....	56
Figure 4.2. Rendering of the Prototype Bridge.....	57
Figure 4.3. Concept #1.....	58
Figure 4.4. Concept #2.....	59
Figure 4.5. Concept #3.....	60
Figure 4.6. Concept #4.....	61
Figure 4.7. Concept #5.....	62
Figure 4.8. Concept #6.....	63
Figure 4.9. Overview of the Workshop Concepts Evaluated.....	63
Figure 4.10. Workshop Reference Concept.....	65
Figure 4.11. Aggregate Equally Weighted Scoring Results during the Workshop.	67
Figure 4.12. Overall Scoring Results at the End of the Workshop.....	68
Figure 4.13. Individual Component Rankings at the End of the Workshop.....	69
Figure 4.14. Selected Concepts for Full-Scale Testing.	70
Figure 5.1. Concept A.....	71
Figure 5.2. Concept B.....	72
Figure 5.3. Concept C.....	72
Figure 5.4. Concept D.....	73
Figure 5.5. Rendering of the Three-Span Benchmark Bridge.	74
Figure 5.6. Rendering of the Transverse Bridge Section.....	75
Figure 5.7. Composite Section of Steel Beam and Concrete Slab.....	75
Figure 5.8. HL-93 Loading—Truck and Lane Load.....	78

Figure 5.9. Critical Load Placement of HL-93 for Maximum Negative Moment Demand.	78
Figure 5.10. Experimental Setup Drawing (Concept A Shown).	81
Figure 5.11. Moment Envelope for the Back-to-Back HL-93 Load Case (Units: kip-ft).....	82
Figure 5.12. Wood Wall Panel Construction.	84
Figure 5.13. Wood Floor Panel Construction.	85
Figure 5.14. Formwork Construction.....	86
Figure 5.15. Painting of Wood Floor Panels.....	87
Figure 5.16. Formwork Assembly.	88
Figure 5.17. Lateral Bracing View.	89
Figure 5.18. Rebar Layout.	90
Figure 5.19. Elevation View of Concept A Connection Area.	96
Figure 5.20. Section View of Concept A Connection Area.....	97
Figure 5.21. Concept A Instrumentation Plan (Plan View).	98
Figure 5.22. Concept A Instrumentation Plan (Elevation View).....	98
Figure 5.23. Concept A Instrumentation Plan (Section View).	99
Figure 5.24. Instrumentation Plan Legend.....	99
Figure 5.25. Clamping of Connection Plate to Top Flange.	101
Figure 5.26. Drilling of Holes in Top Flange of Concept A.....	102
Figure 5.27. Concept A Extended U-Bars.	103
Figure 5.28. Concept A Test Setup Elevation.....	103
Figure 5.29. Bottom Flange Splice Plate.	104
Figure 5.30. Web Surface Preparation.	105
Figure 5.31. Concept A Splice Plates after Sandblasting.	106
Figure 5.32. Skidmore-Wilhelm Bolt Pretension Device.	107
Figure 5.33. Concept A Closure Pour Rebar.	108
Figure 5.34. Concept A Closure Pour Formwork.	108
Figure 5.35. Concept A Bolt Hole Drilling.....	109
Figure 5.36. Concept A Adapter Plate.	110
Figure 5.37. Concept A Hold-Down End.	111
Figure 5.38. Overall Elevation View of Concept A Test Setup.....	112
Figure 5.39. View of Concept A Test Setup from Hold-Down End.....	112
Figure 5.40. View of Concept A Test Setup from Active Loading End.....	113
Figure 5.41. Concept A Static Testing Crack through Lifting Holes.	114
Figure 5.42. Concept A Static Testing Displacement Time History.	115
Figure 5.43. Concept A Static Testing Load Time History.	116
Figure 5.44. Concept A Static Testing Load-Displacement Plot.....	117
Figure 5.45. Concept A Precast Concrete Deck Stresses at E2.	118
Figure 5.46. Concept A Precast Concrete Deck Stresses at E3.	119
Figure 5.47. Concept A Static Testing Rebar Stresses at E1.4.	120
Figure 5.48. Concept A Static Testing U-Loop Rebar Stresses at E0.5.	120
Figure 5.49. Concept A Static Testing Steel Beam Stresses at E1.	121
Figure 5.50. Concept A Static Testing Splice Plate Stresses.	122
Figure 5.51. Concept A Cyclic Testing Closure Pour Crack.	124
Figure 5.52. Concept A Cyclic Testing Cracks on Active Loading End.	124
Figure 5.53. Concept A Ultimate Testing Cracks on Hold-Down End.	126
Figure 5.54. Concept A Ultimate Testing 1 Displacement Time History.	127

Figure 5.55. Concept A Ultimate Testing 1 Force Time History.	127
Figure 5.56. Concept A Ultimate Testing 1 Force Displacement.	128
Figure 5.57. 100-kip Ram Assembly for Concept A.	129
Figure 5.58. Concept A Ultimate Testing 2 Displacement Time History.	130
Figure 5.59. Concept A Ultimate Testing 2 Force Time History.	131
Figure 5.60. Concept A Ultimate Testing 2 Force Displacement.	132
Figure 5.61. Concept A Precast Concrete Deck Stresses at E1.	133
Figure 5.62. Concept A Precast Concrete Deck Stresses at E2.	134
Figure 5.63. Concept A Rebar Stresses at E3.	135
Figure 5.64. Concept A Ultimate Testing 2 U-Loop Rebar Stresses at E0.5.	136
Figure 5.65. Concept A Ultimate Testing 2 Steel Beam Stresses at E1.	137
Figure 5.66. Concept A Ultimate Testing 2 Splice Plate Stresses.	138
Figure 5.67. Concept A Ultimate Testing Structural Strain Profile at E1.	139
Figure 5.68. Concept A Ultimate Testing Structural Strain Profile at E2.	139
Figure 5.69. Concept A Ultimate Testing Structural Strain Profile at W1.	140
Figure 5.70. Concept A Ultimate Testing Structural Strain Profile at W2.	140
Figure 5.71. Concept A Closure Pour Jackhammering.	141
Figure 5.72. Concept A Disposal.	141
Figure 5.73. Transverse Centerline Crack Formed during Cyclic Testing.	142
Figure 5.74. Cyclic Loading Cracks near Gridline E3.	143
Figure 5.75. Cracks on East Side of Concept A after Ultimate Testing.	144
Figure 5.76. Cracks on West Side of Concept A after Ultimate Testing.	145
Figure 5.77. Bottom Flange Splice Plate Scour Marks.	146
Figure 5.78. Web Splice Plate Scour Marks.	147
Figure 5.79. Elevation View of Concept B Connection Area.	149
Figure 5.80. Close-Up Elevation of Steel Bracket Assembly.	150
Figure 5.81. Close-Up Plan View of Steel Bracket Assembly.	150
Figure 5.82. Concept B Instrumentation Plan (Plan View).	151
Figure 5.83. Concept B Instrumentation Plan (Elevation View).	151
Figure 5.84. Concept B Instrumentation Plan (Section View at E1).	152
Figure 5.85. Instrumentation Plan Legend.	152
Figure 5.86. Concept B Notch Formwork.	154
Figure 5.87. Concept B Notch Formwork Close-Up.	155
Figure 5.88. Concept B Beams Stacked.	156
Figure 5.89. Elevation View of Specimen in Testing Area.	157
Figure 5.90. Concept B before Closure Pour.	158
Figure 5.91. Concept B Closure Pour Formwork.	159
Figure 5.92. Concept B Rebar Strain Gauge Overview.	160
Figure 5.93. Application of Rebar Strain Gauge.	161
Figure 5.94. Concept B Instrumentation Elevation View of the Connection Region.	162
Figure 5.95. Steel Strain Gauge Locations.	162
Figure 5.96. Structural Steel Strain Gauge Installation.	163
Figure 5.97. Instrumentation Plan View.	164
Figure 5.98. Concrete Surface Strain Gauge Installation.	164
Figure 5.99. String Pots under Beam.	165
Figure 5.100. Central LVDT Locations.	166

Figure 5.101. Hold-Down LVDT Locations.....	166
Figure 5.102. Whitewashed Steel Beam.	167
Figure 5.103. Concept B Test Setup Elevation.....	168
Figure 5.104. Concept B Adapter Plate.	168
Figure 5.105. Adapter Plate Attachment to the Bottom of the Deck.....	169
Figure 5.106. Adapter Plate Attachment to the Top of the Deck.	170
Figure 5.107. Concept B Hold-Down Actuator.....	171
Figure 5.108. Overall Elevation View of Concept B Test Setup.....	172
Figure 5.109. View of Concept B Test Setup from Hold-Down End.....	172
Figure 5.110. View of Concept B Test Setup from Active Loading End.....	173
Figure 5.111. Concept B Strain on Williams Bars by Hydraulic Wrench.	174
Figure 5.112. Stress at the Deck Surface of E1 While Tensioning the Williams Bars with the Hydraulic Wrench.	175
Figure 5.113. Concept B First Static Testing Closure Pour Interface.	176
Figure 5.114. Concept B First Static Testing Strain on Williams Bars.....	177
Figure 5.115. Concept B Possible Bracket Slippage.	178
Figure 5.116. Concept B First Static Testing Load versus Active Loading End Actuator Vertical Displacement at E7.	179
Figure 5.117. Concept B First Static Testing Rebar in Deck Stress versus Load at E1 (before Slip).	180
Figure 5.118. Concept B First Static Testing-Microstrain on Williams Bars.....	181
Figure 5.119. Concept B First Static Testing Load versus Active Loading End Displacement.....	182
Figure 5.120. End Transverse and Longitudinal Bracket Weld.....	184
Figure 5.121. Inner Transverse and Longitudinal Bracket Weld.....	185
Figure 5.122. Through-Hole Jack Stand.	186
Figure 5.123. Concept B Second Static Testing Strain on Williams Bars during PT.....	187
Figure 5.124. Concept B Second Static Testing Stress on Deck at E1 during PT.....	188
Figure 5.125. Concept B Second Static Testing Strain on Williams Bars.....	189
Figure 5.126. Concept B Second Static Testing Displacement Time History.....	190
Figure 5.127. Concept B Second Static Testing Load versus Displacement.....	191
Figure 5.128. Concept B Second Static Testing Williams Bar Strain versus Load (First Load Application).	192
Figure 5.129. Concept B Second Static Testing Concrete Surface Deck Stress versus Load at E1 (First Load Application).	193
Figure 5.130. Concept B Second Static Testing Concrete Rebar in Deck Stress versus Load at E1 (First Load Application).	194
Figure 5.131. Concept B Second Static Testing Rotation at Center of Rotation (First Load Application).	195
Figure 5.132. Concept B Second Cyclic Loading Displacement at E7 Time History of Selected Cycles.	197
Figure 5.133. Concept B First Cyclic Loading Load Time History of Selected Cycles.....	198
Figure 5.134. Concept B Second Cyclic Loading Load versus Displacement at E7.....	199
Figure 5.135. Concept B Ultimate Testing Strain on Williams Bars.....	200
Figure 5.136. Concept B Ultimate Testing Displacement Time History.....	201
Figure 5.137. Concept B Ultimate Test Actuator Load Time History.....	202

Figure 5.138. Concept B Ultimate Testing Load versus Displacement.....	203
Figure 5.139. Concept B Ultimate Testing Williams Bar Strain versus Displacement.	204
Figure 5.140. Concept B Ultimate Testing Concrete Deck Surface Stress versus Load at E1.	205
Figure 5.141. Concept B Ultimate Testing Rebar in Deck Stress versus Load at W2.	206
Figure 5.142. Concept B Ultimate Testing Steel Beam Strains at E1.	207
Figure 5.143. Concept B Ultimate Testing Structural Strain Profile at E1.....	208
Figure 5.144. Concept B Ultimate Testing Structural Strain Profile at W1.	208
Figure 5.145. Concept B Ultimate Testing Structural Strain Profile at W2.	209
Figure 5.146. Concept B Ultimate Testing Rotation at Center of Rotation.....	210
Figure 5.147. Concept B Dead-End Deck Crack.	211
Figure 5.148. Concept B Active Loading End Deck Cracks.	211
Figure 5.149. Concept B Air Gap between Flange and Haunch.....	212
Figure 5.150. Concept B UHPC/Deck Interface Separation.....	213
Figure 5.151. Elevation View of Concept C Connection Area.....	215
Figure 5.152. Close-Up Elevation of Steel Bracket Assembly.....	216
Figure 5.153. Close-Up Plan View of Steel Bracket Assembly.	216
Figure 5.154. Concept C Instrumentation Plan (Plan View).	217
Figure 5.155. Concept C Instrumentation Plan (Elevation View).	217
Figure 5.156. Concept C Instrumentation Plan (Section View at E1).	218
Figure 5.157. Instrumentation Plan Legend.....	218
Figure 5.158. Couplers and Additional Bolts Acting as Headed Studs for Brackets.	220
Figure 5.159. Concept C Extended U-Bars.	221
Figure 5.160. Finished Specimens for Concept C.	221
Figure 5.161. Finished U-Bars for Concept C.	222
Figure 5.162. Concept C Test Setup Elevation.....	223
Figure 5.163. Concept C Hold-Down Actuator.	224
Figure 5.164. Overall Elevation View of Concept C Test Setup.....	225
Figure 5.165. View of Concept C Test Setup from Hold-Down End.....	225
Figure 5.166. View of Concept C Test Setup from Active Loading End.....	226
Figure 5.167. Concept C Static Testing Strain on Williams Bars during PT.	227
Figure 5.168. Concept C Static Testing Crack through Lifting Hole on Hold-Down End.....	228
Figure 5.169. Concept C Static Testing Crack through Lifting Hole on Active Loading End.	229
Figure 5.170. Concept C Static Testing Vertical Displacement Time History.....	230
Figure 5.171. Concept C Static Testing Load Time History.	231
Figure 5.172. Concept C Static Testing Load-Displacement Plot.....	232
Figure 5.173. Concept C Static Testing Strain on Williams Bars.	233
Figure 5.174. Concept C Precast Concrete Deck Stresses at E1.	234
Figure 5.175. Concept C Precast Concrete Deck Stresses at E2.	235
Figure 5.176. Concept C Precast Concrete Deck Stresses at E3.	236
Figure 5.177. Concept C Static Testing Rebar Stresses at E2.	237
Figure 5.178. Concept C Static Testing U-Loop Rebar Stresses at E0.3.....	238
Figure 5.179. Concept C Static Testing U-Loop Rebar Stresses at W0.3.	239
Figure 5.180. Concept C Static Testing Steel Beam Stresses at E1.	240
Figure 5.181. Concept C Static Testing Steel Beam Stresses at W1.	241

Figure 5.182. 100-kip Ram Setup for Concept C.	243
Figure 5.183. Concept C Ultimate Testing Displacement Time History.....	244
Figure 5.184. Concept C Ultimate Testing Force Displacement.	245
Figure 5.185. Concept C Ultimate Testing Strain on Williams Bars.....	246
Figure 5.186. Concept C Ultimate Testing Williams Bar Strain versus Actuator Load.....	247
Figure 5.187. Concept C Precast Concrete Deck Stresses at E1.	248
Figure 5.188. Concept C Precast Concrete Deck Stresses at E2.	249
Figure 5.189. Concept C Precast Concrete Deck Stresses at W1.	250
Figure 5.190. Concept C Ultimate Testing Rebar Stresses at E2.	251
Figure 5.191. Concept C Ultimate Testing Rebar Stresses at E3.	252
Figure 5.192. Concept C Ultimate Testing U-Loop Rebar Stresses at E0.3.....	253
Figure 5.193. Concept C Ultimate Testing Steel Beam Stresses at E1.....	254
Figure 5.194. Concept C Ultimate Testing Structural Strain Profile at E1.....	255
Figure 5.195. Concept C Ultimate Testing Structural Strain Profile at E2.....	256
Figure 5.196. Concept C Ultimate Testing Structural Strain Profile at W1.	256
Figure 5.197. Concept C Ultimate Testing Structural Strain Profile at W2.	257
Figure 5.198. View of Concept C after Saw Cutting.....	258
Figure 5.199. Concept C Being Taken out of Lab.....	259
Figure 5.200. Cracks on East Side of Concept C after Ultimate Testing.	260
Figure 5.201. Cracks in Closure Pour of Concept C after Ultimate Testing.	261
Figure 5.202. Cracks on West Side of Concept C after Ultimate Testing.	262
Figure 5.203. View of Cracking on South Side of Deck in Closure Pour.	263
Figure 5.204. View of Cracking on North Side of Deck in Closure Pour.	264
Figure 5.205. Elevation View of Concept D Connection Area.	266
Figure 5.206. Section View of Concept D Connection Area.....	267
Figure 5.207. Concept D Instrumentation Plan (Plan View).	267
Figure 5.208. Concept D Instrumentation Plan (Elevation View).....	268
Figure 5.209. Concept D Instrumentation Plan (Section View).	268
Figure 5.210. Instrumentation Plan Legend.....	269
Figure 5.211. Concept D Formwork Assembly.....	271
Figure 5.212. Concept D PVC Pipes for Williams Bars.....	272
Figure 5.213. Concept D Void and Shear Key Forming.	273
Figure 5.214. Concept D Second Pour Concrete.	274
Figure 5.215. Concept D Test Setup Elevation.....	275
Figure 5.216. Epoxy Adhesive Filled Out between the Side Surfaces of the Precast Units.....	276
Figure 5.217. Concept D Hold-Down Actuator.....	277
Figure 5.218. Post-tensioned Williams Rods under Concrete Deck.....	278
Figure 5.219. Overall Elevation View of Concept D Test Setup.....	279
Figure 5.220. View of Concept D Test Setup from Active Loading End.....	280
Figure 5.221. View of Concept D Test Setup from Hold-Down End.....	281
Figure 5.222. Concept D Static Testing Strain on Williams Bars during PT.	282
Figure 5.223. Concept D Static Testing Crack at Top Surface Transverse Joint at 5-kip Load Level.	283
Figure 5.224. Concept D Static Testing Crack at Northside Surface.	284
Figure 5.225. Concept D Static Testing Crack at Southside Surface.	285
Figure 5.226. Concept D Static Testing Vertical Displacement at E7 Time History.	286

Figure 5.227. Concept D Static Testing Load Time History.	287
Figure 5.228. Concept D Static Testing Load-Displacement Plot.	288
Figure 5.229. Concept D Static Testing Strain on Williams Bars.	289
Figure 5.230. Concept D Static Testing Precast Concrete Stresses at E1.	290
Figure 5.231. Concept D Static Testing Precast Concrete Stresses at E2.	291
Figure 5.232. Concept D Static Testing Precast Concrete Stresses at E3.	292
Figure 5.233. Concept D Static Testing Rebar Stresses at E1.	293
Figure 5.234. Concept D Static Testing Rebar Stresses at E3.	294
Figure 5.235. Concept D Static Testing Steel Beam Stresses at E1.	295
Figure 5.236. 100-kip Ram Setup for Concept D.	296
Figure 5.237. Concept D Ultimate Testing Displacement Time History.	297
Figure 5.238. Concept D Ultimate Testing Load-Displacement Plot.	298
Figure 5.239. Concept D Ultimate Testing Stress on Williams Bars Time History.	299
Figure 5.240. Concept D Ultimate Testing Stress on Williams Bars -Load Plot.	300
Figure 5.241. Concept D Ultimate Testing Precast Concrete Deck Stresses at E1.	301
Figure 5.242. Concept D Ultimate Testing Precast Concrete Deck Stresses at E2.	302
Figure 5.243. Concept D Ultimate Testing Rebar Stresses at E1.	303
Figure 5.244. Concept D Ultimate Testing Rebar Stresses at E2.	304
Figure 5.245. Concept D Ultimate Testing Rebar Stresses at W1.	305
Figure 5.246. Concept D Ultimate Testing Rebar Stresses at W2.	306
Figure 5.247. Concept D Ultimate Testing Steel Beam Stresses at E1.	307
Figure 5.248. Concept D Ultimate Testing Structural Strain Profile at E1.	308
Figure 5.249. Concept D Ultimate Testing Structural Strain Profile at E2.	308
Figure 5.250. Concept D Ultimate Testing Structural Strain Profile at W1.	309
Figure 5.251. Concept D Ultimate Testing Structural Strain Profile at W2.	309
Figure 5.252. View of Concept D after Ultimate Testing: (a) Eastside Specimen and (b) Westside Specimen.	311
Figure 5.253. Concept D Being Taken out of Lab.	312
Figure 5.254. Cracks on the West Side of Concept D after Ultimate Testing.	313
Figure 5.255. Cracks in Adhesive Joint of Concept D after Ultimate Testing.	314
Figure 5.256. View of Cracking on South Side in Match-Cast Joint.	315
Figure 5.257. View of Cracking on the North Side of Deck in Match-Cast Joint.	316
Figure 5.258. All Concepts Ultimate Testing Precast Concrete Deck Stresses at E1.	323
Figure 5.259. All Concepts Ultimate Testing Precast Concrete Deck Stresses at E2.	324
Figure 5.260. All Concepts Ultimate Testing Rebar Stresses at E1.	325
Figure 5.261. All Concepts Ultimate Testing Rebar Stresses at E3.	326
Figure 5.262. Concept A Closure Pour Interface Crack.	327
Figure 5.263. Concept A North Side of Closure Pour Cracking.	328
Figure 5.264. Concept A South Side of Closure Pour Cracking.	329
Figure 5.265. Concept B Closure Pour Interface Crack during Cyclic Testing.	330
Figure 5.266. Concept B Closure Pour Interface Crack during Ultimate Testing.	331
Figure 5.267. Concept C Closure Pour Interface Cracks.	332
Figure 5.268. Concept C Closure Pour Transverse Centerline Crack on Underside of Deck.	333
Figure 5.269. Concept C Closure Pour Crack Width North Side.	334
Figure 5.270. Concept C Closure Pour Crack Width South Side.	334

Figure 5.271. Concept D Match-Cast Joint Interface Cracks during Ultimate Testing.....	335
Figure 5.272. Concept D Match-Cast Joint Southside View of Interface Crack.....	336
Figure 5.273. Concept D Match-Cast Joint Northside View of Interface Crack.....	337
Figure 5.274. Concept D Match-Cast Joint Interface Cracks after Sitting on Support Pedestal: (a) Elevation View and (b) Top View.....	338
Figure 5.275. All Concepts Ultimate Testing Precast Concrete Deck Stresses at W1.....	339
Figure 5.276. All Concepts Ultimate Testing Rebar Stresses at W1.....	340
Figure 5.277. Concept A and C Ultimate Testing Rebar Stresses at E0.5 or E0.3.....	341
Figure 5.278. Concept A&C Ultimate Testing Rebar Stresses at W0.5 or W0.3.....	342
Figure 5.279. Concept A Splice Plate Markings.....	344
Figure 5.280. Concept A Top Flange Splice Plate.....	345
Figure 5.281. Ultimate Testing Concept A Top Flange Splice Plate Stress versus Load.....	349
Figure 5.282. Ultimate Testing Concept B, C, and D Williams Bar Stress versus Load.....	350
Figure 5.283. All Concepts Ultimate Testing Top Flange Stress at E1.....	351
Figure 5.284. All Concepts Ultimate Testing Top Flange Stress at W1.....	352
Figure 5.285. Concept A Bottom Flange Splice Plate Markings Pre-slip.....	354
Figure 5.286. Concept A Bottom Flange Splice Plate Markings Post-slip.....	355
Figure 5.287. Concept A Bottom Flange Splice Plate after Testing.....	356
Figure 5.288. Concept A Web Splice Plate after Testing.....	357
Figure 5.289. Concept B Channel Void Gap Filled with Caulk.....	358
Figure 5.290. Concept C Bottom Flange Bearing Plates.....	359
Figure 5.291. Concept D Bottom Shear Key Parts.....	361
Figure 5.292. All Concepts Ultimate Testing Bottom Flange Stress at E1.....	362
Figure 5.293. All Concepts Ultimate Testing Bottom Flange Stress at W1.....	363
Figure 5.294. Load versus Displacement Concept Comparison.....	366
Figure 6.1. (a) Concrete Closure Pour, (b) Rebar in Closure Pour, (c) Rebar in Precast Concrete Slab, (d) Precast Concrete Slab, (e) Steel Girder, (f) Splice Plates with Bolts, and (g) Model Assembly.....	373
Figure 6.2. Typical Stress-Strain Relationship for CDP Model Tension Stiffening Behavior in Abaqus [26].....	376
Figure 6.3. Typical Stress-Strain Relationship for CDP Model Compression Hardening Behavior in Abaqus [26].....	377
Figure 6.4. Proposed Stress-Strain Model for Unconfined and Confined Concrete-Kent and Park Model.....	378
Figure 6.5. Bilinear Stress-Strain Relationship for Concrete Tensile Behavior.....	379
Figure 6.6. Bilinear Stress-Strain Curves of Steel Materials in the FEM.....	380
Figure 6.7. Energy Content Ratio of Kinetic Energy over Inertial Energy during Load Steps.....	381
Figure 6.8. Load-Displacement Curve Comparison between the Concept A FEM and Experimental Test.....	382
Figure 6.9. Bolt Tensile Stresses at the Bottom Flange Splice Plate in the FEM.....	383
Figure 6.10. Stresses at Deck Surface of E1 Comparison.....	384
Figure 6.11. Rebar Stresses at E1.4 Comparison.....	384
Figure 6.12. Stresses at Top Flange Splice Plate Comparison.....	385
Figure 6.13. Stresses at Bottom Flange Splice Plate Comparison.....	386
Figure 6.14. Strain Profile Comparison at E1 for a Load of (a) 30 kips and (b) 73 kips.....	387

Figure 6.15. Bolts Slipped at Bottom Flange Splice Plate in the FEM: (a) Up Splice Plate, (b) Down Splice Plate and Bottom Flange Splice Plate Scour Marks in the Experiment: (c) Up Splice Plate, (d) Down Splice Plate.	388
Figure 6.16. Concrete Damage Patterns at Closure Pour Comparison: (a) FEM Damage Patterns (73 kips) and (b) Experiment Concrete Crack Patterns.	389
Figure 6.17. Concept B Test Setup Model Components: (a) Steel Girder with C-Channel, (b) Rebar, (c) Precast Concrete Deck, (d) UHPC Closure Pour, and (e) Assembly.	390
Figure 6.18. Energy Content Ratio of Kinetic Energy over Inertial Energy during Load Steps.	393
Figure 6.19. Load-Displacement Curve Comparison between the FEM and Experimental Test.	394
Figure 6.20. Stress on the Williams Bar versus Load Curves Comparison.	395
Figure 6.21. Relative Displacement versus Load Comparison.	396
Figure 6.22. Closure Pour Separation at 43 kips in the (a) Ultimate Test and (b) FEM.	397
Figure 6.23. Stress at Structural Steel at E1 When Load Reached 42 kips in the (a) Ultimate Test and (b) the FEM.	398
Figure 6.24. Strain Profile Comparison at E1 for a Load of (a) 28 kips and (b) 42 kips.	399
Figure 6.25. Stress at Deck Surface of E1 versus Displacement at E7 Comparison.	400
Figure 6.26. (a) Concrete Closure Pour, (b) Rebar in Closure Pour, (c) Rebar in Precast Concrete Slab, (d) Precast Concrete Slab, (e) Steel Girder with PT Bracket and Steel Bearing Plate, (f) Williams Bar, and (g) Model Assembly.	401
Figure 6.27. Energy Content Ratio of Kinetic Energy over Inertial Energy during Load Steps.	403
Figure 6.28. Load-Displacement Curve Comparison between the Concept C FEM and Experimental Test.	404
Figure 6.29. Stress on the Williams Bar versus Load at E7 Curves Comparison of Concept C.	405
Figure 6.30. Concrete Damage Patterns at Closure Pour Comparison: (a) FEM Damage Patterns (75 kips) and (b) Experiment Concrete Crack Patterns.	406
Figure 6.31. Strain Profile Comparison at E1 for a Load of (a) 28 kips and (b) 94 kips.	407
Figure 6.32. Stress at Deck Surfaces of E1 versus Displacement at E7 Comparison.	408
Figure 6.33. Relative Displacement at Closure Pour Comparison.	409
Figure 6.34. (a) Precast Unit, (b) Rebar in Precast Unit, (c) Steel Girder, (d) Williams Bars, and (e) Model Assembly.	410
Figure 6.35. Energy Content Ratio of Kinetic Energy over Inertial Energy during Load Steps.	412
Figure 6.36. Load-Displacement Curve Comparison between FEM and Experiment.	413
Figure 6.37. Stress on the Williams Bars versus Displacement at E7 Comparison of Concept D.	414
Figure 6.38. Concrete Damage Patterns at the Side Surface of the Precast Drop Panel Comparison: (a) FEM Damage Patterns at North Side (20 kips), (b) FEM Damage Patterns at North Side (20 kips), (c) Experiment Concrete Crack Patterns at North Side, and (d) Experiment Concrete Crack Patterns at South Side.	415
Figure 6.39. Concrete Damage Patterns at the Front Surface of the Precast Drop Panel Comparison: (a) FEM Damage Patterns (20 kips) and (b) Experiment Concrete Crack Patterns.	415

Figure 6.40. Strain Profile Comparison at E1 When Load at (a) 28 kips and (b) 52 kips.	416
Figure 6.41. Beam Elevation View of the Final System Option 1.	420
Figure 6.42. (a) Precast Concrete Deck with Closure Pour, (b) Splice Plates with Bolts, (c) Steel Beam, (d) Rebar Mat, and (e) Model Assembly.....	421
Figure 6.43. Energy Content Ratio of Kinetic Energy over Inertial Energy during Load Steps.	422
Figure 6.44. Load-Displacement Curve Comparison between the Final System Option 1 Finite Element Model and Concept A.	423
Figure 6.45. Beams and Bearing Plates Stresses at Connection When Load Is 80 kips.	424
Figure 6.46. (a) Precast Concrete Deck with Closure Pour, (b) Splice Plates with Bolts, (c) Steel Beam, (d) Rebar Mat, (e) PT Brackets with Williams Bars, and (f) Model Assembly.....	425
Figure 6.47. Energy Content Ratio of Kinetic Energy over Inertial Energy during Load Steps.	426
Figure 6.48. Load-Displacement Curve Comparison between the Final System Option 1 FEM with PT and Concept C.	427
Figure 6.49. Stress on the Williams Bar versus Displacement at E7 Curves Comparison of Concept C and Final System Option 1 FEM with PT.	428
Figure 6.50. Deck Stresses at the Middle Cut in Longitudinal Direction Cut after PT Comparison: (a) Concept C FEM and (b) Final System Option 1 with PT FEM.....	429
Figure 6.51. Load-Displacement Curve Comparison among the Final System Option 1 FEM, the Final System Option 1 with PT FEM, Concept A, and Concept C.	430
Figure 6.52. Bent Elevation View of Final System Option 2.	431
Figure 6.53. (a) Precast Concrete Deck with the Drop Panel, (b) Rebar Mat, (c) Steel Beam, (d) Williams Bars with Steel Plates, and (e) Model Assembly.	432
Figure 6.54. Energy Content Ratio of Kinetic Energy over Inertial Energy during Load Steps.	434
Figure 6.55. Load-Displacement Curve Comparison between the Final System Option 2 FEM and Concept D.	435
Figure 6.56. Damage Pattern Comparison When Load at 30 kips between (a) Concept D FEM and (b) Final System Option 2 FEM.....	436
Figure 6.57. Load-Displacement Curves Comparison between Final System Option 1 and Final System Option 2.	437
Figure 7.1. TxDOT Standard Design Table Example for a 30-ft Roadway Project [25].	440
Figure 7.2. TxDOT Standard Design (a) Typical Transverse Section and (b) Framing Plan for a 30-ft Roadway [25].....	445
Figure 7.3. TxDOT Standard Design Optional Lateral Support Bent Plate [25].....	446
Figure 7.4. TxDOT Standard Design Framing Plan for a 30-ft Roadway with a 30-Degree Skew Angle [25].	447
Figure 7.5. Stress Distribution Area of Interest.	448
Figure 7.6. Load Case and Area Distribution of the Wheels of the Truck for 0, 15, and 30 Skew.....	449
Figure 7.7. Spacing Distribution for Different Full Bridge Configuration Cases According to the Span Length and Girder Size Presented by the TxDOT Standard Design Tables.....	451
Figure 7.8. General Model Elements.	452

Figure 7.9. General Overview of Concept A Model.....	453
Figure 7.10. Concept C General Model Elements.	454
Figure 7.11. General Overview of Concept C Model.	455
Figure 7.12. Deck and Closure Pour Stress Distribution Example for W40x324 and 120-ft Span Length.	457
Figure 7.13. Maximum Closure Pour Rebar Tensional Stress.....	459
Figure 7.14. Concept C Deck and Closure Pour Stress Distribution for W40×324 and 120 ft Span Length.	462
Figure 8.1. Recommended Steel SDCL Connection Using ABC (Final System Option 1).	465
Figure A.1. Section Properties of Structural Steel and Rebar (Cracked Section).....	471
Figure A.2. Section Properties of Structural Steel, Concrete, and Rebar (Composite Section).	472
Figure C.1. Value of Research per Year.	490

LIST OF TABLES

	Page
Table 5.1. Section Properties for the Composite Section.	76
Table 5.2. Benchmark Bridge Design Parameters.	76
Table 5.3. Dead Load for an Interior Girder.	77
Table 5.4. Live Load Deflection for the Three-Span Benchmark Bridge.	80
Table 5.5. Precast Concrete Deck Compressive Strength Test Results (ksi).....	92
Table 5.6. Concrete Closure Pour Compressive Strength Test Results (ksi).....	93
Table 5.7. Precast Concrete Deck Modulus of Rupture Test Results (ksi).....	94
Table 5.8. Concrete Closure Pour Modulus of Rupture Test Results (ksi).....	94
Table 5.9. Concept A Cyclic Testing Ranges.	123
Table 5.10. Concept B First Cyclic Testing Ranges.	183
Table 5.11. Concept B Second Cyclic Testing Ranges.	196
Table 5.12. Concept C Cyclic Testing Ranges.	242
Table 5.13. Concept D Cyclic Testing Ranges.	295
Table 5.14. Typical Construction Procedures and Time of Concept A.	367
Table 5.15. Typical Construction Procedures and Time of Concept B.	367
Table 5.16. Typical Construction Procedures and Time of Concept C.	368
Table 5.17. Typical Construction Procedures and Time of Concept D.	368
Table 6.1. Major Geometric Information of Concept A Test Setup Model.....	373
Table 6.2. Major Material Properties of the Model.	373
Table 6.3. CDP Model Parameters Used for All Concepts.....	374
Table 6.4. Load Step with Step Time for Concept A Test Setup Model.	380
Table 6.5. Load Step with Step Time for Concept B Test Setup Model.	392
Table 6.6. Load Step with Step Time for Concept C Test Setup Model.	402
Table 6.7. Load Step with Step Time for Concept D Test Setup Model.	411
Table 6.8. Load Step with Step Time for Final System Option 1 FEM.	422
Table 6.9. Load Step with Step Time for Final System Option 1 with PT Model.	425
Table 6.10. Load Steps with Step Time for Final System.	433
Table 7.1. Two- and Three-Span Configuration Bridges, Minimum (Span 1) and Maximum (Span 2) Span Length Configurations in Feet for Texas [34].	442
Table 7.2. Girder Elements Selected from the Standard Design Tables of the 30-ft Roadway Configuration [25].	444
Table 7.3. Parameters Range Summary.	447
Table 7.4. Maximum Longitudinal Stress on the Deck and Closure Pours for Each Case.	456
Table 7.5. Maximum Rebar Tensile Stress of Concept A.	458
Table 7.6. Maximum Longitudinal Stress on the Deck and Closure Pours for Each Case.	460
Table B.1. Concept A Instrumentation List.	473
Table B.2. Concept B Instrumentation List.	476
Table B.3. Concept C Instrumentation List.	479
Table B.4. Concept D Instrumentation List.	482
Table C.1. Functional Areas of Project 0-7112.	485

1. INTRODUCTION

1.1. OBJECTIVE AND SCOPE

The overarching objective of this study was to develop a prefabricated steel accelerated bridge construction (ABC) connection detail at the pier bent locations that allows the structure to behave simply supported for dead load and continuous for live load (SDCL). This connection must be relatively easy to fabricate, fast to assemble, safe, cost-effective, and durable long-term. The project's specific objective was to rigorously evaluate an array of connection concepts so that recommendations could be provided along with design guidance.

The scope of the study included the following:

1. Perform a detailed **literature review** that includes SDCL bridge systems, ABC technology, and SDCL systems used with ABC technologies (Section 2).
2. Conduct a **field assessment** on the recent Texas Department of Transportation (TxDOT) steel girder ABC project in Dallas, Texas (I-635 over Old Seagoville Road) (Section 3).
3. Develop an **array of connection concepts** from information learned in the literature and the field assessment and then present the concepts at a **workshop** to an industry review panel (IRP) and TxDOT for refinement (Section 4).
4. Perform **full-scale experimental testing** for each of the four concepts selected by the IRP and TxDOT (Section 5).
5. Create **analytical finite element models of the tested specimens** to validate the modeling methodology and then analyze variations of the connection detail (Section 6).
6. Perform a **finite element parametric study** to capture the global bridge behavior (Section 7).
7. Identify the **final recommended connection** detail and provide **design guidance** (Section 8).

1.2. SIGNIFICANCE

Currently, there are limited successful research projects on SDCL steel bridges utilizing ABC techniques. A number of SDCL steel bridge research studies, along with many SDCL bridge projects, have been performed. Overall, SDCL has proven to be a viable option for steel bridge

construction. In addition, ABC of steel bridges is a heavily studied area, with numerous successful projects throughout the country. However, the combination of SDCL and ABC has been given limited attention.

The motivation for combining SDCL with ABC is to further improve steel bridge construction. Future steel SDCL-ABC should provide decreased manufacturing and maintenance costs and substantially faster construction speed than conventional construction. As a result, the public is provided a better bridge in a shorter timeframe.

For context, TxDOT already utilizes ABC techniques to build bridges around the state. The precursor to this research study was the first ABC project in the Dallas District. That project was a steel bridge superstructure replacement. However, the bridge was designed and constructed as simply supported for dead and live loading (not SDCL). Although the project was executed in a short timeframe, the structure includes transverse joints at the pier bents, which are typically long-term maintenance issues. In addition, the steel girders are larger than if the bridge was continuous. As a result, TxDOT created and financially supported the research study herein to develop a recommended connection detail that would make similar projects SDCL, which could eliminate the joints and reduce the size of the girders.

1.3. RESEARCH APPROACH

To achieve the objective stated earlier, a series of research tasks were performed. The following subsections summarize each of the primary tasks. Detailed treatment is provided in the following sections.

1.3.1. Literature Review and Synthesis (Section 2)

The research team compiled a comprehensive literature review related to SDCL steel bridges, various ABC techniques, and the combination of SDCL and ABC. The review included papers published in journals and conferences, along with agency reports. Key findings of the literature were documented. These findings were used in this study to guide the development of the experimental program and the determination of the appropriate connection design.

1.3.2. Field Assessment (Section 3)

A field assessment was performed that included field inspection and monitoring of the recent TxDOT steel girder ABC project in Dallas, Texas (I-635 over Old Seagoville Road). The purpose was to understand the current construction method utilized, observe any potential performance issues, and identify the baseline performance of the transverse connection between adjacent spans. This bridge superstructure replacement project was accomplished in a span of 2 weekends. The superstructure portion of the bridge utilized precast twin girder units, and the structure was simple span for dead load and live load. Although the girders on the I-635 bridges were not continuous for live load, the continuous slab details and the structure performance still provided valuable information for the preliminary connection design and experimental test setup. The data from this assessment were also utilized for comparison with the experiments and analytic model results.

1.3.3. System Development (Section 4)

A series of promising connection concepts for constructing prefabricated steel girder bridge units as SDCL with ABC were developed by the research team. These preliminary concepts were created to resist the significant tensile force at the top of the connection and to provide sufficient compressive force at the bottom. A conventional concrete closure pour, an ultra-high-performance concrete (UHPC) closure pour, and a match-cast construction method was considered for the deck region of the connection. For the top of the girder connection, bolted splice plates and a post-tensioning (PT) system were considered. For the bottom of the girder connection, bolted splice plates, UHPC confined in a channel, and steel bearing plates were considered.

An IRP comprised of individuals highly experienced with ABC and related field and research engineers from TxDOT were assembled to provide insight into prefabricated steel girder units made continuous for live loads. The research team hosted a workshop for the IRP and TxDOT panel to help identify the top four systems that would be later subjected to detailed evaluation (experimental testing and numerical modeling). The IRP and TxDOT panel provided valuable feedback and suggestions regarding the connection concepts. Surveys were recorded during the workshop. Data analysis was performed on the survey results and utilized to assemble the final four connection concepts.

1.3.4. Laboratory Testing (Section 5)

Four full-scale bridge connections were constructed and tested at the Center for Infrastructure Renewal on the Texas A&M University RELIS Campus. The final test bridge connection geometry was determined based on the preliminary designs and input from the IRP and TxDOT panel. These experiments were fully instrumented to evaluate the structural performance under service loading and loading to the ultimate capacity. The measured results were also used to validate the finite element modeling (FEM) methodology.

1.3.5. Analytical Modeling of Tested Specimens (Section 6)

Each of the four experimental test specimens was modeled using finite element analysis. The initial purpose was to evaluate the overall structural behavior of the connections. However, the more valuable information came from modeling modifications to the connection (avoiding further testing).

The finite element models were built using Abaqus commercial software package (Version 6.14). These models were developed before the experiments to provide predictive strains, displacements, load capacity, and rotations. They were validated through comparisons with the experimental data. The analytical models allowed for the prediction of the failure mechanisms and other structural behaviors (e.g., the concrete deck cracks). The validated FEM approaches were also utilized for the parametric study.

1.3.6. Parametric Study (Section 7)

A parametric study was conducted to better understand and evaluate the behavior of full bridge configurations with varying materials and parameters. This parametric study connected the laboratory study and analytical modeling with bridge configurations that may be used in practice but were not part of the experimental program. The analysis focused on overall bridge geometry and was conducted using Abaqus and Python. Modeling techniques were aligned with those used in the laboratory modeling.

1.3.7. Recommendations and Design Guidance (Section 8)

Final recommendations were developed for making prefabricated steel ABC connections that are SDCL at the pier bent location. A primary and secondary connection detail was created based on

the experimental testing and numerical modeling. Design guidance was also developed in the form of a comprehensive design example and standard drawings.

2. LITERATURE REVIEW AND SYNTHESIS

2.1. OVERVIEW

This section presents an overview of the state of the art and the state-of-practice in the field of SDCL prefabricated steel ABC units. Steel SDCL bridge systems (not using ABC) have been developed over the past 20 years and are popular in many regions of the United States. These systems provide live load continuity through suitable connections at pier locations. The main advantages of SDCL bridges are they improve the construction process and decrease the manufacturing and maintenance costs [1]. Even as SDCL has gained in popularity for conventional steel bridge systems, they have also begun to be utilized in ABC applications. Section 2.2 provides an overview of SDCL steel bridges and various girder connection details. Next, Section 2.3 reviews the relevant ABC technologies (including three specific types), the advantages of ABC, and experimental applications. Section 2.4 fully reviews the combination of SDCL steel bridges using ABC technologies.

2.2. SDCL STEEL BRIDGE SYSTEMS

2.2.1. Introduction

The concept of bridge construction in which the girders are SDCL has been around for decades. In the 1960s, Freyermuth developed an approach for making precast prestressed concrete girders continuous for bridge live loads to eliminate the maintenance costs associated with deck joints and deck drainage [2]. The overall approach is for the girders to be set and the deck cast without a connection of the girders to adjacent spans. As a result, the girders support the dead load through simple span behavior. A connection is then made between girders at interior supports. The result is a superstructure that supports live load through continuous beam behavior. The primary challenge is the connection at the interior supports.

Steel girder bridges are commonly constructed as continuous for dead and live load through field splices of the girders during erection (typically at the dead load inflection points). However, the SDCL concept has been applied to steel girder bridges over the past 20 years, which requires a splice at the pier bents. The motivation is the cost benefits from easier fabrication and construction [3]. This type of construction requires slightly larger beams and splices at the piers.

However, a more repetitive beam design and easier erection sequence results from SDCL steel bridges [1].

A general illustration of SDCL is provided in Figure 2.1 for a three-span (60 ft–80 ft–60 ft) bridge. Figure 2.1 illustrates different load cases and their corresponding bending moment diagrams (shown to scale). The first load case is the simply supported dead load on each span. The second is an HS-20 truck on the center span when the structure is continuous. Combined Load Case I is the combination of these loading scenarios. The combined moment diagram clearly shows the region of negative bending moment at the interior pier supports (highlighted in red). For context, this area is within roughly a 10 ft region. This information is important in the design process to adequately design the girders and deck reinforcement to minimize cracking.

The third load case illustrated in Figure 2.1 includes HS-20 trucks along the outside spans. This activity induces a negative moment along the entire center span. Combined Load Case II is the combination of the simply supported dead load and the HS-20 trucks in the outer spans. The combined bending moment diagram indicates that roughly 5 ft around interior supports will be subjected negative bending (highlighted in red bold line).

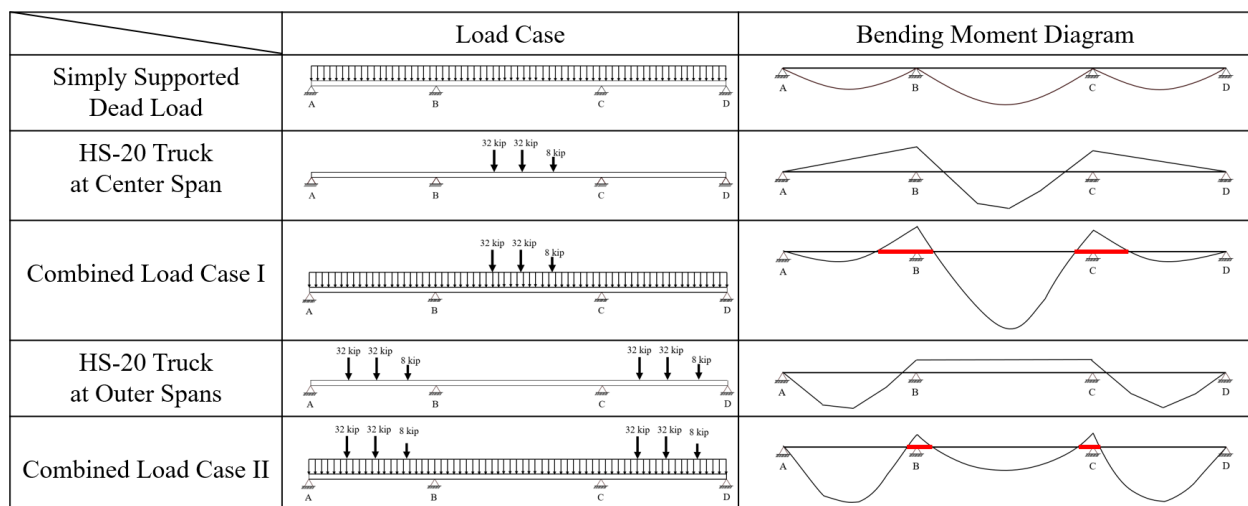


Figure 2.1. Combined Load Cases and Corresponding Bending Moment Diagrams.

The following sections convey various research studies and projects related to steel SDCL bridges.

2.2.2. Steel Bridge SDCL Construction in Tennessee

To improve the performance of short- and medium-span composite steel girder bridges, the Tennessee Department of Transportation (TDOT) applied SDCL construction since it is cost-effective and maintains a good service life. TDOT chose rolled steel beams because they are simple to fabricate and reduce construction time [4]. TDOT's initial application of SDCL construction was used on a bridge replacement project carrying SR-35. This bridge is comprised of four spans of W36×150 grade 50W rolled beams with lengths of roughly 65 ft, 71 ft, 72 ft, and 45 ft. The girders were erected in each span and attached to the piers using drilled and grouted anchor bolts. They used the single-shear bolted connection to meet the requirement of the maximum positive moment. They welded bearing plates at the end of the girders to resist the shear stress. The two-span girders were connected by the concrete diaphragm. Figure 2.2 shows the connection details.

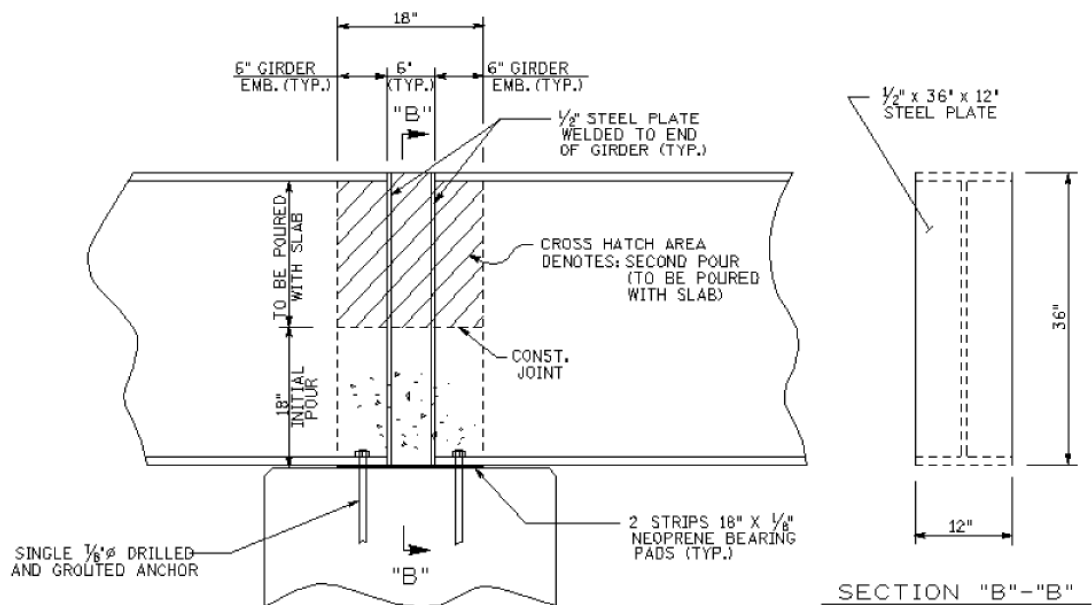


Figure 2.2. TDOT SDCL Initial Connection Detail (Composite Load Only) [4].

For the concrete diaphragm portion, TDOT first cast the lower part of concrete to confine the two girders at the pier. It is vital for this connection to avoid torsion or other stress due to unintended actions. Additionally, the diaphragm provided the compressive connection capacity between the two girders. Therefore, TDOT did not connect the bottom of the flanges of the girders [1]. Next, they cast the upper portion of the diaphragm with the deck cast. The tension force transfer at the top of the detail was limited, so a preformed transverse crack in the deck was

made with a saw cut and then sealed. Overall, this initial application of steel SDCL proved that the strength and displacement requirements were satisfied, but the cost was still more than comparable prestressed beam bridges in Tennessee.

TDOT aimed to increase the economic advantage of steel SDCL construction by improving the connection detail so that it was continuous for the dead load of the wet slab (see Figure 2.3). This new approach was applied to the replacement bridge at the DuPont Access Road over SR-1. The bridge has two spans, and their lengths are 87 ft and 76 ft. It uses six W33×240 grade 50W rolled beams. For the SDCL connection details, they removed the grouted anchors at the bottom flange and added bolted cover plates on the top flange (similar to the SDCL connection details in West Virginia shown later). They also welded cover plates along the bottom flange and added wedge kicker plates between the two girders. The structural performance was not as good as the previous detail (Figure 2.2), but the cost was lower overall. Furthermore, the project delivery time was reduced by 90 calendar days—proving the reduced SDCL construction time—which also decreased traffic interruption [4].

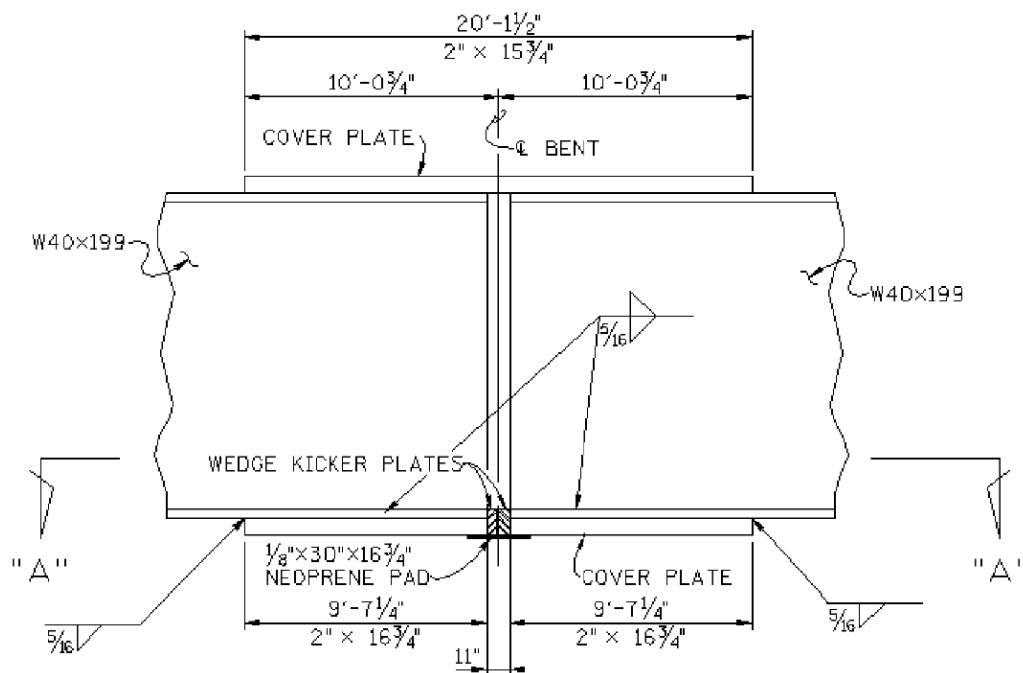


Figure 2.3. TDOT SDCL Revised Connection Detail [4].

2.2.3. Experimental Testing of Steel SDCL Systems in Colorado

The Colorado Department of Transportation developed an innovative approach to the SDCL system using steel diaphragms in 2005 and 2006. They refer to this approach as simple-made continuous (SMC). It was developed as part of a replacement bridge project located at US 36 over Box Elder Creek in Colorado. The bridge had six equal spans of 77 ft and used W33×152 grade 50W rolled steel beams [5]. For the connection details, they welded the sole plate to the bottom flange to make it continuous compression force transfer. W27×84 steel diaphragms were connected to the bearing stiffener. This SDCL connection was without a concrete diaphragm. Figure 2.4 and Figure 2.5 show the connection details and a photo of the bridge, respectively.

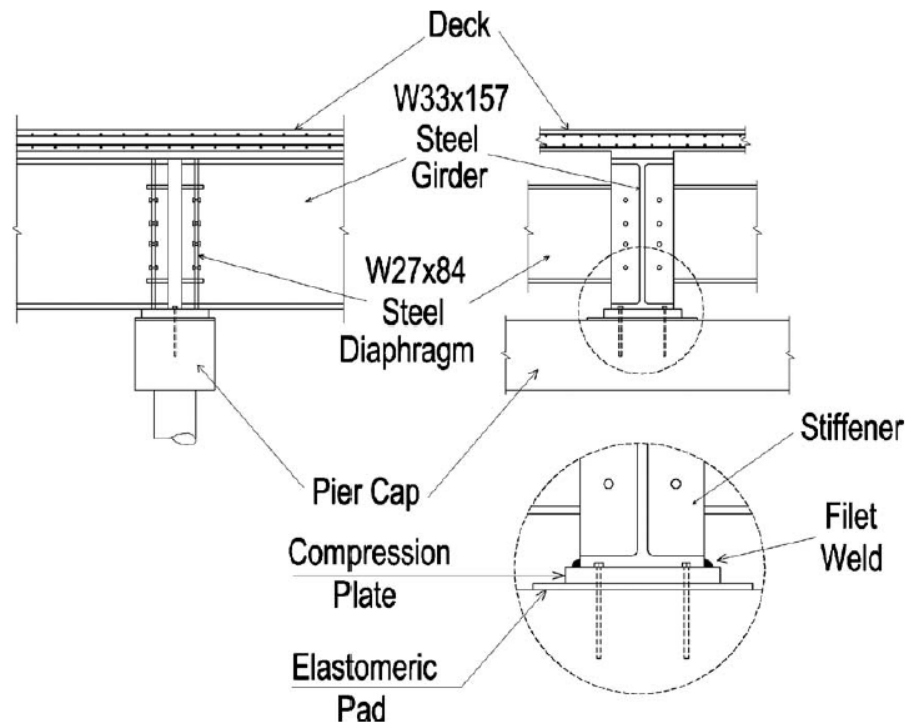


Figure 2.4. Colorado SDCL Connection Details [6].

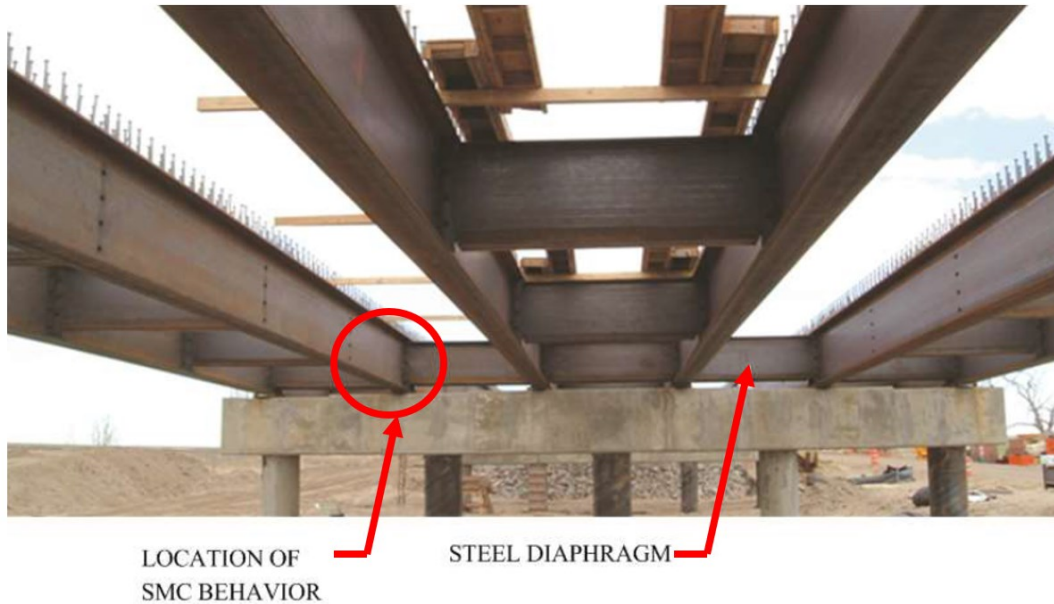


Figure 2.5. Steel Details for SH 36 over Box Elder Creek [6].

Johnson and Atadero conducted FEM for the bridge and conducted a full-scale experimental test for the SDCL system at the Colorado State University Engineering Research Center in 2014 [6]. For the FEM analysis, the model of the specimen combined the dead load and inducing moment by service live load to get the strain at the top flange and the end of the beams. For the experimental test specimen, the two bridge beams were W33×152s with welded sole plates (same original design as the bridge over Box Elder Creek in Colorado). Figure 2.6 shows the full experimental connection details.

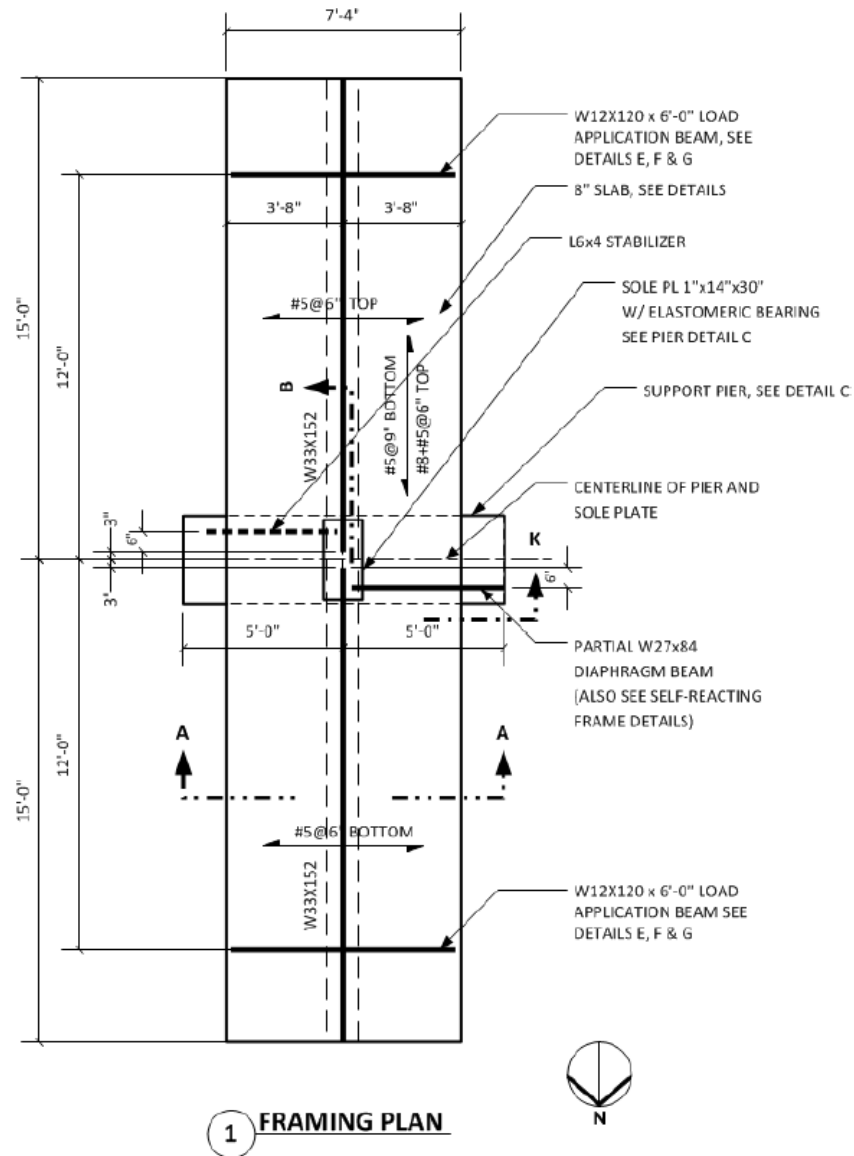


Figure 2.6. Colorado SDCL Connection Details [6].

Strain and displacement gages (potentiometers) were used to record data during the experiments. The maximum moment applied to the setup was close to the theoretical moment in the finite element model. The deflections were also close to the theoretical results [6]. The soleplate connection did not become fully stressed and was considered the vital component to transfer the compressive force. The researchers recommended increasing the weld size to fully transfer forces. It was also critical for the specimen to conduct the fatigue load test since the connection used a steel diaphragm, and they were field welds. The welded connection of the steel soleplate and bottom flange was subjected to compression force.

The research provided future recommendations for the weld between the bottom flanges and the sole part. The fillet weld could be replaced by anchor rods through the soleplate to the pier cap. Wedge compression plates could be added after the girder placement. For the steel-only diaphragm type of connection, the main advantage is reduced construction time since contractors do not need to wait for casting concrete. It is also convenient for engineers to perform the inspection. Compression forces are transferred by steel components, which allows for ductile behavior. The construction procedure can be simplified and accelerated for this type of connection [6].

2.2.4. Steel Bridge SDCL Construction in West Virginia

Ream and Beining designed two steel girder bridges with SDCL construction in West Virginia, which included SDCL connection details. Their work documented the various fabrication, construction, traffic, and construction benefits of SDCL [7]. Both the Three Springs Drive bridge and the Washington Avenue bridge were replaced by two-span SDCL structures that used conventional construction systems. Regarding the Three Springs Drive bridge, the span lengths were 125 ft 6 inches and 95 ft. For the Washington Avenue bridge, the length of spans were 96 ft and 112 ft, which was very similar to the Three Springs Drive bridge. The method of construction and girder connection details were also similar [7]. Figure 2.7 shows the two bridges in West Virginia.

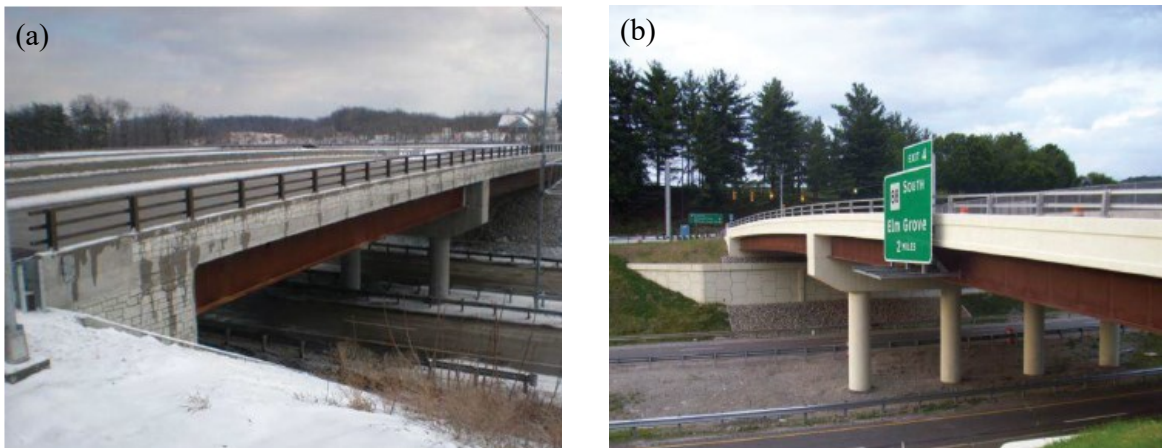


Figure 2.7. (a) Three Springs Drive Bridge, and (b) Washington Avenue Bridge [7].

The SDCL steel girder connection at the pier primarily transferred the live load tension at the top and compression at the bottom through steel connections. These connections were made after the

concrete deck was cured, which was poured within 5 ft of the centerline of the bearing to decrease the non-composite forces. The steel connections then included a bolted splice plate on the top flange joining the two girders (with shear studs to engage the deck). Steel end plates were shop-welded to the bottom end of the girder web. Then, bearing shim plates were added in the field to transfer the compression forces. To supplement the steel connections, a reinforced concrete diaphragm was cast. Holes were drilled into the girder web for transverse bars and shear stirrups. The casting of the diaphragm was the last step. Figure 2.8 shows the steel continuity splice details.

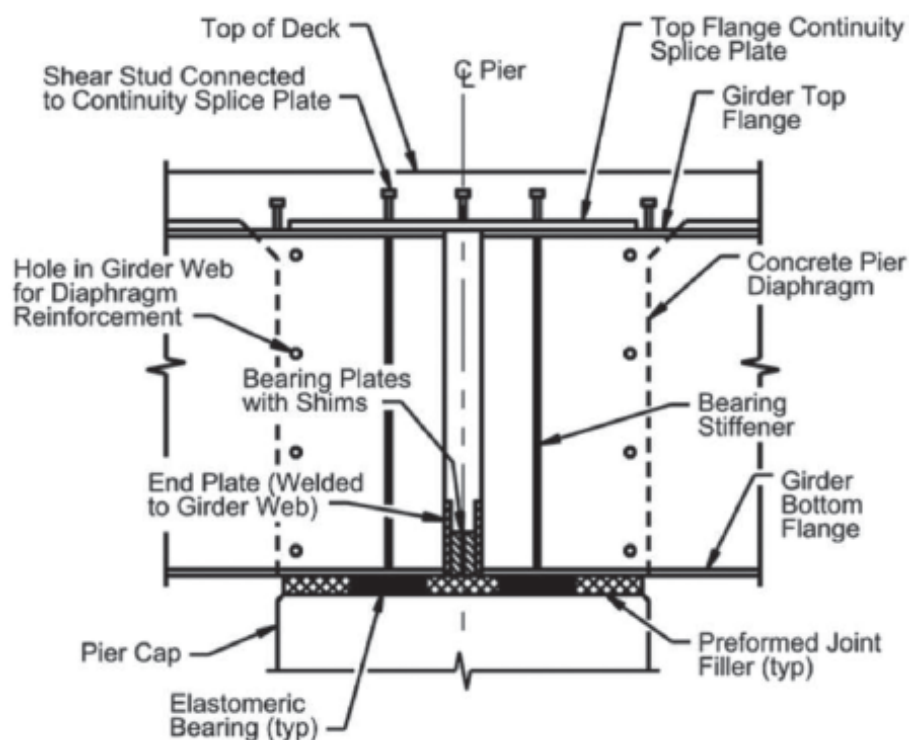


Figure 2.8. West Virginia Steel Continuity Splice Details [7].

This study documented many advantages of steel bridge SDCL. A summary of these advantages observed from the two bridge construction projects is as follows:

- Fabrication—Welded flange transitions were eliminated, which increased the speed of fabrication. Also, the use of concrete diaphragms eliminated the need for complex cross-frames at the supports.
- Construction—Not having in-span field splices and reducing complex steel details increased the speed of construction. The SDCL connection was less complex, which

reduced the labor overall and the skill-level requirements. Also, the crane requirements were reduced.

- Traffic—Only one direction of the highway was required to be under construction as opposed to both directions if it had been a conventional continuous construction.
- Maintenance—The elimination of joints (if simple span construction was chosen) prevented future corrosion of the steel girder ends and pier cap.

2.2.5. Experimental Testing of Steel SDCL Systems in Nebraska

Lampe et al. conducted an experimental study on steel SDCL systems at the University of Nebraska-Lincoln [3]. They designed and constructed three full-scale test specimens. These specimens were subject to two types of loading: cyclic testing and ultimate capacity testing. Farimani et al. also conducted linear and nonlinear finite element numerical modeling for each test specimen to verify the test results [8]. The overall goal of the testing and modeling was to develop a steel SDCL connection for practice. The results of the research show that the SDCL connections adequately transfer the compressive force to maintain an adequate service life. However, the distribution of tensile force may be insufficient due to the potential for long-term cracking issues.

The studied SDCL concept was essentially a composite steel and concrete diaphragm (see Figure 2.9). Three different steel end connection details were tested, as shown in Figure 2.10. For Specimen 1, the bottom flanges of the girders were field-welded together. The detail included welded end-bearing plates along with two triangular stiffening plates at the bottom of the web. Specimen 2 was used as a control group, with no steel connections or details added. Specimen 3 only included steel endplates (no bottom flange connection or triangular stiffeners).

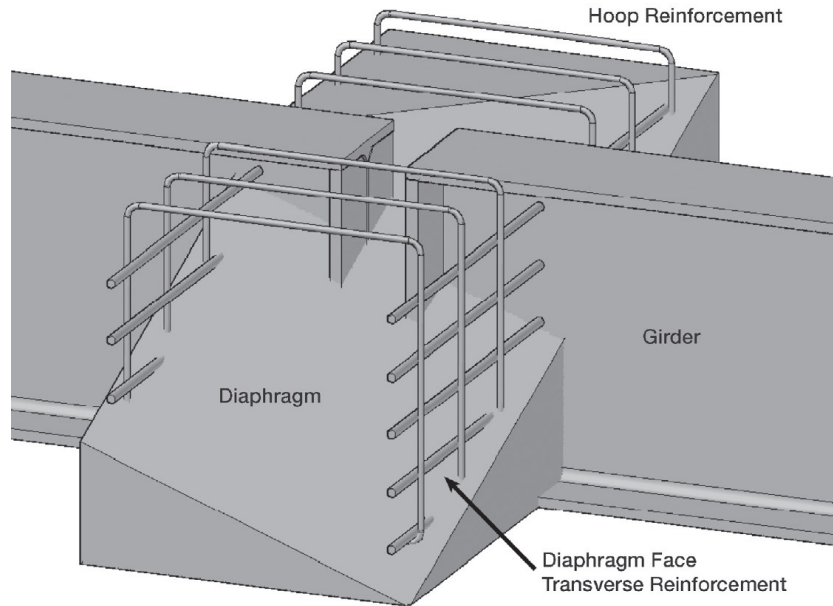


Figure 2.9. Concrete Diaphragm Detail [9].

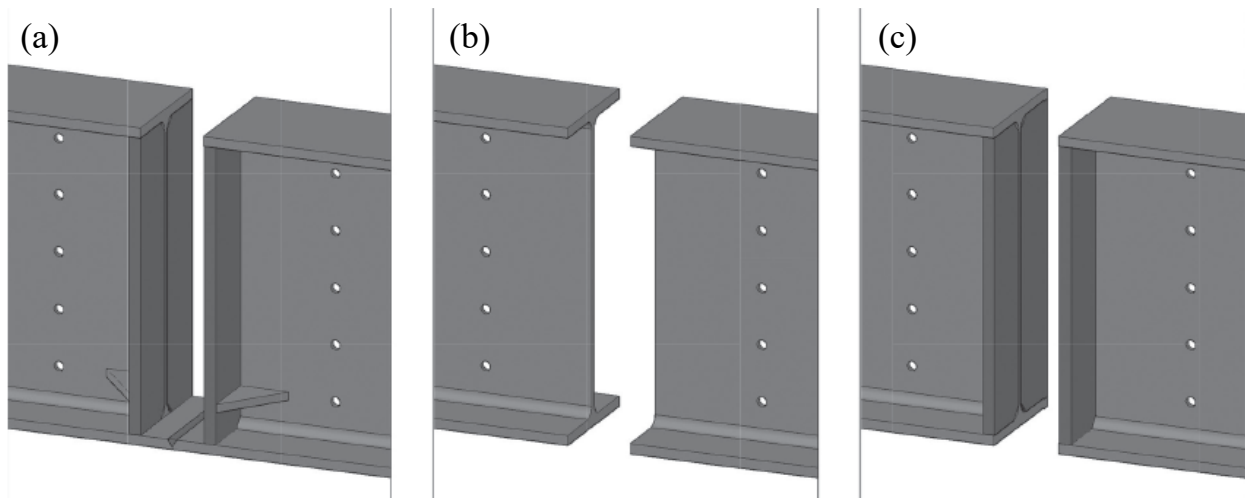


Figure 2.10. Connection Details of the Three Specimens: (a) Specimen 1, (b) Specimen 2, and (c) Specimen 3 [9].

The experimental test setup was comprised of two 16 ft girder sections (W40×215's) supported by a reinforced concrete pier. Continuity was provided by a cast-in-place (CIP)-reinforced concrete deck slab and diaphragm. The concrete diaphragm included #5 stirrups spaced at 12 inches, along with transverse bar through-holes on the web. This diaphragm fully encased the steel connection. Extensive strain and displacement measurements were taken when testing each specimen. Figure 2.11 summarizes the findings for the cyclic and ultimate capacity testing.

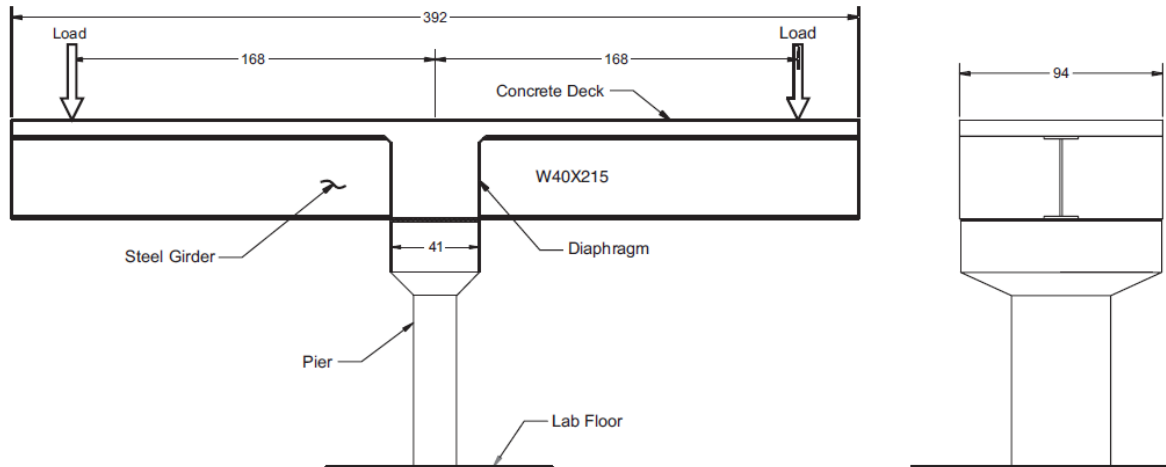


Figure 2.11. Test Specimen Configuration [3].

The cyclic testing aimed to show the long-term effectiveness of the connection details over the pier cap. Researchers applied 220-kip MTS actuators, as shown in Figure 2.12. Cracking was initiated at the edge of the concrete diaphragm for Specimen 1 [9]. The bottom flanges of Specimen 2 penetrated the diaphragm during the cycling test, which indicated a strength failure. The cracks of Specimen 2 initially appeared at the edge of the diaphragm and then spread to the end of the girder. The cracks for Specimen 3 also spread to the end of the cantilever, but the bottom flange did not penetrate the diaphragm. The stiffness variation between Specimens 1 and 3 was similar. However, the strain behavior in the deck was different for the three specimens.



Figure 2.12. Cyclic Test Setup [3].

Ultimate capacity testing was performed after the cyclic testing for each specimen. The results for Specimens 1 and 3 were similar, reaching a capacity of roughly 6,000 kips-ft. For Specimen 1, the yielding of the longitudinal reinforcement occurred in the top layer before the failure of the bottom concrete. Next, the bottom plate yielded about 65 percent of the ultimate load. Finally, the entire rebar top layer and slab rebar yielded. Specimen 2 only reached 4,000 kips-ft during the test. Only two bars yielded before the connection failed for Specimen 2. The concrete at the corner of the bottom flange was crushed, and the transverse bars failed because of the shear force. Specimen 3's performance was similar to Specimen 1. The main exception was that the concrete diaphragm was crushed at the bottom of the flange [9]. Overall, extensive cracking was observed at the connection over the pier in all three specimens. The width of cracks in the slab of Specimen 2 was the largest. Additionally, some large cracks occurred at the centerline of the pier instead of the edge of the diaphragm. Figure 2.13 shows the crack pattern of Specimen 3 from different vantage points.



Figure 2.13. Specimen 3 Crack Patterns after Ultimate Testing: (a) Concrete Slab, Plan View; and (b) Face of the Diaphragm [3].

Based on the results of the two experimental tests, it was recommended that a continuous steel path at the bottom be provided to transfer the compression force. Using a bearing block welded between the bottom flanges instead of directly connecting the bottom flanges was another practical recommendation. The steel reinforcement in the slab yielded at the end of the ultimate load test, which researchers used to justify not providing a continuous top flange steel connection.

Farimani et al. performed nonlinear 3D FEM of the SDCL connections and compared the results with the experimental testing [8]. This modeling was used to develop a new connection that added the bearing block welded at each of the bottom flanges. The FEM showed that the load-displacement behavior was similar to the experimental testing. They concluded that the load resistance mechanisms from the rebar in the deck, bottom connection plates, or the bearing blocks are the vital parts to resist the negative moment over the pier cap.

Simplified moment capacity equations were derived that can be used for the future design of connection details. Azizinamini also suggested a bolted connection at the bottom flanges since the welded connection was vulnerable to fatigue [1]. Another conclusion was that the bonding of the steel girder and the concrete diaphragm was important in increasing the compressive strength. Adding stirrups to the concrete diaphragm was also recommended.

2.3. ABC TECHNIQUE

2.3.1. Introduction

Conventional bridge construction refers to the traditional methods and techniques used to build bridges. The process generally follows a series of well-established steps, including site preparation, foundation work, and the erection of bridge components. It often requires the use of cranes, scaffolding, and formwork to assemble the various structural elements. While conventional bridge construction is time-tested and reliable, it can be labor-intensive and time-consuming and contain potential challenges such as weather delays or disruptions to local traffic during construction.

An alternative to conventional bridge construction is ABC. ABC is a relatively new type of bridge construction method that optimizes design concepts, materials, and construction methods to reduce the on-site time to build or replace a bridge [10]. It can provide a safer and more cost-effective way to improve bridge constructability and minimize the disruption to traffic. ABC is becoming much more common across the United States and within Texas.

The following sections discuss prior research and applications of ABC technology that relate to steel SDCL construction.

2.3.2. Prefabricated Bridge Elements and Systems

Prefabricated bridge elements and systems (PBES) are built off-site or near the site and then transported to the bridge site and installed quickly using various rapid connections. This method is the most common form of ABC since the elements are relatively easy to assemble and connect at the site to form the whole bridge. It can reduce road user impacts, speed the bridge project process, improve the quality of on-site work and constructability, and decrease the interruption to the traveling public. PBES mainly include the superstructure, substructure, connections, and foundations. The Federal Highway Administration (FHWA) has classified prefabricated bridge elements and has specific guidelines for how to use appropriate products [10].

In terms of superstructure components, one ABC example is from Balkos et al., who performed an investigation of the static and fatigue performance of through-bolt shear connectors used between steel girder and concrete slab decks. This study conducted testing of three-beam specimens [11]. The connections did not fail in the fatigue tests but failed by bolt fracture in the

ultimate strength tests. Some recent ABC bridge projects have utilized UHPC to improve the strength and durability of the girder connections. NYSDOT eliminated bridge joints with link slabs by using UHPC, which are shown in Figure 2.14.

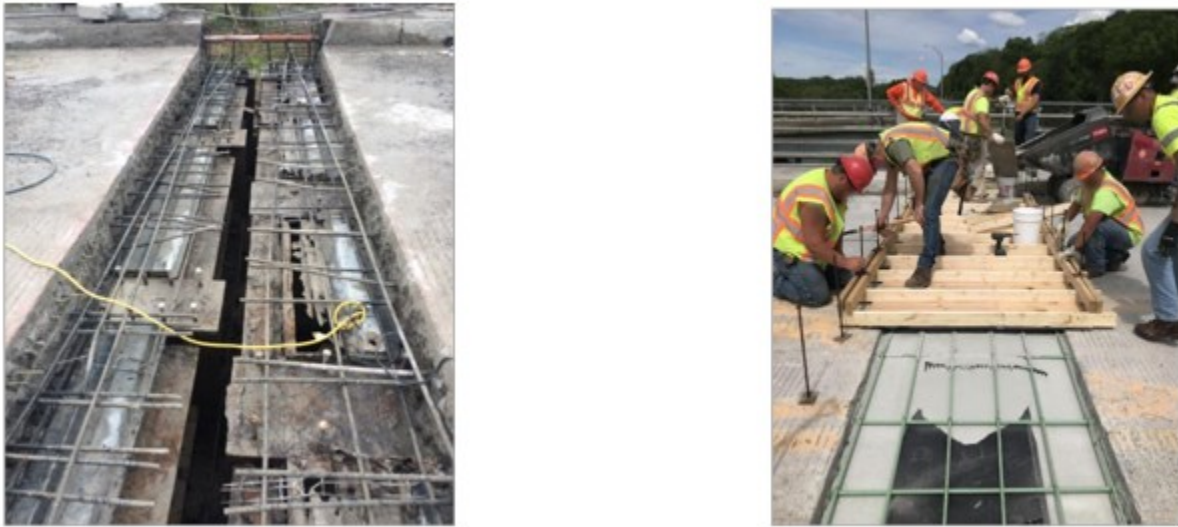


Figure 2.14. Concrete Deck and Joint Removed before Link Slab Installation and Forming of Link Slab [12].

For substructure systems, precast bridge substructures are also used for ABC, which include piers, abutments, etc. Birely et al. presented precast pre-tensioned bent caps as a new application through full-scale experimental testing. The bent caps can significantly reduce cracking and minimize crack width [13]. Additionally, connections are vital for ABC projects since they impact long-term service life and maintenance issues. Different connections between each bridge element exist, like column-to-footing, column-to-cap, SDCL, panel-to-girder connections, etc. Shoushtari et al. developed a large-scale ABC bridge model with various connections. Shake table testing was performed to verify the seismic performance and determine the potential construction methods [14]. This research included the SDCL connection between the girder and cap beam. The performance of the connection was satisfactory, and the damage was restricted to column plastic hinges at the end of the column [15]. Figure 2.15 shows the shake table test for the large-scale bridge model. The various research on PBES can improve the material quality and prolong the service life of bridges.

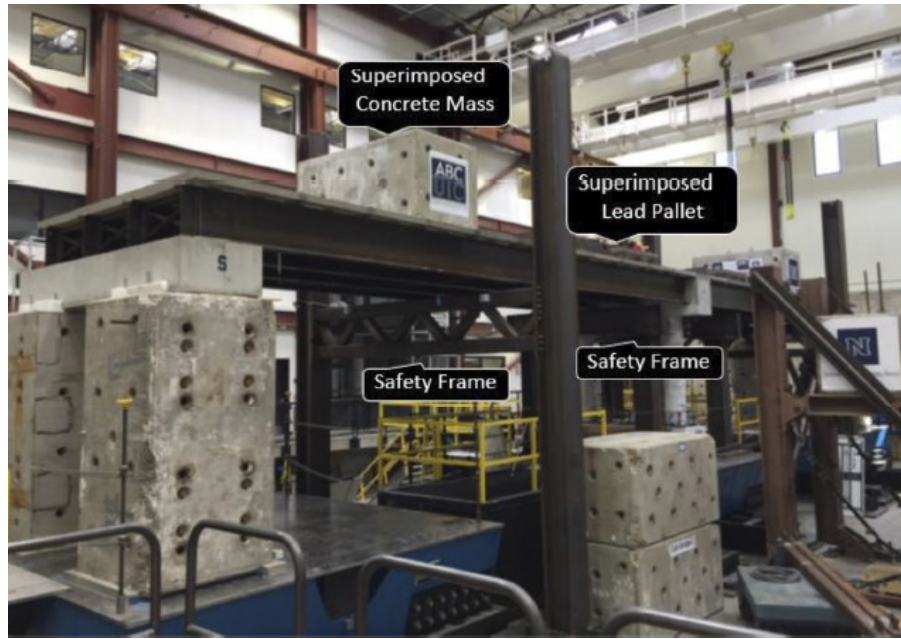


Figure 2.15. Shake Table Test Setup [14].

2.3.3. Slide-In Bridge Construction

Slide-in bridge construction (SIBC), also known as lateral slide, is an ABC technology for rapidly replacing an old bridge. A new bridge superstructure is built and ready for sliding laterally into the existing bridge location once the old one is removed. Attanayake and Aktan presented detailed procedures and guidelines for SIBC. They explored three projects using SIBC completed by the Michigan Department of Transportation [16]. For these lateral slide projects, they present the design considerations and appropriate components for SIBC by using a flowchart that clearly shows the step-by-step procedures and can be used for future designers. Figure 2.16 shows the slide-in construction process when the replacement superstructure is used as a temporary road.



Figure 2.16. Replacement Superstructure Used as Temporary Runaround [16].

2.3.4. Self-Propelled Modular Transporters

A self-propelled modular transporter (SPMT) is an ABC technology that combines multi-axle platforms controlled by a state-of-the-art computer to move, rotate, and carry bridge superstructures to the on-site location. There are several load capacities for SPMTs, like six lanes, 12 lanes with a double-wide, etc. Solae presented a study that observed full-depth deck cracks during construction using SPMTs. The skewed decks are more sensitive than straight decks and might cause cracks using the SPMT method [17]. Thermal movements and dynamic load effects should be considered for the ABC technology. Figure 2.17 shows an example SPMT bridge superstructure move in Utah.



Figure 2.17. SPMT Bridge Moves in Utah [10].

2.4. SDCL STEEL BRIDGE SYSTEMS USED IN ABC TECHNIQUE

2.4.1. Introduction

The application of steel SDCL with ABC has been limited. However, some research and applications have been performed at the state and federal level. The following sections discuss these projects. Overall, there have been challenges with successful application (particularly with reduced deck cracking). Also, the accelerated portion of the construction is questionable due to substantial concrete casting, which is an area in need of improvement.

2.4.2. SDCL System Using ABC at the University of Nebraska-Lincoln

Javidi and Azizinamini developed an SDCL system using pre-topped girders as a modular construction method [18]. Figure 2.18 illustrates the connection detail. This work is an extension of prior SDCL research, which was discussed in Section 2.2.5. As part of this ABC research, they conducted static and cyclic load tests to evaluate the performance of the SDCL specimens. They also explored the resistance mechanism of the connection. In Nebraska, they took advantage of this system and applied it at the 262nd Street bridge over I-80, which confirmed the feasibility and practicality of the system.

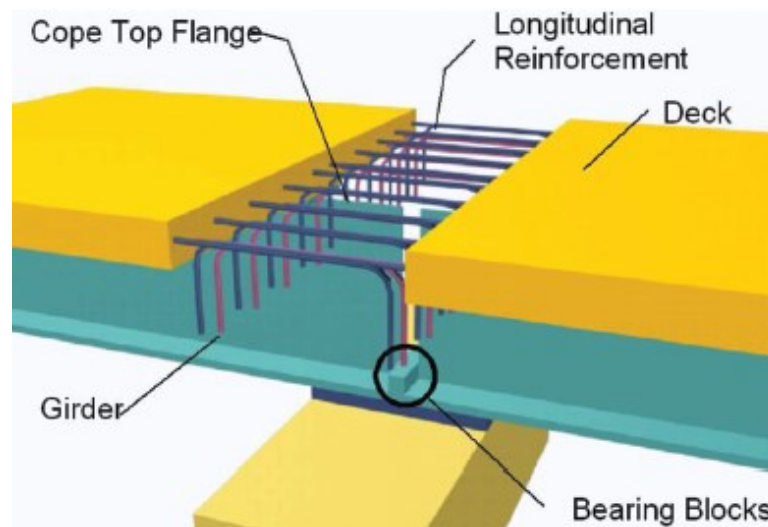


Figure 2.18. Connection Details for Modular System [18].

The experimental testing at the University of Nebraska was similar to the earlier SDCL steel girder testing setup (see Section 2.2.5). After the concrete connection was cured, no visible cracks were observed. Then an initial static load was applied to the specimen (equivalent to the maximum fatigue load), and the deck was inspected. Cracks were observed and mapped. Next,

cyclic loading was conducted, and cracks were continually mapped. Figure 2.19 illustrates the cracks in the top surface of the deck slab. Most of these cracks were present during the first 1 million cycles. Limited growth was observed after that. However, **extensive cracking might be an issue for the long-term durability and service life of the structure.** This cracking allows de-icing chemicals into the slab, thereby accelerating corrosion of the reinforcement.

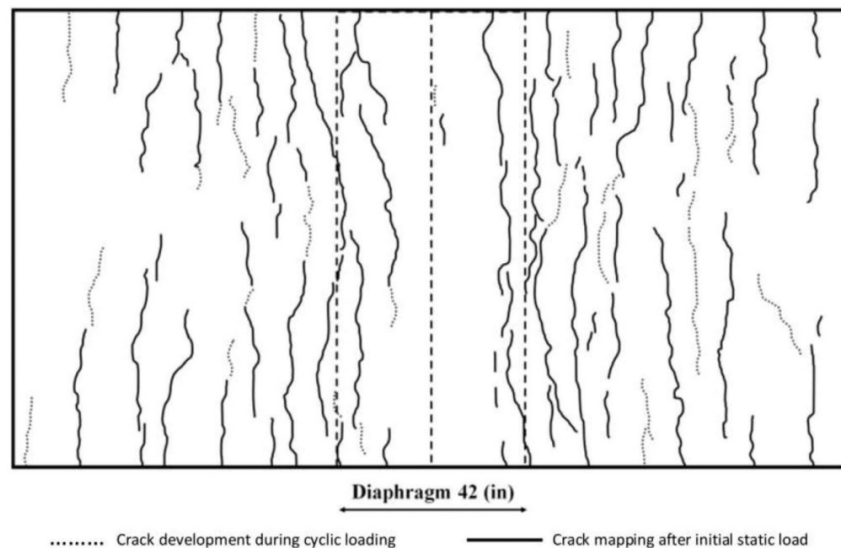


Figure 2.19. Deck Slab Cracking [9].

Ultimate strength testing was performed after the cyclic testing. Researchers applied loading at the westside girder and eastside girder. Both showed similar results for the load-displacement data. The maximum ultimate load was approximately 415 kips, and the displacement was around 6 inches. Overall, this result achieved the desired compression capacity. Additionally, deck cracks formed and developed during the ultimate testing. There were several large cracks since the researchers continued to apply load after the ultimate strength was achieved. The steel bearing blocks welded to the bottom flanges contributed an important part to resisting the compression force. Moreover, the longitudinal reinforcement deck resisted the tension force at the top of the connection.

After the experimental testing, a similar concept was utilized for the 262nd Street bridge over I-80 in Nebraska. This structure is a two-span continuous steel girder bridge with span lengths of 95 ft. For the concrete deck, the longitudinal rebar extended out of the precast portion at the pier within the CIP diaphragm region. The researchers recommended UHPC for joint closures [1]. Bearing blocks were welded at the bottom flange. High-strength bolts along the web (close to the

top flange) prevented slippage from the concrete diaphragm. Figure 2.20 shows the second girder being erected in the second span of the bridge.



Figure 2.20. Erection of the 262nd Street Bridge in Nebraska [18].

2.4.3. SDCL System Using ABC as Part of Strategic Highway Research Program 2

Iowa DOT and HNTB Corporation developed a three-span precast modular steel bridge with SDCL construction using ABC technology. Iowa State University performed UHPC lab tests to assess the performance of the transverse deck joint, which included abrasion and compressive strength tests. This effort was the main part of the Strategic Highway Research Program 2 (SHRP2) R04 project [19]. The previous concrete girder bridge was replaced by a steel bridge. UHPC was cast for the transverse deck joints to resist live load negative moments over the pier (see Figure 2.21). PT bars were later installed on the web to decrease the tensile force at the top of the girder and reduce the deck cracking.

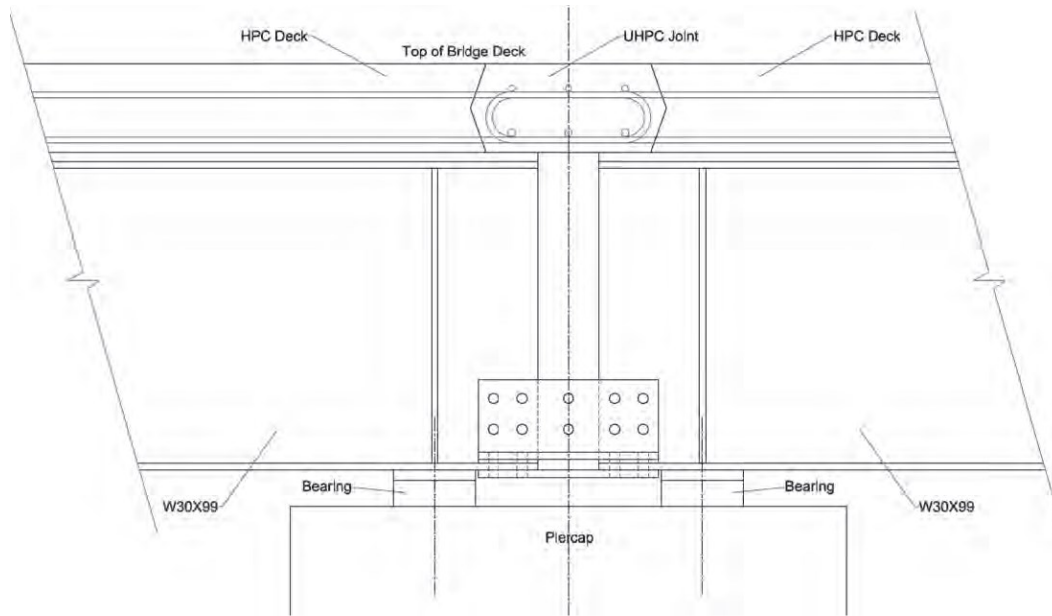
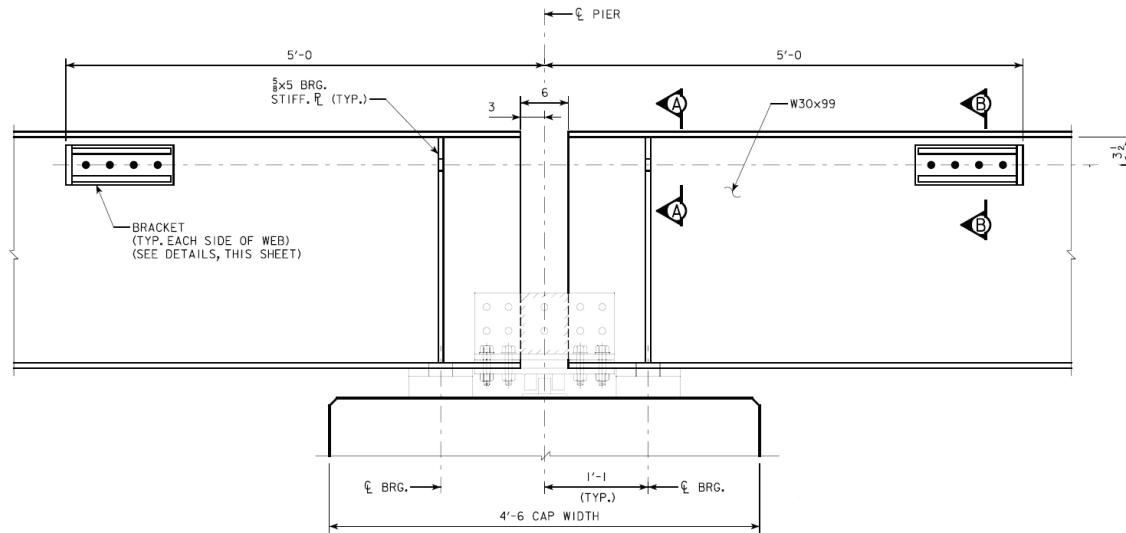


Figure 2.21. SHRP2 Module-to-Module Transverse Connection Detail [19].

For the SHRP2 project, the UHPC lab tests were vital in developing the replacement of an older bridge using ABC. The first part of the tests was an abrasion test for UHPC, which evaluated the grindability of the UHPC material. Researchers built a specimen of the transverse UHPC joint to test the joint constructability and then built the full-scale transverse connection specimen to test its strength and serviceability [19]. Figure 2.21 shows the design details of the transverse deck joint. They constructed the UHPC transverse deck joint and bolted splice plates at the bottom flange. The PT bars were installed as a construction retrofit to minimize the deck crack (Figure 2.22). Service load tests and ultimate moment capacity tests were performed after installing the PT bars on both sides of the girders.



For the joint constructability, a partial-height removable acrylic vertical bulkhead was constructed for the casting sequence to avoid cold joints at the transverse deck joint and get rid of water and chemicals. The early debonding and serious opening between the precast deck and UHPC joint were visually found during the static load tests. Figure 2.23 shows the interface opening and cracks around the UHPC joint. Figure 2.24 shows the UHPC rupture at the top and the bottom of the deck. The steel girders were partially separated from the deck, and UHPC tensile rupture happened around the two large, wide cracks at the top of the deck after the ultimate capacity test. There were also some full-depth cracks in the precast deck within 10 ft of the UHPC joint after the fatigue load tests. As a result, PT rods were selected as a connection retrofit to minimize the tensile force and deck cracks. The 70-kip PT rods were applied, and the strain of rebar at the UHPC joint was lower than the deck cracking strain, which made the connection more durable long-term [19]. The UHPC material proved to be durable and reached a high compression strength, but the tensile strength was a concern for the UHPC joint. The interfacial debonding between the precast deck and UHPC joint was also a problem when subjected to a relatively large negative live load moment.



Figure 2.23. Interface Opening and Crack Propagation [19].



Figure 2.24. UHPC Rupture (Top and Bottom of Deck) [19].

SHRP2 replaced the US-6 bridge in Iowa by using the UHPC joint developed through lab testing. This replacement used ABC technology, and it took about 16 days to re-open the bridge; the replacement included the old bridge demolition, abutment and pier construction, superstructure module assembly, CIP UHPC transverse joints, and the installation of the post-tension rods. Results from the replacement of this existing bridge demonstrated that the bond between the deck and UHPC joint was critical, and the constructability of the joint reinforcement is important.

2.4.4. SDCL System Using ABC as Part of Little Silver Creek Bridge Project

The Little Silver Creek bridge was an accelerated replacement bridge project in fall 2015. Figure 2.25 presents the isolated view of this bridge project. It was a 234 ft by 44 ft and 20-degree skewed steel bridge. It consisted of three spans of modular rolled steel beams, which

were 90 ft, 90 ft, and 50 ft. This project utilized rich ABC experiences from the US 6 over Keg Creek project, also known as SHARP2 Project R04. The whole impact construction duration was 61 days, and the full road closure duration was 21 days, which was a relatively short time compared to conventional bridge construction [20].



Figure 2.25. Little Silver Creek Bridge Isolated View [20].

For the transverse joint details, there was a 10 ft gap between modular beams. For the top part, CIP concrete with additional steel reinforcement was utilized at the deck part and the whole connection part above the pier, which was similar to the Nebraska design (as shown before). For the bottom part, there was a steel compression block anchored on the pier between beam ends. End plates were welded at both beam ends. The shims were placed between end plates and the compression block. Figure 2.26 shows the compression section details of the transverse joint. UHPC was used for the longitudinal joint, which was about 10 inches wide. The rebar details in the concrete deck were also modified for this particular project.

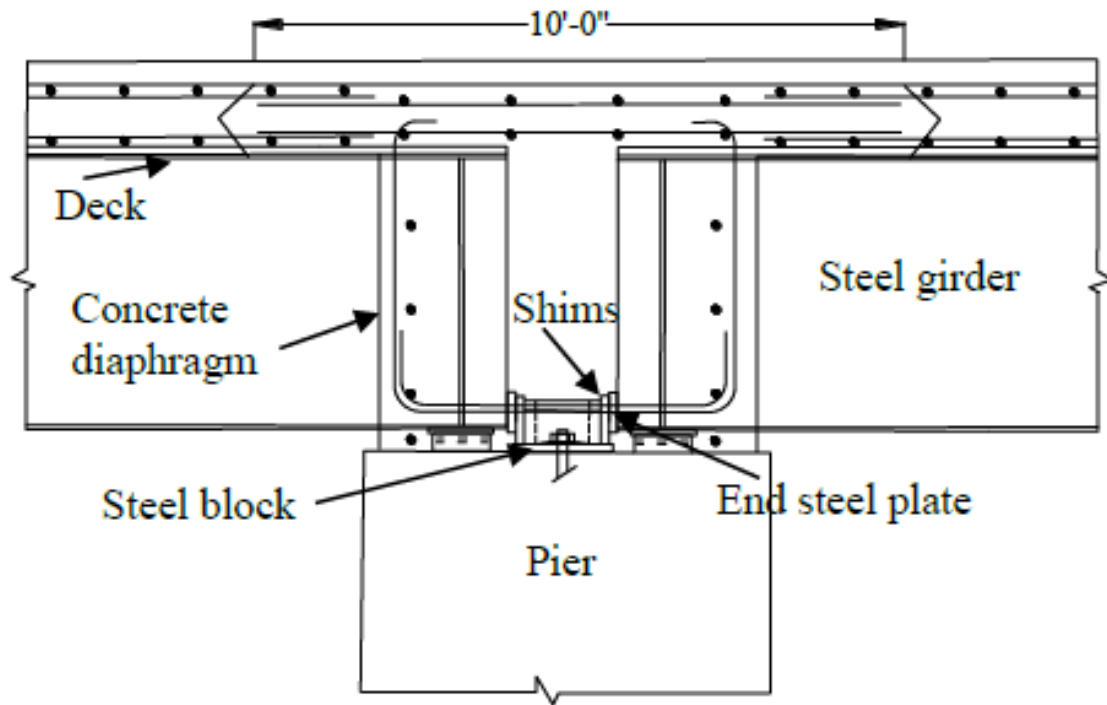


Figure 2.26. Bridge Transverse Joint Details [20].

An experimental program on the transverse joint connection was conducted at Iowa State University in order to explore the structural behavior, strength, and failure mechanism of the connection design utilized for the Little Silver Creek project. The compressive element was the main test element, which was the compression block. Two specimens were designed and tested at the pier locations. One test was conducted with the steel compression block at the bottom of the specimen. Another specimen was not equipped with the block at the bottom part. The full connection detail of the specimen was exactly the same as the connection of the Little Silver Creek project. For the dimensions of the precast specimens, the steel girder section was W40×149. The length of the specimen was about 7 ft 6 inches. For the concrete diaphragm over the pier location, the length was 2 ft 9 inches. The width was 3 ft 11 inches, and the depth was 4 ft 1.5 inches. The connection details were shown in the previous figure.

The strength test was conducted to investigate how the compressive steel block performs under various load levels. Figure 2.27 presents the test setup for the strength test. The actuators were placed at the two ends of the specimens to produce the negative moment at the connection. The load cell was attached to capture the magnitude of the applied load during the testing process. The testing frame was installed to keep the whole specimen load at the vertical location as much

as possible. The test specimen was also fully instrumented with strain gauges and other measure sensors.



Figure 2.27. Strength Test Setup.

Figure 2.28 presents the crack patterns on the deck surface around the connection location. Many of the cracks happened at the connection all the way through the deck width. Figure 2.29 shows another view of the connection for the concrete crack patterns. The vertical cracks occurred at the center of the diaphragm, and these cracks extended down the specimen. The vertical cracks are more significant than the cracks on the deck surface. The top tension-resisting element may still need to be improved since the number of cracks at the top surface were relatively large. The specimen with the bottom compressive steel block performed better than the specimen without an installed block.

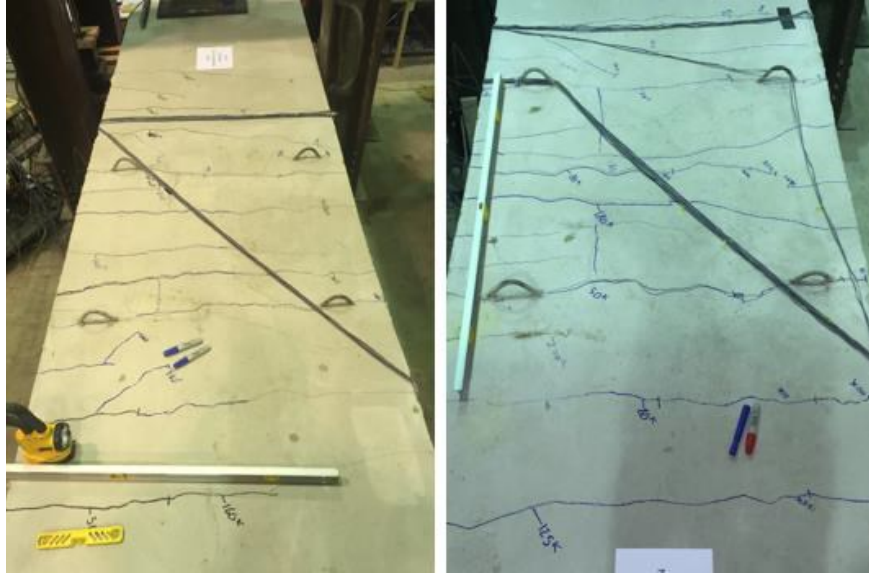


Figure 2.28. Concrete Crack Patterns at the Deck Surface.



Figure 2.29. Concrete Crack Patterns at the Side of the Diaphragm.

2.4.5. SDCL System Using ABC in Seismic Regions

Sadeghnejad et al. modified the steel SDCL-ABC connection developed at the University of Nebraska for seismic loading [21]. The test specimen was a 0.35-scale two-span continuous bridge. Researchers did the cyclic lateral loading test, and the results showed a good performance of ductility. For the developed SDCL-ABC connection for seismic areas, the shear studs and tie bars were on the top flange to prevent large displacement from high vertical excitations. This change was the major difference from the previous SDCL connections. The researchers still used the steel bearing blocks between the girder bottom flanges to transfer the compression force induced by the dead load and live load. An end stiffener was added to each girder, but it was not connected with the bottom flange. The longitudinal reinforcement bars were still 90-degree hook bars at the center of connections. Figure 2.30 shows the SDCL-ABC connection detail for seismic regions.

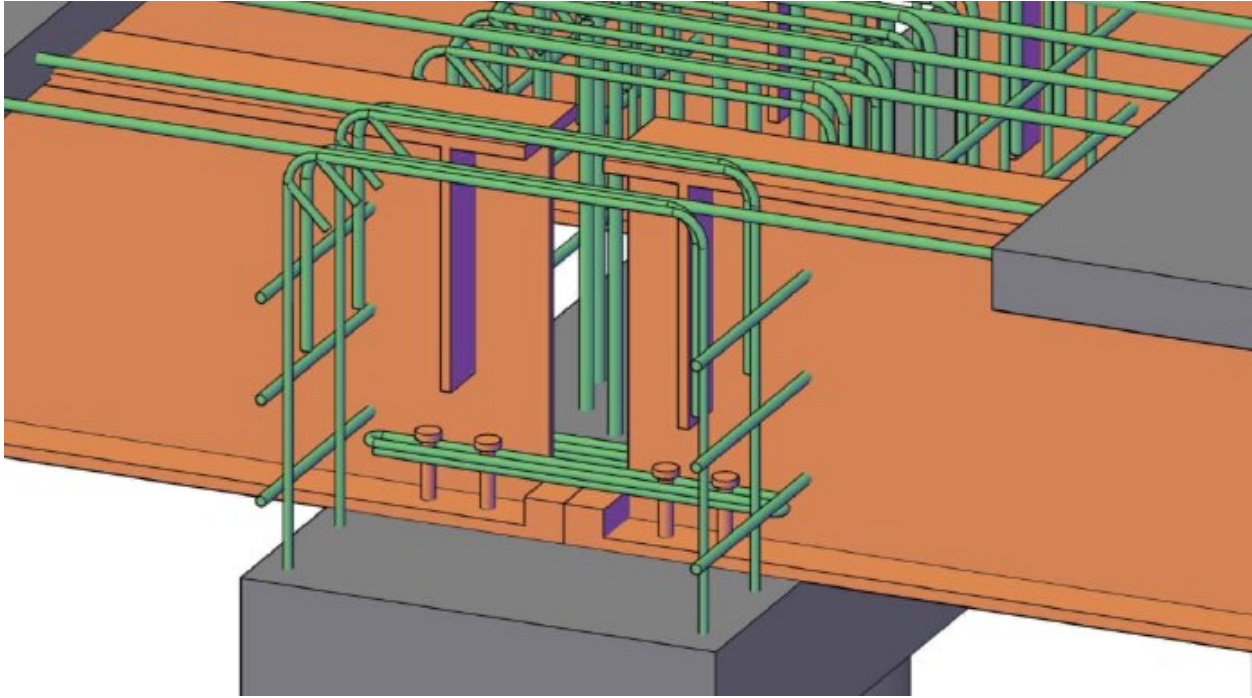


Figure 2.30. SDCL Connection for Seismic Area Details [21].

Further experimental shake table testing was conducted by Shoushtari et al. at the University of Nevada, Reno. They evaluated six different types of ABC connections, including SDCL beam connections, girder-to-deck connections, grouted duct connections, etc. [15]. They tested these connections to make them more practical and effective. For the shake table testing, there was apparent damage and cracking in the plastic hinge region after the third cycle loading. The column buckled at the last cycle of displacement of 6.5 percent drift. The tests proved that the specimen was qualified for the required loading capacity.

3. FIELD ASSESSMENT

3.1. OVERVIEW

A field assessment was performed on the recent TxDOT steel girder ABC project in Dallas, Texas (I-635 over Old Seagoville Road). Figure 3.1 illustrates the overall ABC sequence for the superstructure replacement, and Figure 3.2 provides a construction photo. This was the first ABC project for the Dallas District and was accomplished over 2 weekends.

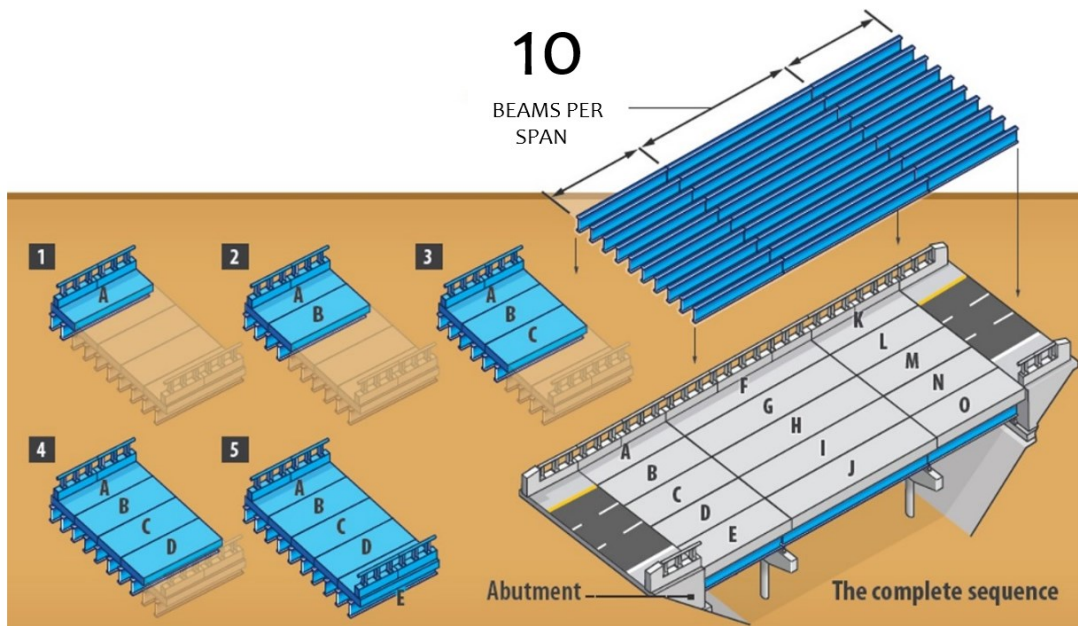


Figure 3.1. Construction Sequence for the I-635 Bridge over Old Seagoville Road in Dallas [22].



Figure 3.2. Construction Photo from the I-635 Bridge [22].

The overall length of the three-span structure is 219 ft, with a width of roughly 70 ft. The cross section of the bridge is shown in Figure 3.3, along with the layout of the prefabricated units. The structure was assembled with the girder's simple span for dead and live load. The deck slab was made continuous with a CIP closure pour between the precast units. Figure 3.4 shows the closure pour location and the reinforcement details.

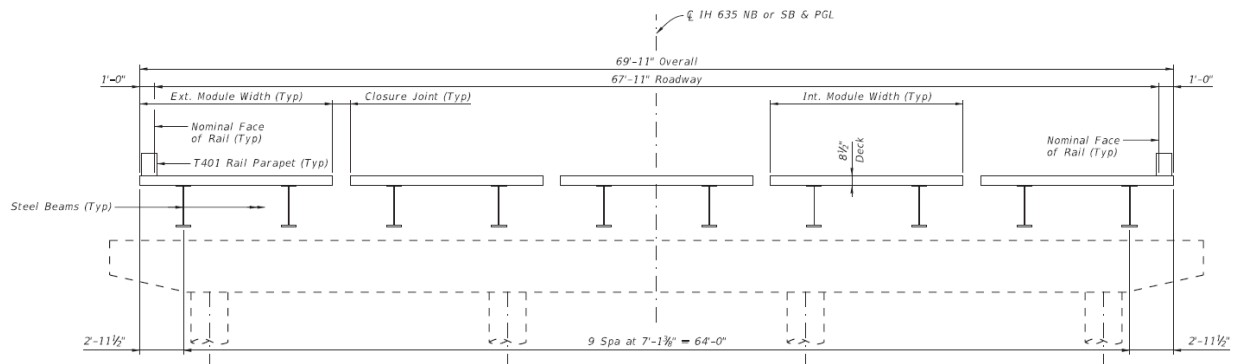


Figure 3.3. Cross Section of the I-635 Bridge.

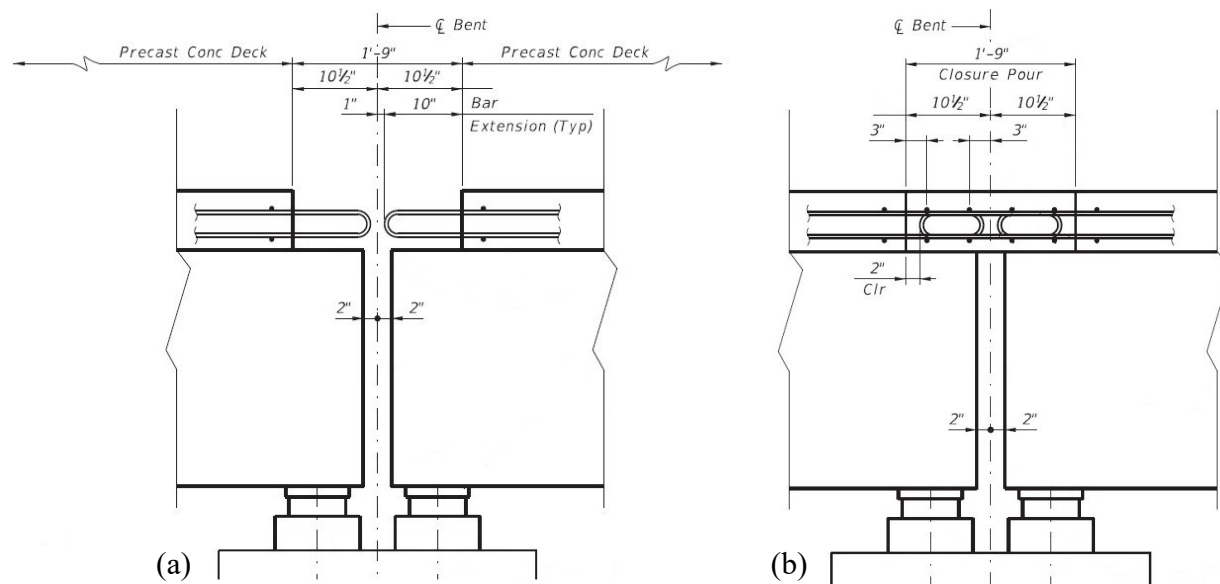


Figure 3.4. I-635 Bridge (a) Initial Prefabricated Unit Placement and (b) Closure Pour Detail.

Even though the girders on the I-635 bridge were not continuous for live load, the research team performed a field assessment to understand the current state of performance for a TxDOT steel ABC project. The field assessment included a visual inspection of the bridge (Section 3.2) along with structural monitoring (Section 3.3). The data from this assessment were utilized for comparison with the laboratory and numerical modeling results obtained later in the study.

3.2. FIELD INSPECTION

A visual inspection was performed on the I-635 bridge superstructure. The scope of this inspection was the region of the structure between spans since it is the focal point of the current research study. The main objective of the visual inspection was to understand the current construction method utilized and observe any potential performance issues. Figure 3.5 provides photos of this location on the northbound structure.

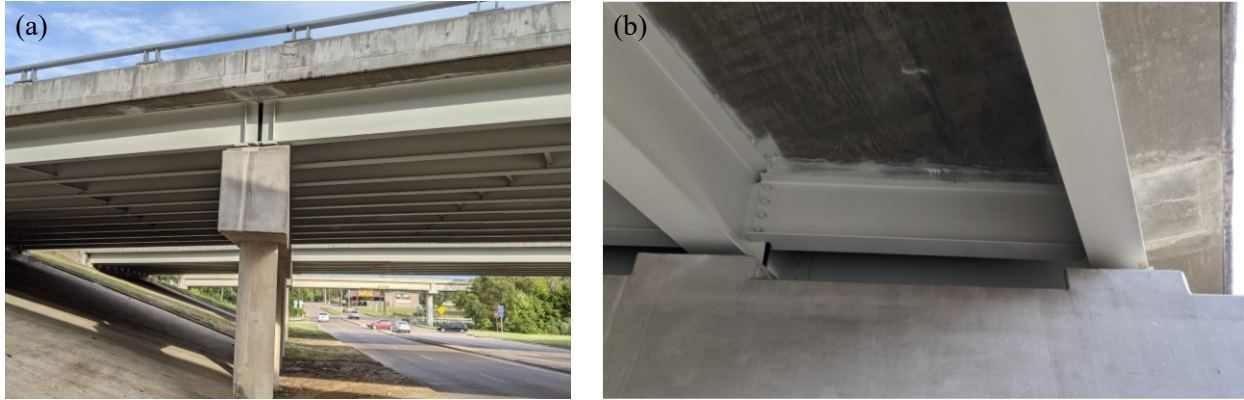


Figure 3.5. Overall Photos of the I-635 Bridge at an Interior Bent: (a) Elevation View and (b) Underside View.

A hands-on inspection was performed using ladder access. The research team members climbed between the steel end diaphragms to access the bottom surface of the deck and the ends of the beams. The primary obstacle was the timber formwork left in place after construction. Therefore, an inspection of the deck slab region between the beams was not possible. Figure 3.6 illustrates this location. Note that traffic control was not performed, so access to the top surface was also not available.



Figure 3.6. Underside of the Deck between the Steel End Diaphragms Obstructed by Timber Formwork.

The bottom surface of the deck slab was accessible in the overhang locations. In all locations, a clear visible crack was present. Figure 3.7 shows two typical photos. The crack patterns follow the angle of the pier bent, which is at roughly a 25-degree skew. These cracks commonly progress up the outside face of the rail. Efflorescence can be clearly seen at most crack locations.



Figure 3.7. Typical Condition of the Underside of the Deck Overhang at the Pier Bents.

A follow-up inspection occurred after it had recently rained. It was observed that water was actively leaking through the deck, primarily at the interface of the deck and the end diaphragms. Water was also observed to be dripping on the pier cap, as illustrated in Figure 3.8. This leakage is cause for concern for the long-term durability of the structure. It appears that water is penetrating the deck slab in this region and being trapped by the timber formwork. This moisture trap could accelerate corrosion of the reinforcement in this region.



Figure 3.8. Evidence of Water Leakage in the Deck Slab through Wet Areas on the Top Surface of the Pier Cap.

3.3. FIELD MONITORING

Field monitoring was also performed on the I-635 bridge superstructure. Similar to the inspection, the monitoring primarily focused on the region of the structure between spans. The objective of the measurements was to identify the baseline performance of the transverse connection between adjacent spans. This information was also utilized later in the study for comparison with the laboratory testing (particularly deck level stresses, which can be extrapolated from the field measurements).

3.3.1. Instrumentation Design

The field monitoring instrumentation was designed to best capture the structural behavior at the connection between Span 1 and Span 2. The concept was to install horizontal displacement gauges at the top and bottom of the girder ends to capture the relative longitudinal movement as well as the rotation. From this rotation, the strains at the top of the slab can be estimated. In addition, strain gauges were installed on the top and bottom flanges of the girders in this region to evaluate if any flexural demands were developed in the girders. Figure 3.9 illustrates the instrumentation approach. Note that the researchers intended to install strain gauges on the bottom surface of the slab, but the timber formwork inhibited this effort.

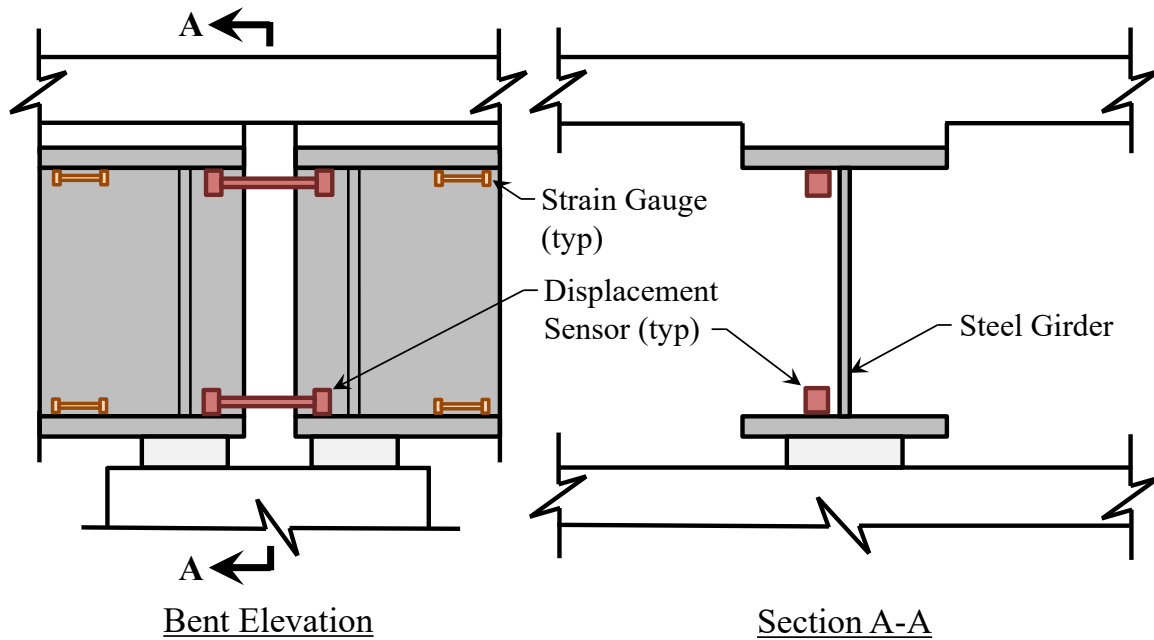


Figure 3.9. General Instrumentation Approach at the Pier Bent.

The primary structural demands of interest were in-service thermal and live load. Therefore, each of these demands was captured through ambient monitoring. To evaluate the thermal behavior, thermistors were included with each strain and displacement gauge. The ambient live load was captured by sampling at 50 Hz. Data covering roughly a week were collected and processed for the study.

A total of 12 sensor locations were selected (24 total sensors, including thermistors), which are shown in the instrumentation plan in Figure 3.10. The research team decided to focus on Girder 8 since it was located under the outside lane of traffic. Additional displacement sensors were added at Girders 9 and 10 to also capture the behavior of the first interior and exterior girders, respectively.

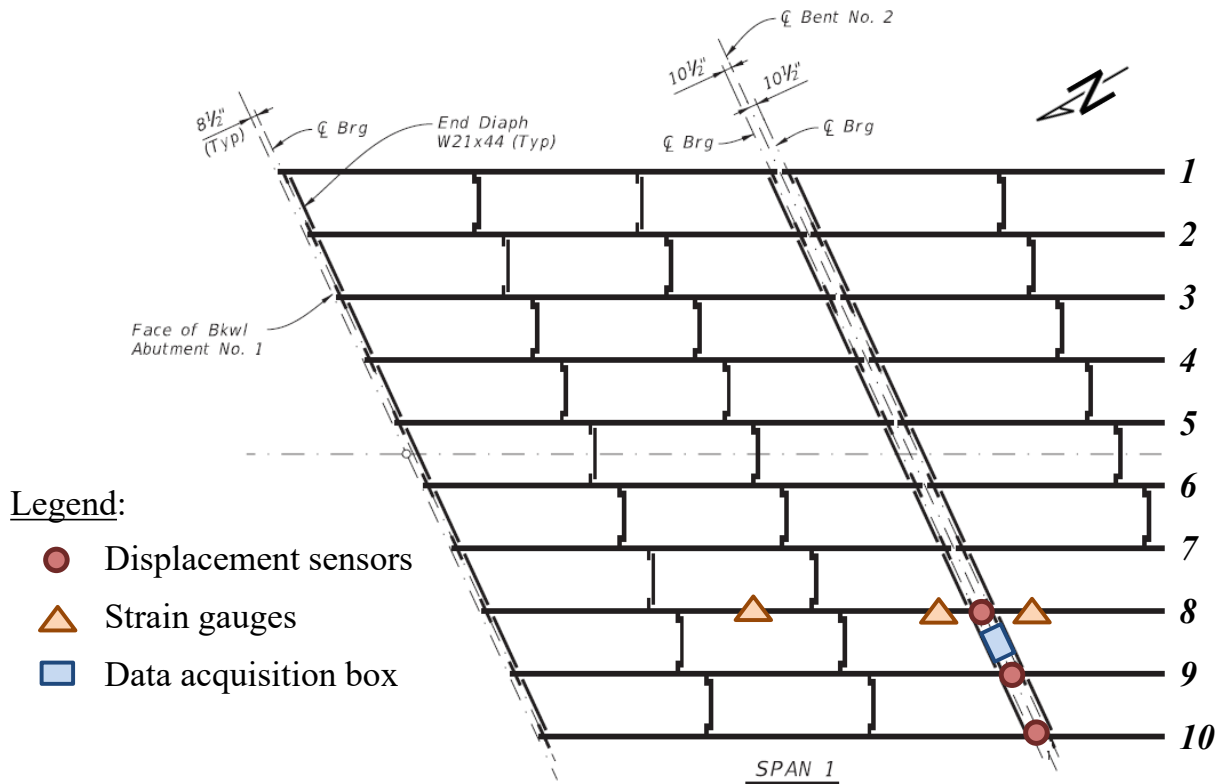


Figure 3.10. Instrumentation Plan for the I-635 Bridge.

The displacement gauges at the pier bent were installed on the top and bottom flanges, as shown in Figure 3.9. The strain gauges at the pier bent were also installed, similar to Figure 3.9, at roughly a distance of 3 ft from the center of the bearing. A cross-section view is provided in Figure 3.11. Two additional strain gauges were installed near midspan along Girder 8. The intent was to capture the primary flexural behavior of the girder. The gauges were installed on the bottom of the bottom flange and at the mid-height of the web. Figure 3.11 shows a cross-section view of the setup. An additional benefit of the midspan gauges is that their measurements were used to verify composite action and trigger the data acquisition system when a sizable truck passed the far right lane on the bridge. As mentioned above, each location included a thermistor.

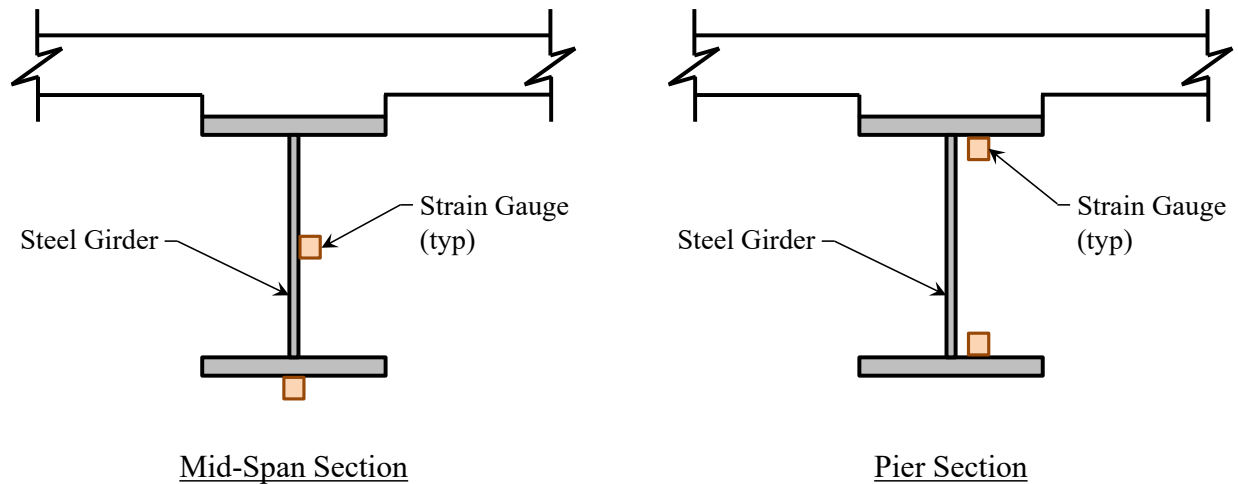


Figure 3.11. Cross-Section View of the Strain Gauge Locations.

The sensor type selected for the study was vibrating wire. This type of sensor has proven reliable for thermal and live load behavior. The Geokon Model 4000 strain gauge and Model 4420 displacement gauge were also utilized. The data acquisition system was from Campbell Scientific since they have the necessary equipment to sample vibrating wire sensors at relatively high speeds. A CR6 datalogger was used with the CDM-VW305 modules (dynamic vibrating wire analyzers). The system was powered with two 100 Ah batteries.

Installation of the setup was performed within a day. Everything was attached with epoxy adhesive to bare metal. Figure 3.12 shows photos of a few installed sensors. Note the sensor locations were painted during installation and after removal to prevent corrosion.

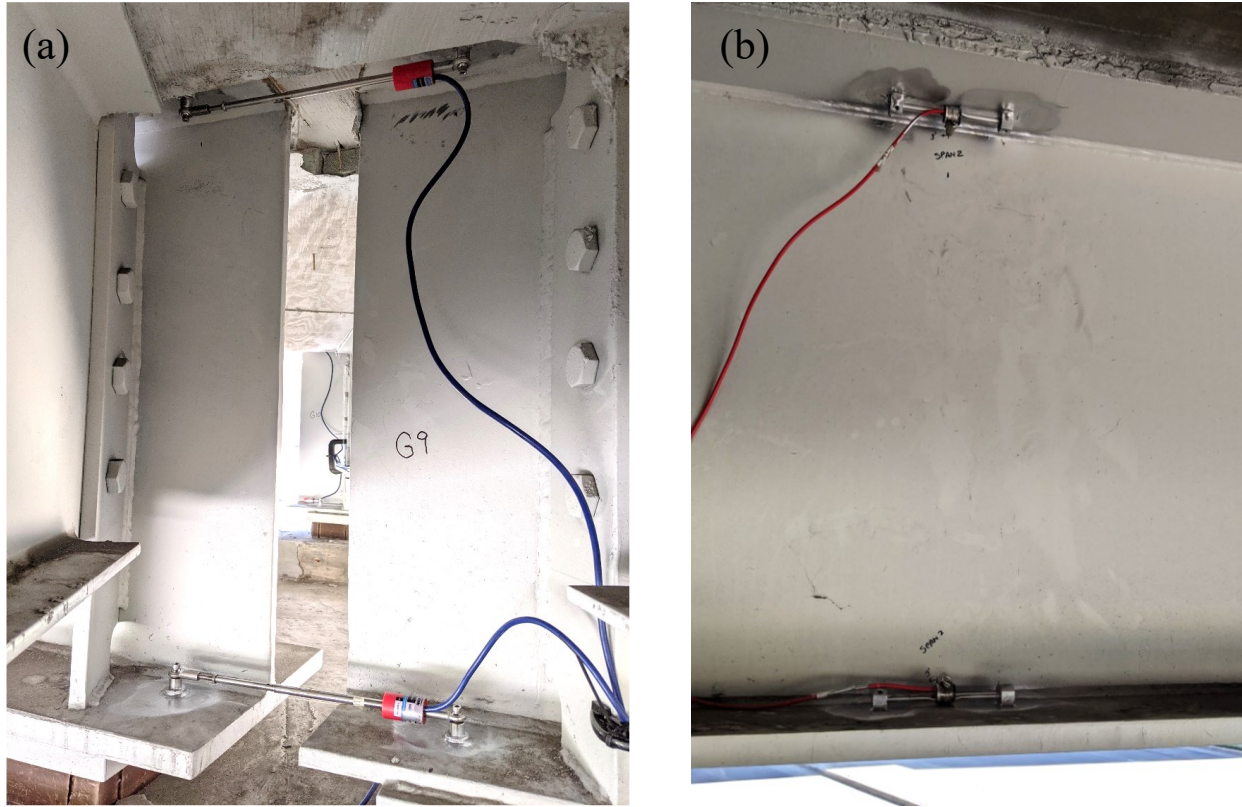


Figure 3.12. Photos of Installed (a) Displacement Gauges and (b) Strain Gauges near the Pier.

3.3.2. Results

The results from the monitoring system provided insight into the behavior of the superstructure at the pier bent between Spans 1 and 2. Over roughly 1 week, the thermal behavior was captured by measurements recorded every minute. Figure 3.13 illustrates the general trend of temperature variations (aka *demand*) over the monitoring period. On December 11, 2021, a significant temperature drop was recorded, followed by several relatively high-temperature increases. Note that the temperatures shown in the time history plot are only at the sensor locations. Therefore, the temperature on the top surface of the deck slab is not provided.

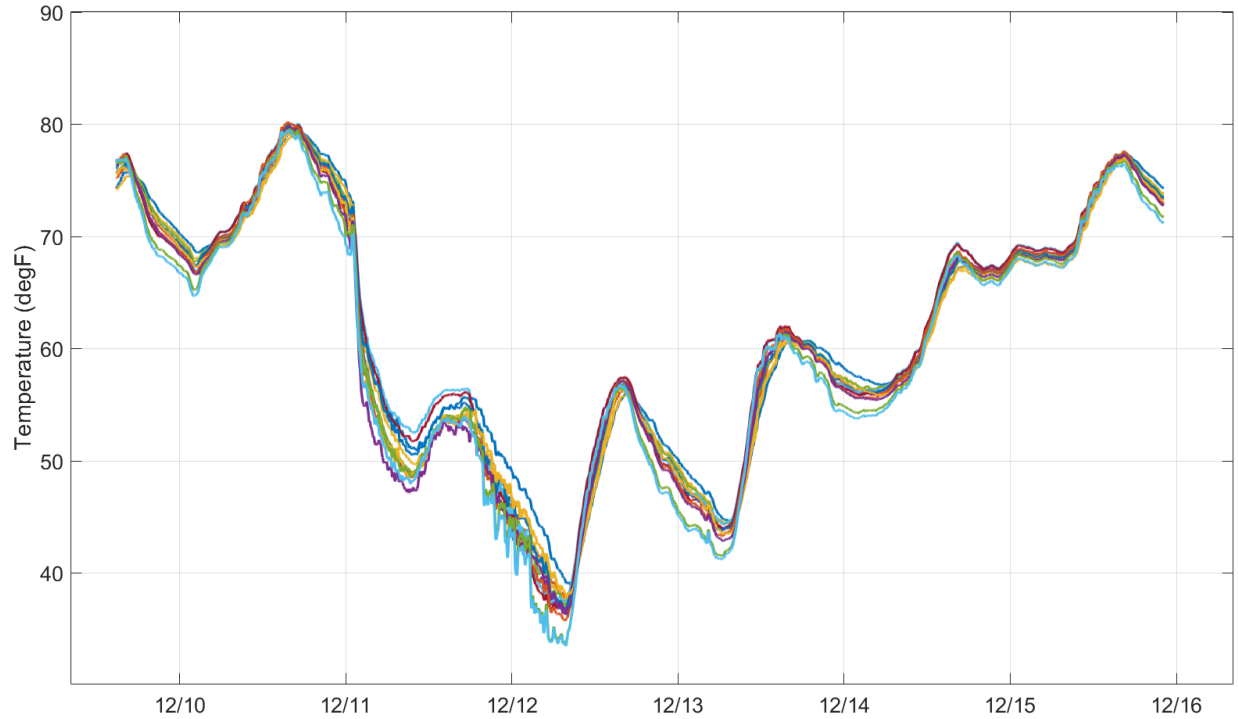


Figure 3.13. Temperature Measurements from All Sensors.

The live load behavior was captured through triggered truck events¹ that recorded the displacement and strain data at 50Hz. Hundreds of relatively heavy trucks were recorded. However, the critical event was a back-to-back truck scenario since it produced the largest response at the pier. Figure 3.14 provides the strain gauge time history at midspan, which shows two large peaks (roughly 160 microstrain) that represent the back-to-back trucks. Other truck events, up to 250 microstrain, were recorded but are not presented herein since they yielded less response at the pier than the back-to-back event.

¹ The midspan bottom flange strain gauge was used to trigger truck events using a threshold of 50 microstrain.

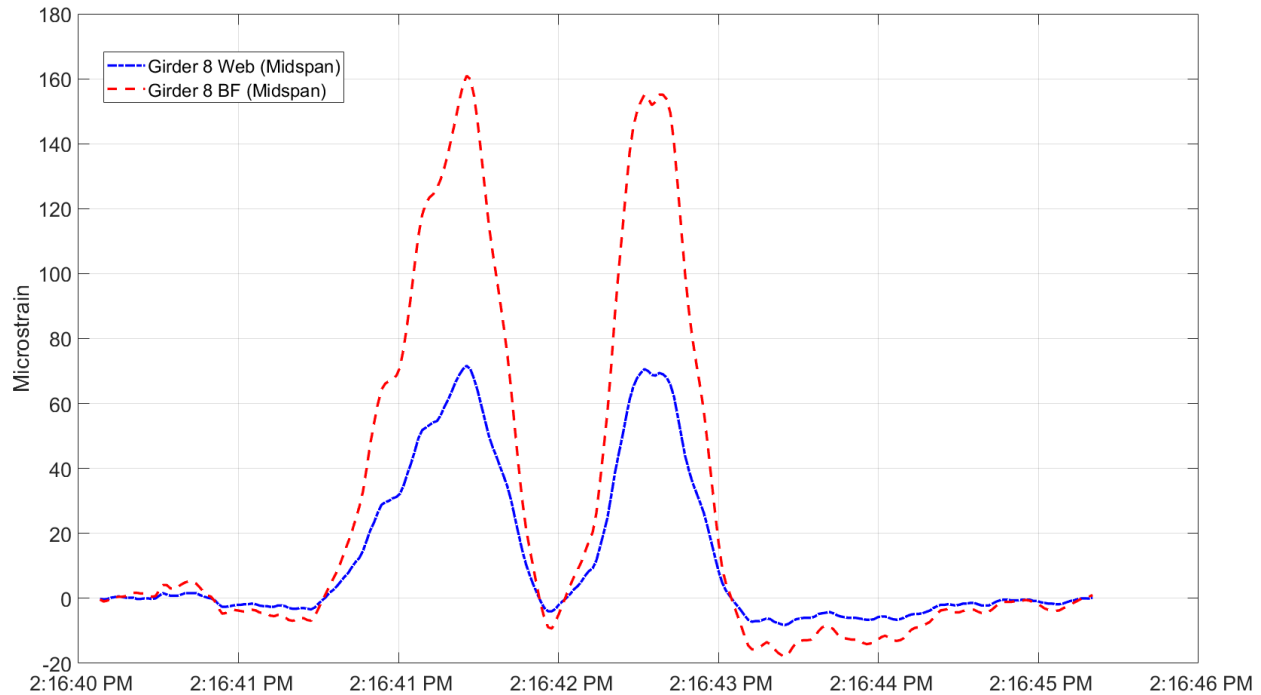


Figure 3.14. Midspan Strain Gauge Measurements for the Recorded Back-to-Back Truck Event Producing the Largest Response at the Pier Bent.

The rotation at the girder ends was calculated from the relative longitudinal displacement measurements. The individual girder end rotations cannot be separated, so the average is provided. Figure 3.15 illustrates the average girder end rotations due to thermal variations. Overall, the vertical thermal gradient drives the girder end rotations and not the absolute temperature change. The average temperature shown in the plot provides insight into the thermal gradients through the slope in the data. The behavior of the interior girders (8 and 9) was relatively similar, producing roughly 7×10^{-4} radians of total girder end rotation. The exterior girder (10) produced higher rotations, up to nearly 1×10^{-3} radians. The exterior girder behavior is different due to the added stiffness of the rail, along with larger variations in temperature due to the exposed outside face of the girder.

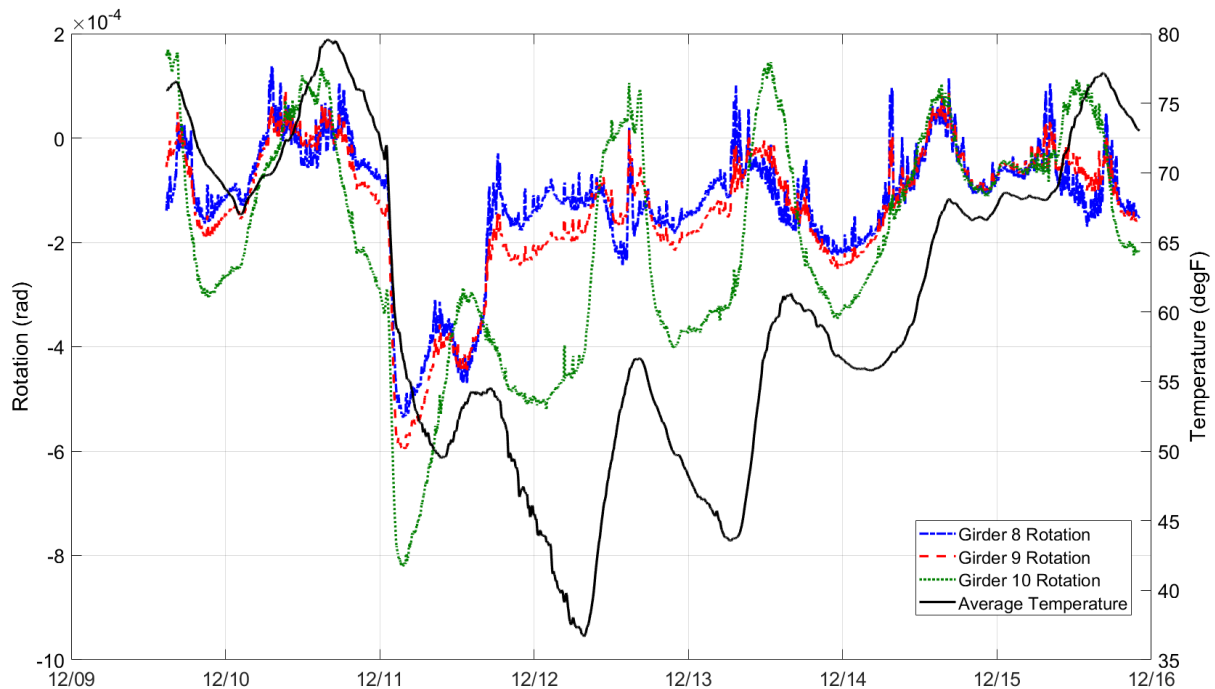


Figure 3.15. Average Girder End Rotations due to Thermal Variations (Positive Is When the Girders Are Concave Up).

The live load girder end rotations were calculated for the significant truckload events.

Figure 3.16 illustrates the rotations from the controlling back-to-back truckload event. The magnitude of response was more significant in Girder 8 due to the position of the girder with respect to the striped lanes. In this truck event, even the Girder 8 end rotation was roughly 1.3×10^{-3} radians, which is nearly double that of thermal demands. Of course, these demands should be combined when evaluating this region of the structure.

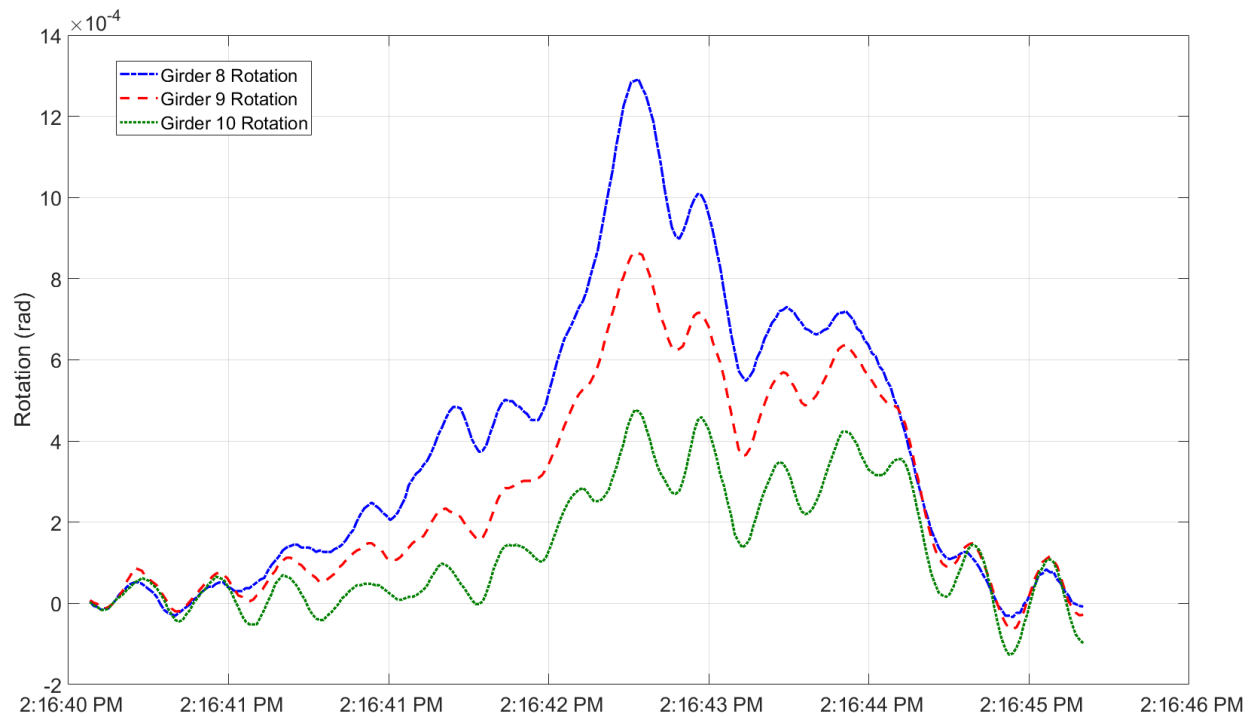


Figure 3.16. Average Girder End Rotations due to the Controlling Live Load Event (Positive Is When the Girders Are Concave Up).

An important performance metric for the deck at the piers is the magnitude of tension at the top surface. As mentioned earlier, the displacement gauge data were used to project a relative displacement at the top of the deck. Figure 3.17 illustrates the displacements at Girder 8. The deformation at the top surface was primarily compressive from thermal demands. However, the live load can induce relatively significant tension at the top of the slab, as shown in Figure 3.18.

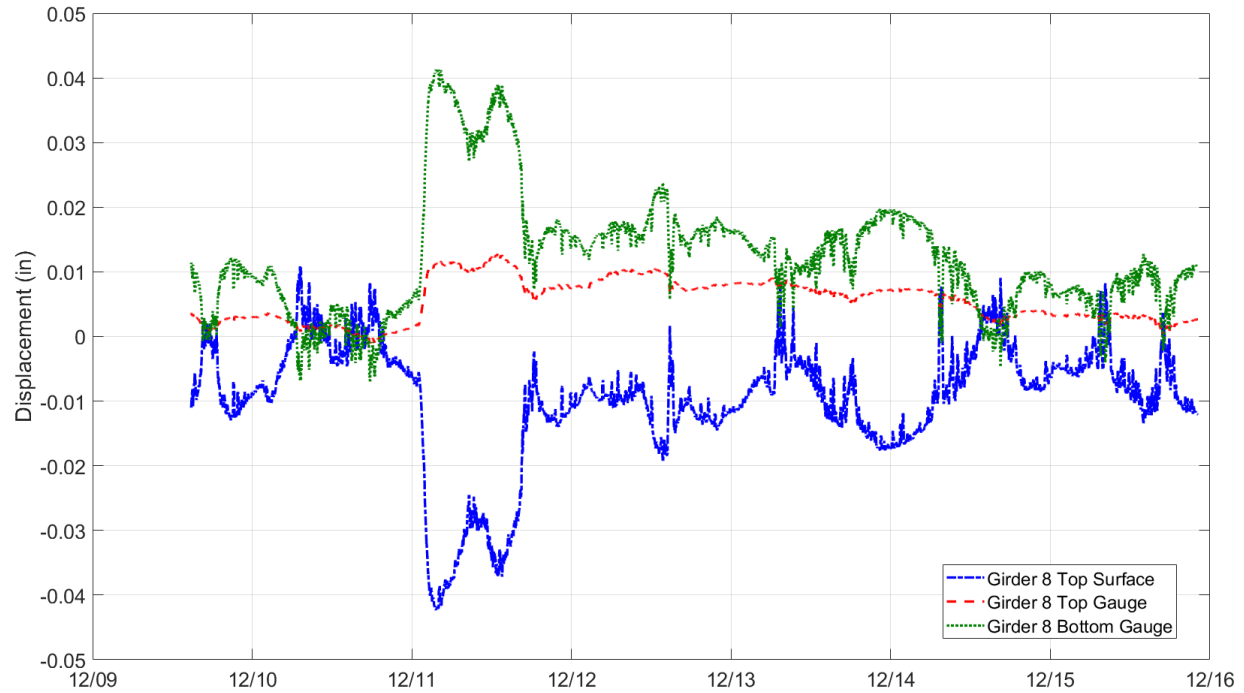


Figure 3.17. Relative Displacements at Girder 8 due to Thermal Variations.

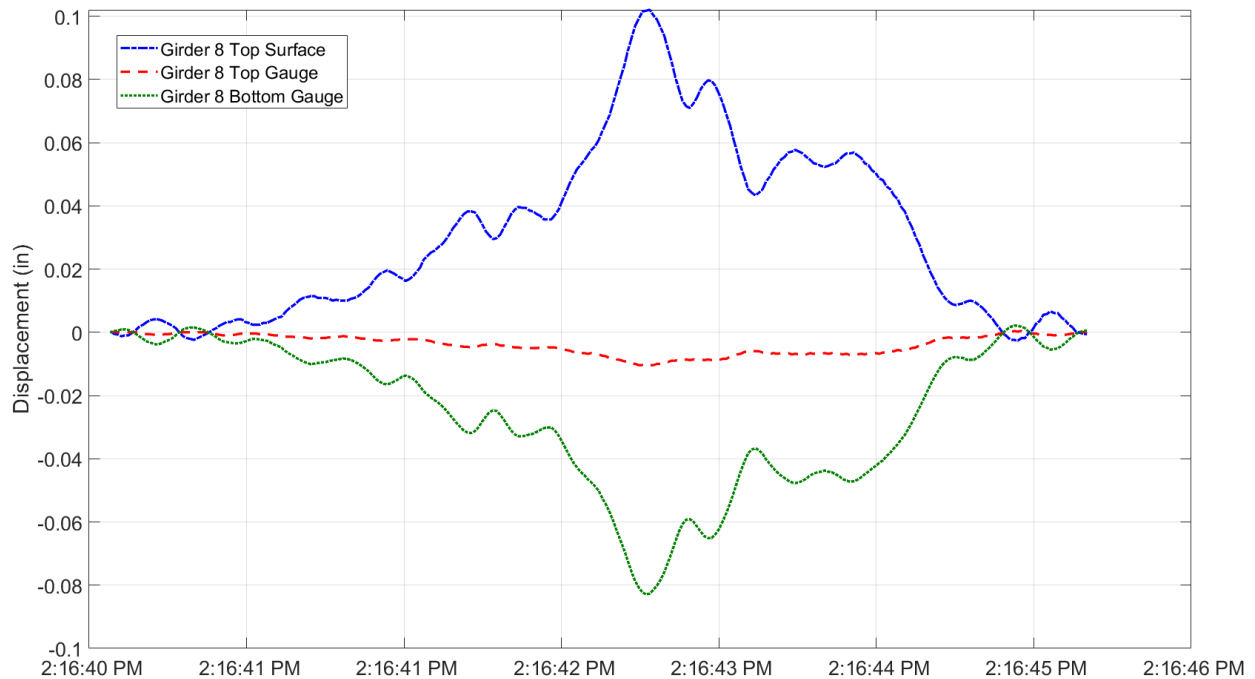


Figure 3.18. Relative Displacements at Girder 8 due to the Controlling Live Load Event.

The projected strains at the top of the slab were calculated for Girders 8, 9, and 10. As mentioned above, thermal variations primarily produced compression at the top of the deck with relatively low tension (see Figure 3.19). The live load stresses were typically well above the cracking

strain. Figure 3.20 illustrates the substantial strain (over 7,000 microstrain in Girder 8) at the top surface of the deck for all the instrumented girders.

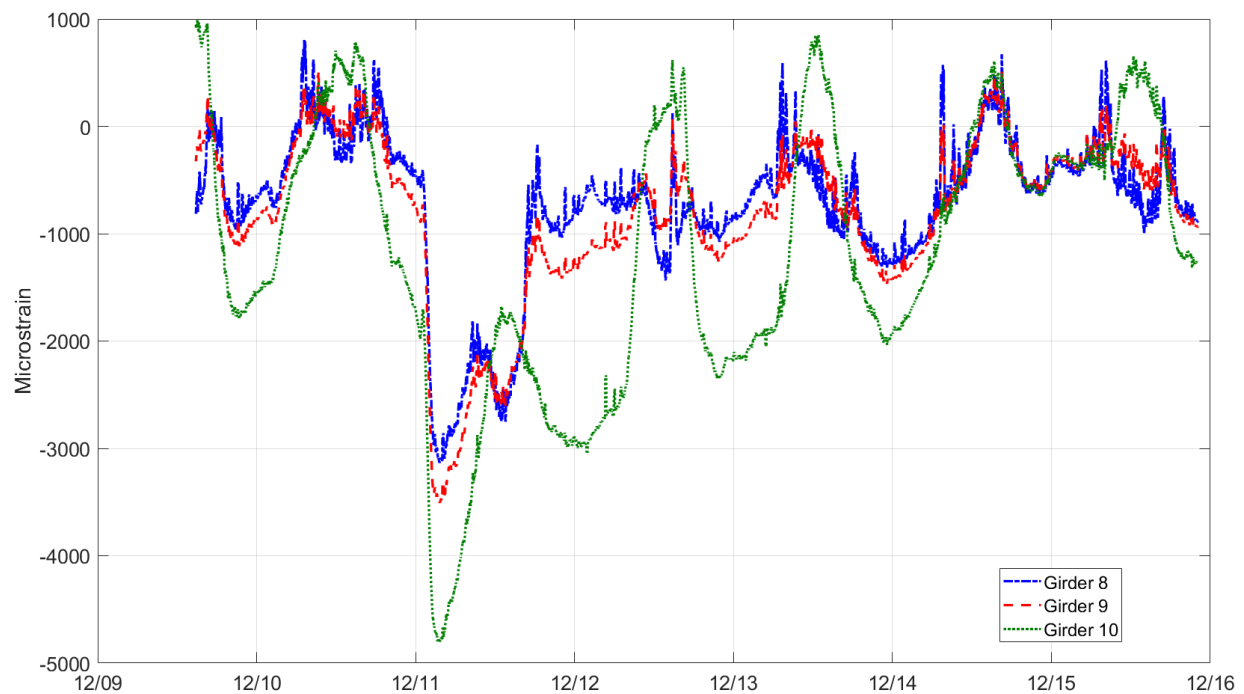


Figure 3.19. Projected Top of Slab Strains at Girders 8, 9, and 10 due to Thermal Variations.

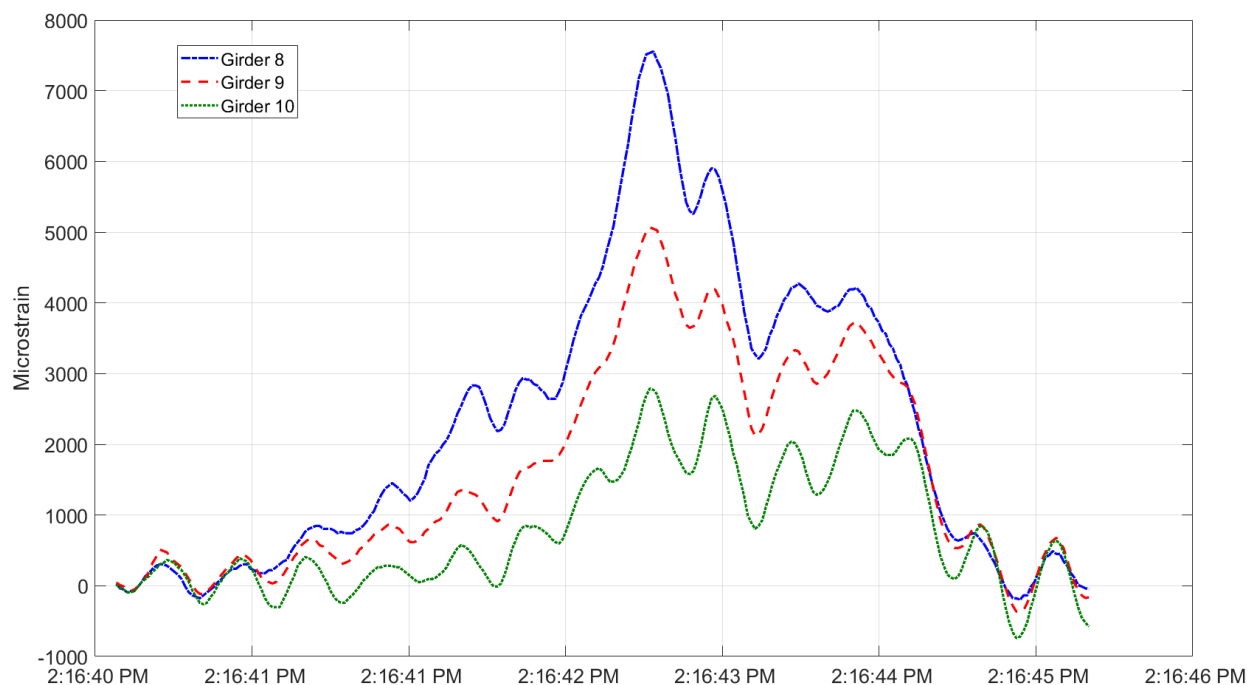


Figure 3.20. Projected Top of Slab Strains at Girders 8, 9, and 10 due to the Controlling Live Load Event.

For additional information, the girders were also instrumented near the pier bent (3 ft from the center of bearing) to observe the magnitude of negative bending. Figure 3.21 and Figure 3.22 show the measured strains along Girder 8 at the pier (Span 1 side) due to thermal variations and the controlling live load event, respectively. Overall, the magnitude of girder strains was relatively moderate (compared to positive bending strains), with a variation of around 40 microstrain (or 1.2 ksi in terms of stress) in both cases. This result is likely due to the relatively low stiffness of the bearings in their new condition. Over time, this strain might increase with an increase in bearing stiffness.

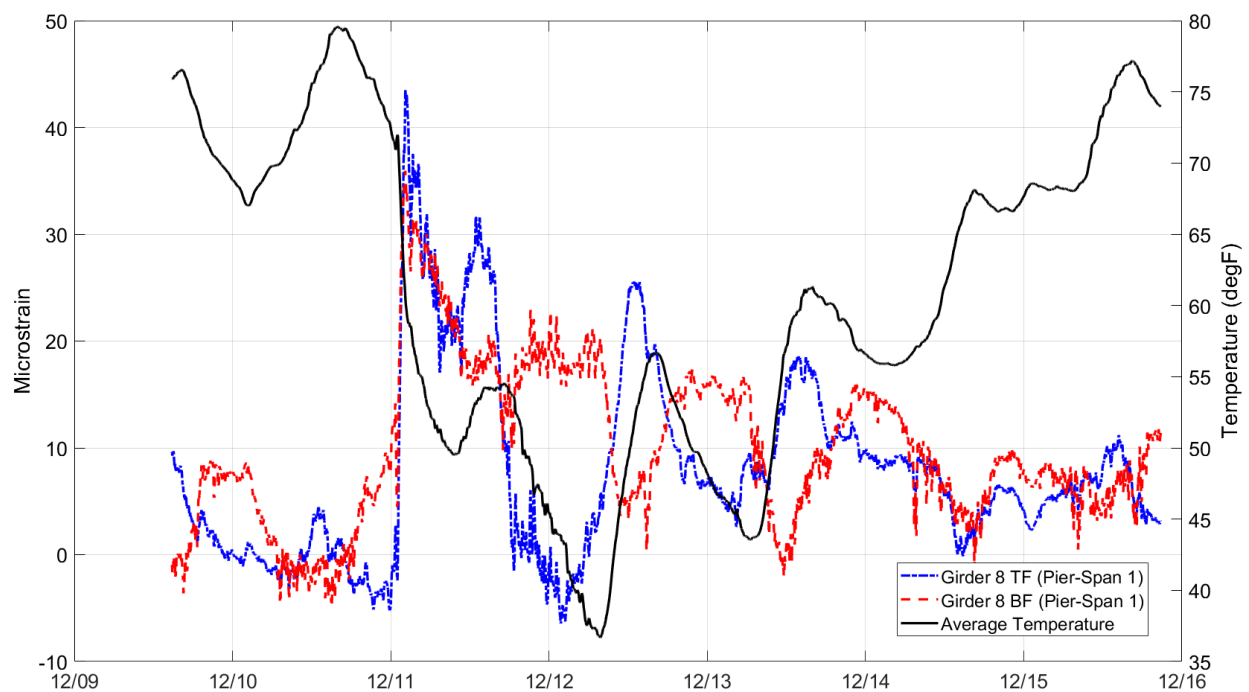


Figure 3.21. Girder 8 Strains at the Pier (Span 1 Side) due to Thermal Variations.

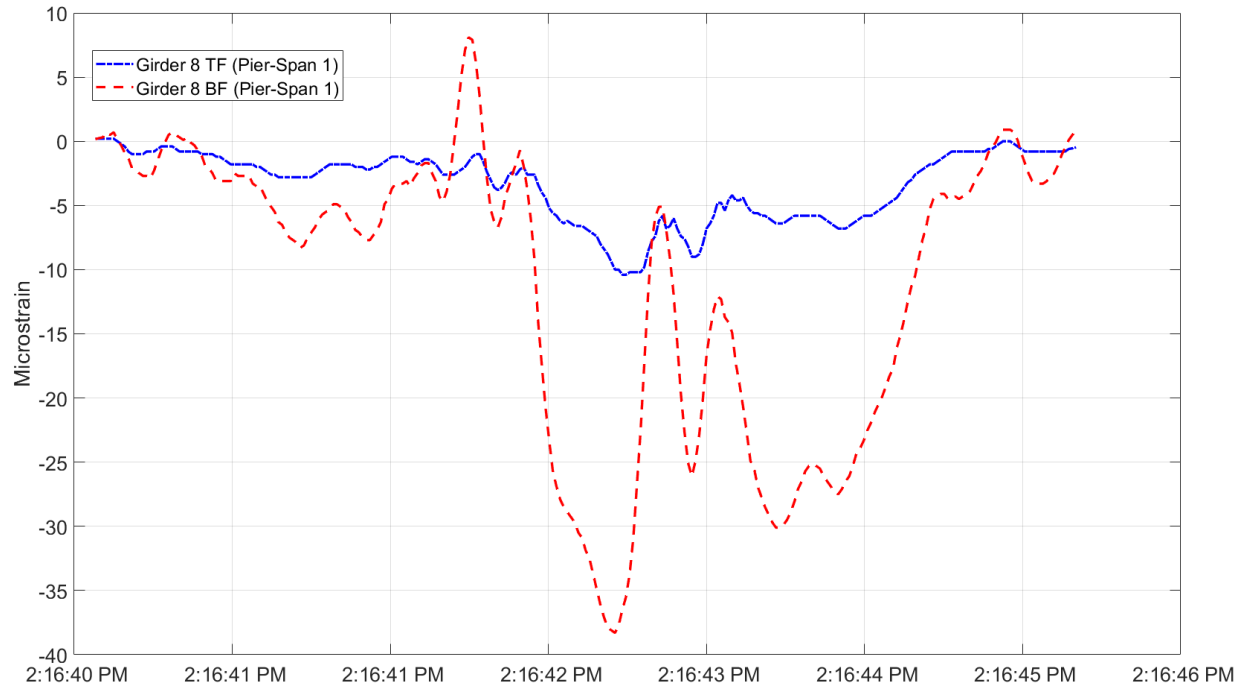


Figure 3.22. Girder 8 Strains at the Pier (Span 1 Side) due to the Controlling Live Load Event.

3.4. FIELD ASSESSMENT SUMMARY

In summary, the visual inspection identified the following long-term performance concerns:

- Cracking and efflorescence were present on the bottom and side surface at every overhang.
- Water was observed leaking through the deck slab at the pier bent location.
- The bottom surface of the slab between beams was not visible due to the timber formwork left in place. This apparatus might trap moisture from the water penetrating the deck and increase the rate of reinforcement corrosion.

The field monitoring of the girder end displacements/rotations, strains, and temperature variations revealed the following:

- The magnitude of girder end rotational demands from thermal variations and live loading were captured and later compared to future experimental testing and numerical modeling.
- Back-to-back truck events produced tensile strains in the top surface of the deck slab well above the cracking strain.

4. SYSTEM DEVELOPMENT

4.1. OVERVIEW

This section presents a comprehensive effort by the research team to identify promising connection concepts for making steel girder bridges continuous for live load while using ABC. This effort began with the development of six preliminary system concepts. These concepts were developed utilizing the information learned in the earlier literature review, along with unique ideas from the research team members. In parallel with this effort, an IRP was assembled. Next, a full-day workshop was designed and executed to elicit expert feedback from TxDOT Panel and industry panel. The information was utilized for the selection of the final system designs that were used for full-scale experimental tests.

4.2. PRELIMINARY SYSTEM CONCEPTS

The research team developed preliminary concepts for prefabricated steel ABC connection details continuous for live load. These connections details are intended to be easy to fabricate, fast to assemble, durable long-term (minimizing cracking), safe, and cost-effective (near-term and long-term).

For any steel ABC connection detail at the pier bent location, there are three main areas of focus: the deck slab, the top of the girder, and the bottom of the girder. The deck slab and the top of the girder are typically subjected to relatively significant tensile force demands from superimposed loads. Conversely, the bottom of the girder is subjected to relatively substantial compression force demands. An array of options exists for these three areas of the connection, which need to adequately transfer these forces while balancing the objectives mentioned above. Figure 4.1 illustrates the alternatives considered for each area.

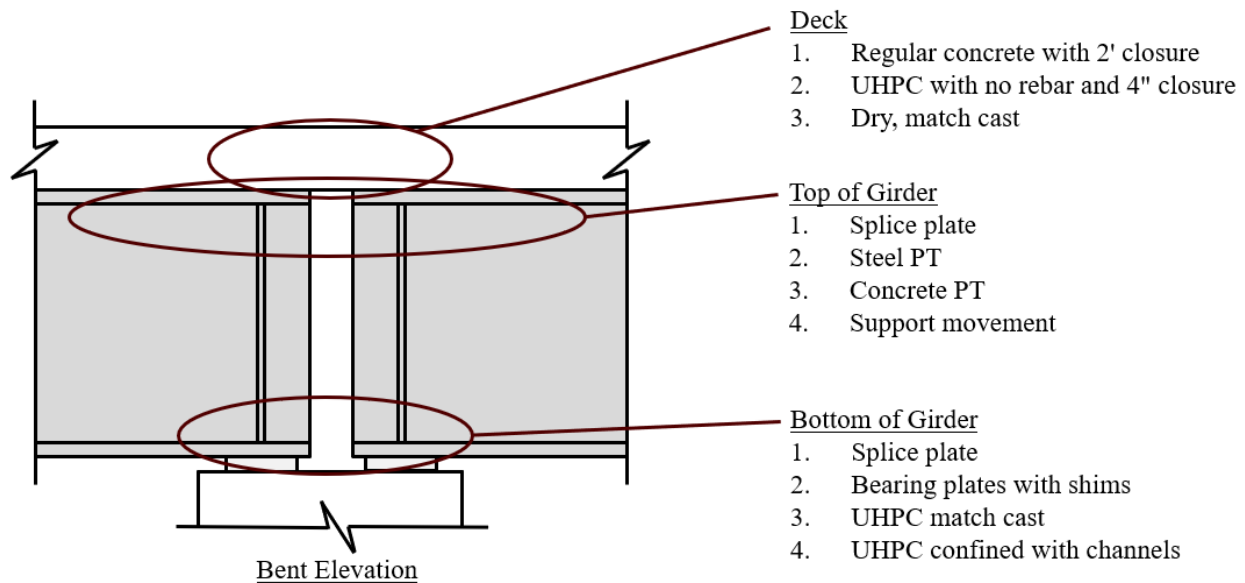


Figure 4.1. Areas of Focus for the Steel ABC Connection.

Six combinations of the details shown in Figure 4.1 were selected for consideration. In order to develop preliminary drawings and renderings of the connection details, a prototype bridge was selected. The structure was three-span continuous, with 60, 80, and 60 ft span lengths. The TxDOT standard bridge designs were utilized, which yielded W33×201 beams spaced at 7 ft (see Figure 4.2). The ABC technique considered was to prefabricate two-beam units with a precast concrete deck slab. These prefabricated units could be assembled rapidly on-site.

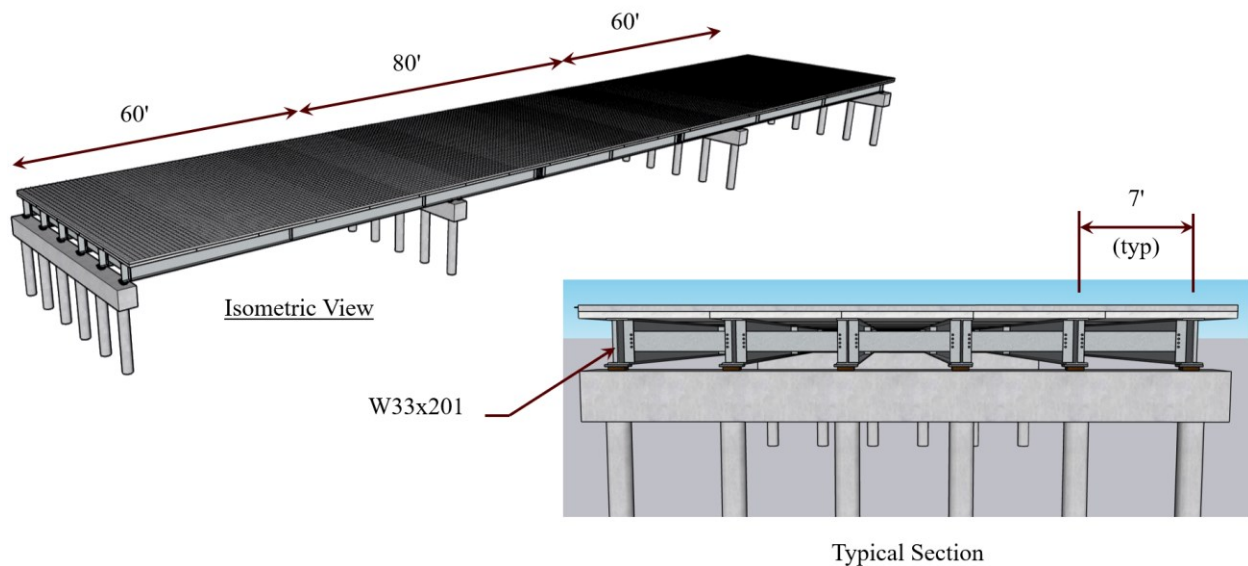


Figure 4.2. Rendering of the Prototype Bridge.

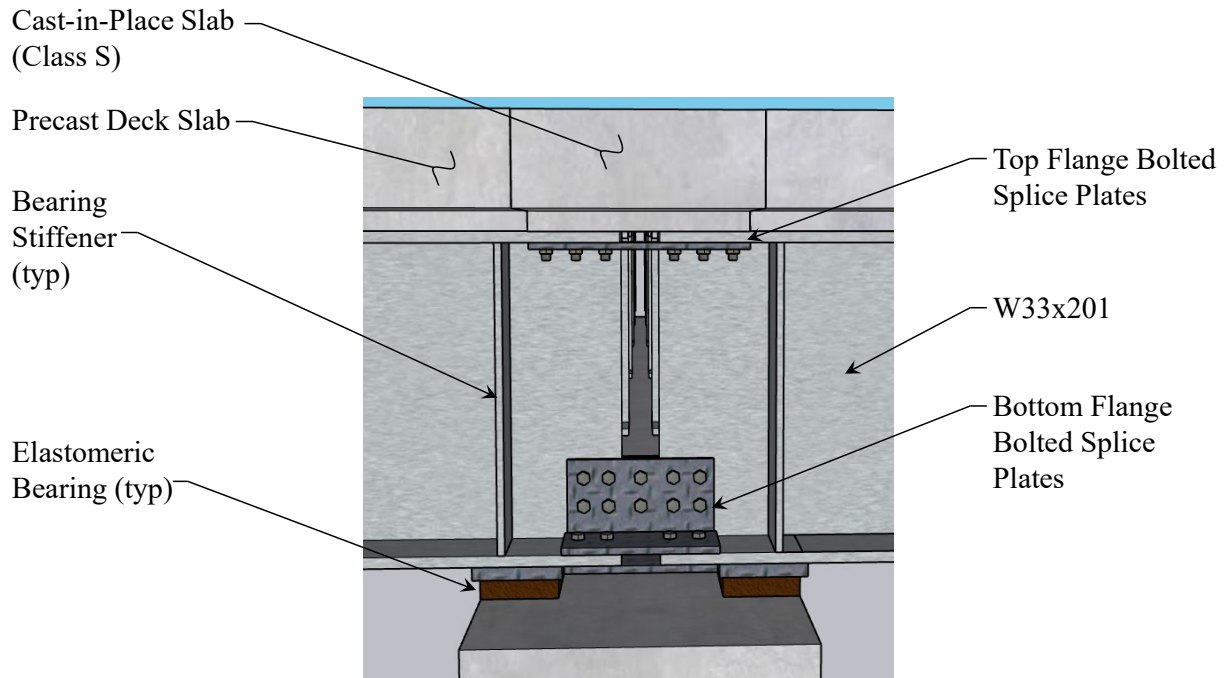
The following subsections present each of the six preliminary concepts. The renderings and details shown are relatively high-level and are based on preliminary calculations. The advantages and disadvantages of each concept are discussed in the workshop section. Also, note that detailed calculations and structural drawings were developed in the next task for the concepts selected for full-scale testing.

4.2.1. Concept #1

The first concept is a passive approach similar to a conventional steel girder splice. The primary details include the following:

- Deck: conventional concrete CIP closure.
- Top of girder: bolted flange splice plates.
- Bottom of girder: bolted flange splice plates.

Figure 4.3 provides a rendering of the final detail. Additional details to note are the bolt hole fabrication. Due to potential fit-up issues, it is anticipated that the splice plates will have shop holes, but the flange holes will be field drilled. In addition, some locations will utilize oversize or slotted holes.



Bent Elevation

Figure 4.3. Concept #1.

4.2.2. Concept #2

The second concept is an active approach intended to eliminate deck cracking and allow for long-term maintenance. The primary details include the following:

- Deck: UHPC.
- Top of girder: PT bars.
- Bottom of girder: steel bearing plates and shims.

Figure 4.4 provides a rendering of the final detail. Additional details to note are that the UHPC closure is not reinforced and is relatively narrow (3 to 4 inches). Reinforcement is not required due to the active compressive force applied by the PT bars. In addition, UHPC has a relatively high tensile strength. The steel bearing plates are to be shop-welded, and the shims are to be applied in the field to accommodate fit-up constraints.

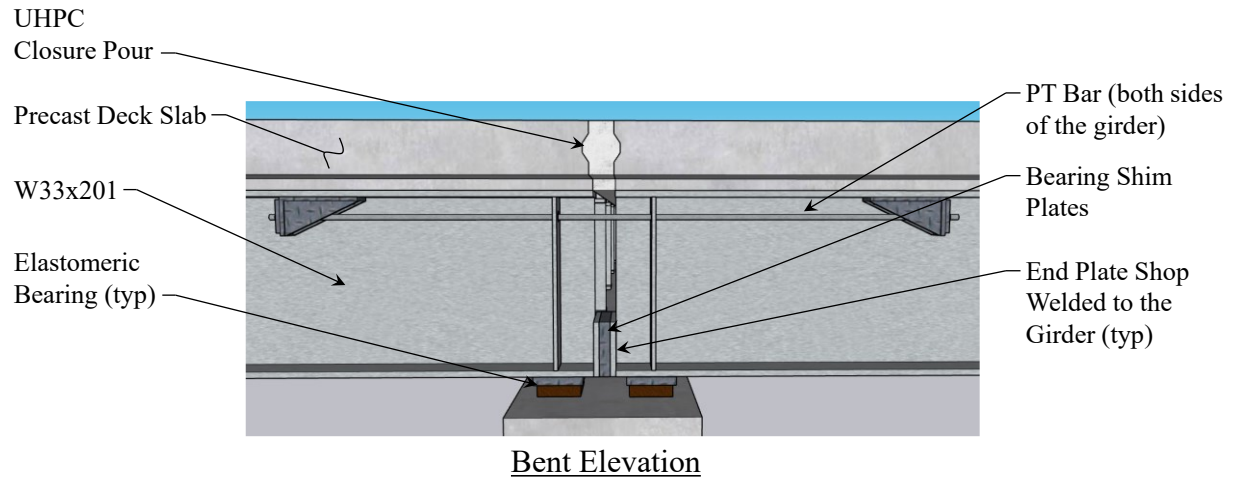


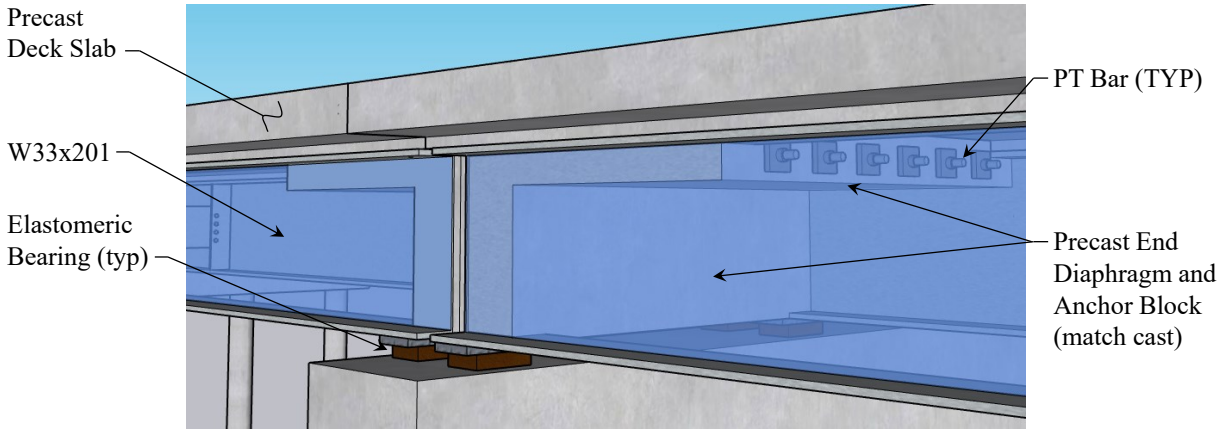
Figure 4.4. Concept #2.

4.2.3. Concept #3

The third concept is an active approach intended to eliminate deck cracking and further increase the speed of construction. The primary details include the following:

- Deck: conventional concrete match cast.
- Top of girder: PT bars.
- Bottom of girder: concrete bearing.

Figure 4.5 provides a rendering of the final detail. The web of the girders is transparent to show the details between the girders. Additional details to note are that this connection is related to segmental concrete box girder bridges. The units can be match cast to improve fit-up during final assembly. A thickened deck section (or anchor block) is provided for the embedded PT bars between the girders.



Bent Isometric View

Figure 4.5. Concept #3.

4.2.4. Concept #4

The fourth concept is an active approach intended to eliminate deck cracking and allow for long-term maintenance (relatively similar to Concept #2). The primary details include the following:

- Deck: conventional concrete CIP closure.
- Top of girder: PT bars.
- Bottom of girder: confined UHPC.

Figure 4.6 provides a rendering of the final detail. Additional details to note are that the deck slab and PT bar assembly are similar to Concept #1 and Concept #2, respectively. The bottom of the girders has end plates that are shop-welded in a C-shape to create a compression zone for confined UHPC. The UHPC is to be poured in the field.

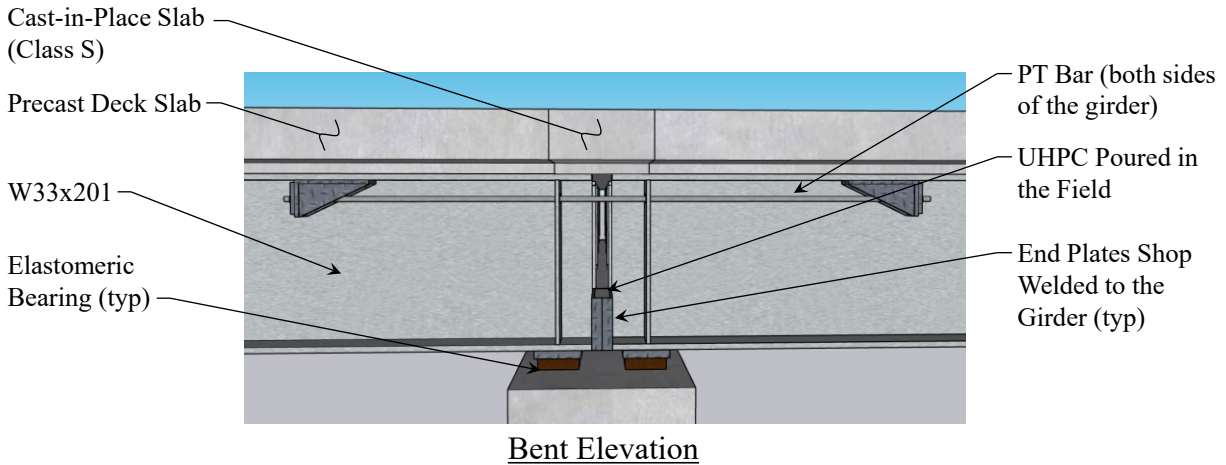


Figure 4.6. Concept #4.

4.2.5. Concept #5

The fifth concept is an active approach intended to eliminate deck cracking and further increase the speed of construction. The primary details include the following:

- Deck: conventional concrete match cast.
- Top of girder: PT bars.
- Bottom of girder: PT bars.

Figure 4.7 provides a rendering of the final detail. Additional details to note are that the deck slab is to be precast for speed and match cast to avoid fit-up issues during assembly. PT bars are included along the top of the girder, similar to earlier concepts. However, PT bars are also included at the bottom of the girder with the brackets reversed. The intent is to provide a force coupling that induces positive bending, which combats the negative bending from live loading.

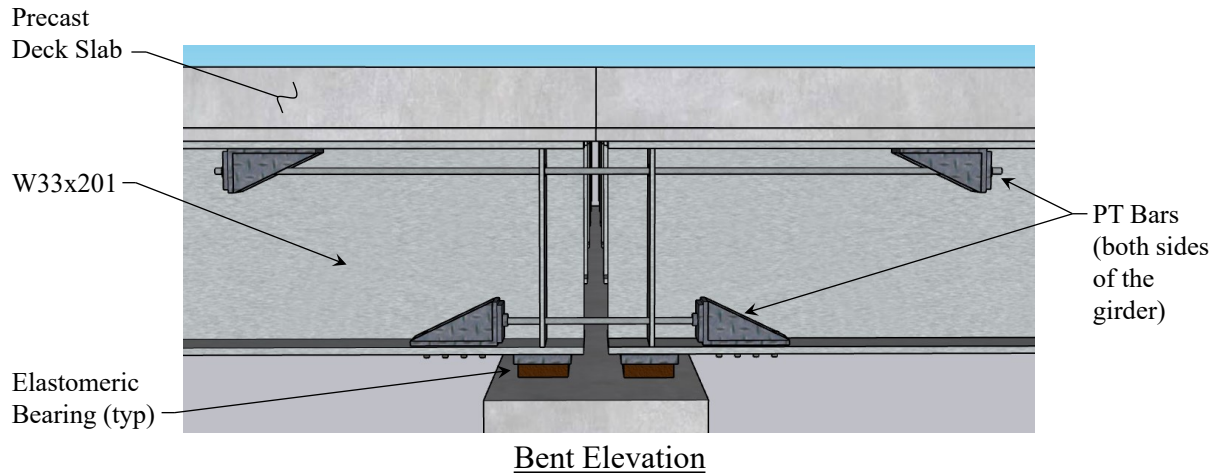


Figure 4.7. Concept #5.

4.2.6. Concept #6

The final concept is an active approach similar to Concept #2 but that includes support movement to reduce deck cracking. The primary details include the following:

- Deck: UHPC (with further compression from support movement).
- Top of girder: PT bars.
- Bottom of girder: steel bearing plates and shims.

The rendering of the final detail in elevation is the same as Concept #2 (Figure 4.4). However, a unique construction sequence is included in Concept #6. The ends of the girders are raised with hydraulic jacks, as shown in Figure 4.8. Then the UHPC closure pour is made for the deck slab. After sufficient strength gain in the closure, the ends of the girders are lowered, which induces a precompression force to the deck slab that reduces deck cracking from superimposed loads.

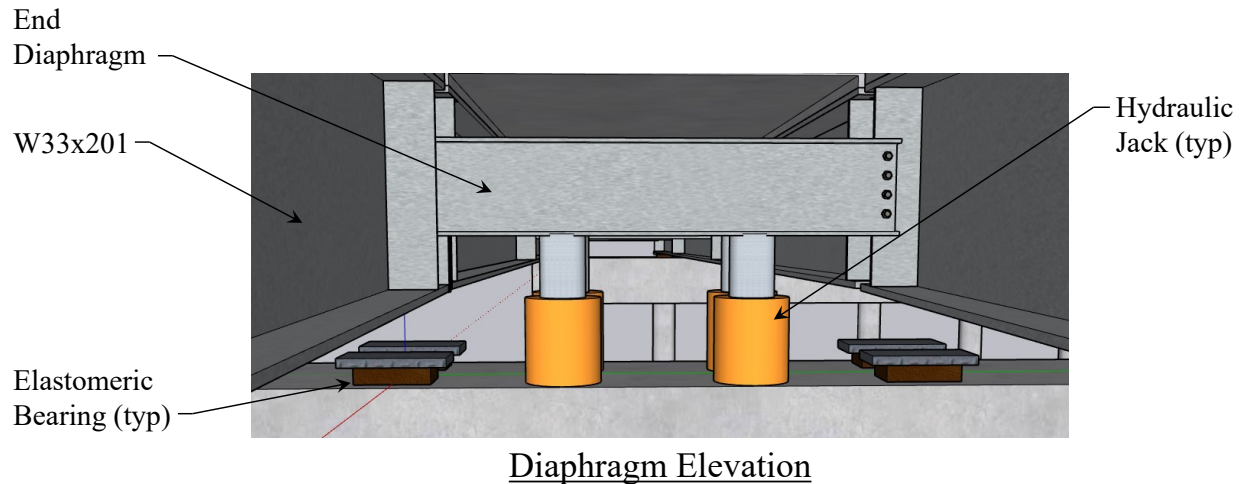


Figure 4.8. Concept #6.

4.3. WORKSHOP

4.3.1. Workshop Objective

The overarching objective of the workshop was to elicit TxDOT panel and industry feedback on a variety of concepts for prefabricated steel ABC girder units constructed continuously for live load. Section 4.2 provided an overview of all six concepts considered (Figure 4.9).

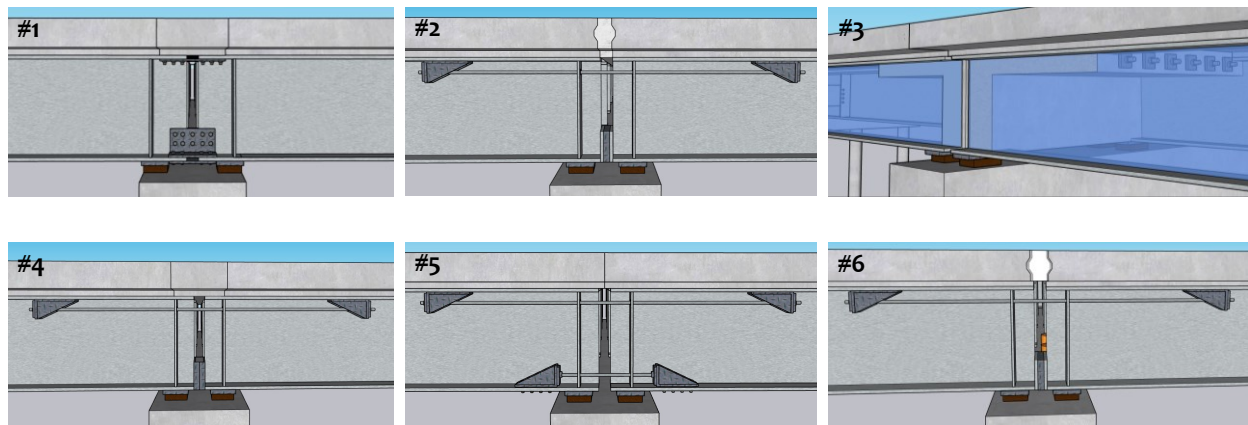


Figure 4.9. Overview of the Workshop Concepts Evaluated.

The emphasis of the workshop was on constructability, speed of assembly, long-term durability, safety, and cost. The target outcome was to obtain sufficient quantitative and qualitative expert input to select three to four connection details for full-scale testing in the laboratory. To achieve this objective, the workshop was designed in a specific manner, as described in the next section.

4.3.2. Workshop Design

A 6-hour, hybrid format (in-person and virtual) workshop was designed to achieve the stated objective. The workshop needed to be well organized and efficient to elicit many opinions in a relatively limited amount of time. The primary agenda was as follows:

1. Workshop introduction and timeline.
2. Overview presentation.
3. Reference connection detail.
4. Connection evaluations (six cycles).
5. Ideation session.
6. Final evaluation.

The first agenda item (workshop introduction and timeline) was essentially how it sounds. The panel members were introduced, and the overall timeline of the workshop was presented. The second agenda item (overview presentation) was a critical item. This item covered background/motivation for the research project, the project objectives, the scope of the study, the objective of the workshop itself, and illustrations of all connection details at a high level.

The third agenda item was to provide the panel with a reference connection detail so they had some context for future numerical scoring. The reference connection was a detail developed at the University of Nebraska and furthered at Florida International University [1]. This connection includes prefabricated steel end plates, cap beam stirrups (dowel bars) over the cap beam, deck longitudinal bars in deck slab, and steel bearing blocks at the bottom of the girders [14, 23]. A rebar cage is provided, and the connection is fully cast in concrete. Figure 4.10 shows a rendering of the connection.

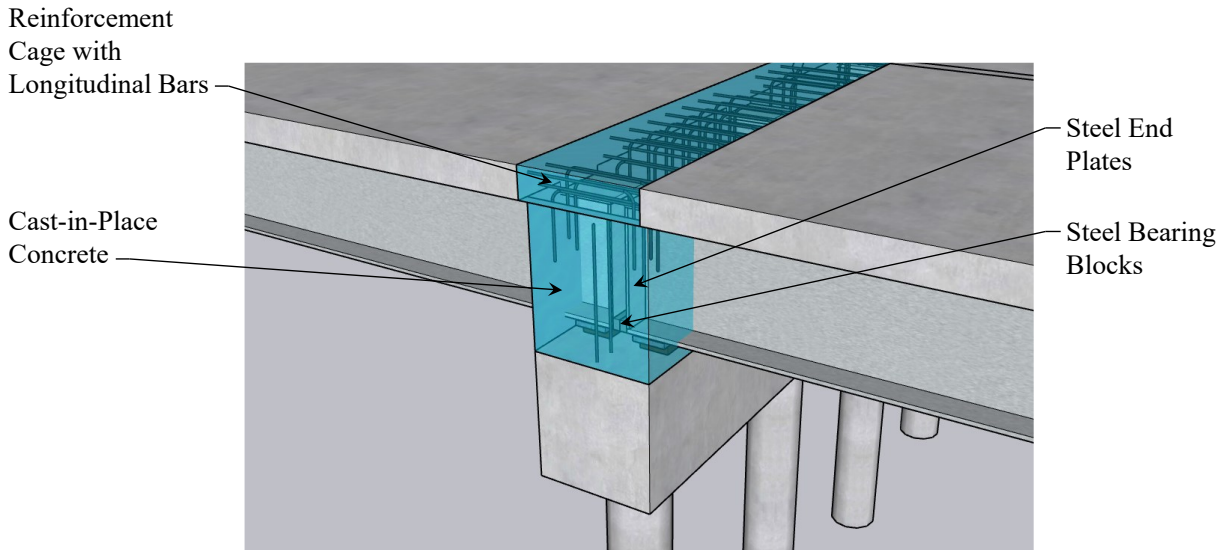


Figure 4.10. Workshop Reference Concept.

The second objective of this item was to familiarize the panel members with the evaluation cycle that would be used for the remainder of the day. The evaluation cycle was 30 minutes and included the following:

1. Brief presentation of the connection (two-dimensional and three-dimensional [3D] fly-through animations) (3 minutes).
2. Individual time to evaluate/document via a Google Forms (2 minutes).
3. Rotating discussion (15 minutes).
4. Open group discussion (5 minutes).
5. Further evaluation via Google Forms (5 minutes).

The purpose of the evaluation before and after the discussion was to obtain unbiased information and then refine information using colleague input. This evaluation process was then used six additional times for the fourth agenda item (connection evaluations). In each case, the full 30 minutes were allotted. In addition, the fifth agenda item (ideation session) was included to allow the panel to create their own connection detail in the event the research team did not include something that should be considered. Overall, the IRP did not propose a different connection detail that made the girders continuous for live load. The consensus was to compare a link slab alternative to the proposed concepts. Finally, the last agenda item (final evaluation) asked the panel members more questions via the Google Form. These questions compared the different connection details among each other.

4.3.3. Workshop Industry Review Panel and TxDOT Panel

The research team assembled an IRP comprised of individuals highly experienced in ABC, steel bridges, and related fields. The primary purpose of the IRP was to provide insight into the concepts discussed above. The TxDOT representatives (seven total) were internally selected from across the organization. Eight industry expert panel members were intentionally assembled to obtain a cross section of the steel bridge community. The industry member subdisciplines include:

- Designers (2).
- Fabricator/erector (2).
- General contractor (1).
- Railroad bridge engineer (1).
- Structural steel detailer (1).
- Trade organization member (1).

The TxDOT Panel included nine TxDOT Project Monitoring Committee members.

4.3.4. Workshop Results

The IRP workshop evaluation form asked the same questions for each concept. In summary, the questions included:

- What are your initial thoughts about this connection concept design?
- How do you score the connection—from poor (1) to high (5)—for the categories *ease of fabrication, ease/speed of assembly, structural performance, construction cost, and life cycle maintenance*?
- Do you have additional feedback?

The IRP survey results were helpful in the concept selection process. In addition, this input was utilized for the design of the full-scale specimens and the development of standard details and specifications.

The scoring results from each concept (second bullet point above) were utilized for final concept selections. Figure 4.11 shows a graphical summary of the results. This summary utilizes equal

weighting of the categories listed above. Interestingly, the TxDOT portion of the panel was relatively consistent with the industry panel members. Concept #3 was the clear preference, followed by Concepts #4 and #2, respectively. The figure provides a graphical ranking of the top concepts.

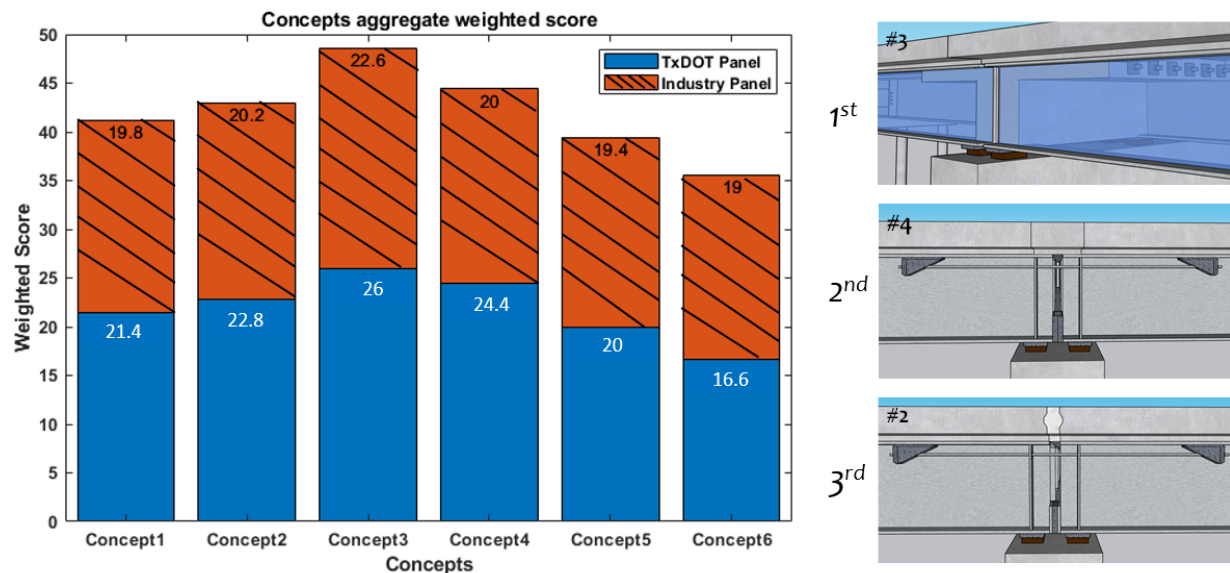


Figure 4.11. Aggregate Equally Weighted Scoring Results during the Workshop.

The latter portion of the IRP evaluation form asked for additional input. The intention was to elicit feedback once the panel was familiar with all concepts. The evaluation form asked for the following (with a request for written justification):

- Overall rankings of the concepts.
- Rankings of the deck connections.
- Rankings of the top of girder connections.
- Rankings of the bottom of girder connections.

The overall rankings produced different results than the prior rankings. Figure 4.12 shows the detailed results. Essentially, Concept #1 jumped to the top of the list, pushing Concepts #3 and #4 to the second and third priority, respectively. Concept #2 was very close as well. Concepts #5 and #6 yielded relatively low scores, essentially ruling them out of consideration. The theory for the preference of Concept #1, as revealed later in the workshop, is that individuals prefer the

more common splice detail when asked to make a final decision. However, this theory reflects present thinking, and with additional study and information, this view may change.

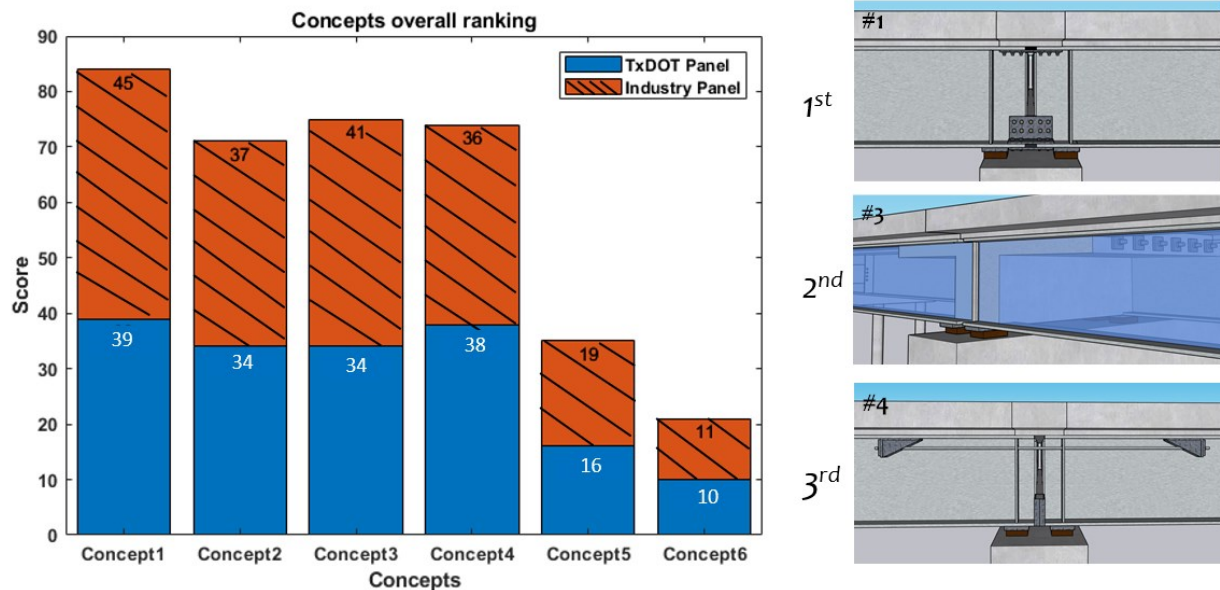


Figure 4.12. Overall Scoring Results at the End of the Workshop.

Ranking the individual connection components (deck, top of girder, and bottom of girder) also produced interesting results. Figure 4.13 graphically summarizes the findings.

The preferred deck connection was clearly conventional concrete, followed by UHPC, which was partly due to the current availability of and expertise with conventional concrete over UHPC. The gap will likely reduce over time. The least preferred deck connection was match cast, which was largely due to fit-up field concerns.

The preference for the top of the girder connection was less decisive. Conventional steel splice plates had the highest score, predominantly due to prior expertise and familiarity with steel splice plating. Interestingly, utilizing support movement to precompress the top of the girders was the second choice over PT alternatives.

The bottom of the girder connection essentially had three preferred choices and two not preferred. The three preferred choices were steel bearing plates with shims, splice plates, and confined UHPC. The panel did not like the idea of steel PT at the bottom of the girder or match-cast UHPC.

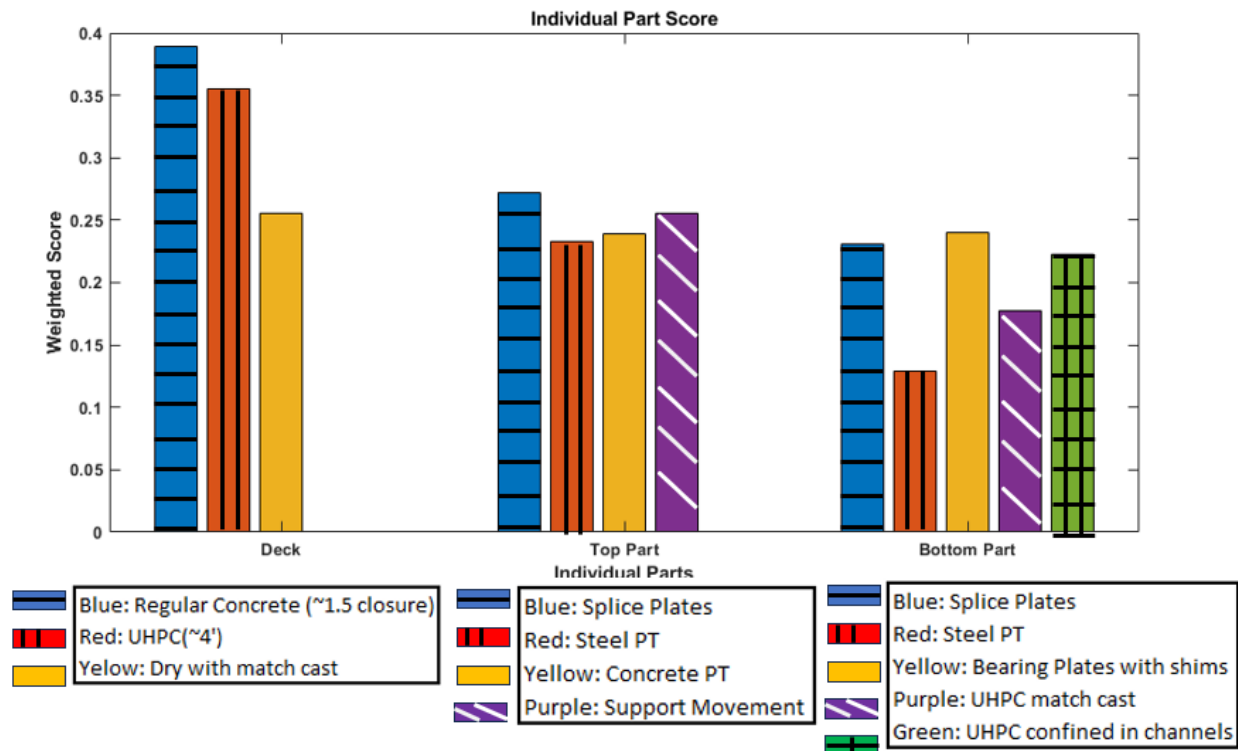


Figure 4.13. Individual Component Rankings at the End of the Workshop.

The written feedback on each concept was extensive. In addition to the Google Forms, detailed notes were taken from the discussions during the workshop. The panel highlighted the following main areas of focus:

- Large concern about the flexibility of the connection to allow sufficient tolerances for rapid field construction.
- UHPC concerns due to relatively high cost and mobilization. It was recommended that an appreciable amount be used if brought on-site.
- Drainage concerns were raised about the bottom of the girder details for fear the girders might experience long-term corrosion/performance issues.
- The appearance of the PT bars was raised as a concern since it may look like a retrofit.

Note that after the workshop, the materials were shared with other TxDOT construction personnel. Feedback was provided, and preference was given to Concepts #1, #2, and #4. One suggestion was to utilize UHPC for the deck and bottom of the girder or not at all. This feedback was utilized in the final system design selections provided in the following section.

4.3.5. System Design for Testing

As a result of the work from this task, four final connection concepts were selected. The order of preference was Concept #1, #4, #2, and #3 (see Section 4.2 for the original concepts). Concept #1 was the clear favorite due to its simplicity. Concept #3 ranked very high from the workshop but was downgraded in preference by the TxDOT construction group feedback. Concepts #4 and #2 ranked well, but the general feedback was that the minimal use of UHPC in each case was not cost-effective. Therefore, Concepts #4 and #2 were modified to switch their deck details. As a result, the final four concepts were relabeled from A to D to avoid confusion going forward in the project. Figure 4.14 illustrates the selected connection concepts for full-scale testing. Note that the scope of work includes four full-scale specimens for testing, which are Concepts A to D.

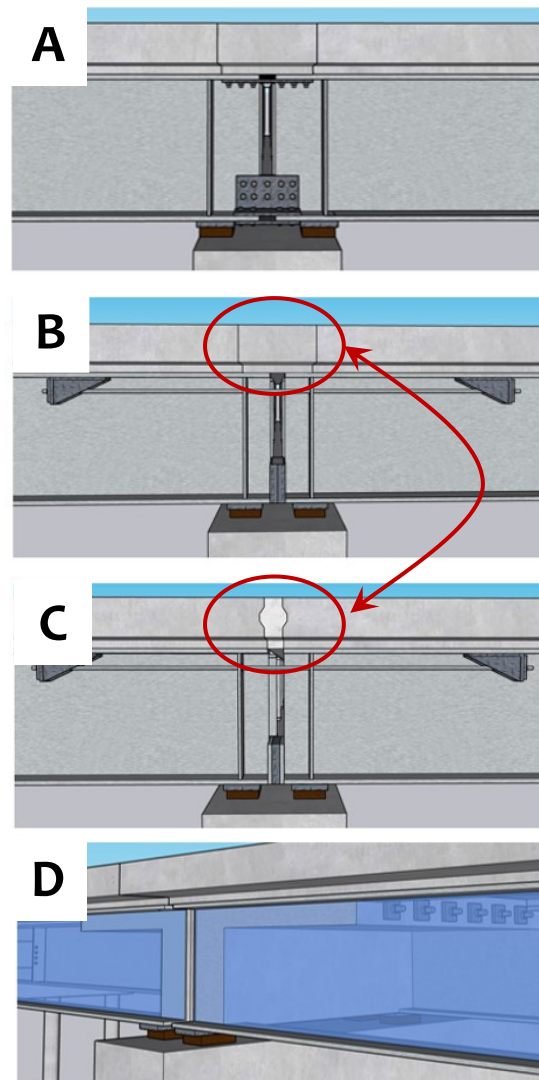


Figure 4.14. Selected Concepts for Full-Scale Testing.

5. LABORATORY TESTING

5.1. GENERAL

One of the project's main goals was to evaluate the structural performance of the connections selected from the workshop by full-scale laboratory testing. As mentioned in the prior section, the final four connection concepts were labeled A, B, C, and D. Concept A is a passive connection similar to a conventional steel splice connection. This detail includes a conventional concrete CIP closure and bolted flange splice plates for the top and bottom of the girder. Figure 5.1 provides a rendering of the Concept A connection.

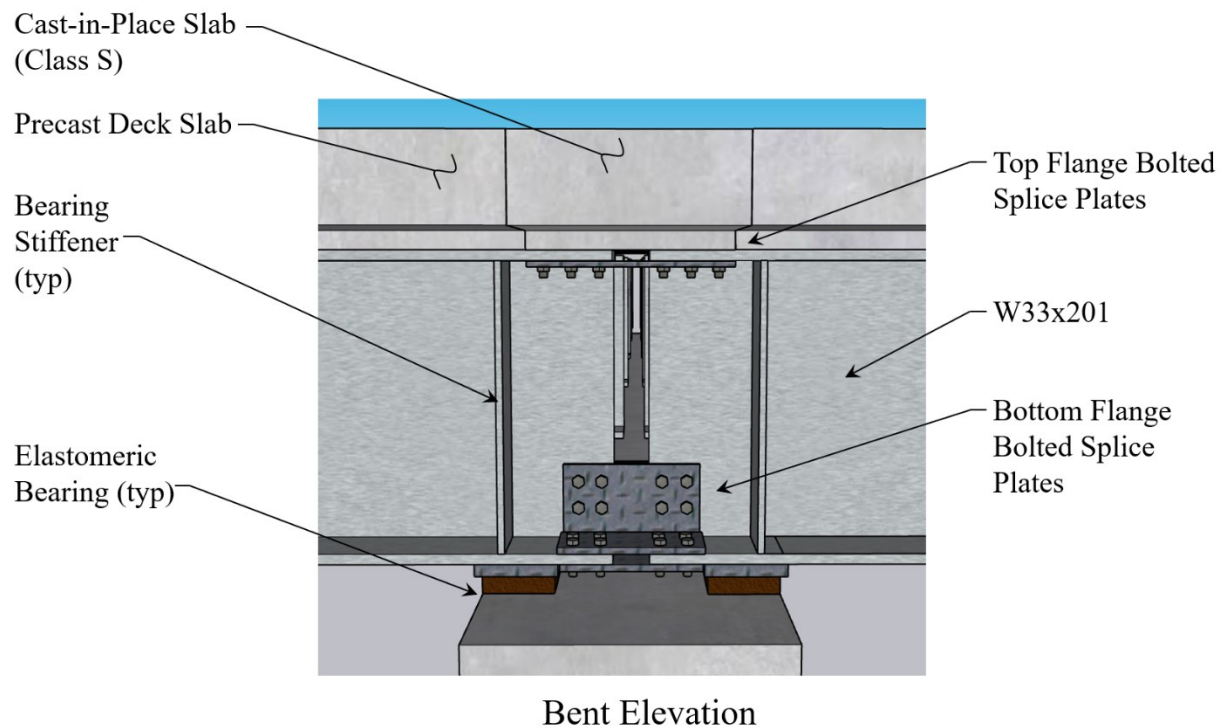


Figure 5.1. Concept A.

Concept B is an active connection in which the deck slab is precompressed. This detail consists of a UHPC CIP closure, Williams bars under the top flange of the girder, and a concrete bearing at the bottom of the girder. Figure 5.2 provides a rendering of the Concept B connection.

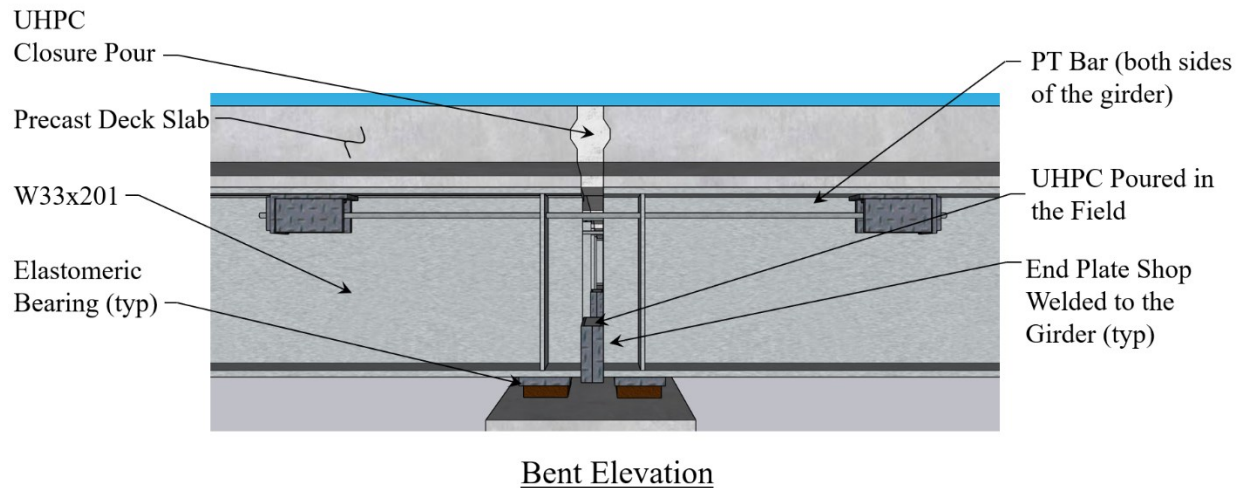


Figure 5.2. Concept B.

Concept C is also an active connection that is related to Concept B. However, this detail includes a conventional concrete CIP closure, Williams bars under the top flange of the girder, and steel bearing plates and shims at the bottom of the girder. Figure 5.3 provides a rendering of the Concept C connection.

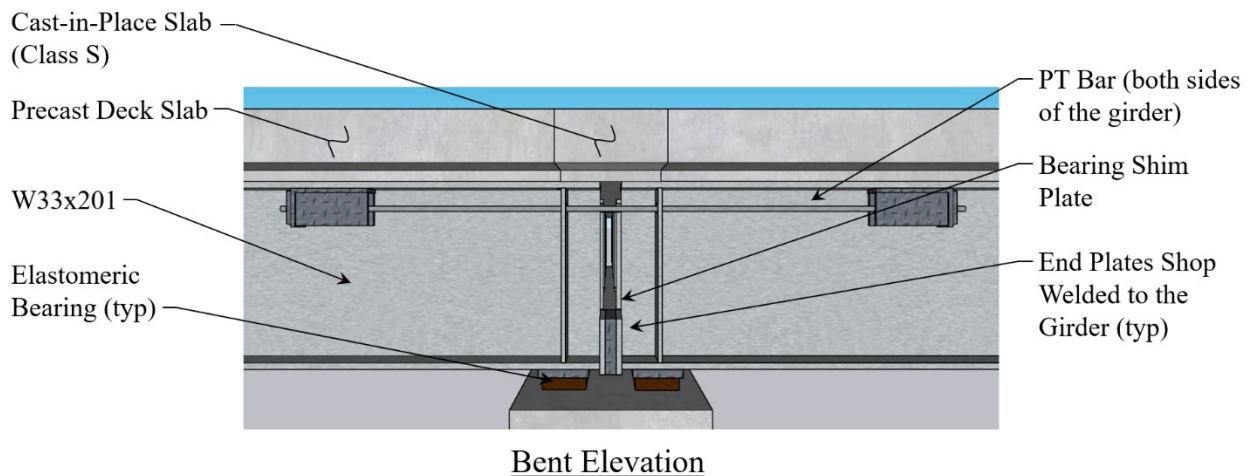
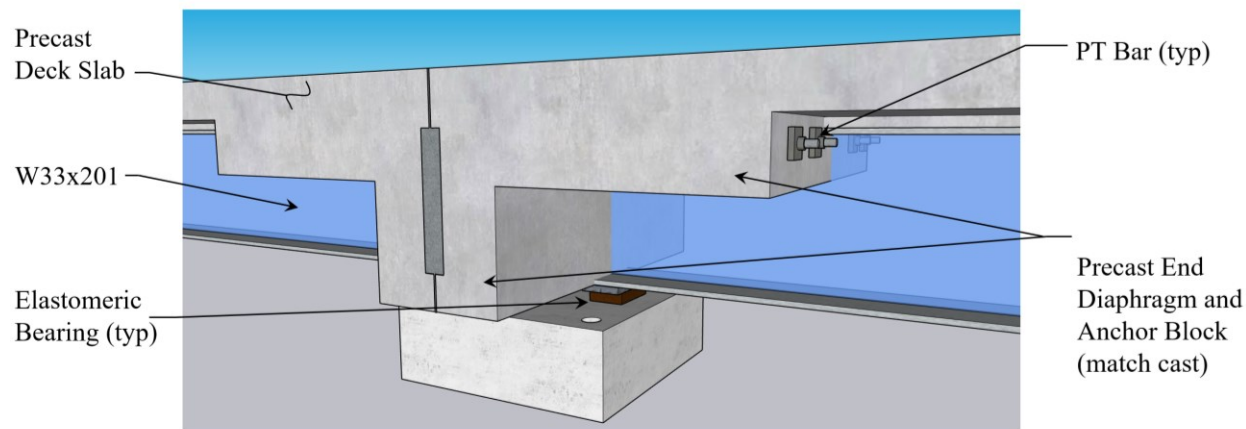


Figure 5.3. Concept C.

Concept D is also an active connection. This concept consists of four Williams bars fed through holes in a full reinforced concrete diaphragm that are post-tensioned to act as the tension-resisting element. The concrete diaphragm was formed on the bottom flange to allow concrete-on-concrete bearing for the compression element. Figure 5.4 provides a rendering of the Concept D connection.



Bent Isometric View

Figure 5.4. Concept D.

5.2. OVERVIEW

The following sections present the findings of the full-scale experimental testing for the development of continuous for live load prefabricated steel ABC. Section 5.3 details the benchmark bridge design, including the bridge configuration, limit states, etc. Section 5.4 presents the general experimental testing sequence taken for each of the concepts. Section 5.5 provides the preparations made for the prefabricated bridge units. Next, Section 5.6 conveys the material testing conducted on all the specimens. Sections, 5.7, 5.8, 5.9, and 5.10 introduce Specimens A, B, C, and D, respectively, along with their experimental testing. Section 5.11 describes the comparison between each concept. Section 5.12 gives a summary of the experimental testing.

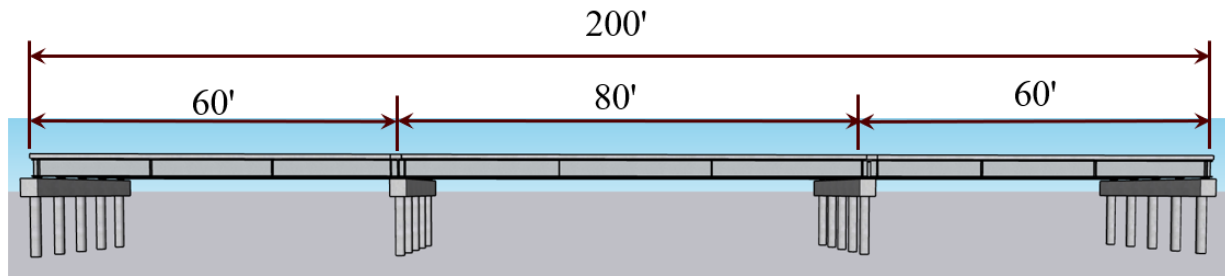
5.3. BENCHMARK BRIDGE DESIGN

A benchmark bridge was designed to ensure realistic component and connection details for the experimental program. Various span lengths and configurations were considered. Once these parameters were selected, a standard TxDOT steel bridge design was used as a basis for the benchmark bridge. In the following sections, the detailed benchmark bridge design is presented.

5.3.1. Bridge Geometry and Girder Cross Section

A three-span SDCL configuration was selected for the benchmark bridge. The center span length was 80 ft, with two end spans of 60 ft (75 percent of the center span). This design was

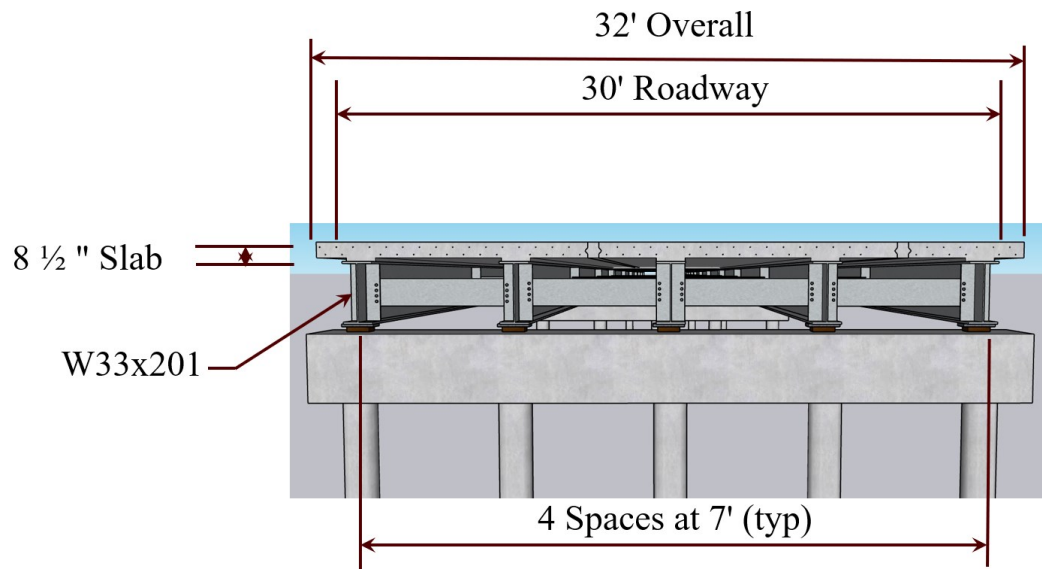
considered a reasonable configuration for the potential future application of ABC. Figure 5.5 presents an elevation view of the benchmark bridge. Note the bridge railing details are not included.



Elevation View

Figure 5.5. Rendering of the Three-Span Benchmark Bridge.

After the span lengths and configuration were set, a total bridge width of 32 ft was selected (28 ft roadway width). Next, the TxDOT standard bridge designs were utilized, which yielded six W33×201 beams spaced at 7 ft, with a 2 ft overhang on each side. The CIP deck was 8.5 inches thick (Class S concrete with a 4.0 ksi compressive strength) and designed to be a composite section with steel beams. Two design lanes were considered for the benchmark bridge design based on the *American Association of State Highway and Transportation Officials (AASHTO) LRFD Specifications* [24]. Figure 5.6 provides a rendering of the bridge cross section.



Typical Section

Figure 5.6. Rendering of the Transverse Bridge Section.

The details of the composite elastic section are shown in Figure 5.7. Also, Table 5.1 presents the composite elastic section properties for the W33×201 girder and concrete slab. The transverse spacing is 5 inches between shear studs. The longitudinal spacing—based on the TxDOT bridge standards—is 4 inches for the eight spaces at the end and 11 inches in the middle [25].

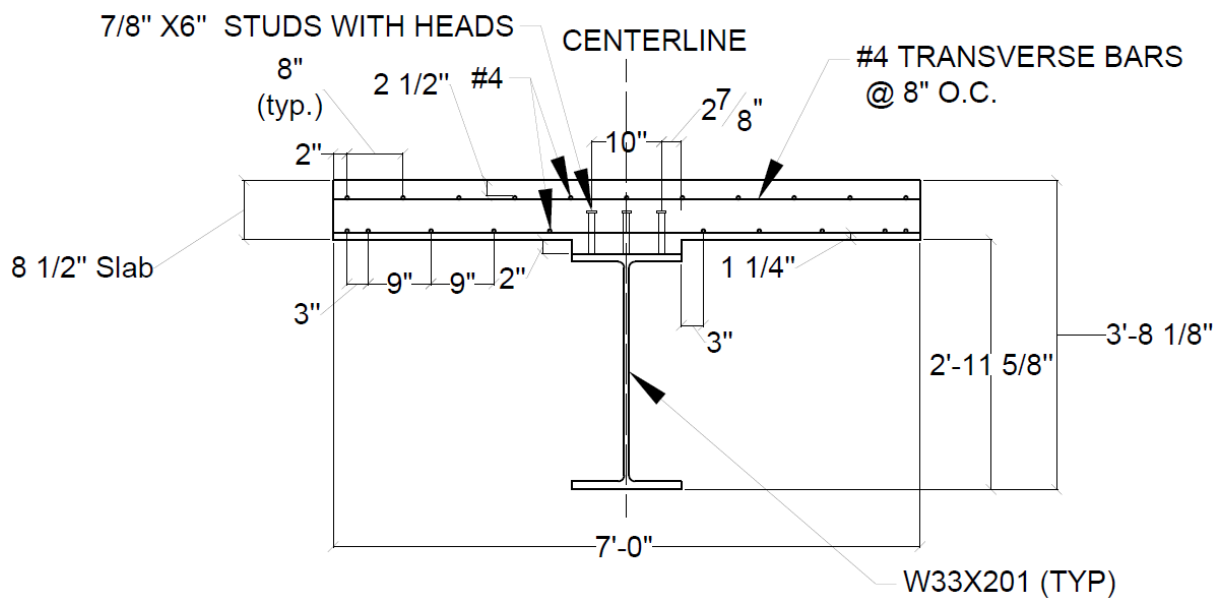


Figure 5.7. Composite Section of Steel Beam and Concrete Slab.

Table 5.1. Section Properties for the Composite Section.

Girder Type	Depth of NA from Top of Girder	Depth of NA from Bottom of Girder	Transformed Area, A	Moment of Inertia, I_x
W33×201	14.5 in	30.8 in	151.6 in ²	3.13 * 10 ⁴ in ⁴

Note: NA = neutral axis.

5.3.2. Design Parameters and Assumptions

Table 5.2 provides a summary of the design parameters for the benchmark bridge. Material parameters are based on the TxDOT bridge standard, like Class S concrete strength, elastomeric bearings, steel reinforcement, etc. Other parameters are based on the *AASHTO LRFD Specification* [24].

Table 5.2. Benchmark Bridge Design Parameters.

Parameter		Value
Concrete Strength at Service for Deck Slab, f'_c		4 ksi
UHPC Strength at Service for Transverse closure pour and Bottom Channel		18 ksi
A588 Steel for Sole Plate	Yield Strength, f_y	50 ksi
	Modulus of Elasticity, E_s	29000 ksi
Grade 60 Reinforcing Steel	Yield Strength, f_y	60 ksi
	Modulus of Elasticity, E_s	29000 ksi
A992 Steel for W33×201	Yield Strength, f_y	50 ksi
	Modulus of Elasticity, E_s	29000 ksi
A572 Steel for Splice Plates	Yield Strength, f_y	50 ksi
	Modulus of Elasticity, E_s	29000 ksi
Williams Bar Threaded Rod	Yield Strength, f_y	120 ksi
	Ultimate Strength, f_u	150 ksi
A325 Bolts for Splice Plate	Minimum Tensile Strength, F_{ub}	120 ksi
A325 Bolts for Bracket	Minimum Tensile Strength, F_{ub}	150 ksi
Class A Surface Condition	Coefficient of Friction, K_s	0.30
Class B Surface Condition	Coefficient of Friction, K_s	0.50

The following assumptions were also made for the benchmark bridge design:

- The bridge is straight and has no skew angle.
- The Williams bars used for Concepts B, C, and D are external and under the top flange of the steel beam.
- The slab of each specimen is cast in a single operation.
- The CIP slab thickness is a constant 8.5 inches, and a 2-inch thick haunch is present between slab and steel beam.
- The temporary formworks, diaphragms, and other temporary components are minor and neglected in the benchmark design.
- The steel beams are sufficiently braced when casting the slab for the prefabricated bridge units.

5.3.3. Loading

5.3.3.1. Dead Loads

The dead loads for the benchmark bridge include the steel girder self-weight and weights of the reinforced concrete slab, haunch, and future wearing surface. The slab tributary width is the center-to-center spacing between girders. This slab weight is distributed to the interior girders. The wearing surface is not considered a part of the composite section, but it is included in the dead load, which is distributed equally to all the girders. The dead load unit weights utilized were from the *AASHTO LRFD Specifications* Article 3.5.1 [24]. Table 5.3 presents the various dead load magnitudes acting on an interior girder for the benchmark bridge.

Table 5.3. Dead Load for an Interior Girder.

Load Type	Value (kip/ft)
Self-weight steel girder	0.201
Haunch weight	0.032
Slab weight	0.657

5.3.3.2. Live Loads

The benchmark bridge was designed for live load demands of two design lanes due to the 28 ft roadway width. The HL-93 live load model (*AASHTO LRFD Specifications* Article 3.6) was

primarily used for sizing the various connection details [24]. HL-93 is a notional load that includes combinations of a tandem axle load, HS20 truck load, and lane load. The tandem axle load did not control any of the design. The HS20 truck component of HL-93 includes one 8.0-kip axle and two 32.0-kip axles. The lane load is 0.64 k/ft, which is uniformly distributed along the design lane. Figure 5.8 illustrates one load combination of HL-93 loading that combines the HS20 truck with the lane load. This combination produced the largest positive bending moment for the design. Note that the HS20 truck can be at any position along the bridge.

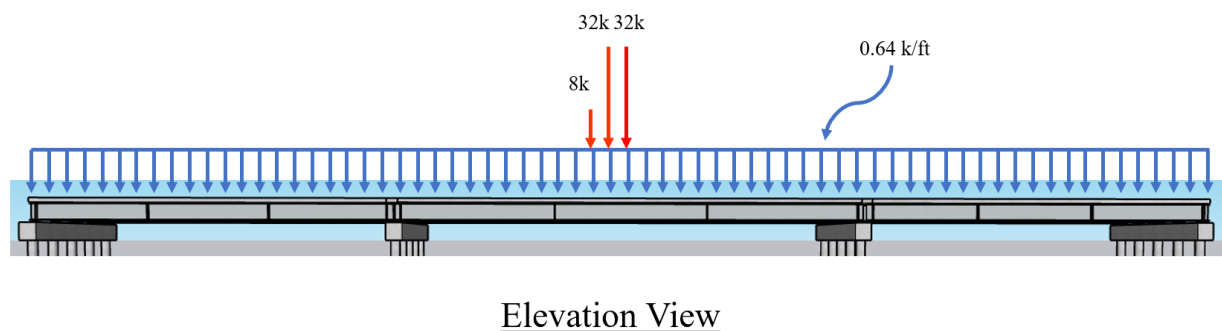


Figure 5.8. HL-93 Loading—Truck and Lane Load.

The maximum negative moment case for HL-93 is two HS20 trucks spaced 50 ft between the front axle of one truck and the rear axle of another truck. This pair of trucks are positioned to produce the maximum effect. However, AASHTO only requires 90 percent of the effect to be utilized for design. Figure 5.9 illustrates the maximum negative moment case for HL-93 loading.

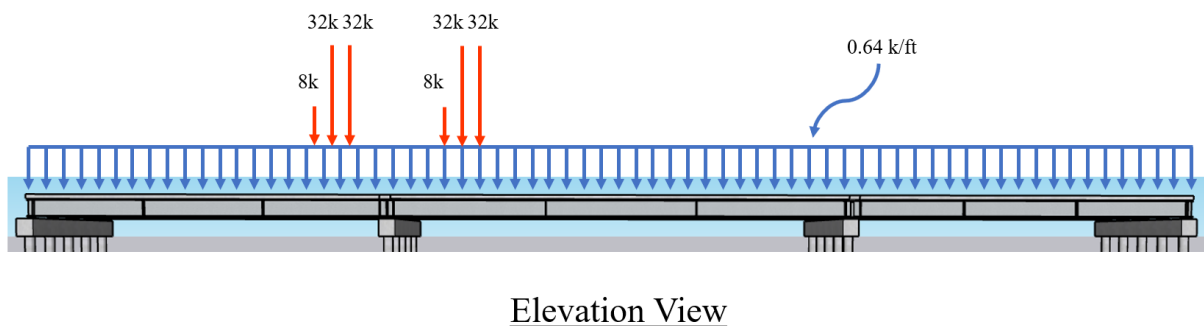


Figure 5.9. Critical Load Placement of HL-93 for Maximum Negative Moment Demand.

To convert the design lane load to loading on individual girders, live load distribution factors (LLDFs) (addressed in *AASHTO LRFD* Table 4.6.2.2) were included. These values included the multiple presence factor. The magnitude of the LLDF for the moment in interior beams is 0.597.

Another factor included was for dynamic load allowance factor (IM) to account for the dynamic amplification of a moving live load. This factor has a magnitude of 1.33.

5.3.4. Limit States

5.3.4.1. Service Limit State

This load combination is related to normal operations with loads taken at their normal design levels based on the *AASHTO LRFD Specifications* Article 3.4.1 [24]. The Service II limit state is also considered since it can control yield (permanent set) and slip of slip-controlled connections due to vehicular live load. Equation (1) expresses the Service I limit state combined loading (Q_{ServI}). Equation (2) describes the Service II limit state combined loading (Q_{ServII}).

$$Q_{\text{ServI}} = 1.0(\text{DC} + \text{DW}) + 1.0(\text{LL} + \text{IM}) \quad (1)$$

$$Q_{\text{ServII}} = 1.0(\text{DC} + \text{DW}) + 1.3(\text{LL} + \text{IM}) \quad (2)$$

Where:

DC = Dead load due to the components (girder and slab).

DW = Dead load of wearing surface.

LL + IM = Live load with dynamic load allowance.

5.3.4.2. Fatigue Limit State

Fatigue I is usually used to prevent fatigue and fracture of a component and for the infinite fatigue life check. In addition, this element can limit crack growth under repetitive loads during the design life of the bridge. The crack growth is the function of stress change and the number of applied loads. A factor of 1.75 is used with only live load and dynamic allowance for the fatigue limit state. The fatigue load is one design truck, with a constant spacing of 30 ft between the 32-kip axles and 14 ft between the center of the first rear axle group and the steering axle. It is different from HL-93. The single-lane average daily truck traffic is used as the frequency of the fatigue load, which is applied to all components of the bridge.

5.3.4.3. Strength I Limit State

It is vital to check the flexural strength limit state to ensure safety at ultimate load conditions. Strength I is the basic load combination for vehicular traffic and is primarily used for the total ultimate design bending moment and shear forces, according to the *AASHTO LRFD Specifications* [24]. Equation (3) shows the Strength I limit state combined load effect (Q_{StrI}).

$$Q_{StrI} = 1.25(DC) + 1.5(DW) + 1.75(LL + IM) \quad (3)$$

5.3.5. Deflection Check

For the deflection evaluation under service loading, the composite girders were checked for the maximum deflection under service live load with dynamic allowance based on the *AASHTO LRFD Specifications* Article 2.5.2.6.2 [24]. The limit of the deflection is $L/800$, where L is the span length. The deflection should be taken as the larger of the following:

- The deflection resulting from the HL-93 alone.
- The deflection resulting from 25 percent of the HL-93 taken together with the design lane load.

Table 5.4 shows the deflection results, which are within the allowable limit.

Table 5.4. Live Load Deflection for the Three-Span Benchmark Bridge.

Deflection	End Span	Center Span
Allowable (in.)	0.90	1.20
Actual (in.)	0.58	0.76

5.4. EXPERIMENTAL TESTING APPROACH

The following section details the general experimental testing sequence taken for each of the concepts (for experiment methodology, see Section 5.2). A typical experiment setup is shown in Figure 5.10 (the figure is from Concept A, but the overall setup is similar for each concept). Before testing, the Williams bars for Concepts B and C had to be post-tensioned. The details for PT can be found in section 5.8.1 for Concept B and section 5.9.1 for Concept C. No Williams bars were present for Concept A.

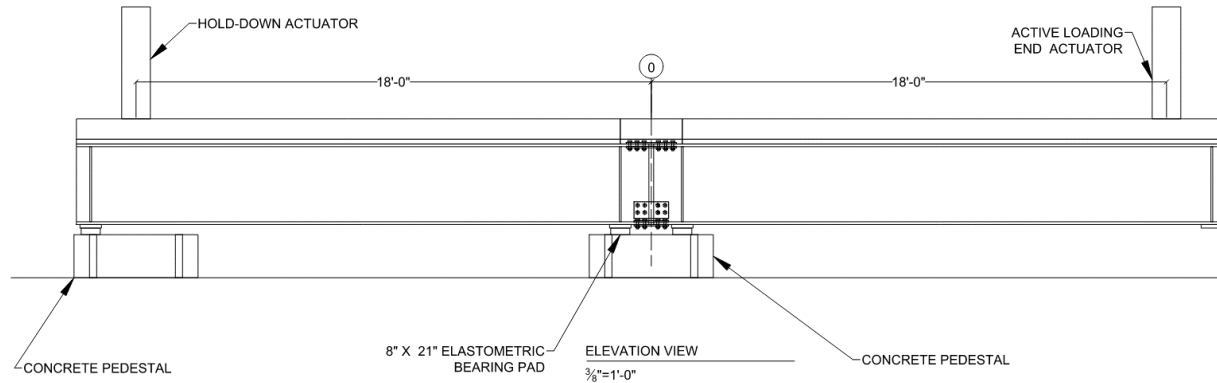


Figure 5.10. Experimental Setup Drawing (Concept A Shown).

The first step in the experimental testing approach was to load the hold-down end of the specimen (the left side of Figure 5.10). The load that was used on this end varied from test to test. For example, for Concept B, it was at 200 kips for the entirety of testing, while for Concept A and Concept C, it varied depending on which part of testing was being conducted. This information is provided later in the report.

On the active loading end of the specimen, which is on the right side in Figure 5.10, a 55-kip actuator was placed so that the center was 2 ft 1 inches from the end of the specimen. After the hold-down end was loaded, the loading end was raised using from 10 to 20 kips so that the pedestal under that end could be removed. To pick up the loading end, an adapter plate had to be fabricated. This adapter plate had holes in it that allowed threaded rods to be fed through the deck to provide a positive connection.

After the pedestal was removed, the specimen was lowered so that the active loading actuator read 0 kips on the load cell. This figure was considered the zero point for the testing. At this zero point, the specimen effectively acted as a cantilever, inducing some negative bending moment at the center connection (magnitude provided later).

The previous steps were carried out before static, cyclic, and ultimate testing. Static testing was performed with load control for the active loading end actuator. Load control tells the actuator what load it should impart on the specimen; conversely, displacement control tells the actuator how much to displace the specimen.

The magnitude of applied vertical load for static testing was selected from the equivalent HL-93 demands for the benchmark bridge described in the prior section. Figure 5.11 illustrates the HL-93 (unfactored) moment envelope for the benchmark bridge. The unfactored maximum negative moment (per lane) was 1102 kip-ft at the pier bents. The negative moment per girder was 658 kip-ft, and the minimum negative moment per girder was 87 kip-ft over the pier when the LLDF was applied. For static testing, the required demand (based on HL-93) was 658 kip-ft negative bending.

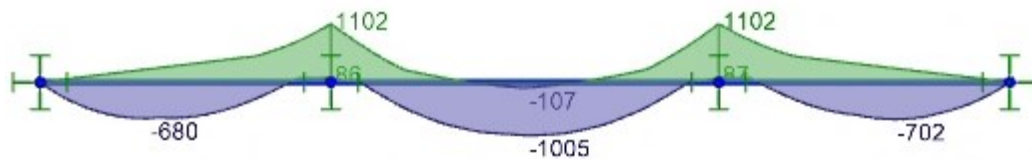


Figure 5.11. Moment Envelope for the Back-to-Back HL-93 Load Case (Units: kip-ft).

To achieve these magnitudes of bending at the center connection during testing, two factors were considered. The first was the self-weight of the specimen. While the specimen was in a cantilever state at the zero point, the self-weight was already inducing a portion of the moment to meet the HL-93 requirements. The moment that was provided by the self-weight was about 178 kip-ft. The remainder of the moment had to be met by the second factor, which was the load imparted by the loading end actuator. The remaining 480 kip-ft was met by pushing down with 30 kips (the actual required loading was 28 kip, but 5-kip loading increments were used, so it was decided to go slightly higher). After the equivalent HL-93 moment load was reached, the load on the active loading end actuator was reduced, and the specimen was left to rebound to the zero-point state to check for repeatability and signs of damage. If no signs of damage were noticed, the load was applied a second time, and then a third time to check for repeatability. At all load steps during testing, the results were checked with calculated deflections and strains for verification. If no major signs of damage were seen and the results were close to what was expected, the static testing was considered complete.

For the cyclic testing, the specimen was taken off the pedestal like it was before the static testing. Displacement control was used for the cyclic testing. The ranges for the displacement of the specimen were determined based on the results of the static testing. The downward displacement matched the displacement that corresponded with the 28-kip load level, and the upward

displacement matched up with the displacement that corresponded to the load required to meet the positive bending moment from the HL-93 loading. The total number of cycles depended on several factors, including the availability of the lab and the timeline of laboratory testing. Generally, a minimum of 125,000 cycles were run for each concept. The frequency of the cyclic loading was 1.0 Hz, which was the limit of the active loading end actuator for the displacement levels that were required. The frequency of the cyclic loading was reduced for a portion of the cycles to evaluate the specimen. After each day's testing was completed, the specimen was put back on the pedestal so that the specimen would be ready for testing the next day.

Ultimate testing was the final portion of the experiment that was conducted for each concept. Ultimate testing was performed using displacement control as well. One-quarter-inch increments were used for the starting downward displacement of the specimen. This displacement increment was lowered to 1/8-inch increments as testing approached failure of the specimen. Once failure was reached, the specimen was placed back on the support pedestal, and the specimen was inspected for signs of damage. After the specimen was inspected and signs of damage were documented, the instrumentation was taken off, and the specimen was discarded.

5.5. PREFABRICATED BRIDGE CONSTRUCTION PREPARATIONS

Wood formwork was constructed that could be reused for each of the four concepts. To save on material costs, lab space, and assembly time, the formwork was constructed so that it would fit each of the concepts with only minor modifications as needed. The following section describes the overall construction of this formwork.

Overall, 36 wall panels were constructed out of 2 × 4 inch wood studs spaced at 1 ft 4 inches o.c. (on center). The vertical wall studs were 2 ft 6 inches tall and attached to the continuous 2 × 4 inch top and bottom plate with two #9 screws each. See Figure 5.12 for typical wall panel construction.



Figure 5.12. Wood Wall Panel Construction.

For the bottom of the precast concrete deck to pour against, wood floor panels were constructed out of 2×4 inch wood studs spaced at 1 ft 4 inches o.c. The studs were cut to fit a typical $4 \text{ ft} \times 8 \text{ ft}$ plywood sheet. Therefore two 8 ft studs were laid along the length of the plywood and shorter 3 ft 9 inch studs were used to fill the space between. See Figure 5.13 for typical wood floor panel construction.



Figure 5.13. Wood Floor Panel Construction.

The studs were fastened together with two #9 screws, like the wall panels. After the studs had been put together, a sheet of plywood was laid on top and fastened to the perimeter studs with #9 screws at approximately 1 ft o.c. The plywood used was 23/32-inch structural grade plywood. Overall, 12 of these floor panels were constructed. To fill in the gaps at the ends of the steel beams, four smaller floor panels were constructed similarly. See the foreground of Figure 5.14 for an example of one of these panels.



Figure 5.14. Formwork Construction.

The exposed surface that the precast concrete deck was to be cast against was painted with a glossy white paint to help with the removal of the formwork after the deck had sufficiently cured. See Figure 5.15 for a picture of the painting process.



Figure 5.15. Painting of Wood Floor Panels.

Wood side forms were also constructed to form the sides of the precast concrete deck. These forms were made of 2×10 inch members shaved down from 9.25 inches to 8.5 inches wide. The base of the side forms was made from 2×8 inch members to form an L shape. To provide stiffness to the side forms, small sections of 2×4 inch members were spaced at 1 ft 4 inches o.c. See Figure 5.14 for an example of the side forms. The face of the shaved 2×10 inch member was also painted white like the floor panels to aid with form removal.

Once all the formwork was constructed, the steel beams were brought into the lab to begin assembly. Three wall panels were used for each floor panel. Two of the wall panels were placed

under each of the long sides of the floor panels, with one wall panel being placed at the midpoint of the floor panels. See Figure 5.16 for a view of this assembly.



Figure 5.16. Formwork Assembly.

As can be seen in Figure 5.16, small lengths of 2×4 inch studs were placed on the bottom plates of the wall panels to control the spacing of the wall panels. The end of one wall panel was attached to the end of the next wall panel with one #9 screw at the top and bottom of the last wall stud. The wall panels were attached to the floor panels with three #9 screws per panel. Each side of the beam used three floor panels and nine wall panels.

The side forms were laid on the floor panels at the appropriate distance from the beam to achieve the required 7 ft deck width. The side forms were attached to floor panels using at least eight screws per side form.

One concern that was brought up while in the design stage was that the formwork was prone to separate from each other, which would result in concrete spilling in between the gap between the beam and the formwork. Therefore a $\frac{3}{8}$ -inch \varnothing threaded rod was used to hold the two sides of the

formwork together. This threaded rod was installed 10 ft from the connection end of the beams. It was then tightened using a nut and washer. This threaded rod was cast into the concrete.

To increase the stability of the system, several 2×4 inch lateral braces were added to the wall panels. These braces can be seen in Figure 5.17.



Figure 5.17. Lateral Bracing View.

After all formwork had been assembled, silicon caulk, backing rod, and duct tape were used to seal all cracks in the formwork. Once the silicon caulk dried, form-release oil was spread on the surfaces that would be in contact with the concrete to allow the formwork to separate after the concrete had cured. The form oil was allowed to cure overnight to allow it to soak into the formwork. Another layer of form-release oil was applied the next day. Rebar was laid after the form-release oil was applied. The bottom transverse bars were #4 bars at 8 inches o.c. and had a bottom cover of 1.5 inches. Therefore, 1.5-inch continuous bolsters were used to achieve this required cover distance. Once the transverse rebar was laid, the longitudinal rebar was laid and fastened to the transverse rebar. After the bottom mat of steel had been laid, 5.5-inch rebar chairs

were used to achieve the required 2 inches clear distance to the top of the slab. However, due to a calculation error, the 5.5-inch rebar chairs were too tall since laying the longitudinal bars on top of the transverse bars would have resulted in only 1.5-inch clear cover. Therefore, the longitudinal bars were attached to the rebar chairs and the transverse bars were hung underneath with rebar ties. See Figure 5.18 for a view of the completed rebar layout.



Figure 5.18. Rebar Layout.

5.6. MATERIAL PROPERTIES

This section provides the properties of the actual experimental test specimens. The first subsection provides the methodology and results for the concrete material testing. The second subsection provides the steel material testing. However, only the results are provided since this testing was performed by the steel mill producing the steel. The information was obtained from the mill test reports.

5.6.1. Concrete Material Testing

Concrete compression tests were performed for every concrete pour on the project to obtain the compressive strength of the concrete. The results for the precast concrete deck are provided in Table 5.5. The results for the concrete closure pours are shown in Table 5.6. Conventional 4 × 8 inch concrete cylinders were used for these tests. A minimum 28-day compressive strength of 4 ksi concrete for the deck slab was required, which was achieved. Concrete compression tests were conducted 7, 14, and 28 days after pouring, as well as on test day. The test result values were calculated using the equation shown in Equation (4), taken from ASTM C39 which is Standard Test Method for Compressive Strength of Cylindrical Concrete Specimens . For clarity and consistency, **bold** text is used in table notes throughout the report to emphasize key terms, instructions, or critical information.

Table 5.5. Precast Concrete Deck Compressive Strength Test Results (ksi).

Test Date	Specimen No.	Concept A	Concept B	Concept C	Concept D Unit A	Concept D Unit B
7 Day	1	5.02	4.14	5.08	5.33	5.78
	2	5.44	3.86	5.39	5.43	5.43
	3	5.39	4.32	5.65	5.66	5.69
	Average	5.28	4.11	5.37	5.48	5.63
14 Day	4	6.04	5.19	5.84	6.09	6.58
	5	5.93	5.23	6.05	6.10	6.25
	6	5.66	5.24	6.29	6.24	6.20
	Average	5.88	5.22	6.06	6.14	6.34
28 Day	7	6.36	4.67	6.26	6.43	6.89
	8	6.67	5.45	6.23	6.75	6.17
	9	6.50	5.11	5.70	6.13	6.45
	Average	6.51	5.08	6.06	6.44	6.50
Test Day	10	7.11	5.57	6.12	7.76	8.05
	11	7.72	6.65	6.67	8.05	7.61
	12	8.10	5.33	7.31	8.34	7.63
	Average	7.65	5.85	6.70	8.05	7.76

Table 5.6. Concrete Closure Pour Compressive Strength Test Results (ksi).

Test Date	Specimen No.	Concept A	Concept B	Concept C
7 Day (1 day for Concept B)	1	3.60	6.31	4.04
	2	3.53	6.10	3.88
	3	3.59	6.56	3.73
	Average	3.57	6.32	3.88
14 Day	4	4.03	n/a	3.67
	5	4.39	n/a	4.26
	6	4.46	n/a	4.38
	Average	4.29	n/a	4.10
28 Day	7	4.96	13.08	5.04
	8	4.76	16.87	4.81
	9	4.82	11.56	4.91
	Average	4.84	13.84	4.92
Test Day	10	4.62	15.71	4.08
	11	4.90	15.15	5.27
	12	5.23	16.75	5.23
	Average	4.92	15.87	4.86

Note: "n/a" denotes not applicable.

$$f_{cm} = \frac{4P_{max}}{\pi D^2} \quad (4)$$

Where:

f_{cm} = compressive strength (psi).

P_{max} = maximum load (lbf).

D = average measured diameter (inches).

Table 5.7 shows the results from the modulus of rupture tests for the deck slab concrete. The results for the closure pour concrete can be seen in Table 5.8. These tests were conducted using third-point flexural bending. The tests were conducted 28 days after pouring, as well as on test

day. These values were calculated using the equation shown in Equation (5), taken from ASTM C78.

Table 5.7. Precast Concrete Deck Modulus of Rupture Test Results (ksi).

Test Date	Specimen No.	Concept A	Concept B	Concept C	Concept D Unit A	Concept D Unit B
28 Day	7	0.66	0.56	0.51	0.58	0.68
	8	0.83	0.58	0.79	0.66	0.77
	9	0.77	0.55	0.56	0.63	0.73
	Average	0.75	0.57	0.62	0.62	0.73
Test Day	10	1.07	0.94	0.83	0.92	0.98
	11	0.92	0.96	0.90	0.92	0.79
	12	0.94	1.07	0.73	0.98	0.90
	Average	0.98	0.99	0.82	0.94	0.89

Table 5.8. Concrete Closure Pour Modulus of Rupture Test Results (ksi).

Test Date	Specimen No.	Concept A	Concept B	Concept C
28 Day	7	0.49	n/a	0.75
	8	0.53	n/a	0.58
	9	0.54	n/a	0.75
	Average	0.52	n/a	0.69
Test Day	10	0.62	n/a	0.73
	11	0.71	n/a	0.64
	12	0.71	n/a	0.58
	Average	0.68	n/a	0.65

$$R = \frac{PL}{bd^2} \quad (5)$$

Where:

R = modulus of rupture (psi).

P = maximum applied load indicated by the testing machine (lbf).

L = span length (inches).

b = average width of specimen at the fracture (inches).

d = average depth of specimen at the fracture (inches).

The modulus of elasticity was also obtained for the precast concrete deck slabs. These tests were conducted 28 days after pouring, as well as on test day. These values were calculated using the equation shown in Equation (19) taken from ASTM C469.

$$E = \frac{S_2 - S_1}{\epsilon_2 - 0.000050} \quad (6)$$

Where:

E = chord modulus of elasticity (psi).

S_2 = stress corresponding to 40 percent of the ultimate load (psi).

S_1 = stress corresponding to a longitudinal strain, ϵ_1 , of 50 millionths (psi).

ϵ_2 = longitudinal strain produced by stress S_2 .

5.6.2. Steel Material Testing

The steel material properties were obtained from the steel mill material test reports. The steel W33×201 beams were Grade A992 steel. The yield and ultimate tensile strength for the beams were 59 ksi and 74 ksi, respectively. Fortunately, the beams were all from the same batch.

The steel plate used for the specimens was Grade A572-50. The 0.75-inch splice plates for Concept A had yield and ultimate tensile strengths of 52 ksi and 75 ksi, respectively. The 1 inch plates for Concept B and C PT brackets had yield and ultimate tensile strengths of 64 ksi and 84 ksi, respectively. Also, the channels at the bottom of Concept B were Grade A992. Their yield and ultimate strengths were 56 ksi and 76 ksi, respectively.

The PT bars as part of Concepts B, C, and D were provided by Williams. Grade A722 steel with a tensile strength of 150 ksi, was used.

5.7. CONCEPT A

5.7.1. Design, Construction, and Pretest Behavior of Concept A

5.7.1.1. Specimen Design

This subsection discusses how the Concept A test specimen was designed to achieve the features of the benchmark bridge. Section 5.3 previously described the benchmark bridge design, which is the basis of the specimen design. An elevation view of the connection area of Concept A is shown in Figure 5.19, and a section view is shown in Figure 5.20.

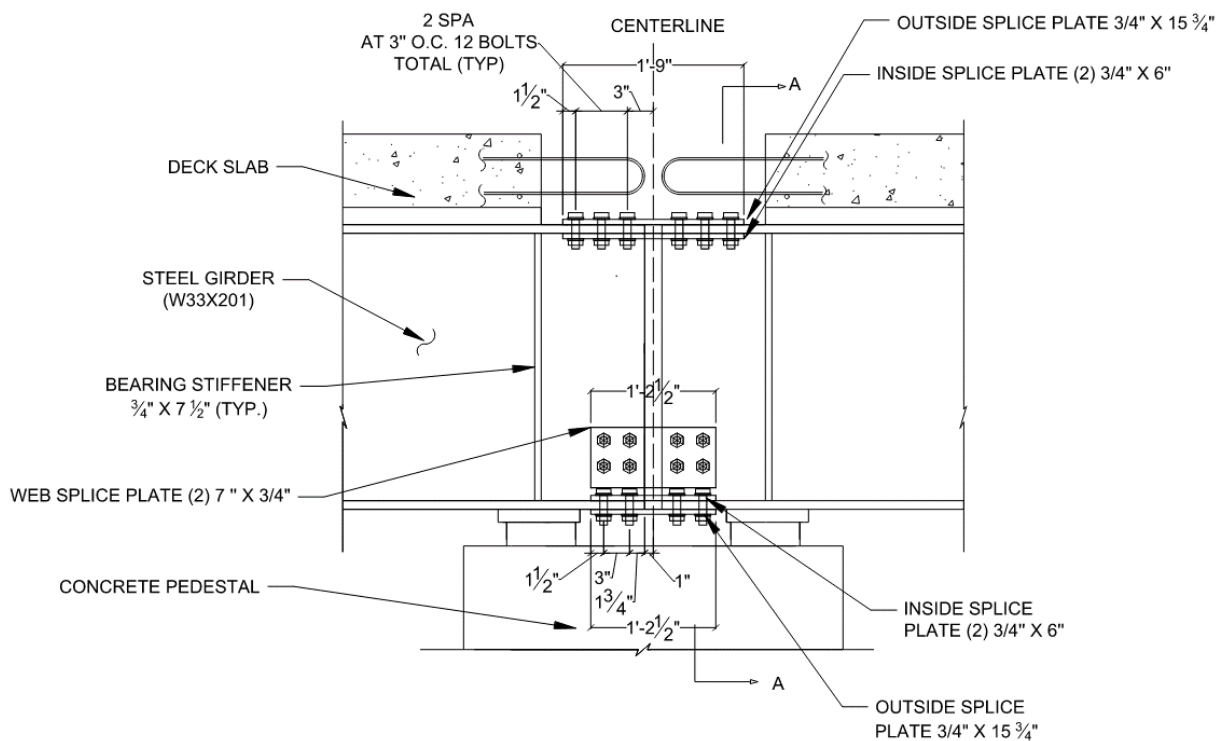


Figure 5.19. Elevation View of Concept A Connection Area.

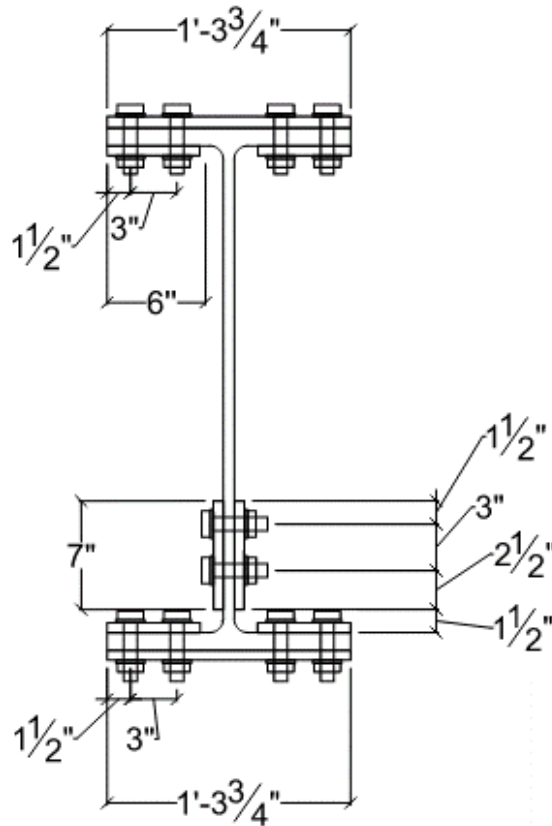


Figure 5.20. Section View of Concept A Connection Area.

This concept uses a passive design approach with steel plates and a reinforced precast concrete deck slab acting as the moment-resisting system. The plates, bolts, and beams were checked to ensure they met all design criteria. The primary design checks calculated from the *AASHTO LRFD Bridge Design Specifications 9th Edition* and corresponding AASHTO articles include:

- Shear resistance of bolts (Article 6.13.2.7).
- Slip resistance of bolts (Class B surface condition) (Article 6.13.2.8).
- Bearing resistance at bolt holes (Article 6.13.2.9).
- Tensile yielding and tensile rupture of connection plates (Article 6.8.2.1).
- Compression of connection plates (Article 6.13.6.1.2).

Figure 5.20 shows a cross section of the connection area for Concept A. All steel plates used were 0.75 inches thick, with varying widths and lengths. All bolts used in Concept A were 0.875-inch Ø A325 and were pre-tensioned to be slip-critical with a Class B faying surface. The concrete closure pour region was 2 ft 2 inches wide to allow for the installation of steel

connection plates during erection. Holes in one beam were left undrilled to allow for field drilling to remove any possibility of hole misalignment when erecting the beams. This step was previously recommended by the IRP.

5.7.1.2. Instrument Plan and Data Acquisition

The instrumentation of this concept focused mainly on the connection of the two composite beams. A plan view, elevation view, and section view of the instrumentation plan can be seen in Figure 5.21, Figure 5.22, and Figure 5.23, respectively. A legend for the symbols can be found in Figure 5.24. The final instrumentation lists for each concept can be found in Appendix B.

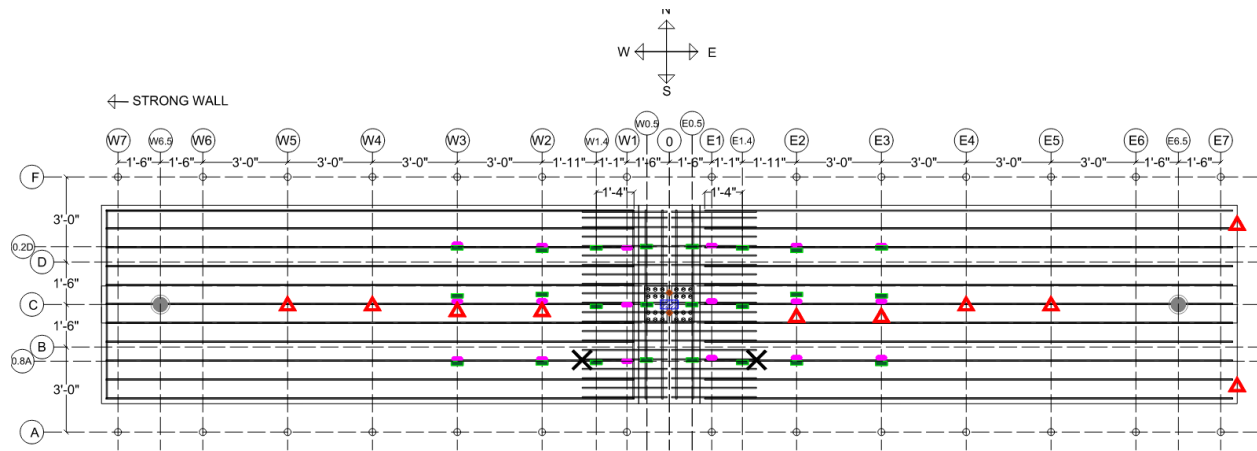


Figure 5.21. Concept A Instrumentation Plan (Plan View).

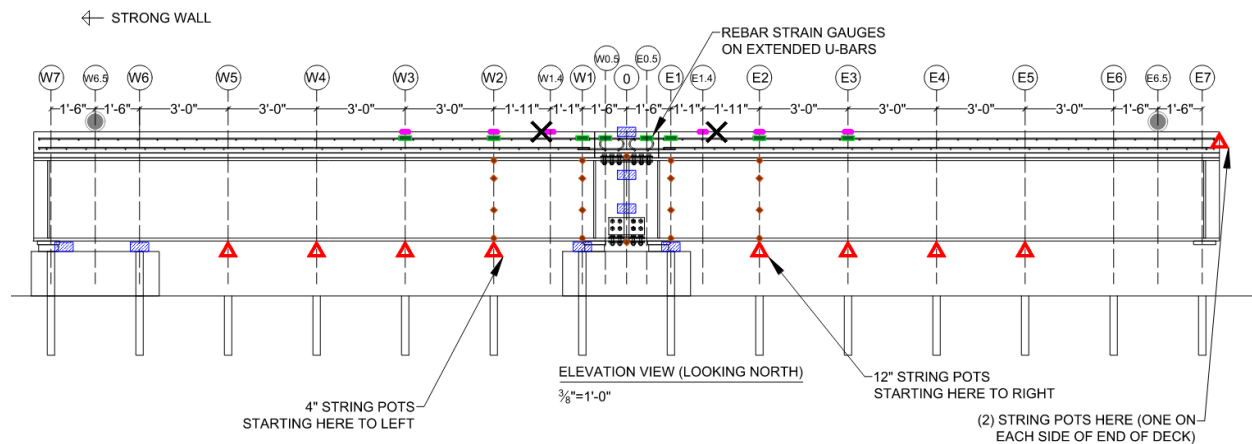


Figure 5.22. Concept A Instrumentation Plan (Elevation View).

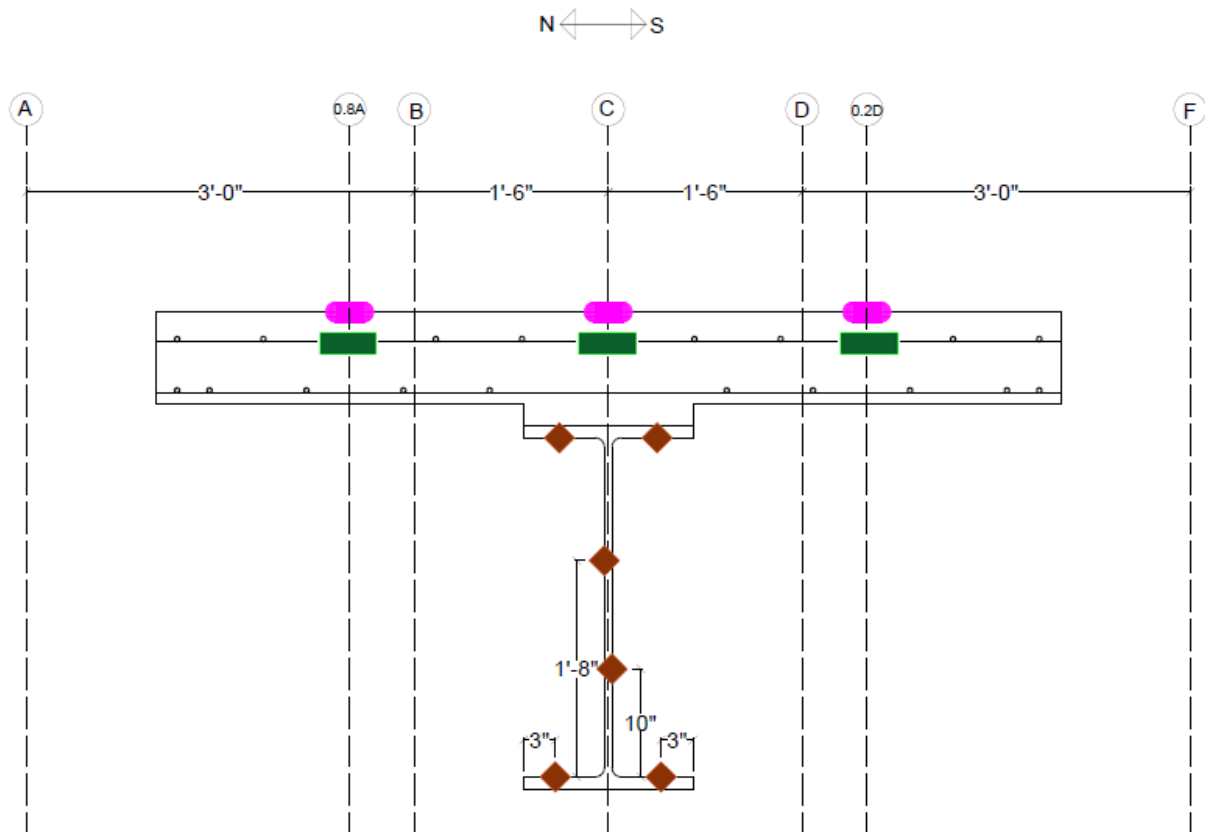


Figure 5.23. Concept A Instrumentation Plan (Section View).

Symbol	Item	Concept A Count
	Actuator and Load Cell	2
	Embedded Rebar Strain Gauge	24
	Concrete Surface Strain Gauge	18
	Structural Steel Surface Strain Gauge	28
	String Potentiometer	11
	LVDT	7
	Wire Exits	2

Figure 5.24. Instrumentation Plan Legend.

Most strain gauges were located on gridlines so that after testing the results could easily be turned into strain profiles to see how the strain differs relative to the closure pour. Strain gauges were also located on the top surface of the top connection plate and the bottom surface of the bottom connection plate so that the strain in the connection plates at the beam interface could be measured. String potentiometers (string pots) were located every 3 ft so that the displacement curve could be seen during and after testing. For areas that have higher precision displacements, linear variable differential transformers (LVDTs) were used. LVDTs were used near the supports of the beams (to measure deflection near the supports), on the web of the steel beams (to measure the relative rotation of the beams), and above the slab on the closure pour (to measure the elongation of the closure pour).

The rebar strain gauges used were FLAB-5-350-11 from Texas Measurements. The first rebar strain gauges were located starting at 1 ft 4 inches from the end of the longitudinal bars. The second rebar strain gauges were located 1 ft 11 inches beyond the first, and the third rebar strain gauges were located 3 ft beyond the second. Rebar strain gauges were located within 7 ft 6 inches of the centerline of the closure pour since that was the primary focus area for the testing.

Concrete surface strain gauges used were PL-60-11 from Texas Measurements. Concrete strain gauges were located directly on the major gridlines (E1, E2, etc.) so that the change in strain could be seen in regular increments moving farther away from the centerline of the closure pour.

The structural steel strain gauges used were also FLAB-5-350-11 from Texas Measurements. Structural steel strain gauges were located starting 1 ft 6 inches from the centerline of the closure pour with another line 3 ft from that. As previously stated, structural steel strain gauges were also located on the connection plates.

5.7.1.3. Specimen Preparation

The general formwork construction was previously discussed in Section 5.5. The following subsections are unique to Concept A.

Prior to all the formwork being connected, the holes in the top flange of the beam that were not shop-drilled had to be drilled because once the extended U-bars were installed in the deck slab,

access to the top flange would be very difficult (revision to the U-bar spacing is recommended for easier field drilling). The top connection plate was used as a guide for drilling the holes in the beam. The top connection plate was lifted into place and clamped down to the top flange. Once the plate had been adequately secured, a magnetic drill press was used to drill the holes into the top flange of the beam. After all the holes had been drilled, the rest of the formwork could be assembled. See Figure 5.25 and Figure 5.26 for views of the clamping plate and drilling holes.



Figure 5.25. Clamping of Connection Plate to Top Flange.



Figure 5.26. Drilling of Holes in Top Flange of Concept A.

To install the extended U-bars, holes were cut into the side forms at the connection end of the beams. These holes were slightly offset from the spacing of the longitudinal bars in the slab so that the extended u-bars lined up directly next to them. Three layers of wood forms were used so that the formwork could be easily removed without demolishing it and reused for Concept C. See Figure 5.27 for a view of the extended U-bars protruding through the formwork.



Figure 5.27. Concept A Extended U-Bars.

5.7.2. System Experiment Testing Program, Experiment Results, and Observations

5.7.2.1. Concept A Test Setup

Section 5.4 provides the general steps taken during the experimental testing. The test setup for Concept A included several unique steps. See Figure 5.28 for an elevation view of the overall test setup.

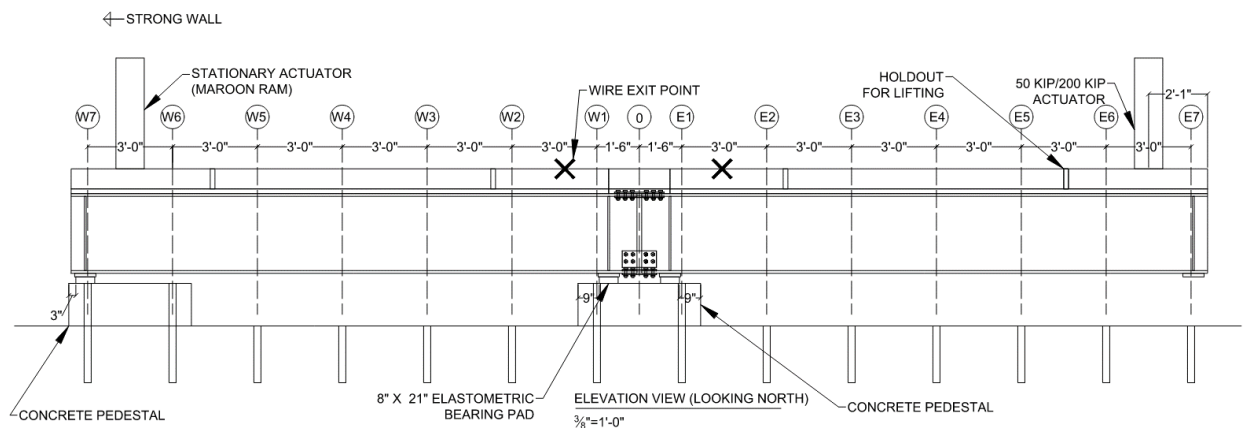


Figure 5.28. Concept A Test Setup Elevation.

Once the specimens were placed on the concrete pedestals, the first step was to bolt the top flange splice plates together. These plates had to be put into place before the closure pour because there was no access to the top flange after the concrete was poured. Before bolting the top flange splice plates, it was noticed that the splice plates did not appear to have a Class B faying surface preparation applied to them. The surface of the splice plates was very smooth when compared to the surface of the beam. See Figure 5.29 for a view of a bottom flange splice plate surface and Figure 5.30 for a view of the web surface preparation.



Figure 5.29. Bottom Flange Splice Plate.



Figure 5.30. Web Surface Preparation.

It can be seen that the splice plate had a smooth surface, while the web was rougher. The research team decided that the surface preparation of the splice plate was not adequate and needed to be fixed. The solution was to use a sandblaster to roughen up the surface of the splice plate that would be in contact with the steel beam. After sandblasting, the surfaces of the splice plates became much rougher. Figure 5.31 shows the splice plates after they were sandblasted. The top plate in that figure is the surface before sandblasting, while the middle and bottom plates are after sandblasting.

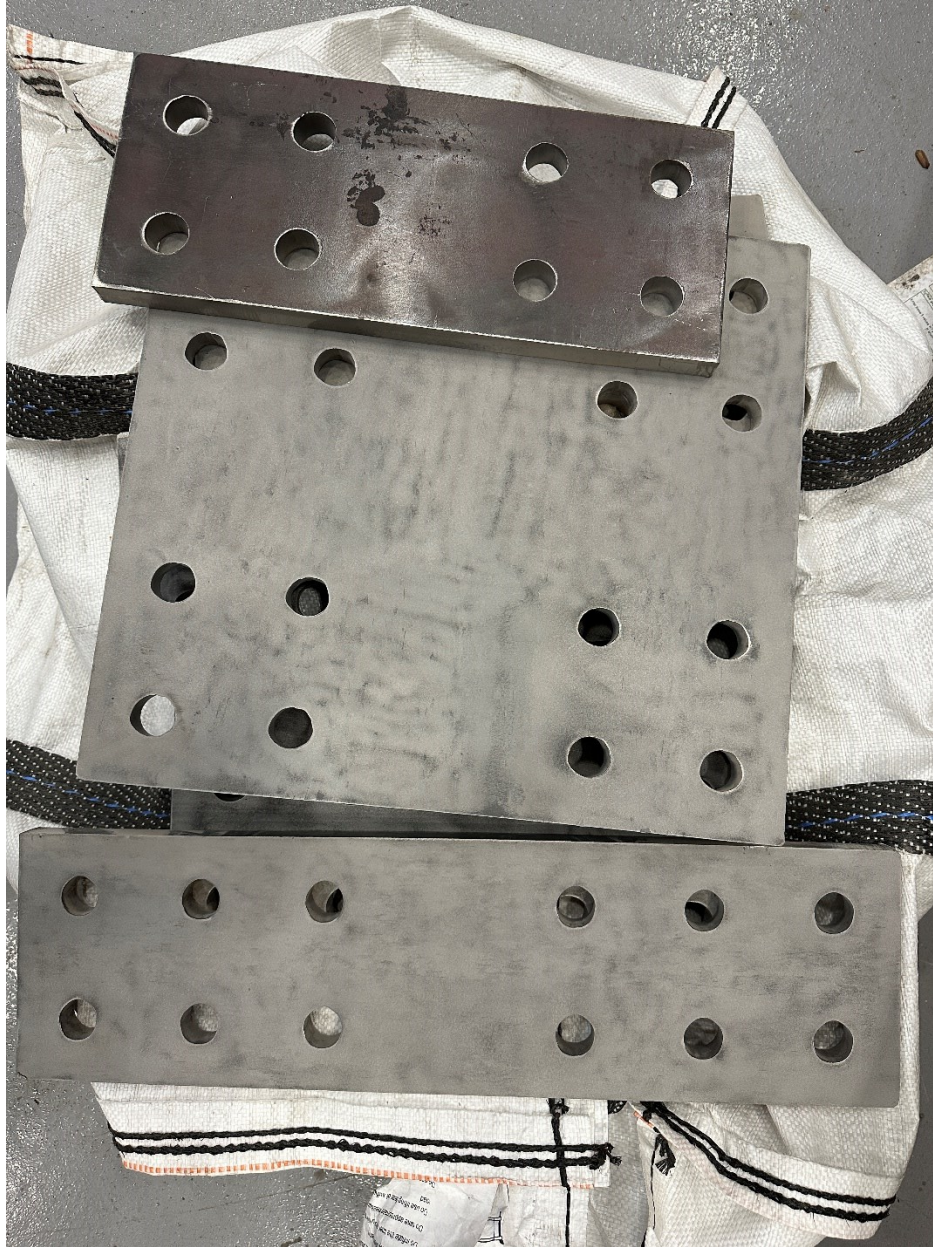


Figure 5.31. Concept A Splice Plates after Sandblasting.

The bolts that were originally supposed to be used for the connection were A325 bolts, but to increase the clamping force, new A490 bolts were ordered and used instead. The bolts were fed through the splice plates and the flange and were pre-tensioned using the turn-of-the-nut method. Before pre-tensioning the bolts, however, a Skidmore-Willhelm device was used to verify the turn-of-the-nut method provided adequate pretension to the bolts. See Figure 5.32 for a view of this process. The team determined from using the Skidmore-Willhelm device that to meet the required pretension force for the bolts, only 1/4 to 1/3 of a turn was required instead of the

one-half turn bolt specification required. Therefore, at least one-third of a turn was used for all bolts, but for most of them, half of a turn was used.

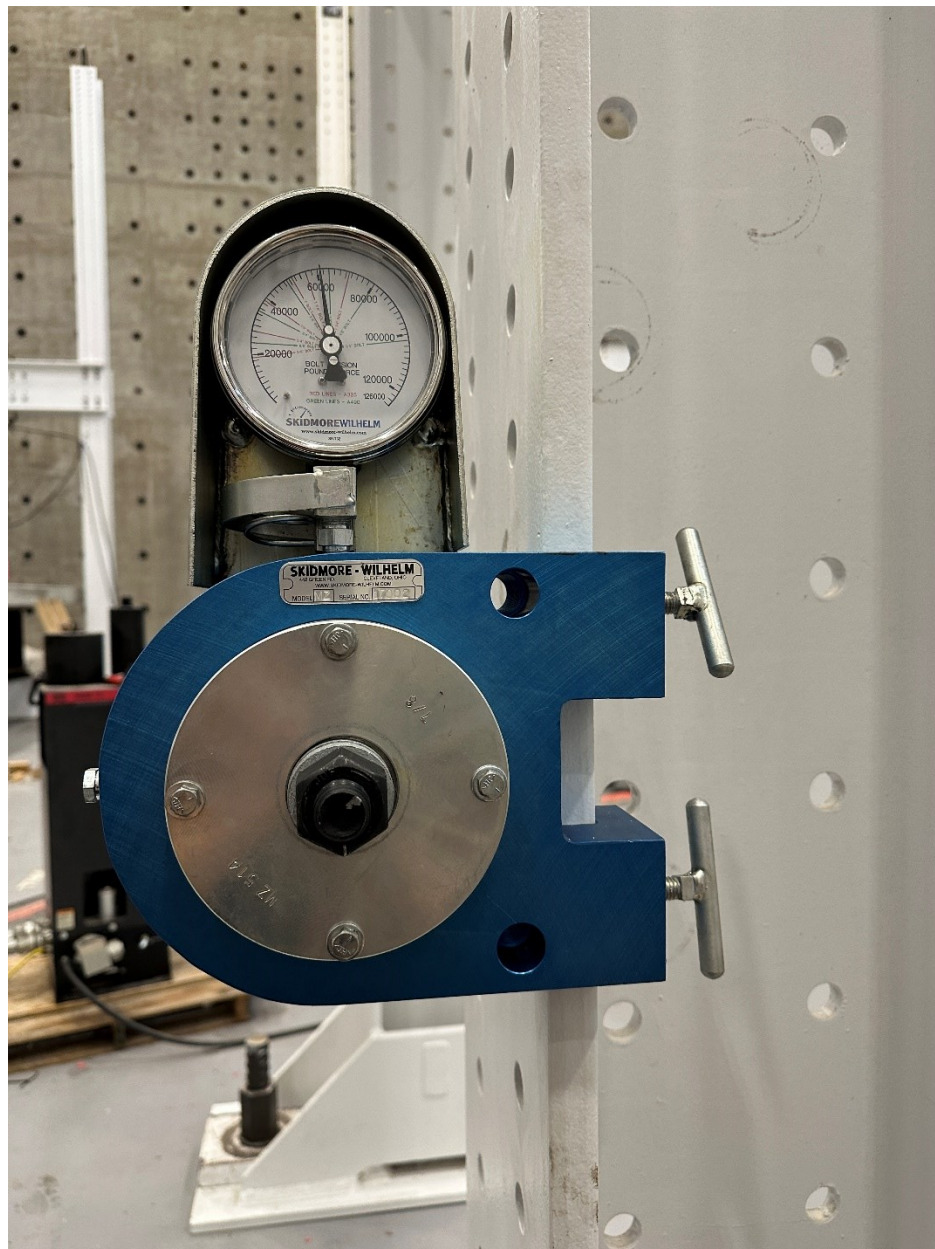


Figure 5.32. Skidmore-Wilhelm Bolt Pretension Device.

After the top flange splice plates were attached, the closure pour rebar was tied to the extruding U-bars. See Figure 5.33 for a view of the rebar in the closure pour.



Figure 5.33. Concept A Closure Pour Rebar.

After the rebar was tied, the formwork for the closure pour was assembled. The formwork that was used for the main precast concrete deck was used and modified to fit the setup. See Figure 5.34 for a view of the formwork after assembly.



Figure 5.34. Concept A Closure Pour Formwork.

After the closure pour was completed, the next step was to drill the bolt holes in the web and bottom flange of the beam that did not have the bolt holes shop-drilled. This process was achieved by using a mag drill and a 15/16-inch drill bit. See Figure 5.35 for a view of the mag drill drilling holes in the bottom flange.



Figure 5.35. Concept A Bolt Hole Drilling.

Once all the bolt holes were drilled in the steel beam, the splice plates were added, and the bolts were pre-tensioned using the turn-on-the-nut method. After the beams were bolted together, the rest of the test setup was conducted.

A 1.5-inch thick adapter plate was fabricated with a hole pattern that fit the actuator and the holdouts that were placed in the precast concrete deck. This adapter plate can be seen in Figure 5.36.



Figure 5.36. Concept A Adapter Plate.

The inner hole pattern is for the 55-kip actuator, the middle hole pattern is for the 200-kip actuator (if needed), and the outer hole pattern is for the connection to the deck. The connection to the actuator was made by making threads in the holes so that bolts could be fed through the foot of the actuator and connected to the plate. The connection to the deck was made by feeding threaded rods through the outer hole pattern. On the bottom of the deck, large plate washers were used to spread the load out. On the top of the deck, the rods were fastened with a small washer and a nut.

On the hold-down side of the test setup (the left side is shown in Figure 5.28), a stationary actuator was used to hold down the specimen during testing. This actuator was used to keep the

hold-down side in place. A load cell was placed under the end of the actuator so that it could be determined how much load was being put into it. Several plates were also used to distribute the load across a greater area of the slab. See Figure 5.37 for a view of this actuator.



Figure 5.37. Concept A Hold-Down End.

The following images show the actual test setup of the entire concept in the lab. The overall test setup, a view from the hold-down end, and a view from the active loading end can be seen in Figure 5.38, Figure 5.39, and Figure 5.40, respectively.

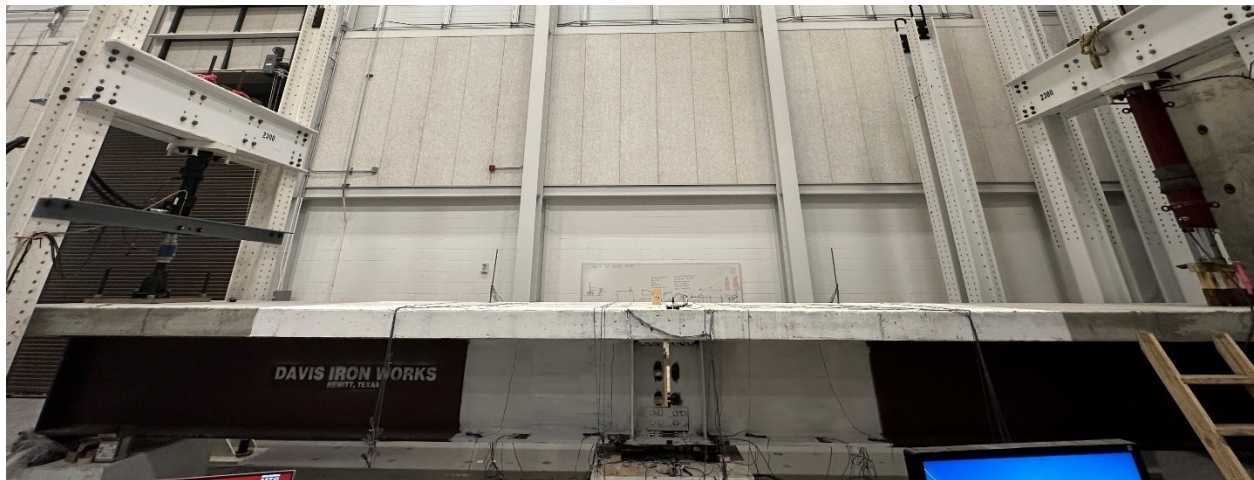


Figure 5.38. Overall Elevation View of Concept A Test Setup.



Figure 5.39. View of Concept A Test Setup from Hold-Down End.



Figure 5.40. View of Concept A Test Setup from Active Loading End.

5.7.2.2. Concept A Static Testing

Testing on Concept A started with static testing. Since there were no Williams bars in this concept, no PT had to be done before testing started. The specimen was pulled up with approximately 19 kips on the active loading end so that the support pedestal could be pulled out. The specimen was lowered until the active loading end actuator read 0 kips, which was considered the zero point for the static testing. Note that even though the actuator read 0 kips, there was negative bending due to the connection being made due to the cantilever setup. The specimen was then pushed down on the active loading end in 5-kip increments. After each 5-kip increment, the specimen was inspected for signs of damage. There was no observable damage in

the specimen until 15 kips was reached. At this load level, it was observed that cracks were forming in the construction joint between the deck and the closure pour. Seeing cracks start to form at this location was expected. The load on the specimen was increased in 5-kip increments up to 35 kips. Although the equivalent HL-93 loading was only approximately 28 kips, the specimen performed very well, so it was decided to push it a little further up to the 35-kip load level. No new cracks formed between the 15-kip load and the 30-kip load. At 35 kips, a crack was observed running through the lifting holes on the active end of the specimen. This crack can be seen in Figure 5.41.

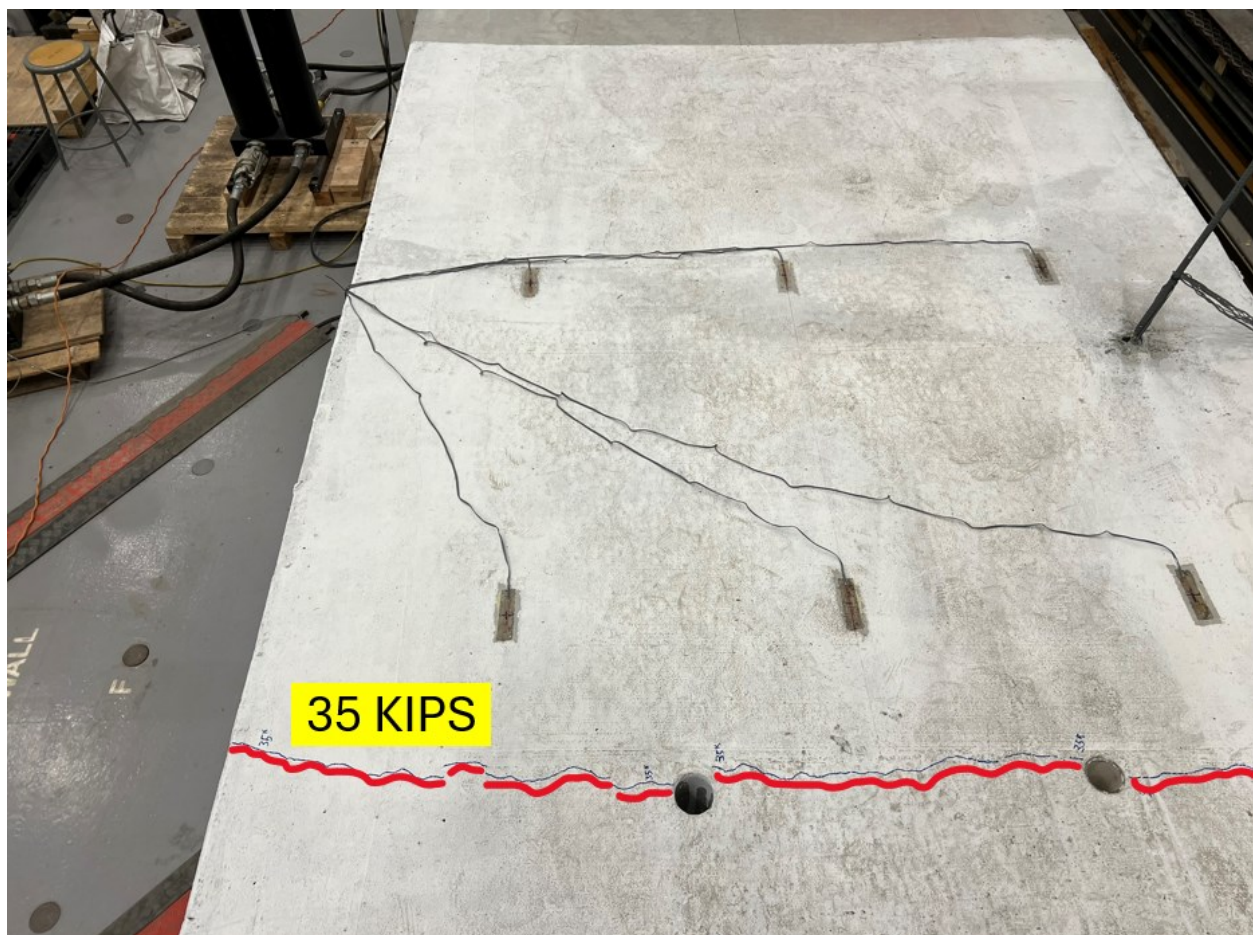


Figure 5.41. Concept A Static Testing Crack through Lifting Holes.

The load was taken off the specimen, and then up to 30 kips was placed on the specimen two more times to check for repeatability. See Figure 5.42 for the displacement time history plot. This plot shows the displacement at the different times of the testing. E7N and E7S are the string pots located on gridline E7 on the north and south side of the specimen, respectively. The stroke

is the displacement of the active loading end actuator. See Figure 5.43 for the load time history plot. It can be seen from this plot that the load level drops off at each load step. This process occurred because as the specimen was sitting there while being inspected, it started to creep, which caused the actuator load to fall off slightly.

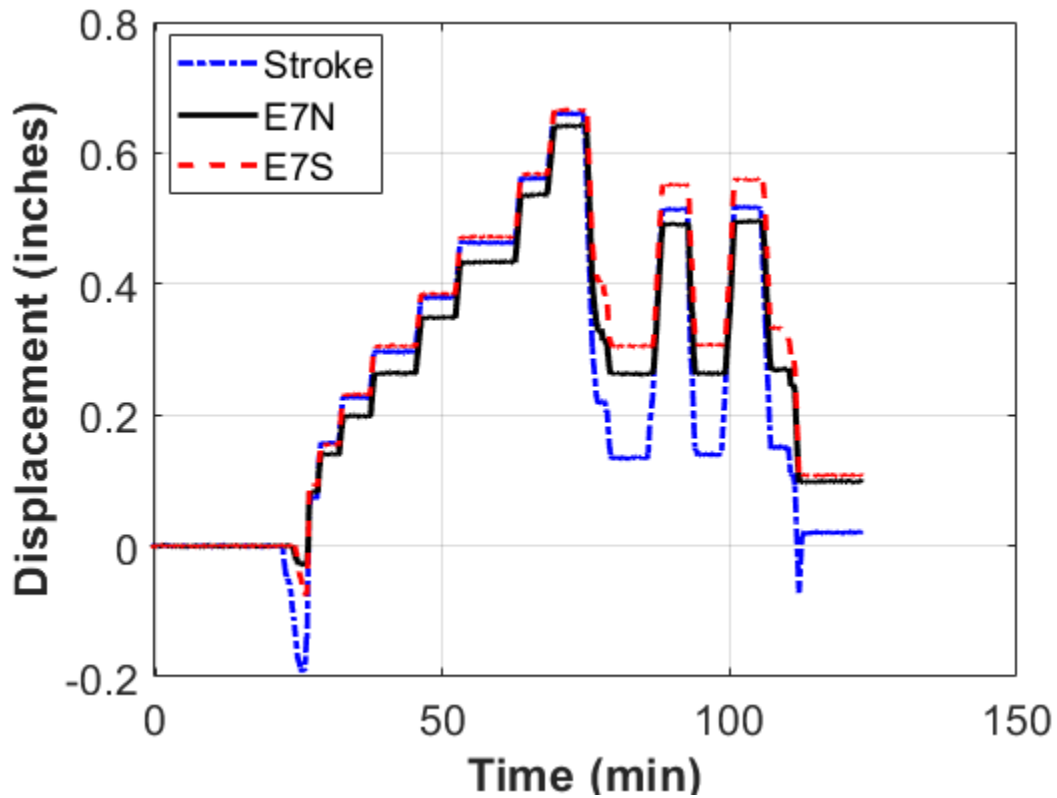


Figure 5.42. Concept A Static Testing Displacement Time History.

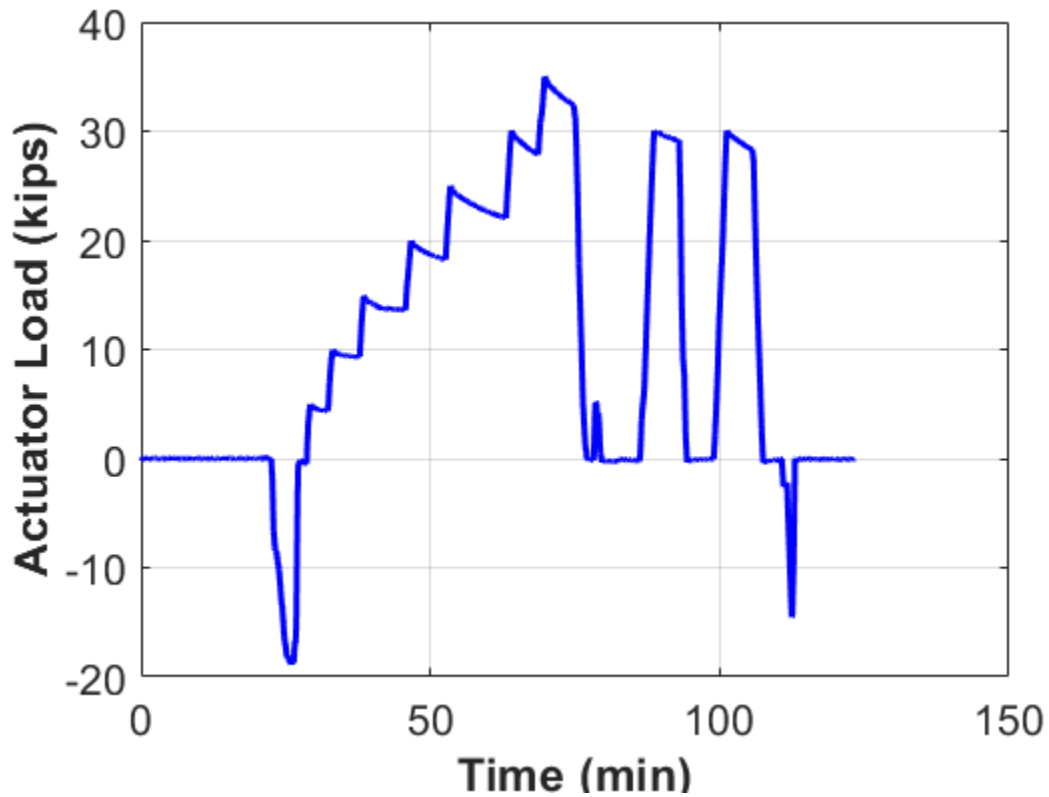


Figure 5.43. Concept A Static Testing Load Time History.

Figure 5.44 shows the actuator load versus displacement plot. At the zero-load level, it shows that the displacement of the specimen was approximately 0.10 inches (cantilever deflection). The maximum displacement of the specimen at the 35-kip load level was approximately 0.65 inches. It can be seen that the data from the second and third load application were repeatable. The reason that the blue line is shifted is because of the creep that was happening after each load step during the first load application.

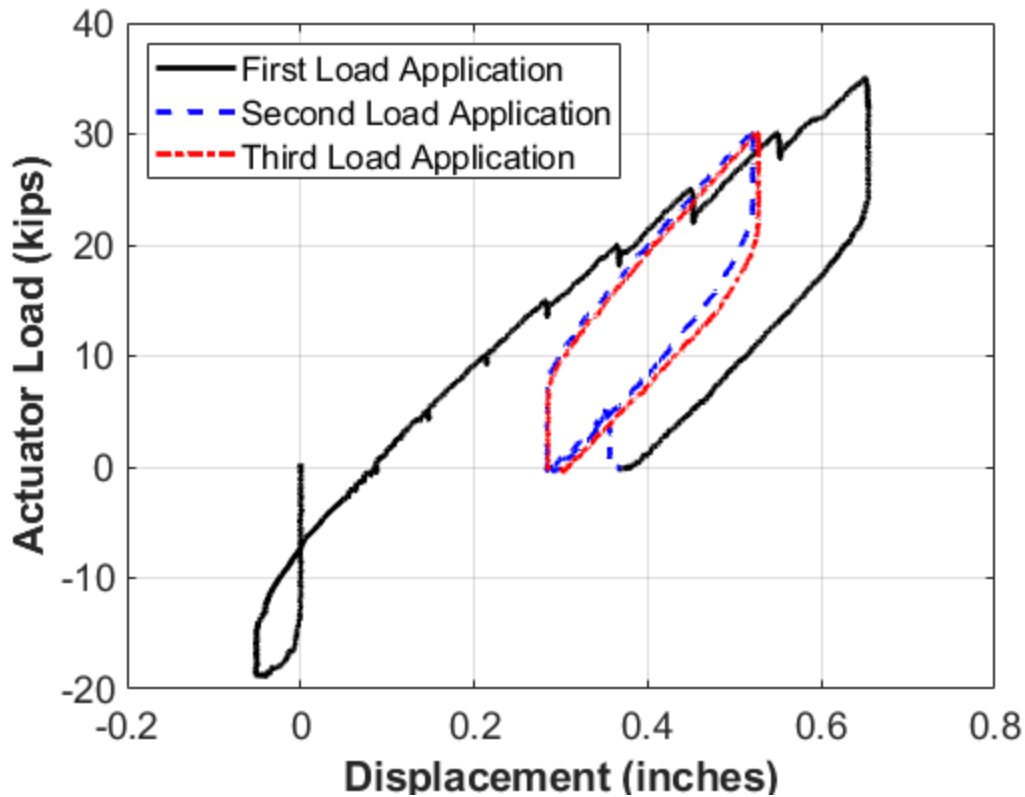


Figure 5.44. Concept A Static Testing Load-Displacement Plot.

The stress at the surface of the precast concrete deck at gridline E2 can be seen in Figure 5.45. SG62 is located on the longitudinal centerline, while SG61 and SG63 are located 2 ft on either side of the centerline. At the zero-load level, the strain on the precast concrete deck was approximately 0.05 ksi. It was not at zero because the self-weight of the specimen was causing the precast concrete deck to experience some minor stresses. As the load increased, the stresses followed a nearly linear path until just past the 30-kip load level. Between 30 kips and 35 kips, the crack formed through the lifting holes in the deck near these strain gauges. This crack forming released some of the stresses in the deck, which is why the stresses dropped off at that point.

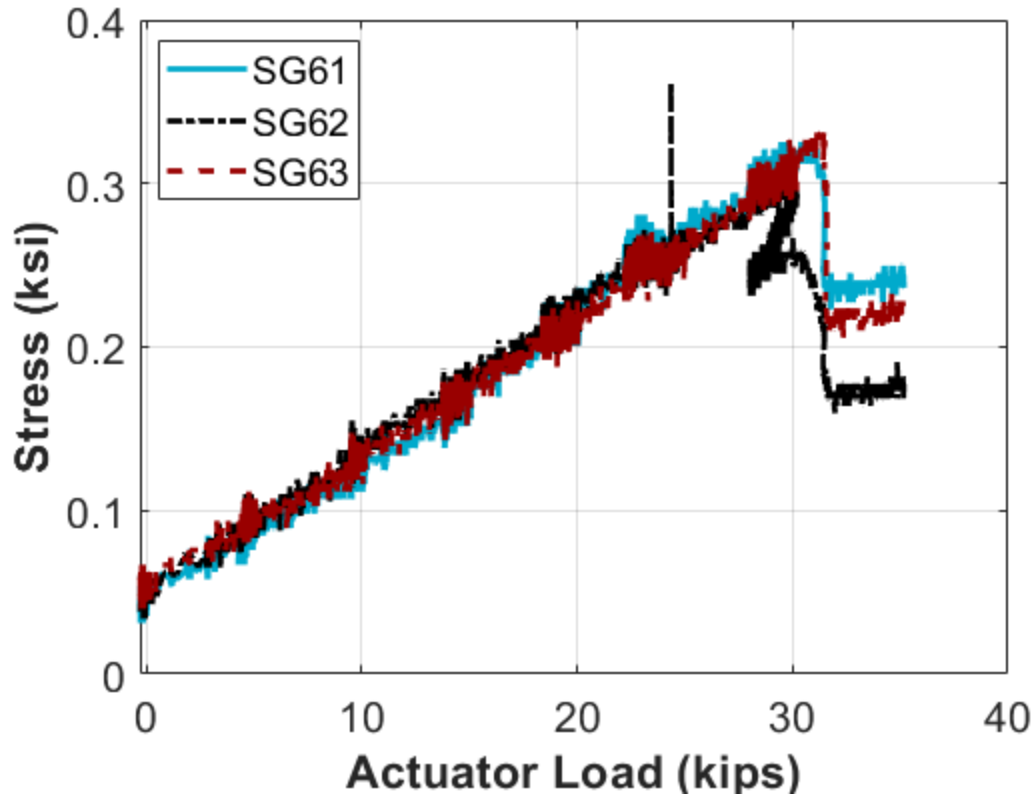


Figure 5.45. Concept A Precast Concrete Deck Stresses at E2.

Figure 5.46 shows the stresses on the surface of the precast concrete deck at gridline E3. SG65 was located on the longitudinal centerline, while SG64 and SG66 were located 2 ft on either side of the centerline. Similar to gridline E2, the stresses in the deck increased linearly as the load was increased. There was not a significant drop-off of stress at this location once the crack formed through the lifting holes.

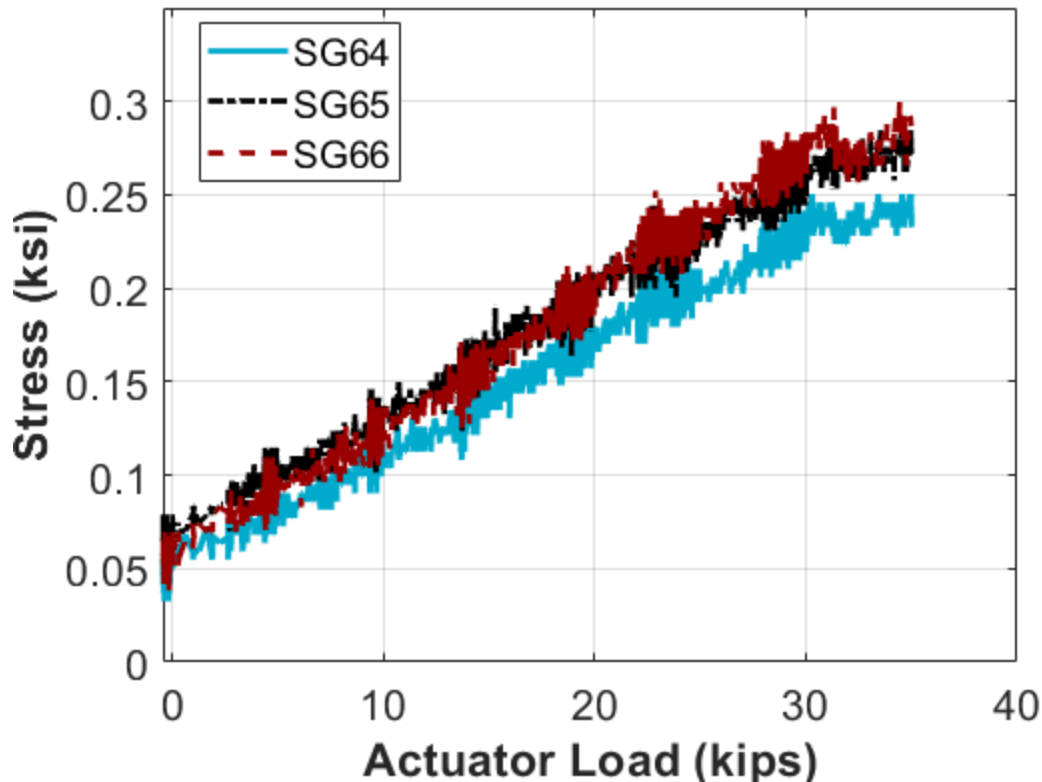


Figure 5.46. Concept A Precast Concrete Deck Stresses at E3.

The stresses in the longitudinal rebar at gridline E1.4 can be seen in Figure 5.47. SG11 was located on the longitudinal centerline, while SG10 and SG12 were located approximately 2 ft on either side of the centerline. The stresses increased linearly as the load proceeded, which was to be expected. However, the magnitude of the stresses was quite low. The magnitude of the stresses at gridlines E2, E3, W1.4, W2, and W3 were similar to these as well. However, the magnitude of the stresses in the U-loop rebar at E0.5 was much higher and closer to what would be expected. These stresses can be seen in Figure 5.48. The reason that the stresses in the U-loop rebar are shown to be so much higher than in the longitudinal rebar might be that the rebar is not fully developed.

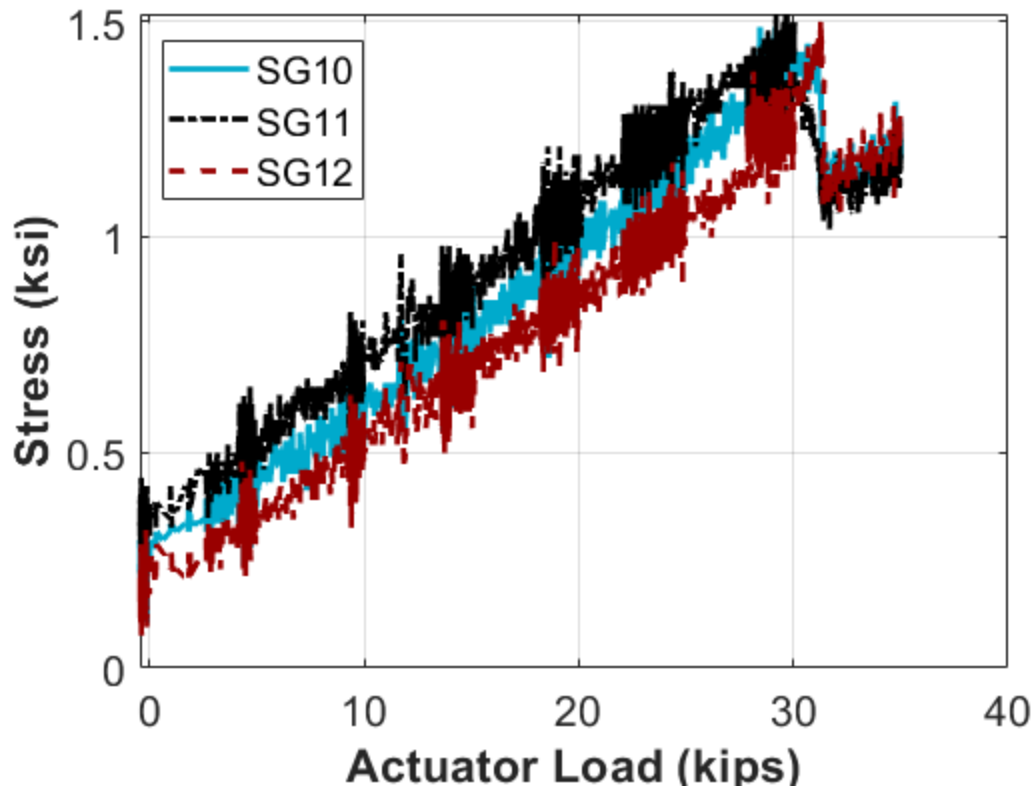


Figure 5.47. Concept A Static Testing Rebar Stresses at E1.4.

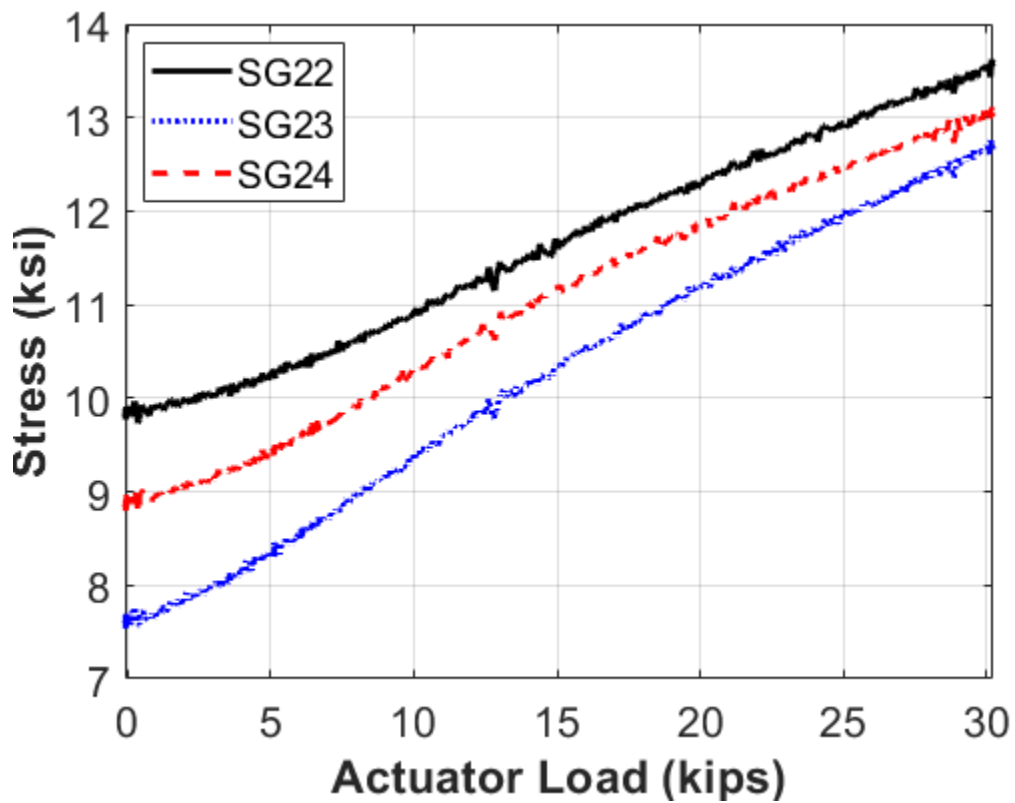


Figure 5.48. Concept A Static Testing U-Loop Rebar Stresses at E0.5.

The stresses in the steel beam at E1 can be seen in Figure 5.49. SG35 and SG36 were located on the top flange, SG37 was located on the top portion of the web, SG38 was located on the bottom portion of the web, and SG39 and SG40 are located on the bottom flange. All the gauges show a very linear path as the load increased, with the strain gauges on the top flange showing an increase in tension, and the strain gauges on the bottom flange showing an increase in compression, which was to be expected. SG37 stayed almost completely the same during the testing, indicating that it was located almost perfectly on the neutral axis (NA).

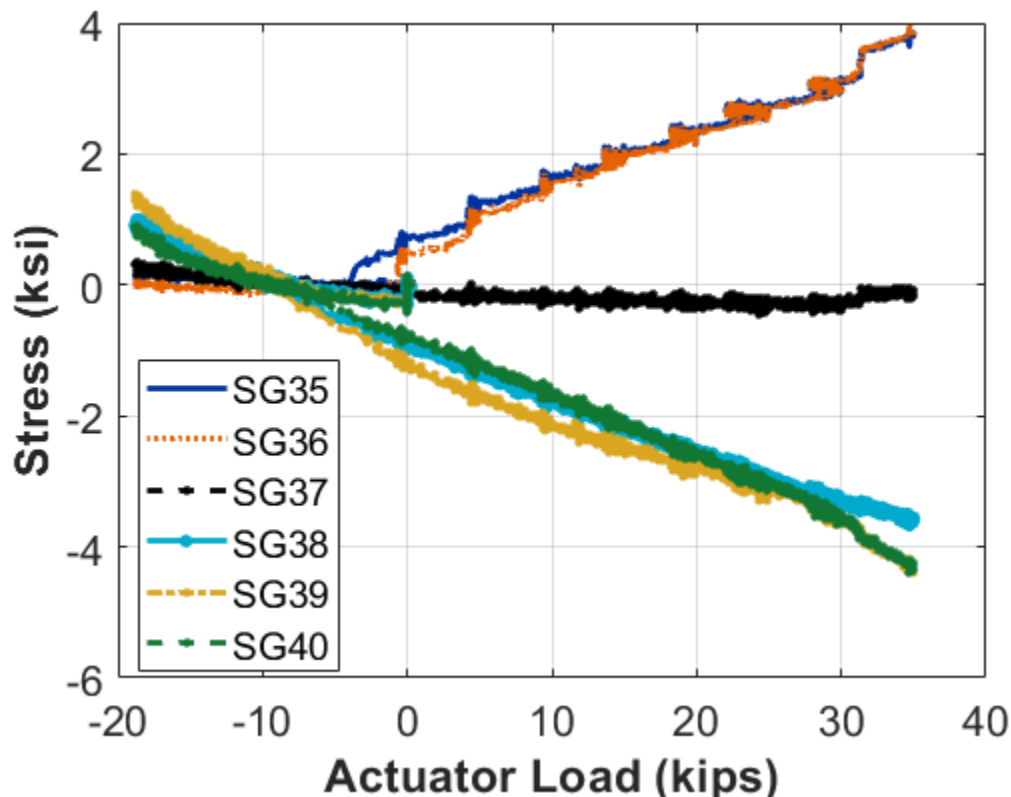


Figure 5.49. Concept A Static Testing Steel Beam Stresses at E1.

The stresses in the splice connection plates can be seen in Figure 5.50. SG45 and SG46 were located on the top flange connection plates, while SG47 and SG48 were located on the bottom flange connection plates. The changes in stress can be seen as almost perfectly linear, with the stresses in the top flange increasing in tension, while the stresses in the bottom flange increase in compression.

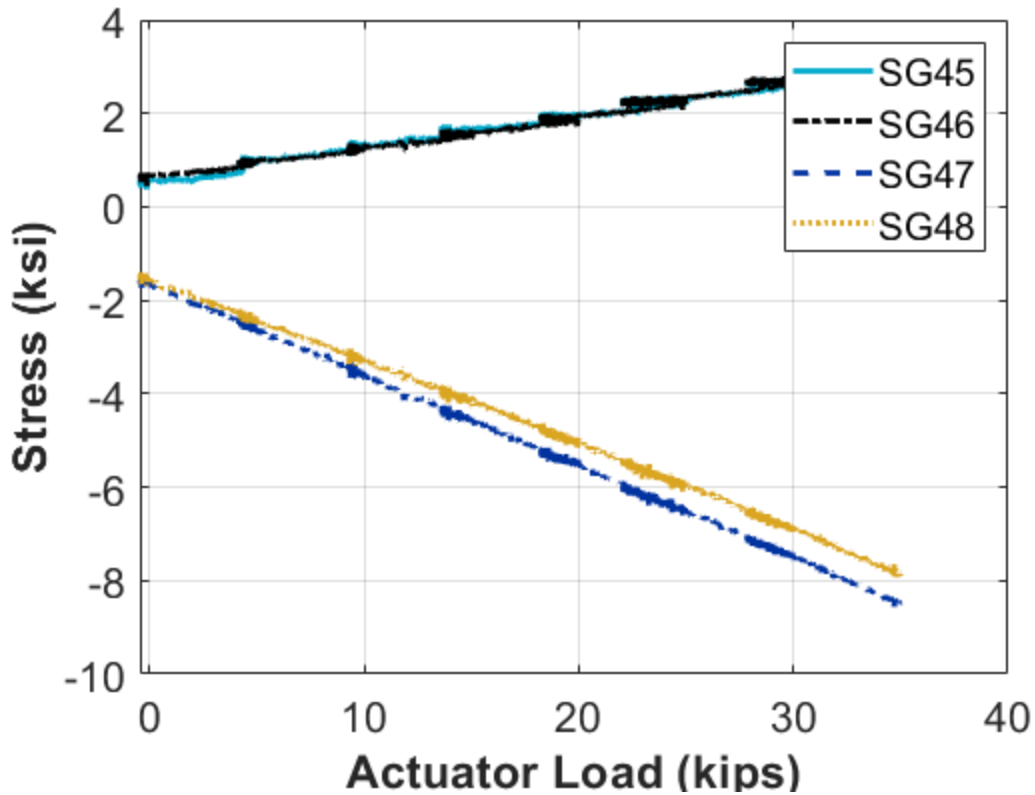


Figure 5.50. Concept A Static Testing Splice Plate Stresses.

The static testing was considered complete at this point. The specimen was put back on the pedestal and was inspected for any new cracks that may have formed. The data were analyzed, and based on the recorded displacements and forces, a testing regimen for the cyclic portion of testing was formulated.

5.7.2.3. Concept A Cyclic Testing

A total of 430,000 cycles were run during the cyclic testing, with 7,200 cycles run at a lower displacement level at the beginning of the cyclic testing to see how the specimen would react. After these cycles, the rest were run at the higher displacement level (equivalent to +30 kips to -15 kips). See Table 5.9 for an overview of the cyclic testing ranges.

Table 5.9. Concept A Cyclic Testing Ranges.

Day	Number of Cycles	Load Rate (Hz)	Displacement Control Range
1	7,200	1	(−0.30") to (+0.10")
2	16,200	1	(−0.4") to (+0.15")
3	82,800	1	(−0.4") to (+0.15")
4	19,800	1	(−0.4") to (+0.15")
5	79,200	1	(−0.4") to (+0.15")
6	82,800	1	(−0.4") to (+0.15")
7	72,000	1	(−0.4") to (+0.15")
8	70,000	1	(−0.4") to (+0.15")
Total	430,000		

The specimen was periodically inspected for signs of damage throughout the cyclic testing. Three major cracks formed during the cyclic testing. One crack formed down the transverse centerline of the closure pour region at approximately 8,000 cycles. This crack can be seen in Figure 5.51. Two more cracks formed around 130,000 cycles approximately 7 ft away from the transverse centerline on the active loading end. These cracks can be seen in Figure 5.52.

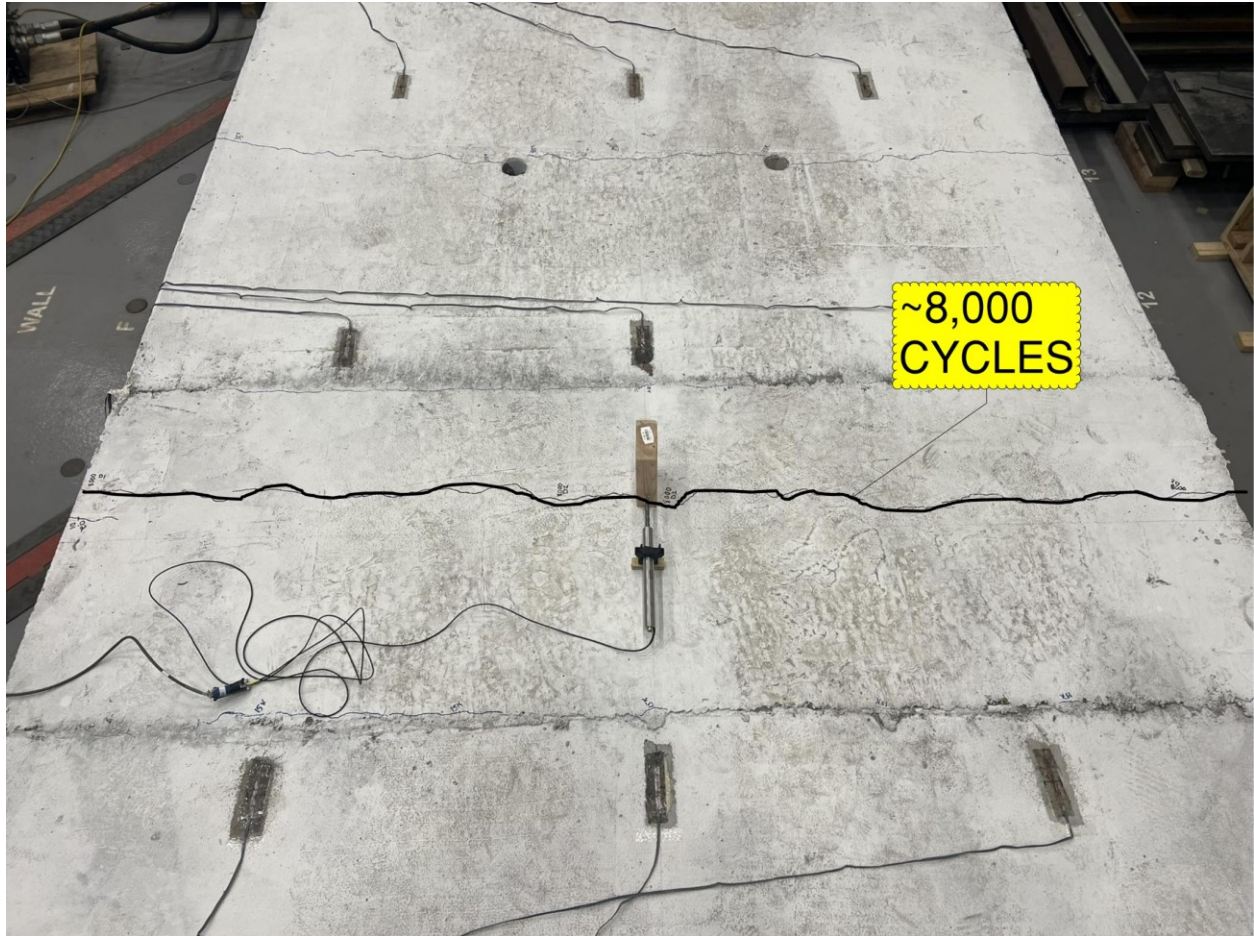


Figure 5.51. Concept A Cyclic Testing Closure Pour Crack.

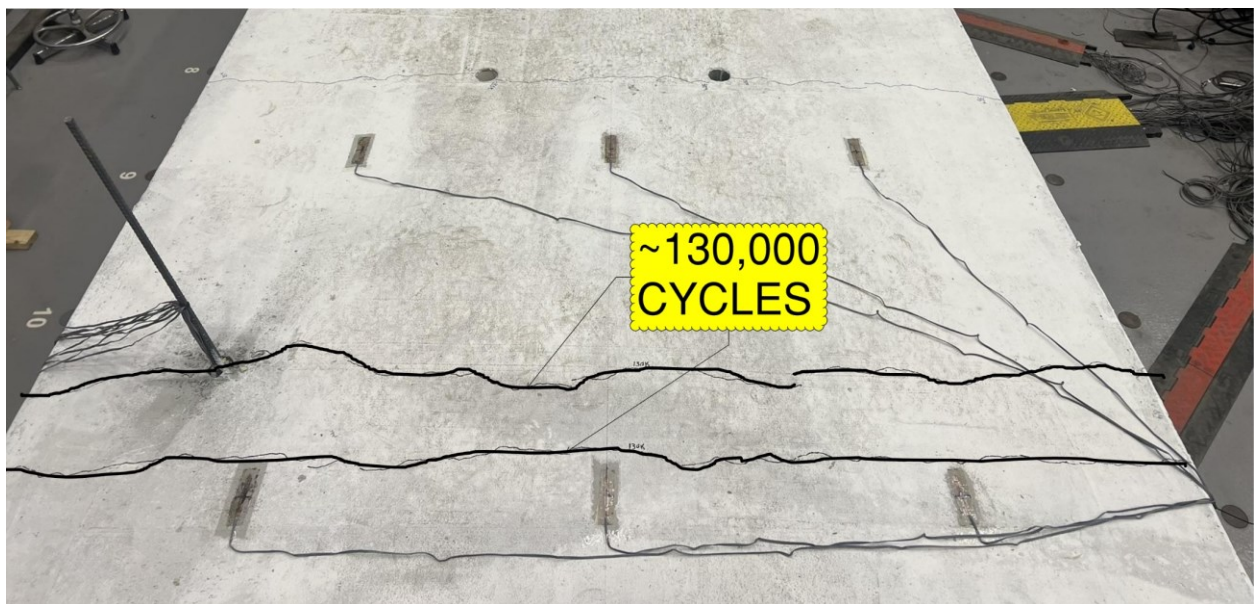


Figure 5.52. Concept A Cyclic Testing Cracks on Active Loading End.

5.7.2.4. Concept A First Ultimate Testing

The first ultimate testing for Concept A began by lifting the specimen off the support pedestal on the active loading end. This effort required approximately 15 kips to achieve, which was slightly lower than before the static testing, likely because the specimen was worn out from the static and cyclic testing, so it was less stiff. The specimen was lowered so that the actuator read 0 kips, which was considered the zero point for this test. The displacement at this point was 0.066 inches down from when the specimen was on the pedestal. The ultimate testing of this concept was carried out using displacement control on the active loading end actuator. The specimen was pushed down in $\frac{1}{8}$ -inch increments. After each increment, the specimen was inspected for signs of damage. Only two new signs of damage were noticed during this testing. A crack formed through the lifting holes on the hold-down end of the specimen at the equivalent force of 35 kips. Another crack formed approximately 7 ft 6 inches away from the transverse centerline on the hold-down end of the specimen at the equivalent force of 53 kips. A loud crack was heard when this crack formed. These cracks can be seen in Figure 5.53.

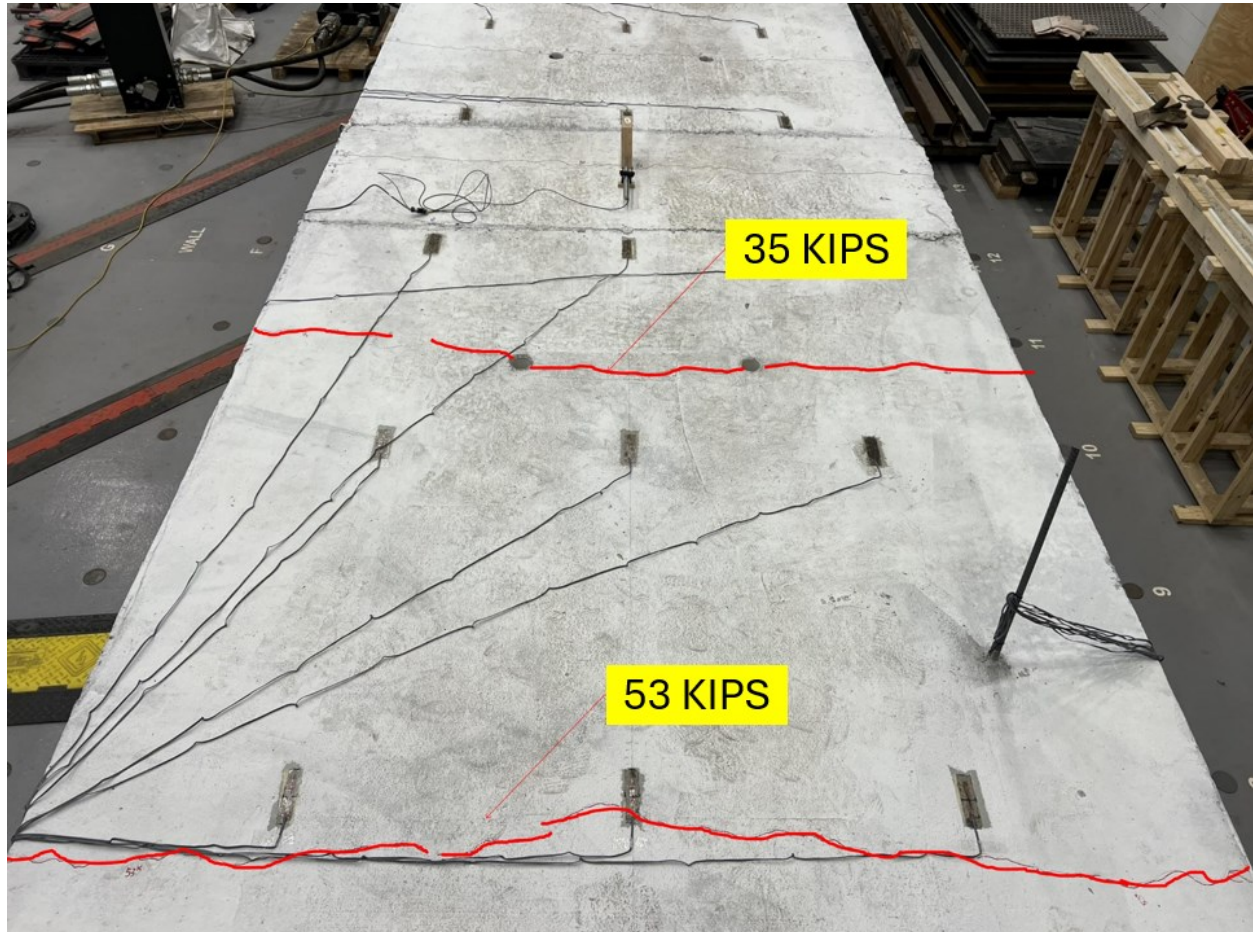


Figure 5.53. Concept A Ultimate Testing Cracks on Hold-Down End.

The displacement time history plot and the actuator load time history plot can be seen in Figure 5.54 and Figure 5.55, respectively. E7N and E7S on the displacement time history plot are the string pots on the north and south side of the specimen at gridline E7. The string pots slightly deviated from one another during the test because the loading of the specimen from the active loading end was not perfectly concentric, so the specimen did experience some minor torsional effects during the testing.

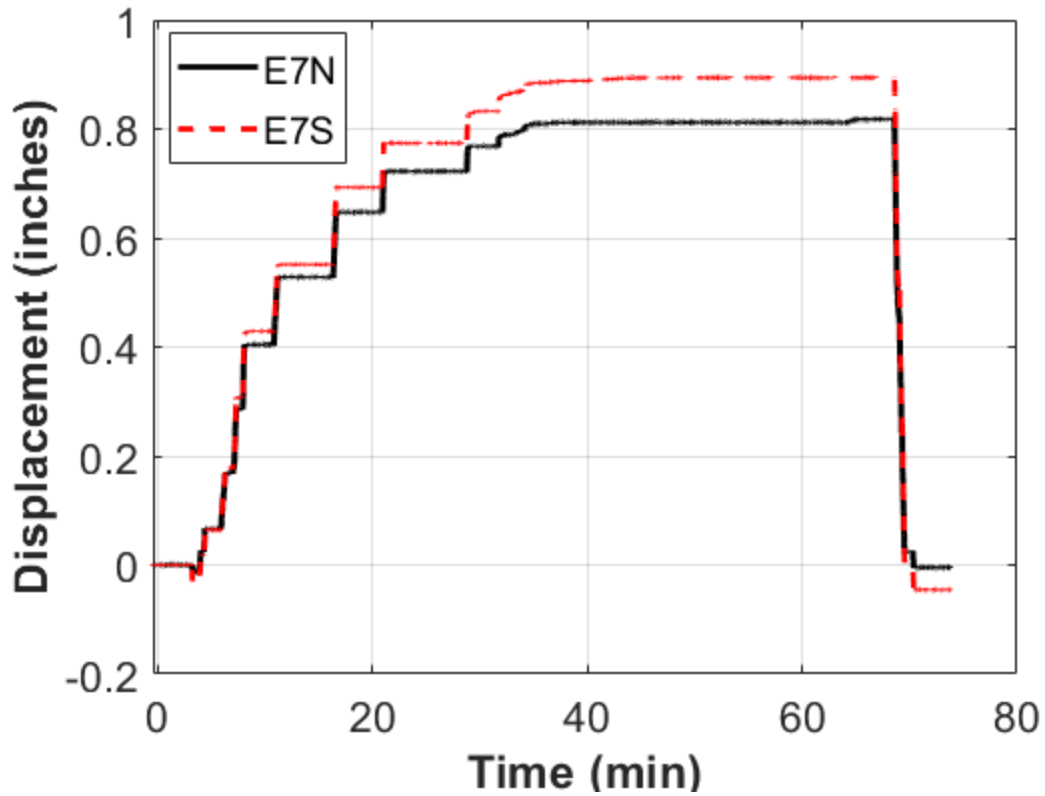


Figure 5.54. Concept A Ultimate Testing 1 Displacement Time History.

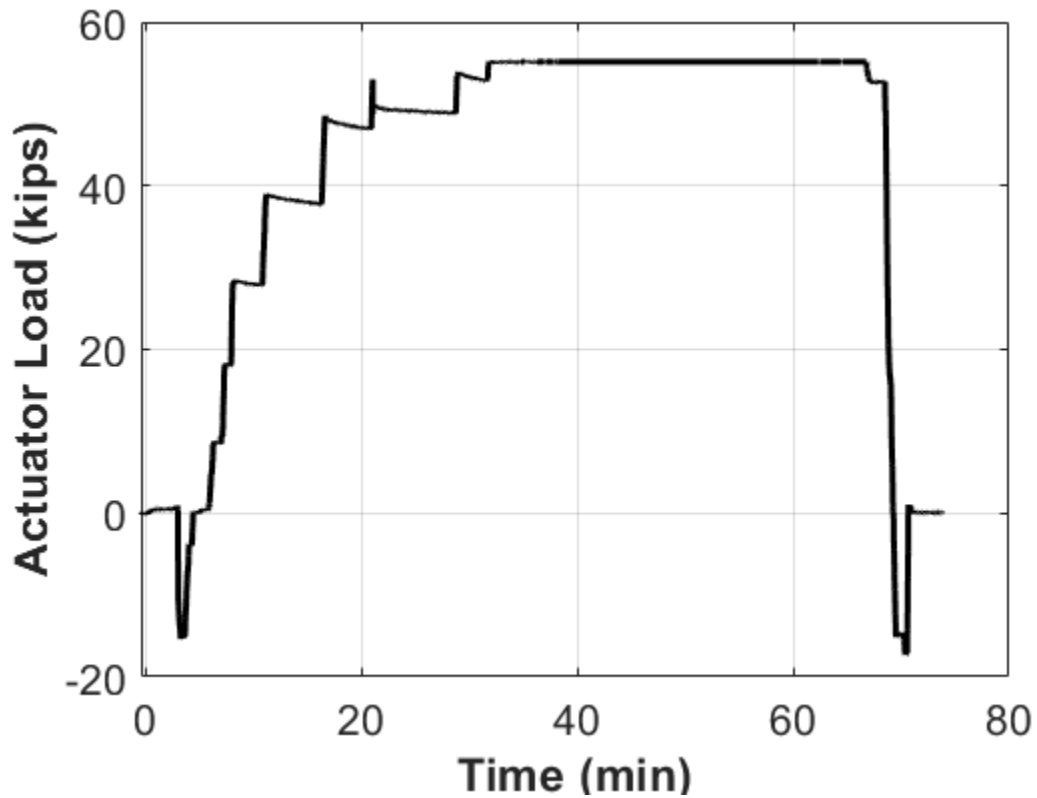


Figure 5.55. Concept A Ultimate Testing 1 Force Time History.

The actuator load versus displacement plot can be seen in Figure 5.56. The negative load and negative force indicate the portion of the testing in which the specimen was being pulled up to remove the support pedestal. The plot is linear up to 53 kips, which is when the previously mentioned crack formed, thereby lowering the stiffness of the specimen.

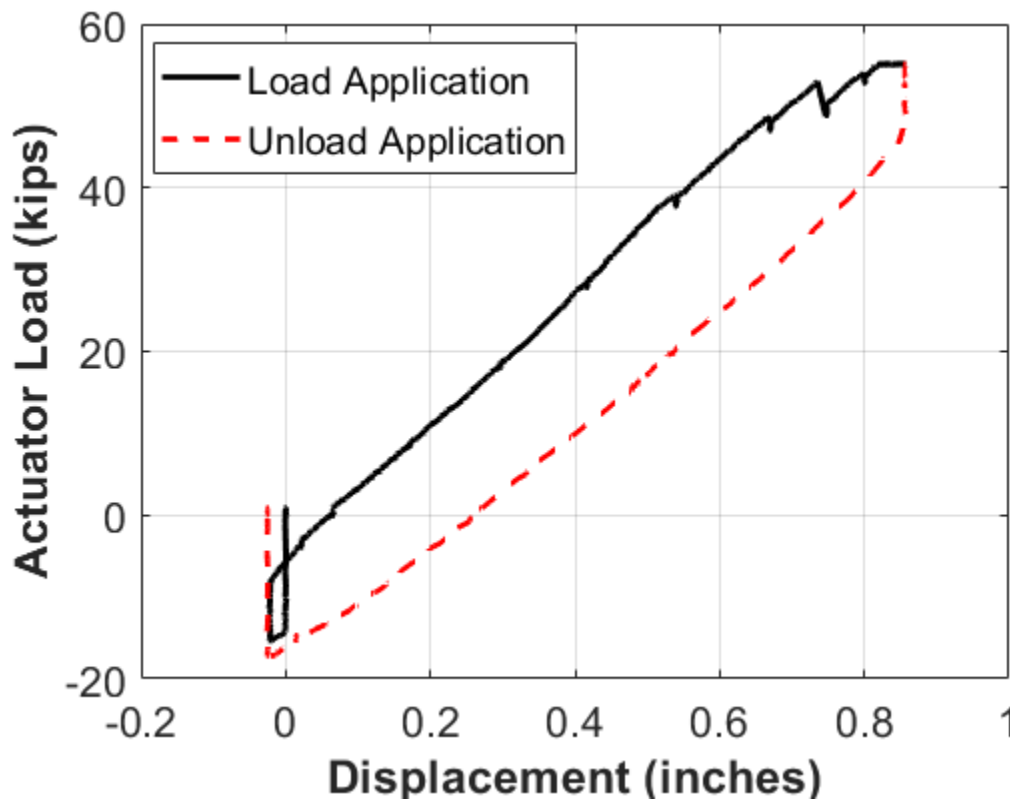


Figure 5.56. Concept A Ultimate Testing 1 Force Displacement.

Because the capacity of the active loading end actuator was only 55 kips and the data indicated the specimen had additional capacity, the team decided more force was required to complete the ultimate testing.

5.7.2.5. Concept A Second Ultimate Testing

To allow for a higher ultimate testing load, the 55-kip actuator was replaced by a 100-kip ram. This ram was placed on a different frame (with the header beam lowered) and was put into the same position on the beam that the 55-kip actuator had been in. See Figure 5.57 for a view of the ram being attached to the frame.



Figure 5.57. 100-kip Ram Assembly for Concept A.

This ram was not connected to the specimen because it was only pushing down on the specimen and not pulling up. To lift the specimen and remove the support pedestal, a through-hole jack was placed under the bottom flange, and the specimen was jacked up. Because the 100-kip ram did not have a string pot attached to it, the displacement of the specimen was measured purely by the string pots on gridline E7.

The time-displacement history plot can be seen in Figure 5.58. The specimen was pushed down in 1/8-inch increments—the same as in the first ultimate test. The specimen was inspected after each increment to check for signs of damage. The string pot on the north side of the specimen was showing a larger displacement than the one on the south side, indicating that the specimen was undergoing torsion. This result was likely due to the 100-kip ram not being exactly on the longitudinal centerline of the specimen.

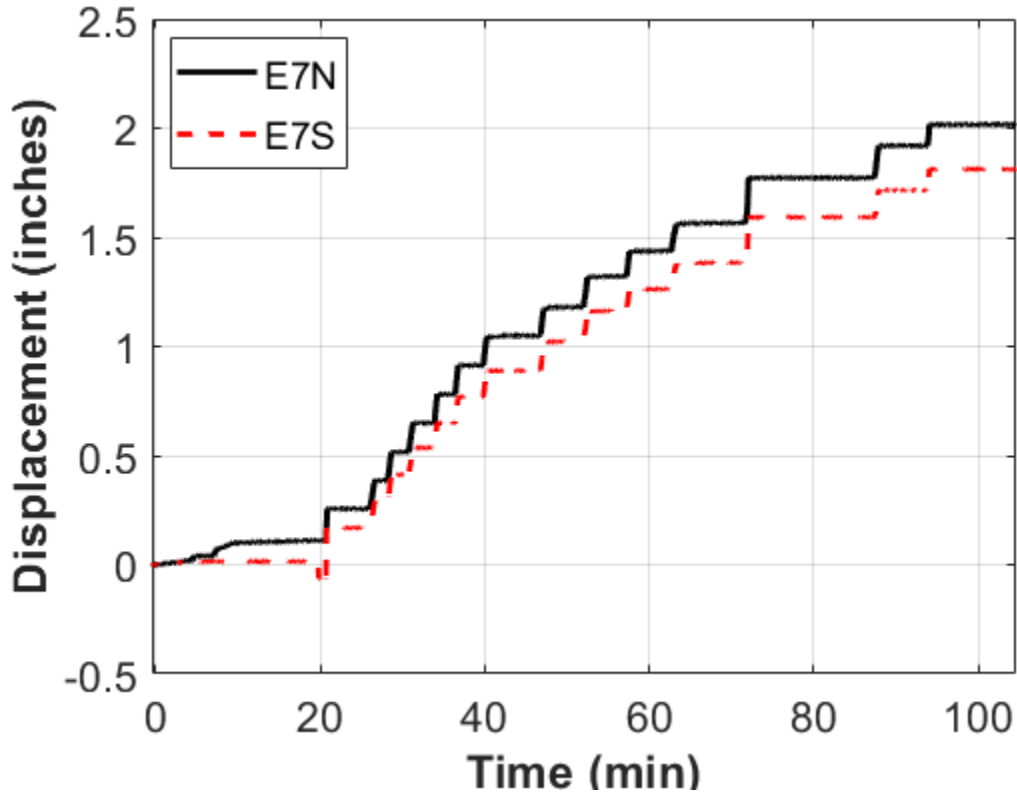


Figure 5.58. Concept A Ultimate Testing 2 Displacement Time History.

The load time history plot can be seen in Figure 5.59. The plot shows that after each step up to about 56 kips, the load dropped slightly due to the specimen relaxing. Past this point, after each increment that the specimen was displaced, the specimen lost a significant amount of stiffness. Many new cracks formed after this load level. The significant gap at approximately 70 minutes was when the bottom flange plates slipped. A very loud bang was heard and was accompanied by a large drop in load. The load on the specimen at slip was 74 kips. It was determined that the test should continue and that the load that was on the specimen at the time of slip should be put back on the specimen. A second loud bang was heard at approximately 72 kips, which was most likely the plates on the web slipping. After hearing this second bang, researchers ended the test, and the cause of failure was plate slippage.

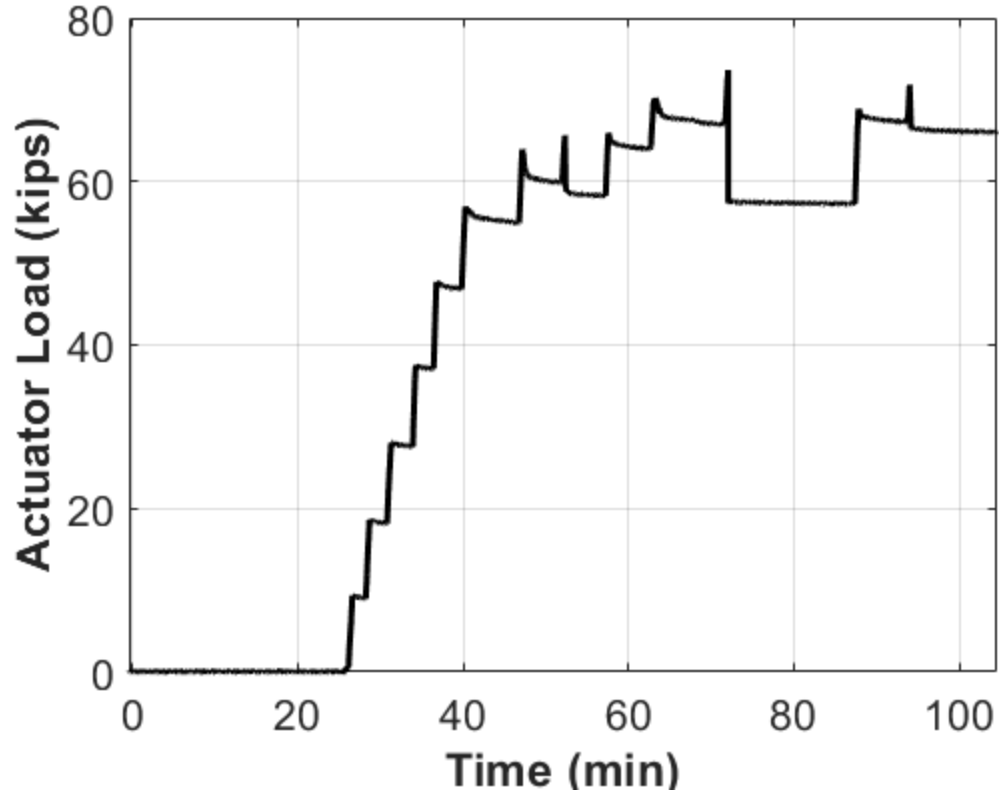


Figure 5.59. Concept A Ultimate Testing 2 Force Time History.

The actuator load versus displacement plot can be seen in Figure 5.60. This plot follows a linear path until approximately 56 kips (roughly twice the HL-93 design load negative bending demand), which is when the specimen started dropping load. After each subsequent increment, the load dropped significantly. The first large jump indicates the bottom flange plates slipping, while the second smaller jump indicates the web plates slipping. From the plot, it can be seen that some damage occurred to the specimen because when the load was taken off the specimen did not return to its original position. It had over an inch of deformation.

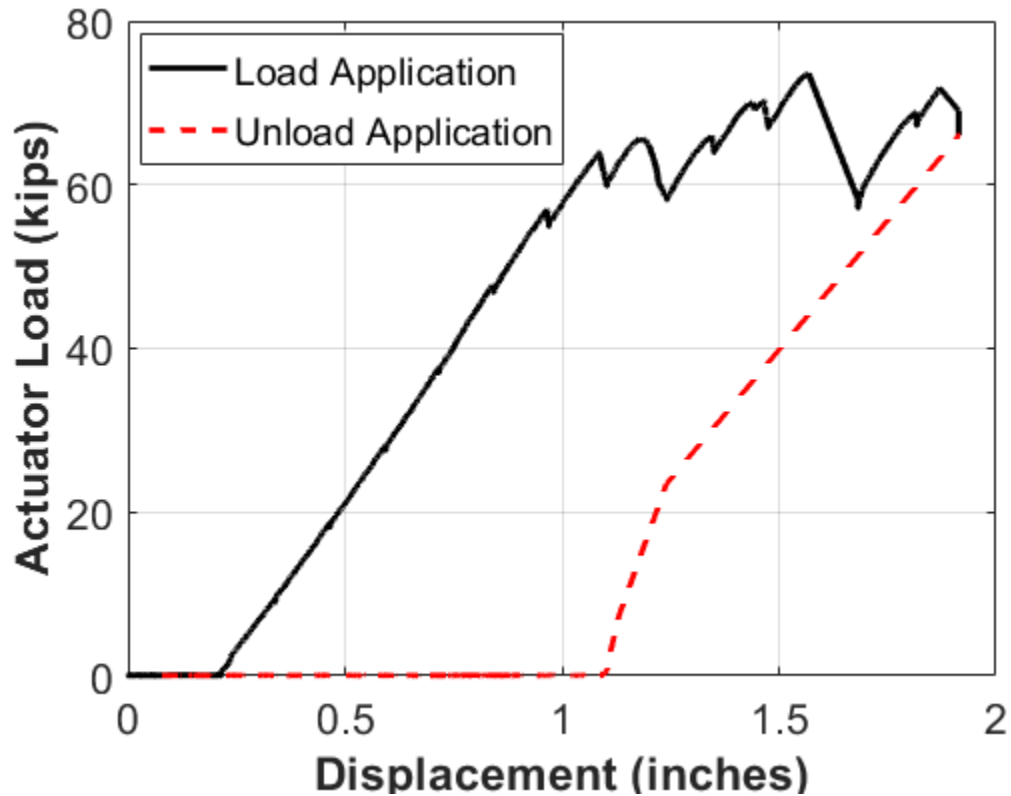


Figure 5.60. Concept A Ultimate Testing 2 Force Displacement.

The stresses on the surface of the precast concrete deck at gridline E1 can be seen in Figure 5.61. SG59 was located on the longitudinal centerline, and SG58 and SG60 were located 2 ft on either side. The stresses on the outer strain gauges increased in more tension as the load increased, which made sense. The middle strain gauge does not show an increase in stress because a crack had formed that ran directly through the strain gauge, so it was not reading correctly.

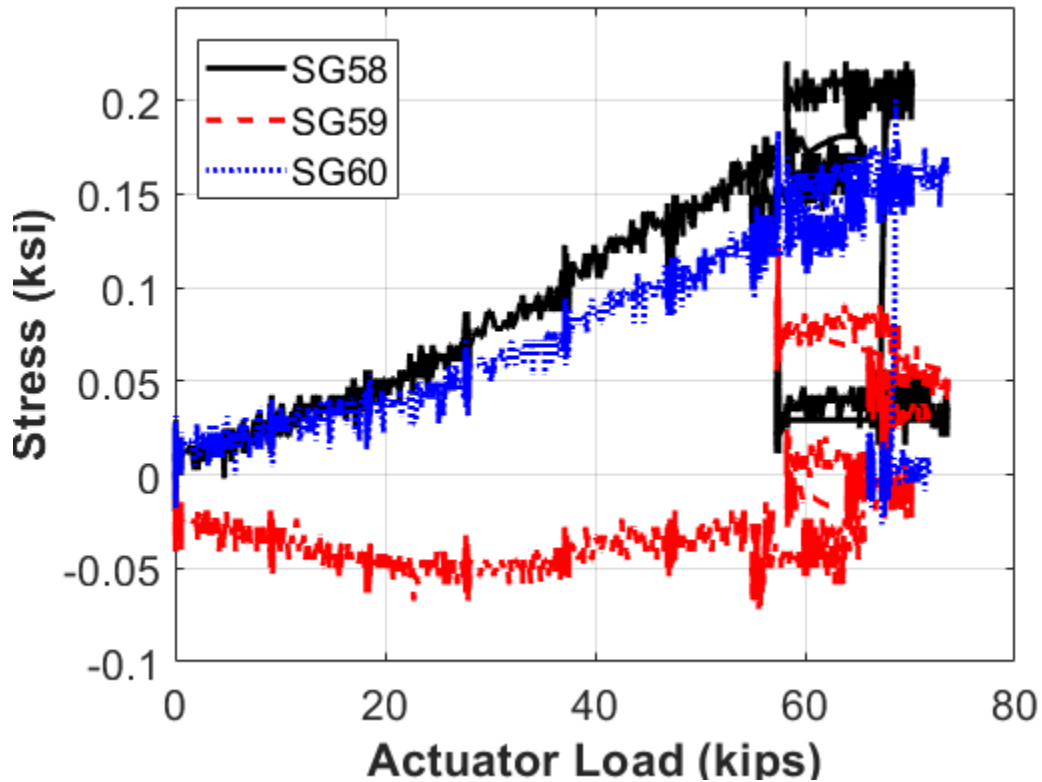


Figure 5.61. Concept A Precast Concrete Deck Stresses at E1.

The deck stresses at gridline E2 can be seen in Figure 5.62. SG62 was located on the longitudinal centerline, and SG61 and SG63 were located 2 ft on either side. Similar to the stress at E1, as the load increased on the specimen, the stress greatly increased very linearly in the tensile direction. Toward the end, the data appear to show a lot more noise, which was when the bottom plates slipped, so the vibrating of the specimen along with the loss of stiffness caused additional noise in the data.

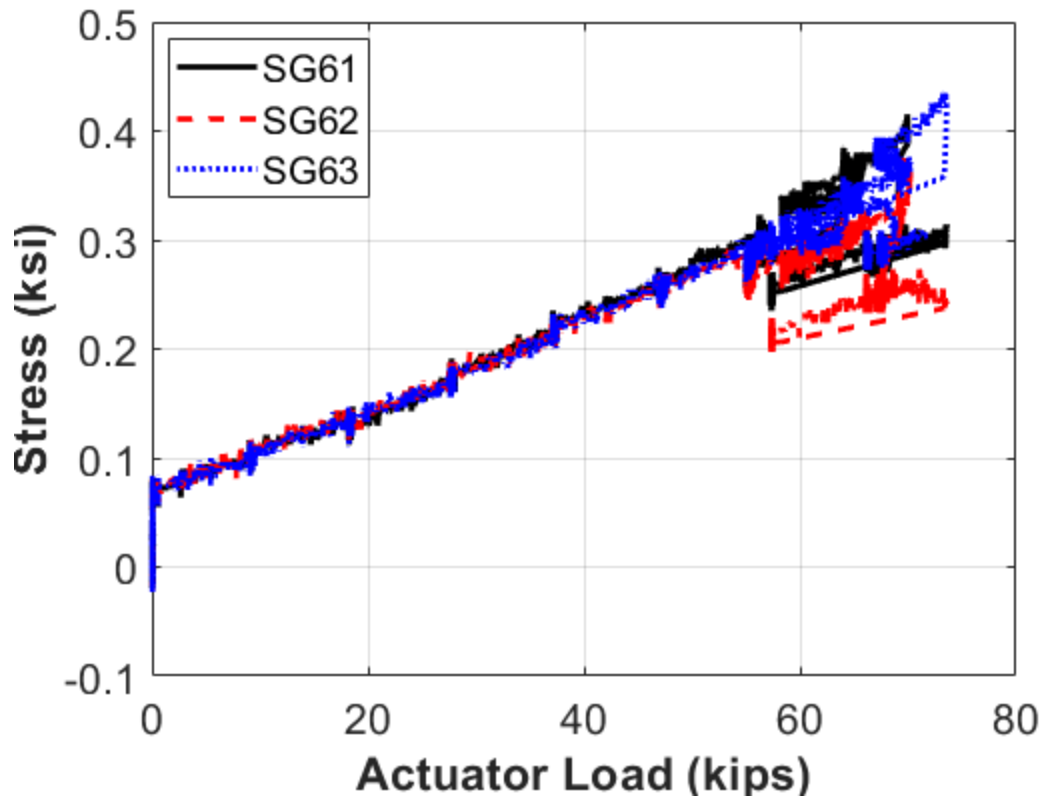


Figure 5.62. Concept A Precast Concrete Deck Stresses at E2.

The stresses on the longitudinal rebar at gridline E3 can be seen in Figure 5.63. SG17 was located on the centerline, while SG16 and SG18 were located 2 ft on either side. The initial stress at zero-load was due to the self-weight of the structure as it was in its cantilevered state. After the load on the active loading end was applied, the stress increased fairly linearly. There are several jumps in the data because the 100-kip ram was not attached to the specimen, so when it stopped pushing on the specimen, it kept going toward the floor and then rebounded. The noise at the end of the plot is due to the plates slipping on the bottom flange and then the web.

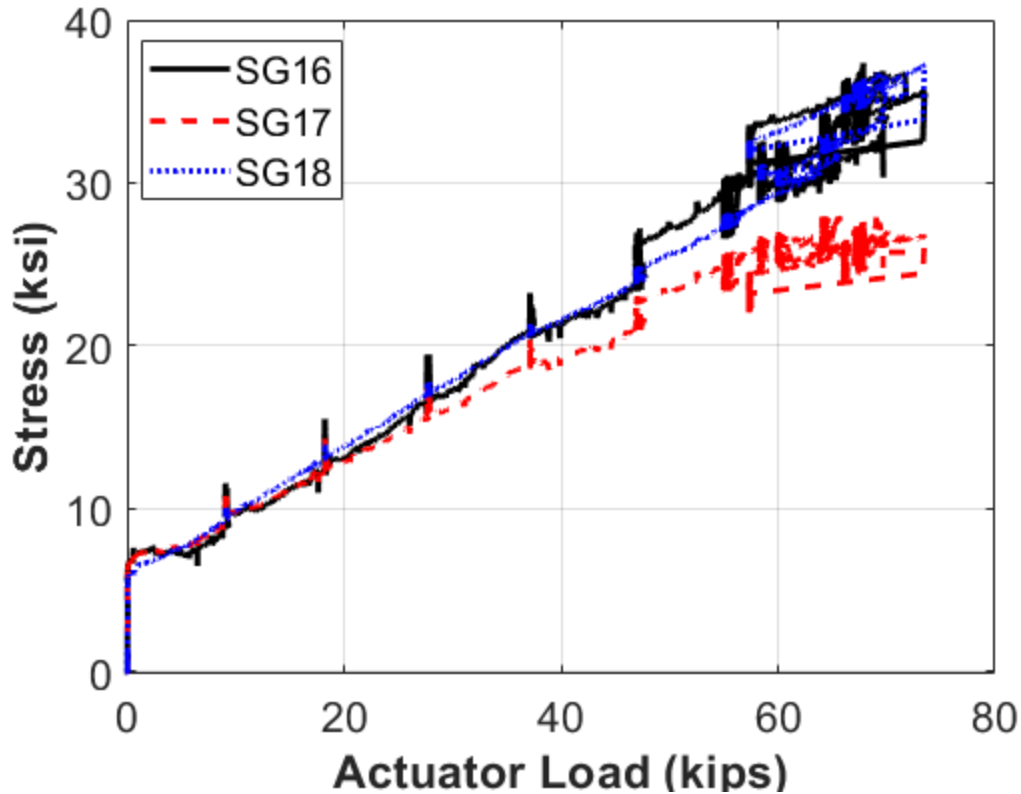


Figure 5.63. Concept A Rebar Stresses at E3.

The stresses in the U-loop rebar at gridline E0.5 can be seen in Figure 5.64. Only one set of data on the plot exists because the other two strain gauges on this gridline failed at some point during the testing. SG22 was located 2 ft on the north side of the centerline (gridline 0.2D in Figure 5.21). Similar to the longitudinal rebar, the initial stress in the U-loop is due to the self-weight of the specimen. The stresses increased linearly here as well to approximately 65 kips. At that point, the strain gauge displays a lot of noise, which could be due to microcracks forming in this area.

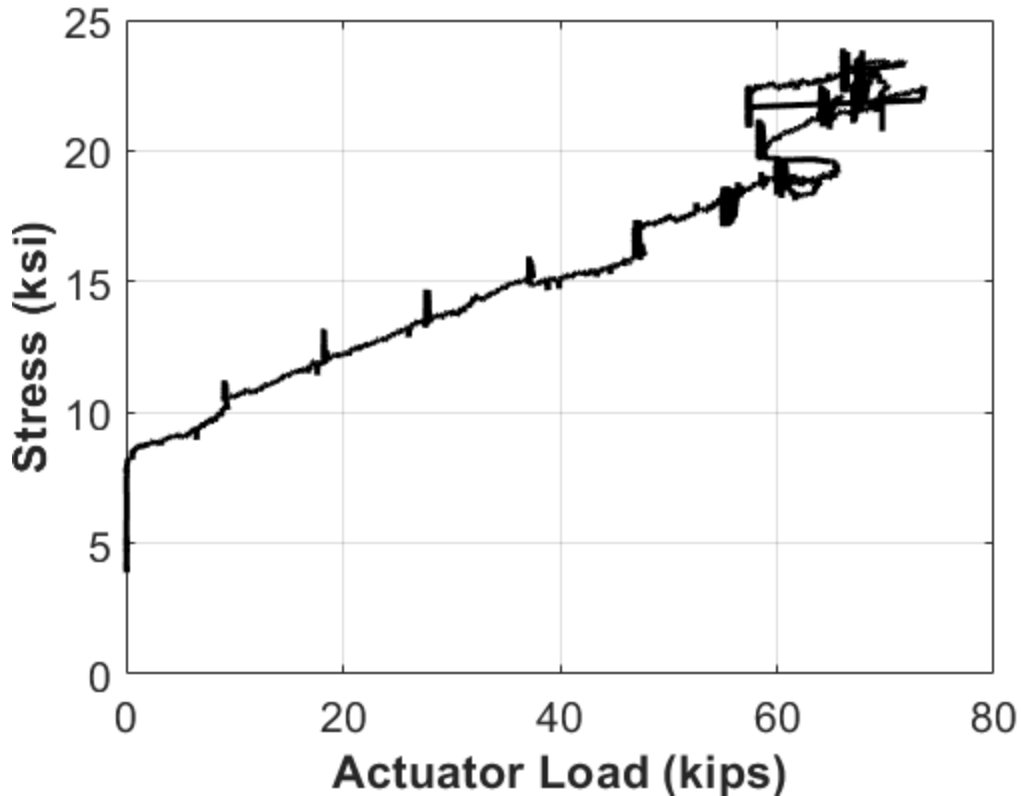


Figure 5.64. Concept A Ultimate Testing 2 U-Loop Rebar Stresses at E0.5.

The stresses in the steel beam at gridline E1 can be seen in Figure 5.65. SG35 and SG36 were located under the top flange on either side of the web, SG37 was located on the upper portion of the web, SG38 was located on the bottom portion of the web, and SG38 and SG39 were located on the top of the bottom flange on either side of the web. SG35 and SG36 both trended toward more tension as the loading increased, while SG38, SG39, and SG40 all trended toward more compression. These results make sense because the top flange was in tension, while the bottom flange and bottom portion of the web were in compression. SG37 stayed almost the same during the testing, indicating that it was located very near the NA. The noise at the end of the data is from the plates slipping on the bottom flange and the web.

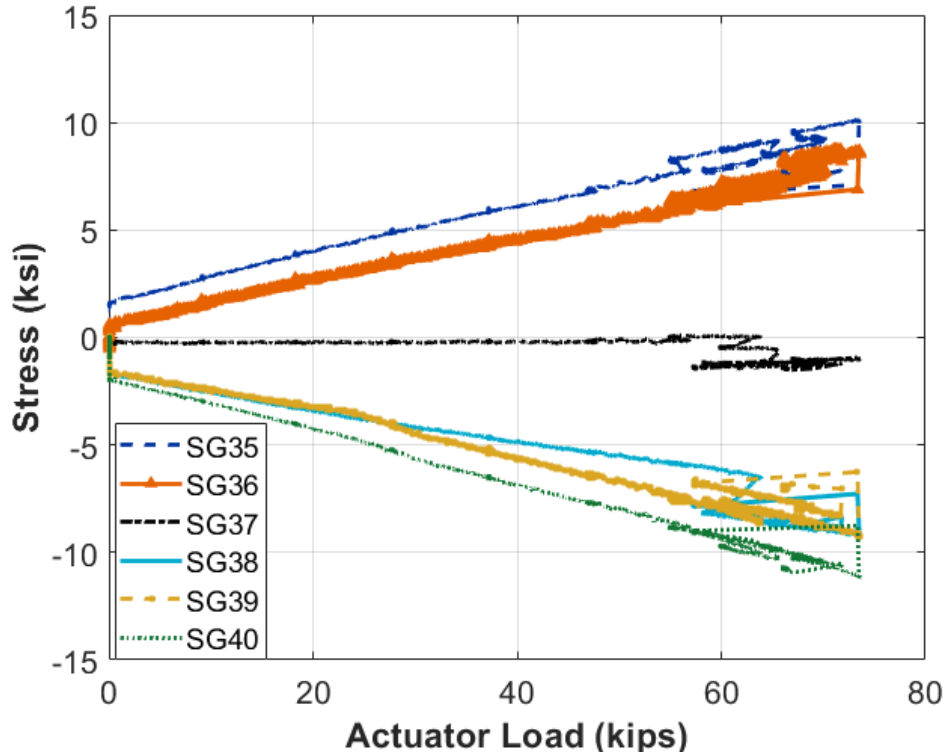


Figure 5.65. Concept A Ultimate Testing 2 Steel Beam Stresses at E1.

The stresses on the splice plates can be seen in Figure 5.66. SG45 and SG46 were located on the top flange connection plates, while SG47 and SG48 were located on the bottom flange connection plates. This plot reveals that the stresses in the top flange trended toward more tension, while the stresses in the bottom flange trended more toward compression. The top flange stresses exhibited spikes at each of the loading increments, but interestingly the bottom flange did not exhibit these jumps. The stresses in the bottom plate were linear until 64 kips, when they started to relax after each loading increment. From this plot, it appears there may have been some minor slippage happening, starting at approximately 64 kips. There are two significant jumps in the bottom flange data, both indicated by red arrows in the figure. The larger jump was 74 kips when the bottom plates slipped, and the second smaller jump was when the web plates slipped.

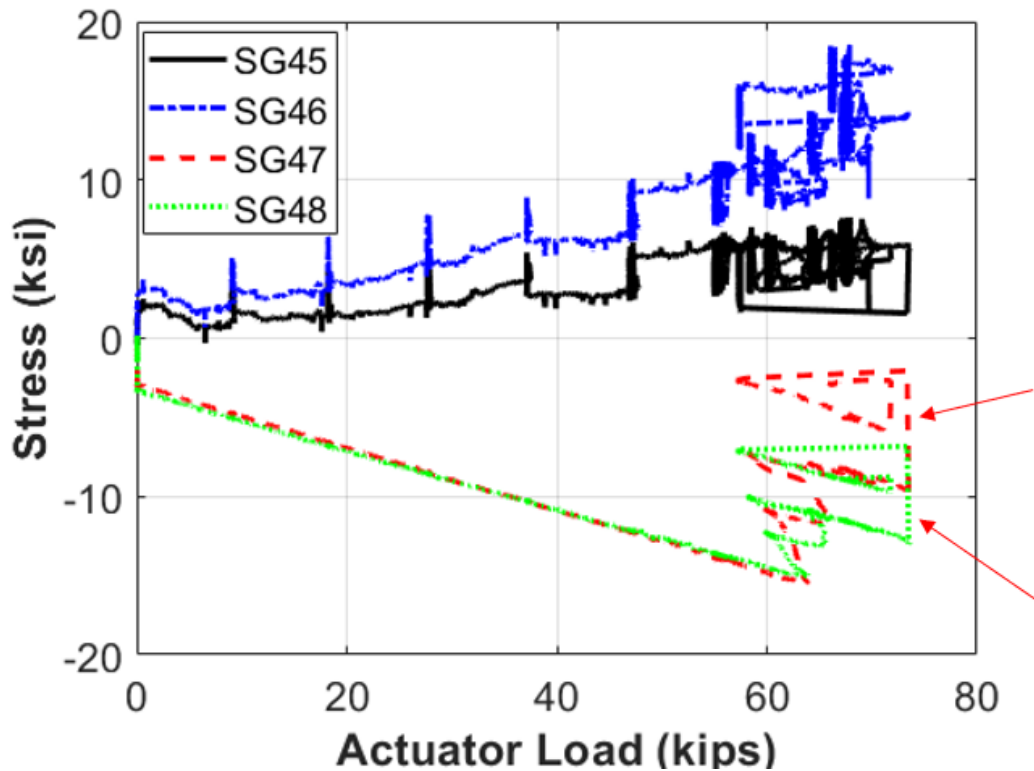


Figure 5.66. Concept A Ultimate Testing 2 Splice Plate Stresses.

Several plots show the location of the NA. Figure 5.67 to Figure 5.70 show the NA based on the strains from the structural steel strain gauges at E1 E2, W1, and W2, respectively. The load of 30 kips was chosen because that was the maximum load that was used during all three iterations of the static testing, and 73 kips was chosen because that was the maximum load of ultimate testing prior to slippage of the splice plates. These plots reveal that the NA stayed consistent at approximately 20 inches above the bottom of the bottom flange. This finding is consistent with the data because, as seen in Figure 5.65, SG37 showed almost no change in strain during the entirety of testing, and this strain gauge was located 20 inches from the bottom of the specimen. The composite NA of the cracked section was calculated as being 18.3 inches above the bottom of the specimen (see Appendix A for NA calculations), which very nearly matches the height of the NA that was computed using the results of the testing.

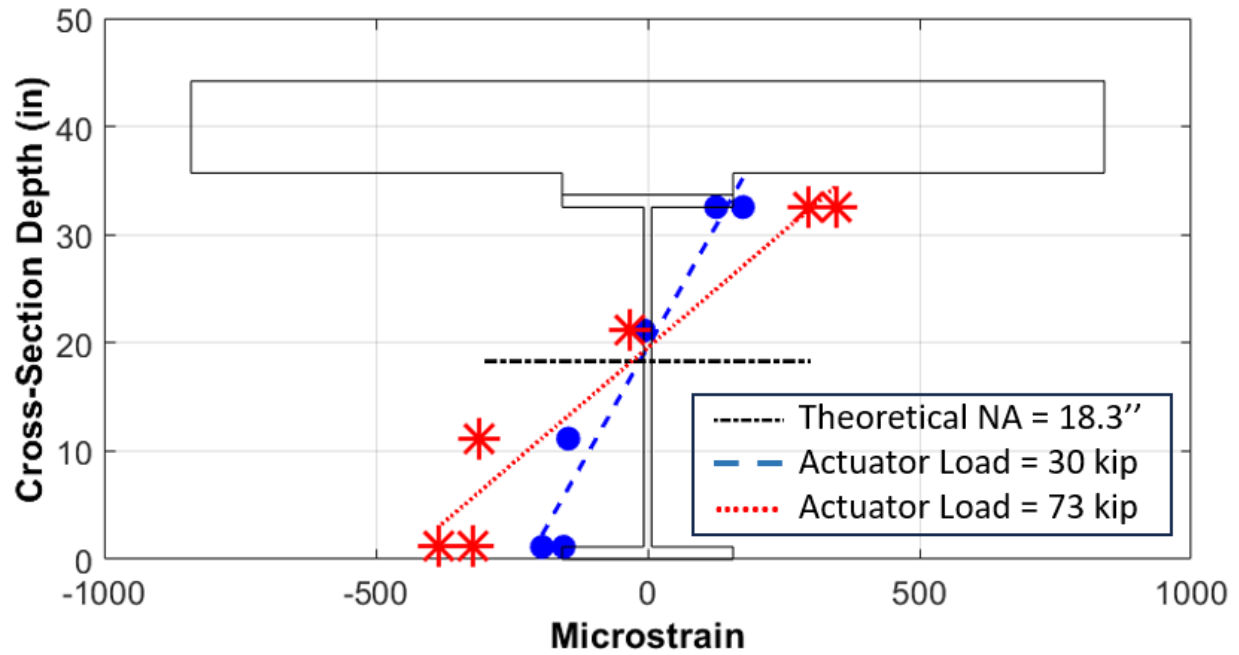


Figure 5.67. Concept A Ultimate Testing Structural Strain Profile at E1.

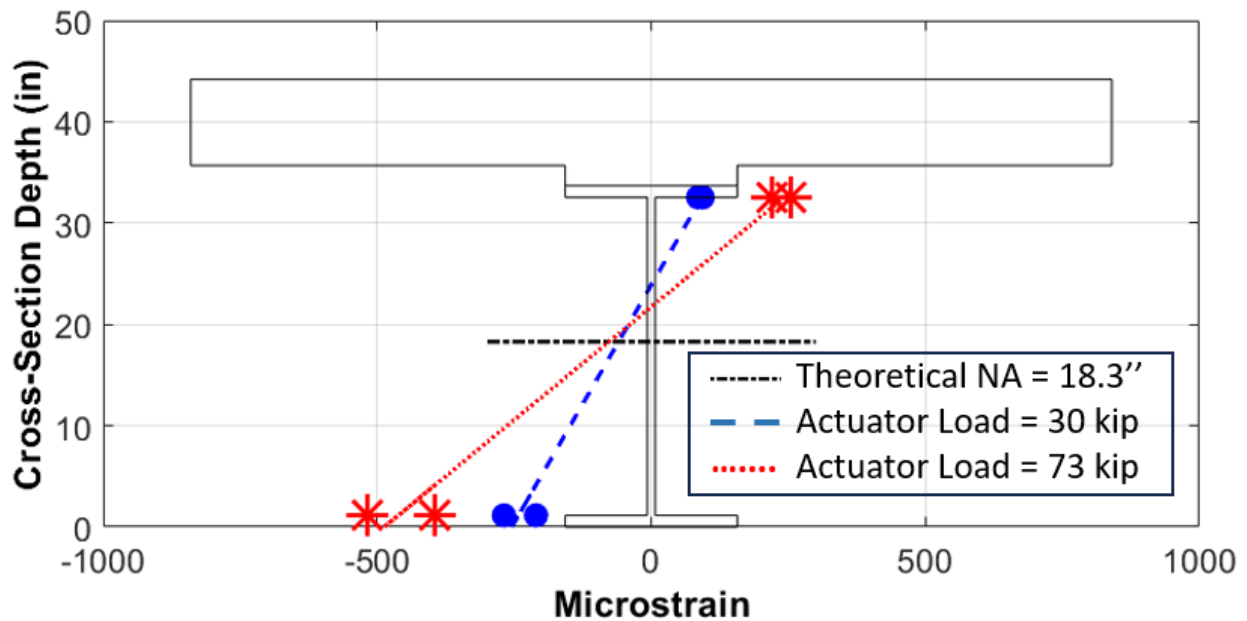


Figure 5.68. Concept A Ultimate Testing Structural Strain Profile at E2.

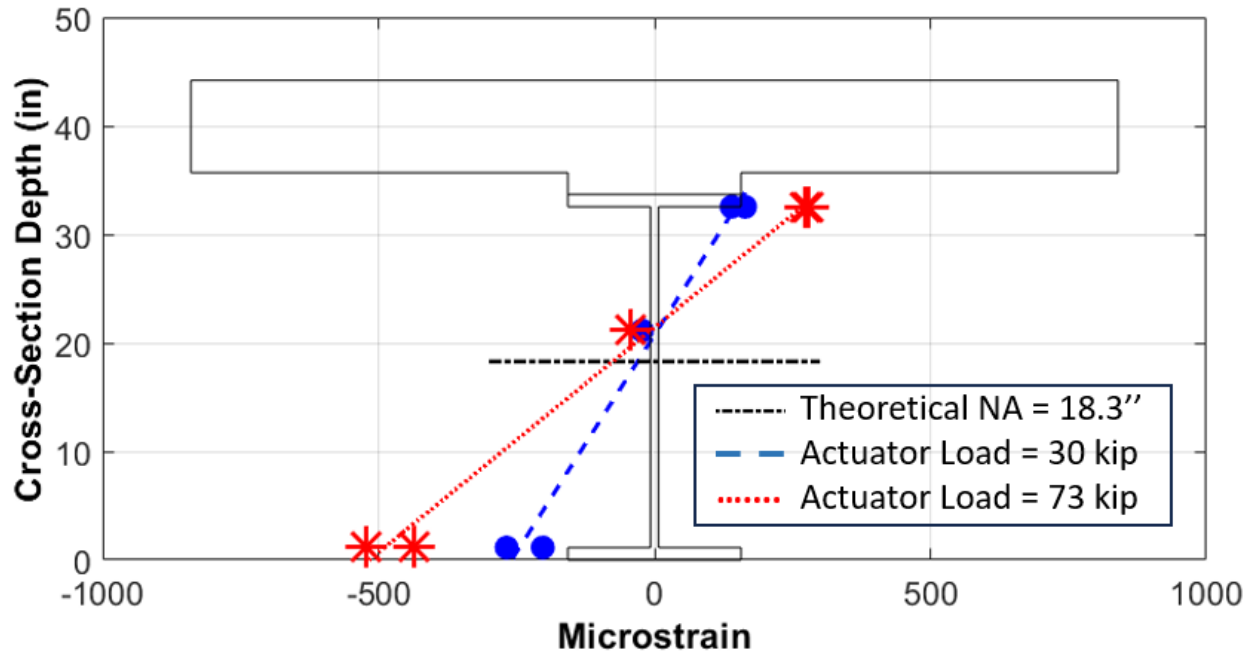


Figure 5.69. Concept A Ultimate Testing Structural Strain Profile at W1.

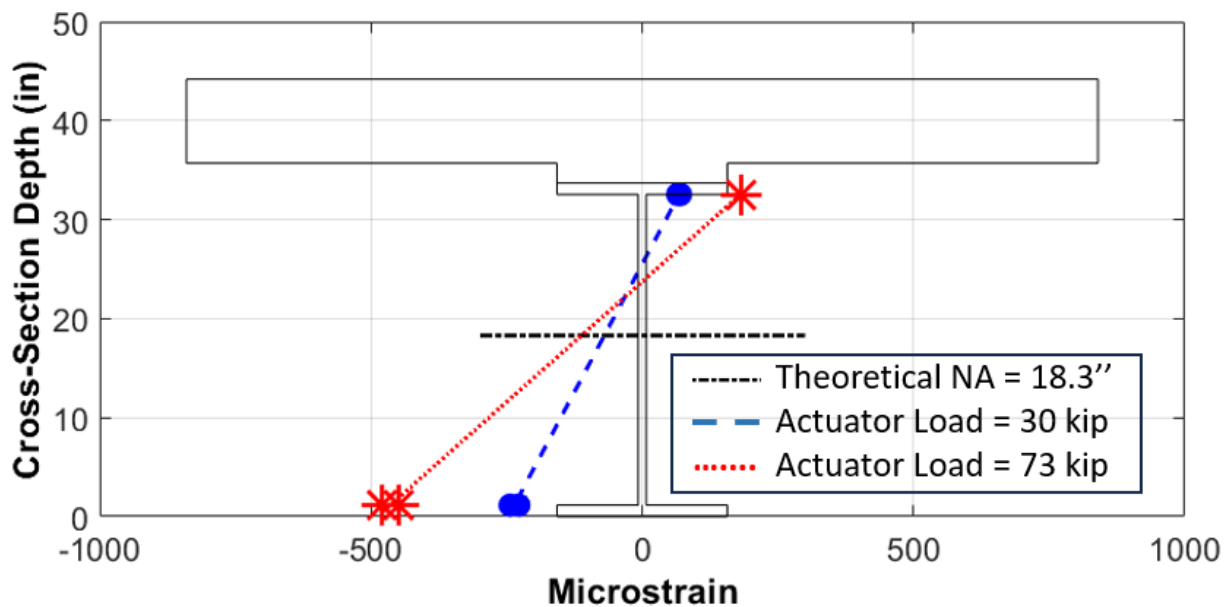


Figure 5.70. Concept A Ultimate Testing Structural Strain Profile at W2.

The load was taken off the specimen, and the through-hole jack was used to lift the specimen enough so the support pedestal could be placed under the end. After the specimen was placed back on the pedestal, the instrumentation was taken off, and the specimen was prepared for disposal. The specimen had to be broken in half by using a concrete saw to make a transverse cut down the center of the closure pour in order to remove it from the lab. A jackhammer was also

used to remove the concrete directly above the top plate on the top flange so that a cutting torch could get at it. See Figure 5.71 for a view of this process. The specimen was disposed of after being broken apart (See Figure 5.72).



Figure 5.71. Concept A Closure Pour Jackhammering.



Figure 5.72. Concept A Disposal.

5.7.2.6. Concept A Posttesting Observations

After the ultimate testing was completed, many observations were made from inspecting the specimen. The most obvious observation was that there were many cracks on the deck of the specimen that had formed over the course of testing. During the static testing, one visible crack formed (see Figure 5.41). During the cyclic testing, several more cracks formed that either stayed the same size or propagated. One of these cracks can be seen in Figure 5.73. This crack formed very early in the cyclic loading testing, and traveled almost exactly over the entire transverse centerline of the specimen.

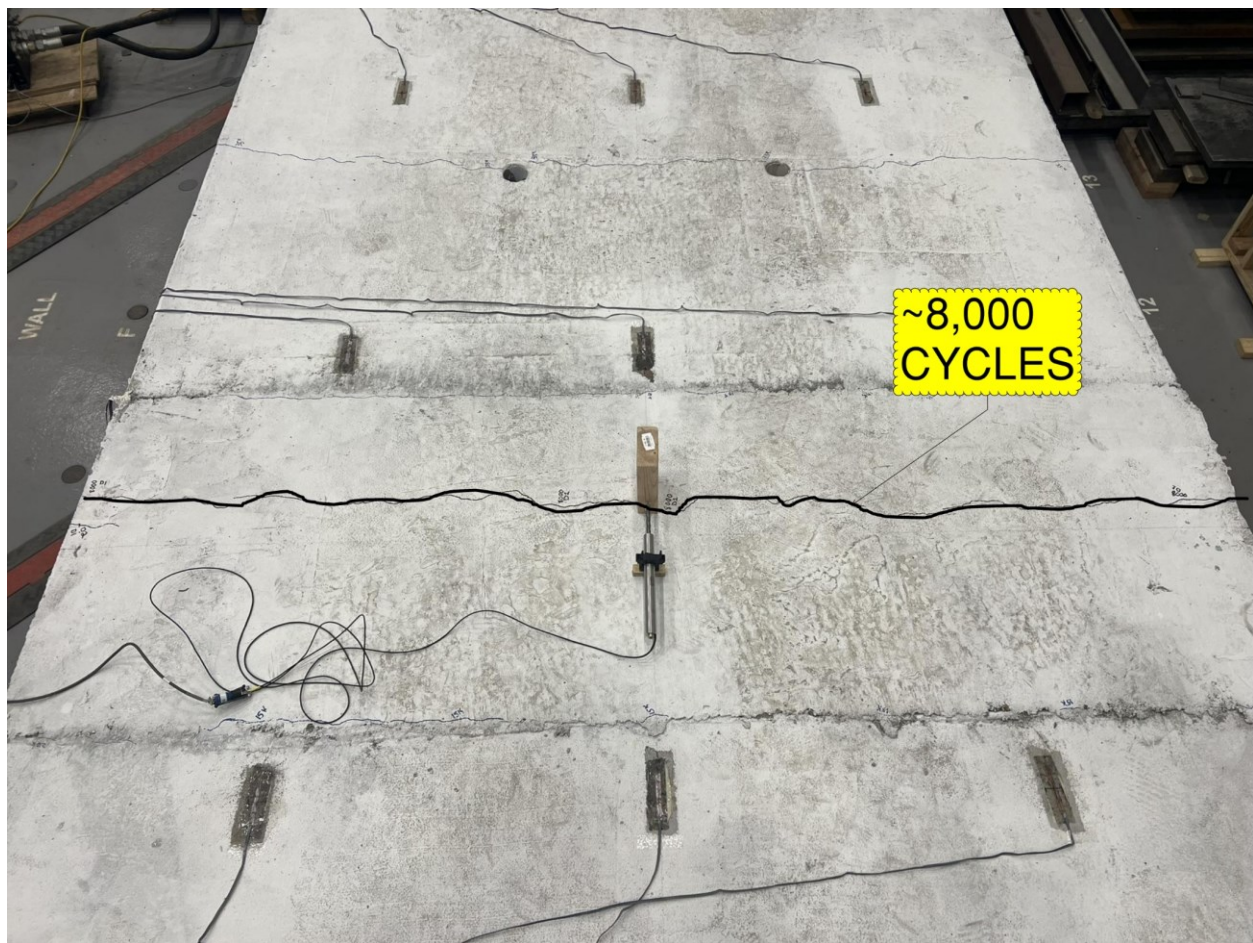


Figure 5.73. Transverse Centerline Crack Formed during Cyclic Testing.

Two more significant cracks that formed during the cyclic testing can be seen in Figure 5.74. These cracks formed very near each other around 130,000 cycles in and were located approximately 7 ft away from the transverse centerline of the specimen. The one on the bottom

may have formed due to the instrumentation coming out of the top of the slab on the left of the picture.

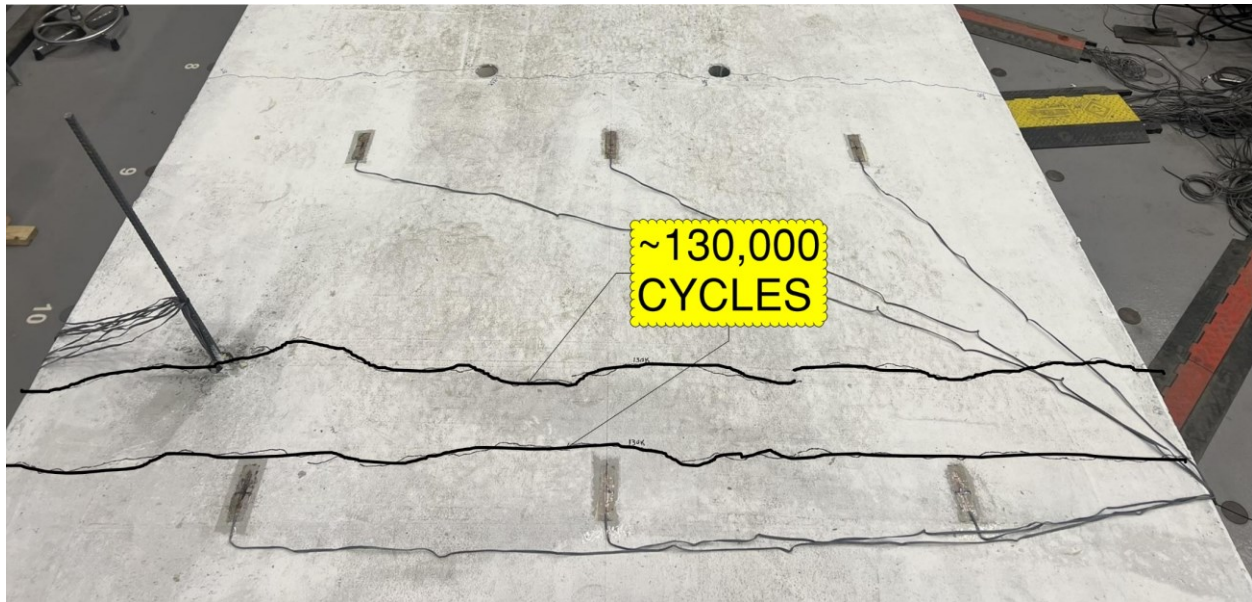


Figure 5.74. Cyclic Loading Cracks near Gridline E3.

A multitude of cracks formed during the ultimate testing. The cracks on the east side of the specimen can be seen in Figure 5.75, while the cracks on the west side can be seen in Figure 5.76. The cracks have been drawn over so that they can be seen better, and the loads next to them are the approximate loads at which they formed.

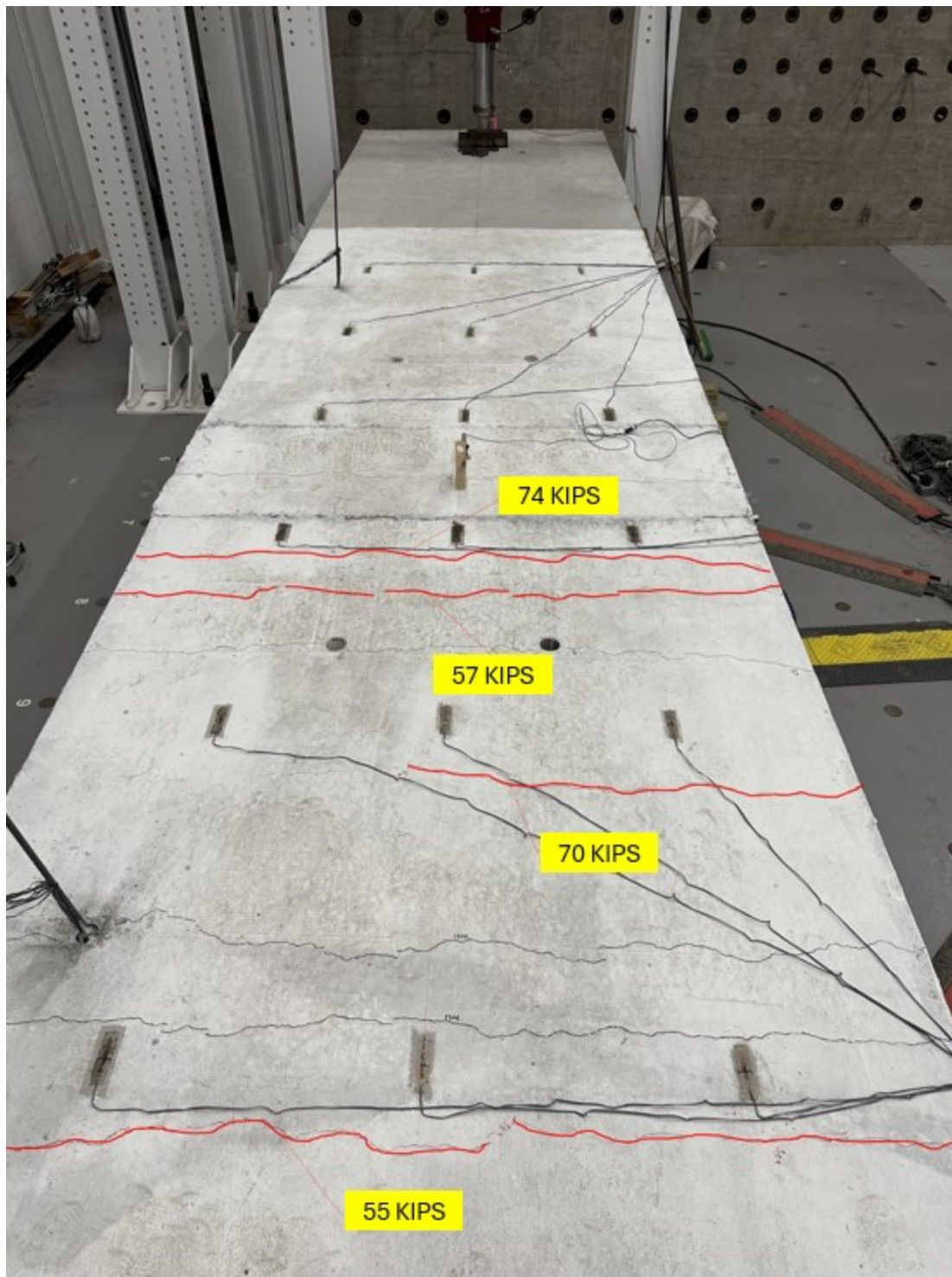


Figure 5.75. Cracks on East Side of Concept A after Ultimate Testing.

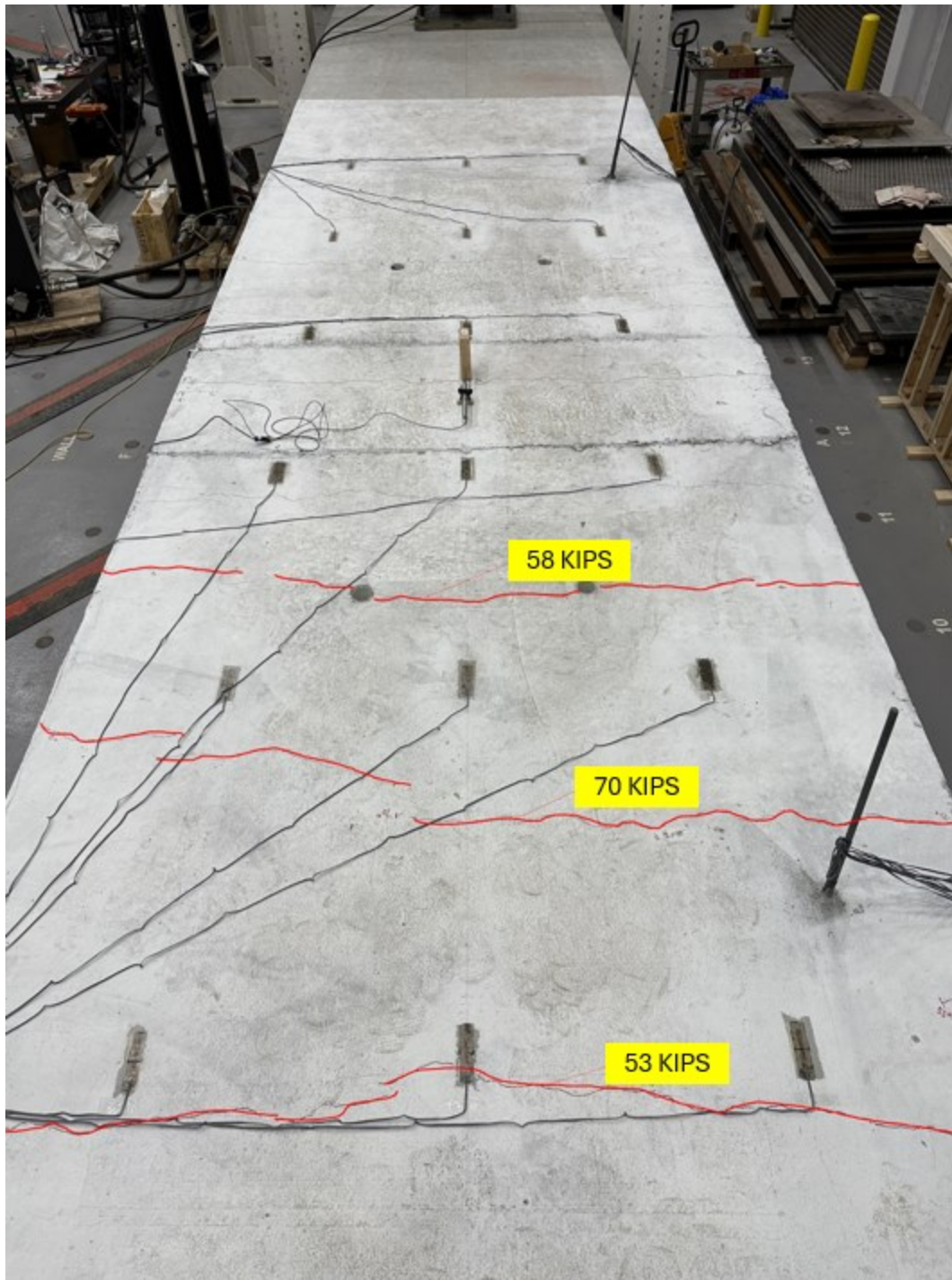


Figure 5.76. Cracks on West Side of Concept A after Ultimate Testing.

Overall, the number of cracks that formed on this specimen were generally evenly spaced along the length of the specimen.

Another major observation was made after the splice plates were taken off the specimen. Scour marks in the longitudinal direction could be seen on the surface that was in contact with the steel beam, indicating that movement between the plates had occurred. See Figure 5.77 and Figure 5.78 for a view of the scour marks on the bottom flange splice plates and the web splice plates, respectively. The original surface can be seen in Figure 5.31. Each end of the plate on the bottom flange had scour marks, indicating that both ends had slipped. However, the splice plate on the web only had scour marks on the east side.



Figure 5.77. Bottom Flange Splice Plate Scour Marks.

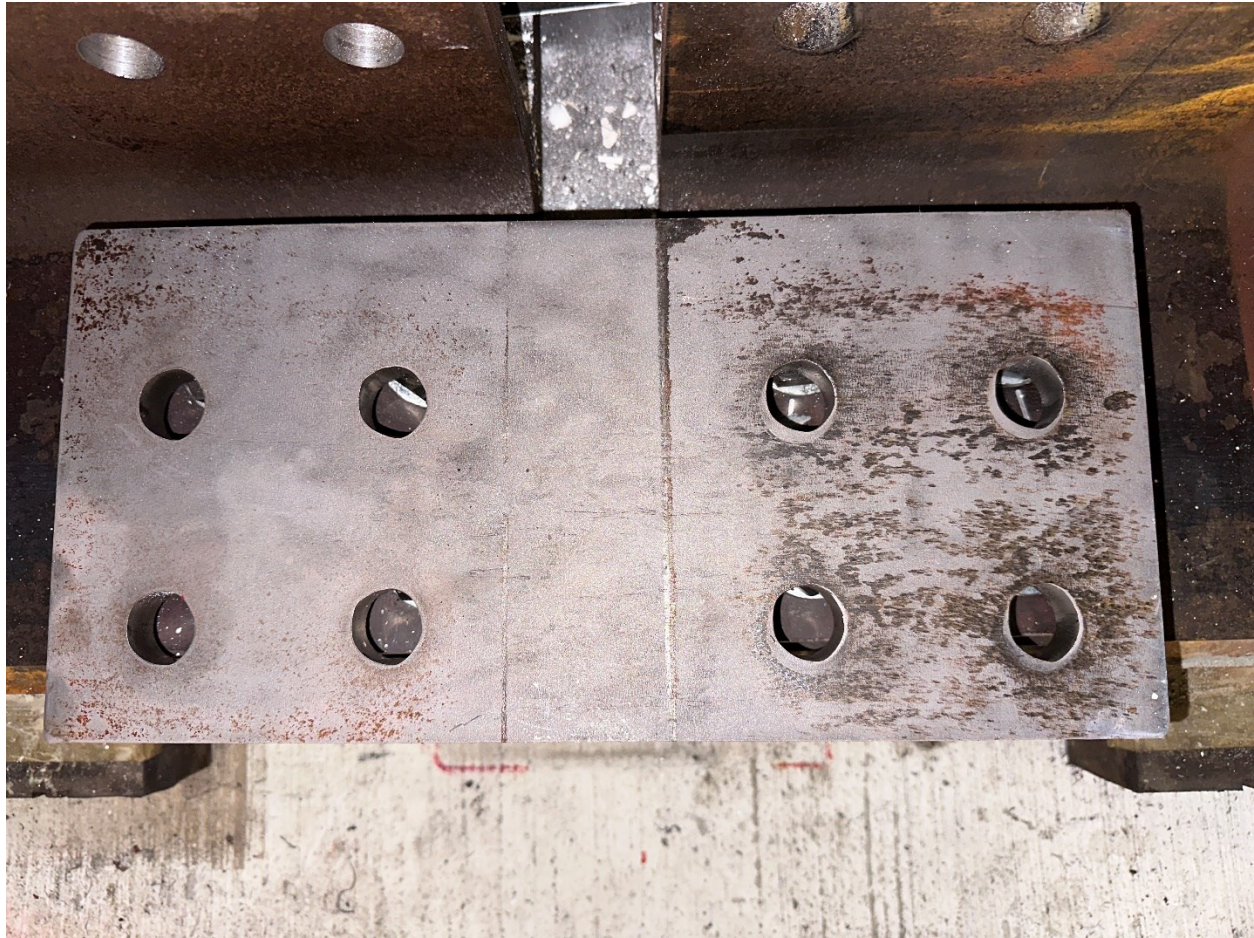


Figure 5.78. Web Splice Plate Scour Marks.

5.7.2.7. Concept A Findings

Several findings emerged from the Concept A experimental testing. The primary findings are summarized as follows:

- *Splice Plate Connection Stiffness*: The splice plate connections for this concept were relatively stiff. The initial stiffness of the specimen was ~ 75 kip/in (above the theoretical stiffness for a continuous girder, ignoring the tension provided by the slab). During the cyclic testing, it was possible to see the specimen moving in the longitudinal direction as the active loading end was being pushed down. The bottom flange was going into compression as the specimen was being pushed down, which caused the entire specimen to shift. The elastomeric bearing pads were observed being sheared as the compression was happening. After many cycles, such conditions may cause the beams to slip off the

supports if they are not fastened down adequately. See Section 5.11.5 for an in-depth comparison of each concept's stiffnesses.

- *Closure Pour*: The interface between the closure pour and the deck was the first place that cracks were observed during testing. Although these cracks were generally hairline or slightly larger, they formed as early as during 70 percent of the equivalent HL-93 loading.
- *Crack Propagation*: At up to 62 kips (roughly two times the HL-93 load level), eight visible cracks formed. These cracks were not concentrated in one area and were spread fairly evenly across the surface. Most of the cracks formed at relatively high loading. They were also full-depth cracks, meaning they went all the way through the slab.
- *Slip-Critical Connection*: The slip-critical nature was extremely important to the function of this connection. Prior to testing, it was observed that the incorrect faying surface preparation was applied to the splice plates. Had this issue not been rectified, the connection may not have performed as designed. The equivalent moment on the specimen when the connection slipped was at 1547 kip-ft (which is 235 percent of the equivalent HL-93 loading). The slippage of the bottom flange connection plates was the controlling limit state of the specimen. Therefore, the correct pretension of the bolts is a major factor in the effectiveness of this connection. Although the turn-of-the-nut method is generally adequate to achieve the required pretension, if these loads are not achieved, it may have negative consequences on the serviceability of this connection. One way to improve this connection is to increase the bolt diameter. Because altering the faying surface is costly and may not be done correctly, a Class A faying surface is the preferred surface preparation. Using a 1-inch diameter A325 bolt instead of a $\frac{7}{8}$ -inch diameter A325 bolt gives an additional 30 percent increase. If the bolt diameter increase is still inadequate, then A490 bolts can be used instead of increasing the bolt diameter further.

5.8. CONCEPT B

5.8.1. Design, Construction, and Pretest Behavior of Concept B

5.8.1.1. Specimen Design

This subsection introduces how the Concept B test specimen was designed to achieve the features of the benchmark bridge. Section 5.3 previously described the benchmark bridge design that is the basis of the specimen design. An elevation view of the connection area of Concept B is shown in Figure 5.79.

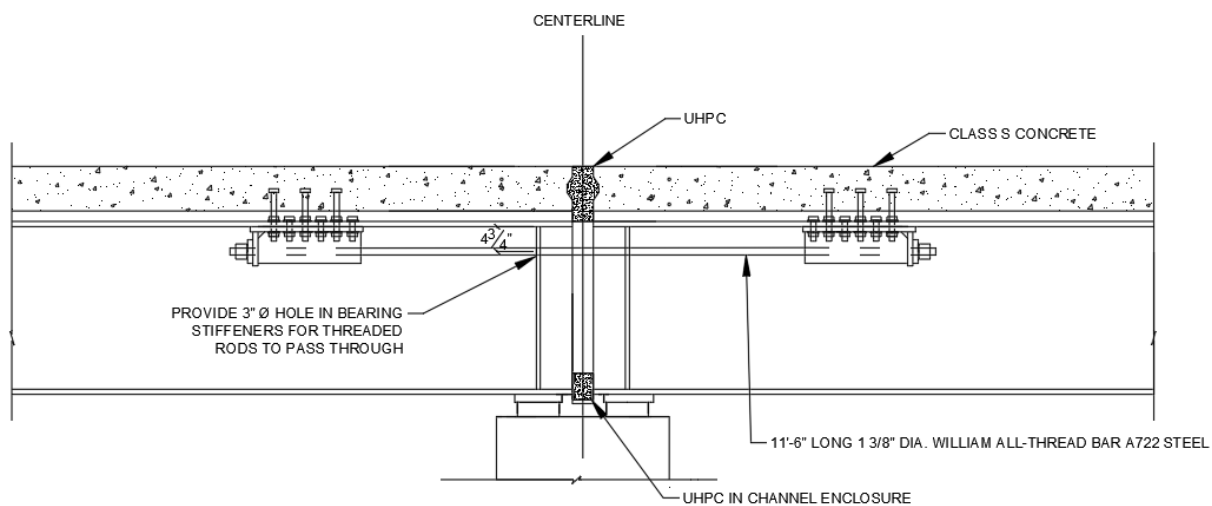


Figure 5.79. Elevation View of Concept B Connection Area.

The Williams bar design involves the service load balancing technique, which has been applied to the design of the continuous structure. The connection is designed for service loads and checked for the ultimate capacity and tensile stress at the slab under the service load. The force magnitude of the Williams bar design is 120-kip per bar, which is based on the stress-strain profile to achieve the net stress at the center of the closure pour surface equal to 0.0 ksi. The confined UHPC at the bottom of the connection is designed to ensure adequate compressive resistance.

For the bolted bracket design, the *AASHTO LRFD Bridge Design Specification 9th Edition* was followed [24]. The primary design checks and the AASHTO articles include:

- Shear resistance of bolts (Article 6.13.2.7).
- Slip resistance of bolts (Class B surface condition) (Article 6.13.2.8).

- Bearing resistance at bolt holes (Article 6.13.2.9).
- Bolt tensile resistance (Article 6.13.2.10.2).
- Prying action of the bolts or the flange or plate bending, which may result in the formation of a plastic hinge (Article 6.13.2.10.4).
- Combined bolt tension and shear resistance (Article 6.13.2.11).
- Fillet-welded connections (Article 7.12.3).

This concept consists of two W33×201 steel sections that are each 20 ft long with steel brackets located under each side of the top flange approximately 5 ft from the connection end of the beam. The steel brackets consist of 1-inch thick plate steel arranged in a three-sided configuration. See Figure 5.80 and Figure 5.81 for the layout of steel brackets.

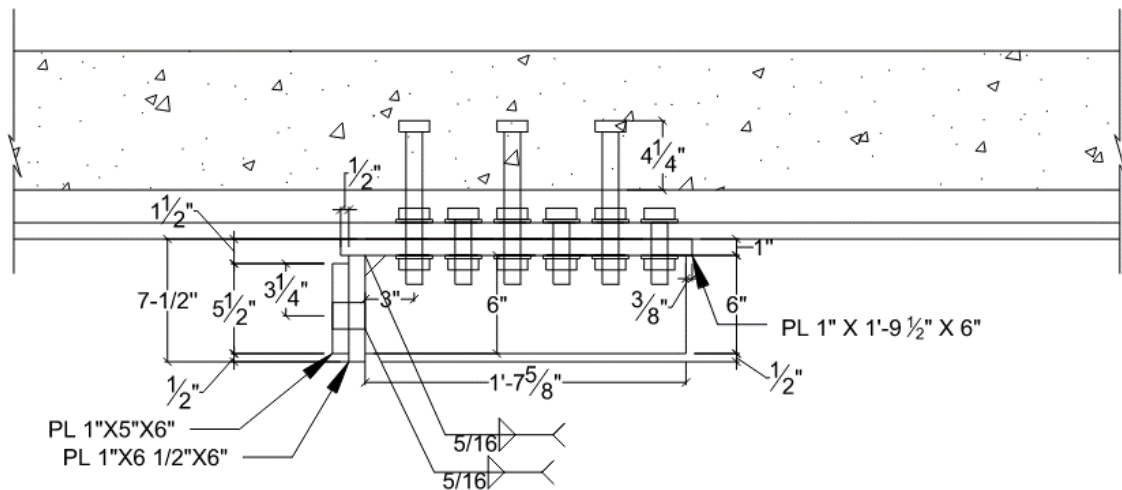


Figure 5.80. Close-Up Elevation of Steel Bracket Assembly.

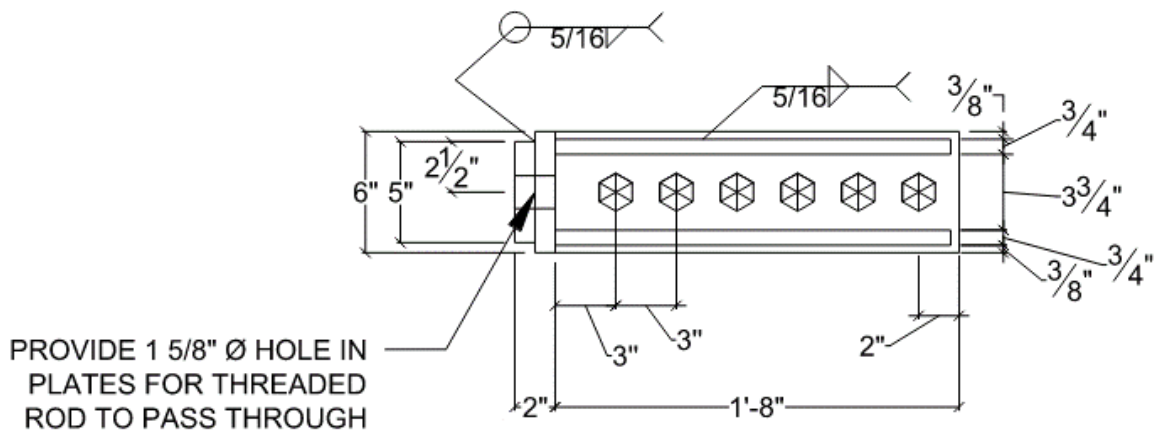


Figure 5.81. Close-Up Plan View of Steel Bracket Assembly.

A 150-ksi 1 $\frac{3}{8}$ -inch Williams bar was fed through these brackets and post-tensioned to bring the deck slab into compression. Two channels face-to-face filled with UHPC were welded to the bottom of the web and bottom flange to be used as the compression element during loading. A small plate was welded to the bottom of the channel to prevent the UHPC from leaking out. UHPC was also used in the closure pour region to bridge the gap between the deck slabs.

5.8.1.2. Instrument Plan and Data Acquisition System

The instrumentation of this concept focused mainly on the connection of the two composite beams. A plan view, elevation view, and section view of the instrumentation plan can be seen in Figure 5.82, Figure 5.83, and Figure 5.84, respectively. A legend for the symbols can be found in Figure 5.85. The final instrumentation lists for each concept can be found in Appendix B.

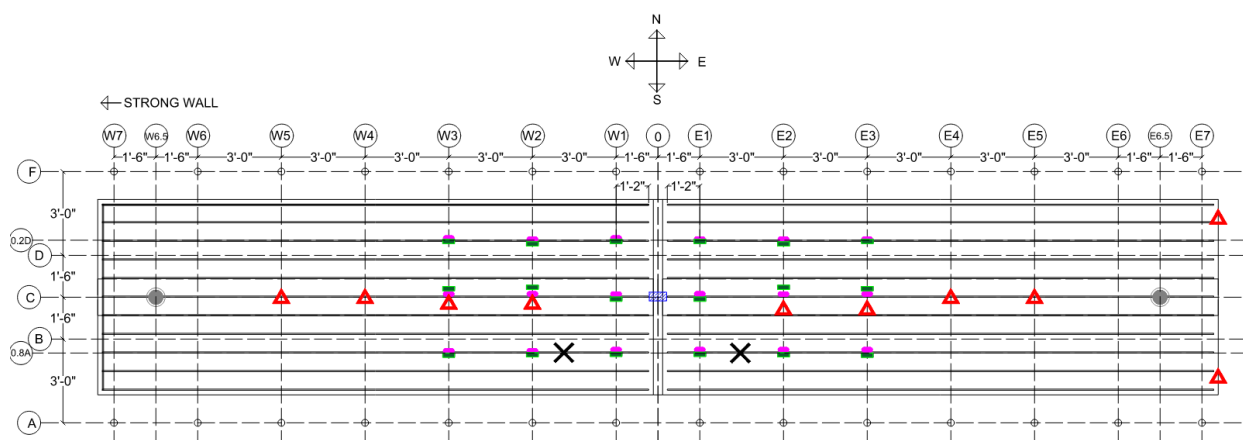


Figure 5.82. Concept B Instrumentation Plan (Plan View).

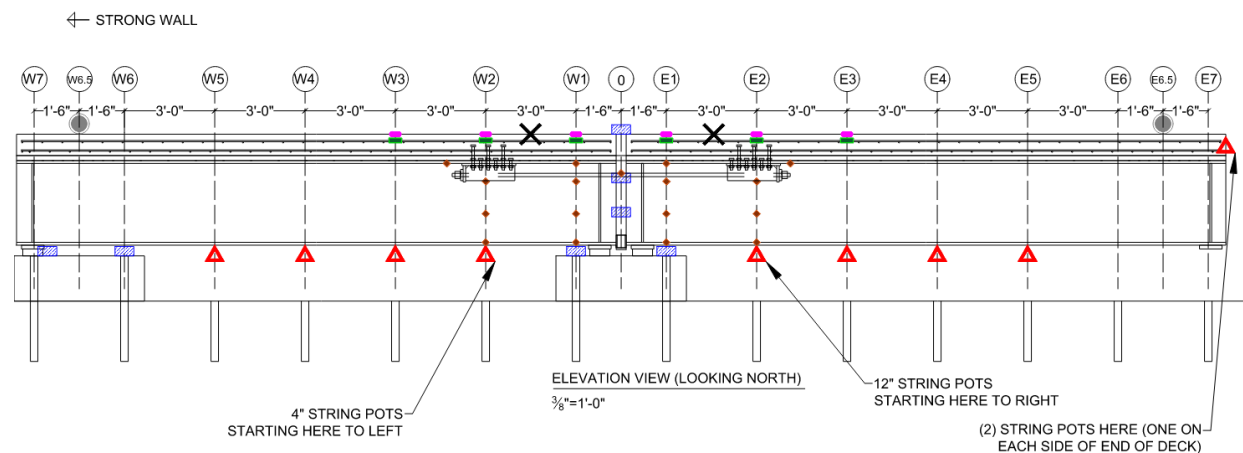


Figure 5.83. Concept B Instrumentation Plan (Elevation View).

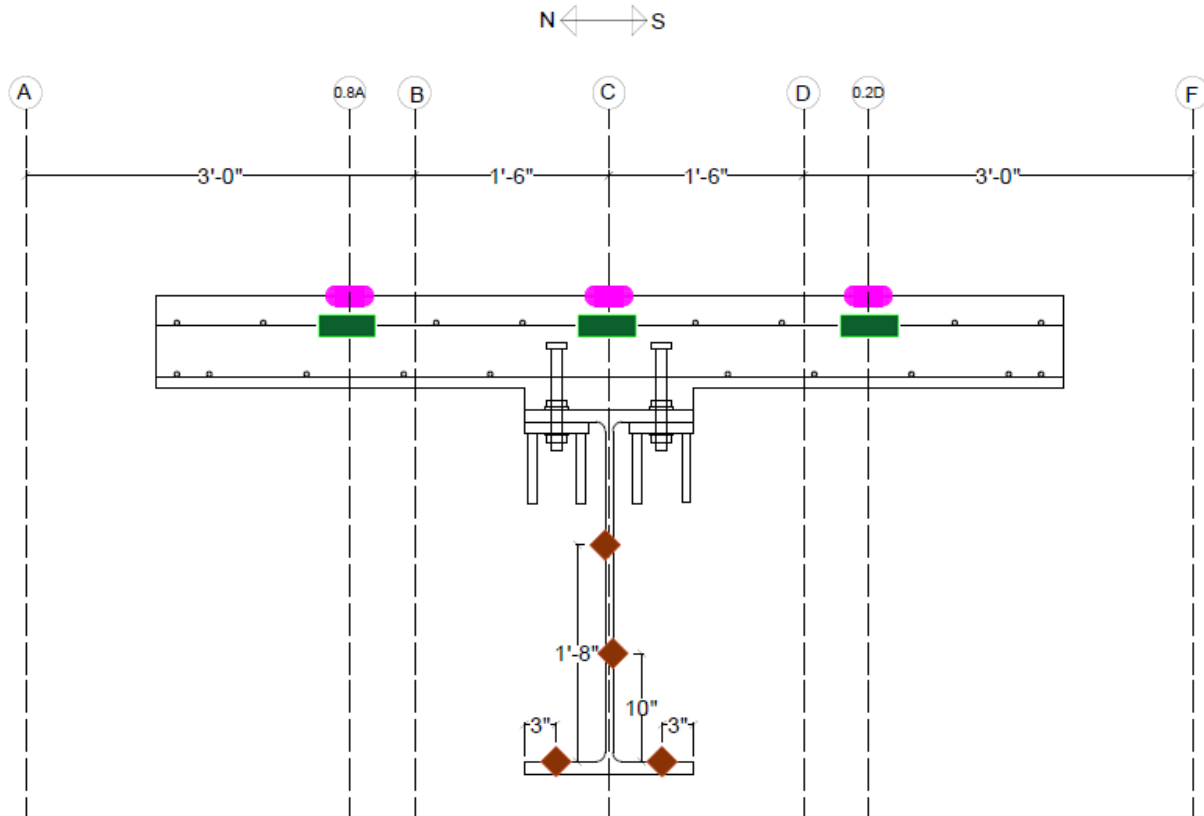


Figure 5.84. Concept B Instrumentation Plan (Section View at E1).

Symbol	Item	Concept B Count
	Actuator and Load Cell	2
	Embedded Rebar Strain Gauge	18
	Concrete Surface Strain Gauge	18
	Structural Steel Surface Strain Gauge	26
	String Potentiometer	11
	LVDT	7
	Wire Exits	2

Figure 5.85. Instrumentation Plan Legend.

All strain gauges were located on gridlines so that after testing they could easily be turned into strain profiles to see how the strain differed relative to the closure pour. Strain gauges were also located on the 1 $\frac{3}{8}$ -inch \varnothing Williams bars so that the proper amount of post-tension could be put into the bars. String pots were located every 3 ft so that a displacement curve could be seen during and after testing. For areas that had higher precision displacements, LVDTs were used. LVDTs were located near the supports of the beams (to measure deflection near the supports), on the web of the steel beams (to measure the relative rotation of the beams), and above the slab on the closure pour (to measure the elongation of the closure pour).

The rebar strain gauges used were FLAB-5-350-11 from Texas Measurements. Rebar strain gauges were located starting 1 ft 2 inches from the end of the longitudinal bars and spaced every 3 ft beyond that for two more spaces. Rebar strain gauges were located within 7 ft 6 inches from the closure pour since that was the primary focus area for the testing.

Concrete surface strain gauges used were PL-60-11 from Texas Measurements. Concrete strain gauges were applied directly above the rebar strain gauges so that a clear comparison could be made between them.

The structural steel strain gauges used were also FLAB-5-350-11 from Texas Measurements. Structural steel strain gauges were located starting 1 ft 6 inches from the center of the closure pour with another line 3 ft away from that. Structural steel strain gauges were also applied on the 1 $\frac{3}{8}$ -inch \varnothing Williams bars directly at the centerline. Structural steel strain gauges were located within 4 ft 6 inches of the closure pour.

5.8.1.3. Specimen Preparation

The general formwork construction was previously discussed in Section 5.5. The following subsections are unique to Concept B.

Prior to the formwork being connected, the brackets were lifted into place under the flange and were attached using six 1-inch \varnothing A490 bolts. The bolts were tightened to the required pretension using a combination of the turn-of-the-nut method and direct tension indicators (DTIs). The bolts were tightened starting at the innermost bolt in the pattern and working outwards. Due to a lack

of couplers and time constraints, the additional bolts that were to be connected to the ends of the bracket bolts were unable to be added to this concept.

At the connection end of the formwork, a notch had to be fashioned for the future closure pour. To achieve create the notch, a 2×4 inch member was shaved at an angle. See Figure 5.86 and Figure 5.87 for a view of this notch.



Figure 5.86. Concept B Notch Formwork.



Figure 5.87. Concept B Notch Formwork Close-Up.

To allow for future movement of the specimens, four 2-inch Ø PVC pipes were installed in the slab approximately 4 ft from each end of the specimen and 6 inches away from the beam top flange. The pipes were cut to approximately 8.375 inches so that they would not interfere with screeding the concrete. These PVC pipes can be seen in Figure 5.18.

Once all the PVC pipe, rebar, and threaded rod was installed, the slab was poured. The total amount of concrete poured was approximately 8.5 cubic yards. The concrete was allowed to cure for 3 days, and then the formwork was removed. Due to space limitations in the lab, the beams were not able to be immediately transported to the testing area. Instead, the beams were stacked on top of each other to save space. See Figure 5.88 for a view of how the beams were stacked.



Figure 5.88. Concept B Beams Stacked.

Once space had been cleared, the specimens were transported to the testing area. To transport the specimens, four steel rods were hollowed out and had threads put through them. These steel rods were inserted into the cavity left by the PVC pipes in the slab. A shackle was screwed into the top of the rod while a bolt with a large washer was inserted into the bottom of the rod under the slab. A rope was then fed through the shackle and attached to a crane. While transporting this specimen, the research team attempted to use a forklift to guide the specimen between two existing columns in the lab. The forks were adjusted so that they would straddle the steel beam. However, the angle of the forks relative to the beam was off so that the weight of the beam was concentrated on the edge of the slab. This caused minor cracking on the bottom surface of the slab near the closure pour region. This cracking was documented, and another way to move the specimens was used to ensure the cracking would not happen again.

Before placing the specimens in the testing area, three concrete pedestals were put into place. Neoprene bearing pads were placed on the pedestals so that they would be directly under the steel bearing plates. The pedestal on the active loading end of the specimen was orientated so that it could be easily removed once testing began. The overhead crane was then used to move the specimen into place in the testing area. See Figure 5.89 and Figure 5.90 for views of specimens in the testing area.



Figure 5.89. Elevation View of Specimen in Testing Area.



Figure 5.90. Concept B before Closure Pour.

Once the specimen was in place, formwork for the closure pour region was installed. This formwork consisted of previously used formwork that was slightly modified. See Figure 5.91 for closure pour formwork.



Figure 5.91. Concept B Closure Pour Formwork.

After the closure pour formwork was constructed, UHPC was used to fill the closure pour. The UHPC in the closure pour region was left to cure for 1 day before the formwork was removed.

After the closure pour formwork was removed, the instrumentation was installed. Before the deck slab was poured, rebar strain gauges were installed on a total of six longitudinal bars in the top mat of steel. Each one of these bars had three strain gauges installed on them. The strain gauges were installed 1 ft 2 inches, 4 ft 2 inches, and 7 ft 2 inches from the end of each rebar so

they would line up with the other instrumentation on the specimen. See Figure 5.92 and Figure 5.93 for applications of rebar strain gauges.



Figure 5.92. Concept B Rebar Strain Gauge Overview.



Figure 5.93. Application of Rebar Strain Gauge.

The next instrumentation installed was steel strain gauges on the W33×201. These strain gauges are depicted as diamonds in Figure 5.94.

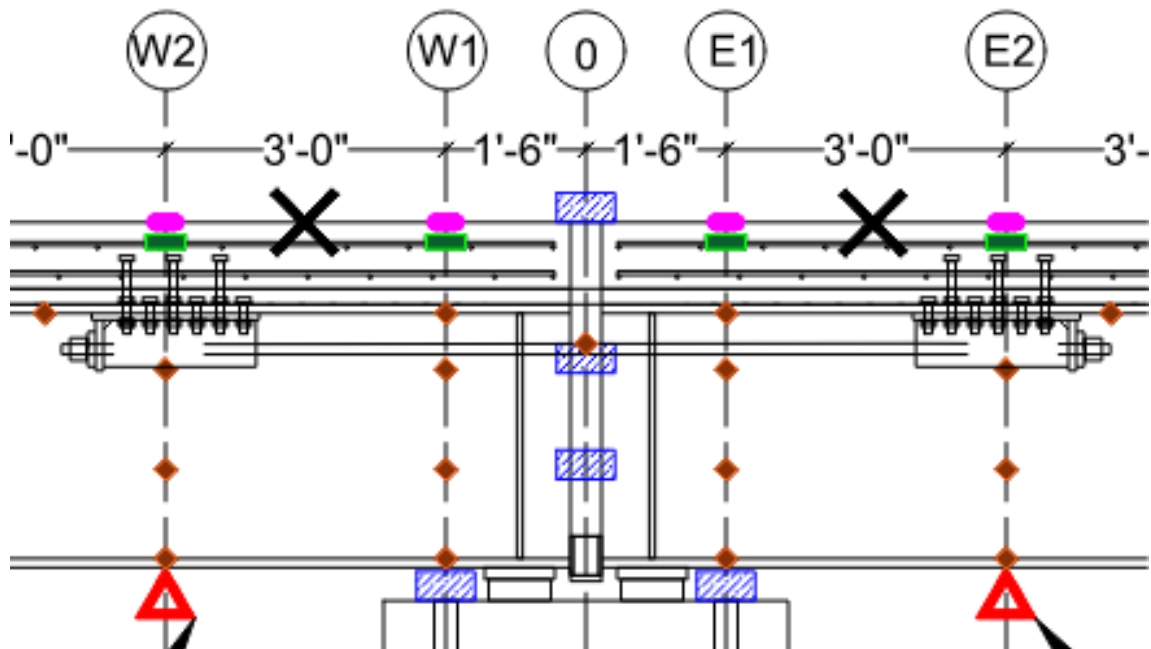


Figure 5.94. Concept B Instrumentation Elevation View of the Connection Region.

These steel strain gauges consisted of one strain gauge under each side of the top flange, one gauge on the top third of the web, one gauge on the bottom third of the web, and one gauge on top of each side of the bottom flange. See Figure 5.95 for these locations and Figure 5.96 for a view of the installation.

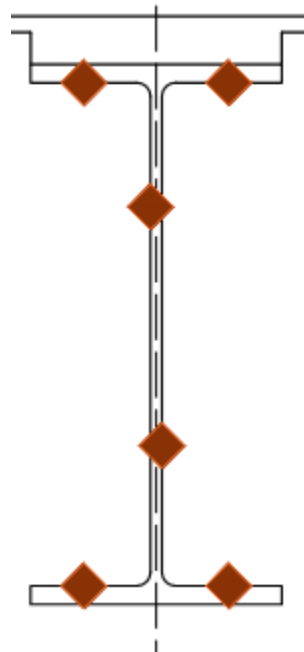


Figure 5.95. Steel Strain Gauge Locations.



Figure 5.96. Structural Steel Strain Gauge Installation.

Before installing any instrumentation on the precast concrete deck, the top and side surfaces of the deck were painted white with a mixture of two parts water with one part matte white paint. The deck was painted white to allow any cracks that formed during testing to be easily seen and recorded.

A total of 18 concrete surface strain gauges were installed on the top of the precast concrete deck. Their locations can be seen as pink ovals in Figure 5.97. These concrete strain gauges were installed directly above the rebar strain gauges, and their locations can be seen in Figure 5.98.

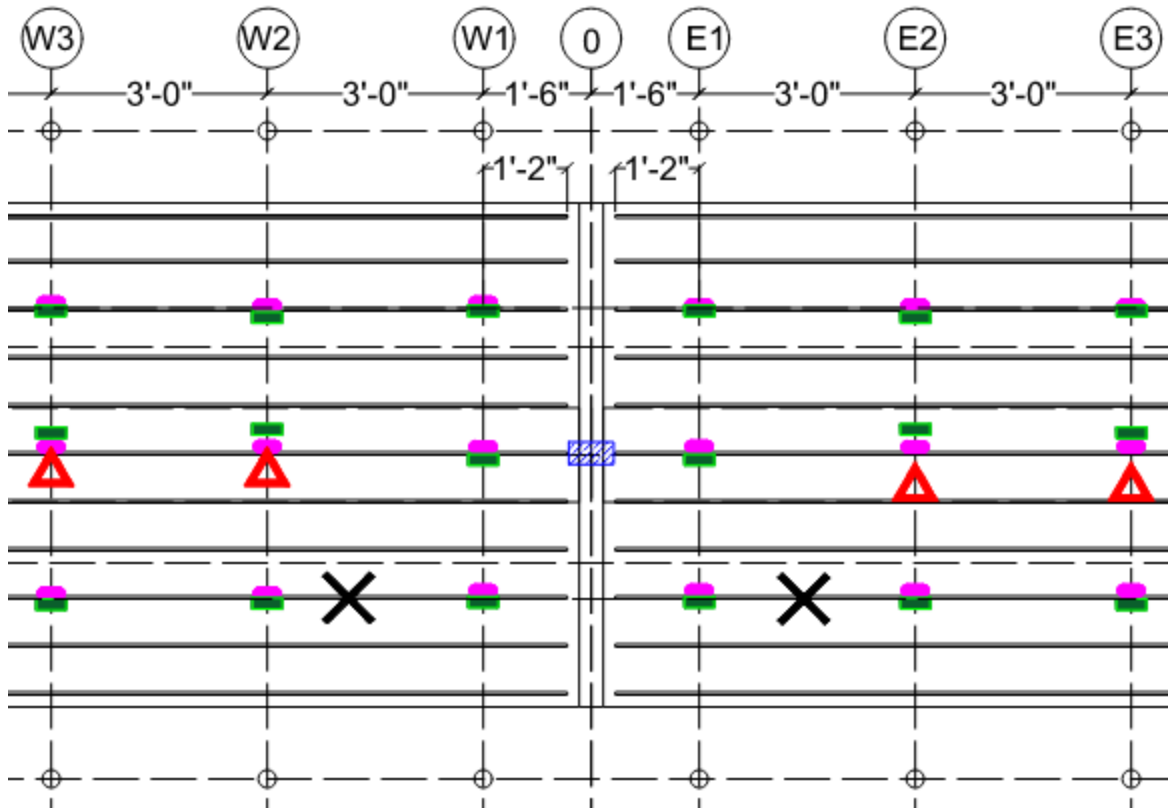


Figure 5.97. Instrumentation Plan View.



Figure 5.98. Concrete Surface Strain Gauge Installation.

String pots were installed at 3 ft increments along the length of the beam under the bottom flange. These string pots were used to measure the deflection of the beam during loading. Two different lengths of string pots were used. In the areas where substantial amounts of deformation were anticipated, 12-inch string pots were used. In smaller deformation areas, 4-inch string pots were used. These string pots can be seen in Figure 5.99.



Figure 5.99. String Pots under Beam.

LVDTs were used to measure displacement in select areas, as indicated in the prior section. The LVDT locations are shown in Figure 5.100 and Figure 5.101. The LVDTs under the beam on grids E1, W1, W6, and W7 were used to measure relatively small amounts of deformation near the neoprene bearing pads. The LVDTs on the beam web were used to measure the relative

rotation of the connection area, while the LVDT on the concrete surface was used to measure the elongation of the closure pour.

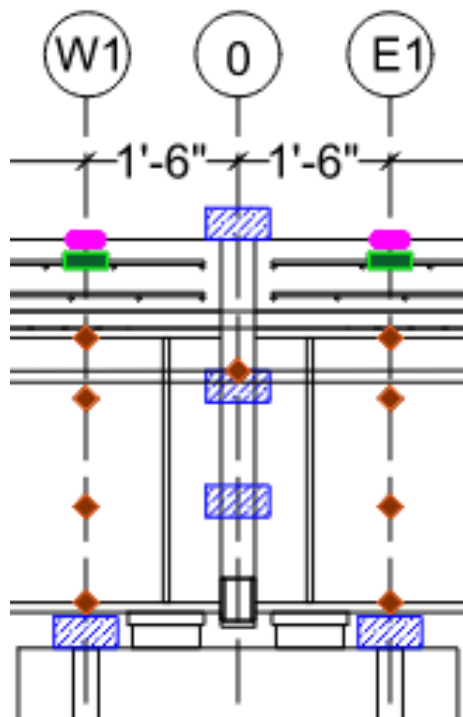


Figure 5.100. Central LVDT Locations.

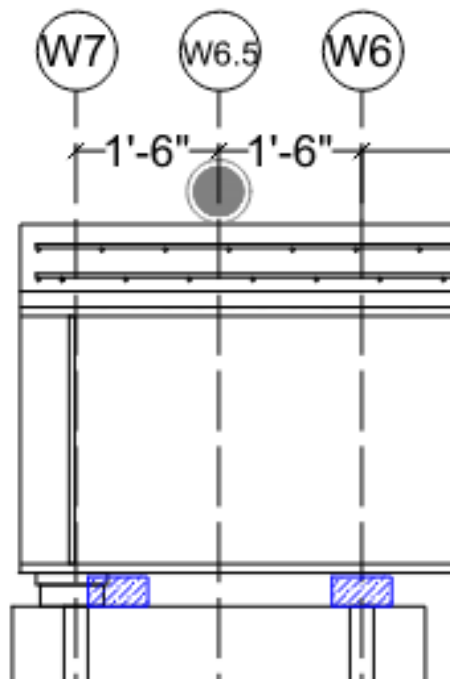


Figure 5.101. Hold-Down LVDT Locations.

In addition to instrumentation, a portion of the steel beam was whitewashed with a mixture of lime and water. Only 10 ft on each side of the connection point on one side of the beam was whitewashed. The steel was whitewashed so that as the beam moved from the elastic range to the plastic range during testing, the deformation of the beam can be seen more clearly. The whitewash can be seen in Figure 5.102.

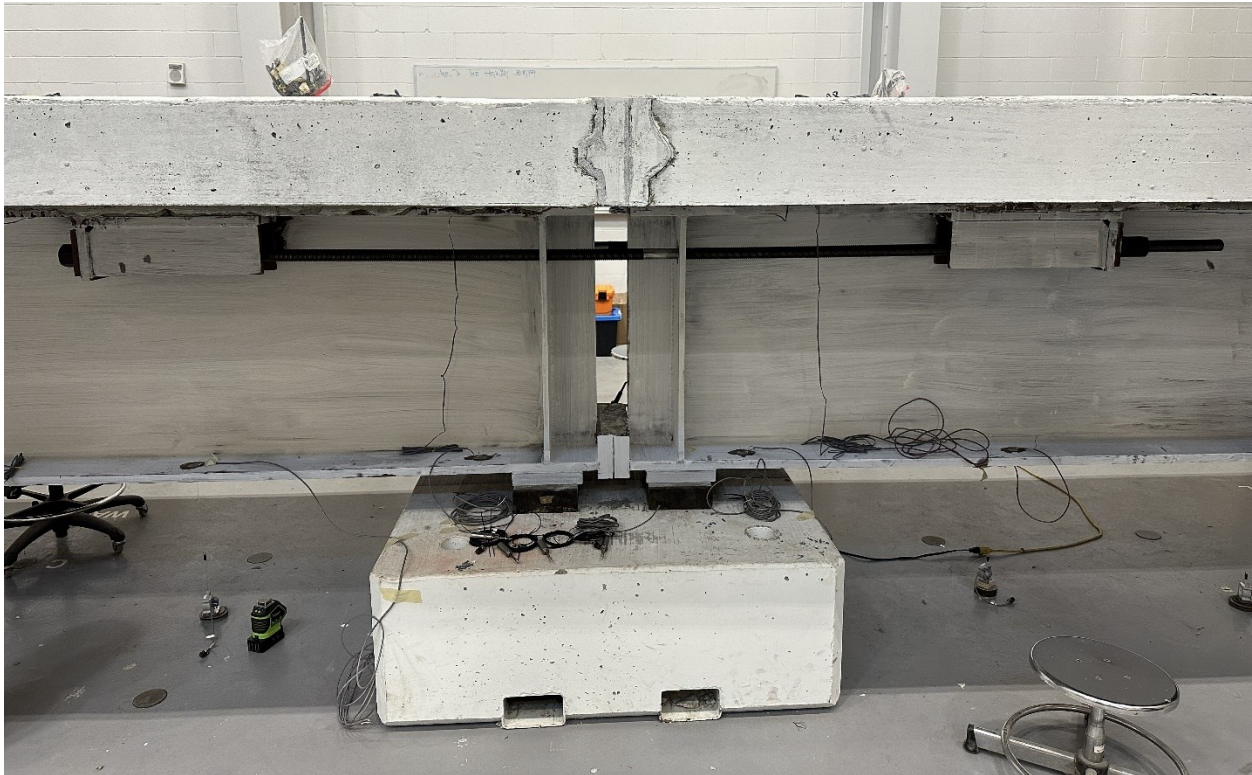


Figure 5.102. Whitewashed Steel Beam.

5.8.2. System Experiment Testing Program, Experiment Results, and Observations

5.8.2.1. Concept B Test Setup

Section 5.4 provides the general steps taken during the experimental testing. The test setup for Concept B included several unique steps. See Figure 5.103 for an elevation view of the overall test setup.

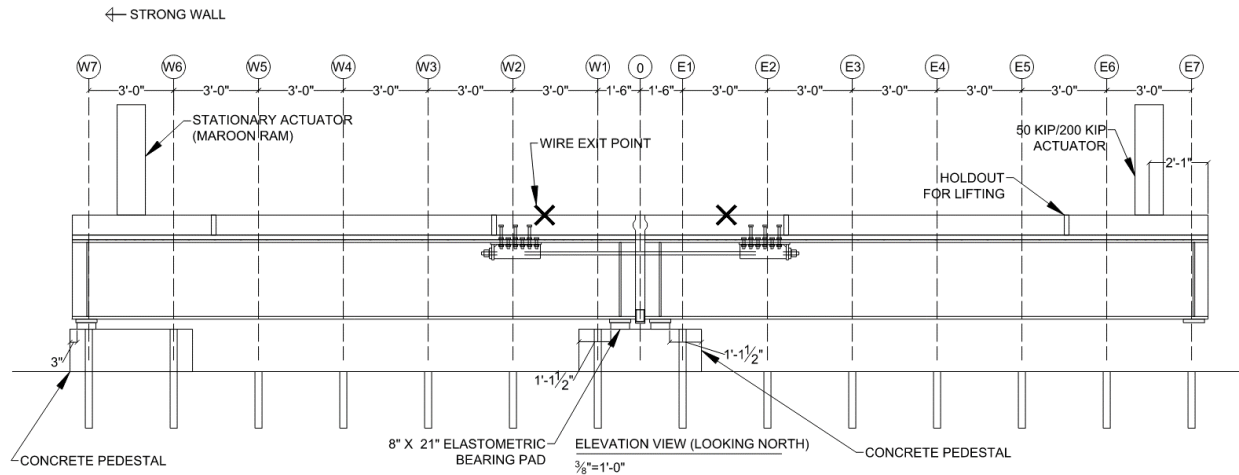


Figure 5.103. Concept B Test Setup Elevation.

A 1.5-inch thick adapter plate was fabricated with a hole pattern that fit the actuator and the holdouts that were placed in the precast concrete deck. This adapter plate can be seen in Figure 5.104.

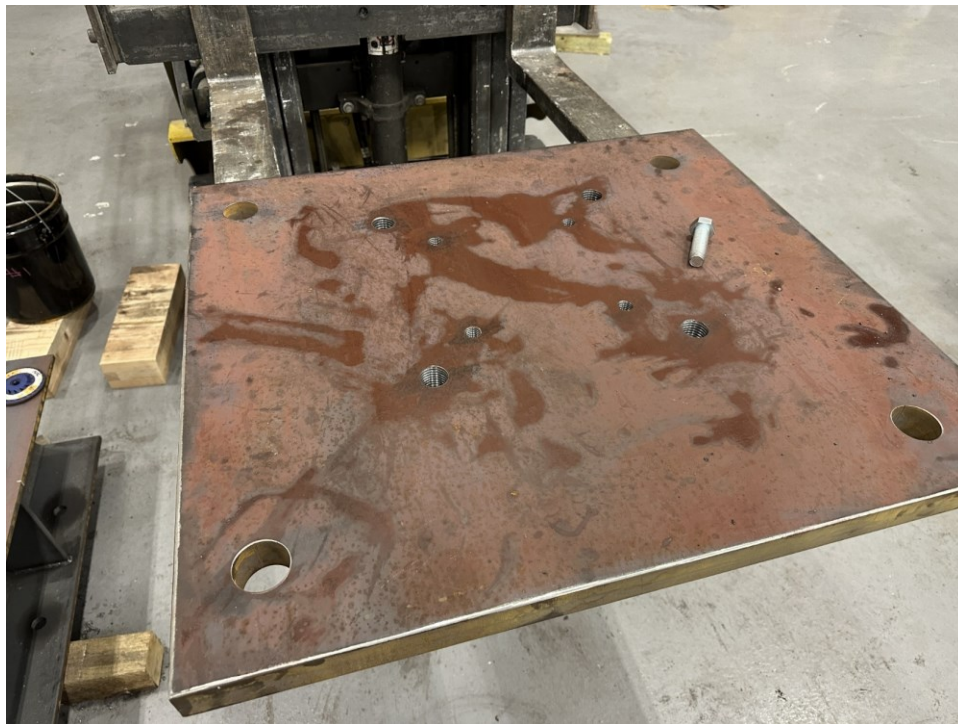


Figure 5.104. Concept B Adapter Plate.

The inner hole pattern was for the 55-kip actuator, the middle hole pattern was for the 200-kip actuator (if needed), and the outer hole pattern was for the connection to the deck. The connection to the actuator was made by making threads in the holes so that bolts could be fed

through the foot of the actuator and connected to the plate. The connection to the deck was made by feeding threaded rods through the outer hole pattern. On the bottom of the deck, large plate washers were used to spread the load out. On the top of the deck, the rods were fastened with a small washer and a nut. See Figure 5.105 and Figure 5.106 for both of these attachments.



Figure 5.105. Adapter Plate Attachment to the Bottom of the Deck.



Figure 5.106. Adapter Plate Attachment to the Top of the Deck.

On the hold-down side of the test setup (the left side shown in Figure 5.103), a stationary actuator was used to hold down the specimen during testing. This actuator used 200 kips to keep the hold-down side in place. A load cell was placed under the end of the actuator so that it could be determined how much load was being put into it. Several plates were also used to distribute the load across a greater area of the slab. See Figure 5.107 for a view of this actuator.

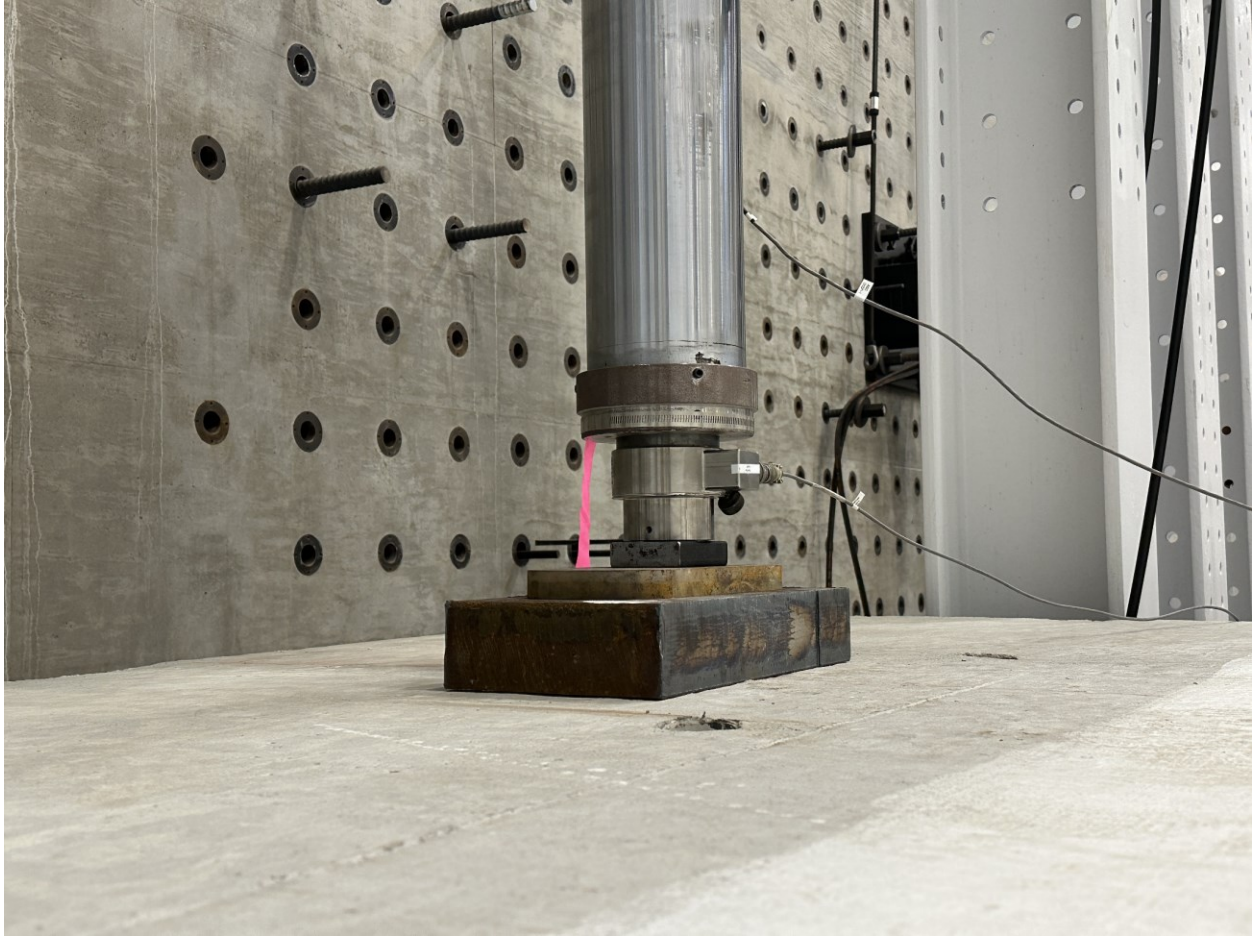


Figure 5.107. Concept B Hold-Down Actuator.

The following images show the actual test setup of the entire concept in the lab. The overall test setup, a view from the hold-down end, and a view from the active loading end can be seen in Figure 5.108, Figure 5.109, and Figure 5.110, respectively.



Figure 5.108. Overall Elevation View of Concept B Test Setup.

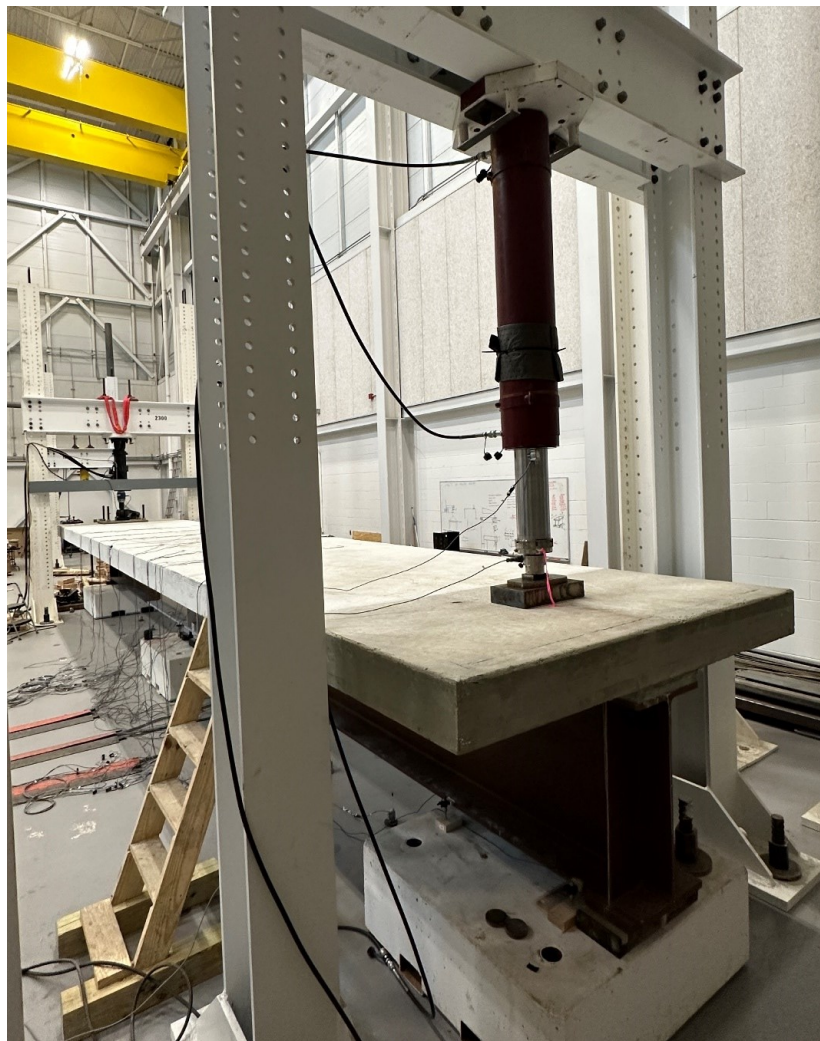


Figure 5.109. View of Concept B Test Setup from Hold-Down End.

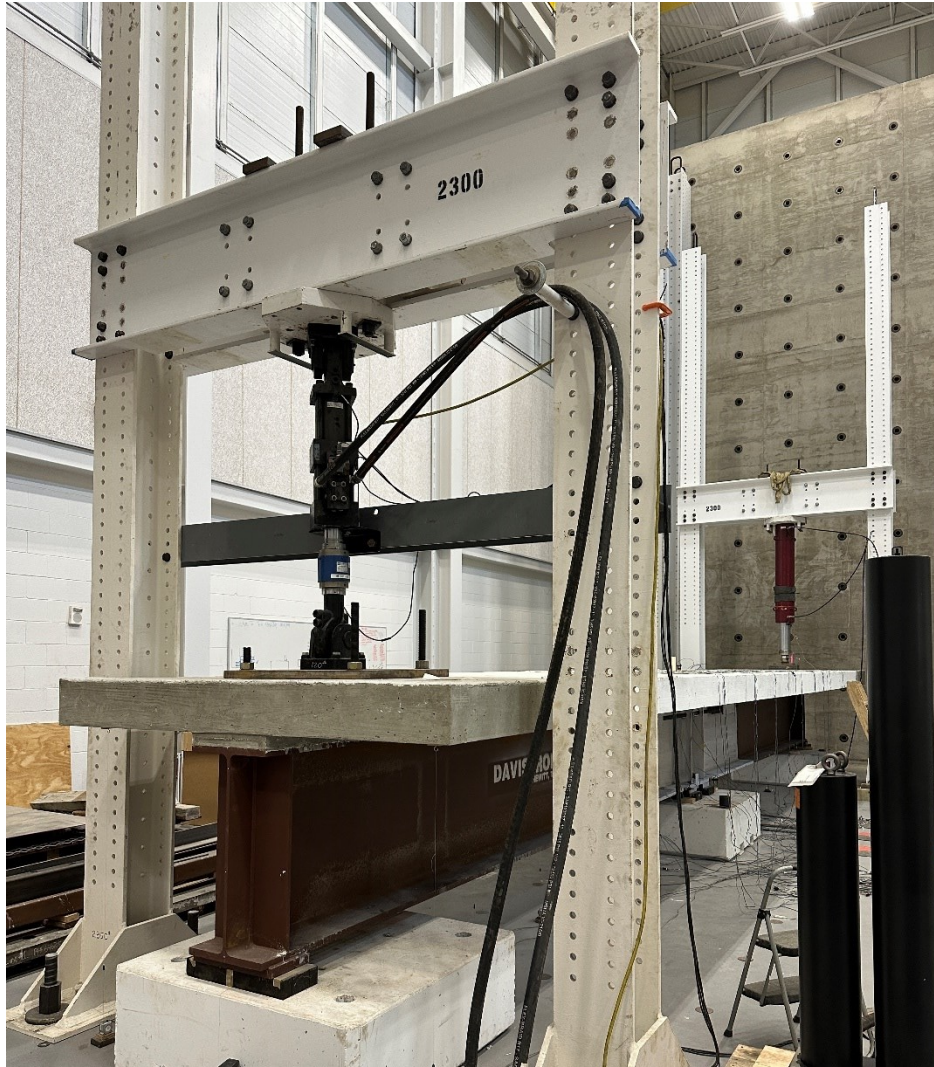


Figure 5.110. View of Concept B Test Setup from Active Loading End.

5.8.2.2. Concept B First Static Testing

Testing on Concept B started with static testing. The Williams bars were initially post-tensioned by hand to approximately 500 microstrain. Next, they were post-tensioned by using a hydraulic torque wrench to approximately 2500 microstrain on the test day, which equates to 115 kips of axial tension in the Williams bars. This equates to approximately 49 percent of the theoretical ultimate strength of the bars. Figure 5.111 presents the strain on the Williams bars at each side when they were post-tensioned by using a hydraulic wrench. SG43 is located on the north Williams bar and SG44 is located on the south Williams bar.

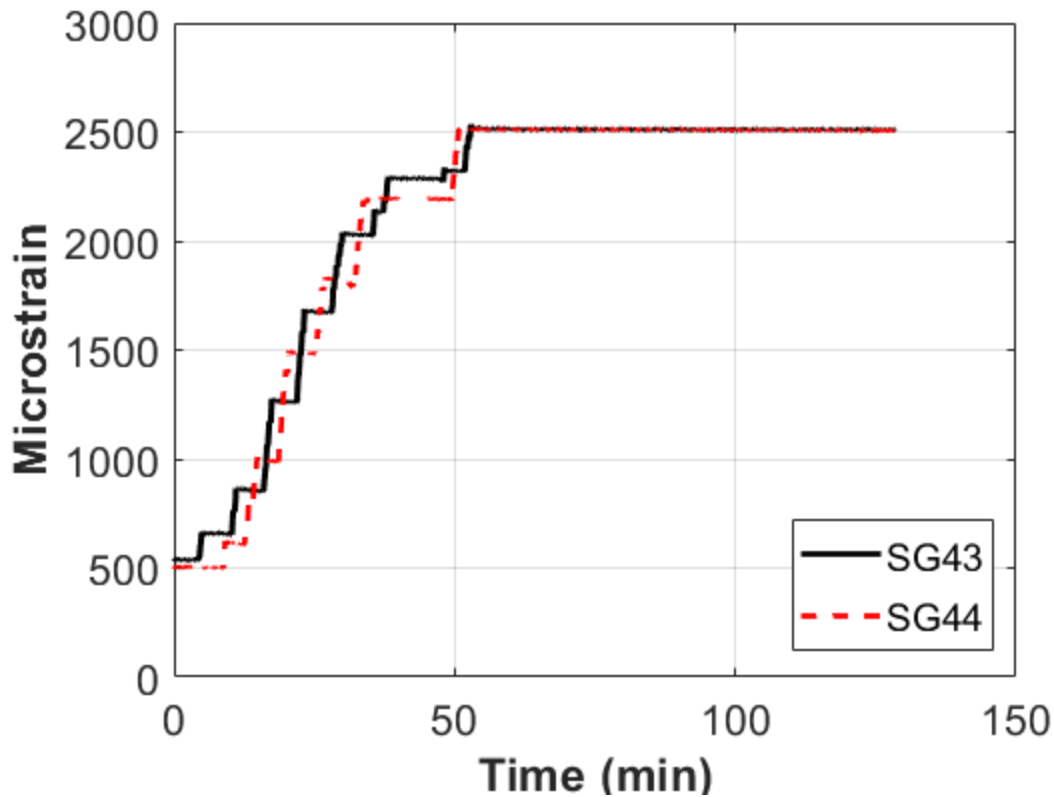


Figure 5.111. Concept B Strain on William Bars by Hydraulic Wrench.

Data were taken from the PT process and evaluated to show the initial stress and strain in the deck slab, steel reinforcement, and steel girders. The Williams bars were designed to precompress the slab in the range of the Williams bars. For the experimental test, the design experimental load balanced the equivalent live load moment induced by the HL-93 back-to-back load case. The data from the concrete strain gauges and embedded steel strain gauges were calculated, and they were compared with analytical model results. Figure 5.112 presents the initial post-tension stress using the hydraulic wrench from the selected embedded steel strain gauge at E1. Strains gauges SG58 and SG60 were located 2 ft on either side of the longitudinal centerline of the specimen, while SG59 was located on the centerline. The stress at SG59 increased more rapidly because it was located on the centerline of the specimen, and the elements along the centerline were experiencing a pseudo shear-lag effect. SG58 and SG60 also experience more compressive stress but at a slower rate. This was consistent with all other instrumentation on this specimen.

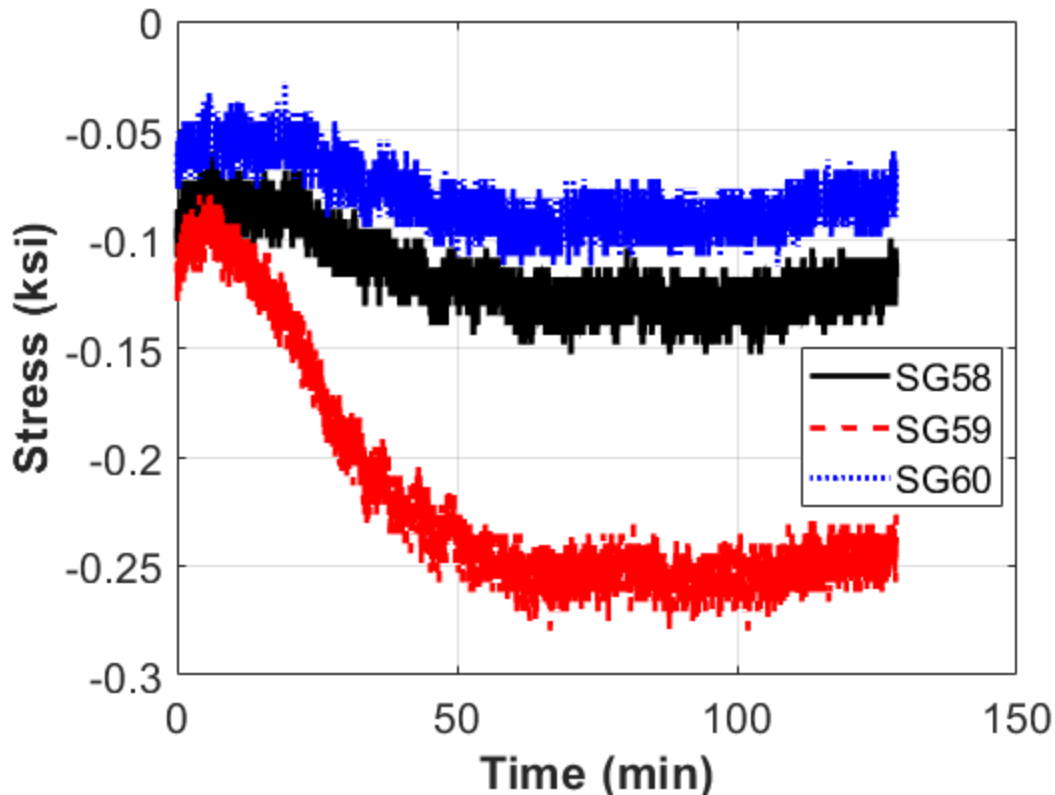


Figure 5.112. Stress at the Deck Surface of E1 While Tensioning the Williams Bars with the Hydraulic Wrench.

The active loading end of the specimen was pulled up with approximately 15 kips so that the pedestal it was resting on could be removed. The beam was lowered until the actuator read 0 kips. At that point, the specimen was essentially supporting itself as a cantilever. This location was considered the zero-reference point. Downward was set as the positive load direction. The specimen was then loaded in 5-kip increments pushing down. At each 5-kip increment, testing was paused, measurements were taken, and cracks in the deck slab were mapped. Once the 15-kip load level was reached, the strain in the Williams bars started to increase. The displacement was not linear at this point. The specimen was displaced at a greater rate without an increase in load once 15 kips were reached. Between 15 and 20 kips, it was very difficult to apply any more load. The interface between the precast concrete deck and the UHPC closure pour was starting to open up at this point. See Figure 5.113 for a view of this occurrence.



Figure 5.113. Concept B First Static Testing Closure Pour Interface.

At approximately 20 kips, a loud bang was heard, and the active loading end actuator started to vibrate. The strain in the Williams bars dropped to between 1500–1700 microstrain after the bang was heard. The static test was aborted at this point. Figure 5.114 shows the strain on the Williams bars during the loading process, and there is a clear strain drop at about 50 mins. The cracks in the deck were mapped at this point, and the specimen was inspected for signs of damage. Some signs of slippage of the brackets were found. See Figure 5.115 for a view of the indication of possible bracket slippage.

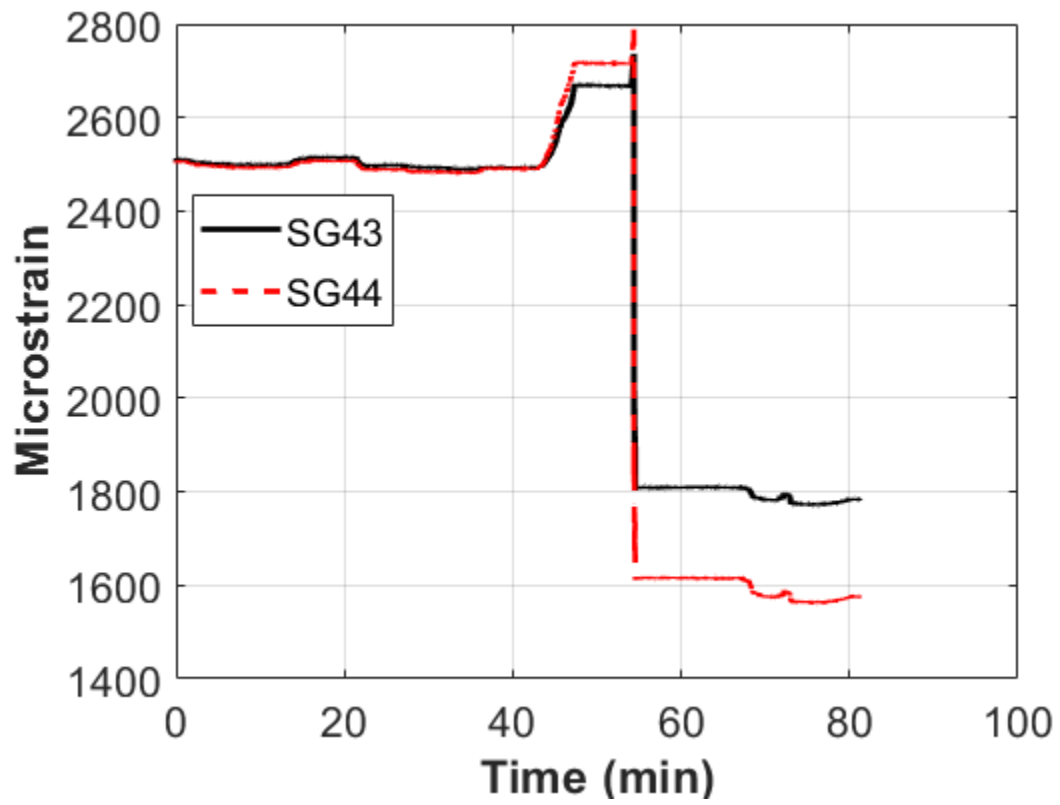


Figure 5.114. Concept B First Static Testing Strain on William Bars.



Figure 5.115. Concept B Possible Bracket Slippage.

Figure 5.116 presents the plot of actuator load and vertical displacement at the active loading end of the specimen. The displacement at the load end of the specimen was about 0.4 inches when the load started to drop and the actuator began to vibrate.

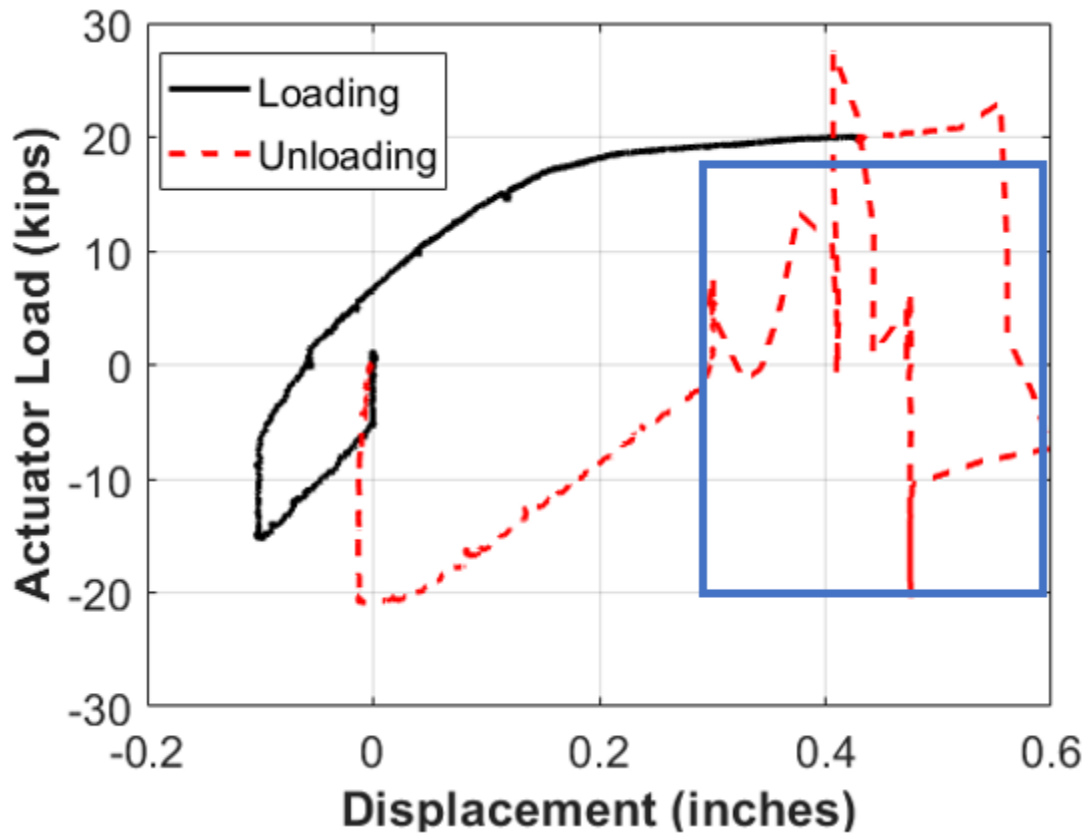


Figure 5.116. Concept B First Static Testing Load versus Active Loading End Actuator Vertical Displacement at E7.

Figure 5.117 shows the deck surface stresses at E1 before slip. At the zero-load location on the plot, there is an increase in stress without any change in loading because, on the hold-down end, the maroon ram was not located directly above the bearing pad. It was located approximately 1 ft 6 inches away from the bearing location. Therefore, the load that was imparted to hold down this end was inducing a moment on the specimen that caused the strain gauges near the closure pour to experience additional tensile stresses. As the specimen was lifted (negative actuator load), the top of the deck showed more compression, which makes sense. When the specimen was being pushed down (positive actuator load), the deck showed more tension until the 10-kip mark, when the precast concrete deck started to go into more compression because, around the 10-kip to 15-kip mark, the closure pour started to open excessively, which released most of the tension in the slab.

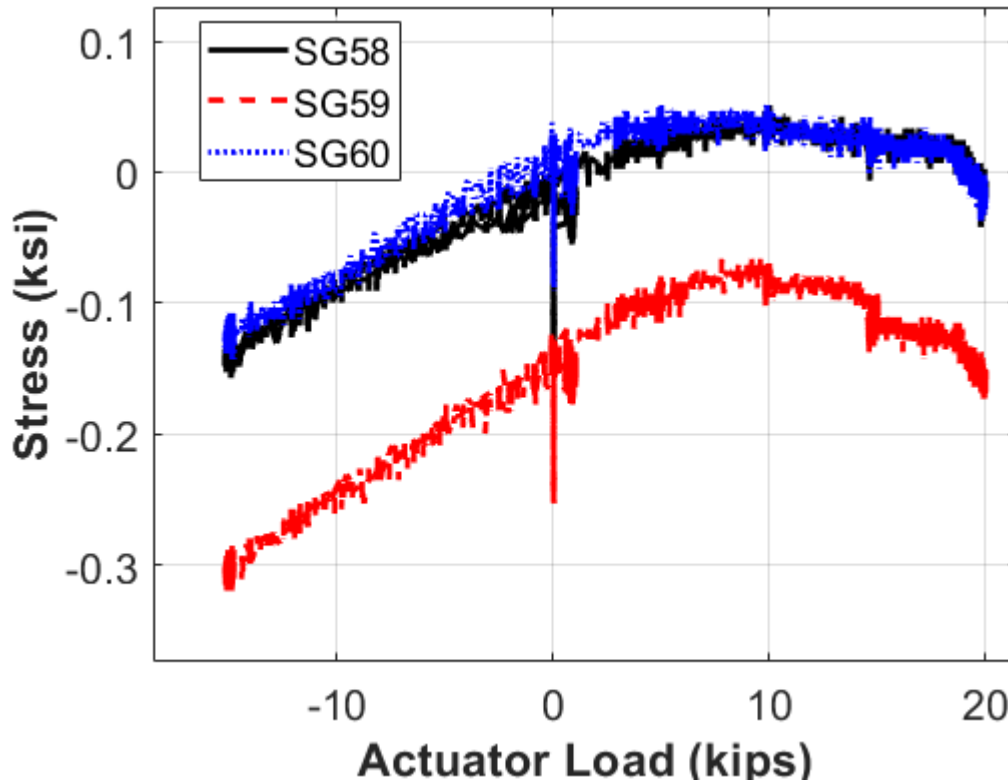


Figure 5.117. Concept B First Static Testing Rebar in Deck Stress versus Load at E1 (before Slip).

The specimen was placed back on the pedestal. After discussion with the rest of the research team, it was decided to post-tension the Williams bars back to 2500 microstrain and do another round of static testing.

Several possible causes for the brackets slipping were identified. The most likely cause was the faying surface between the brackets and beam flange was not correctly prepared. Another possible reason is that the bolts were not properly pre-tensioned, which would reduce the friction between the bracket and flange.

In the next round of static testing, the specimen was pushed down with 22.5 kips before the deflection started to dramatically increase without an increase in load. The specimen was unloaded and pushed down with 22.5 kips again. The data were found to be repeatable. It was decided to proceed with a lower displacement level for the cyclic testing for the first few days to see how the specimen reacted. If no detrimental effects occurred, then a larger displacement level could be used for the rest of the testing.

Figure 5.118 shows the strain on Williams bars for the two applications of the first static loading. Figure 5.119 presents each application of the load versus displacement. The target load during the static testing was at least 30 kips. With the combination of the 30 kips from the actuator and the self-weight of the specimen, the equivalent HL-93 load should have been reached. However, Figure 5.119 reveals that the maximum load that was achieved by the actuator was 22–23 kips. The displacement of the specimen at these load levels was also very high, with almost 0.8 inches of total deflection. This displacement level was unacceptable and was due to insufficient levels of precompression from the Williams bars. These results directly led to the need to increase the post-tension in the Williams bars and do a second round of static and cyclic testing.

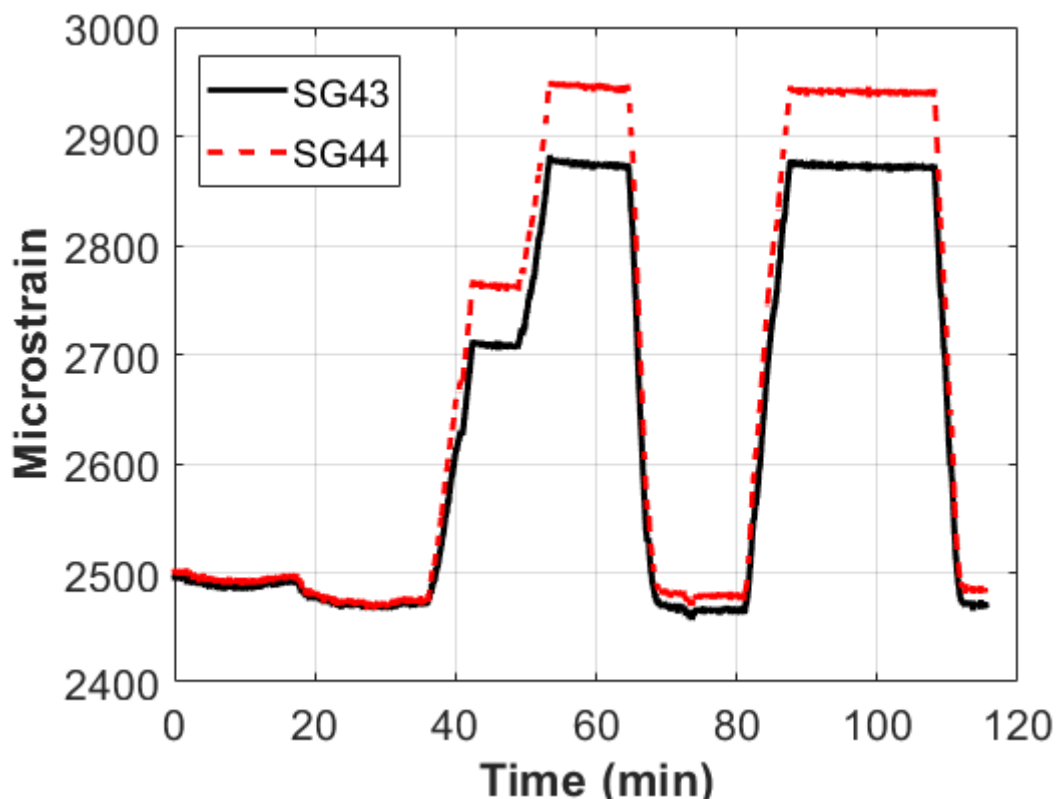


Figure 5.118. Concept B First Static Testing-Microstrain on Williams Bars.

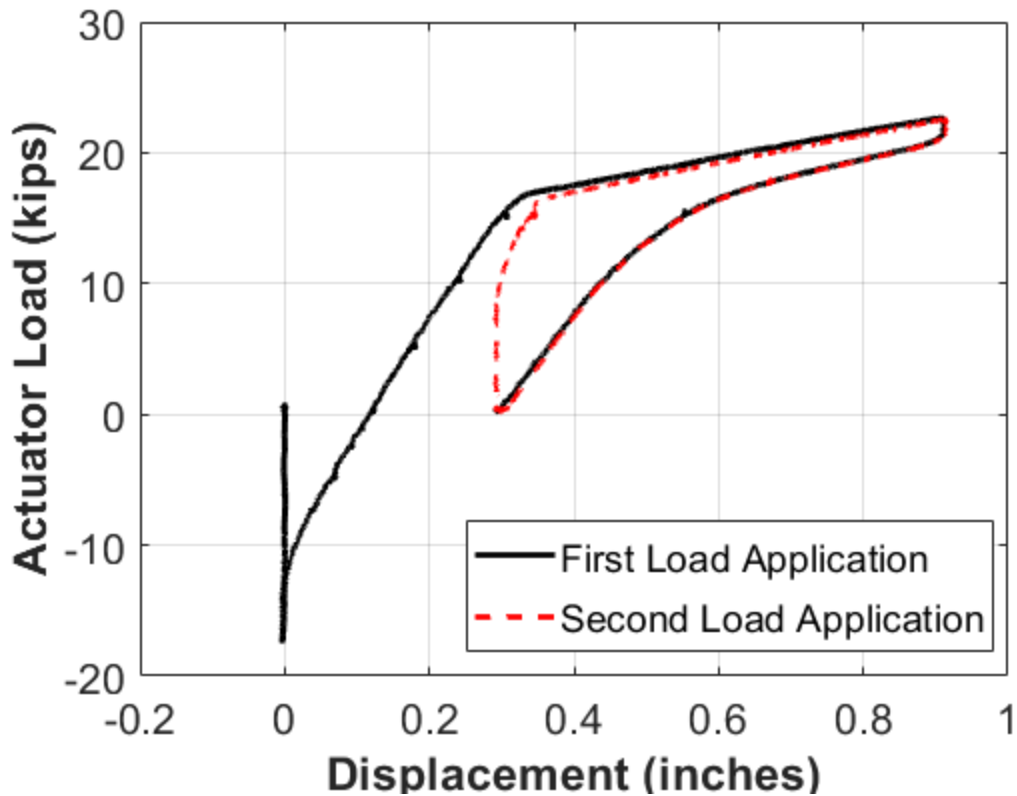


Figure 5.119. Concept B First Static Testing Load versus Active Loading End Displacement.

5.8.2.3. Concept B First Cyclic Testing

After the first round of static testing was completed, 67,600 cycles were run on the specimen using a lower corresponding displacement range than the HL-93 loading. A lower range was selected so that the specimen would not be damaged and so the research team could see how it fared against cyclic loading. No damage was seen after the 67,600 cycles were completed, and the research team decided to make several changes to the specimen, which are described in Section 5.8.2.4. See Table 5.10 for a summary of the number of cycles run as well as the corresponding displacement ranges.

Table 5.10. Concept B First Cyclic Testing Ranges.

Day	Number of Cycles	Load Rate (Hz)	Displacement Control Range
1	3,600	1.0	−0.3" to 0.1"
2	21,600	1.0	−0.3" to 0.1"
3	900	0.5	−0.3" to 0.1"
4	16,200	1.0	−0.3" to 0.1"
5	25,300	1.0	−0.3" to 0.1"
Total	67,600		

5.8.2.4. Concept B Second Static Testing

After consultation, the research team decided that the brackets should be welded to the bottom of the top flange to eliminate the slip of the brackets from the failure mechanism. The team also decided to run the static test again after the welding was completed. A $\frac{3}{8}$ -inch full-width fillet weld was used in the transverse direction on the ends of the brackets to the flange. In addition, a full-length longitudinal weld was used on the outside of the bracket to the flange. Since the bracket and the flange tip were flush, a channel had to be arc-gouged between the bracket and the flange tip. This step allowed the gap to be filled with a $\frac{3}{8}$ -inch minimum partial penetration groove weld. The side of the bracket nearest to the web could not be welded because the welder did not have access. The welds were designed so that they had enough strength to reach the ultimate strength of the Williams bar, which is at least 237 kips. See Figure 5.120 and Figure 5.121 for a view of the bracket welds.



Figure 5.120. End Transverse and Longitudinal Bracket Weld.



Figure 5.121. Inner Transverse and Longitudinal Bracket Weld.

The hydraulic torque wrench that was originally used to post-tension the Williams bars was not able to tension the bars past approximately 2500 microstrain. To reach the new target of 166 kips, the wrench needed to reach 3600 microstrain. An Enerpac through-hole jack was used to post-tension the bars to the new required level. Due to the heavy weight of the through-hole jack, a stand had to be constructed to hold the jack while the PT was taking place. See Figure 5.122 for a picture of this stand in use.



Figure 5.122. Through-Hole Jack Stand.

Once the bars were post-tensioned to the required level, another round of static testing was carried out. The same regimen was followed as the first time. The pedestal under the active loading end was pulled out, and 5-kip load increments were imparted on the specimen. After each load increment, the specimen was inspected. This time, the specimen maintained linear deflection behavior up to the 30-kip point. The maximum deflection at the 30-kip point was approximately 0.48 inches. The specimen was brought back to 0 kips and then back to 30 kips two more times to check for repeatability.

The strain on each of the Williams bars due to PT by the through-hole jack is shown in Figure 5.123. SG43 is located on the north Williams bar and SG44 is located on the south Williams bar. The Williams bars were tensioned so that there was never a difference of more than approximately 800 microstrain between the two bars. It was necessary to go slightly past the target tension of 3600 microstrain because once the pressure in the through-hole jack was

released, the tension in the bars dropped slightly due to not being able to hand-tighten the nut on the end of the bar as tight as possible, which meant there was going to be some slack in the bar.

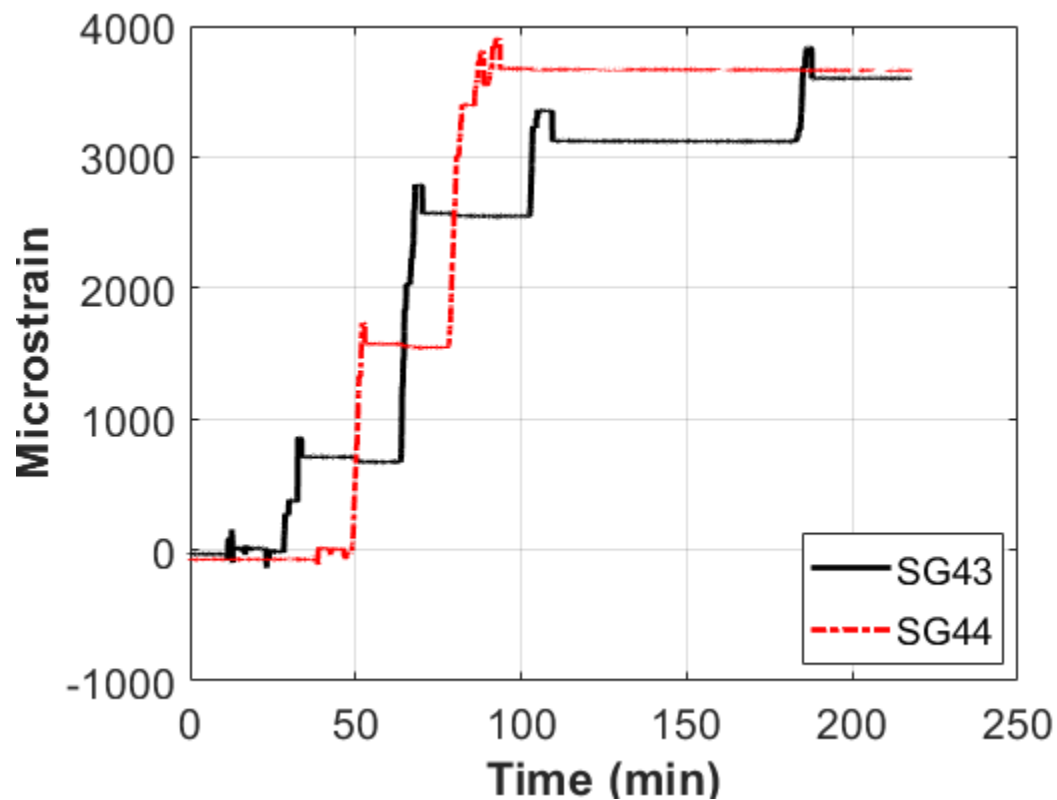


Figure 5.123. Concept B Second Static Testing Strain on Williams Bars during PT.

The stress in the deck at gridline E1 due to the tensioning of the Williams bars can be seen in Figure 5.124. The stress on the surface of the deck started at 0 ksi, and as the bars were post-tensioned, the stress in the deck began to show more compression. SG59, which was located on the longitudinal centerline of the specimen, showed the most compressive stress, while strain gauges 58 and 60, which were located on either side of SG59, showed less compressive stress due to a pseudo shear-lag effect, whereas the elements closest to the post-tensioned elements showed a greater effect due to the PT.

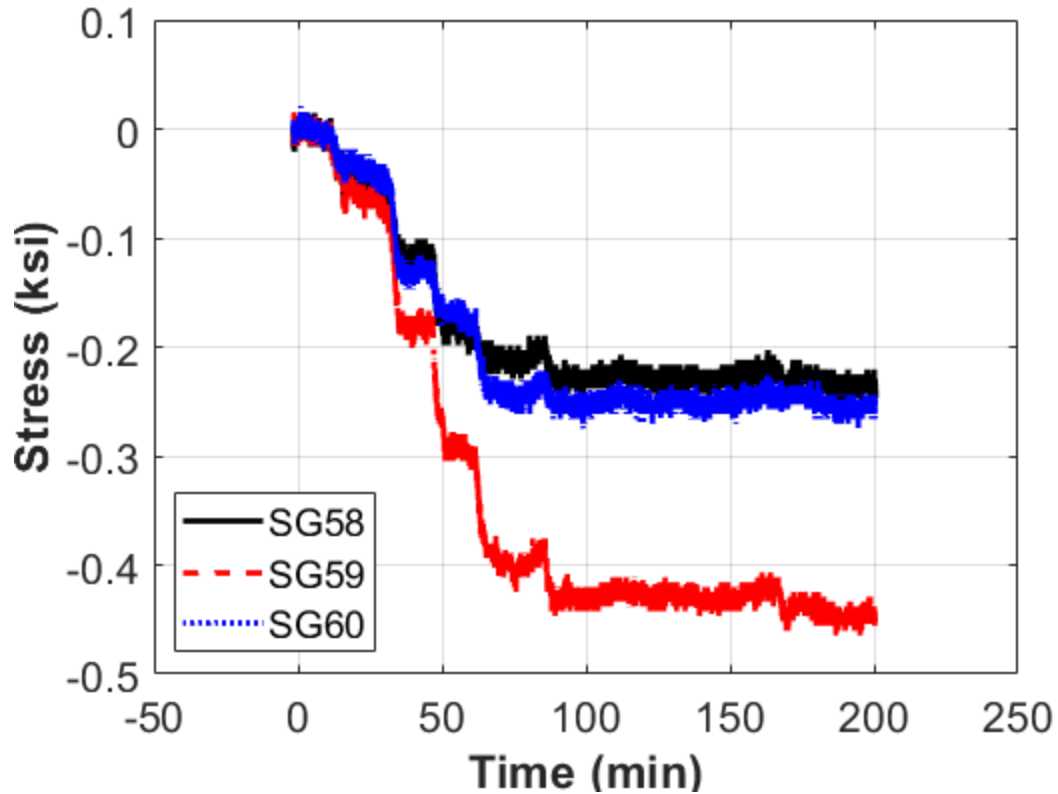


Figure 5.124. Concept B Second Static Testing Stress on Deck at E1 during PT.

A time history of the strain on the Williams bars during the static testing can be seen in Figure 5.125. As the testing progressed, it can be seen that up to a certain point, the tension in the bars decreased before increasing, which indicates that the NA was located above the bars until a certain load level; then, once this load level was exceeded, the NA went below the bars, and the bars started to experience more tension. The maximum strain in the bars at the maximum load level was approximately 3720 microstrain. This load was repeated two more times to check for repeatability of the system. As the figure shows, these results were repeatable.

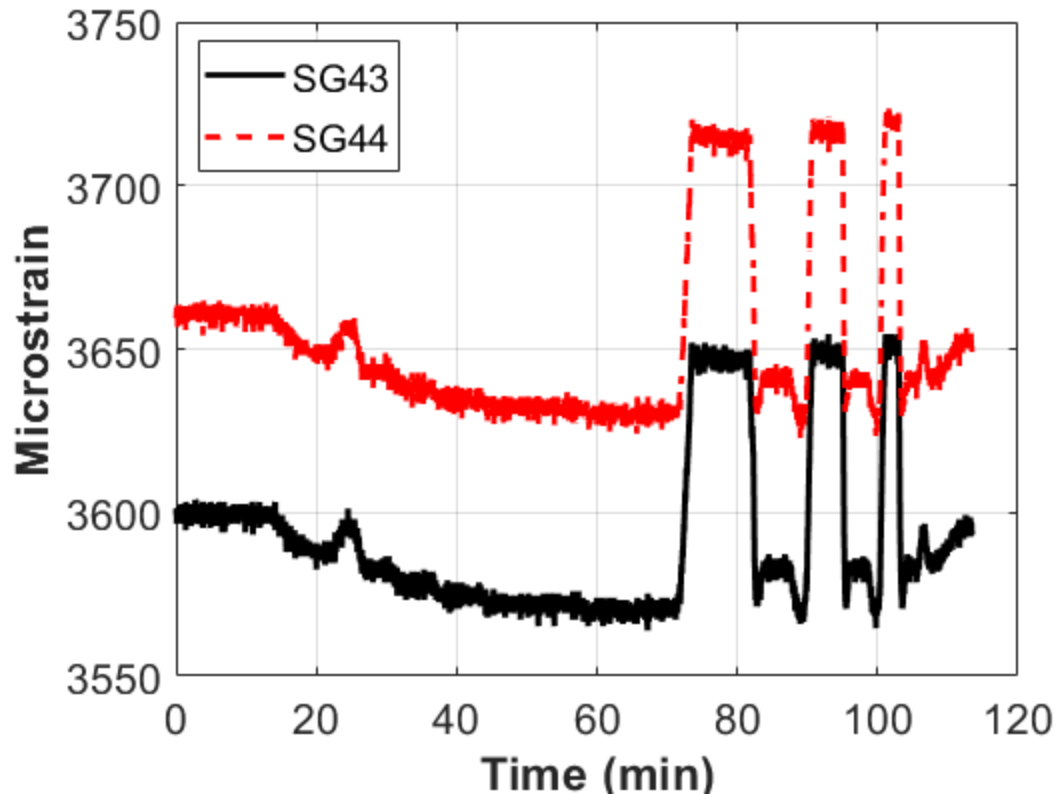


Figure 5.125. Concept B Second Static Testing Strain on Williams Bars.

A time history of the vertical displacement at E7 of the system is shown in Figure 5.126. The two data sets are for two separate string pots located on the active loading end of the specimen—one under the precast concrete deck on each side of the specimen (see Figure 5.82 and Figure 5.85 for these string pot locations). The string pot data showed similar results; however, one string pot showed a larger displacement than the other. This result is due to several reasons, including the specimen not being loaded perfectly on the centerline of the specimen, and each Williams bar not having the same post-tension at the beginning of testing. The specimen was loaded three times, and each time the specimen's displacement increased slightly. This feature can be attributed to a loosening of the system as it was undergoing load.

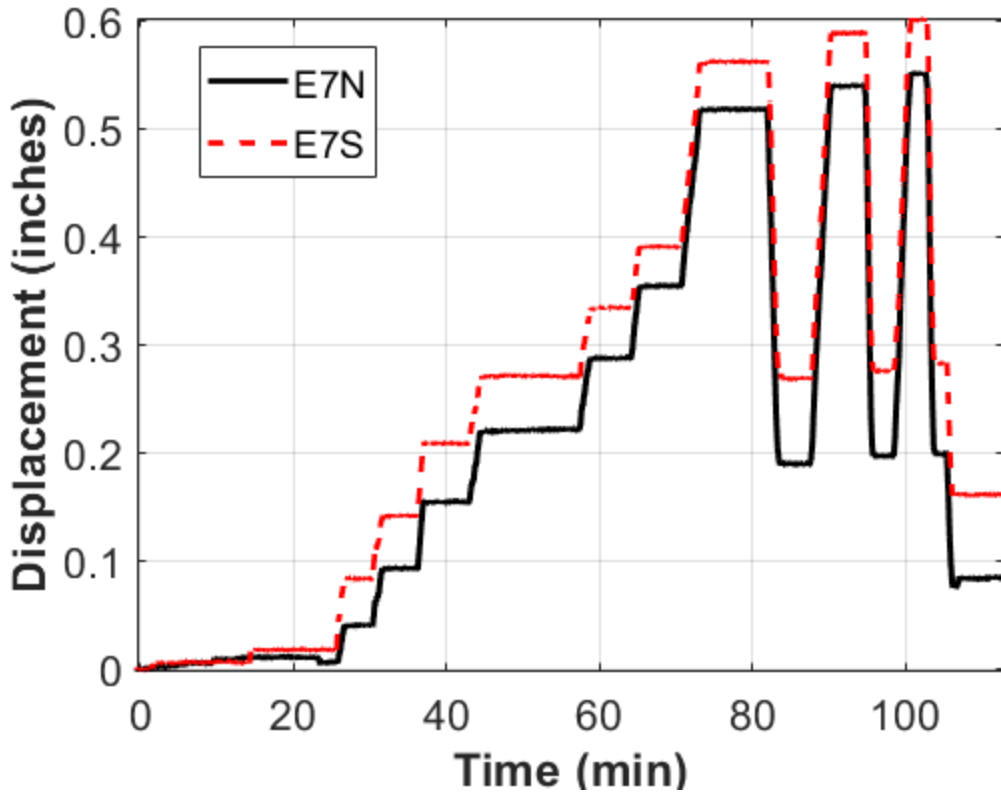


Figure 5.126. Concept B Second Static Testing Displacement Time History.

The actuator load versus displacement plot of the specimen can be seen in Figure 5.127, with negative displacement meaning pulling up and negative load meaning pulling up. The specimen had to be pulled up with approximately 12 kips to remove the pedestal support under the active loading end. Once the pedestal was pulled out, the specimen was returned to its original position. As the specimen was loaded, it maintained a linear relationship up to the 28–29-kip level. At that point, the stiffness of the specimen started to reduce (deformation increased at a faster rate). The maximum load reached was 30 kips, and the displacement at that load level was approximately 0.5 inches.

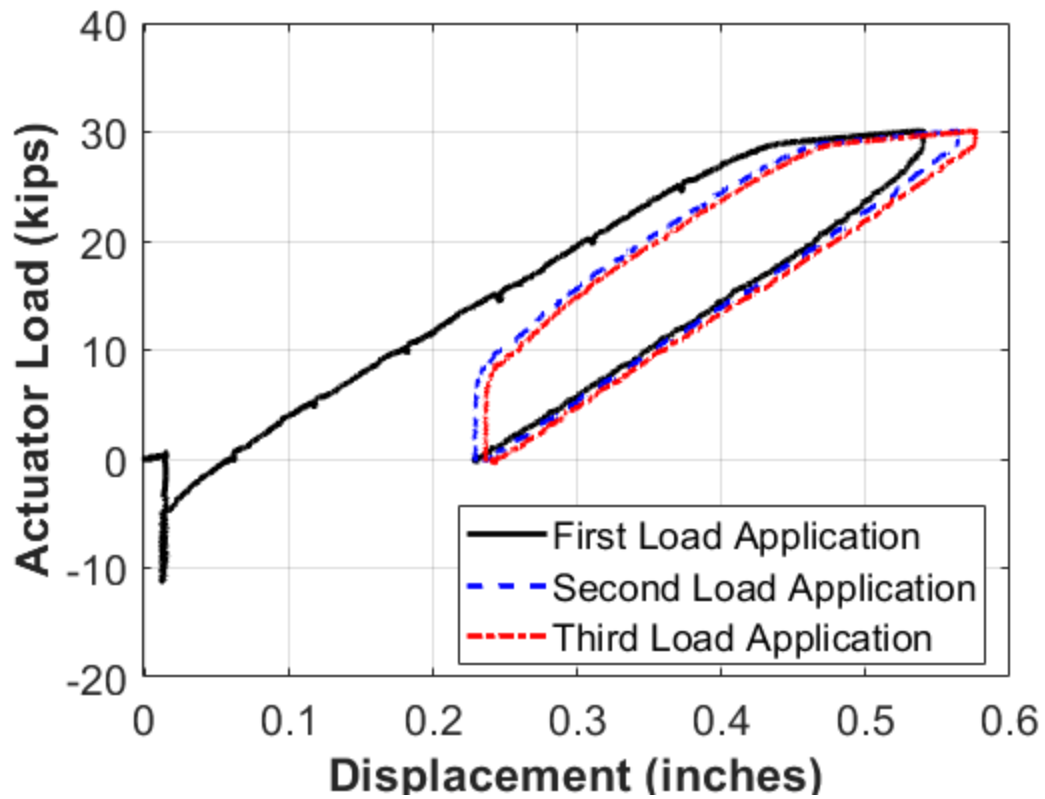


Figure 5.127. Concept B Second Static Testing Load versus Displacement.

The strain in the Williams bars due to the load of the specimen can be seen in Figure 5.128. Similar to Figure 5.125, this figure shows the strain decreasing slightly as the specimen displaces, and then once the load reaches approximately 29 kips, the strain in the bars increases rapidly.

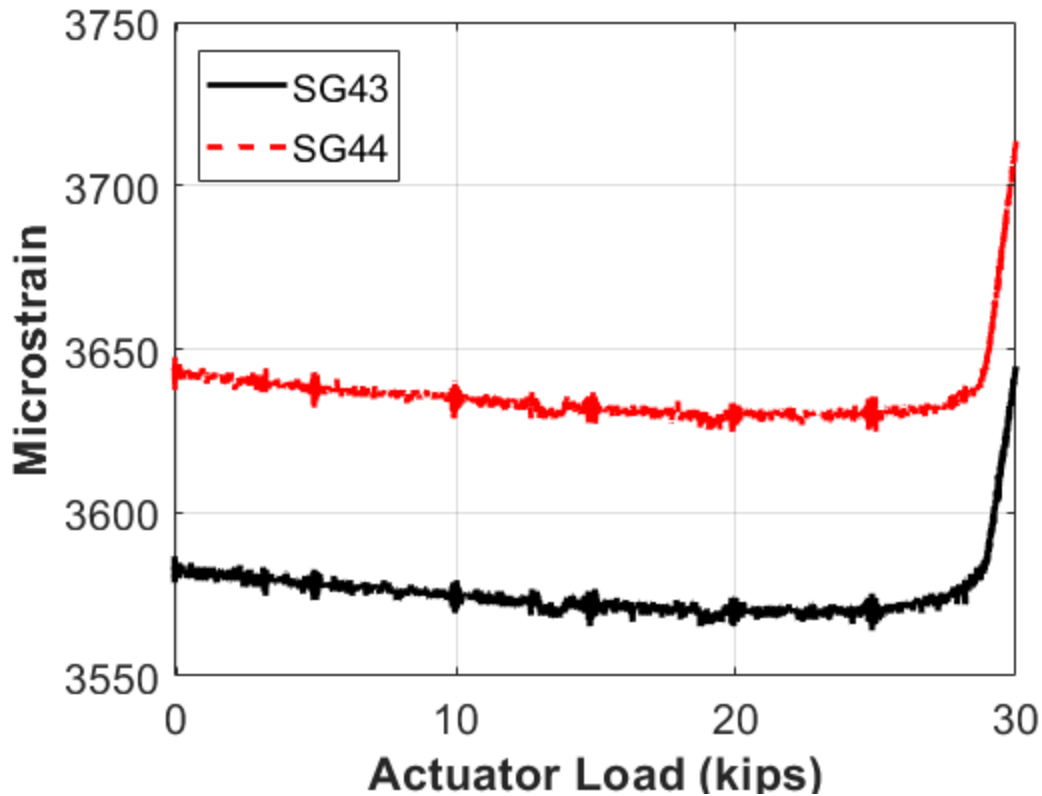


Figure 5.128. Concept B Second Static Testing Williams Bar Strain versus Load (First Load Application).

The stress on the surface of the deck can be seen in Figure 5.129, with negative load meaning pulling up and negative displacement meaning pushing down. SG 59 was located on the longitudinal centerline of the beam on gridline E1, and SG58 and SG60 were located 2 ft on either side of SG59. The specimen was initially pulled up to remove the pedestal, which created compression at the top of the deck. As the specimen was pushed down, tension developed at the top of the deck. The trend of the data seems to follow a mostly linear path up to the 30-kip load level.

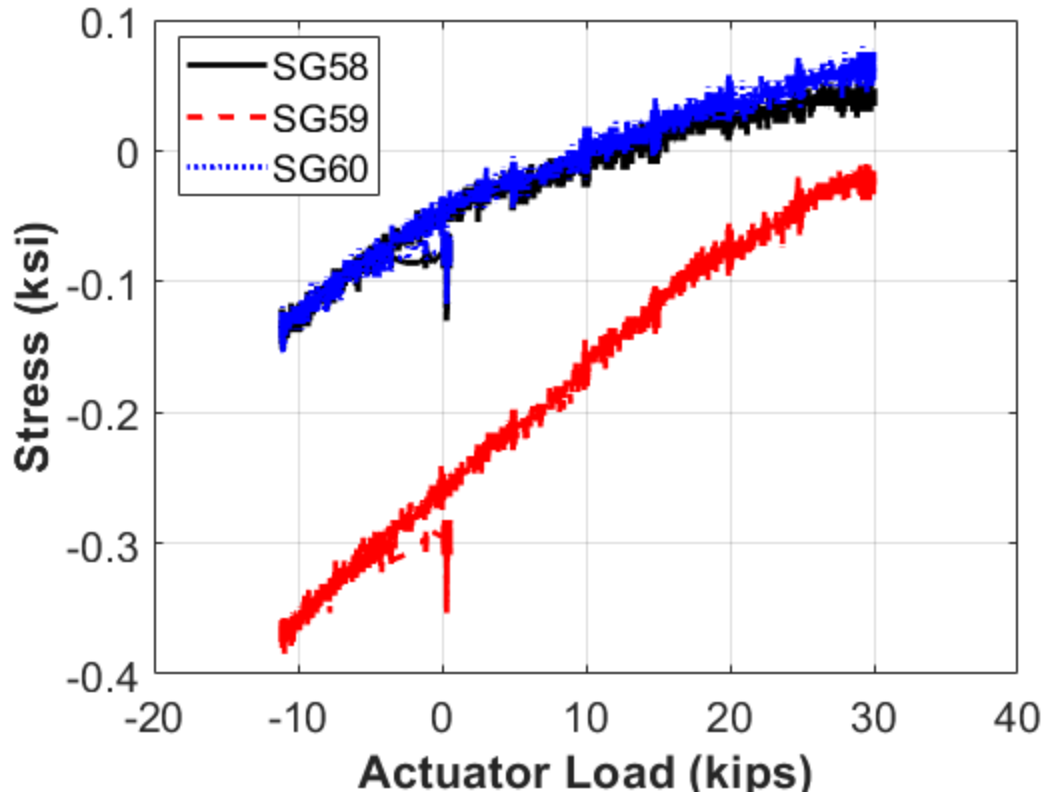


Figure 5.129. Concept B Second Static Testing Concrete Surface Deck Stress versus Load at E1 (First Load Application).

Similar to Figure 5.129, Figure 5.130 shows the stress in the deck rebar at gridline E1 versus the load applied on the specimen. The stress in the rebar followed a linear path to more tension as the load was increased, with SG11 (located on the longitudinal centerline) increasing at a faster rate than SG10 and SG12 due to the shear-lag effect described earlier.

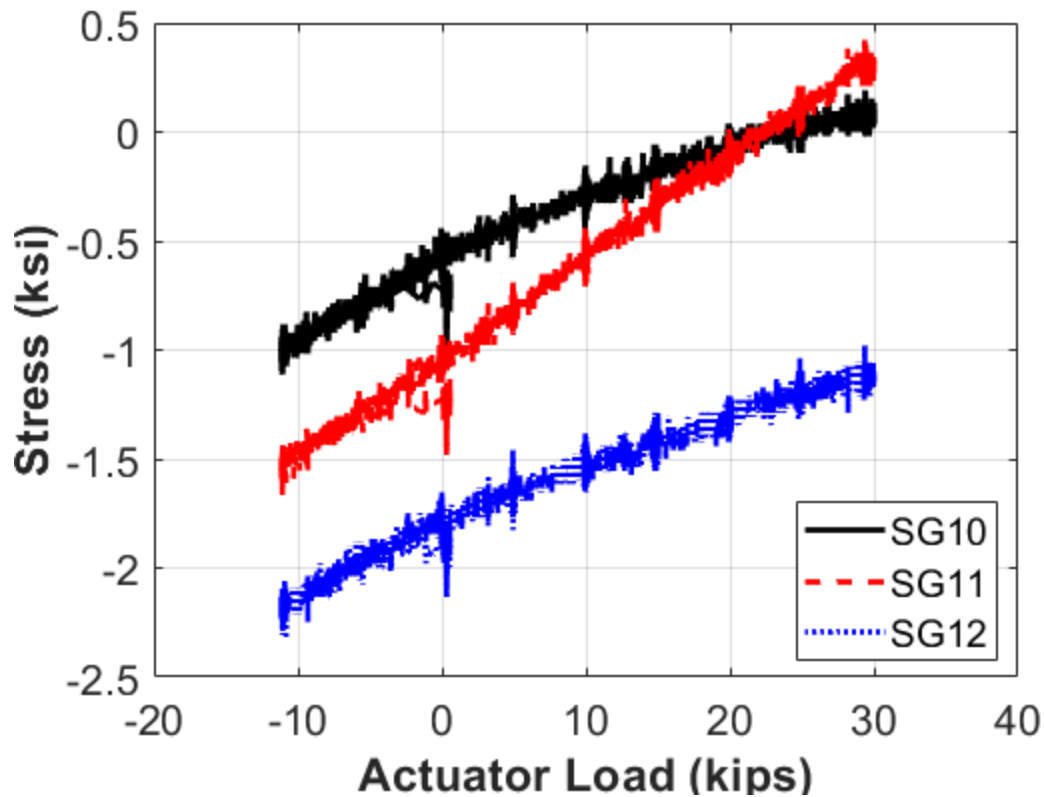


Figure 5.130. Concept B Second Static Testing Concrete Rebar in Deck Stress versus Load at E1 (First Load Application).

The rotation of the specimen versus the actuator load can be seen in Figure 5.131. The rotation of the specimen was found by taking the data from the LVDT that was on top of the deck on the longitudinal centerline of the specimen. The elongation of the LVDT was divided by the distance to the NA to find the rotation of the specimen at the closure pour. There are two distinct regions shown in this plot. The first region is the set of data up to the 28-kip mark. Up to then, the data are linear, and there is not much rotation of the specimen. Once the load exceeds 28-kips, the rotation of the specimen starts to increase exponentially. The stiffness of the specimen drops significantly once the load exceeds 28-kips.

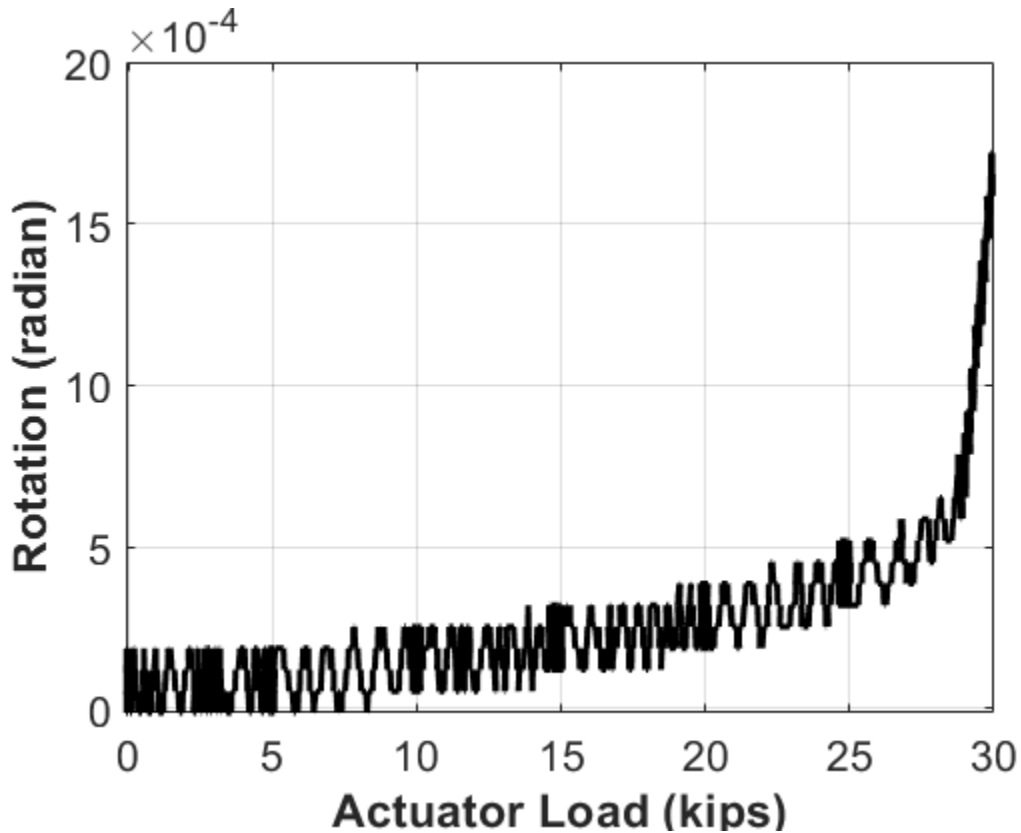


Figure 5.131. Concept B Second Static Testing Rotation at Center of Rotation (First Load Application).

The second round of static testing was considered complete at this point. The specimen was put back on the pedestal and was inspected for any new cracks that had formed. It was noted that the interface between the precast concrete deck and the UHPC closure pour stayed closed more with the added post-tension of the Williams bars.

5.8.2.5. Concept B Second Cyclic Testing

After the second round of static testing had been completed, cyclic testing resumed. A smaller deflection range of +0.10 inches to -0.30 inches to match the first round of cyclic testing was used for the first 9,000 cycles to see if the specimen had any loosening effects. After those 9,000 cycles were completed, the specimen was examined and found to have no new cracks or loosening of any of the components. The rest of the cyclic testing was run at a deflection level of +0.15 inches to -0.40 inches. A total of 125,000 cycles were run at this deflection range. At the beginning of this round of cyclic testing, the lowest strain in the Williams bars was at approximately 3565. At the end of the 125,000 cycles, the strain in the Williams bars remained

steady at 3565 microstrain. See Table 5.11 for a summary of the number of cycles and the ranges that were run per day.

Table 5.11. Concept B Second Cyclic Testing Ranges.

Day	Number of Cycles	Load Rate (Hz)	Displacement Control Range
1	9,000	1	(−0.30") to (+0.10")
2	9,000	1	(−0.4") to (+0.15")
3	16,000	1	(−0.4") to (+0.15")
4	15,000	1	(−0.4") to (+0.15")
5	25,000	1	(−0.4") to (+0.15")
6	26,000	1	(−0.4") to (+0.15")
7	25,000	1	(−0.4") to (+0.15")
Total	125,000		

In total, 192,600 cycles were run throughout both cyclic tests. Tightening the Williams bars to the higher post-tension level allowed the specimen to experience a larger displacement range with no (or minimal) loss of stiffness. After the cyclic testing was completed, the specimen was inspected for any new cracks or other signs of damage that occurred due to the cyclic testing. The separation of the UHPC closure pour and the precast concrete deck had closed completely, indicating that the post-tension from the Williams bars still provided enough compressive force to close this gap.

A time-displacement plot can be seen in Figure 5.132. The sampling rate during the cyclic loading was 5 Hz, so due to the large amount of data that were collected, this figure only shows a snapshot of data from the testing. It can be seen from this figure that displacement during the testing was very consistent, going from −1.05 inches to −1.55 inches.

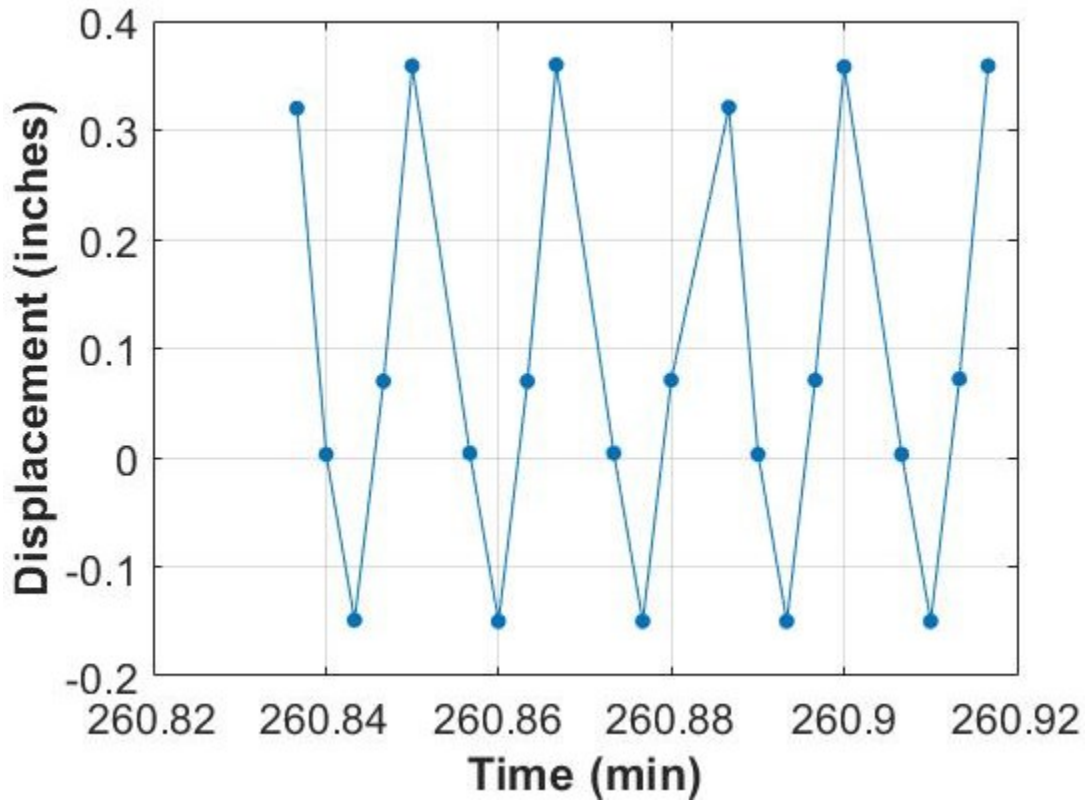


Figure 5.132. Concept B Second Cyclic Loading Displacement at E7 Time History of Selected Cycles.

Similar to Figure 5.132, Figure 5.133 shows a load time history plot. The target loads the team was trying to hit were approximately 15 kips pulling up and 29 kips pushing down. The plot reveals that the team was hitting the 15-kip goal, but the goal of 29 kips pushing down seemed short, which was due to the sampling rate. Since the sampling rate could not be increased further, the maximum points only show ~25 kips, when in reality, during the testing, the actuator hit 29 kips consistently.

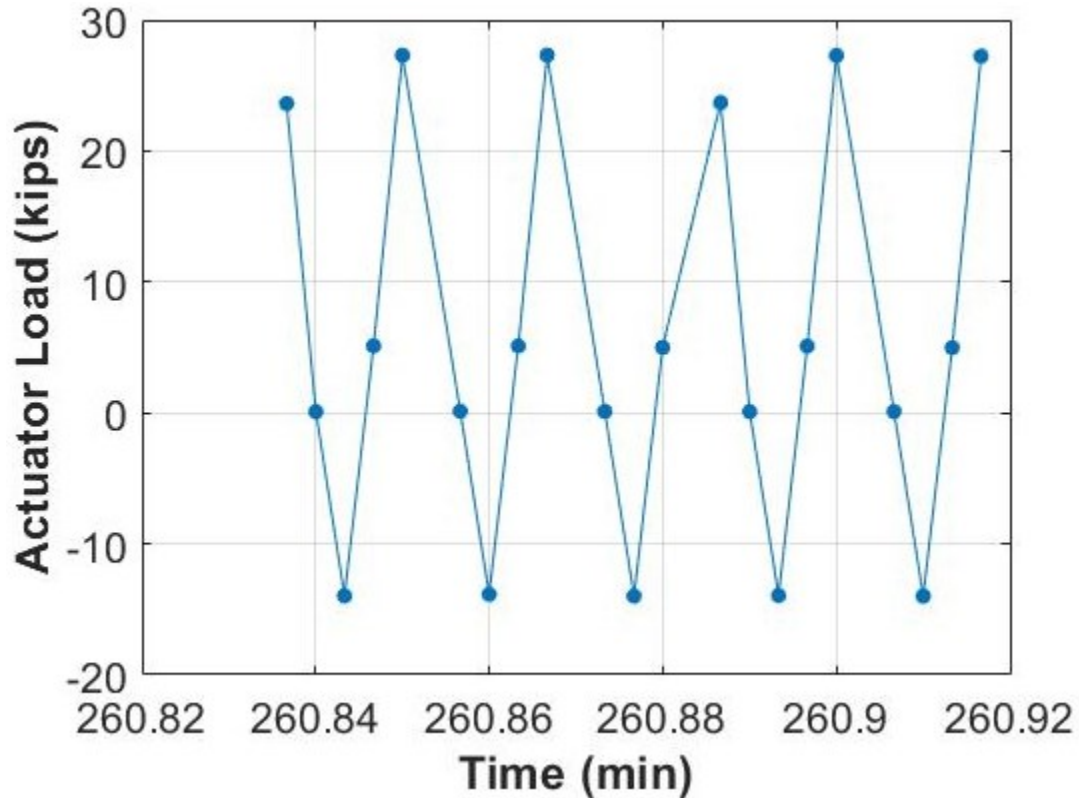


Figure 5.133. Concept B First Cyclic Loading Load Time History of Selected Cycles.

Figure 5.134 shows the load versus displacement plot for a sample of data points, which reveals that the load versus displacement stayed linear during the entirety of the sample that was pulled. The gaps in the data are due to the sampling rate. Only using 5 Hz as the sampling rate made it inevitable that gaps were going to be seen in the test data, but the main point of focus of this plot was to see if there was not any loss of stiffness of the system during the cyclic loading testing.

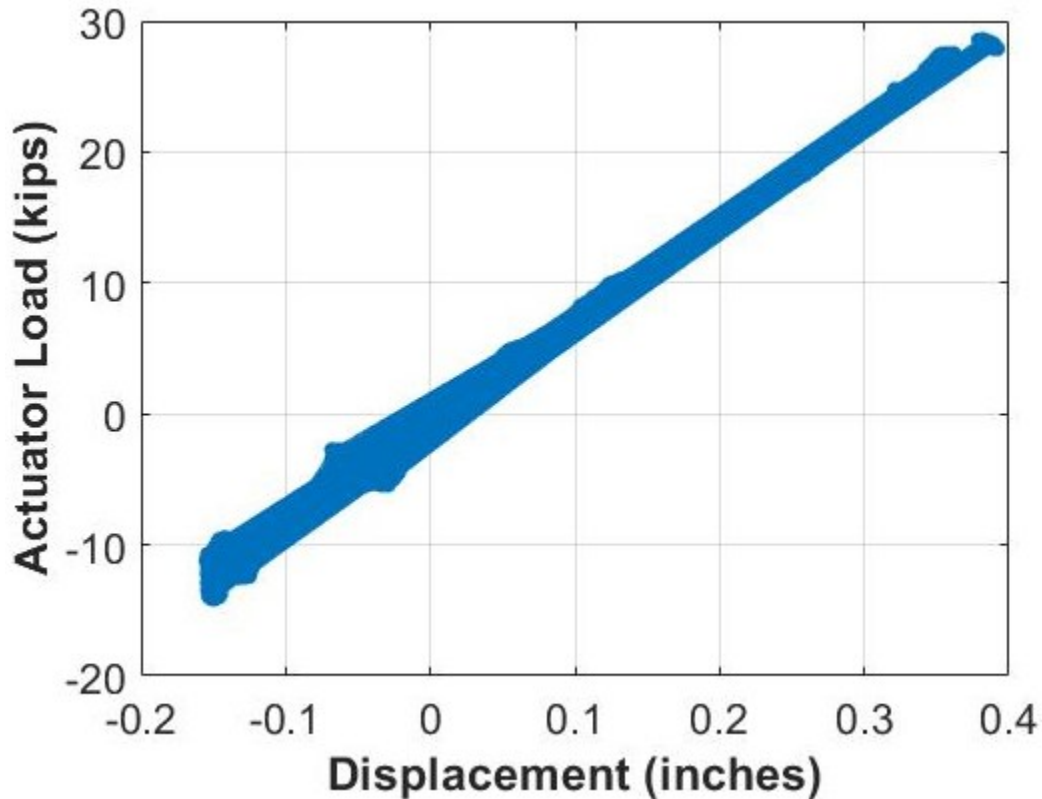


Figure 5.134. Concept B Second Cyclic Loading Load versus Displacement at E7.

Once the cyclic testing was completed, the final part of testing was started, which was ultimate testing.

5.8.2.6. Concept B Ultimate Testing

Ultimate testing for Concept B was conducted using displacement control. The specimen was pushed down in 0.25-inch increments to start. After each increment, the specimen was inspected for new cracks and other signs of damage. At 0.5-inch of deflection, the specimen started to behave nonlinearly, which matched the results of the static testing. Once the specimen reached 1.5 inches of deflection, the strain in the Williams bars reached 4800 microstrain (yielding of the bars was expected at 4100 microstrain). The deflection increment was changed to 0.125 inch after this point. The research team continued to displace the specimen in 0.125-inch increments until 5100 microstrain was reached, which correlated to the ultimate strength of the Williams bars and a deflection of the specimen of 2 inches. It was decided to keep displacing the specimen until a total deflection of 2.5 inches was reached without a failure of the Williams bars. The strain in the Williams bars read 6200 microstrain at this point, which is 1100 microstrain higher

than the theoretical ultimate strain. Testing was stopped because catastrophic failure seemed imminent, and the specimen was well beyond the typical deflection limits of a bridge. The cracks in the slab were documented, and many pictures were taken. See Figure 5.135 for a plot of the strains on the Williams bars. As the testing proceeded, the strain difference between each Williams bar increased due to several factors, including the specimen being loaded slightly off-center and the Williams bars being loaded slightly differently to start.

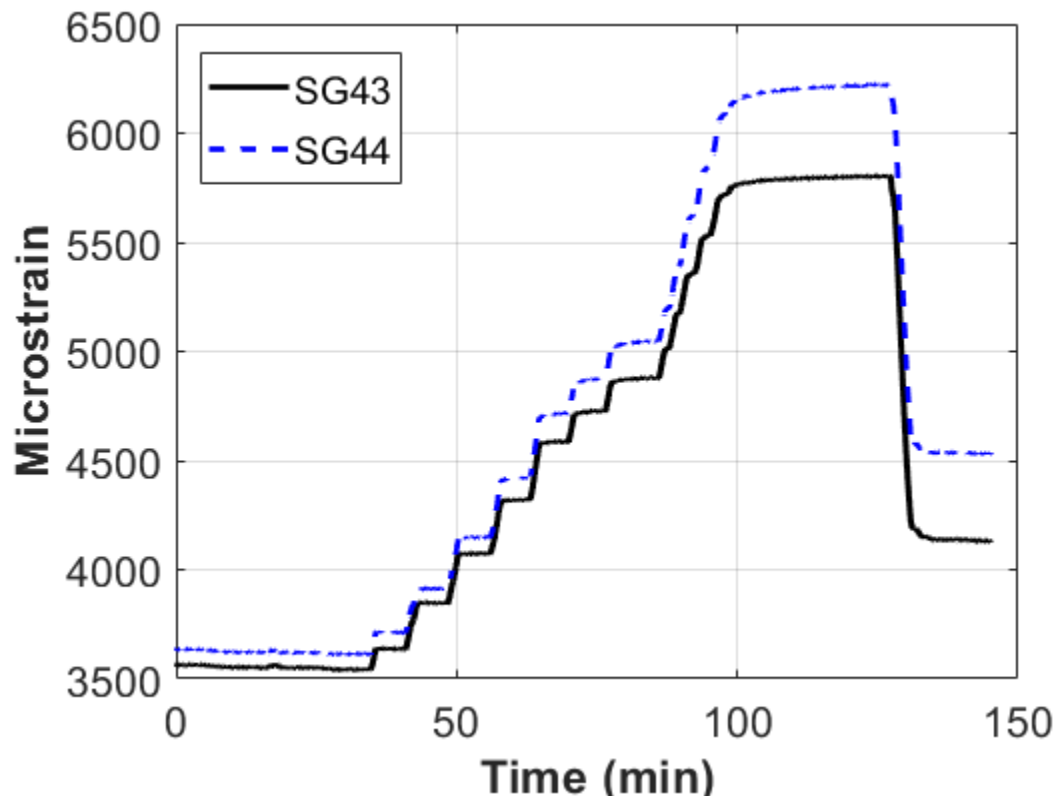


Figure 5.135. Concept B Ultimate Testing Strain on Williams Bars.

The total vertical deflection of the specimen on the active loading end can be seen in Figure 5.136, with negative values being down. The initial positive displacement is due to lifting the specimen so that the pedestal could be removed. Each displacement step can be seen clearly, and the maximum deflection approached 2.5 inches.

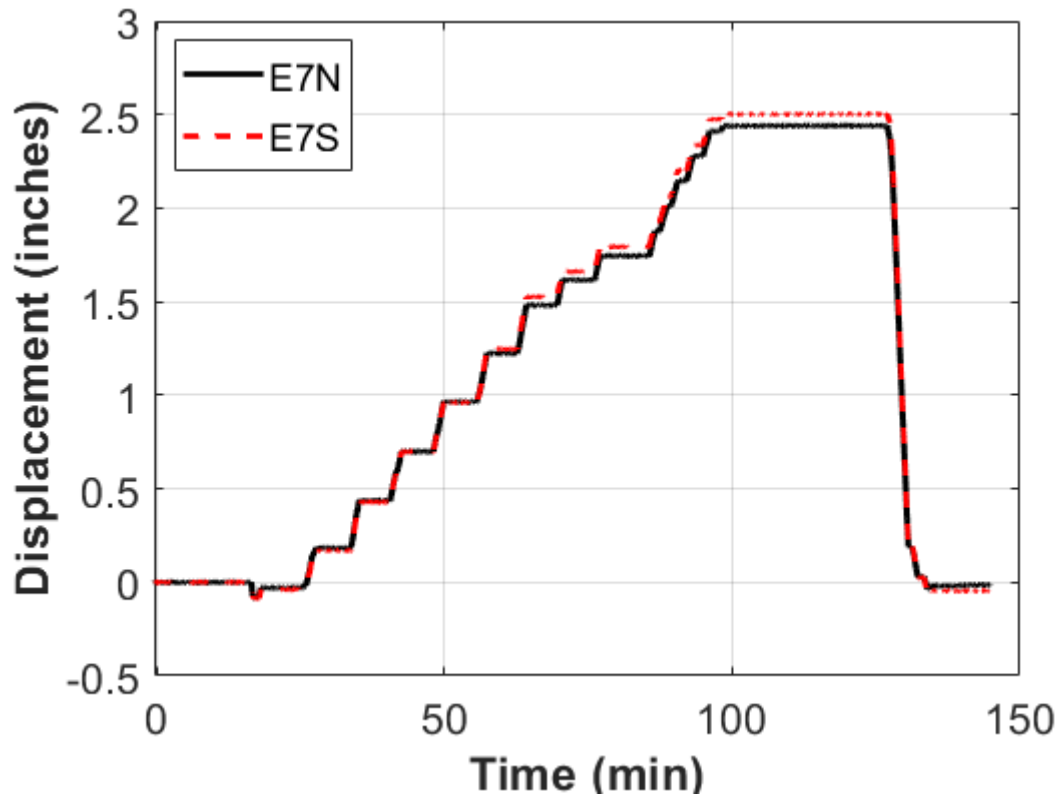


Figure 5.136. Concept B Ultimate Testing Displacement Time History.

The load imparted on the specimen by the active loading end actuator can be seen in Figure 5.137, with positive load meaning the specimen is being pushed down. The initial negative load is due to pulling the specimen up so that the support pedestal could be pulled out from under it. This effort required slightly more than 10 kips to achieve. As the testing progressed, it became harder to increase the load as the displacement was increasing, which can be seen in Figure 5.137, in which the steps got smaller and smaller as testing progressed. The maximum load that was achieved was approximately 41–42 kips.

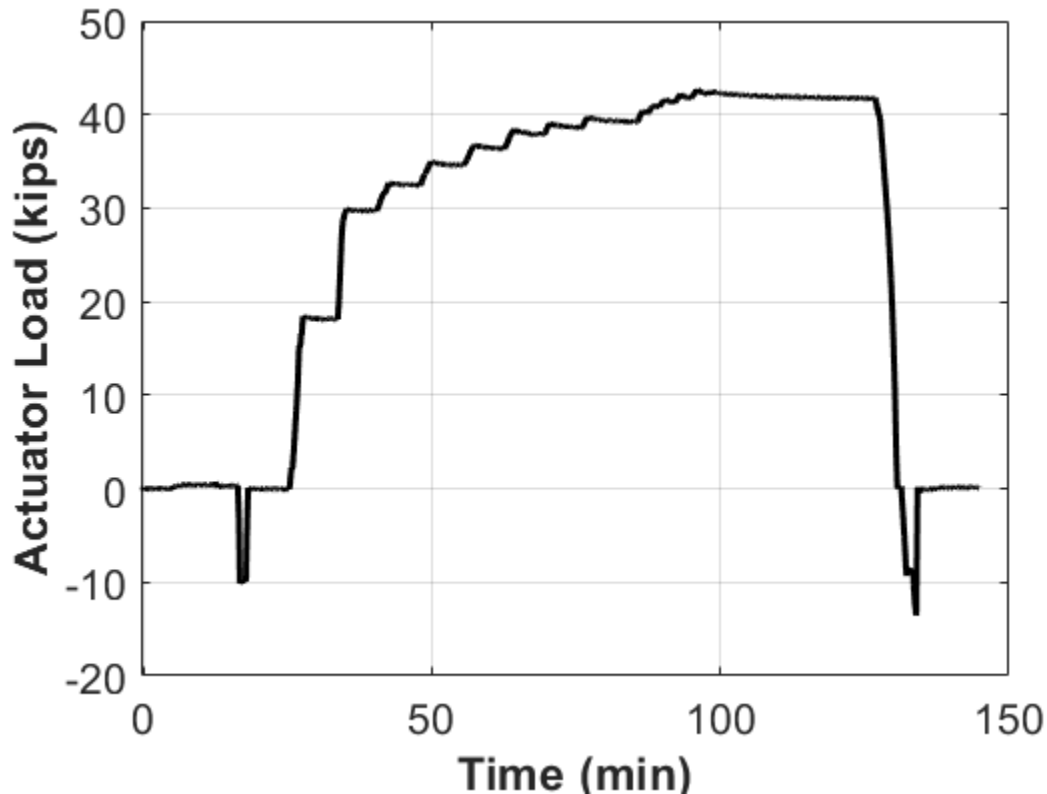


Figure 5.137. Concept B Ultimate Test Actuator Load Time History.

The actuator load versus displacement plot can be seen in Figure 5.138. The top line indicates the load being imparted on the specimen, while the bottom line indicates the load being taken off the specimen. As explained before, the negative load and displacement at the bottom left of the plot are due to the specimen being lifted to remove the support pedestal. The initial portion of the plot shows a fairly linear relationship of load versus displacement. This line peaks at approximately 28 kips of load and 0.3 inches of displacement. After this point, however, the displacement started to increase at a greater rate than the load, which indicates a region of yielding/plastic deformation. This result can also be seen in the bottom line of the plot. As the load was being taken off the specimen, the load versus displacement line did not follow the initial line, indicating that some plastic deformation occurred.

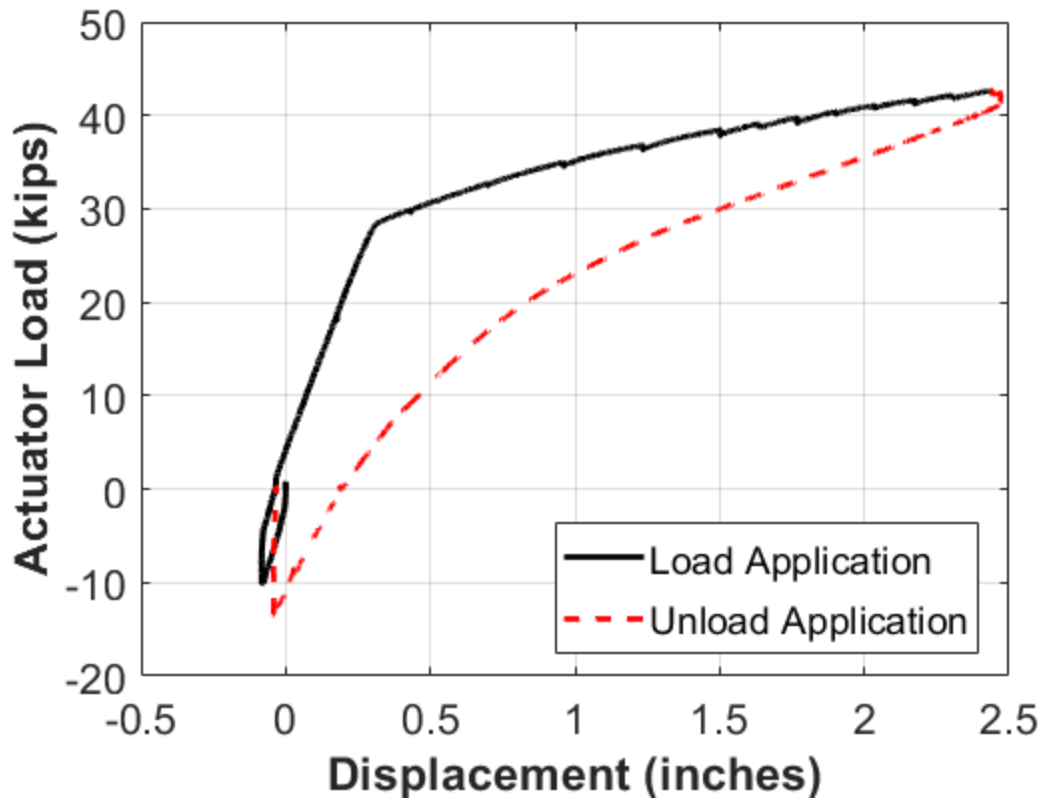


Figure 5.138. Concept B Ultimate Testing Load versus Displacement.

This plastic deformation can also be seen in Figure 5.139. This plot shows the strain in each Williams bar versus the displacement of the specimen. The bottom set of lines is from the load being imparted on the specimen, while the top set of lines is from the load being taken off the specimen. The strain in the Williams bars started to increase at approximately 0.4 inches of displacement. At each displacement step, the strain in the Williams bars increased as well. As the test progressed, the strain in the bars appeared to increase at a greater rate, with the maximum strain in the bars reaching 6200 microstrain, well above the theoretical ultimate strain limit. As the load was taken off the specimen, the strain in the bars did not return to their original levels, indicating that yielding had occurred.

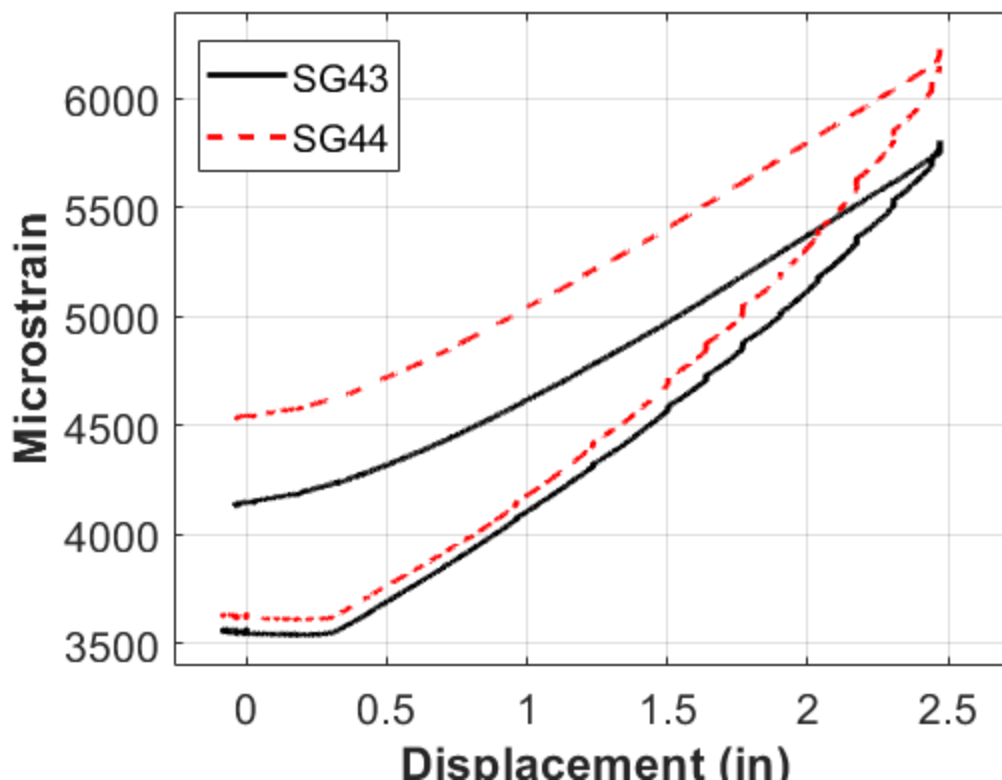


Figure 5.139. Concept B Ultimate Testing Williams Bar Strain versus Displacement.

An example of the strains in the deck slab can be seen in Figure 5.140. A negative stress indicates compressive stress, and a negative load indicates pulling up on the specimen. This figure shows the strains in the deck at the E1 grid location (refer to Figure 5.82 for a view of the instrumentation plan). This location was the first set of strain gauges on the active loading end of the specimen closest to the closure pour. SG59 was the concrete strain gauge down the longitudinal centerline of the specimen, with SG58 and SG60 being on each side of it. The initial negative stress in the strain gauges was due to the compression from the Williams bars being post-tensioned. The center strain gauge having more stress than the outer strain gauges indicates a shear-lag effect, wherein the elements on the centerline of the specimen closest to the brackets see a higher compression than elements farther away from the brackets. As the specimen was lifted to remove the support pedestal, the deck strain gauges read more compression, which is correct since the top of the deck undergoes more compression during this process. As the specimen was being pushed down, the stress in the deck became more positive, indicating more tension in the top fibers of the precast concrete deck, which also makes sense. All three strain gauges maintained a net compressive stress during the entirety of the test, indicating that at these regions the deck remained in compression.

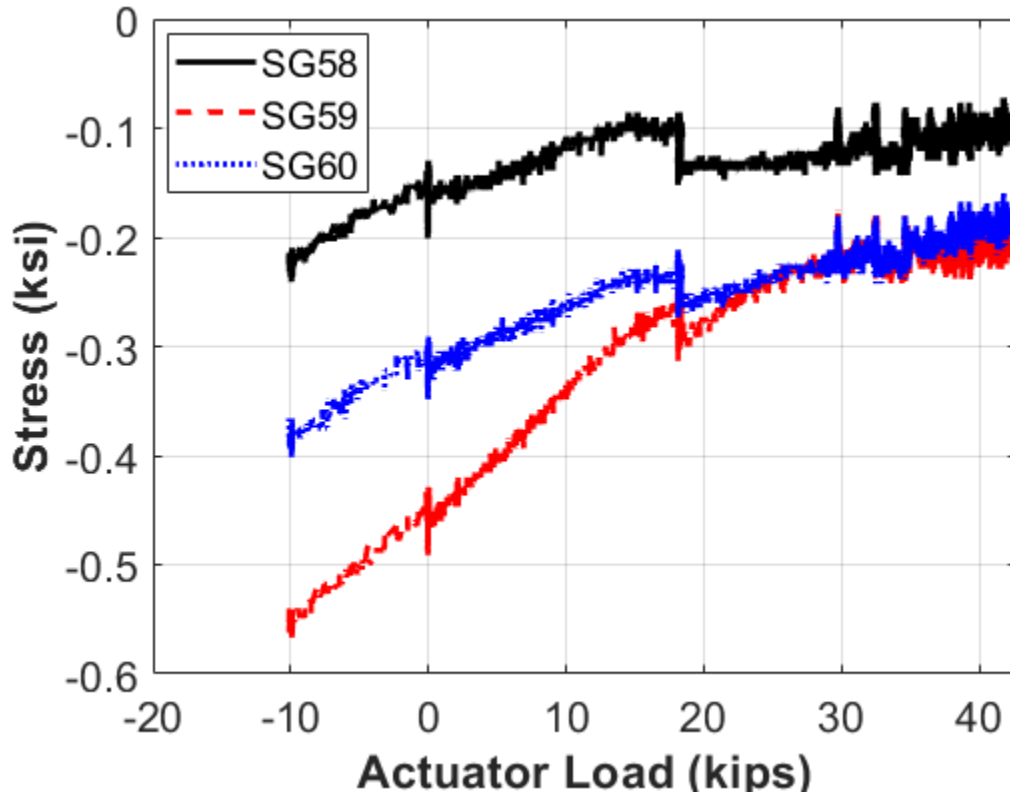


Figure 5.140. Concept B Ultimate Testing Concrete Deck Surface Stress versus Load at E1.

Similar to Figure 5.140 above, Figure 5.141 shows the stress in the rebar embedded in the deck at the E1 gridline. These strain gauges started with negative stress due to the precompression from the Williams bars. The initial vertical jump at the zero-load mark was due to the maroon ram on the hold-down side of the specimen. The maroon ram pushed down on the dead-end side with 200 kips, which caused the strain gauges to experience tension because they were in the negative bending region over the support. The rebar strain gauges experienced compressive stress while the pedestal was being pulled out, and then they showed tension as the specimen was being loaded. SG11 was the rebar strain gauge on the longitudinal centerline of the specimen. SG10 and SG12 were on either side of SG11. SG10 and SG12 followed very similar slopes as the test was going on, while SG11 appeared to grow at a much faster rate toward the tension stress zone. This finding further demonstrates that the specimen experienced a shear-lag effect. The magnitude of the stresses were relatively low in this area, likely because as the load was increased, the specimen started to pivot about the bottom flange and experienced rigid body motion, which removed most tension from forming in the deck.

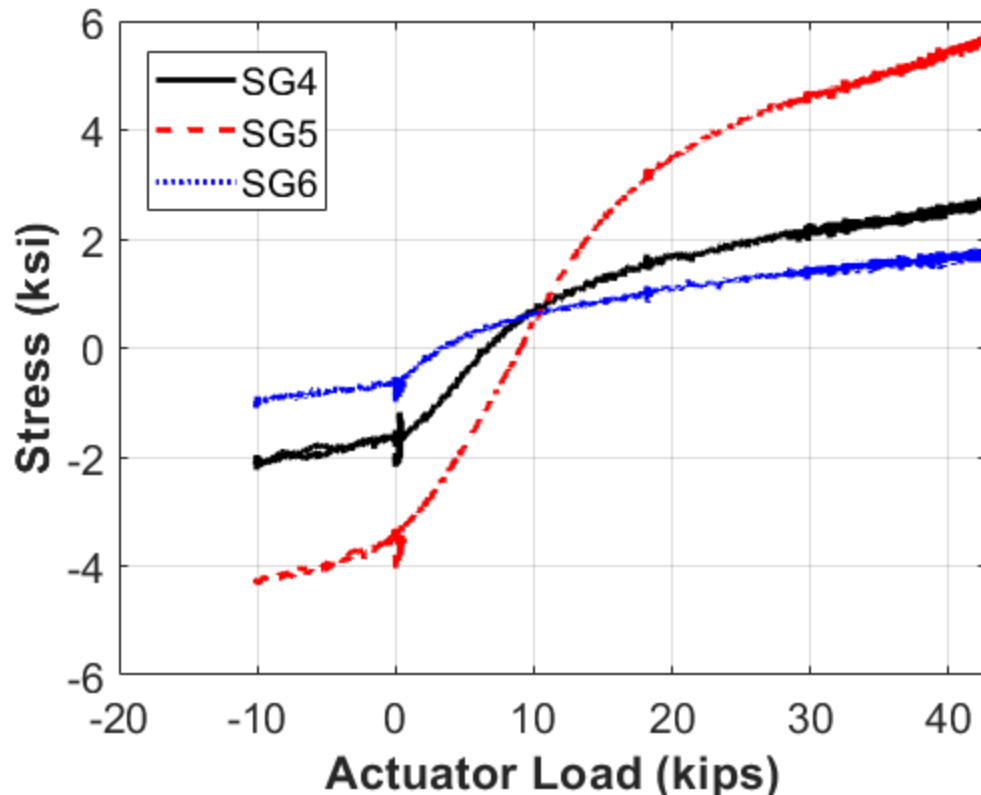


Figure 5.141. Concept B Ultimate Testing Rebar in Deck Stress versus Load at W2.

The strain values on the steel beam at gridline E1 can be seen in Figure 5.142. SG31 and SG32 are on the top flange, SG33 is on the top of the web, SG34 is on the bottom of the web, and SG35 and SG36 are on the bottom flange. All the strain gauges on the steel stayed the same or experienced tension while the pedestal was being pulled out. This finding makes sense since the NA was around the top flange, so the bottom flange will experience tension as this is happening. As the test progressed, SG34-36 started to experience more and more compressive strains because the bottom flange was in compression. As more load was imparted on the active loading end of the specimen, the NA moved down. The strain gauges on the top flange stayed the same or showed slight tension toward the end of the test, which makes sense since the top fibers of the steel experience tension as the NA moves down.

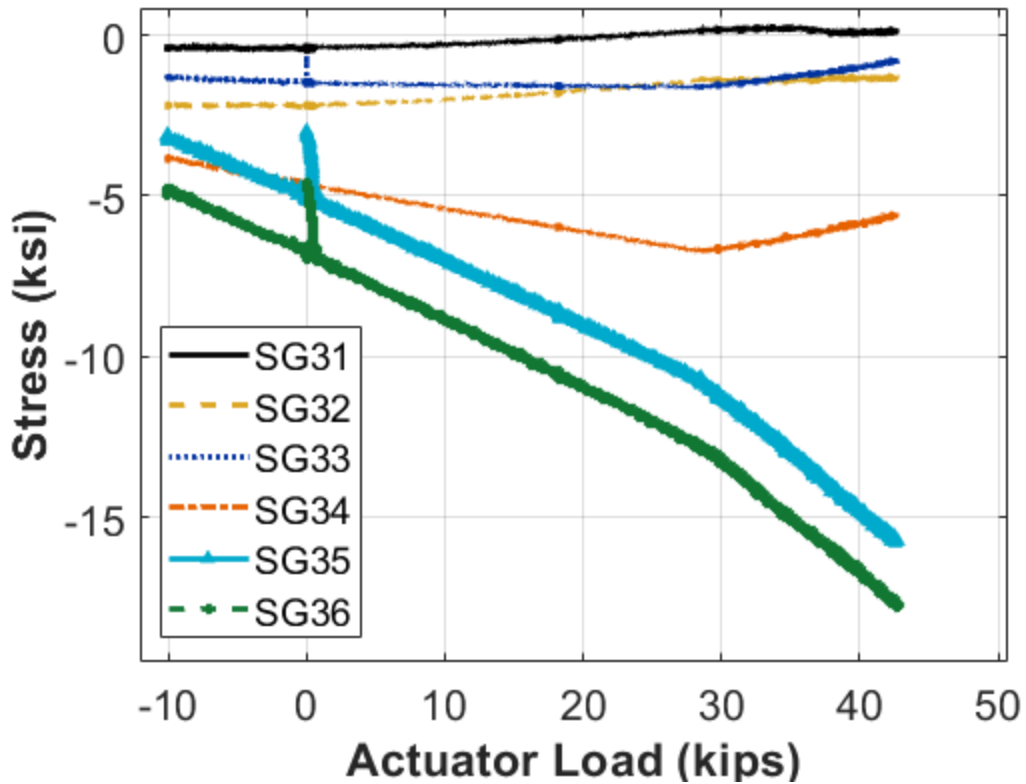


Figure 5.142. Concept B Ultimate Testing Steel Beam Strains at E1.

Several plots show the location of the NA. Figure 5.143 to Figure 5.145 show the NA based on the strains from the structural steel strain gauges at E1, W1, and W2, respectively. The NA at gridline E1 was very near the top flange, which put it at approximately the same height as the Williams bars. This finding was also the case at gridline W1. The NA at gridline W2 was lower, approximately 22 inches above the bottom flange. The composite NA of the cracked section was calculated as being 17.5 inches above the bottom of the specimen.

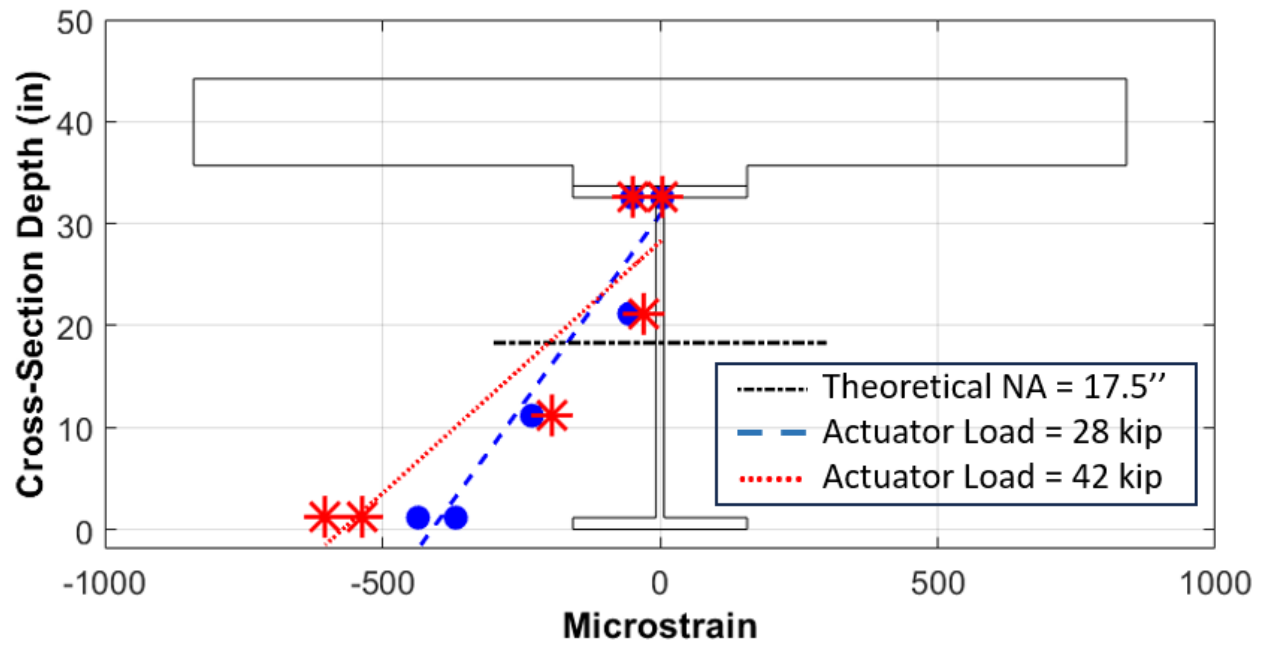


Figure 5.143. Concept B Ultimate Testing Structural Strain Profile at E1.

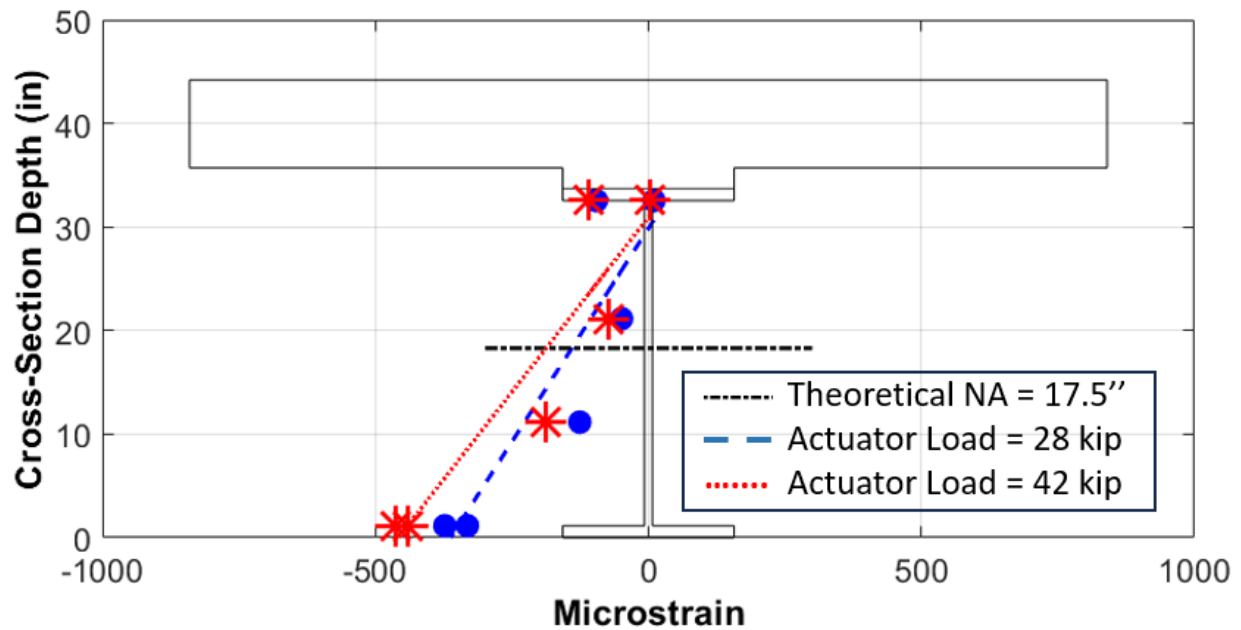


Figure 5.144. Concept B Ultimate Testing Structural Strain Profile at W1.

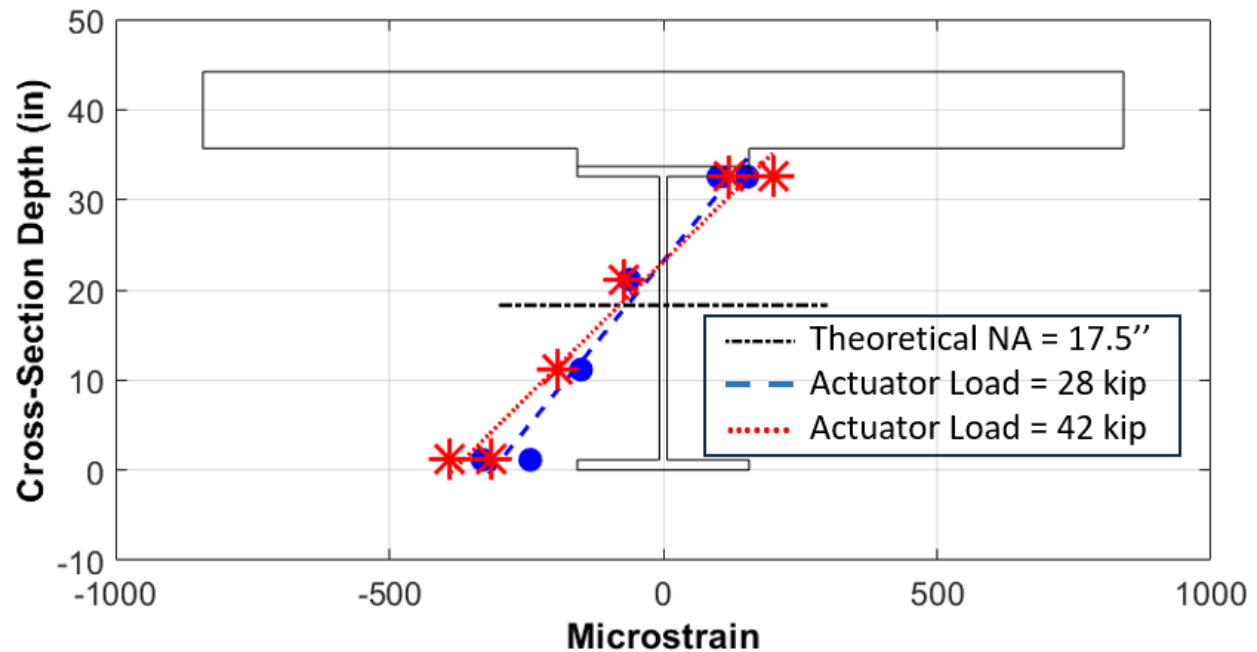


Figure 5.145. Concept B Ultimate Testing Structural Strain Profile at W2.

The rotation of the specimen versus the actuator load can be seen in Figure 5.146. Similar to static testing, there are two distinct regions in this plot. The first region is up to 30 kips. Up to that point, the data are linear, but once that load is exceeded, the stiffness of the system drops drastically, and the specimen rotates more as the load is increased.

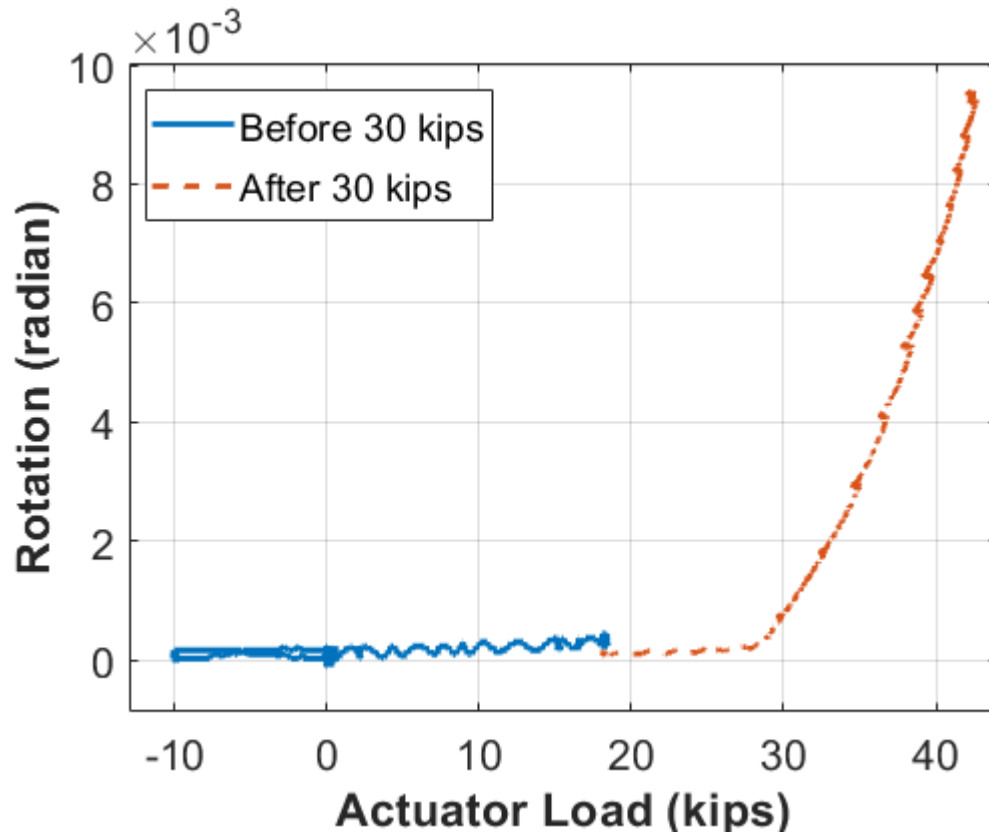


Figure 5.146. Concept B Ultimate Testing Rotation at Center of Rotation.

The gap between the precast concrete deck and the UHPC closure pour was very large at the end of the ultimate testing. The other cracks in the deck stopped expanding once 0.5-inch of deflection was reached. It seemed all the movement in the deck was transferred to the interface between the deck and UHPC. The specimen was brought back to its original deflection level of 1.22 inches; however, the strains in the Williams bars did not return to their original level. The strain readings on the bars were between 4200 and 4500, indicating that yielding had occurred. The specimen was put back on the pedestal, and the ultimate testing was completed. Final pictures were taken (shown in the next section), and the specimen was disposed of.

5.8.2.7. Concept B Posttesting Observations

After ultimate testing was completed, several major observations were made concerning the specimen. The first was that three significant transverse cracks appeared on the top of the deck during the testing. The first crack occurred on the dead-end side of the deck. The crack started propagating approximately 4 ft 6 inches from the transverse centerline of the specimen. This location is directly above the bracket location. This crack can be seen in Figure 5.147. The other

two significant cracks appeared on the active loading end of the specimen, approximately 3 ft and 4 ft 6 inches away from the transverse centerline. The crack that was 3 ft away from the transverse centerline is approximately where the end of the bracket lands, and the 4 ft 6 inches crack was in the middle of the bracket. These cracks can be seen in Figure 5.148. It is thought that the tension of the Williams bars in this area and the additional force imparted on the bars during testing caused the flange to slightly bend at this location, therefore causing cracking in the concrete. These were the only locations on the specimen where deck cracking was observed (outside of the closure pour interfaces).



Figure 5.147. Concept B Dead-End Deck Crack.



Figure 5.148. Concept B Active Loading End Deck Cracks.

Another major observation of this concept was that on the deck end side of the specimen, a visible air gap could be seen between the top of the top flange and the bottom of the haunch directly above the bracket. See Figure 5.149 for a picture of this air gap. It is hypothesized that as the specimen was undergoing vertical loading, the tension from the Williams bar was prying on

the bracket, causing the flange to separate from the haunch. This process was further exacerbated by there being no headed studs in this area. Originally, the research team planned to use a threaded coupler to extend the vertical bolts into the haunch (acting similar to shear studs), but these couplers were not available at the time of construction of this specimen. Therefore, there was nothing in this area to hold the haunch and the flange together.



Figure 5.149. Concept B Air Gap between Flange and Haunch.

The last major observation was the cracks that occurred between the interface of the UHPC closure pour and the precast concrete deck. These cracks grew at approximately the same rate up to the 30-kip load level (or its corresponding deflection level). However, once 30 kips was exceeded, the three transverse cracks did not widen (meaning rigid body rotation was occurring). The interface between the UHPC and the deck was the only location where the widening happened. After ultimate testing, this crack had widened substantially. See Figure 5.150 for a view of this separation.

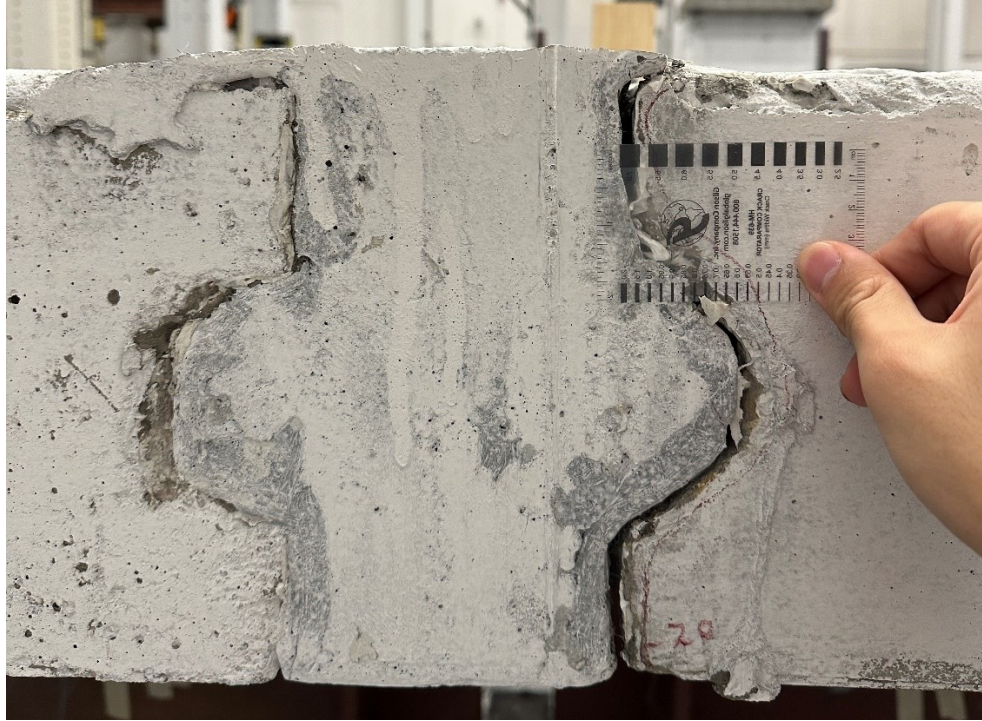


Figure 5.150. Concept B UHPC/Deck Interface Separation.

5.8.2.8. *Concept B Findings*

Several findings were determined from conducting the Concept B experimental testing. The primary findings are summarized as follows:

- *Loss of Stiffness:* There was a loss of stiffness of the specimen once design loading was exceeded. The initial stiffness of the specimen was ~ 80 kip/in. Past approximately 28 kips (which is the equivalent HL-93 load), the specimen acted nonlinearly (rigidly rotating). The stiffness of the specimen after it started acting nonlinear was ~ 7 kip/in, a drastic decrease. One reason for this issue was insufficient PT force. Future designs with this type of detail need to better account for the PT losses and provide additional reserve capacity such that the stiffness is maintained at much higher load levels. See Section 5.11.5 for an in-depth comparison of each concept's stiffnesses.
- *UHPC Interface:* The cyclic loading completely broke the interface bond between the UHPC closure pour and the normal concrete. The insufficient PT force (described above), combined with an unreinforced closure pour, allowed for a hinge to form at the UHPC interface. Although the narrow unreinforced closure pour is logistically desirable for

ABC, the structural performance is inadequate. Future design recommendations include a reinforced closure.

- *Welded Brackets*: The PT brackets should be shop-welded rather than bolted to the beam flanges because it is difficult to know for certain whether the required pretension of the bolts has been achieved. These bolts are an essential part of the design, therefore it is unacceptable if they are not adequately pre-tensioned. In addition, using slip-critical bolts will require special surface prep for the beams and the bracket assembly. These surface preps can be expensive and may not always provide the necessary coefficient of friction required by design. Welding the brackets to the beam flange eliminates this problem because welding can be controlled much better than slip-critical bolts. Moreover, in certain cases, the required number of bolts to resist the shear and tensile loads may become large, which will require a large bracket assembly. Such large bracket assemblies get very heavy, and on a construction site may become dangerous to handle. Also, without bolts attached to the top flange, shear studs can be welded, which reduces local flange bending.
- *Bar Tensioning*: To provide adequate tension in the Williams bars, a through-hole jack is a reliable method. For virtually all designs a 100-ton through-hole jack is the minimum jack size. These jacks weigh more than 100 lb; therefore, this factor must be accounted for when considering the constructability of the setup.

5.9. CONCEPT C

5.9.1. Design, Construction, and Pretest Behavior of Concept C

5.9.1.1. Specimen Design

This subsection introduces how the Concept C test specimen was designed to achieve the features of the benchmark bridge. Section 5.3 previously described the benchmark bridge design, which is the basis of the specimen design. An elevation view of the connection area of Concept C is shown in Figure 5.151.

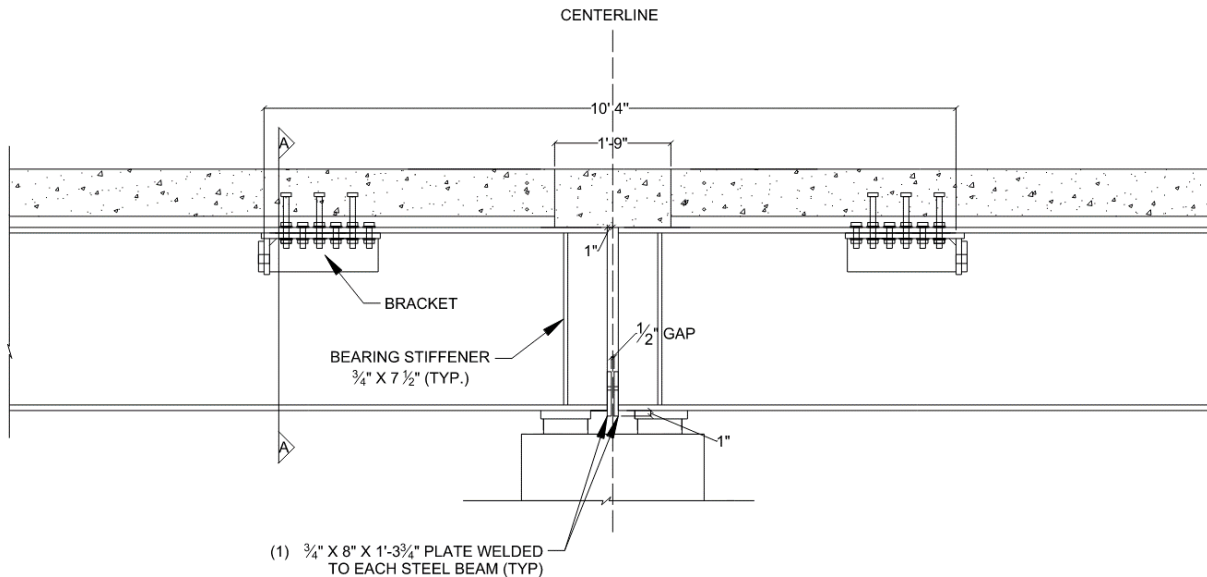


Figure 5.151. Elevation View of Concept C Connection Area.

The Williams bar design involved the service load balancing technique, which has been applied to the design of the continuous structure. The connection is designed for service loads and checked for the ultimate capacity and tensile stress at the slab under the service load. The force magnitude of the Williams bar design was 120-kip per bar, which was based on the stress-strain profile to achieve the net stress at the center of the closure pour surface equal to 0.0 ksi. The steel plates located on the bottom portion of the web and bottom flange were designed as compression-resisting elements.

For the bolted bracket design, the *AASHTO LRFD Bridge Design Specification 9th Edition* was followed [24]. The primary design checks and the AASHTO articles include:

- Shear resistance of bolts (Article 6.13.2.7).
- Slip resistance of bolts (Class B surface condition) (Article 6.13.2.8).
- Bearing resistance at bolt holes (Article 6.13.2.9).
- Bolt tensile resistance (Article 6.13.2.10.2).
- Prying action of the bolts or the flange or plate bending, which may result in the formation of a plastic hinge (Article 6.13.2.10.4).
- Combined bolt tension and shear resistance (Article 6.13.2.11).
- Fillet-welded connections (Article 7.12.3).

This concept consists of two W33×201 steel sections that are each 20 ft long with steel brackets located under each side of the top flange approximately 5 ft from the connection end of the beam. The steel brackets consist of 1-inch thick plate steel arranged in a three-sided configuration. See Figure 5.152 and Figure 5.153 for the layout of steel brackets.

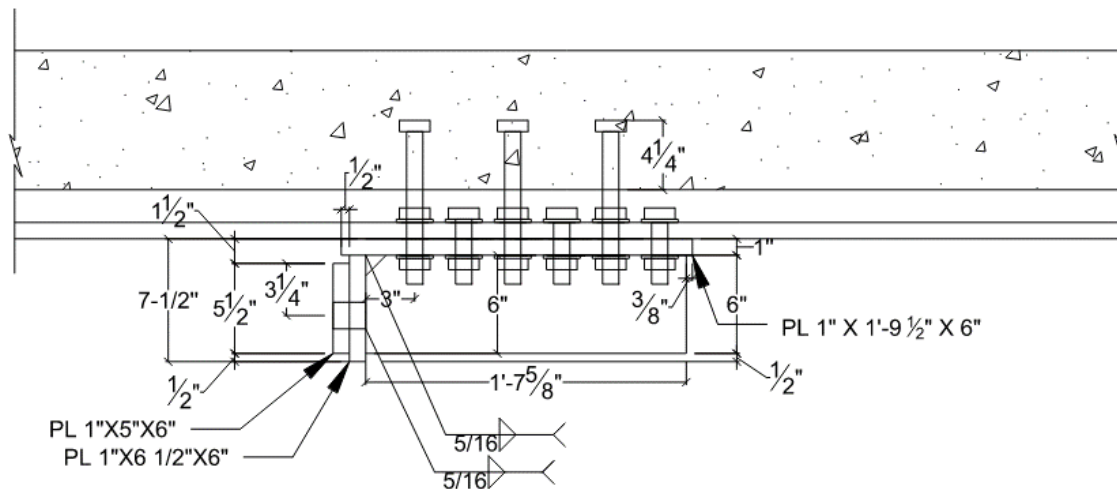


Figure 5.152. Close-Up Elevation of Steel Bracket Assembly.

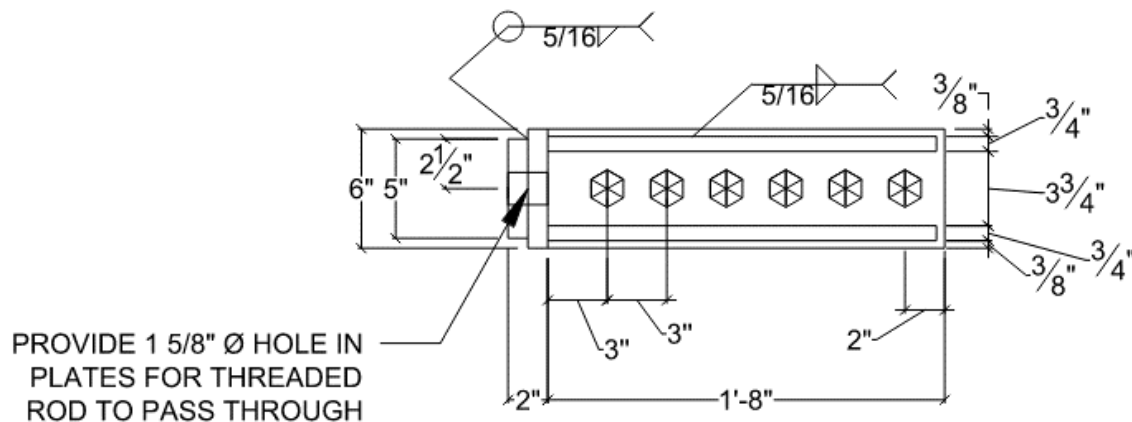


Figure 5.153. Close-Up Plan View of Steel Bracket Assembly.

A 150 ksi 1.375-inch Williams bar was fed through these brackets and post-tensioned to bring the deck slab into compression. Although Concept B utilized UHPC, Concept C used a wider closure pour region with Class S concrete.

5.9.1.2. Instrument Plan and Data Acquisition

The instrumentation of this concept focused mainly on the connection of the two composite beams. A plan view, elevation view, and section view of the instrumentation plan can be seen in

Figure 5.154, Figure 5.155, and Figure 5.156, respectively. A legend for the symbols can be found in Figure 5.157. The final instrumentation lists for each concept can be found in Appendix B.

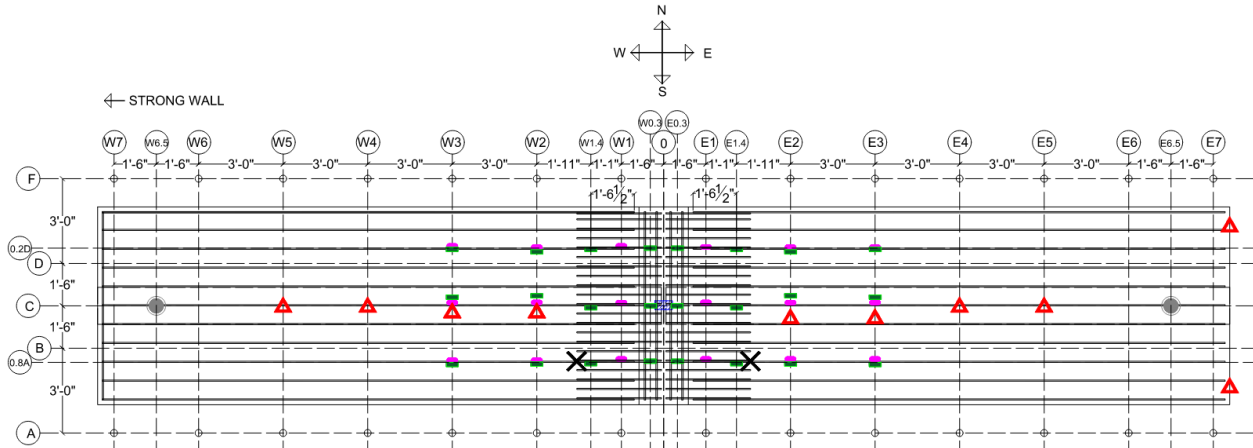


Figure 5.154. Concept C Instrumentation Plan (Plan View).

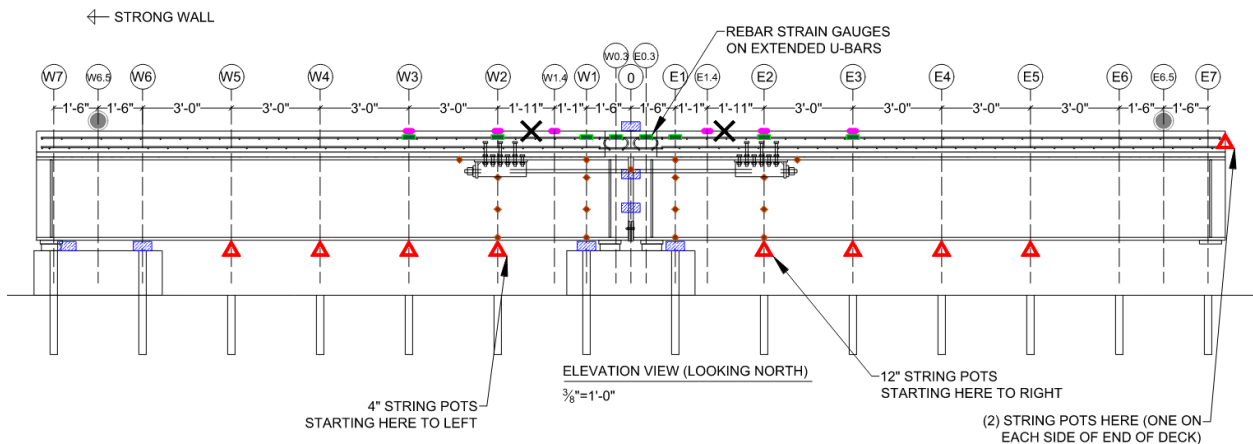


Figure 5.155. Concept C Instrumentation Plan (Elevation View).

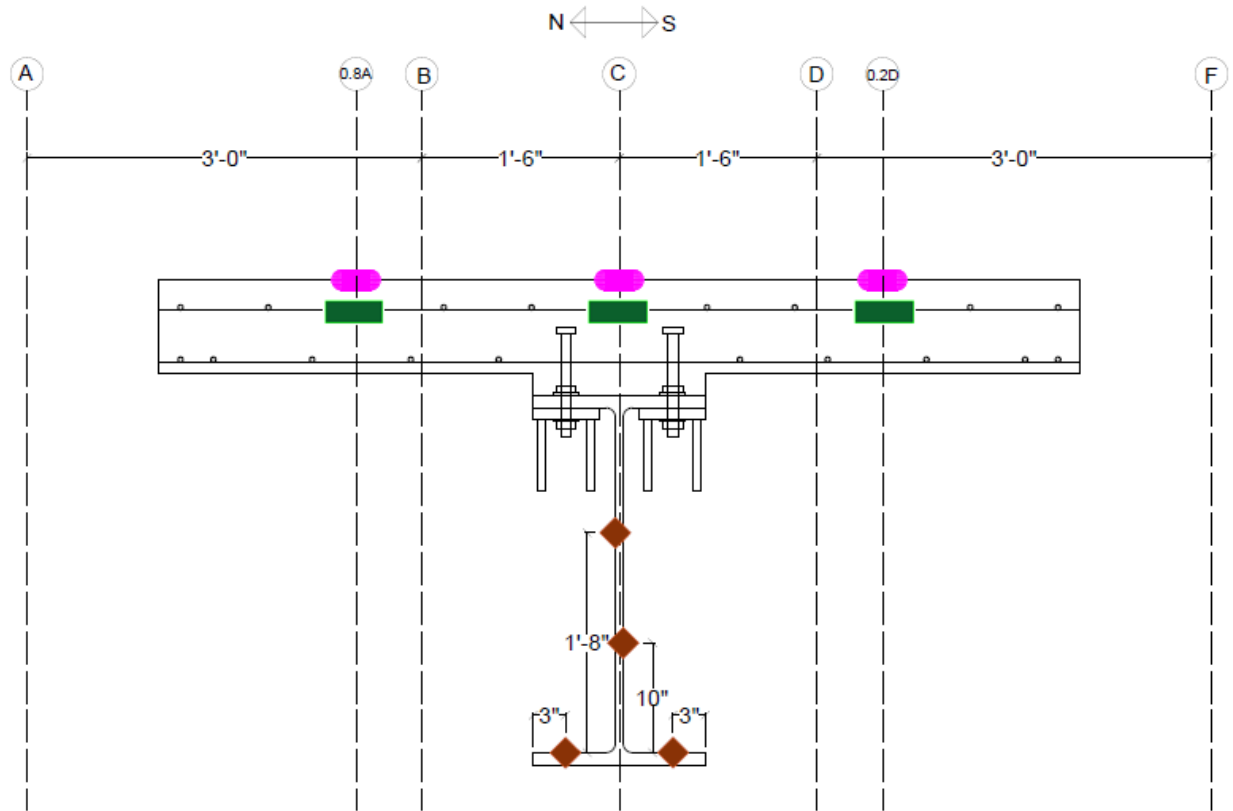


Figure 5.156. Concept C Instrumentation Plan (Section View at E1).

Symbol	Item	Concept C Count
	Actuator and Load Cell	2
	Embedded Rebar Strain Gauge	24
	Concrete Surface Strain Gauge	18
	Structural Steel Surface Strain Gauge	26
	String Potentiometer	11
	LVDT	7
	Wire Exits	2

Figure 5.157. Instrumentation Plan Legend.

Most strain gauges were located on major gridlines (E1, E2, etc.) so that, after testing, they could easily be turned into strain profiles to see how the strain differs relative to the closure pour. Strain gauges were also located on the 1.375-inch Ø Williams bars so that the proper amount of post-tension could be put into the bars. String pots were located every 3 ft so that a displacement curve could be seen during and after testing. For areas with higher precision displacements, LVDTs were used. LVDTs were located near the supports of the beams (to measure deflection near the supports), on the web of the steel beams (to measure the relative rotation of the beams), and above the slab on the closure pour (to measure the elongation of the closure pour).

The rebar strain gauges used were FLAB-5-350-11 from Texas Measurements. The first rebar strain gauges were located starting 1 ft 6.5 inches from the end of the longitudinal bars, with the second strain gauges 1 ft 11 inches after that, and the third 3 ft beyond that. Rebar strain gauges were located within 7 ft 6 inches of the centerline of the closure pour since that was the primary focus area for the testing.

The concrete surface strain gauges used were PL-60-11 from Texas Measurements. Concrete strain gauges were located directly on the major gridlines (E1, E2, etc.) so that the change in strain could be seen in regular increments farther away from the centerline of the closure pour.

The structural steel strain gauges used were also FLAB-5-350-11 from Texas Measurements. Structural steel strain gauges were located starting 1 ft 6 inches from the center of the closure pour, with another line 3 ft away from that. Structural steel strain gauges were also applied on the 1.375-inch Ø Williams bars directly at the centerline. Structural steel strain gauges were located within 4 ft 6 inches of the closure pour.

5.9.1.3. Specimen Preparation

The general formwork construction was previously discussed in Section 5.5 The following subsections are unique to Concept C.

Prior to the formwork being connected, the brackets were lifted into place under the flange and were attached using six 1-inch Ø A490 bolts. The bolts were tightened to the required pretension using a combination of the turn-of-the-nut method and DTIs. The bolts were tightened by starting at the innermost bolt in the pattern and working outward. The bolts were also fitted with

couplers and additional bolts to the ends to act as headed studs for a more efficient transfer of load to the slab. These couplers and bolts can be seen in Figure 5.158.

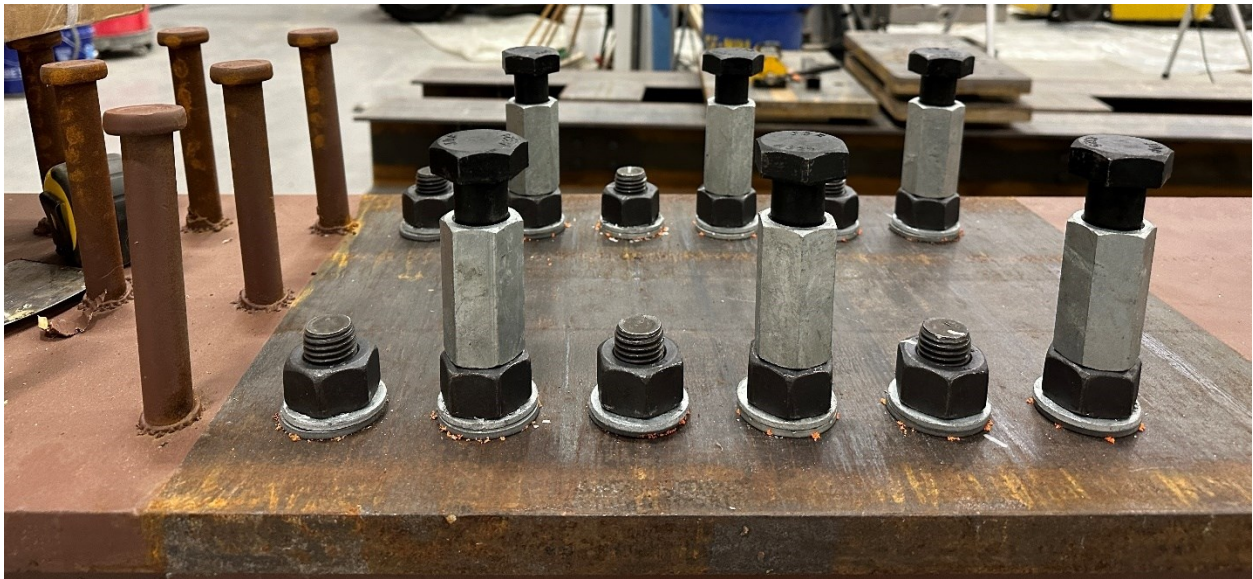


Figure 5.158. Couplers and Additional Bolts Acting as Headed Studs for Brackets.

Like in Concept A, holes were cut into the side forms at the connection end of the beams to install the extended U-bars. These holes were slightly offset from the spacing of the longitudinal bars in the slab so that the extended U-bars lined up directly next to them. The same formwork that was used for the Concept A extended U-bars was used for Concept C. See Figure 5.159 for a view of the extended U-bars protruding through the formwork.



Figure 5.159. Concept C Extended U-Bars.

See Figure 5.160 for the finished specimens for Concept C and Figure 5.161 for the finished U-bars protruding from the end of the slab.



Figure 5.160. Finished Specimens for Concept C.



Figure 5.161. Finished U-Bars for Concept C.

5.9.2. System Experiment Testing Program, Experiment Results, and Observations

5.9.2.1. Concept C Test Setup

Section 5.4 provides the general steps taken during the experimental testing. The test setup for Concept C included several unique steps. See Figure 5.162 for an elevation view of the overall test setup.

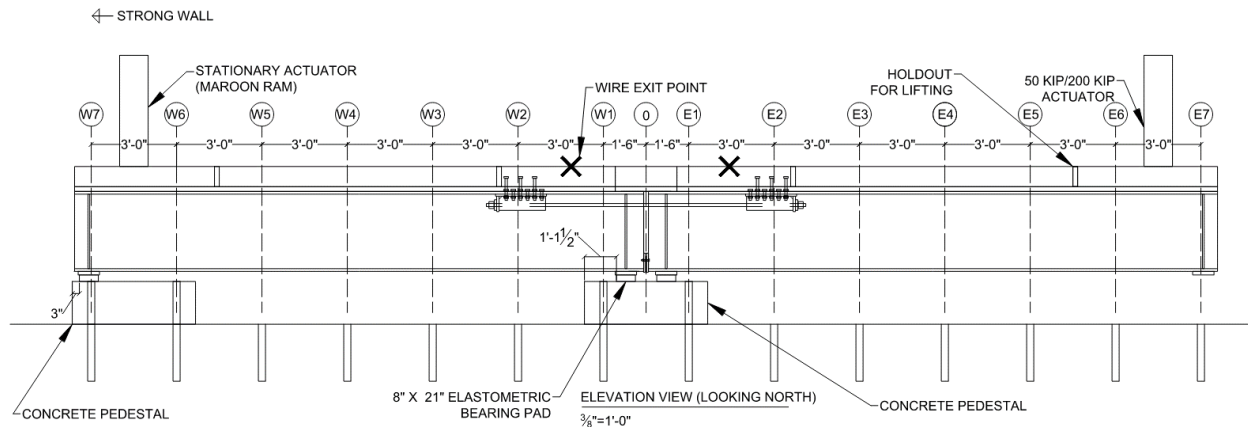


Figure 5.162. Concept C Test Setup Elevation.

A 1.5-inch thick adapter plate was fabricated with a hole pattern that fit the actuator and the holdouts that were placed in the precast concrete deck. This adapter plate is similar to the one that can be seen in Figure 5.104. This plate was fastened to the specimen the same way it was for Concept A and Concept B. See Figure 5.105 and Figure 5.106 for photos of how the adapter plate was attached to the deck.

On the hold-down side of the test setup (the left side shown in Figure 5.162), a stationary actuator was used to hold down the specimen during testing. This actuator used a variable load to keep the hold-down side in place. A load cell was placed under the end of the actuator so that it would be known how much load was being put into it. Several plates were also used to distribute the load across a greater area of the slab. See Figure 5.163 for a view of this actuator.

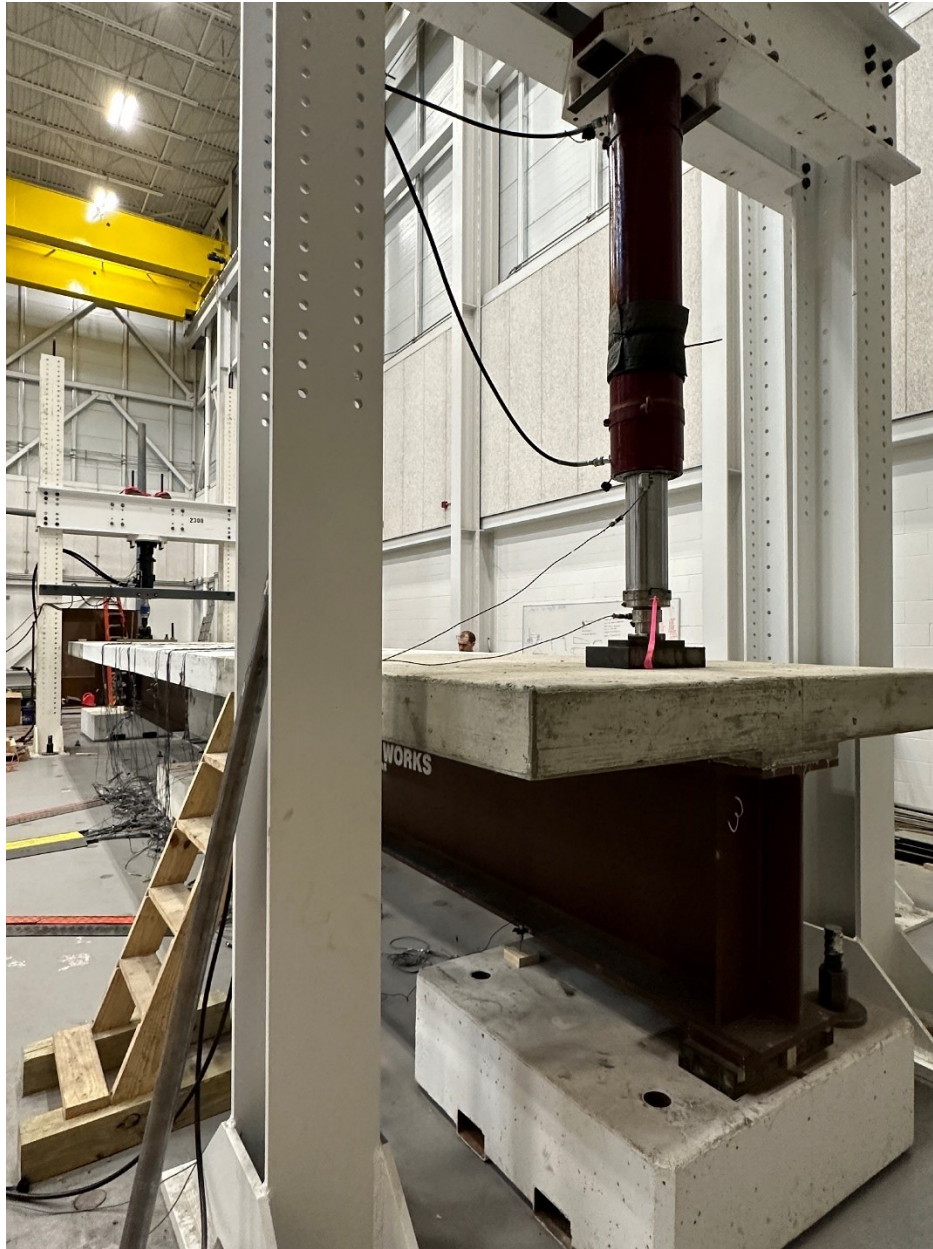


Figure 5.163. Concept C Hold-Down Actuator.

Similar to Concept B, the brackets had to be welded to the bottom of the top flange to eliminate the possibility of slippage occurring during testing. A 0.375-inch full-width fillet weld was used in the transverse direction on the ends of the brackets to the flange. In addition, a full-length longitudinal weld was used on the outside of the bracket to the flange. Since the bracket and the flange tip were flush, a channel had to be arc-gouged between the bracket and the flange tip. This channel allowed the gap to be filled with a 0.375-inch minimum partial penetration groove weld. The side of the bracket nearest to the web could not be welded because the welder did not have

access. The welds were designed so that they had enough strength to reach the ultimate strength of the Williams bar, which is at least 237 kips. See Figure 5.120 and Figure 5.121 for a similar view of the bracket welding.

The following images show the actual test setup of the entire concept in the lab. The overall test setup, a view from the hold-down end, and a view from the active loading end can be seen in Figure 5.164, Figure 5.165, and Figure 5.166, respectively.



Figure 5.164. Overall Elevation View of Concept C Test Setup.



Figure 5.165. View of Concept C Test Setup from Hold-Down End.



Figure 5.166. View of Concept C Test Setup from Active Loading End.

5.9.2.2. Concept C Static Testing

The static testing for Concept C began similarly to Concept B. First, the Williams bars had to be post-tensioned. This process was done just like it was done in the second static testing for Concept B—by using a through-hole jack. The same stand to support the through-hole jack was used during the PT. See Figure 5.122 for a view of this stand being used.

The through-hole jack was used to post-tension the Williams bars to at least 166 kips, which is 70 percent of the theoretical ultimate strength of the bars. This load level corresponds to 3600 microstrain in the Williams bars. The Williams bars were post-tensioned, alternating on each side of the specimen in approximately 900–1000 microstrain lifts. This step was done to eliminate uneven stresses/strains from developing in the specimen before testing began. See Figure 5.167 for a plot of this process. SG47 was on the north Williams bar, and SG48 was on

the south Williams bar. The bars had to be post-tensioned slightly higher than the target value because of losses that would occur when the through-hole jack was released.

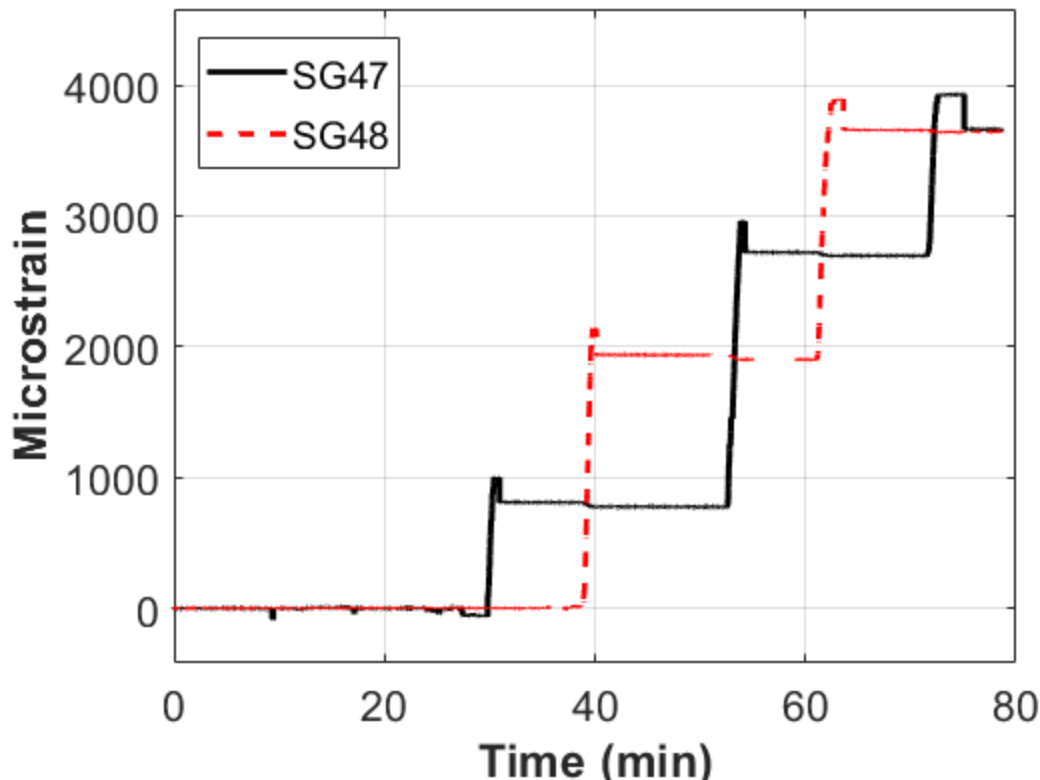


Figure 5.167. Concept C Static Testing Strain on Williams Bars during PT.

Once the PT was completed, the static portion of the testing commenced. The specimen was pulled up with approximately 24 kips on the active loading end so that the support pedestal could be removed. The specimen was lowered until the active loading end actuator read 0 kips, which was considered the zero point for the static testing. Note that even though the actuator read 0 kips, there was negative bending due to the connection being made because of the cantilever setup. The specimen was then pushed down on the active loading end in 5-kip increments. After each 5-kip increment, the specimen was inspected for signs of damage. The first signs of damage on the specimen occurred at the 10-kip load level. At this load level, cracks began forming in the construction joint between the deck and the closure pour. It was not unexpected to see cracks start to form at this location. The load on the specimen was increased in 5-kip increments up to 35 kips. Although the equivalent HL-93 loading was only approximately 28 kips, the specimen was performing very well, so it was decided to push it a little further—up to the 35-kip load level. At the 20-kip load level, it was observed that the specimen had cracks running through the

lifting holes on both sides, approximately 4 ft away from the transverse centerline. These cracks were the only ones observed during the first set of static tests. These cracks can be seen in Figure 5.168 and Figure 5.169.



Figure 5.168. Concept C Static Testing Crack through Lifting Hole on Hold-Down End.

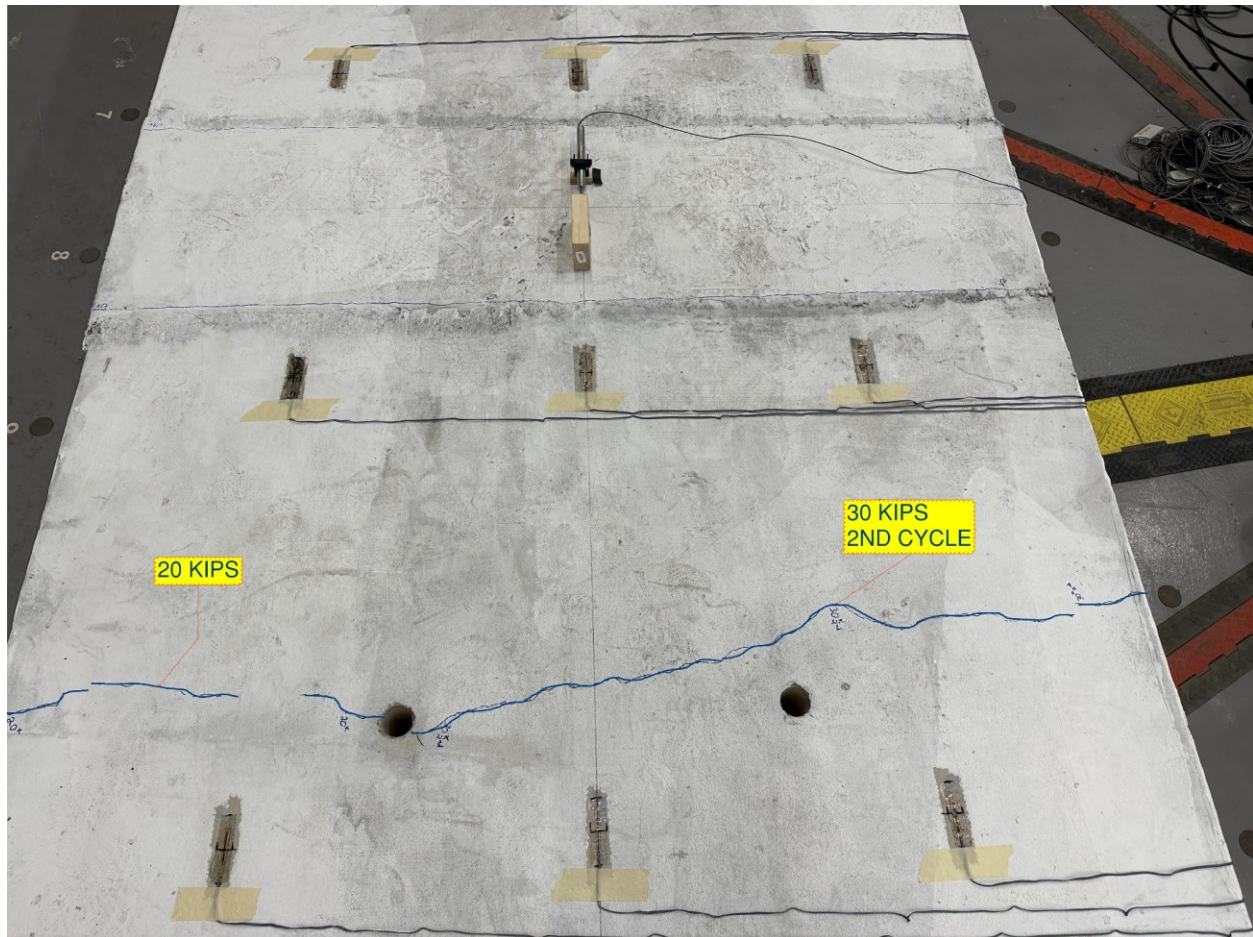


Figure 5.169. Concept C Static Testing Crack through Lifting Hole on Active Loading End.

The load was taken off the specimen, and then up to 30 kips was placed on the specimen two more times to check for repeatability. During the second set of static testing, it was observed that, at approximately 30 kips of load, the cracks running through the lifting holes on the active loading end of the specimen had expanded to run across the entire width of the specimen. See Figure 5.170 for the vertical displacement time history plot. This plot shows the displacement of the end of the specimen at different times of testing. The stroke data are from the active loading end actuator, and the SP average is the average of the two string pots located on gridline E7.

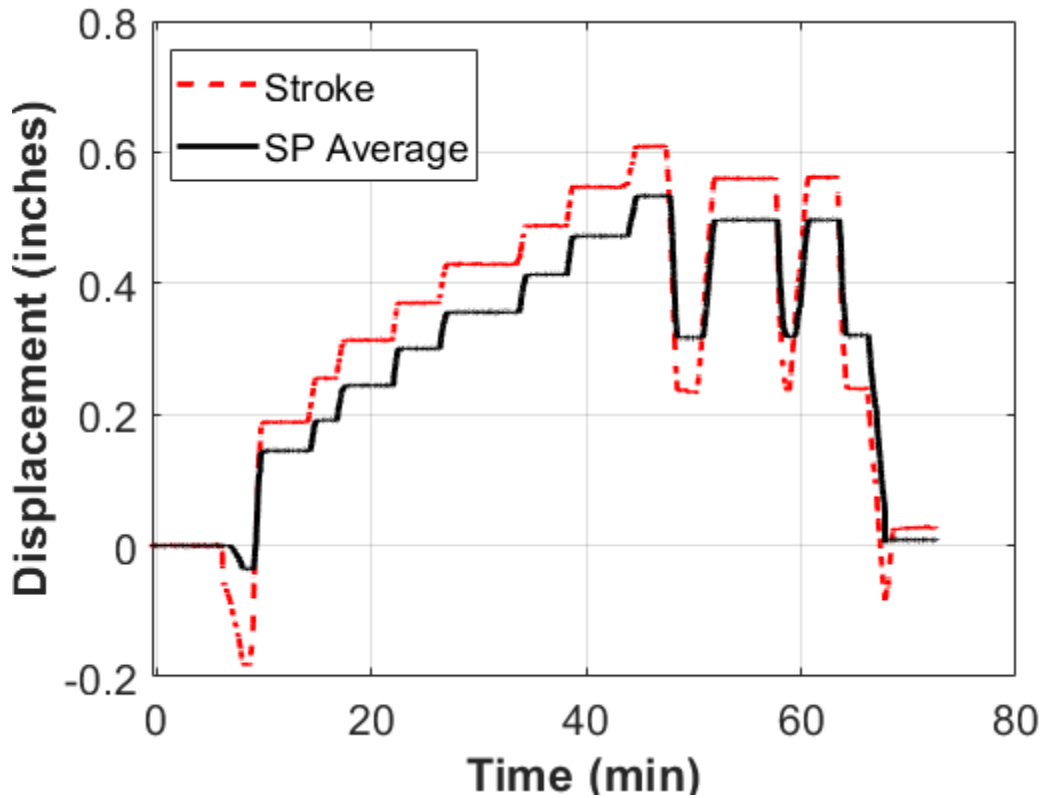


Figure 5.170. Concept C Static Testing Vertical Displacement Time History.

The load time history plot can be seen in Figure 5.171. The negative load at the beginning is from picking up on the specimen so that the support pedestal on the active loading end could be removed. Each load increment of 5 kips can be seen on the plot. Next, the load was brought back down to zero and then back to 30 kips again two more times.

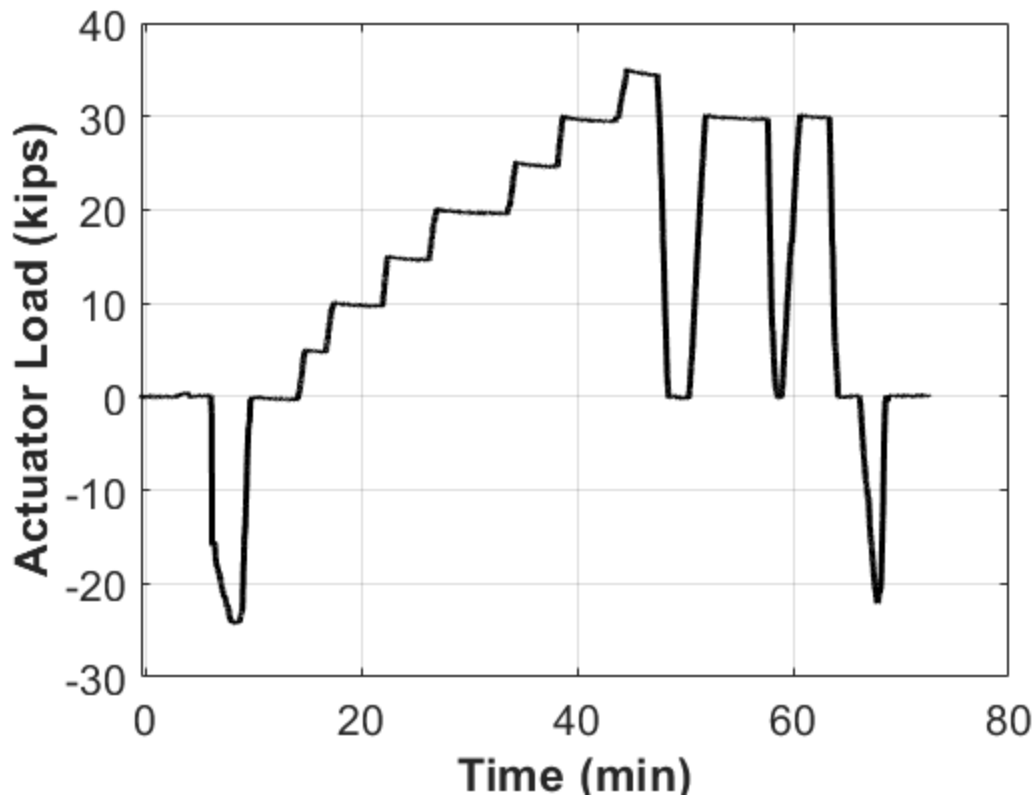


Figure 5.171. Concept C Static Testing Load Time History.

Figure 5.172 shows the actuator load versus displacement plot. At the zero-load level, it shows that the displacement of the specimen was approximately 0.14 inches (cantilever deflection). The maximum displacement of the specimen at the 35-kip load level was approximately 0.53 inches. It can be seen that the data from the second and third load applications were repeatable. The reason that the data from the first load application are shifted is because as the specimen was sitting there and being observed between each 5-kip load application, it was starting to creep. Therefore, once it was returned to the zero-load level, the displacement was at approximately 0.31 inches and no longer at 0.14 inches.

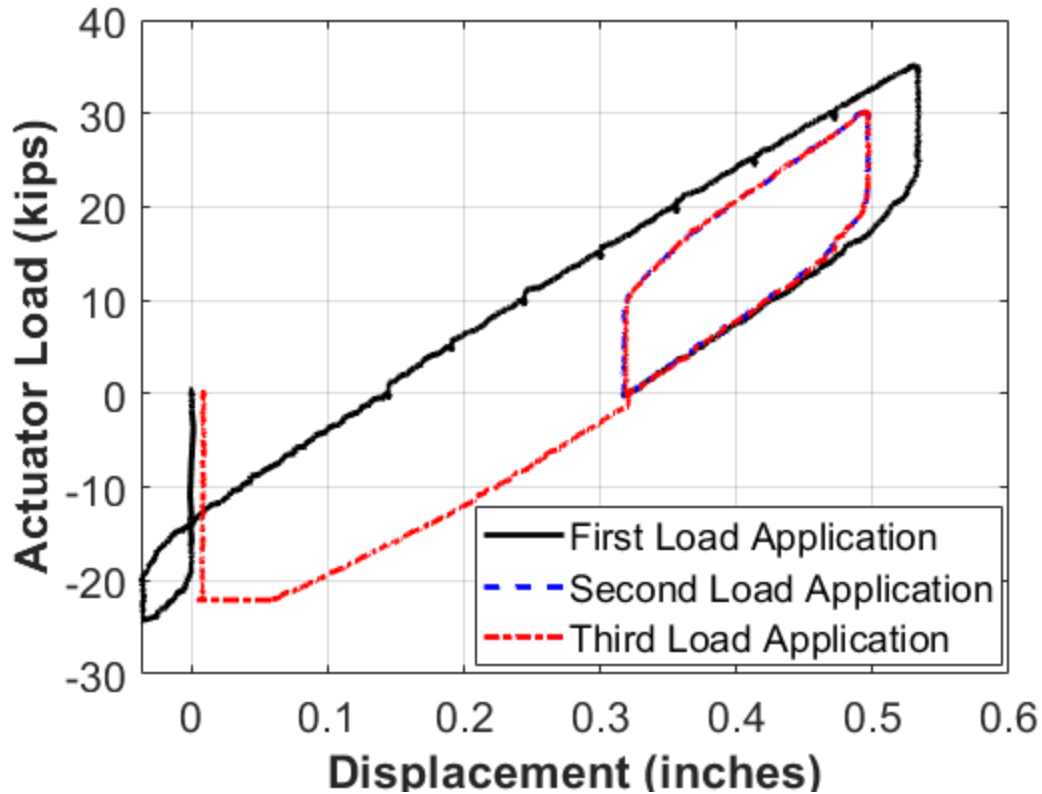


Figure 5.172. Concept C Static Testing Load-Displacement Plot.

The strain on the Williams bars can be seen in Figure 5.173. SG47 was located on the north Williams bar, and SG48 was located on the south Williams bar. The strains on the bars started between 3620 and 3660 microstrain at the beginning of the test. The initial increase in strain is due to the lifting of the specimen so that the support pedestal could be removed. The increase in strain at this time indicates that the NA of the specimen was still above the Williams bars, thus putting more tension on them. This finding is further confirmed by the fact that as the specimen was being pushed down, the strain in the Williams bars was decreasing because they were having some of the tension in them released. At the end of the static testing, the strains had been reduced to between 3600 and 3620 microstrain, indicating some losses due to the loading applications.

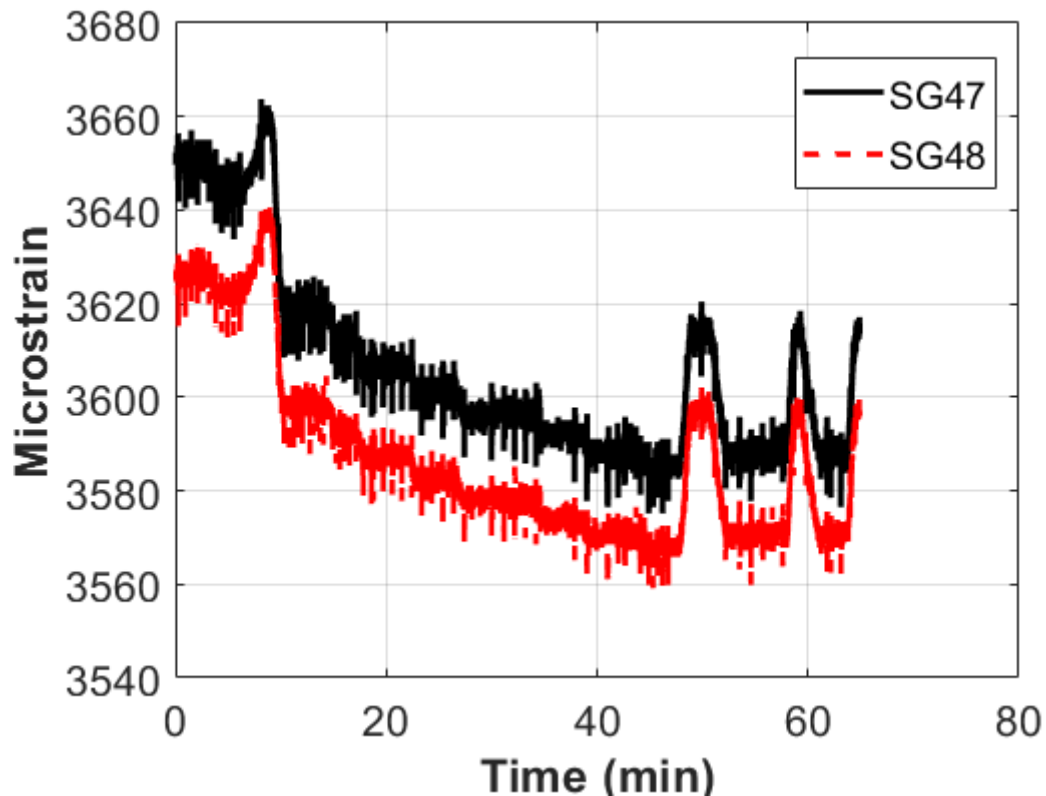


Figure 5.173. Concept C Static Testing Strain on Williams Bars.

The stresses in the precast concrete deck at gridline E1 can be seen in Figure 5.174. SG59 was located on the longitudinal centerline, while SG58 and SG60 were located 2 ft on either side of the centerline. At the zero-load level, the stresses in SG59 and SG60 were approximately -0.15 ksi, while SG58 was approximately -0.40 ksi. The stresses in SG59 and SG60 remained in net compression during the entirety of the static testing, while SG58 went into slight tension and leveled off around 0.10 ksi. The data show that the stresses stopped increasing between 10 and 20 kips, most likely due to stresses being relieved because the cracks in the nearby interface of the closure pour region opened up.

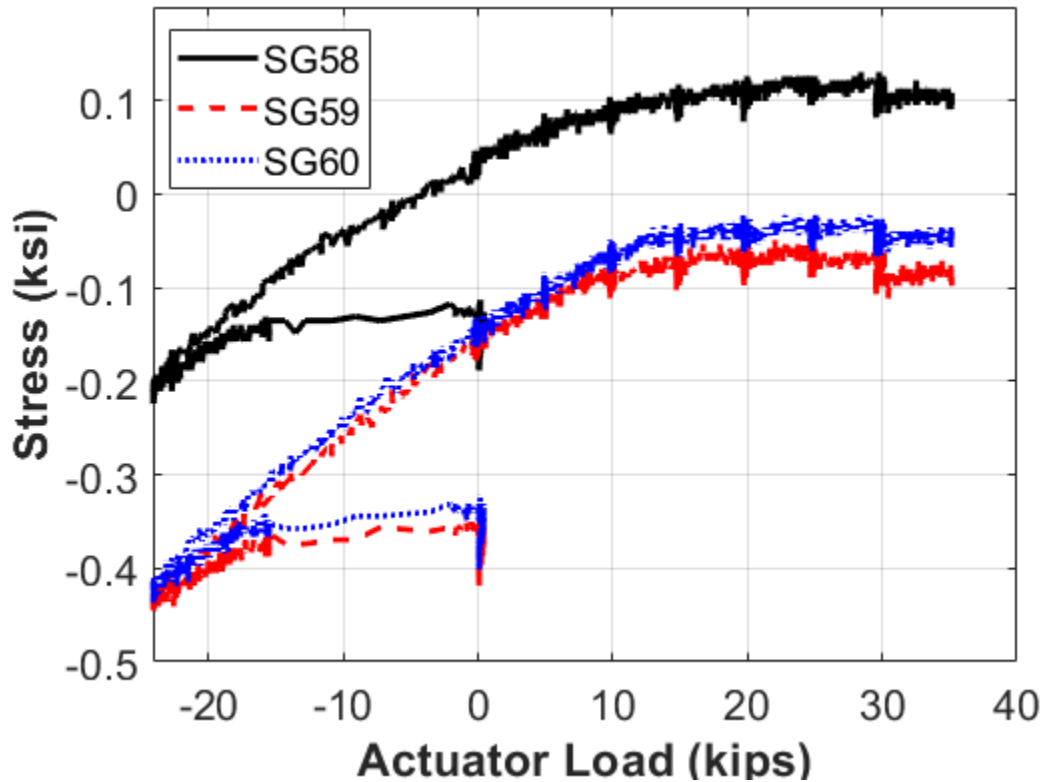


Figure 5.174. Concept C Precast Concrete Deck Stresses at E1.

The stresses in the precast concrete deck at gridline E2 can be seen in Figure 5.175. SG62 was located on the longitudinal centerline, while SG61 and SG63 were located 2 ft on either side of the centerline. All the stresses remained in net compression until 15 to 20 kips, at which point both of the outside strain gauges showed that the slab was going into tension. However, the center strain gauge shows compression during the entirety of the static testing. Since these strain gauges were located almost directly above the Williams bar brackets, the shear-lag effect is likely what caused the center strain gauge to remain in compression while the outside strain gauges went into tension.

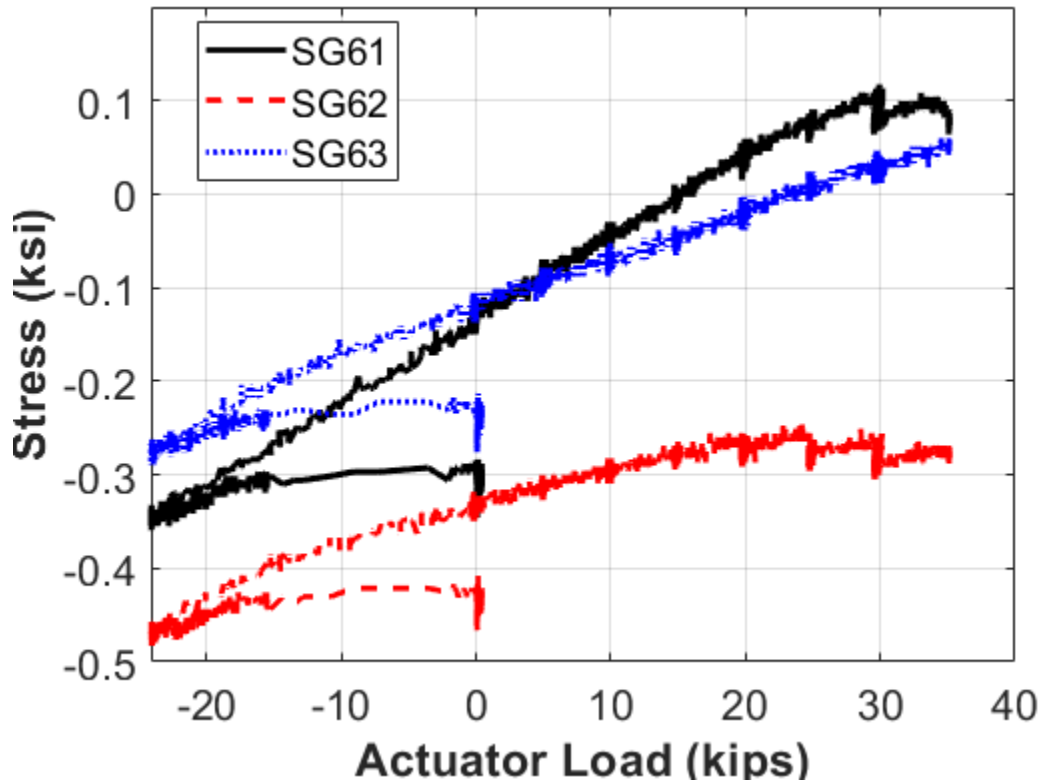


Figure 5.175. Concept C Precast Concrete Deck Stresses at E2.

The stresses in the precast concrete deck at gridline E3 can be seen in Figure 5.176. SG65 was located on the longitudinal centerline, while SG66 was located 2 ft on the side of the centerline. The stresses are shown in net compression until approximately 10 kips have been reached, at which point the strain gauge on the centerline goes into net tension. Since these strain gauges are located past the Williams bar brackets, they are not subject to the same shear-lag effect as the strain gauges between the brackets, which is why these strain gauges show an almost identical change in stress throughout the static testing.

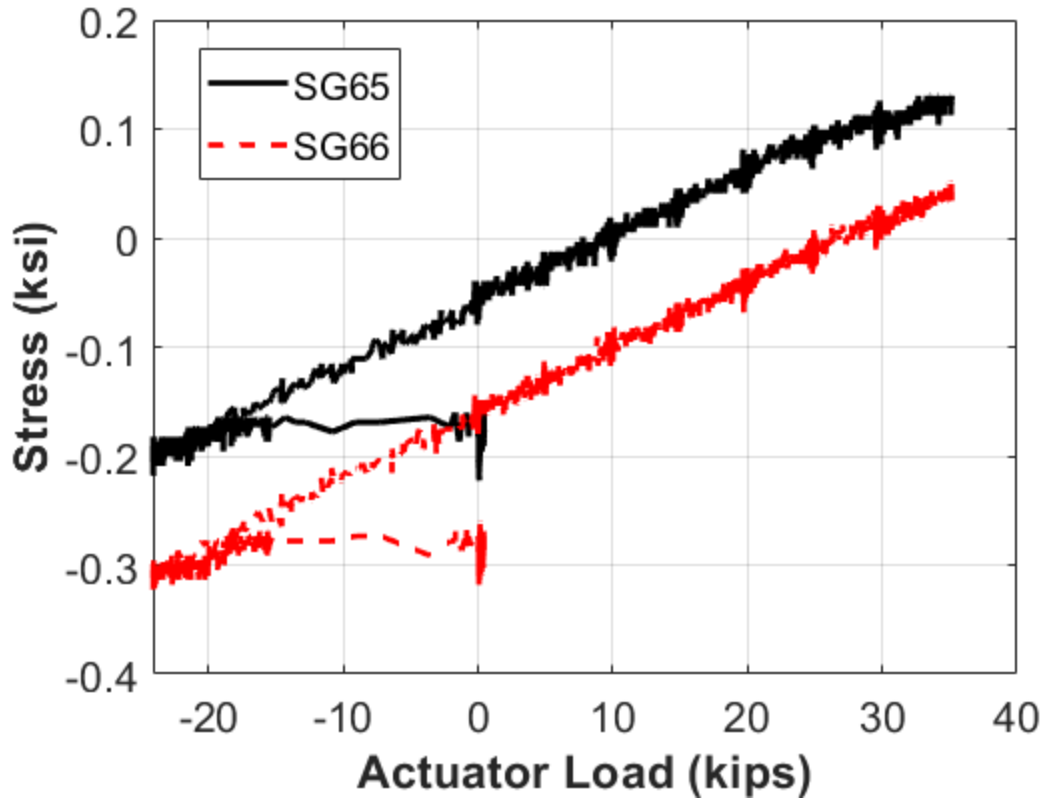


Figure 5.176. Concept C Precast Concrete Deck Stresses at E3.

The stresses in the rebar at gridline E2 can be seen in Figure 5.177. SG14 was located on the longitudinal centerline of the specimen, while SG13 and SG15 were located 2 ft on either side of the centerline. The strain gauges show that the rebar only remained in net compression up to a maximum of approximately 5 kips. However, the overall stresses of the rebar were not high. The stresses at gridline E1 were low because the longitudinal rebar had not yet been developed at the location of the strain gauge. However, the gauge locations at E2 should have been developed, leading to larger strains. The results at gridline E3 show a similar result. The reason that the strain gauges at E2 and E3 show relatively small stresses is possibly because of an excess amount of cracking.

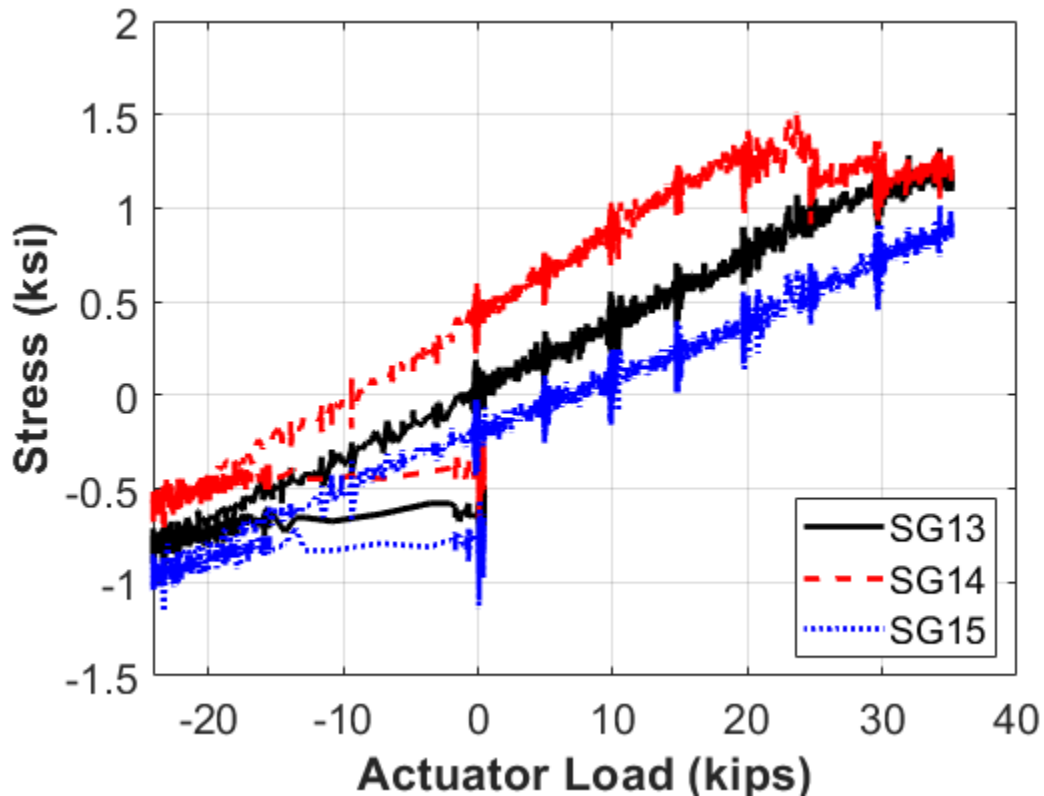


Figure 5.177. Concept C Static Testing Rebar Stresses at E2.

Unlike the results shown at gridline E2, the results from the U-loop bars at gridline E0.3 in Figure 5.178 show a larger increase in stress during testing. SG23 was located on the longitudinal centerline of the specimen, while SG22 was located 2 ft on the side of the specimen. At the zero-load level, the rebar in the closure pour experienced near-zero net stress. As the static testing proceeded, the stresses in the rebar experienced an almost exponential increase in stress, with the maximum reaching almost 8 ksi (which is still relatively low).

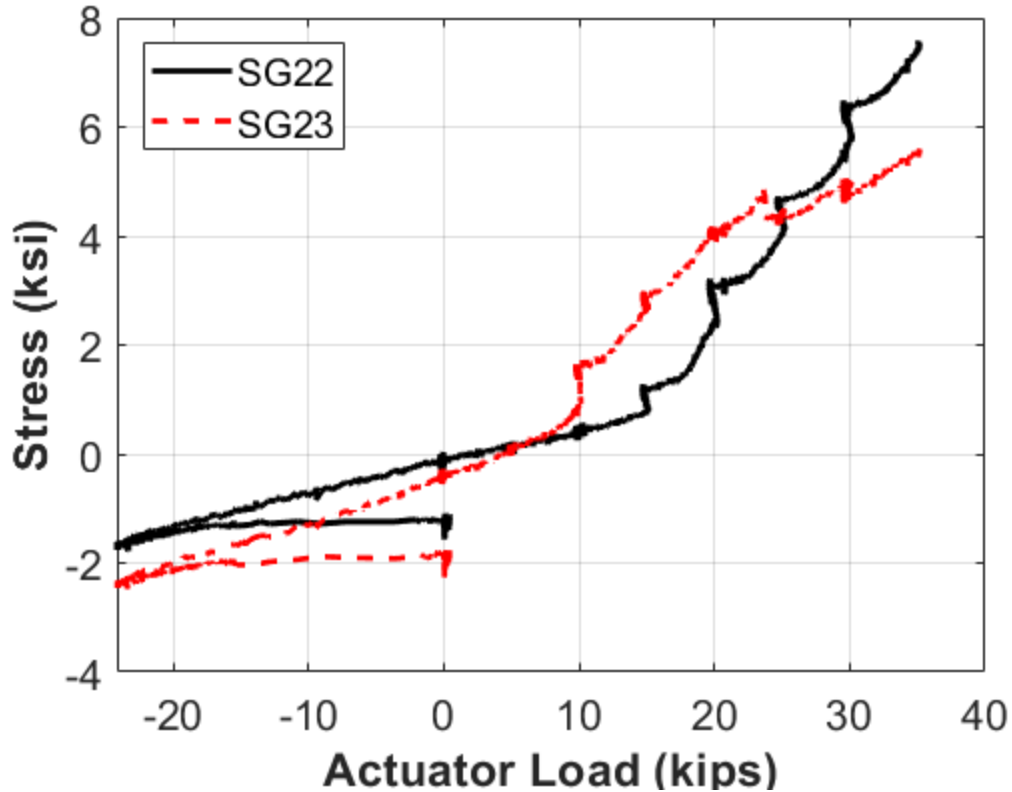


Figure 5.178. Concept C Static Testing U-Loop Rebar Stresses at E0.3.

The results at gridline W0.3 in Figure 5.179 show a similar trend to the results at gridline E0.3. SG20 was located on the longitudinal centerline of the specimen, while SG19 and SG21 were located 2 ft on either side of the centerline. The rebar remained in net compression until between 5 to 15 kips, which is a slightly higher load level than what the rebar at gridline E0.3 was showing. The overall maximum magnitude of the stresses at this gridline approached 6 ksi of tension, which is slightly lower than the magnitudes at gridline E0.3.

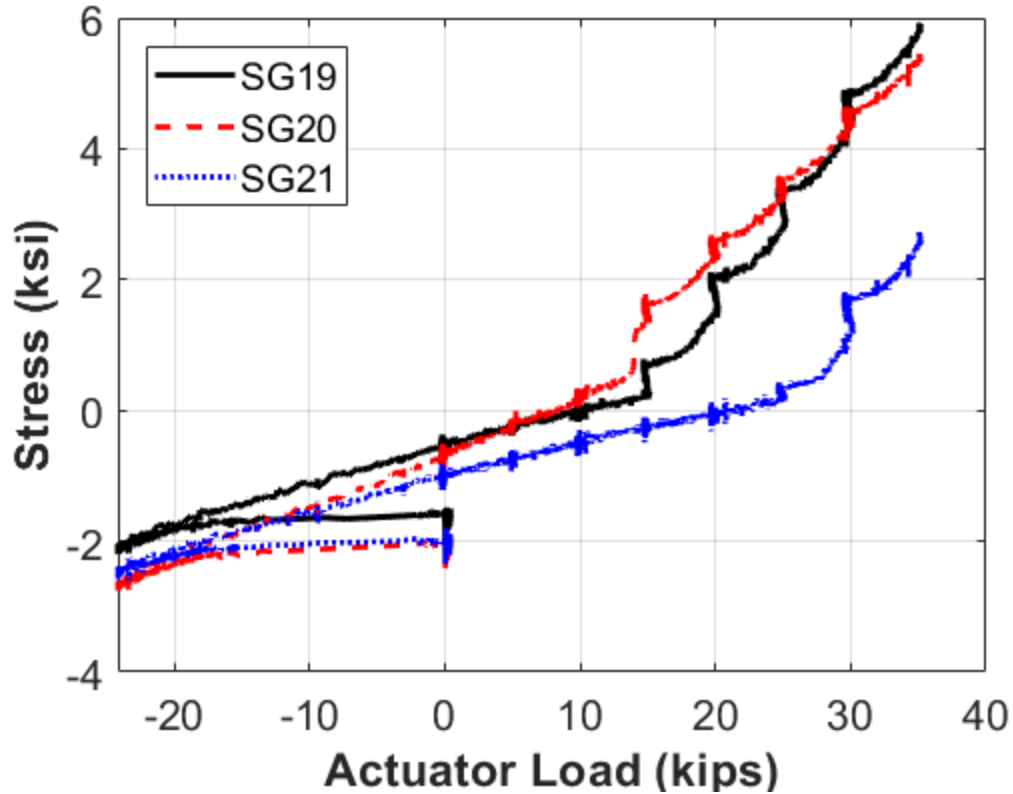


Figure 5.179. Concept C Static Testing U-Loop Rebar Stresses at W0.3.

The stresses in the steel beam at gridline E1 can be seen in Figure 5.180. SG35 and SG36 were located on the top flange, SG37 was located on the top portion of the web, SG38 was located on the bottom portion of the web, and SG40 was located on the bottom flange. All of the strain gauges show net compression during the entirety of static testing. SG35 through SG37 show very little change, while SG38 went into slightly more compression, and SG40 shows a more significant increase in compressive stresses. SG39 was removed from the plot because it was showing faulty data.

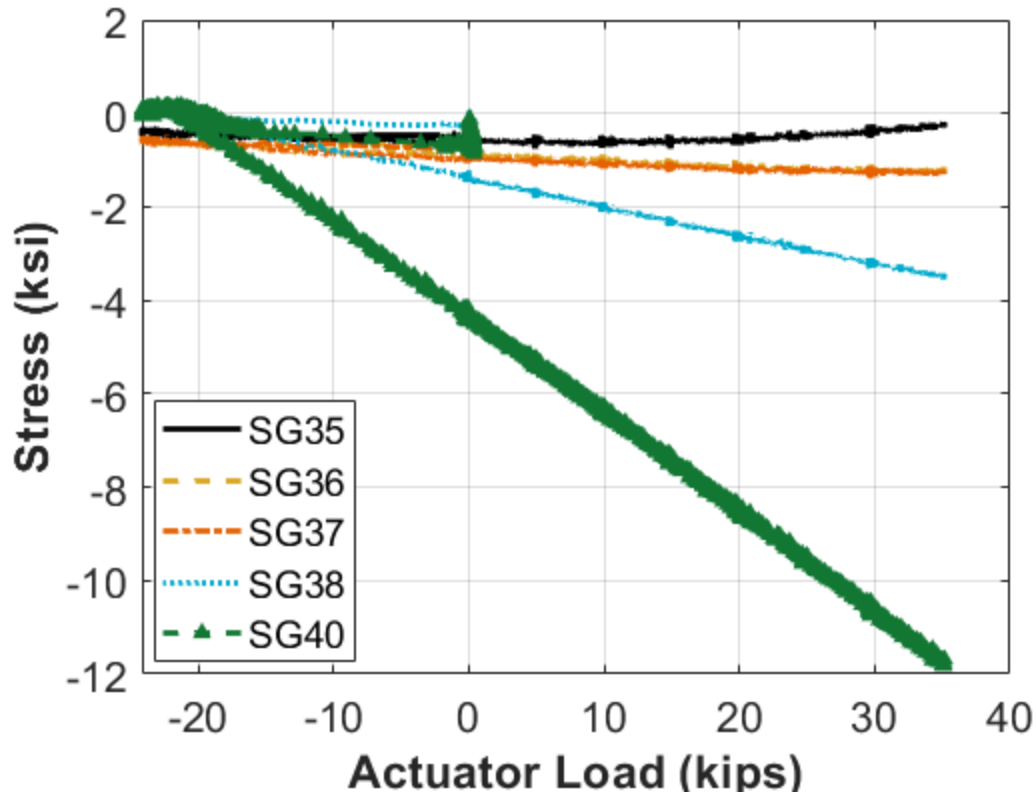


Figure 5.180. Concept C Static Testing Steel Beam Stresses at E1.

The stresses in the steel beam at gridline W1 can be seen in Figure 5.181. SG29 and SG30 were located on the top flange, SG31 was located on the top portion of the web, SG32 was located on the bottom portion of the web, and SG33 and SG34 were located on the bottom flange. All of the strain gauges showed net compression during the entirety of static testing. SG29 and SG30 showed little change, while SG31 and SG32 go into slightly more compression while SG33 and SG34 show a more significant increase in compressive stresses. Similar to the previous plot, all the strain gauges started at close to zero stress, while SG33 and SG34 started with a large offset of approximately 2–3 ksi, which is likely due to the same reasons cited with SG39.

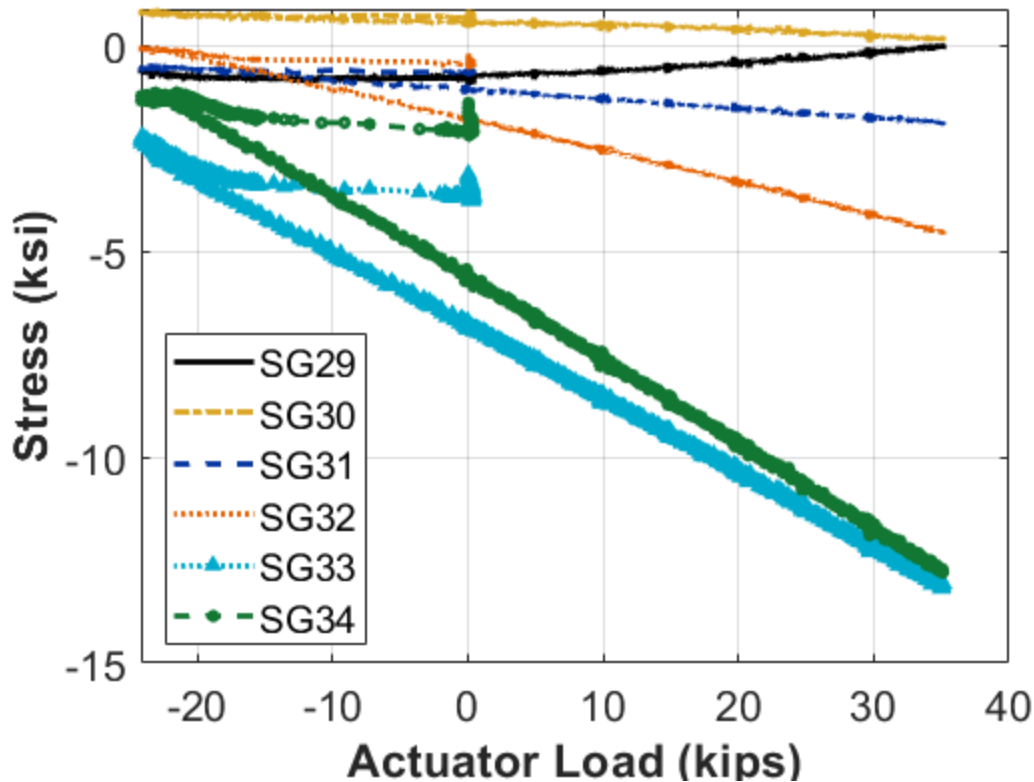


Figure 5.181. Concept C Static Testing Steel Beam Stresses at W1.

The static testing was considered complete at this point. The specimen was put back on the pedestal and was inspected for any new cracks that had formed. The data were analyzed, and based on the recorded displacements and forces, a testing regimen for the cyclic portion of testing was formulated.

5.9.2.3. Concept C Cyclic Testing

A total of 514,800 cycles were run during the cyclic testing, with 3,600 cycles run at a lower displacement level at the beginning of the cyclic testing to see how the specimen would react. After these cycles, the rest were run at the higher displacement level (equivalent to +28 kips to -10 kips). See Table 5.12 for an overview of the cyclic testing ranges.

Table 5.12. Concept C Cyclic Testing Ranges.

Day	Number of Cycles	Load Rate (Hz)	Displacement Control Range
1	3,600	1	(−0.20") to (+0.05")
2	86,400	1	(−0.30") to (+0.10")
3	86,400	1	(−0.30") to (+0.10")
4	252,000	1	(−0.30") to (+0.10")
5	86,400	1	(−0.30") to (+0.10")
Total	514,800		

The specimen was periodically inspected for signs of damage throughout the cyclic testing. No visible cracks were observed to have formed during the cyclic testing. In addition, no other forms of damage were recorded. The strain in the Williams bars remained steady between 3590 and 3610 microstrain, and none of the other gauges saw any massive changes during the cyclic testing.

5.9.2.4. Concept C Ultimate Testing

Similar to Concept A, the 55-kip actuator had to be replaced with a 100-ton ram because the 55-kip actuator did not provide enough force or displacement to adequately take the specimen to failure. The ram was placed on a different frame (with the header beam lowered) and was put into the same position on the beam that the 55-kip actuator was in. See Figure 5.182 for a view of the ram setup for this concept.

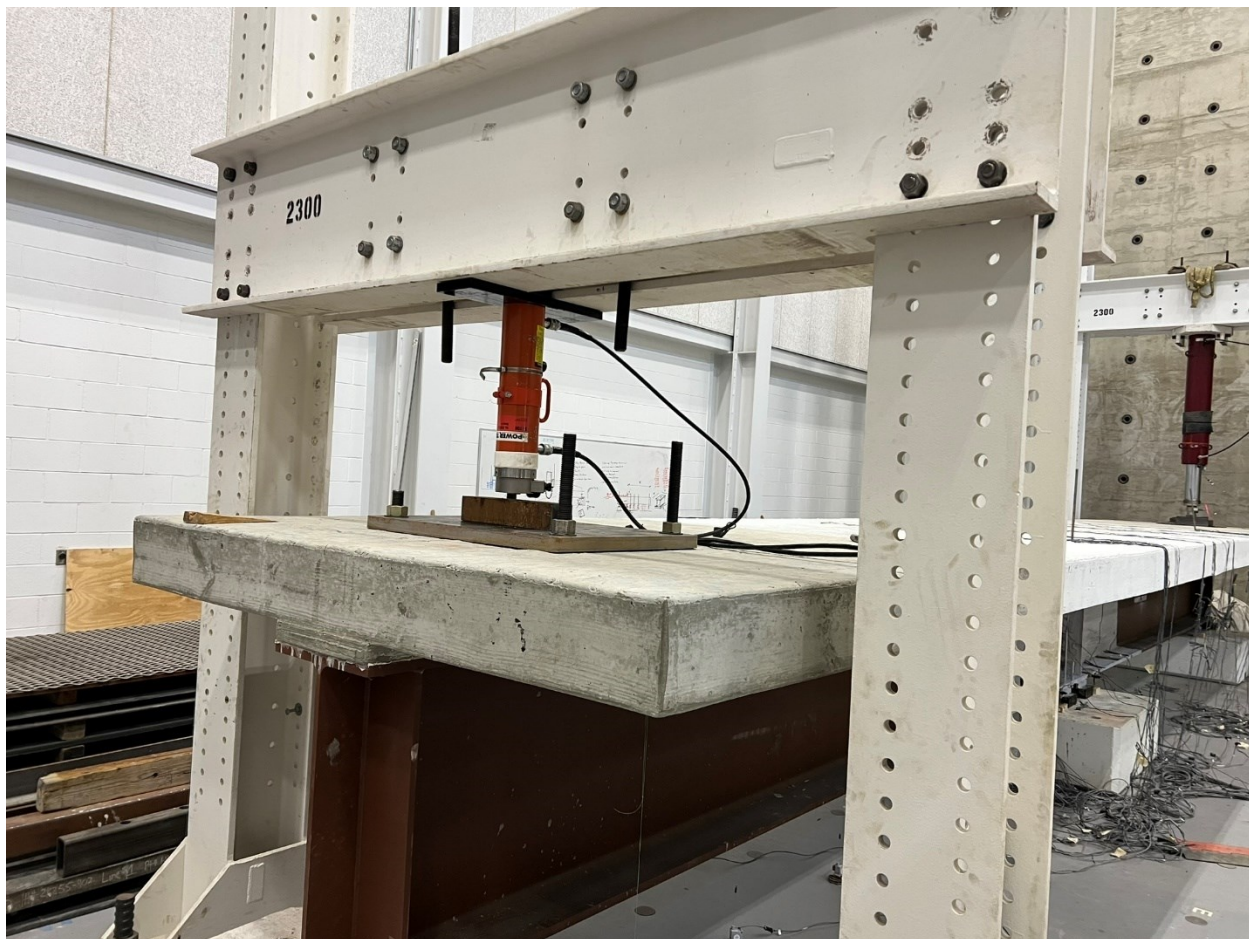


Figure 5.182. 100-kip Ram Setup for Concept C.

This ram was not connected to the specimen because it was only pushing down on the specimen and not pulling up. To lift the specimen and remove the support pedestal, a through-hole jack was placed under the bottom flange, and the specimen was jacked up. Because the 100-kip ram did not have a string pot attached to it, the displacement of the specimen was measured purely by the string pots on gridline E7.

The vertical displacement time history plot can be seen in Figure 5.183. The displacement data were taken as the average of the two string pots on gridline E7, which are SP9 and SP10. The specimen was pushed down in 0.125-inch increments through displacement control. The specimen was inspected after each increment to check for signs of damage. A maximum displacement of 2.5 inches was reached, after which point the specimen was brought back to the zero-displacement level.

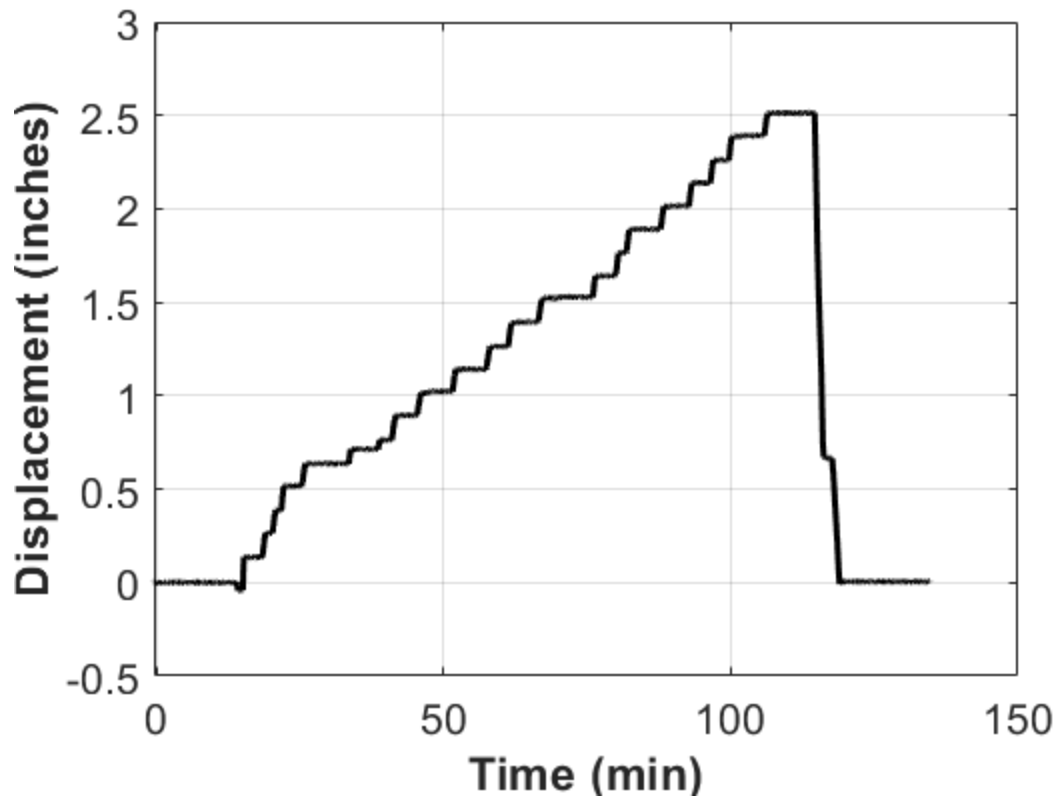


Figure 5.183. Concept C Ultimate Testing Displacement Time History.

The actuator load versus displacement plot can be seen in Figure 5.184. This plot starts with an initial displacement without an increase in force because since the specimen is self-supporting, an initial displacement due to its self-weight occurs. The plot shows that there is a linear relationship between the load and displacement up to approximately 50 kips, or approximately 0.7 inches of displacement. The specimen relaxes slightly after this point and then returns to a linear relationship until approximately 60 kips. After that point, the specimen starts to lose load after each displacement increment. The specimen's stiffness starts to lessen after this point, as indicated by the change in slope of the following plot. A maximum load of 94 kips was reached, which corresponded to 2.5 inches of total deflection. At that point, the specimen was inspected for signs of damage, which were numerous. Many cracks had formed on the surface of the precast concrete deck, and most of those cracks went through the slab. Several loud bangs were also heard during the ultimate testing. When the source of these bangs were investigated, new full-width cracks were found to have formed. After all the signs of damage had been recorded, the load was slowly taken off the specimen. Once the load reached zero, the overall displacement

of the specimen was approximately 0.7 inches, indicating that damage to the specimen had occurred (primarily in the slab).

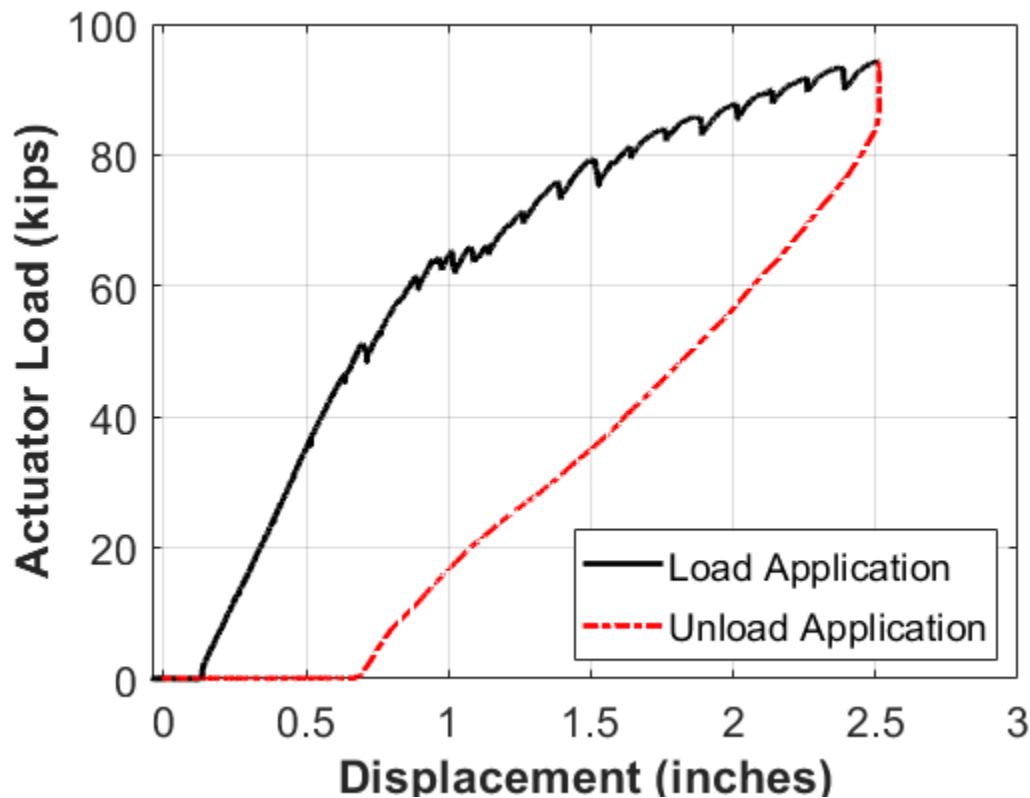


Figure 5.184. Concept C Ultimate Testing Force Displacement.

The strain time history on the Williams bars can be seen in Figure 5.185. SG47 was located on the north Williams bar and SG48 was located on the south Williams bar. The strain in both bars started at approximately 3600 microstrain, which equates to 70 percent of the theoretical ultimate strain of the bars. During the testing, the Williams bars showed a decrease in strain before a dramatic increase after about 50 min of testing. Once the strain in the Williams bars started increasing, the NA dipped below the level of the bars. The maximum strain that was reached was 4650 microstrain on the north one and 4570 microstrain on the south one (roughly 90 percent of the theoretical ultimate strain). When the load was taken off the specimen, the strain in the Williams bars dropped to between 3800 and 3900 microstrain, indicating that they were yielded.

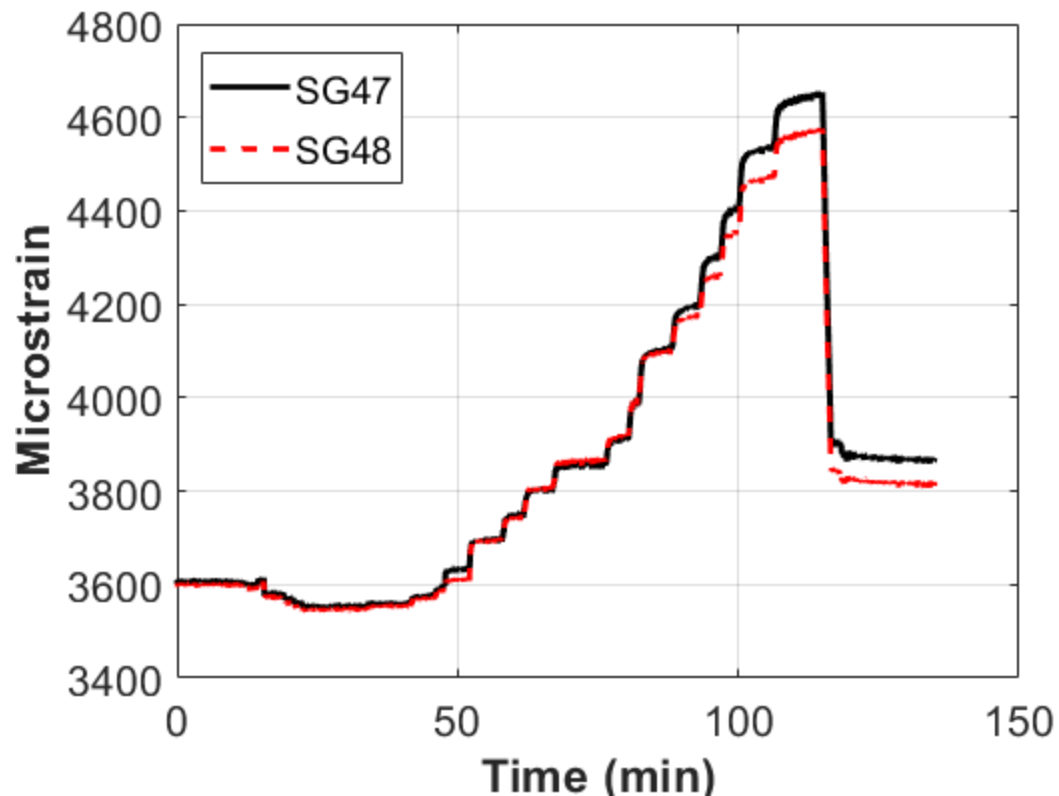


Figure 5.185. Concept C Ultimate Testing Strain on Williams Bars.

The actuator load versus strain in the Williams bars can be seen in Figure 5.186. The strain in the Williams bars is shown to decrease until an actuator load of approximately 60 kips. After this point, the strain in the Williams bars increases. After each displacement increment, the load slightly drops off, indicating a softening of the specimen. The strain in the north and south bars stays relatively the same until about 85 kips of load. At that point, the strain in the bars starts to diverge slightly, possibly due to a slight eccentricity in the loading of the specimen.

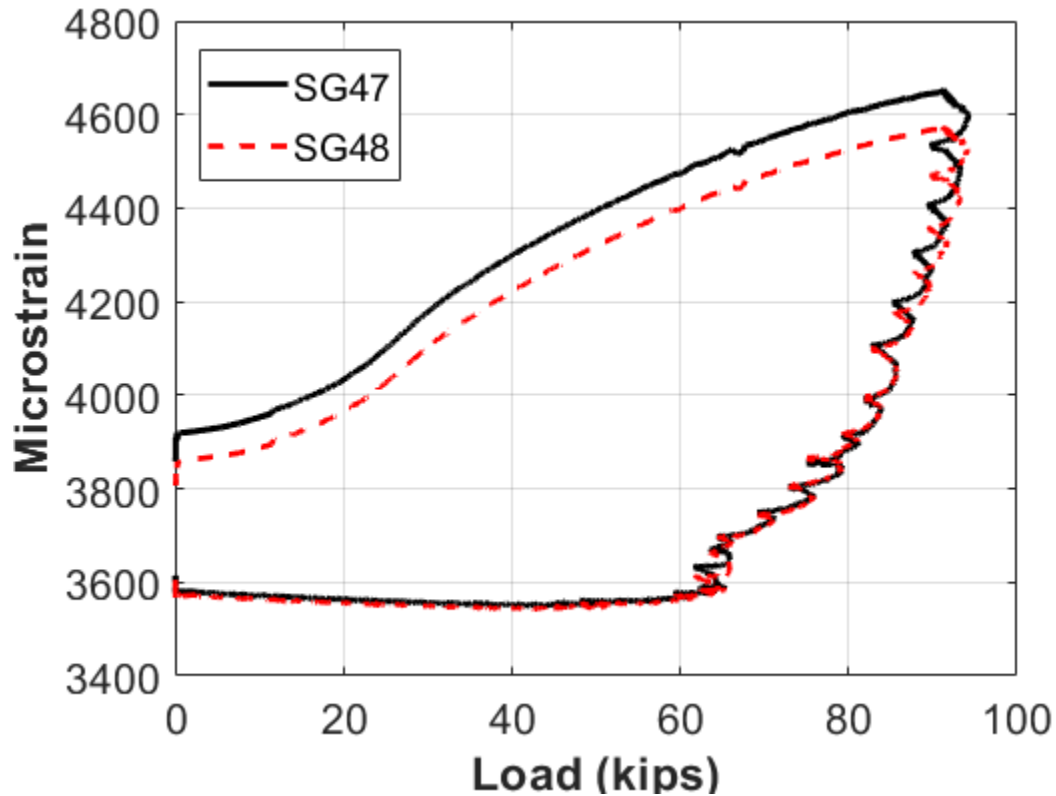


Figure 5.186. Concept C Ultimate Testing Williams Bar Strain versus Actuator Load.

The stresses on the surface of the precast concrete deck at gridline E1 can be seen in Figure 5.187. SG59 was located on the longitudinal centerline, while SG58 and SG60 were located 2 ft on either side of the centerline. All of the gauges started in net compression and saw a jump in stress at the zero-load level in the actuator because while the specimen was self-supporting, the top of the specimen was going into tension. The strain gauges all remained in net compression until approximately 30 kips, which is when one gauge went into tension. The other two gauges remained in compression during the entire test except for a jump around 65–70 kips. It was at this load level when two cracks formed near gridline E1, which might explain the sudden jump in stresses. The gauges all dropped back down in stress at approximately 75 kips, indicating that cracking around that area relieved most of the tensile stresses.

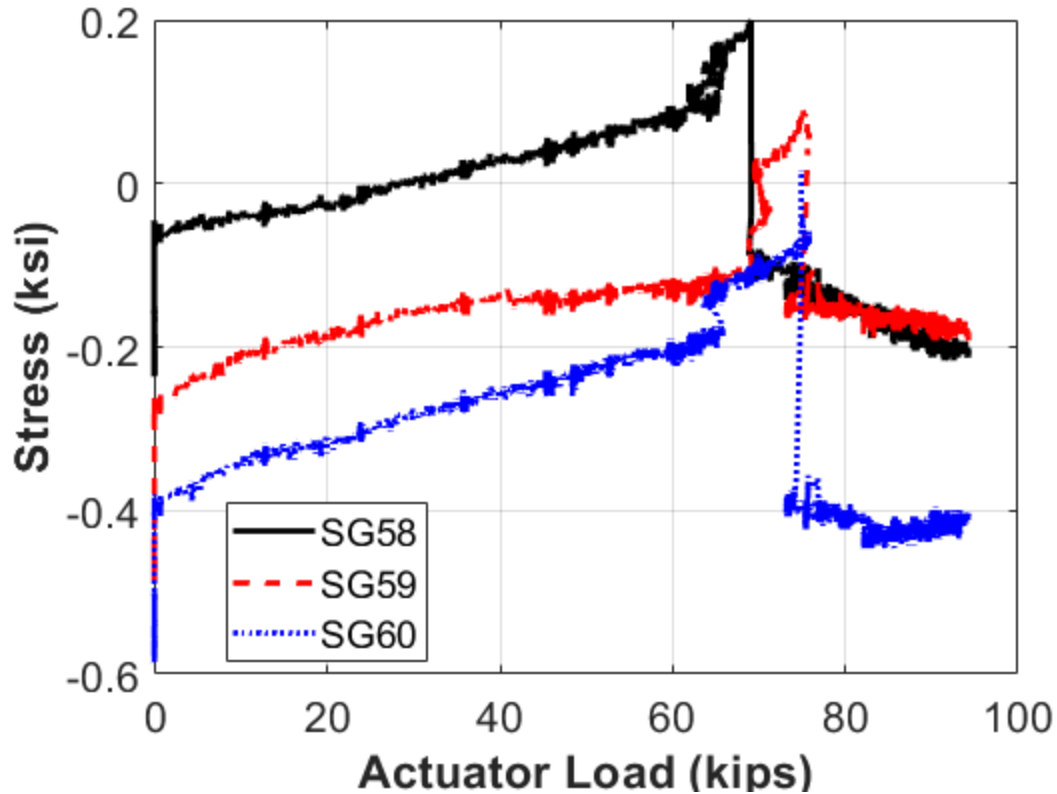


Figure 5.187. Concept C Precast Concrete Deck Stresses at E1.

The stresses on the surface of the precast concrete deck at gridline E2 can be seen in Figure 5.188. SG62 was located on the longitudinal centerline, while SG61 and SG63 were located 2 ft on either side of the centerline. Similar to gridline E1, the strain gauges all started in net compression. However, when the specimen was self-supporting, the stresses all increased into net tension. Since these gauges were almost directly over the PT brackets, they likely did not see as much precompression from the Williams bars as the gauges on E1. All the gauges showed an increase in tensile stress during the ultimate test. The jump in SG61 that formed at approximately 75 kips was due to a crack developing in that area at around that load level.

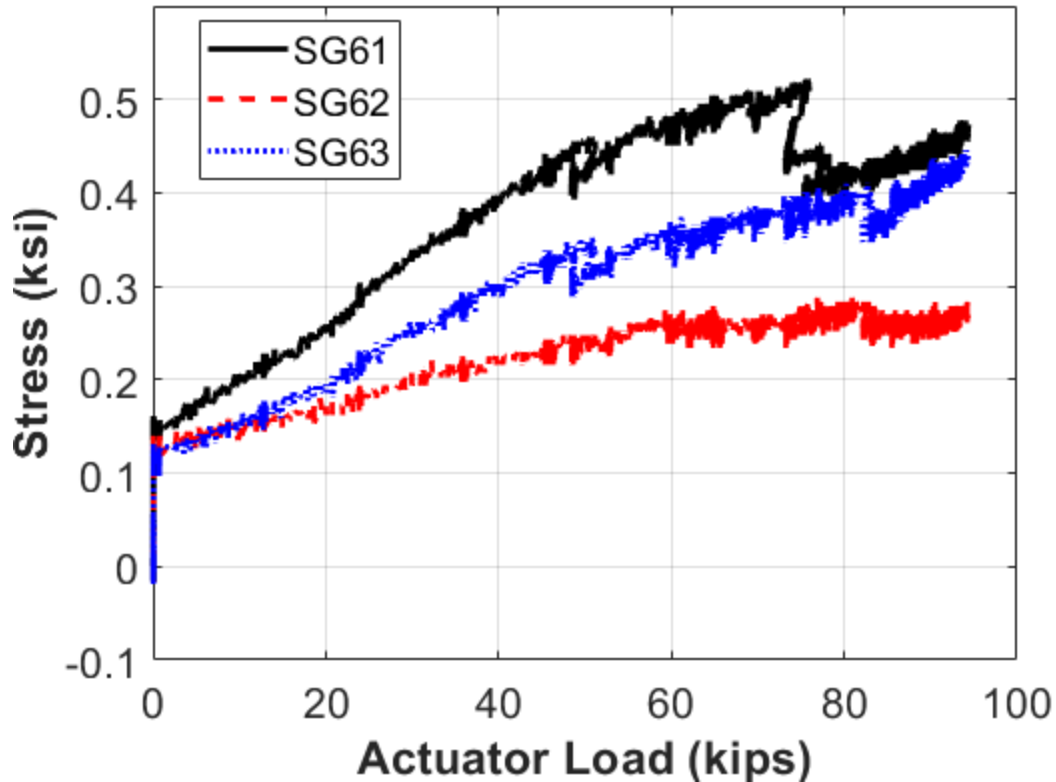


Figure 5.188. Concept C Precast Concrete Deck Stresses at E2.

The stresses on the precast concrete deck at gridline W1 can be seen in Figure 5.189. They are very similar to the results found at gridline E1. SG56 was located on the longitudinal centerline, while SG55 and SG57 were located 2 ft on either side of the centerline. SG57 and SG55 remained in net compression until about 10 kips and 20 kips, respectively. SG56 remained in net compression during most of the testing. All the gauges exhibited a small jump in stress at 65 kips, which was likely due to microcracks. A larger jump can be seen at approximately 79 kips, which is when several larger cracks formed near this area.

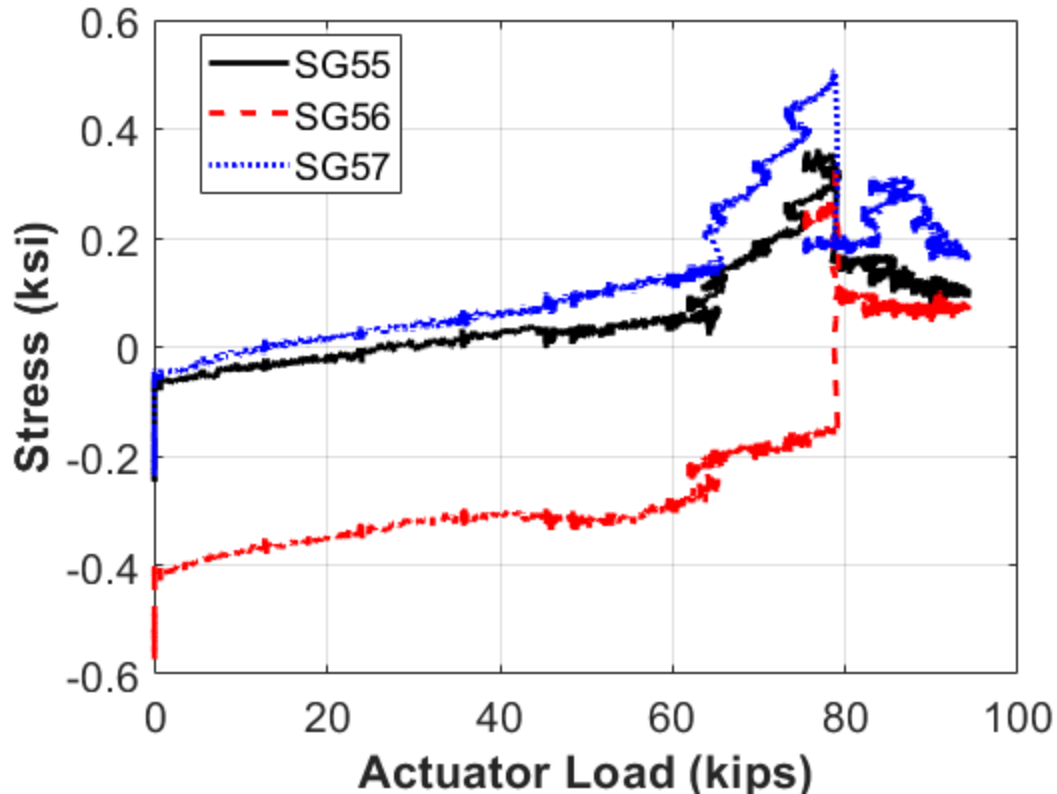


Figure 5.189. Concept C Precast Concrete Deck Stresses at W1.

The stresses in the longitudinal rebar at gridline E2 can be seen in Figure 5.190. SG14 was located on the longitudinal centerline, while SG13 and SG15 were located 2 ft on either side of the centerline. All gauges initially started in net compression. After the specimen was lifted off the pedestal and was left self-supporting, SG14 showed slight net tension. As the test progressed, all gauges showed an increase in tension fairly linearly up to about 45 kips. At that point, the data started to show more noise but still maintained the same mostly linear increase in tension. No new cracks were observed to have formed in this area at this load level, so it is unknown what caused the noise to occur in the data past 45 kips. The location of the strain gauges on the rebar at E2 should have been far enough from the end of the bar that it was developed; however, the stresses are still relatively low. It is unknown why the stresses remained low during the entirety of the test. It is possible that the cracking of the slab during the ultimate testing caused the low stresses.

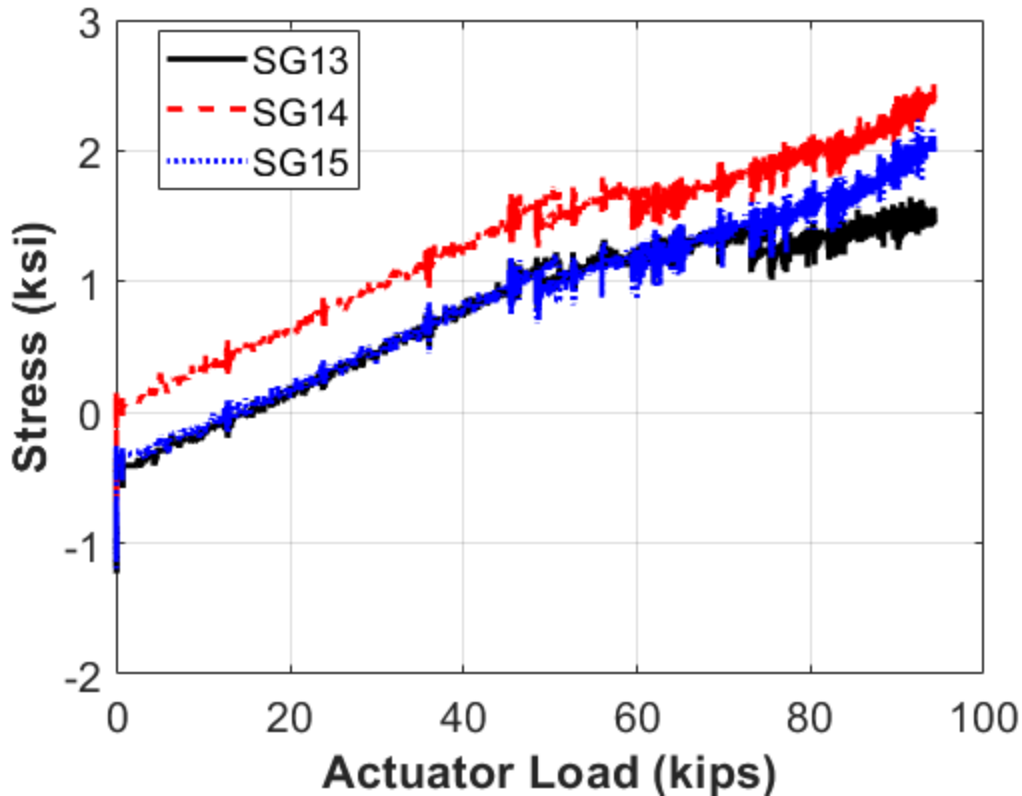


Figure 5.190. Concept C Ultimate Testing Rebar Stresses at E2.

The stress in the longitudinal rebar at gridline E3 can be seen in Figure 5.191. SG17 was located on the longitudinal centerline, while SG16 and SG18 were located 2 ft on either side of the centerline. The stresses in the rebar at this gridline remained relatively small until about 55 kips was reached. At that point, the stress at the location of SG16 increased rapidly to almost 20 ksi. At about 61 kips, the stress at the location of the other two strain gauges also increased rapidly. A crack did form very near to these strain gauges at 61 kips. Due to the concrete being cracked near this location at that load magnitude, all of the tension that the concrete was carrying got transferred into the rebar.

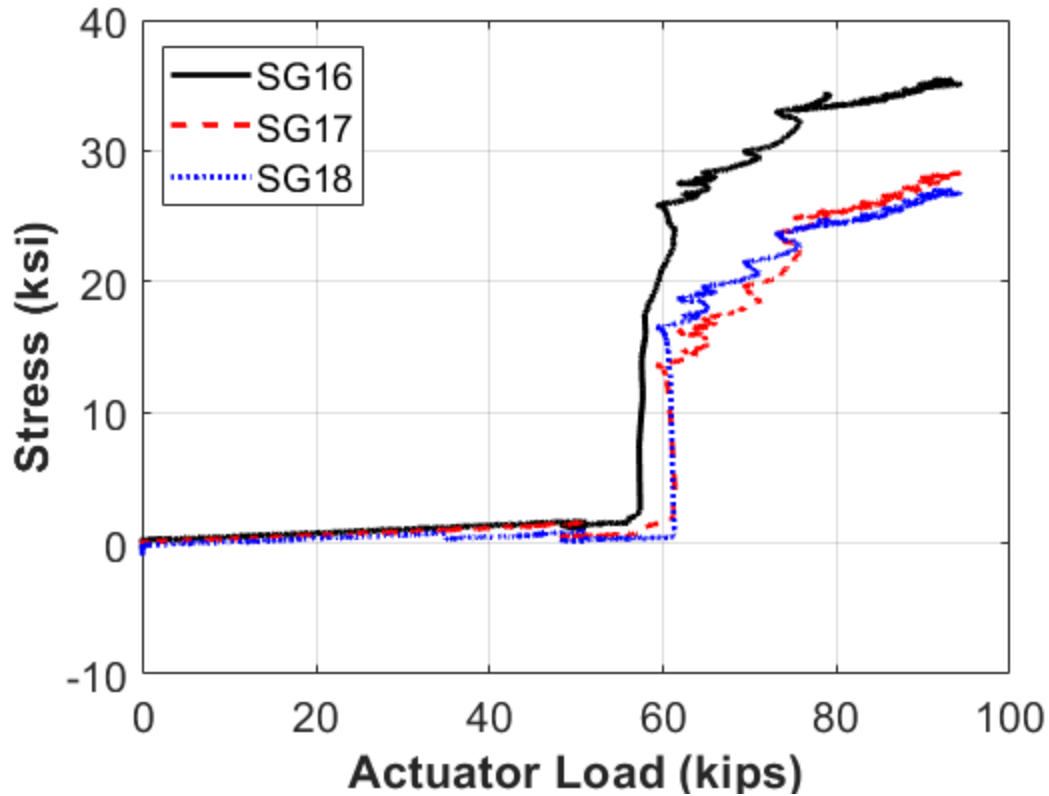


Figure 5.191. Concept C Ultimate Testing Rebar Stresses at E3.

The stresses in the rebar at gridline E0.3 in the closure pour can be seen in Figure 5.192. SG23 was located on the longitudinal centerline of the specimen, and SG22 was located 2 ft to the side of it. Both strain gauges showed a gradual increase in stress as the testing proceeded. SG23 showed a jump at approximately 75 kips, and SG22 showed a jump at about 85 kips. Many cracks started forming in the closure pour around this load level, which caused many variations in the data.

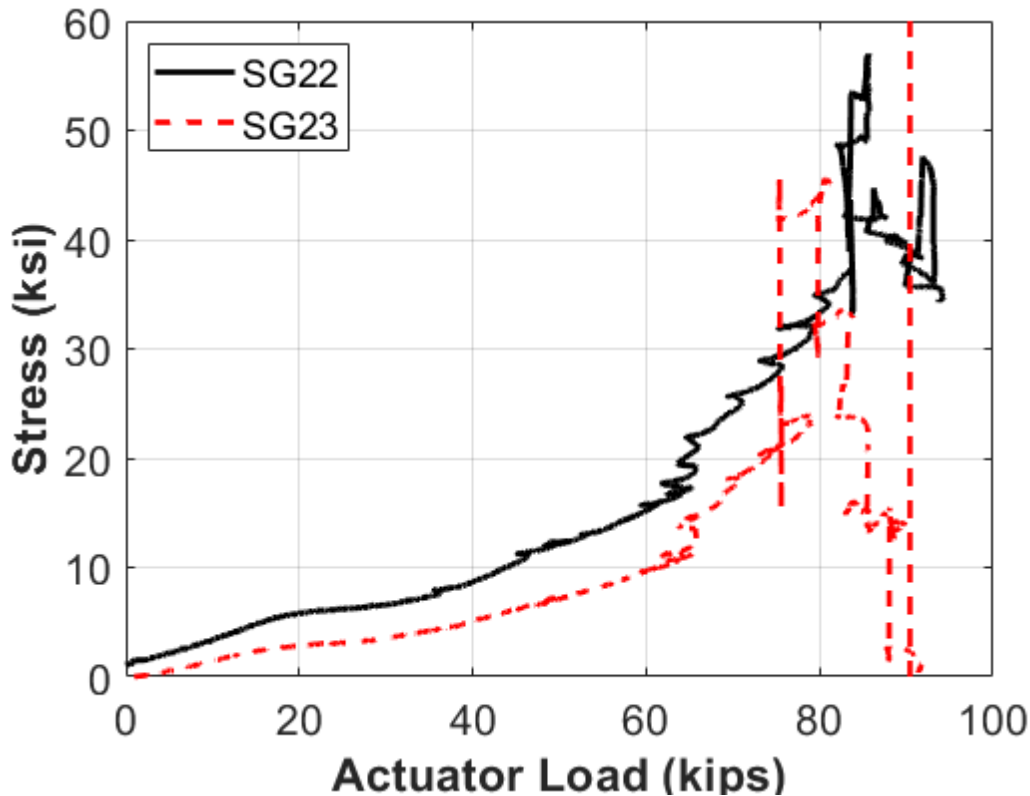


Figure 5.192. Concept C Ultimate Testing U-Loop Rebar Stresses at E0.3.

The stresses in the steel beam at gridline E1 can be seen in Figure 5.193. SG35 and SG36 were located on the top flange, SG37 was located on the top portion of the web, SG38 was located on the bottom portion of the web, and SG40 was located on the bottom flange. SG39 was removed from the plots because it was showing faulty data. SG36 and SG37 showed almost no change in stress, while SG35 showed an increase in tension, and SG38 showed a slight increase in compression. SG40 showed a large increase in compression, approaching 30 ksi of compression by the end of ultimate testing, which is still well below the yield strength of 50 ksi, indicating that the steel still had more capacity, even at the maximum load level.

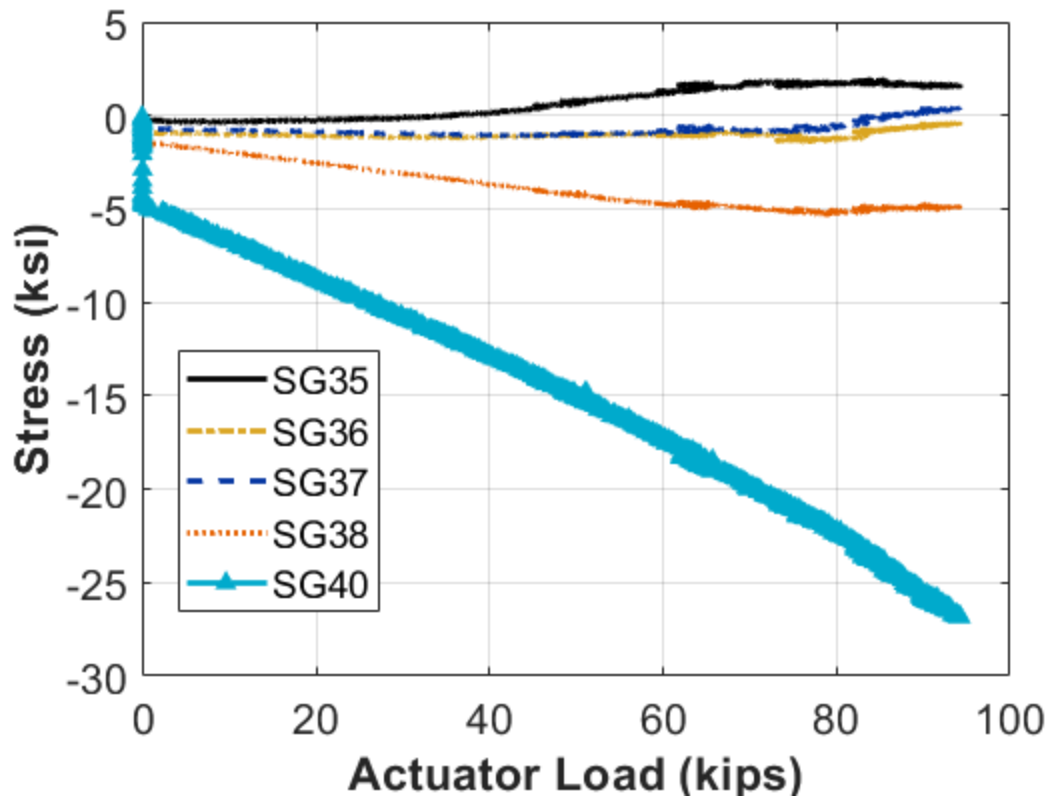


Figure 5.193. Concept C Ultimate Testing Steel Beam Stresses at E1.

Several plots show the location of the NA. Figure 5.194 to Figure 5.197 shows the NA based on the strains from the structural steel strain gauges at E1, E2, W1, and W2, respectively. The NA at gridline E1 varied slightly as the testing progressed. At 28 kips, the NA was approximately 27 inches above the bottom flange, but at the maximum load that was reached (94 kips), the NA was slightly lower—approximately 25 inches. The NA at gridline E2 varied more than at E1. At 28 kips, the NA was approximately 29 inches above the bottom flange, but at 94 kips, it dropped to around 22 inches. Similar results were seen at gridlines W1 and W2, with the NAs being close at W1 and farther apart at W2. The composite NA of the cracked section was calculated as being 18.7 inches above the bottom of the specimen.

The NA calculated from the testing results was consistently higher than the theoretical NA, which ignored the tensile resistance of the concrete. For the 28-kip load level, the NA was significantly higher because the deck had yet to have a significant amount of cracking. Therefore, the deck slab provided tensile force resistance, which drove the NA up on the specimen. As the testing progressed, the deck started to crack, which caused the NA to drop

closer to the theoretical NA. At the maximum load level, the deck had cracked extensively, which transformed the section into mainly a steel beam and rebar.

The NA calculated from the test results was also higher than the NA from Concept A. This is consistent with the expectation that due to the PT from the Williams bars the NA would be raised.

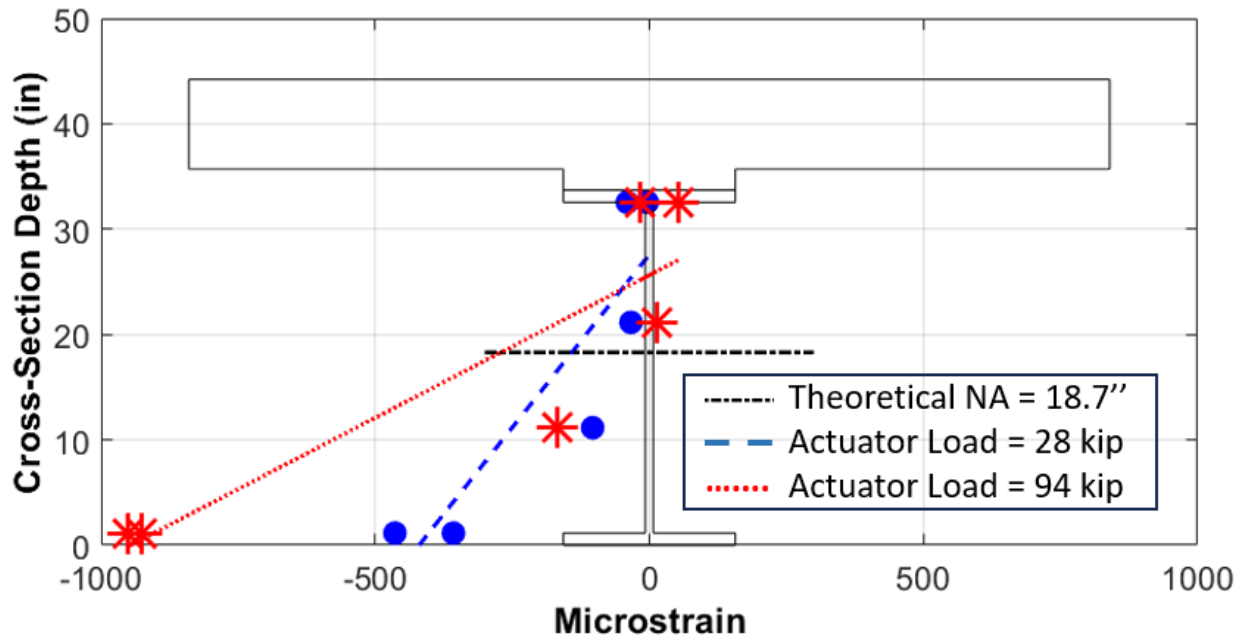


Figure 5.194. Concept C Ultimate Testing Structural Strain Profile at E1.

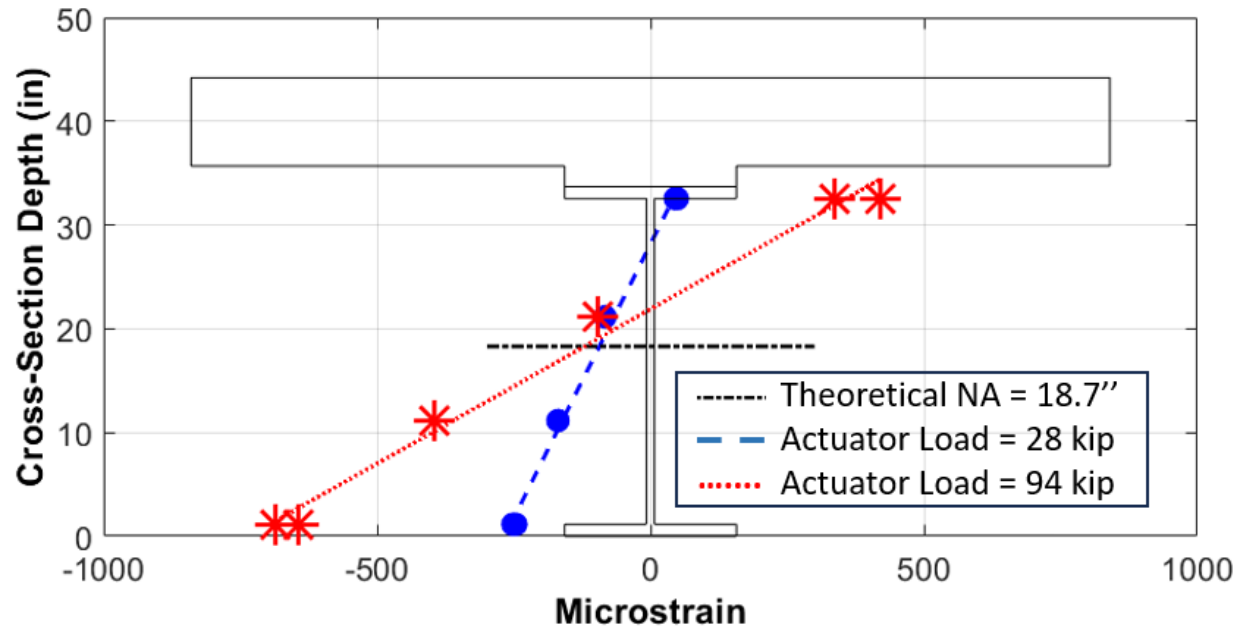


Figure 5.195. Concept C Ultimate Testing Structural Strain Profile at E2.

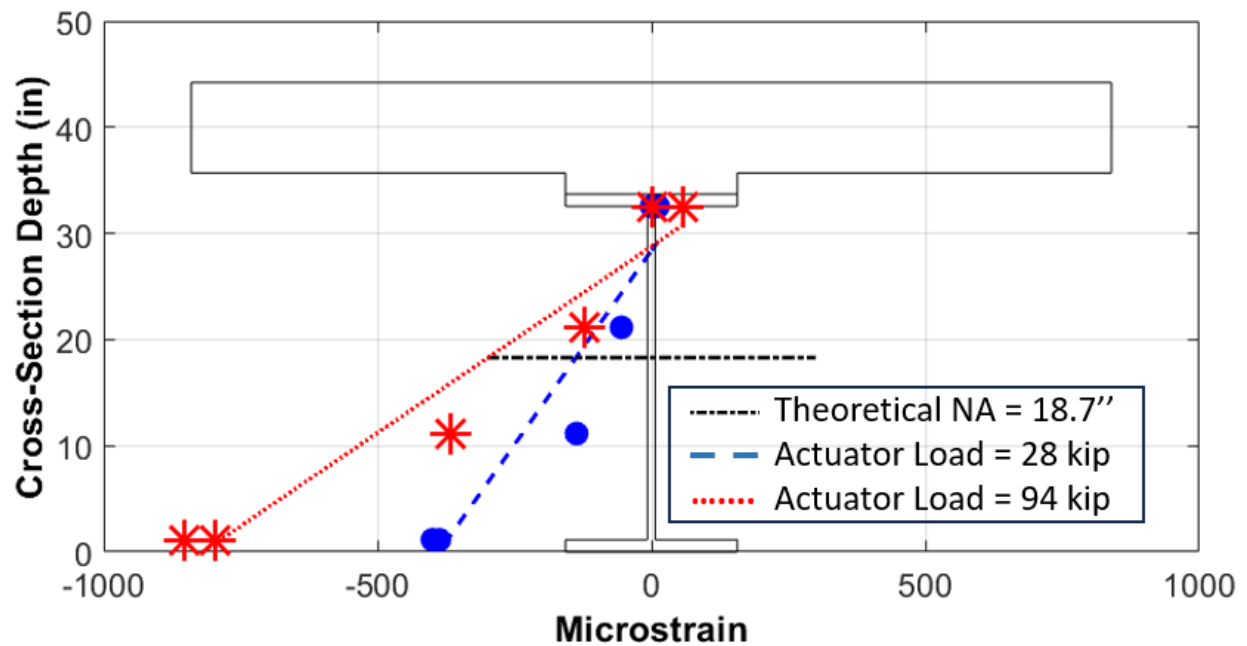


Figure 5.196. Concept C Ultimate Testing Structural Strain Profile at W1.

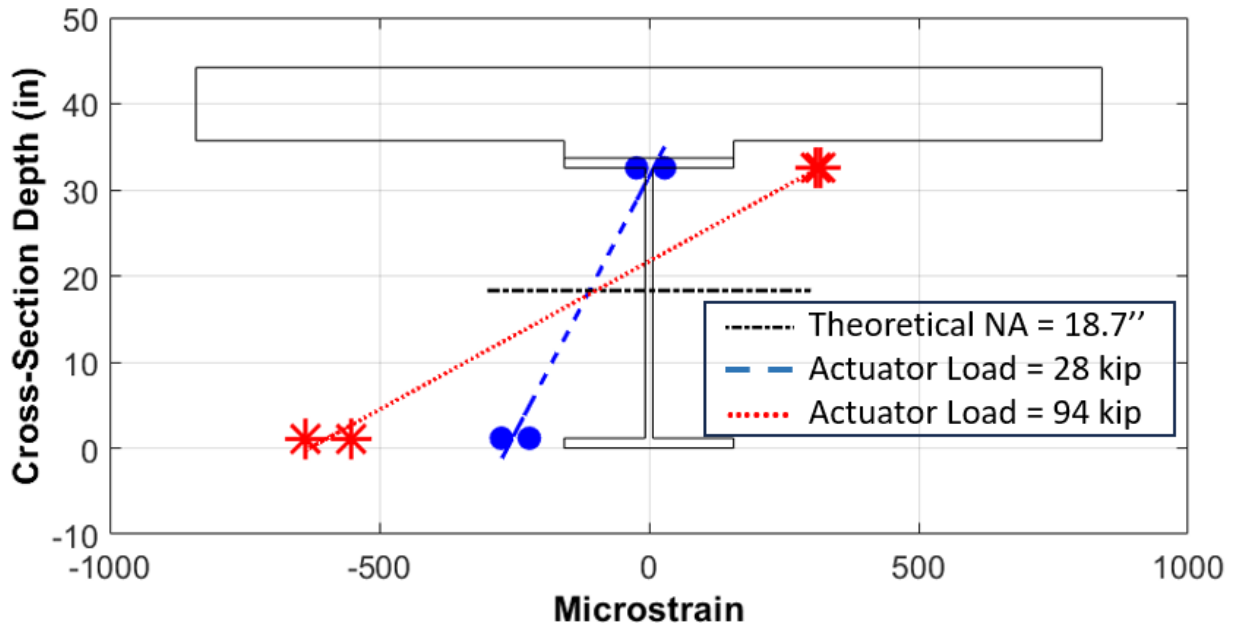


Figure 5.197. Concept C Ultimate Testing Structural Strain Profile at W2.

The load was taken off the specimen, and the through-hole jack was used to lift the specimen enough so the support pedestal could be placed under the end. After the specimen was placed back on the pedestal, the instrumentation was taken off, and the specimen was prepared for disposal. The specimen had to be broken in half to remove it from the lab. To do so, a concrete saw had to be used to make a transverse cut down the center of the closure pour. See Figure 5.198 for a view of the specimen after it had been cut in half and Figure 5.199 for view of the specimen leaving the lab.

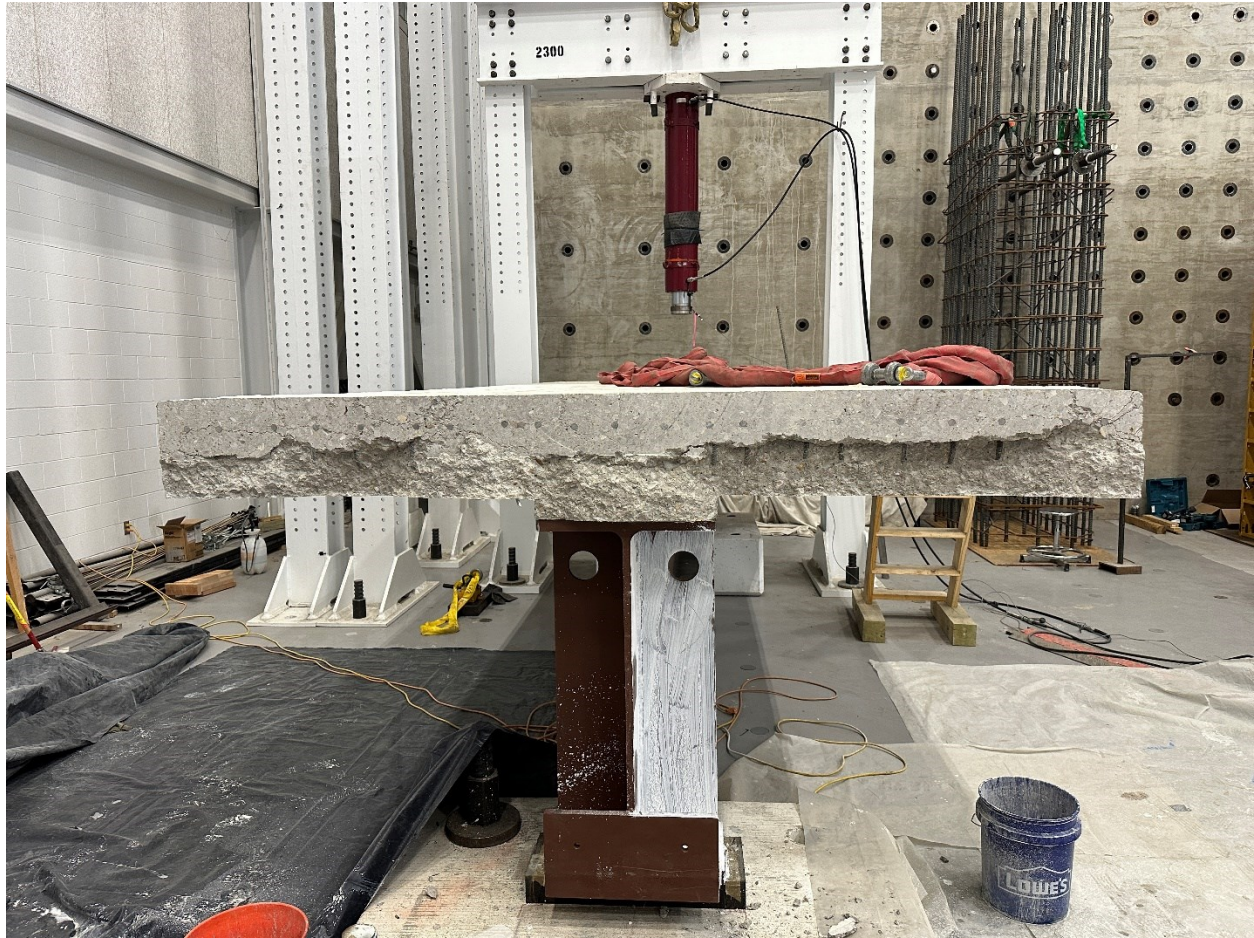


Figure 5.198. View of Concept C after Saw Cutting.



Figure 5.199. Concept C Being Taken out of Lab.

5.9.2.5. Concept C Post testing Observations

Many observations were made about the specimen after testing had concluded. Various signs of damage were reported, the main one being the multitude of cracks that formed on the surface of the deck at various points of the testing. The fact that only two cracks formed during static testing (besides the cracks in the construction joint) and no cracks formed during cyclic testing means the vast majority of cracks were formed during ultimate testing. The earliest crack that formed during ultimate testing was at 45 kips, which is equivalent to 154 percent of the HL-93 loading. Most of the rest of the cracks that formed after this point formed after 65 kips, which is equivalent to 210 percent of the HL-93 loading.

Many cracks were observed to have formed during ultimate testing. The cracks on the east side of the specimen can be observed in Figure 5.200, the cracks around the closure pour region are

shown in Figure 5.201, and the cracks on the west side of the specimen are shown in Figure 5.202.

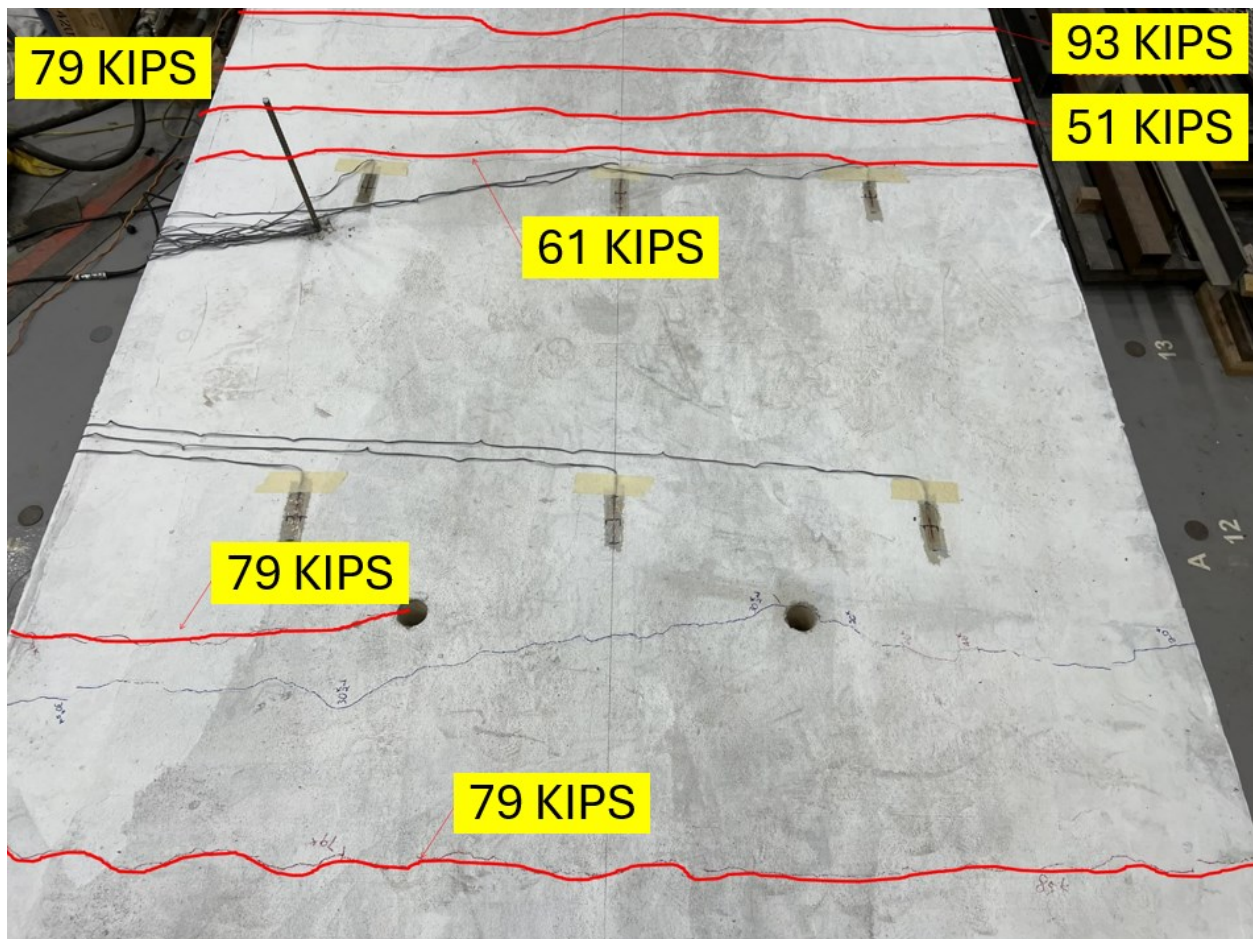


Figure 5.200. Cracks on East Side of Concept C after Ultimate Testing.

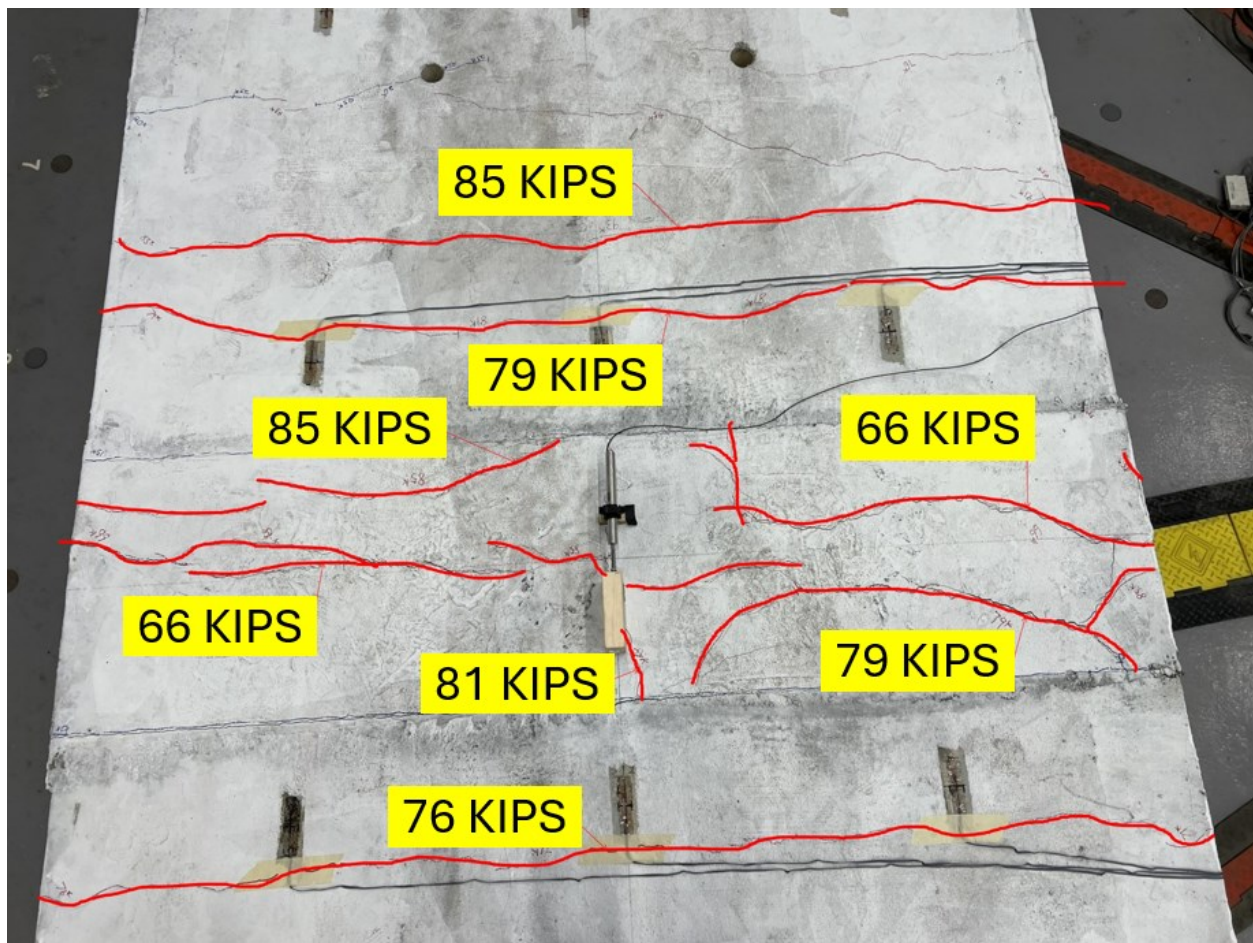


Figure 5.201. Cracks in Closure Pour of Concept C after Ultimate Testing.

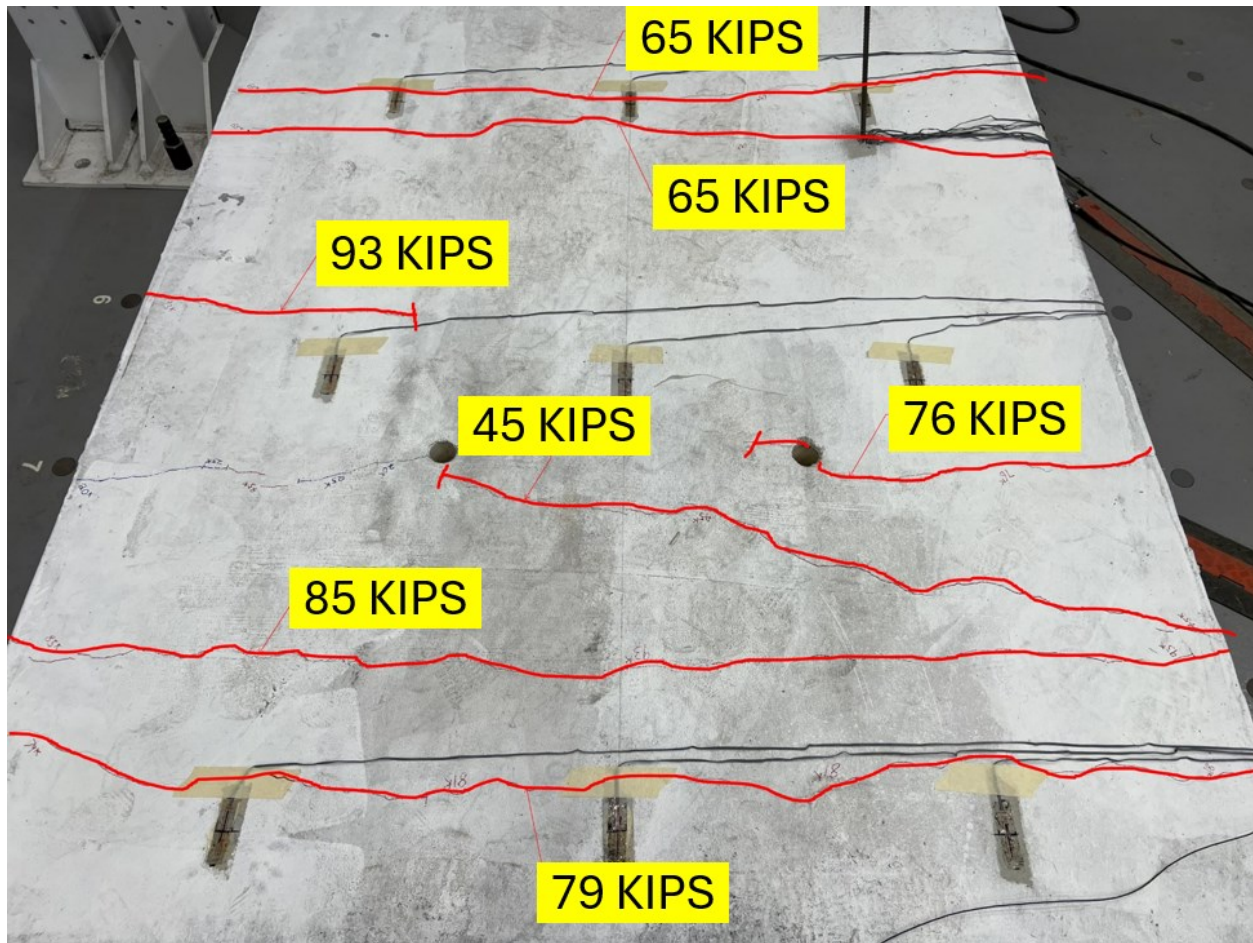


Figure 5.202. Cracks on West Side of Concept C after Ultimate Testing.

Many cracks were observed on the sides of the deck as well; the most major cracks are shown in Figure 5.203 and Figure 5.204. The bottom of the crack on the south side of the specimen measured over 0.2 inch across. This crack split into several smaller cracks as they traveled to the top of the slab, while on the north side of the specimen, the main crack remained one large crack as it traveled to the top of the deck.

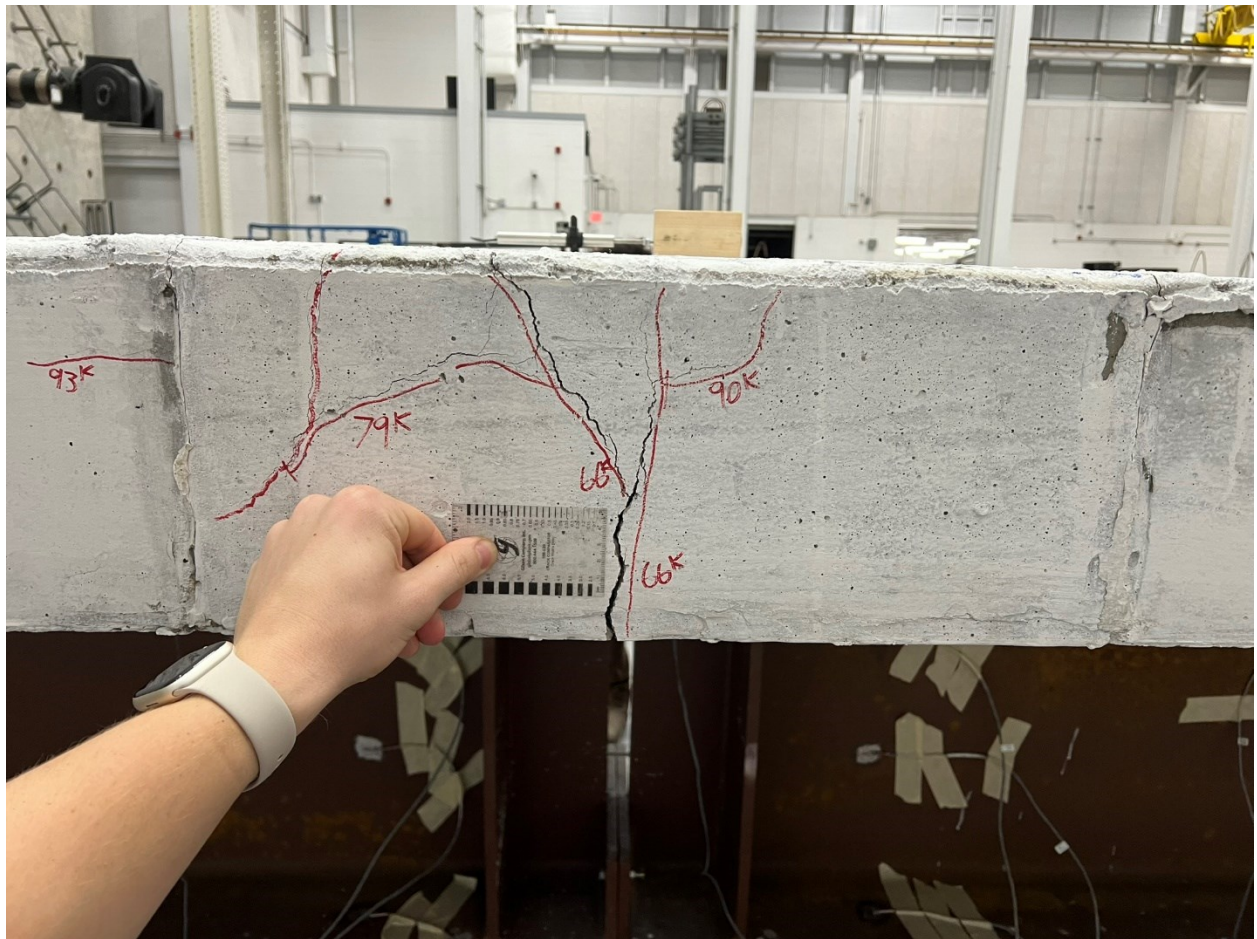


Figure 5.203. View of Cracking on South Side of Deck in Closure Pour.

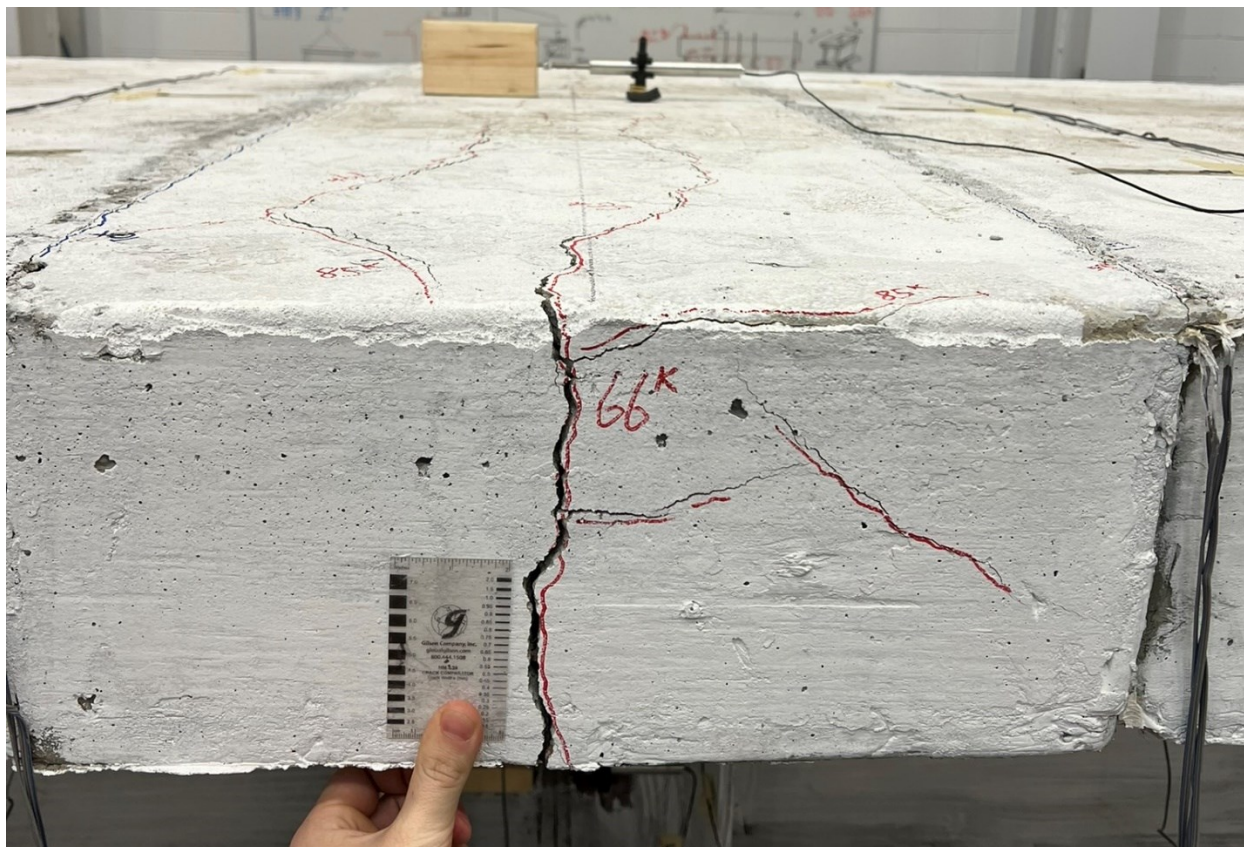


Figure 5.204. View of Cracking on North Side of Deck in Closure Pour.

5.9.2.6. *Concept C Findings*

Several findings arose from the Concept C experimental testing. The primary findings are summarized as follows:

- *Stiffness*: The initial stiffness of Concept C was greatest of all specimens, with it being ~90 kip/in (above the theoretical stiffness for a continuous girder, ignoring the tension provided by the slab). This stiffness was maintained until approximately 50 kips (equivalent to 168 percent of the HL-93 loading) was reached. After this point, the specimen started to relax after each displacement increment due to cracks forming on the deck, causing the specimen to act more non-composite in nature. See Section 5.11.5 for an in-depth comparison of each concept's stiffnesses.
- *Closure Pour*: Similar to Concept A, the first place that cracks started to appear during testing was at the interface between the closure pour and the deck. These cracks formed

as early as 55 percent of the HL-93 loading. These cracks were approximately 0.02 inch wide at the end of ultimate testing.

- *Crack Propagation:* Up to 62-kips load level (roughly two times the HL-93 load level), only three visible cracks formed besides the ones at the interface of the closure pour and deck (five fewer cracks than Concept A). All of these cracks formed at least 4 ft 6 inches away from the transverse centerline of the specimen, with two of them forming over 7 ft 6 inches away from the transverse centerline. They were also full-depth cracks, meaning they went all the way through the slab.
- *Welded Brackets:* Similar to Concept B, the PT brackets should be shop-welded rather than bolted to the beam flanges because it is difficult to know for certain whether the required pretension of the bolts has been achieved. These bolts are an essential part of the design; therefore, it is unacceptable if they are not adequately pre-tensioned. Moreover, using slip-critical bolts will require special surface prep for the beams and the bracket assembly. These surface preps can be expensive and may not always provide the necessary coefficient of friction required by design. Welding the brackets to the beam flange eliminates this problem since welding is a much better controlled process than using slip-critical bolts. Additionally, in certain cases, a large number of bolts may be required to resist the shear and tensile loads, thus necessitating a large bracket assembly. Such large bracket assemblies get heavy, and on a construction site, they may become difficult to handle. Also, without bolts attached to the top flange, shear studs can be welded, which reduces local flange bending.
- *Bar Tensioning:* To provide adequate tension in the Williams bars, a through-hole jack is a reliable method. For virtually all designs, a 100-ton through-hole jack is the minimum jack size. These jacks weigh more than 100 lb; therefore, the weight must be accounted for when considering the constructability of the setup.
- *Steel Bearing Plates:* The steel bearing plates provided an excellent way for the compressive forces to be transferred across the bottom flange. The one issue with the bottom-flange steel bearing plates is that if they are not welded to the bottom flange perfectly parallel to each other, then there will be a gap on one of the edges. This issue can be remedied by using steel shim plates or by using bolts to tighten the plates together.

In the experimental test setup, there was a small gap that was minimized by inserting a bolt into the already present bolt hole and tightening it to pull the plates together.

5.10. CONCEPT D

5.10.1. Design, Construction, and Pretest Behavior of Concept D

5.10.1.1. Specimen Design

This subsection introduces how the Concept D test specimen was designed to achieve the features of the benchmark bridge. Section 5.3 previously described the benchmark bridge design, which is the basis of the specimen design. An elevation view of the connection area of Concept D is shown in Figure 5.205.

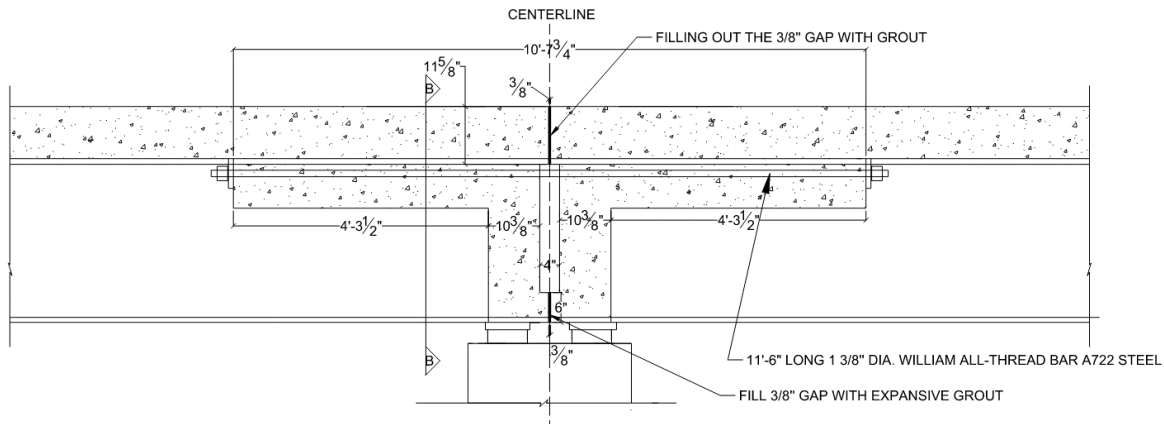


Figure 5.205. Elevation View of Concept D Connection Area.

A section view of the connection through the diaphragm can be seen in Figure 5.206. In this section, it can be seen that this concept has four Williams bars rather than the two Williams bars in Concept B and Concept C due to a slightly different NA and cross section of the post-tension design. The Williams bar design involved the service load balancing technique, which has been applied to the design of the continuous structure. The connection is designed for service load and checked for the ultimate capacity and tensile stress at the slab under service load. The force magnitude of the Williams bar design was 160 kip per bar, which was based on the stress-strain profile to achieve the net stress at the center of the match-cast joint surface equal to 0.0 ksi. The concrete shear key design was applied at the top and bottom of the concrete block connection along the width of the specimen. A 150 ksi 1.375-inch Williams bar was fed through these four tunnels and post-tensioned to bring the deck slab into compression. While Concept A, B, and C

used a closure pour region, Concept D applied the match-cast method and used epoxy resin to fill between the two precast units.

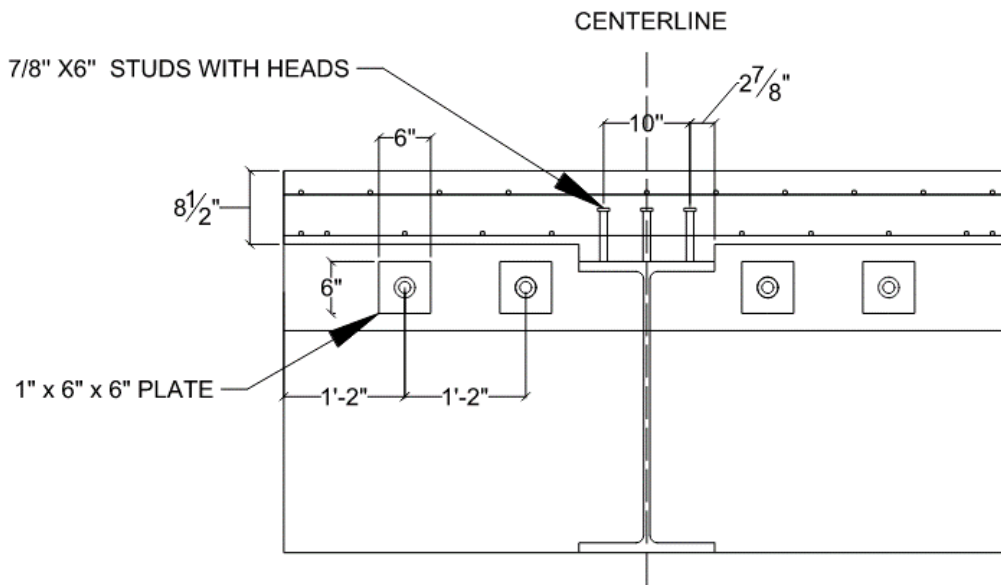


Figure 5.206. Section View of Concept D Connection Area.

5.10.1.2. Instrument Plan and Data Acquisition

The instrumentation of this concept focused mainly on the connection of the two composite beams. A plan view, elevation view, and section view of the instrumentation plan can be seen in Figure 5.207, Figure 5.208, and Figure 5.209, respectively. A legend for the symbols can be found in Figure 5.210. The final instrumentation lists for each concept can be found in Appendix B.

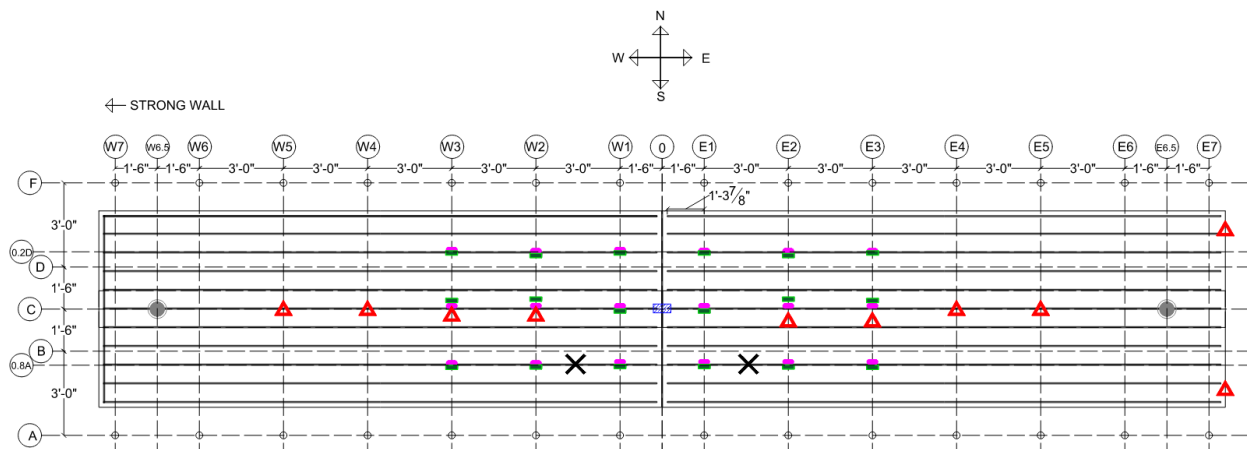


Figure 5.207. Concept D Instrumentation Plan (Plan View).

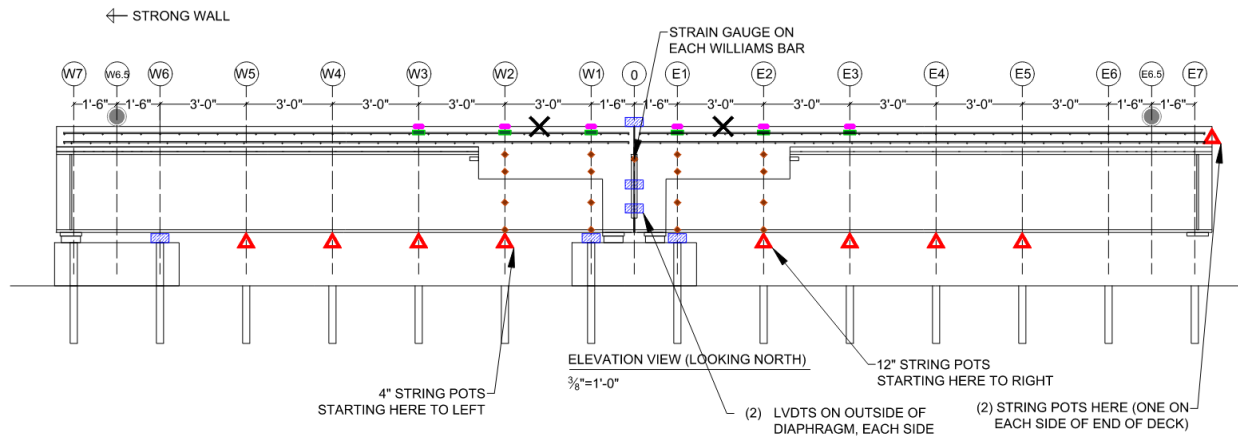


Figure 5.208. Concept D Instrumentation Plan (Elevation View).

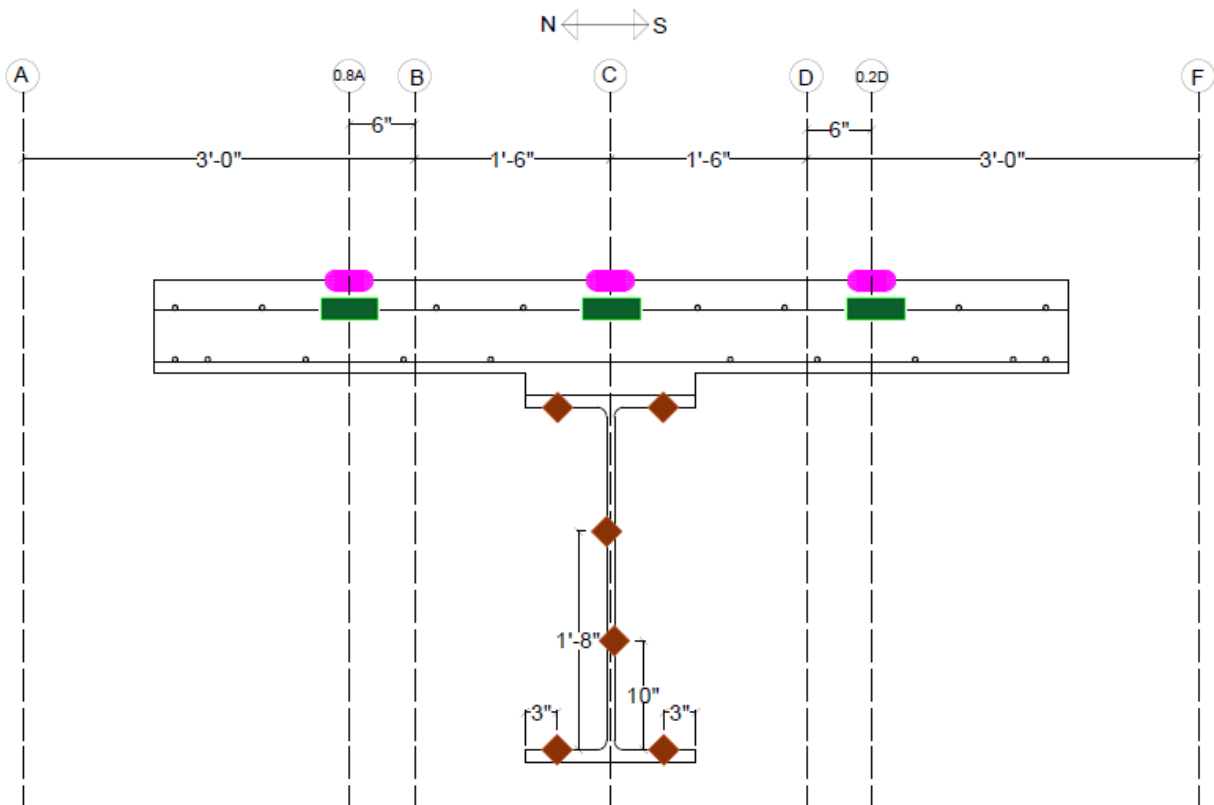


Figure 5.209. Concept D Instrumentation Plan (Section View).








Symbol	Item	Concept D Count
	Actuator and Load Cell	2
	Embedded Rebar Strain Gauge	18
	Concrete Surface Strain Gauge	18
	Structural Steel Surface Strain Gauge	28
	String Potentiometer	10
	LVDT	8
	Wire Exits	2

Figure 5.210. Instrumentation Plan Legend.

Most strain gauges were located on major gridlines (E1, E2, etc.) so that after testing, they could easily be turned into strain profiles to see how the strain differs relative to the match-cast joint. Strain gauges were also located on the 1.375-inch Williams bars so that the proper amount of post-tension could be put into the bars. String pots were located every 3 ft so that a displacement curve could be seen during and after testing. For areas that have higher precision displacements, LVDTs were used. LVDTs were located near the supports of the beams (to measure deflection near the supports), on the sides of the concrete diaphragm (to measure the relative rotation of the beams), and above the slab on the match-cast joint (to measure the elongation of the match-cast joint).

The rebar strain gauges used were FLAB-5-350-11 from Texas Measurements. The first rebar strain gauges were located starting 1 ft 6.5 inches from the end of the longitudinal bars, with the second strain gauges 1 ft 11 inches after that, and the third 3 ft beyond that. Rebar strain gauges were located within 7 ft 6 inches of the centerline of the match-cast joint since that was the primary focus area for the testing.

Concrete surface strain gauges used were PL-60-11 from Texas Measurements. Concrete strain gauges were located directly on the major gridlines (E1, E2, etc.) so that the change in strain

could be seen in regular increments moving farther away from the centerline of the match-cast joint.

The structural steel strain gauges used were also FLAB-5-350-11 from Texas Measurements. Structural steel strain gauges were located starting 1 ft 6 inches from the center of the pier cap, with another line 3 ft away from that. Structural steel strain gauges were also applied on the 1.375-inch Williams bars directly at the centerline.

5.10.1.3. Specimen Preparation

The general formwork construction was previously discussed in Section 5.5. The following subsections are unique to Concept D.

Due to the unique nature of the connection area of this concept, a portion of the concrete formwork had to be redesigned and constructed. Multiple new panels were constructed and assembled so that the diaphragm could be effectively constructed. See Figure 5.211 for a view of the formwork while it was being assembled.



Figure 5.211. Concept D Formwork Assembly.

To resist the relatively large lateral forces from the concrete, several 0.625-inch threaded rods were fed through the side forms and were tensioned so that they would hold the formwork together. In addition, the used Williams bars from the previous concepts were fed through PVC pipes to hold the top portion of the formwork together. These PVC pipes were also used to feed the Williams bars through for the experimental testing. These PVC pipes can be seen in Figure 5.212.



Figure 5.212. Concept D PVC Pipes for Williams Bars.

To ensure that the contact between the two halves of the concept was at a known point, a 2-inch void was formed between the two halves. This void was formed by gluing a 1-inch foamboard insulation panel to the end formwork panel. This panel was cut so that there was a portion on the top and bottom of the specimen that was in contact. A shear key was also made on the top and bottom portion of the contact area so that the specimen would fit together better. See Figure 5.213 for a view of the void and shear key forming.



Figure 5.213. Concept D Void and Shear Key Forming.

To ensure that the two ends of the specimen would fit together as closely as possible, it was decided to use the first half of the specimen that was cast as a form for the second half. A plastic sheet was laid between the two halves so that they could be separated easily after pouring. The result after the second half of the specimen was cast can be seen in Figure 5.214.



Figure 5.214. Concept D Second Pour Concrete.

5.10.2. System Experiment Testing Program, Experiment Results, and Observations

5.10.2.1. Concept D Test Setup

Section 5.4 provides the general loading procedure taken during the experimental testing. For the Concept D experimental test setup, it included several unique steps. Figure 5.215 presents an elevation view of the overall Concept D test setup.

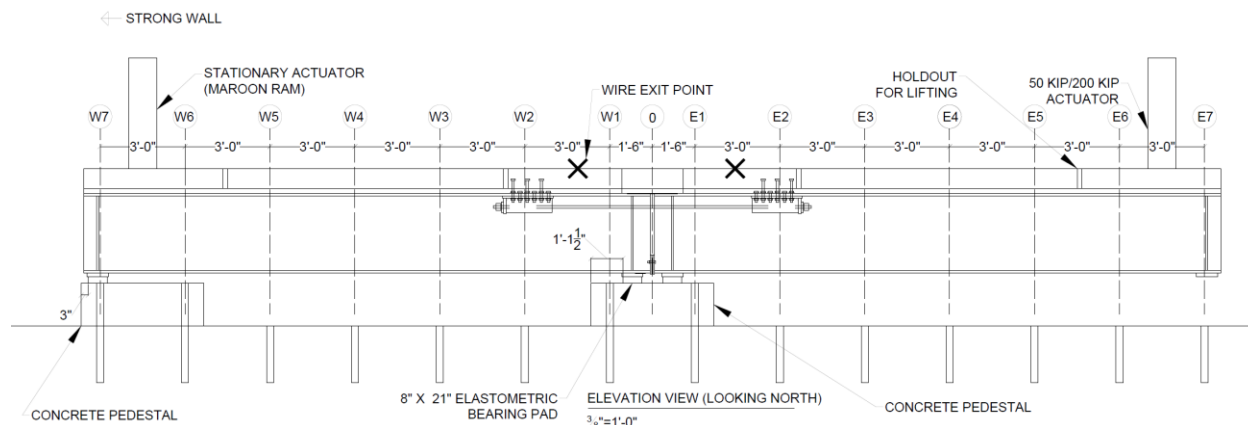


Figure 5.215. Concept D Test Setup Elevation.

After the Concept D precast units were placed on the concrete pedestals, the first step was to fill the epoxy resin between these precast units. The precast segmental epoxy adhesive called DURAL 106-EUCLID CHEMICAL has been used as a bonding agent for precast segmental concrete construction. It is a non-sag paste and can provide 6 hours of contact time before the PT process, which was a good fit for the Concept D test setup. Before applying the epoxy adhesive, the side surfaces were prepared at the top and bottom parts of the precast units. They were dry and structurally sound. This epoxy adhesive came with two individual parts and needed to be fully mixed before use. Figure 5.216 shows the epoxy adhesive applied to both the top and bottom side surfaces of the Concept D precast units. The PT step will be shown in Section 5.10.2.2, Concept D static testing. The next construction procedure was post-tensioning Williams bars in order to create compressive stress at the top deck surface.



Figure 5.216. Epoxy Adhesive Filled Out between the Side Surfaces of the Precast Units.

Similar to the previous concepts, a 1.5-inch thick adapter plate was fabricated with a hole pattern that fit the 50-kip capacity actuator and the holdouts that were placed in the precast concrete deck. A similar adapter plate for Concept A is shown in Figure 5.36. The plate was fastened to the specimen in the same manner as in Concepts A, B, and C. Figure 5.105 shows how the adapter plate was attached to the concrete deck.

For the hold-down side of the test setup (the left side is shown in Figure 5.216), a stationary actuator was applied to hold down the specimen during testing. Figure 5.217 shows the side view of this actuator. This actuator used a variable load to keep the hold-down side in place. A load cell was placed under the end of the actuator to measure the actual load magnitude during testing. Several steel plates were under the load cell to distribute the load across a larger area of the concrete deck.



Figure 5.217. Concept D Hold-Down Actuator.

For the Concept D PT part setup, the precast concrete drop panel was designed for holding the four Williams bars and also provided enough contact surface at the top and bottom shear key part between precast units. The upper part of the drop panel was about 5 ft wide for one unit in order to provide adequate precompression force at the connection location. The lower part of the drop panel was about 10 inches wide since it needed to be accommodated with the bearing pad size of the TxDOT bridge standard. The steel plate was used to distribute the concentrated compressive force at the nut and acted as the base plate for the through-hole jack during the post-tension

process. Figure 5.218 shows the Williams bars were on one side of the specimen. There were no additional construction procedures for Concept D before testing.



Figure 5.218. Post-tensioned Williams Rods under Concrete Deck.

Figure 5.219 shows the overall view of the Concept D test setup. The view from the active loading side is shown in Figure 5.220. Figure 5.221 presents the view from the hold-down end side.



Figure 5.219. Overall Elevation View of Concept D Test Setup.



Figure 5.220. View of Concept D Test Setup from Active Loading End.



Figure 5.221. View of Concept D Test Setup from Hold-Down End.

5.10.2.2. Concept D Static Testing

Static testing for Concept D was performed in similar fashion as in the previous concepts. Four Williams bars were already post-tensioned right after the application of epoxy adhesive, just as it was done during the static testing for Concepts B and C, by using a through-hole jack. The same stand but at a different height was used to support the through-hole jack during the whole PT process. Figure 5.122 shows a view of the stand used for the previous concepts.

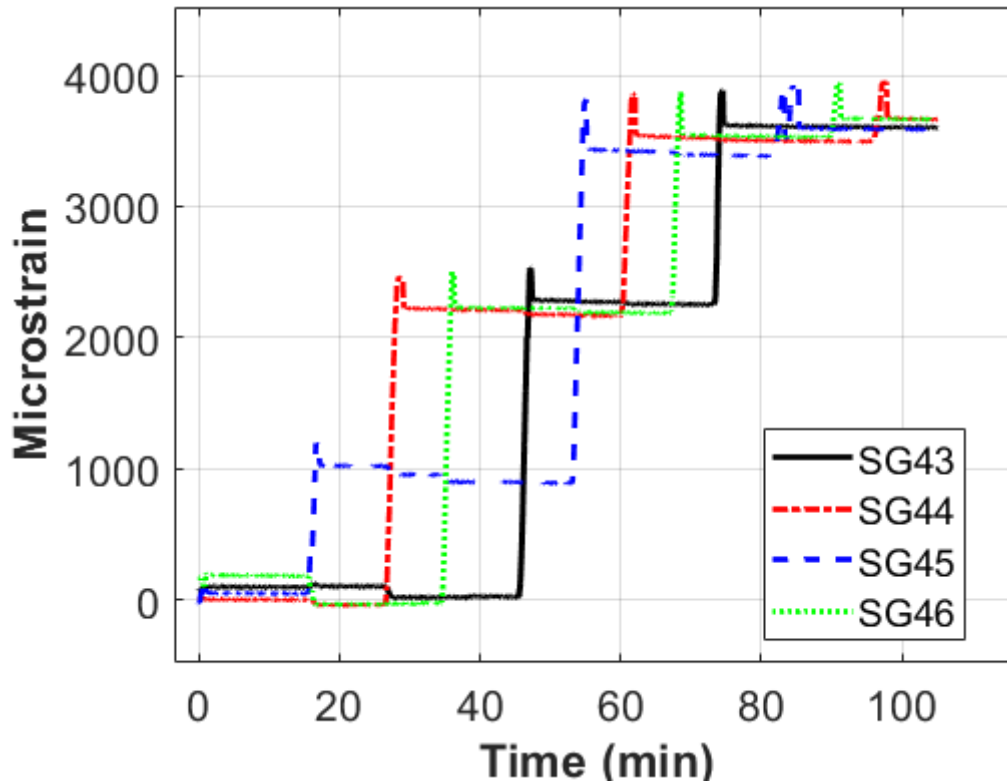


Figure 5.222. Concept D Static Testing Strain on Williams Bars during PT.

The through-hole jack was used to post-tension the Williams bars to at least 166 kips, which is 70 percent of the theoretical ultimate strength of the bars. This required post-tensioned load level corresponds to 3600 microstrain in Williams bars. The four Williams rods were post-tensioned three times per rod to reach the desired stress value, alternating on each side of the specimen in approximately 1000 microstrain lifts. This procedure aimed to eliminate uneven stresses/strains developing in the specimen before the testing had begun. Figure 5.222 shows the time history of the strain on four Williams bars. SG43 was on the north outside Williams bar. SG44 was on the north inside Williams bar. SG45 was on the south inside Williams bar. SG46 was on the south outside Williams bar. All the Williams bars were post-tensioned slightly higher than the target value since the strain losses would occur when the through-hole jack was released.

The static testing commenced once the PT process was completed. The active loading end of the specimen was pulled up using approximately 22 kips so that the temporary support pedestal could be removed. The specimen was lowered until the active loading end actuator was about 0 kips, which was considered the zero point for the static testing. Although the actuator was 0 kips, the negative moment induced by the cantilever setup was about 200 kip-ft at the active

loading end. The active loading end of the specimen was then pushed down in 0.125-inch increments. The test specimen was inspected for signs of damage every increment. The first sign of damage on the specimen occurred at the 5-kip load level. It was observed that minor cracks were forming in the transverse joint at the top concrete deck surface between the two precast units. Figure 5.223 shows the minor crack location and the crack card measurement. A minor crack formed at the interface of the precast concrete drop panel of the hold-down end side at the 5-kip load level.

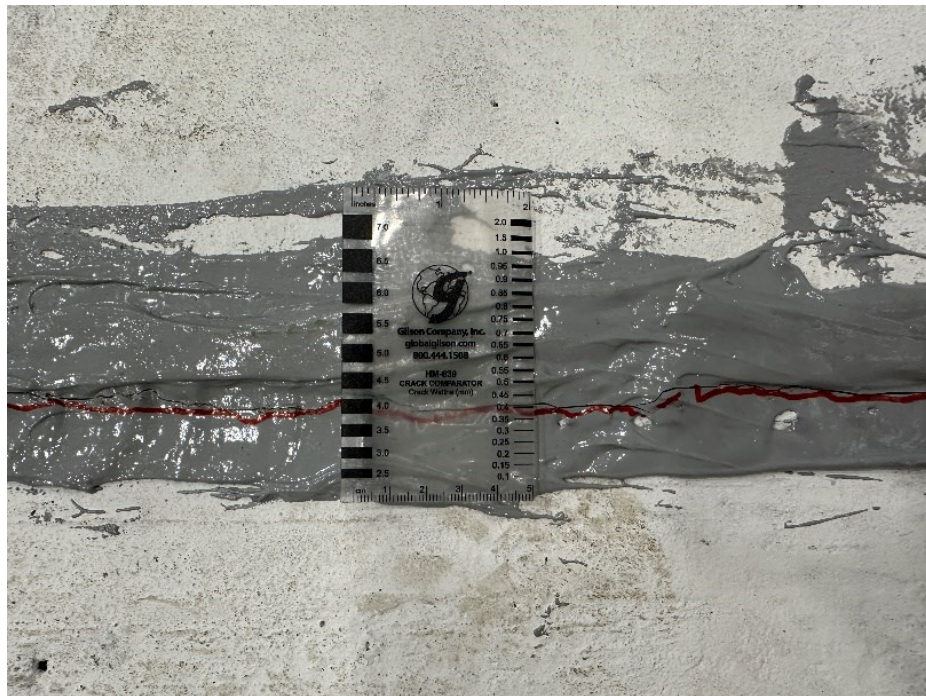


Figure 5.223. Concept D Static Testing Crack at Top Surface Transverse Joint at 5-kip Load Level.

One of the minor cracks formed at the interface of the precast concrete drop panel of the active north side at the 21-kip load level. In addition, minor cracks formed at a similar location on the south side at a 5-kip load level. Figure 5.224 reveals the crack that developed at the active north side when the load was about 21 kips. Figure 5.225 depicts the crack that developed at the active south side when the load was about 5 kips and 21 kips.

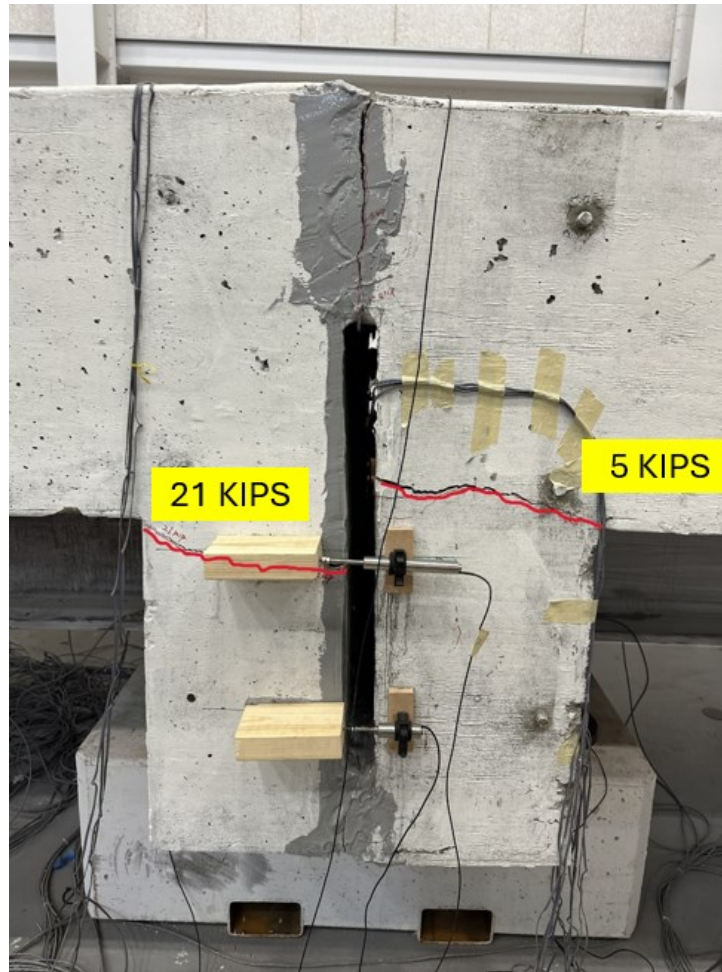


Figure 5.224. Concept D Static Testing Crack at Northside Surface.

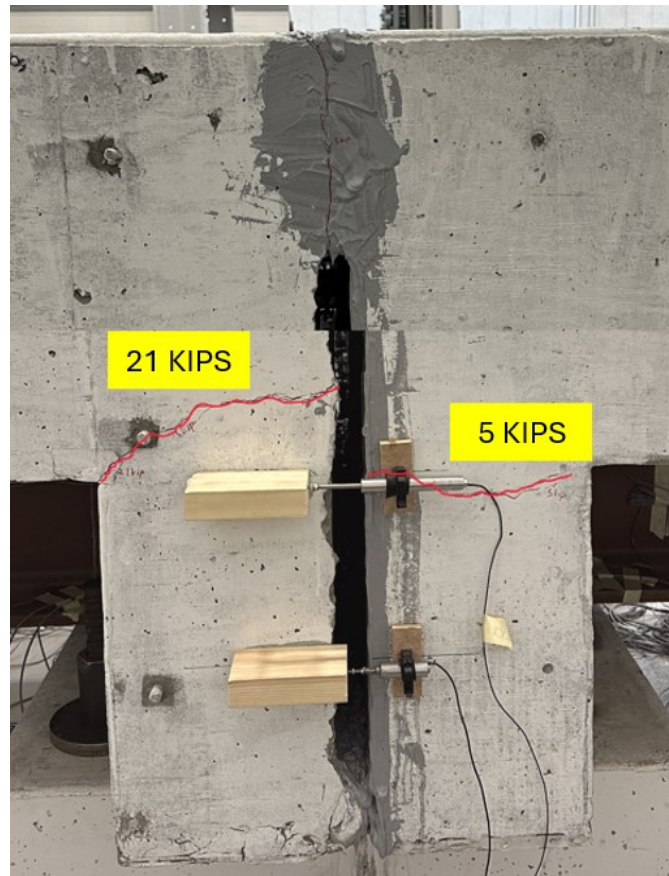


Figure 5.225. Concept D Static Testing Crack at Southside Surface.

The load on the specimen was increased in 5-kip increments up to 30 kips. Although the equivalent HL-93 notional loading was only about 28 kips, the Concept D specimen performed relatively well. There was no other crack forming until the static test was completed. The complete loading process was repeated twice after the load was released from 30 kips to check for repeatability. The vertical displacement at the gridline E7 time history plot is depicted in Figure 5.226. The load data were from the active loading end actuator. The displacement data were the average of the two string pots attached to the bottom of the concrete deck on gridline E7. The maximum displacement reached about 1.7 inches. The final displacement was about 0.1 inches due to the elastomeric bearing pad rebounding after the end of the specimen was lifted. The total static testing process lasted about 100 mins long.

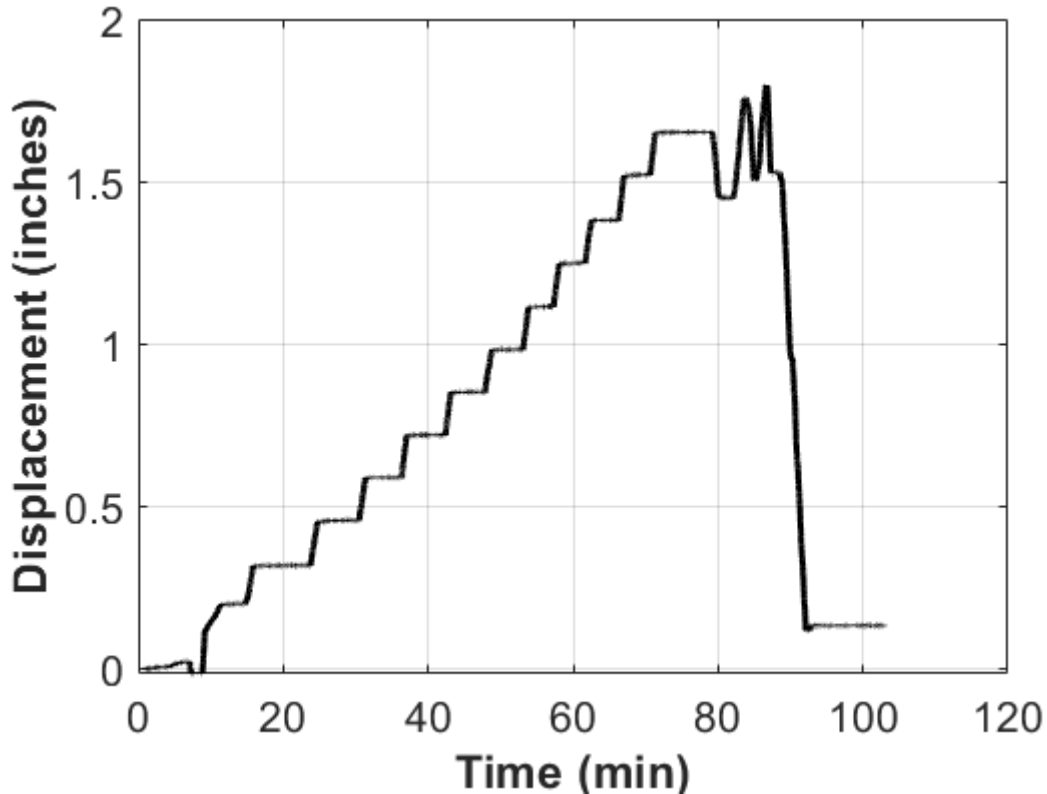


Figure 5.226. Concept D Static Testing Vertical Displacement at E7 Time History.

Figure 5.227 presents the load data along with the testing time. The initial negative load indicated the active ending was lifted in order to remove the concrete pedestal under the specimen. The actuator started to release the specimen, and the load was lowered back down to 0.0 kip. Each load increment can be seen on the plot. The concrete creep behavior was happening during the static testing since the load dropped a little bit once it reached each desired displacement stage. The maximum load was about 30 kips, which was a little bit above the HL-93 notional loading (28 kips). The plot also shows the load back to zero and then back to 30 kips again two more times.

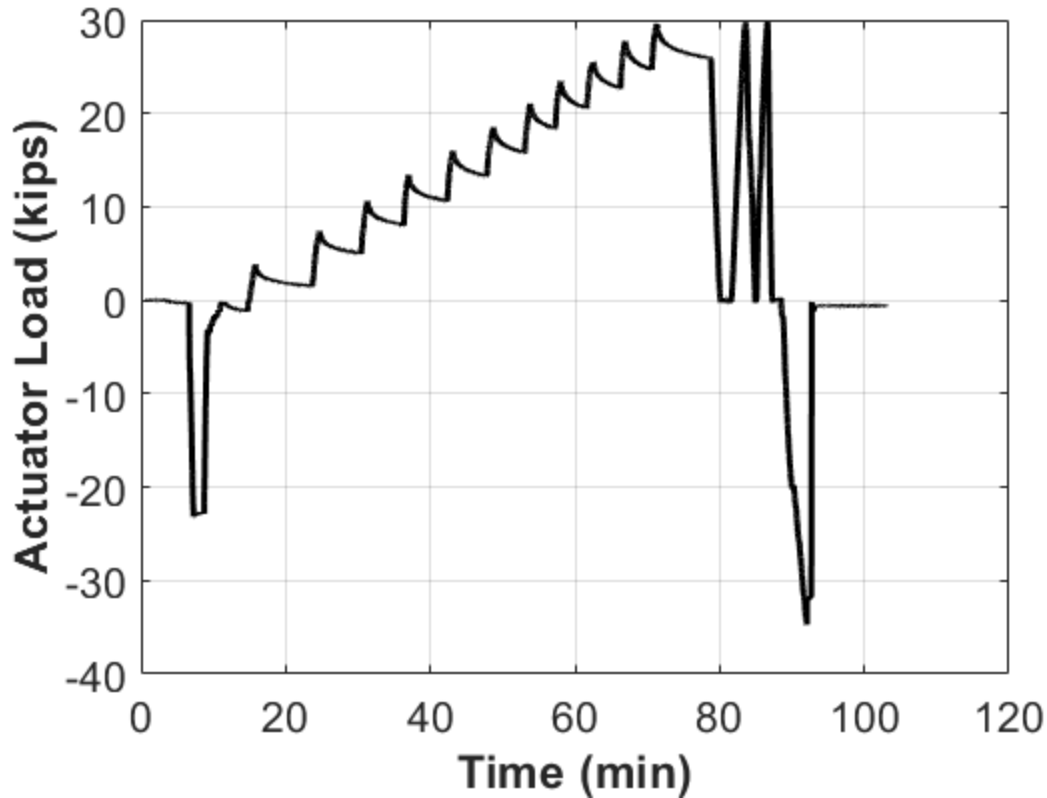


Figure 5.227. Concept D Static Testing Load Time History.

The end load versus vertical displacement at gridline E7 was presented in Figure 5.228, which shows the plot of load versus displacement of the static testing. The end displacement was about 0.2 inches when the specimen was at the zero-load level. The maximum deflection of the specimen at a 30kip load level was approximately 1.5 inches. The maximum load of the other two loading processes also reached the 30-kip load level. During the first loading process, the specimen started to keep creeping due to each displacement increment. The load dropped about 1 to 3 kips when the displacement increased. Therefore, once it was returned to the zero-load level, the displacement was at approximately 1.5 inches instead of 0.2 inches. The last two loading processes did not creep much due to the short load time. The structure stiffness from the last two loading processes was about 98 kips/in and ignored the creep behavior due to the first-time load process, which was relatively larger than the one from the first time.

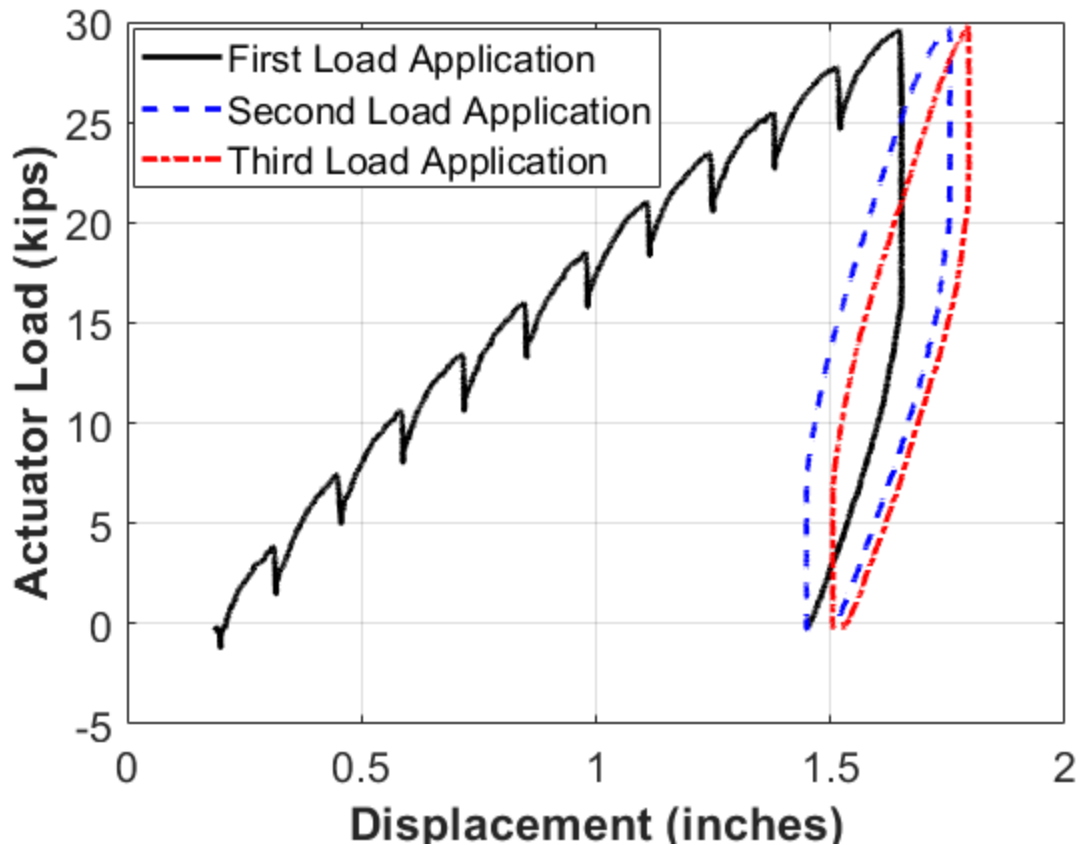


Figure 5.228. Concept D Static Testing Load-Displacement Plot.

The time history of the stresses on the Williams bars was analyzed, and Figure 5.229 shows the four Williams bars stresses during the static testing. Each location of the four strain gauges was described earlier. Due to the curing of the epoxy adhesive process, a little bit of stress loss happened. However, the bars were still very close to the desired design stress (106 ksi). The initial stresses increased by about 1 ksi because the specimen was lifted so that the concrete pedestal could be removed. The increase in stress at that time indicates that the NA was above the Williams bars. As the specimen was being pushed down, the compressive stresses induced by the actuator kept adding to the Williams bars since the NA of the specimen was still above the Williams bars. Therefore, the gradual reduction of stress in Williams bars was measured between approximately 2 to 6 ksi. The stresses had been reduced by 1 to 3 ksi in the Williams bars at the end of the static loading, which showed some losses due to the loading applications.

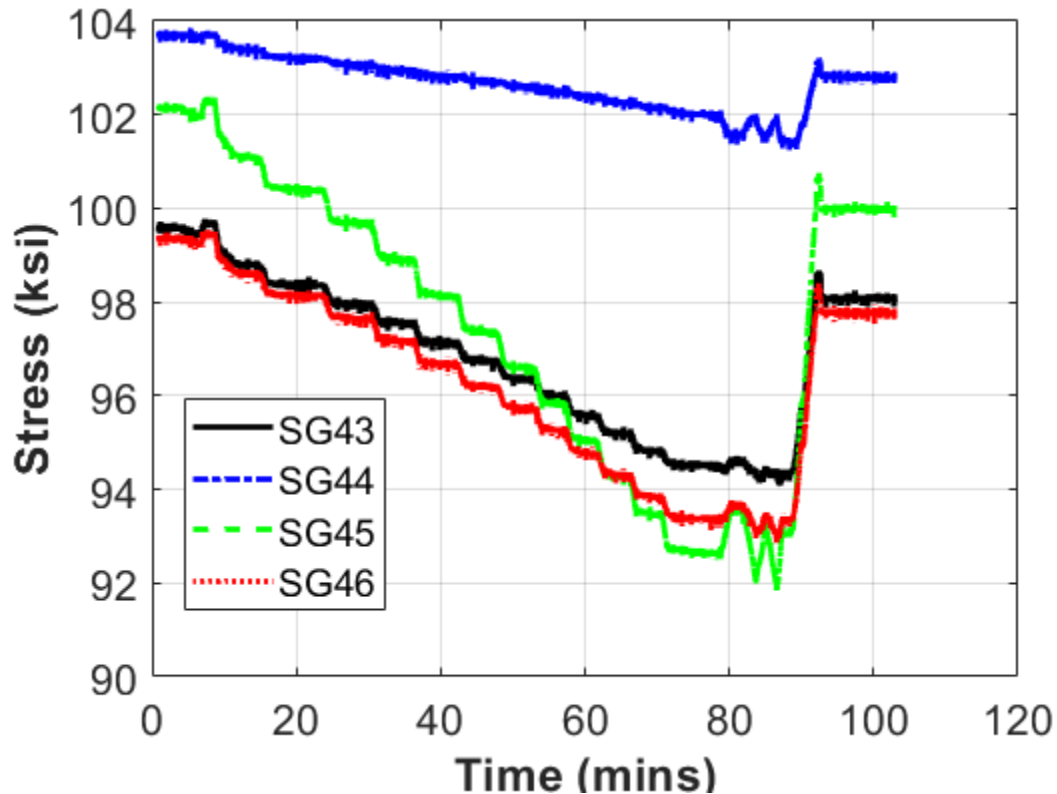


Figure 5.229. Concept D Static Testing Strain on Williams Bars.

The stresses in the precast concrete deck at gridline E1 were plotted. Figure 5.230 illustrates the stresses kept increasing during the first loading application. SG58 and SG60 were located 2 ft on either side of the longitudinal centerline of the specimen. SG59 was located on the centerline. At the zero-load level, the stresses in SG58 and SG59 were about -0.3 ksi, while SG59 was about -0.9 ksi. The stresses in SG58, SG59, and SG60 all remained in net compression during the whole loading application, which indicated that the compressive stresses induced by post-tensioned Williams bars were adequate for the HL-93 notional loading. The deck service-level behavior performed well at gridline E1.

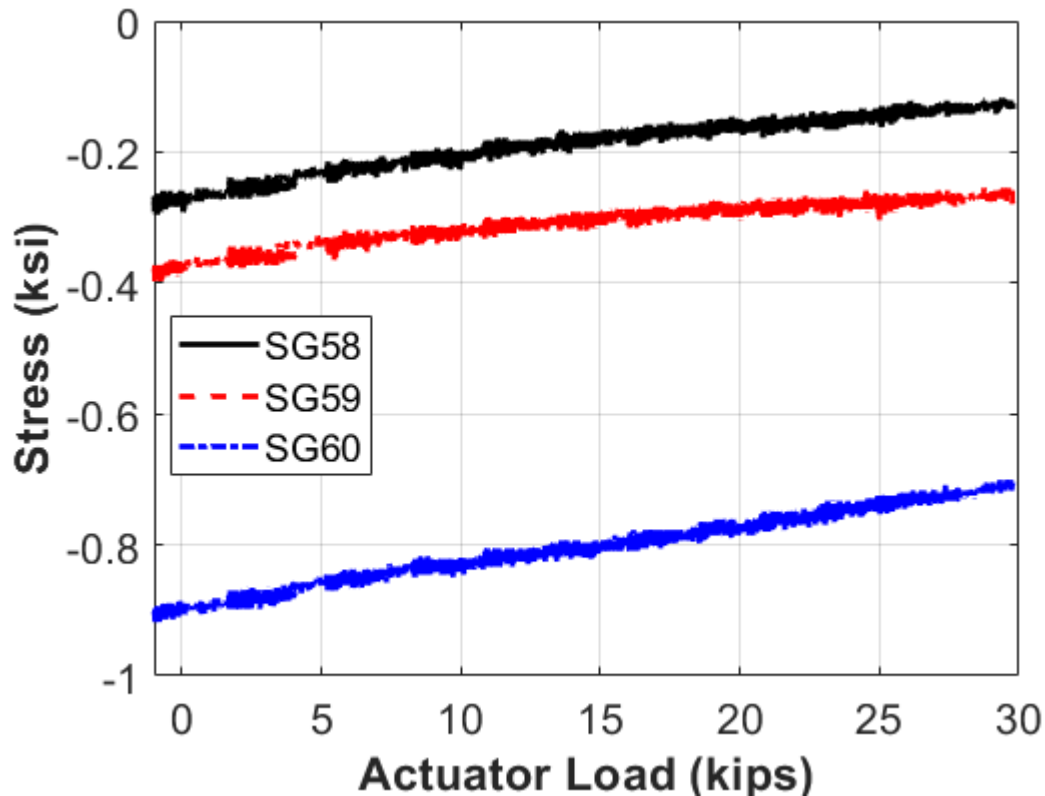


Figure 5.230. Concept D Static Testing Precast Concrete Stresses at E1.

The stresses in the precast concrete deck at gridline E2 are illustrated in Figure 5.231, which shows the stresses in SG61, SG62, and SG63. SG62 was located at the centerline, while SG61 and SG63 were located on either side of the centerline. The initial stress in SG62 was about -0.4 ksi, which was slightly higher than the stresses in SG61 and SG63. The initial stresses at E2 were also similar to stresses at E1 except for SG60 since they were both in the length of Williams bars. All the stresses in SGs were in net compression during the whole loading application. They all went to about -0.1 ksi, which demonstrated that the post-tensioned effect performed relatively well at gridline E2.

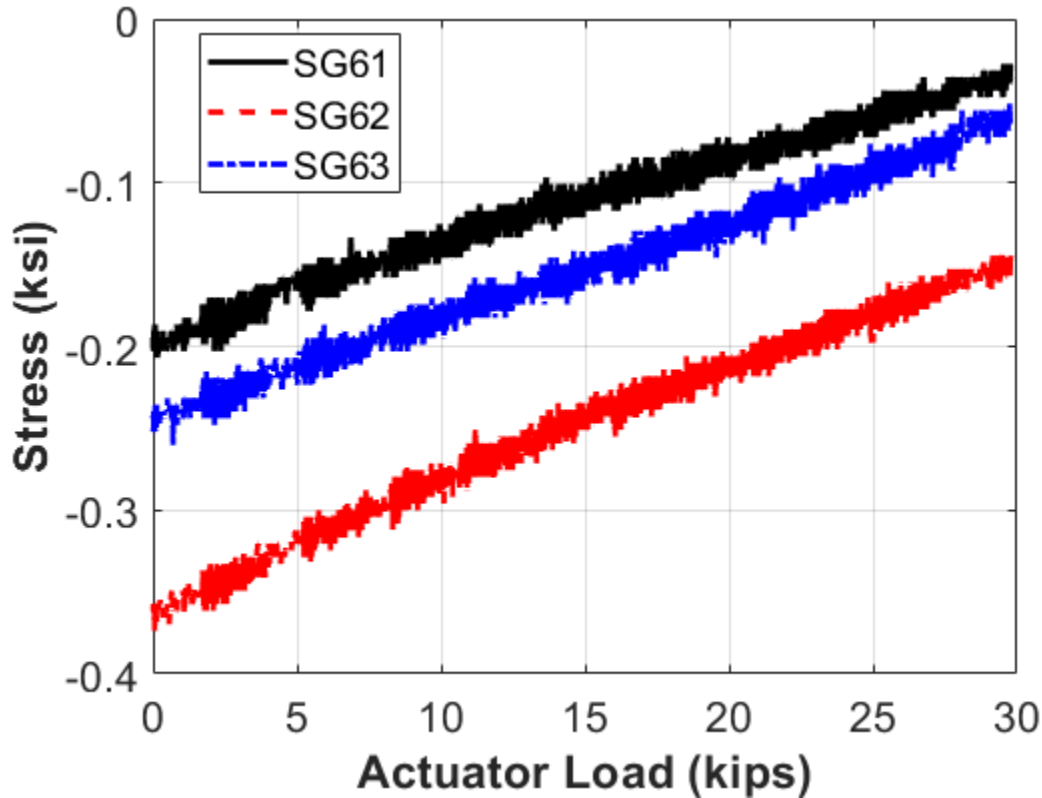


Figure 5.231. Concept D Static Testing Precast Concrete Stresses at E2.

The stresses in the precast concrete deck at gridline E3 were plotted. Figure 5.232 shows the stresses in SG65 and SG66. SG65 was located at the centerline, and SG66 was located at one side of the centerline. The initial stress in SG65 was about -0.7 ksi, which was slightly higher than the stresses in SG66. All the stresses in SGs at gridline E3 were in net compression during the whole loading application. The stress in SG66 reached about 0 ksi at a 30-ksi load level, which was a little bit higher than the stresses at E1 and E2 since these strain gauges were positioned beyond the length of Williams bars.

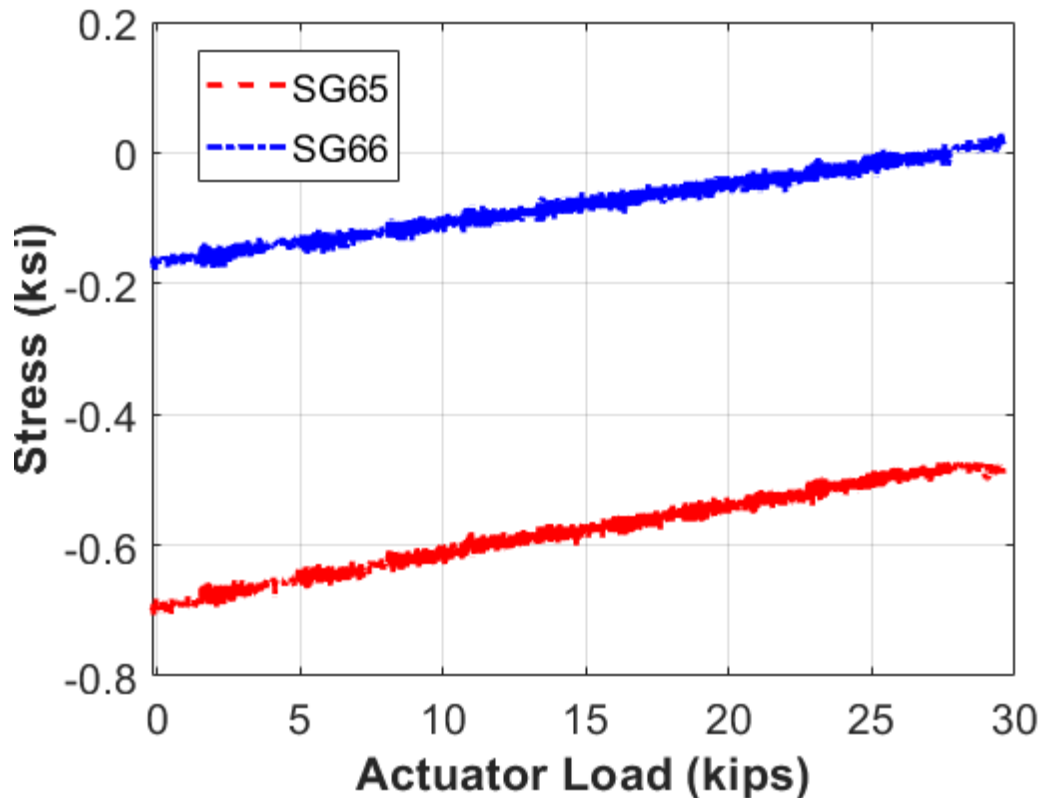


Figure 5.232. Concept D Static Testing Precast Concrete Stresses at E3.

The stresses in the rebar at gridline E2 were plotted. Based on the instrumentation setup shown before, the strain gauges were also attached to the rebar embedded in the precast concrete deck. Figure 5.233 presents the stresses in SG10 and SG12 versus the actuator load. SG10 and SG12 were located 2 ft on either side of the centerline. The initial stresses in these strain gauges were negative values because of the post-tension effect. The stresses remained in net compression during the whole static loading. However, the overall stresses of the rebar were not relatively high since the specimen kept the relative full composite behavior and no major cracks occurred for the concrete deck surface of the two precast units except for the adhesive joint between the two precast units. Another possible reason for the relatively low stresses might be that the reinforcement was not developed through the adhesive joint between the two units. The precast deck over 5-kip load level did not behave as continuous at the adhesive joint. Therefore, it did not transfer much of the tensile force through reinforcement in the deck.

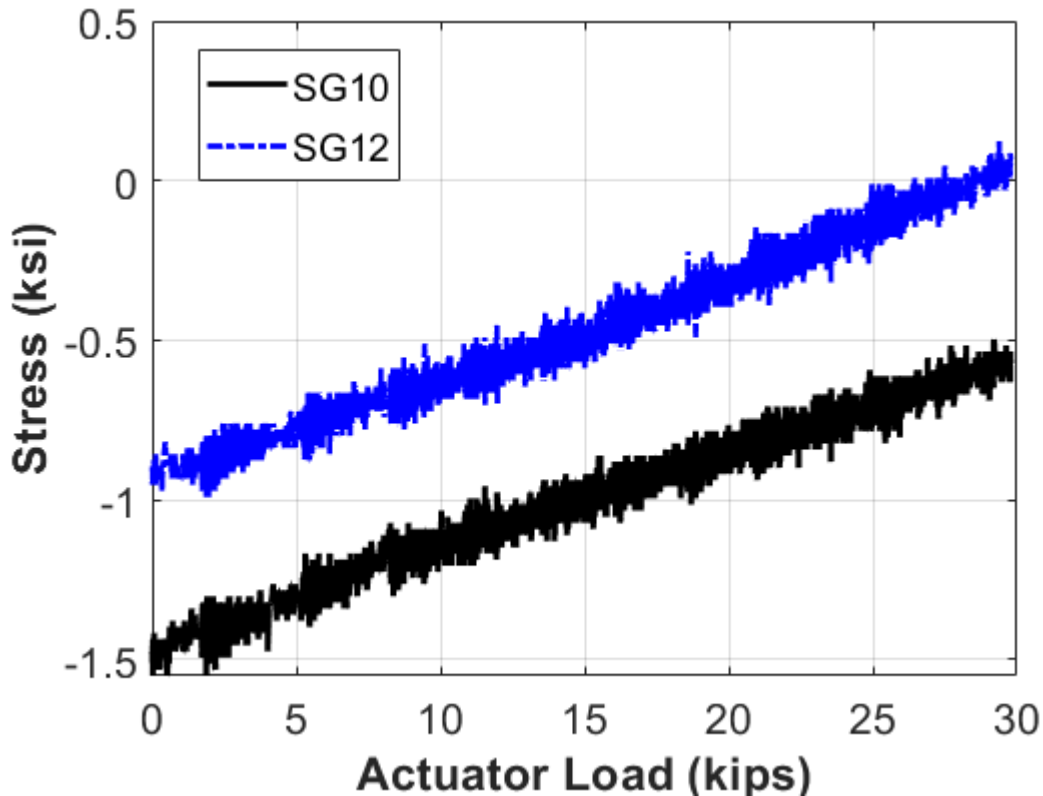


Figure 5.233. Concept D Static Testing Rebar Stresses at E1.

The stresses in the rebar at gridline E3 are depicted in Figure 5.234, which provides the stresses in SG16, SG17, and SG18 versus the actuator load. SG16 and SG18 were located 2 ft on either side of the centerline. SG17 was located at the centerline. The initial stresses in SG16 and SG18 were about -0.1 ksi. The initial stress in SG17 was about 0.1 ksi, which was above the net compression since the SGs at E3 were positioned beyond the length of Williams bars. Therefore, the pos-tensioned Williams bars did not produce much compressive stress in rebar at E3. The stresses in rebar at E3 were in tension during the static loading application. The rebar stress increased by about 1 ksi at E3 when the load was at the 30-kip load level.

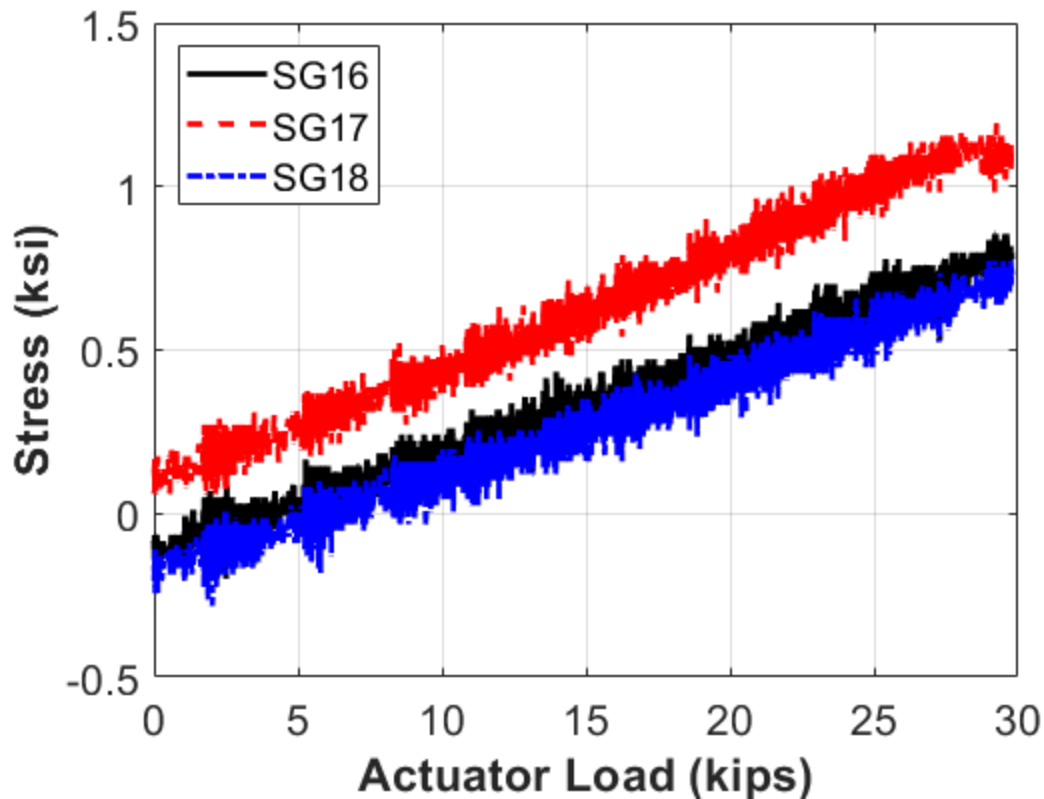


Figure 5.234. Concept D Static Testing Rebar Stresses at E3.

The stresses in the steel beam at gridline E1 were plotted, and Figure 5.235 presents the stresses in SG31, SG32, SG34, SG35, SG36. SG31 and SG32 were located on the top flange. SG34 was located at the bottom portion of the web. SG35 and SG36 were located at the bottom flange. All the strain gauges were under compression during the whole static loading application. SG31 and SG32 showed little change, while SG34 went into slightly more compression. SG35 and SG36 showed a more significant increase in compressive stresses. SG31 and SG32 started close to zero stress, while SG33 and SG34 started with a large offset of approximately 2 to 3 ksi because of the PT effect.

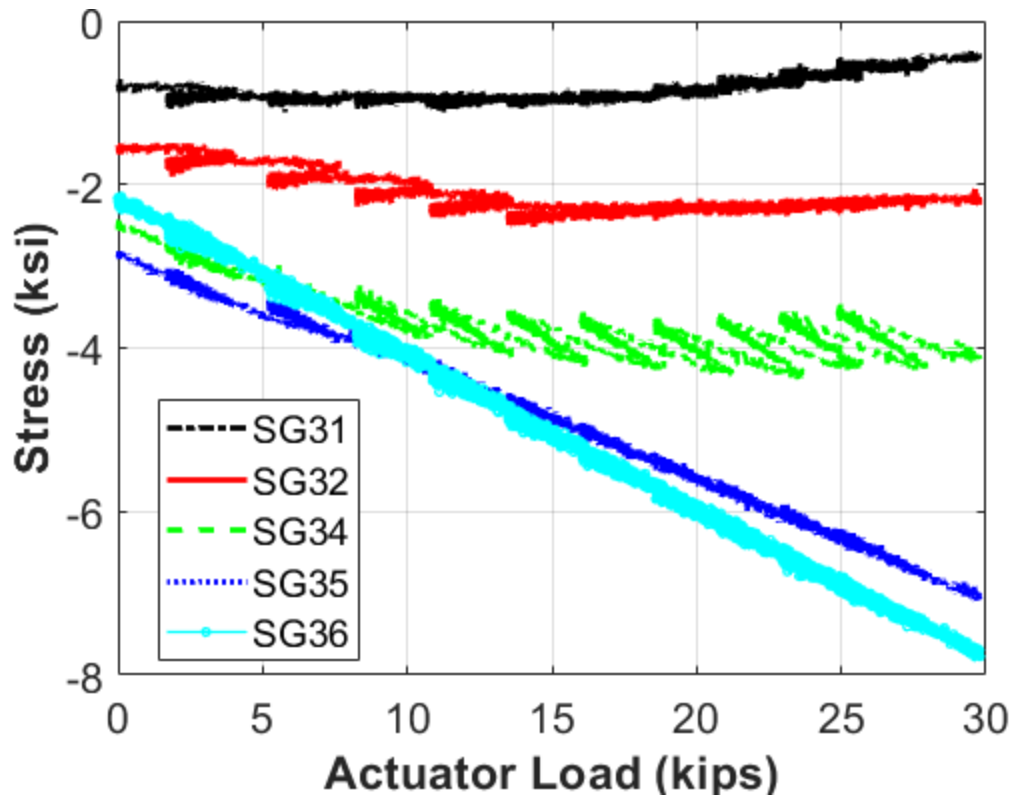


Figure 5.235. Concept D Static Testing Steel Beam Stresses at E1.

5.10.2.3. Concept D Cyclic Testing

A total of 154,800 cycles were run during the cyclic testing. The first 3,600 cycles were run at a relatively lower displacement to verify the corresponding HL-93 notional loading range. After these cycles, the displacement range was adjusted to the HL-93 notional loading range, which is 0.5 inches down to 0.1 inches up. Table 5.13 illustrates the overview of the cyclic loading process.

Table 5.13. Concept D Cyclic Testing Ranges.

Day	Number of Cycles	Load Rate (Hz)	Displacement Control Range
1	3,600	0.25	(-0.40") to (+0.05")
2	22,500	0.25	(-0.50") to (+0.10")
3	22,500	0.25	(-0.50") to (+0.10")
4	63,000	0.25	(-0.50") to (+0.10")
5	43,200	0.25	(-0.50") to (+0.10")
Total	154,800		

During the cyclic test, only one minor crack formed at the top deck surface of the active end, which was about 7 ft away from the adhesive joint. No other visible cracks were observed. The strain in the Williams bars remained steady at around 3400 microstrain, and none of the other gauges recorded any massive changes during the cyclic testing process.

5.10.2.4. Concept D Ultimate Testing

For Concept D ultimate testing, a 50-ton ram was used to test the specimen because the required load capacity was larger than the 55-kip capacity. The stroke length was also a concern for Concept D based on the static testing behavior because concrete deck creep behavior occurred during the static testing. This ram was placed on the same frame (with the header beam lowered) and was put into the same position on the beam that the 55-kip actuator was in. Figure 5.236 shows the view of the ram setup for Concept D.

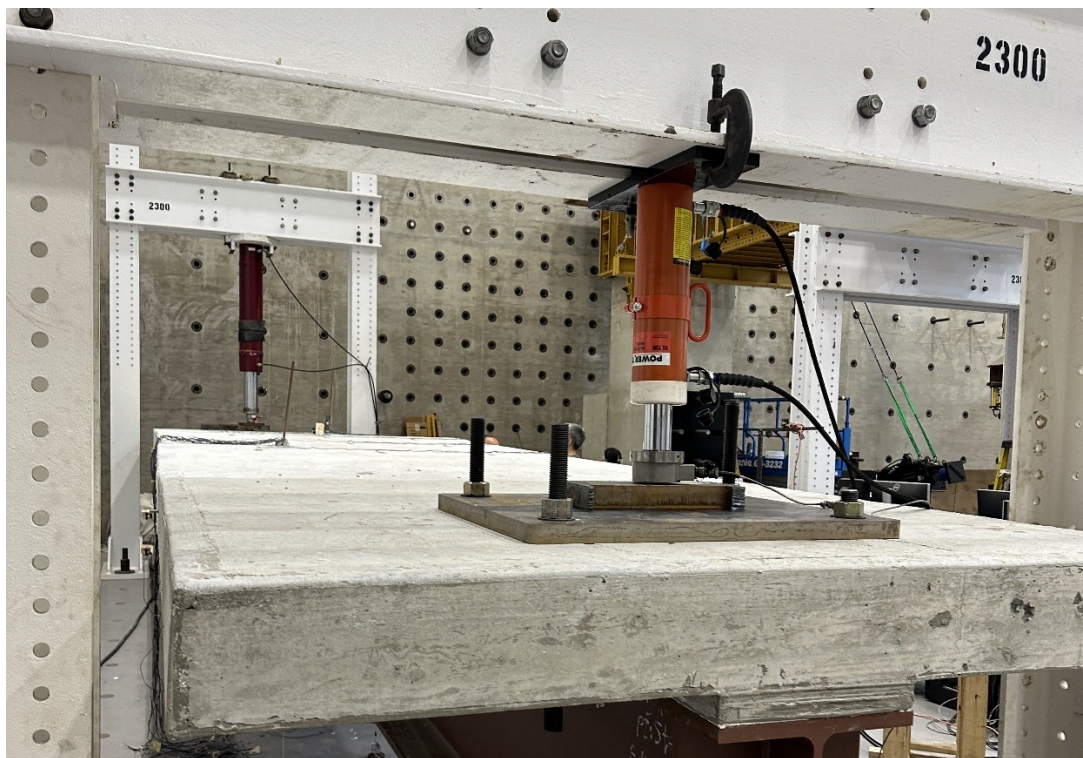


Figure 5.236. 100-kip Ram Setup for Concept D.

This 100-kip ram was not connected to the specimen since it only pushed down on the concrete deck and did not pull up. In order to lift the specimen and remove the concrete pedestal, a through-hole jack was placed under the bottom flange of the steel beam at gridline E6, and the

specimen was jacked up. The displacement of the specimen was still measured by the two string pots attached to the concrete deck at E7.

The vertical displacement at E7 time history was plotted, and the ultimate loading application process lasted about 2 hours. Figure 5.237 shows the displacement time history during this process. The displacement data were taken as the average of the two string pots on gridline E7, which were SP9 and SP10. The specimen was pushed down in 0.125-inch increments through displacement control. The specimen was inspected after each increment to check for signs of damage. A maximum displacement of 5.8 inches was achieved, after which point the specimen was brought back to the zero-displacement level.

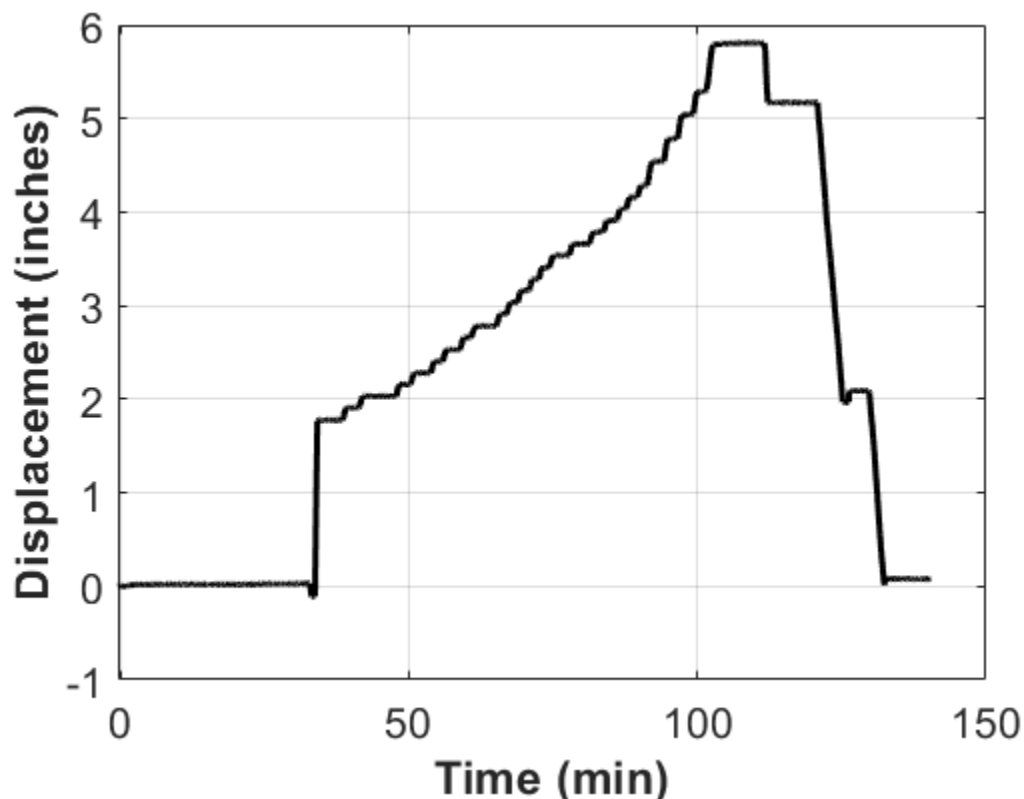


Figure 5.237. Concept D Ultimate Testing Displacement Time History.

The vertical displacement at E7 versus the actuator load is depicted in Figure 5.238, which shows the load-displacement relationship during the entire loading application. The specimen was self-supporting after removing the support pedestal under the steel beam, so there was an initial displacement due to the specimen's self-weight. Therefore, the plot started with an initial displacement without an increase in force, which was about 1.8 inches. The plot shows that there

is a linear relationship between the load and displacement up to approximately 35 kips, or approximately 2.7 inches of displacement. The specimen relaxed slightly after that point and started to lose load after each displacement increment. The displacement increment changed from 0.125 inches to 0.25 inches to minimize the effect of creep behavior. The specimen's stiffness started to lessen after 35-kip load level, indicated by the change in slope of the following plot. A maximum load of 52 kips was reached, which corresponded to 5 inches of total deflection. At this point, the specimen was inspected for signs of damage; one crack was forming on the concrete deck surface, and several cracks had formed on the side surfaces of the precast concrete deck drop panel. There were no loud bangs during the ultimate testing. After all the signs of damage were recorded, the load was slowly taken off the specimen. Once the load reached zero, the overall displacement of the specimen was approximately 5.1 inches, indicating that damage to the specimen had occurred (primarily in the concrete drop panel).

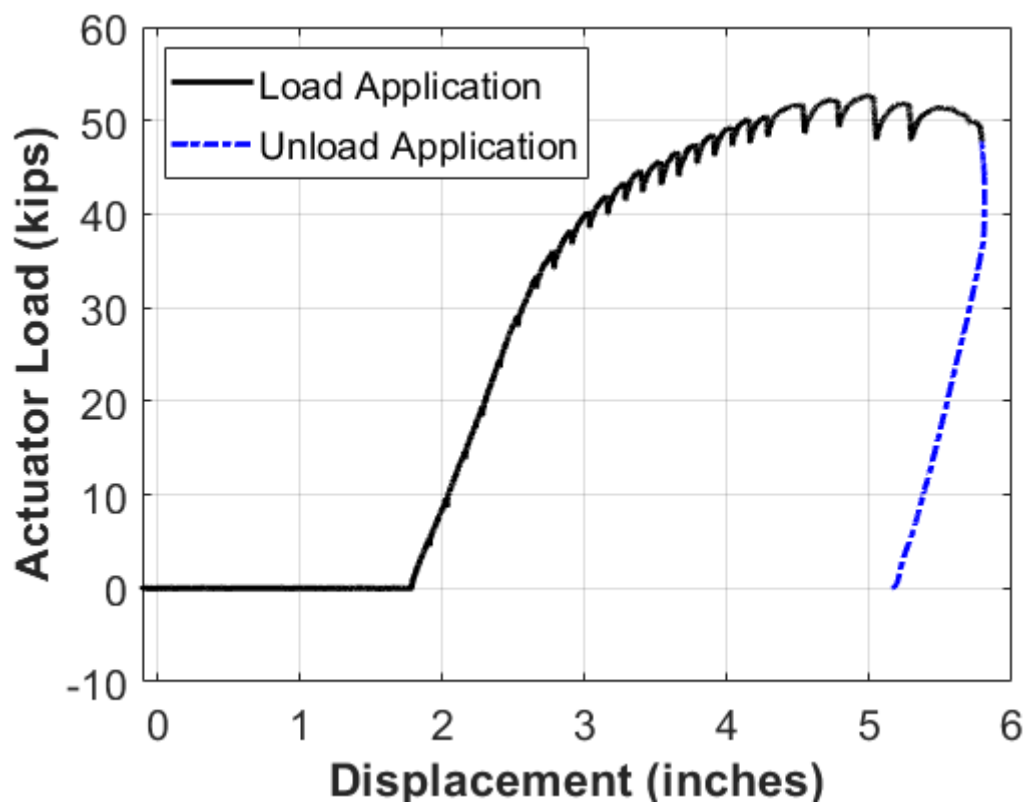


Figure 5.238. Concept D Ultimate Testing Load-Displacement Plot.

The stresses on the four Williams bars during the ultimate testing are presented in Figure 5.239. SG43 is on the north outside Williams bar. SG44 was on the north inside Williams bar. SG45 was on the south inside Williams bar. SG46 was on the south outside Williams bar. The stresses

in the four Williams bars started close to the desired design value (105 ksi), which was equal to 70 percent of the stress of the theoretical ultimate strength. There were some stress losses during the static testing and the cyclic testing. The post-tensioned stresses dropped about 3 to 7 ksi due to the removing support pedestal process. The specimen end was jacked up and there were some compressive stress losses. The stresses of SG43, SG44, and SG46 were relatively stable before 80 minutes. After about 80 minutes, once the stresses of these three Williams bars started increasing, the specimen's NA dipped below the level of the bars. When the load was taken off the specimen, the stresses in the Williams bars still dropped back to the original stresses, which indicated that the Williams bars had not yielded.

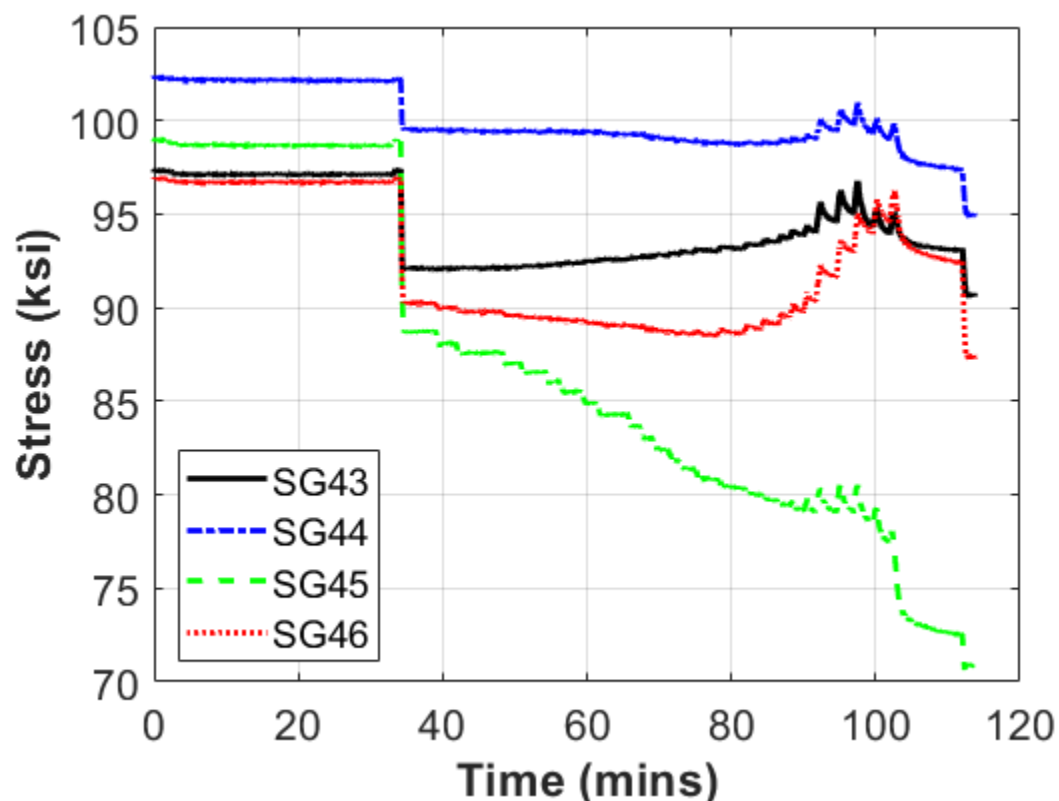


Figure 5.239. Concept D Ultimate Testing Stress on Williams Bars Time History.

Figure 5.240 presents the four William bars' stresses during the ultimate loading application. The strain gauge locations were mentioned earlier. SG44 and SG46 decreased a little bit until an actuator load of approximately 46 kips was reached. SG45 dropped about 10 percent in compressive stresses during the loading process. All of the stresses increased when the load was about 46 kips. SG45 may have been affected by some friction losses during the ultimate testing and decreased by about 20 percent in compressive stresses.

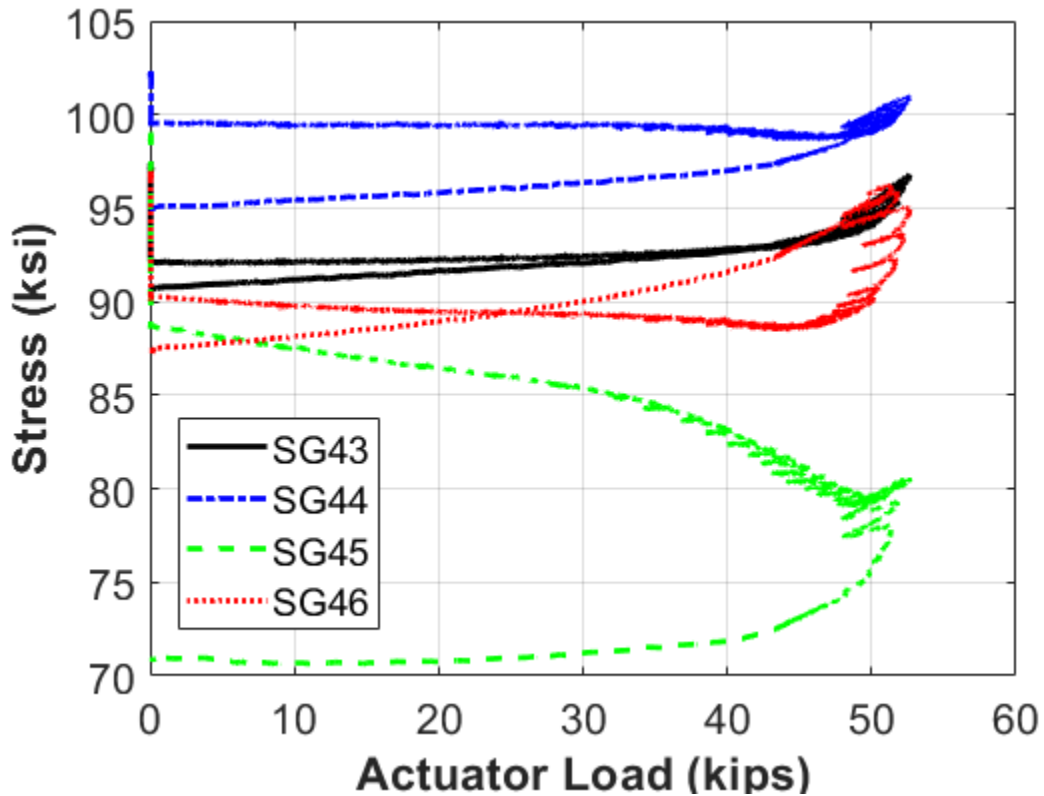


Figure 5.240. Concept D Ultimate Testing Stress on Williams Bars -Load Plot.

The stresses on the surface of the precast concrete deck at gridline E1 versus the actuator load are depicted in Figure 5.241, which shows the stresses in SG58, SG59, and SG60. SG58 and SG60 were located 2 ft on either side of the centerline. SG59 was located on the longitudinal centerline. All the strain gauges were in net compression during the whole ultimate testing. There was a jump in stresses at the zero-load level since the specimen was self-supporting and the top surface of the specimen was going into tension. There was not a stress jump after the actuator load increased since no cracks formed near gridline E1.

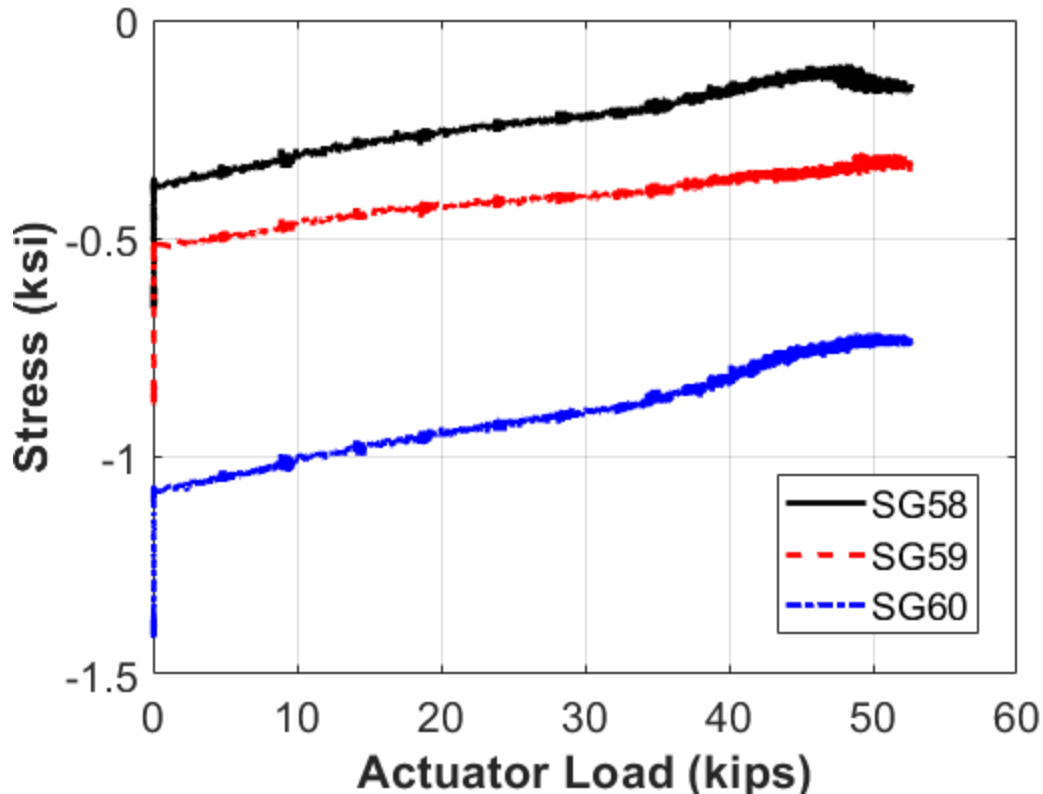


Figure 5.241. Concept D Ultimate Testing Precast Concrete Deck Stresses at E1.

The stresses on the surface of the precast concrete deck at gridline E2 versus the actuator load are depicted in Figure 5.242, which shows the stresses in SG61, SG62, and SG63. SG61 and SG63 were located 2 ft on either side of the centerline. SG62 was located on the longitudinal centerline. All the strain gauges were in net compression during the whole ultimate testing. SG62 captured the stress increase quickly during the last several displacement increments.. Similar to the stresses at E1, the stresses at E2 exhibited an initial jump of approximately 0.3 ksi due to the specimen's self-supporting behavior. The compressive stresses at E2 were comparable to those at E1, as both locations were within the length of the Williams bars.

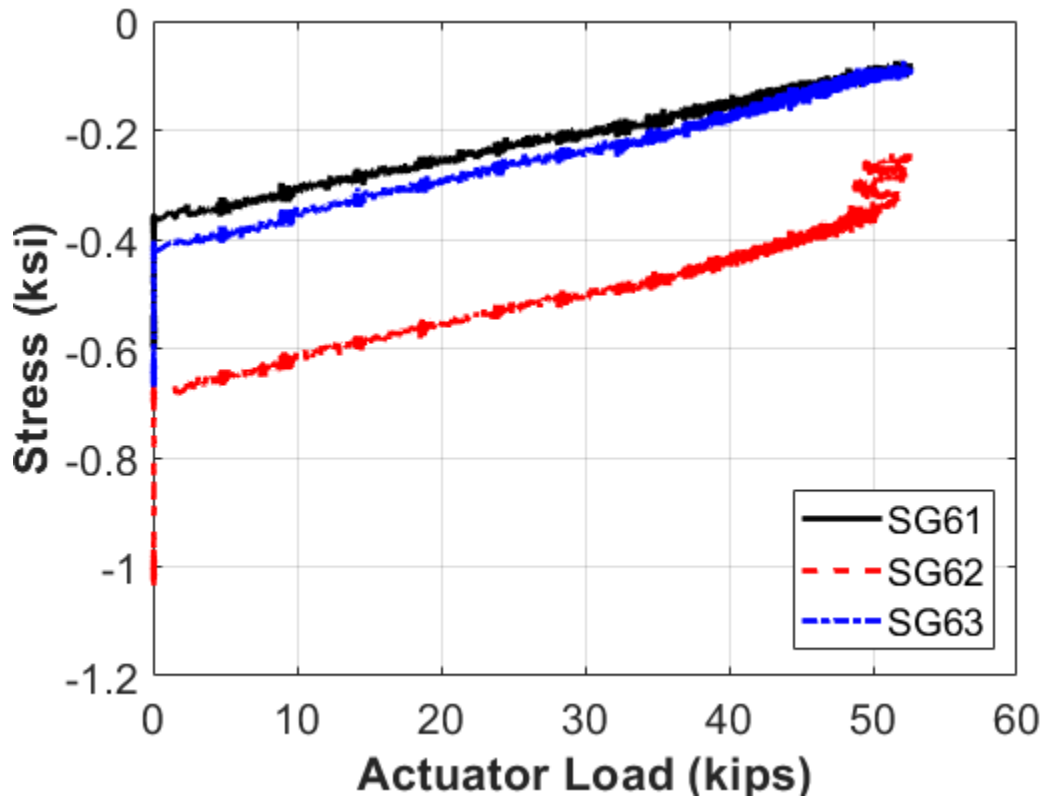


Figure 5.242. Concept D Ultimate Testing Precast Concrete Deck Stresses at E2.

The stresses in longitudinal rebar at gridline E1 versus the actuator load are depicted in Figure 5.243, which shows the stresses in SG10 and SG12. SG10 and SG12 were located 2 ft on either side of the centerline. All strain gauges remained in net compression during the whole ultimate testing. After the specimen was lifted off the pedestal and was left self-supporting, a stress jump of about 1 ksi occurred. As the test progressed, all gauges showed an increase in compression fairly linearly up to about 35 kips. No new cracks were observed to form in this area at this load level, so it is unknown what caused the noise to occur in the data past 40 kips. Similar to the static testing, the stresses were still relatively low. It is possible that the cracking of the adhesive joint during the ultimate testing caused the low stresses in reinforcement.

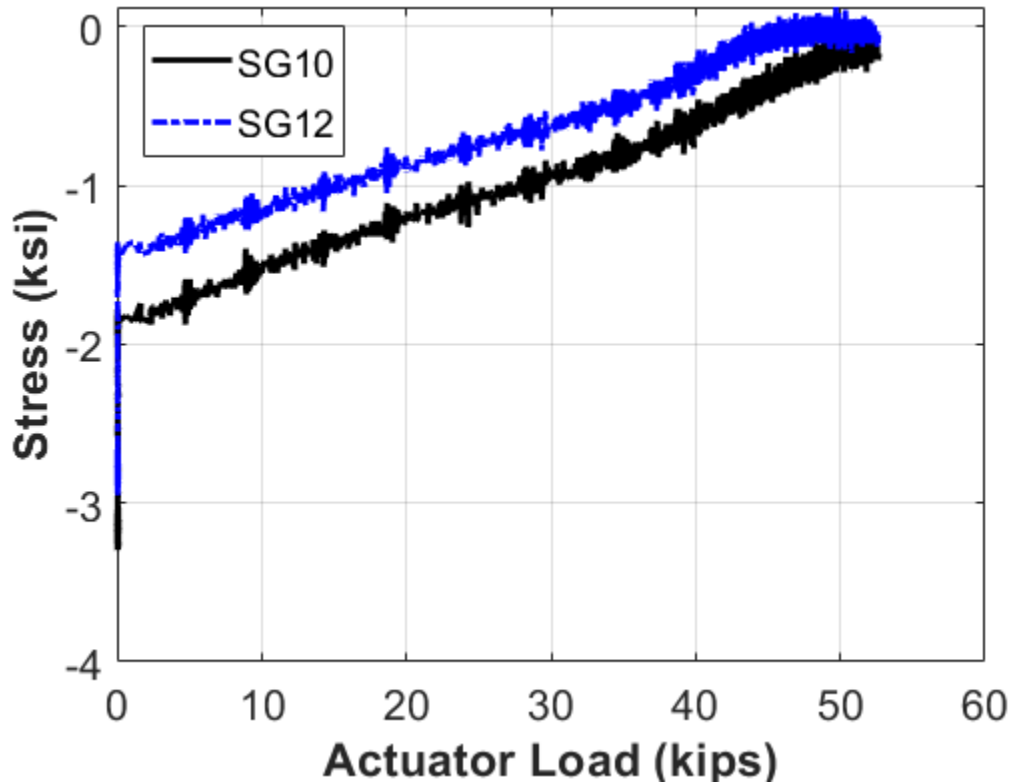


Figure 5.243. Concept D Ultimate Testing Rebar Stresses at E1.

The stresses in longitudinal rebar at gridline E2 versus the actuator load are depicted in Figure 5.244. It shows the stresses in SG13, SG14, and SG15. SG13 and SG15 were located 2 ft on either side of the centerline. SG14 was located at the centerline. Similar to the stresses at E1, the stress jumped at the beginning because of the support pedestal removal. SG13 and SG15 were in net compression through the ultimate testing. The stress in SG14 increased rapidly after the 35-kip load level, and the structure stiffness also decreased at this moment. A minor crack may have developed within the concrete deck at the SG14 location, leading to increased tensile

force being carried by the reinforcement.

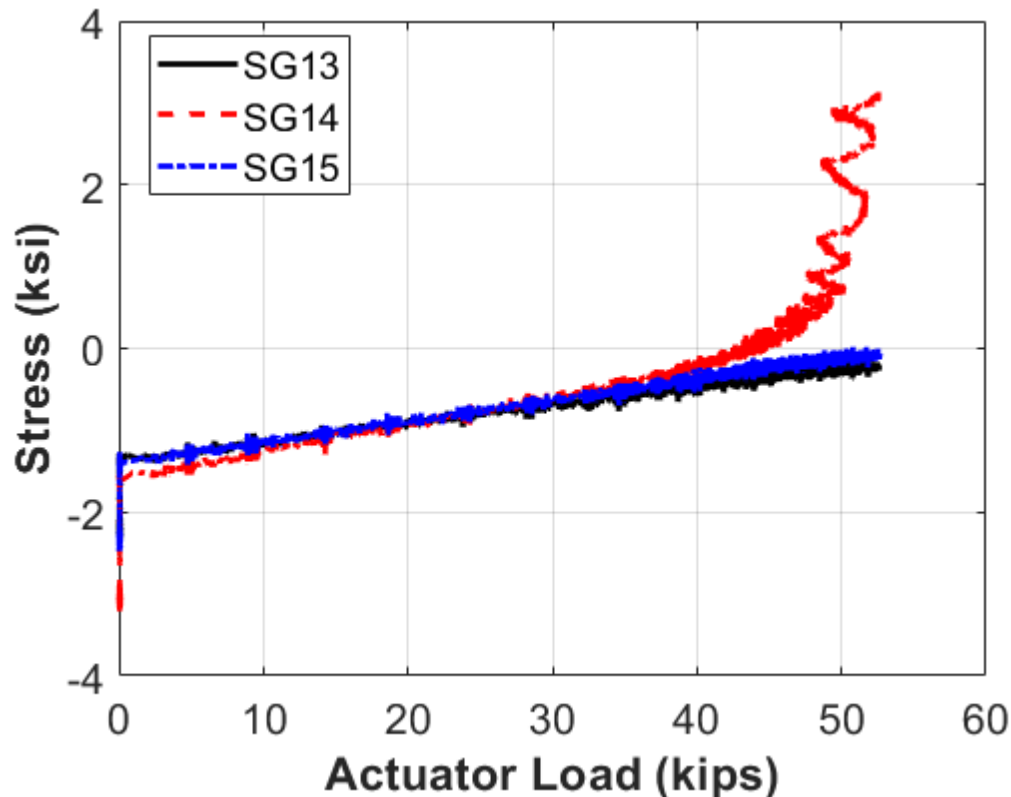


Figure 5.244. Concept D Ultimate Testing Rebar Stresses at E2.

The stresses in longitudinal rebar at gridline W1 versus the actuator load were plotted and shown in Figure 5.245, which depicts the stresses in SG7 and SG8. SG7 was located at the centerline. SG8 was located 2 ft to one side of the centerline. All strain gauges were maintained in net compression during the whole ultimate testing. The stresses had a jump at the beginning because of the self-supporting of the specimen. After that, no crack formed near this area, and the stresses increased at a stable rate.

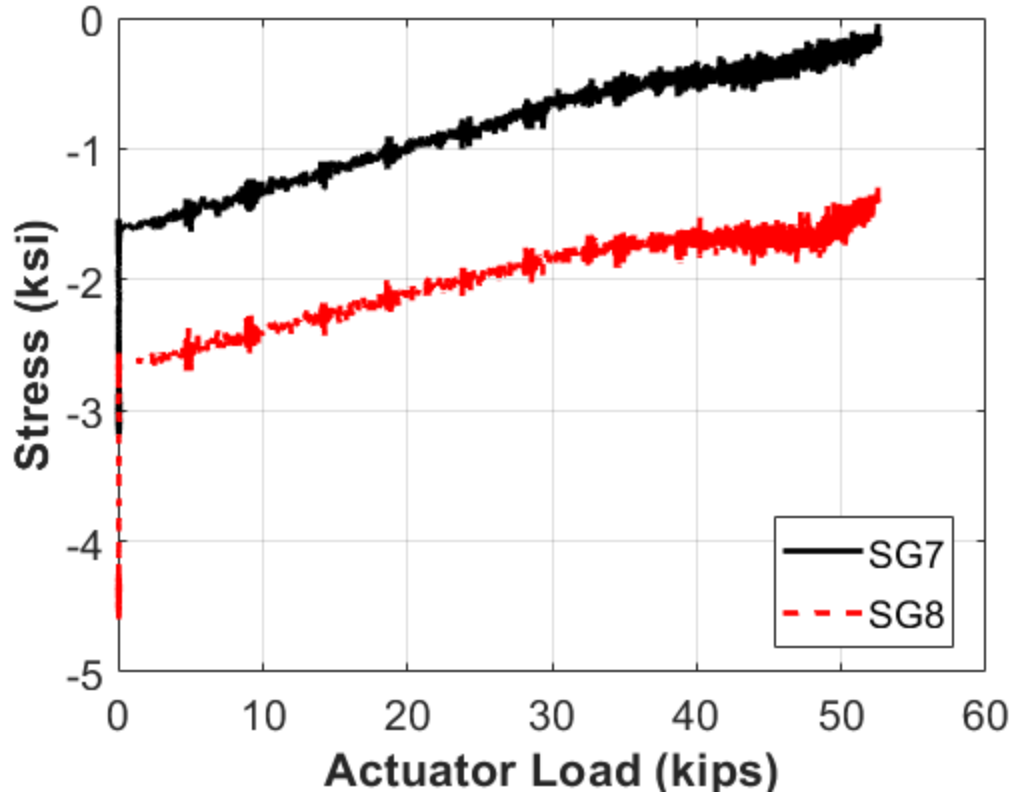


Figure 5.245. Concept D Ultimate Testing Rebar Stresses at W1.

The stresses in longitudinal rebar at gridline W2 versus the actuator load were plotted. Figure 5.246 shows those stresses in SG5 and SG6. SG5 was located at the centerline. SG6 was located 2 ft to one side of the centerline. The stresses in SG5 and SG6 were in net compression during the ultimate testing. All the gauges exhibited a small jump in stress at 42 kips, which is likely due to microcracks. The initial jump for the stresses was due to the self-supporting of the specimen at the beginning. All of the stresses were also relatively low—between -3.5 ksi and 0 ksi. It is possible that the cracking of the adhesive joint during the ultimate testing caused the low stresses in reinforcement.

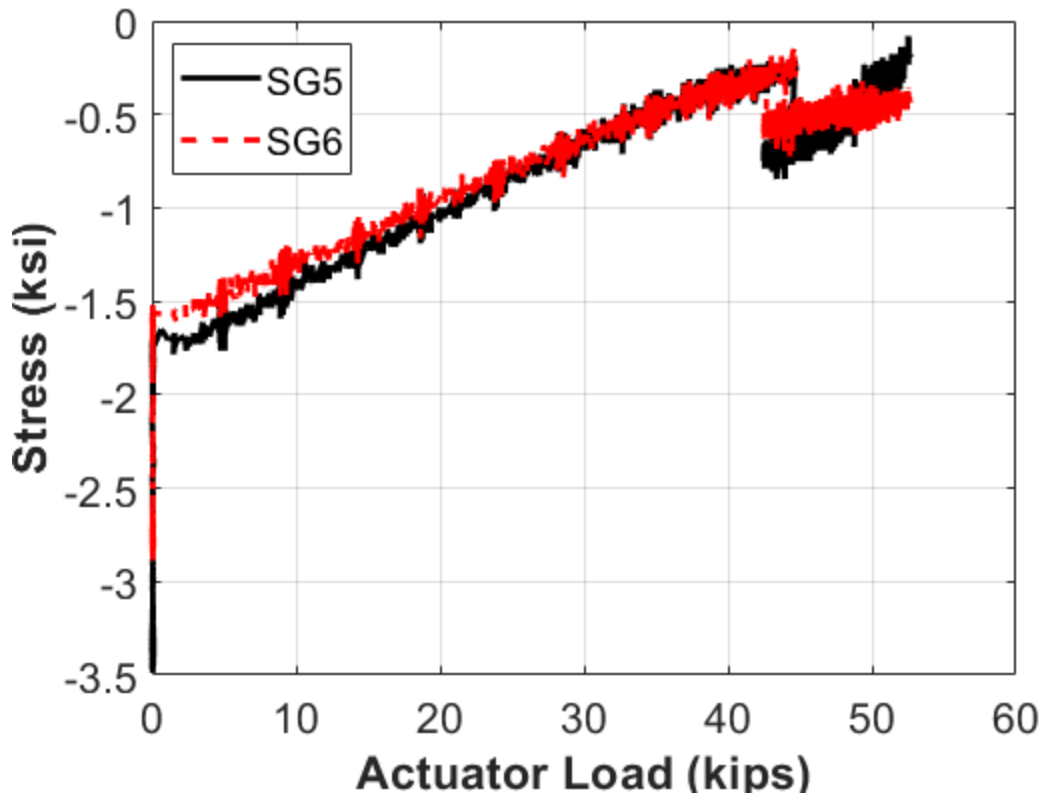


Figure 5.246. Concept D Ultimate Testing Rebar Stresses at W2.

The stresses in the structural beam at gridline E1 are depicted in Figure 5.247, which presents the stresses in SG31, SG32, SG34, SG35, and SG36. SG33 was removed from the plot because it showed faulty data. SG31 and SG32 were located on the top flange. SG34 was located on the bottom portion of the web. SG35 and SG36 were located on the bottom flange. All the strain gauges were in net compression except for SG31 during the whole ultimate testing. SG31 and SG32 showed slightly increasing stresses. The stress in SG34 started compress, and then the compressive stress was released a little bit after the 40-kip load level, probably because the specimen kept creeping under higher load levels, and the section behaved as a relatively low partial composite section. The NA went down. SG35 and SG36 showed a large increase in compression, approaching 10 ksi of compression by the end of ultimate testing, which is still well below the yield strength of 50 ksi, indicating that the steel still had more capacity even at the maximum load level.

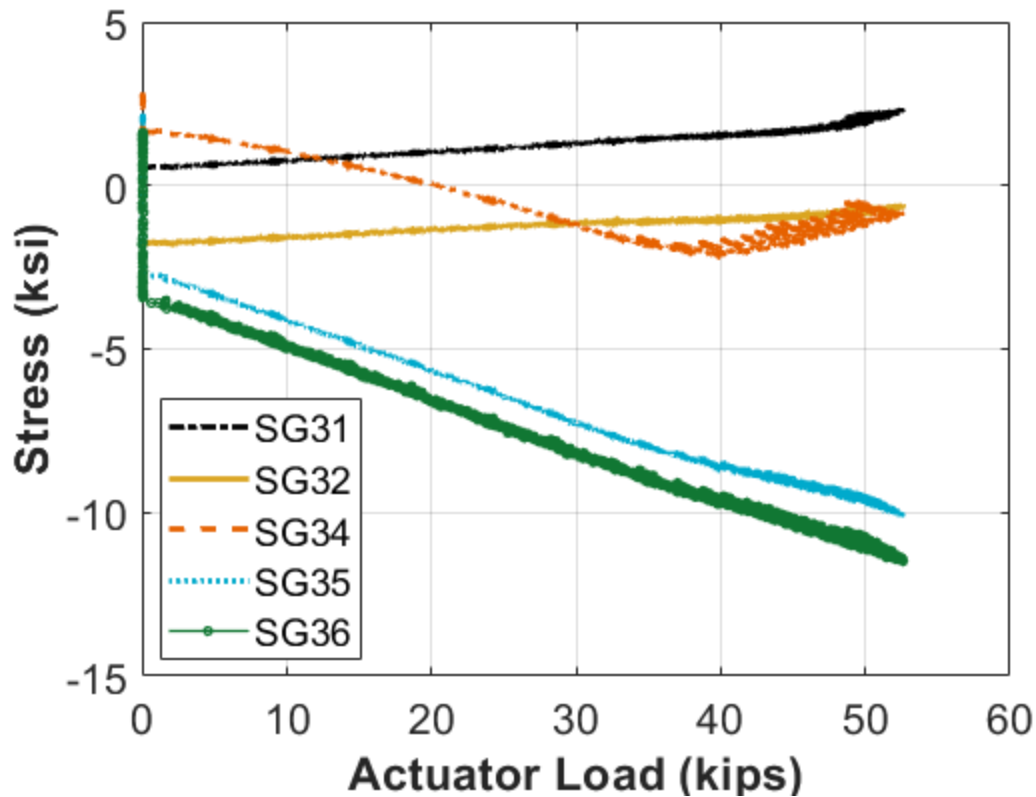


Figure 5.247. Concept D Ultimate Testing Steel Beam Stresses at E1.

The structural strain profiles at different cross sections were extracted and plotted. Figure 5.248 illustrates Concept D's ultimate testing of steel beam stresses at E1. Structural strain profiles were captured at different cross sections and are shown in subsequent figures for various gridlines under actuator loads of 28 and 52 kips. Figure 5.249 details strain at gridline E2, Figure 5.250 at W1, and Figure 5.251 at W2. The NA at gridline E1 varied slightly as the testing progressed. At 28 kips, the NA was approximately 28 inches above the bottom flange, but at the maximum load that was reached (52 kips), the NA was slightly lower—approximately 26 inches. The NA at gridline E2 varied similar to the NA at E1. At 28 kips, the NA was approximately 30 inches above the bottom flange, but at 52 kips, it dropped to around 27 inches. Similar results were seen at gridlines W1 and W2, with the NAs being close at W1 and farther apart at W2. The composite NA of the cracked section was calculated as being 18.1 inches above the bottom of the specimen.

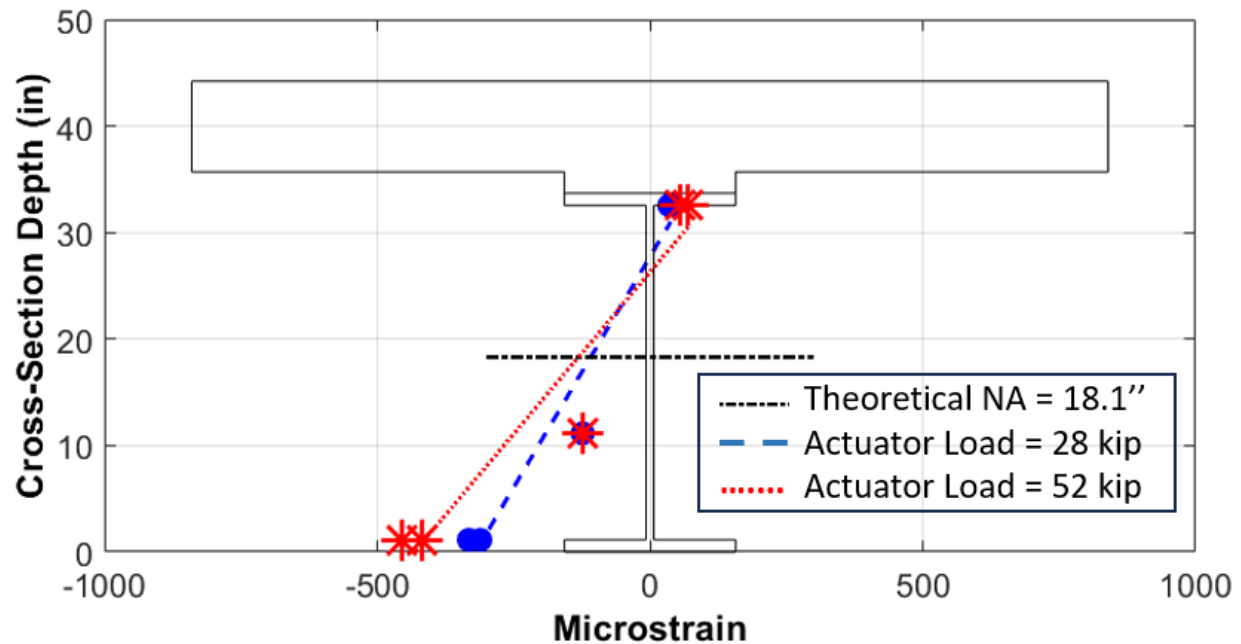


Figure 5.248. Concept D Ultimate Testing Structural Strain Profile at E1.

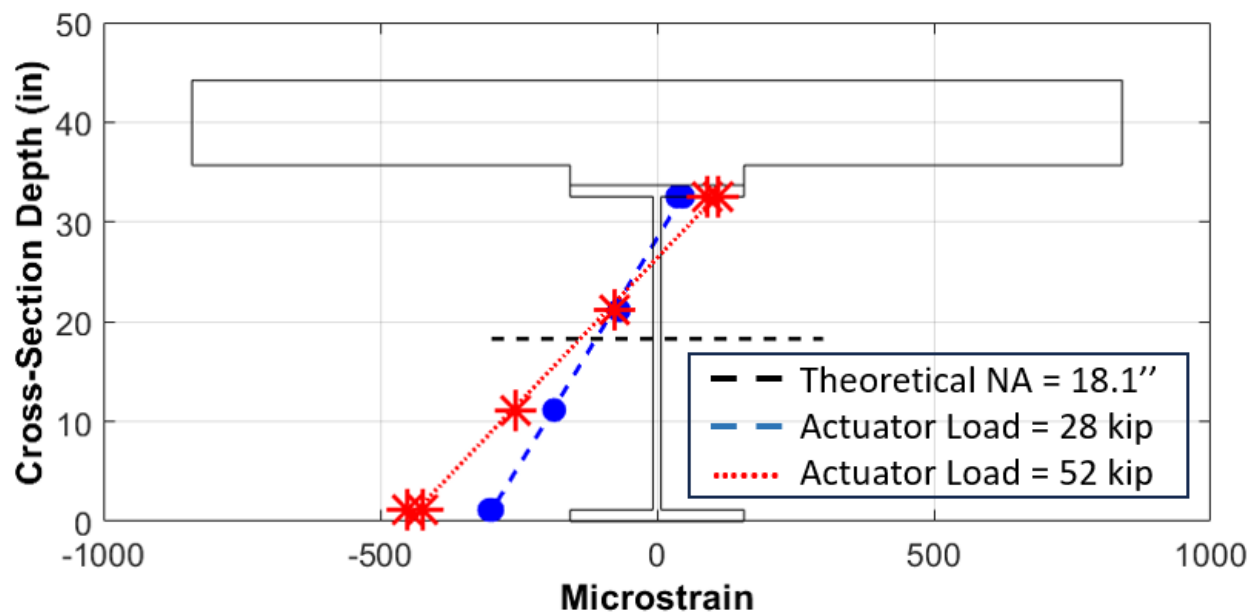


Figure 5.249. Concept D Ultimate Testing Structural Strain Profile at E2.

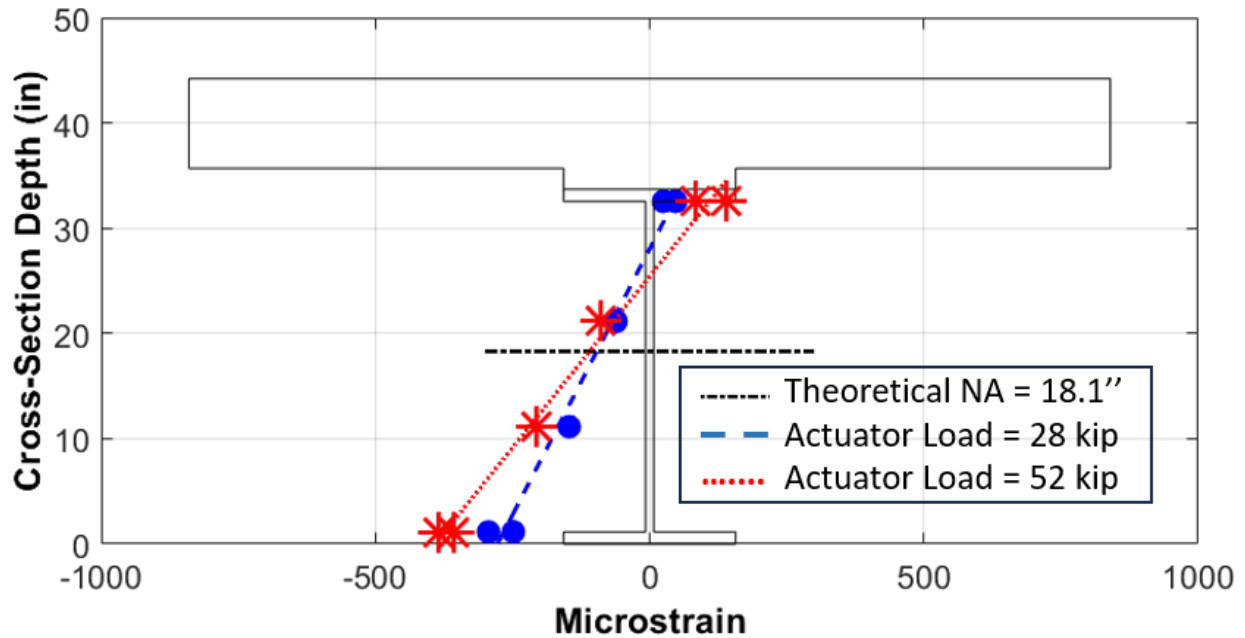


Figure 5.250. Concept D Ultimate Testing Structural Strain Profile at W1.

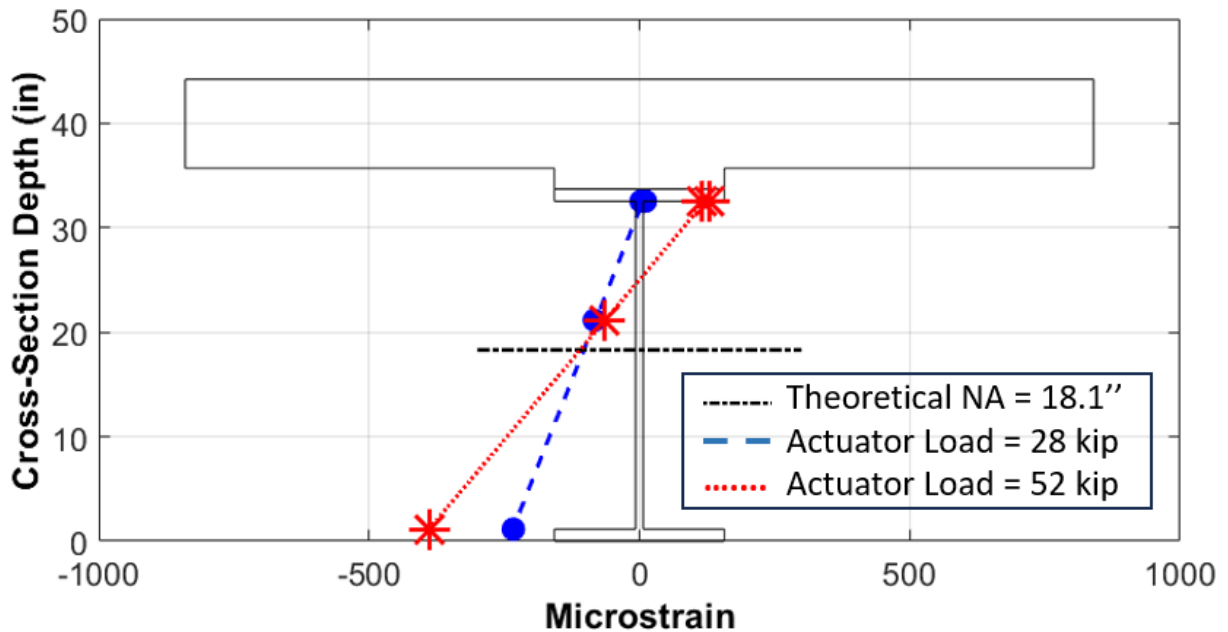


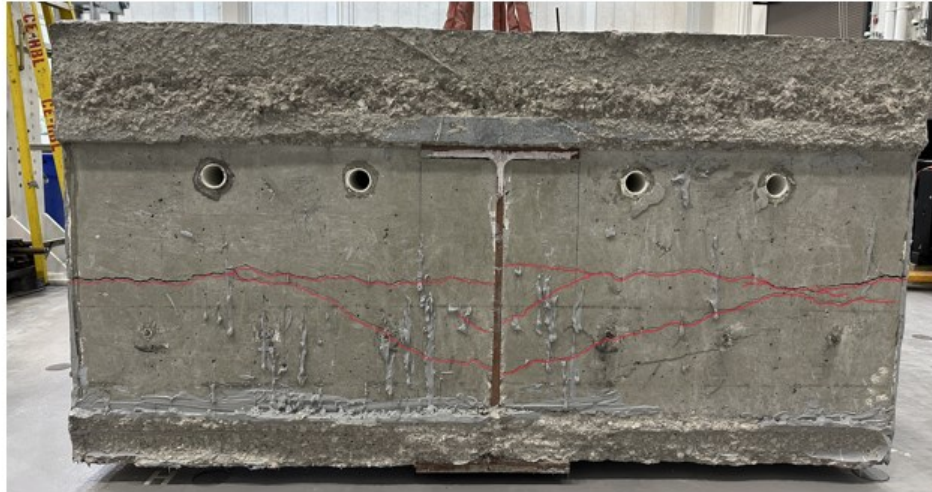
Figure 5.251. Concept D Ultimate Testing Structural Strain Profile at W2.

Similar observations were noted at W1 and W2, with the NAs closely aligned at W1 and more varied at W2. The calculated composite NA for the cracked section was positioned 18.1 inches above the specimen's base. Testing results indicate a higher NA than theoretical values due to the concrete's initial tensile resistance and the structure acting as a full composite section. As the test was going on, cracking in the deck, especially near adhesive joints, caused the NA to shift

toward its theoretical position. At maximum load, cracks in both the adhesive joint and the precast concrete deck transformed the section into a main steel beam with reinforcement.

The NA calculated from the test results is also higher than the NA from Concept A. This finding is consistent with the expectation that—due to the PT from the Williams bars—the NA would be raised.

The load was taken off the specimen, and the through-hole jack was used to lift the specimen enough so the support pedestal could be placed under the bearing pad. After the specimen was placed back on the pedestal, the instrumentation was taken off, and the specimen was prepared for disposal. The specimen had to be broken in half to remove it from the lab. The crane was used to lift the specimen, and there was no need to use a concrete saw since they were joined by epoxy adhesive. Figure 5.252 shows the elevation view of the two parts of the specimen. The side surface cracks did go through the back surface of the concrete drop panel; several cracks were forming at mid-height of the specimen. Figure 5.253 provides the view of the specimen leaving the lab.



(a)



(b)

Figure 5.252. View of Concept D after Ultimate Testing: (a) Eastside Specimen and (b) Westside Specimen.



Figure 5.253. Concept D Being Taken out of Lab.

5.10.2.5. Concept D Post testing Observations

Many observations were made regarding the specimen after ultimate testing concluded. Various signs of damage were reported, the main one being the crack that had formed on the adhesive joint at various points of the testing. Along with only two cracks forming during the static testing (besides the crack in the adhesive joint) and one crack forming at the top deck surface during the cyclic testing, only one crack formed at the top deck surface during the ultimate testing. The crack that formed during the ultimate testing was at 46 kips, which is equivalent to about 160 percent of the HL-93 notional loading. Figure 5.254 presents the crack formed at the deck surface at the hold-down end side when the load was about 46 kips. Figure 5.255 shows the crack formed at the adhesive joint between the two precast units. The crack width developed during ultimate testing and reached about 0.16 inches at 50 kips.

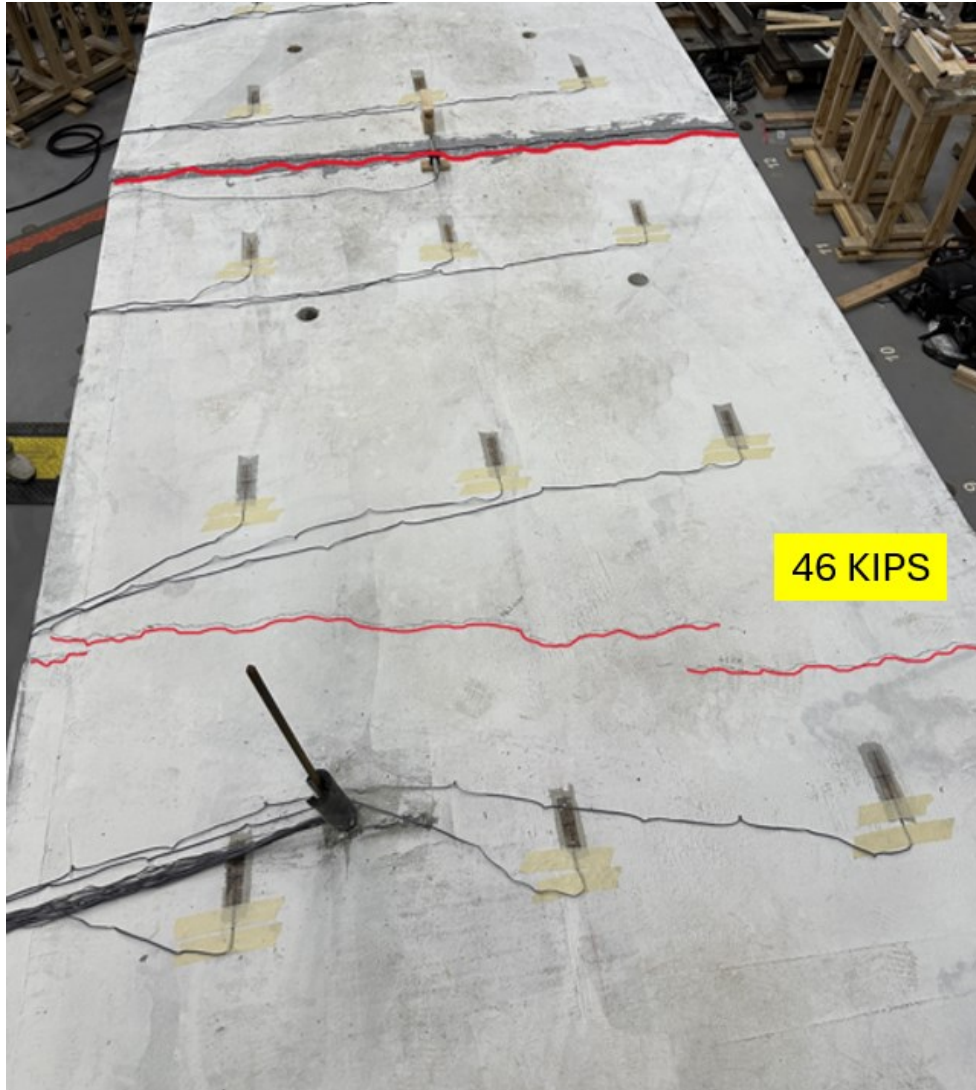


Figure 5.254. Cracks on the West Side of Concept D after Ultimate Testing.

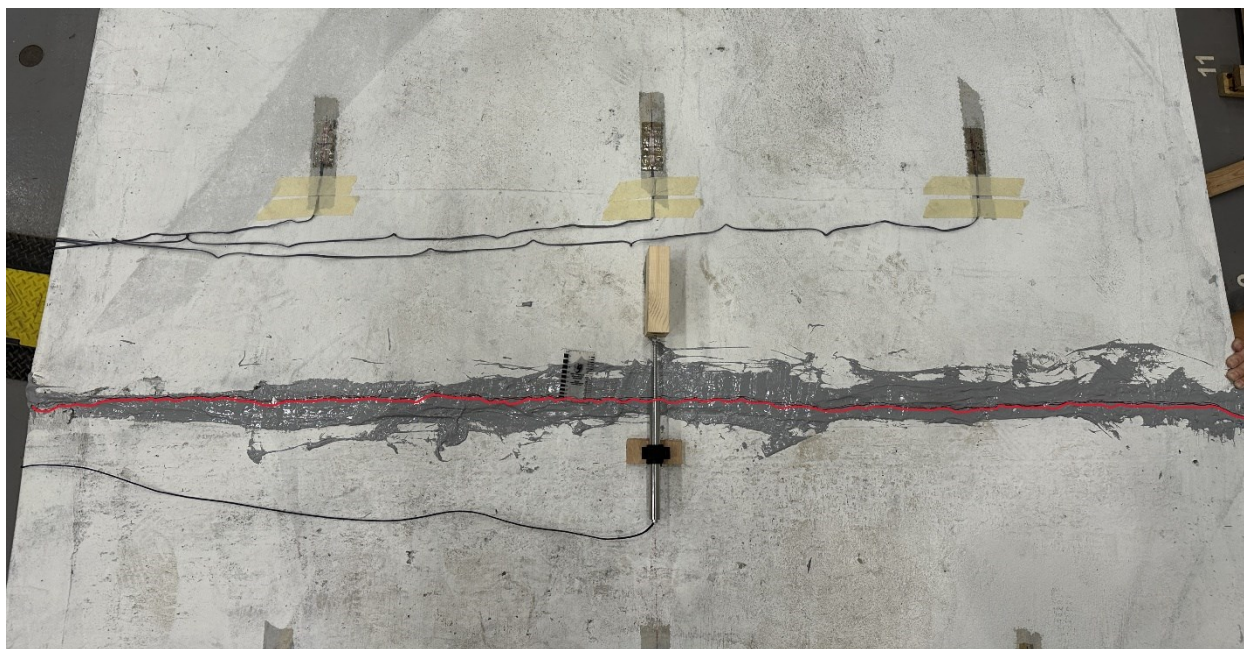


Figure 5.255. Cracks in Adhesive Joint of Concept D after Ultimate Testing.

Cracks developed at the side surface of the precast specimens were recorded during ultimate testing. Figure 5.256 shows the cracks that developed in the side surface on the south side of the specimen. Two cracks formed at both the active load end and the hold-down end. Figure 5.257 presents the opposite side surface of the precast specimen. The concrete damage patterns and crack locations were similar to the southside surface. Both cracks formed at the beginning of the static testing and developed during the cyclic testing and the ultimate testing. The maximum crack width for the crack that happened at the northside surface of the active load end was about 0.04 inch.

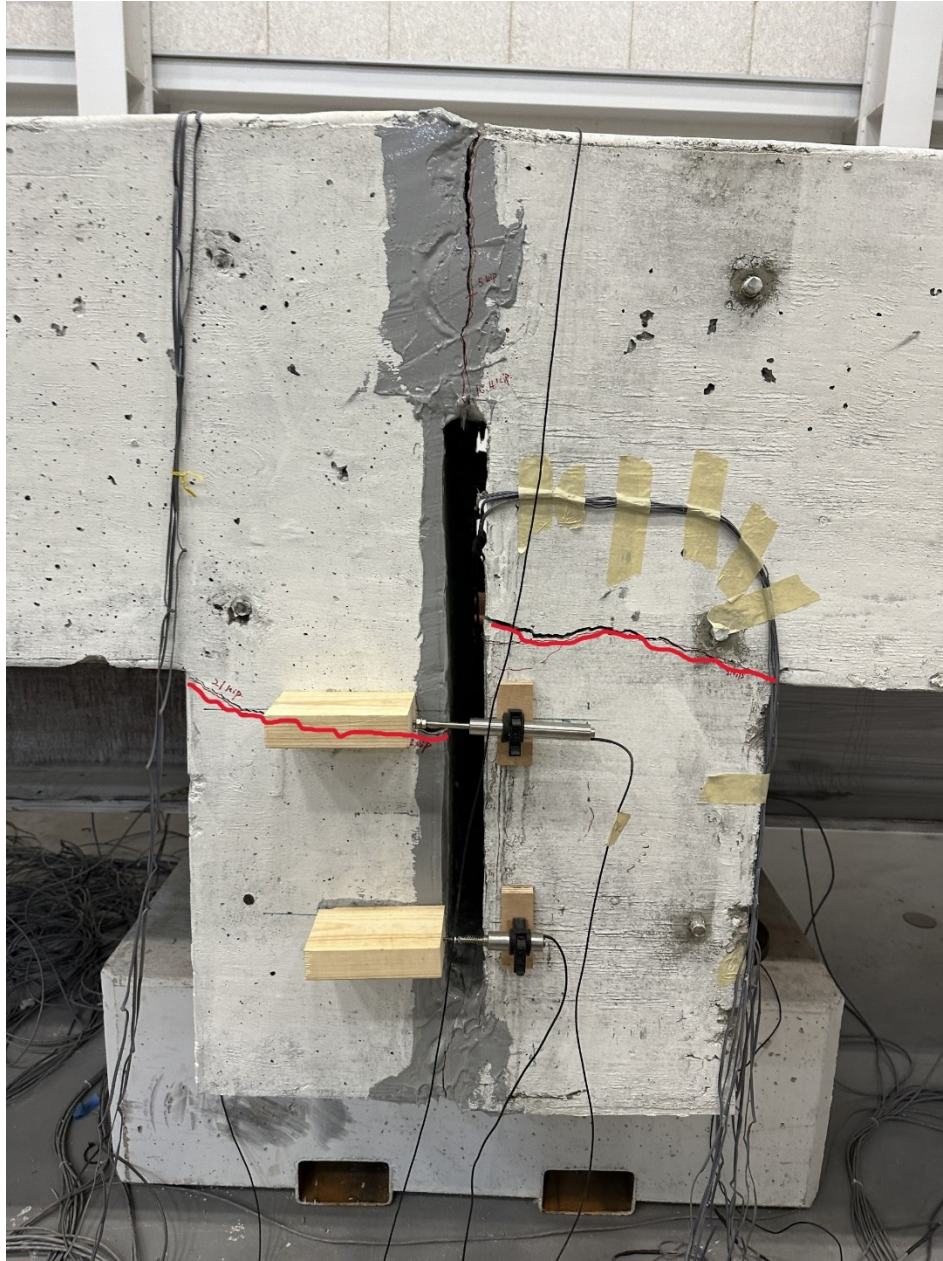


Figure 5.256. View of Cracking on South Side in Match-Cast Joint.

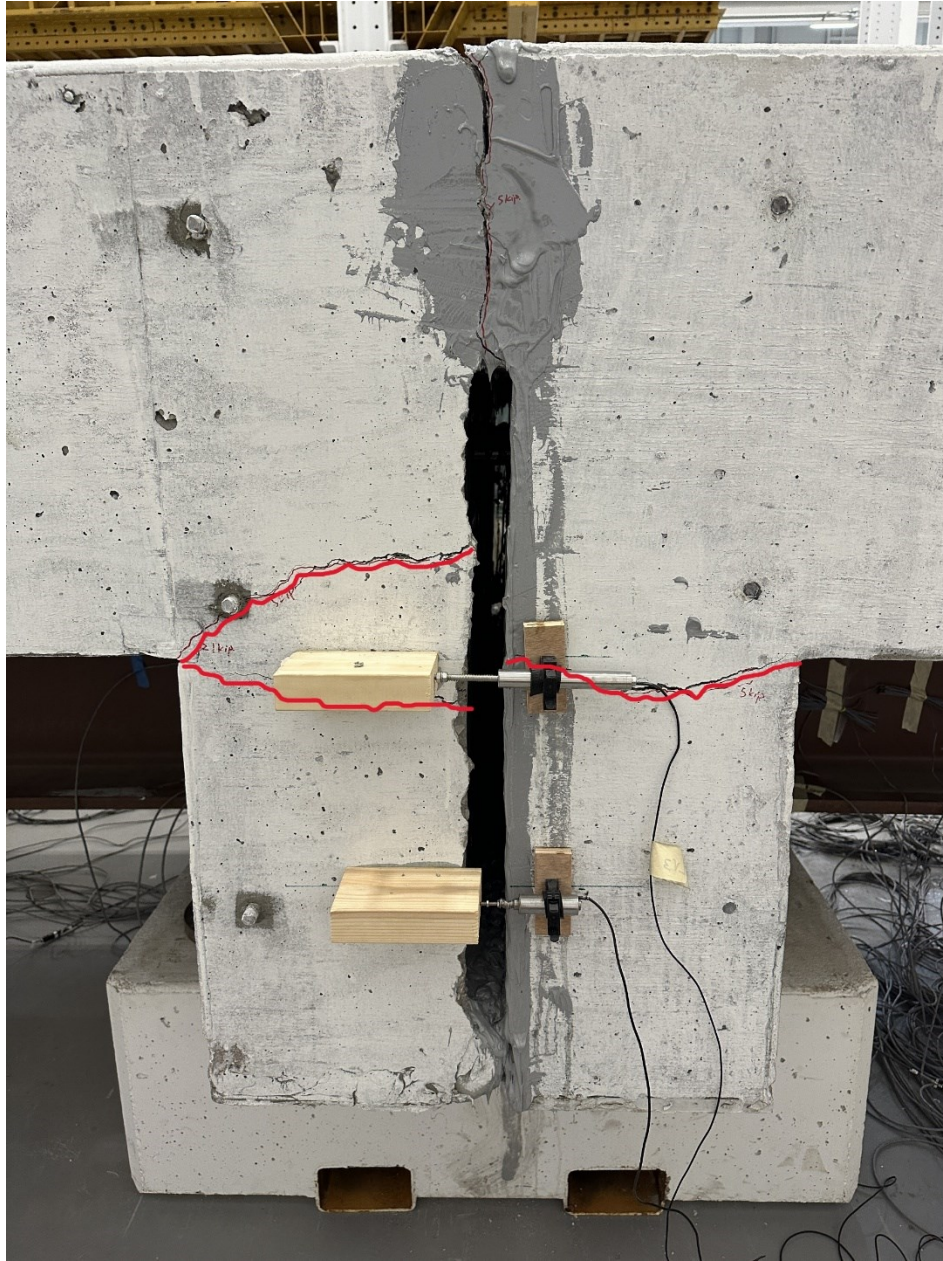


Figure 5.257. View of Cracking on the North Side of Deck in Match-Cast Joint.

5.10.2.6. Concept D Findings

The Concept D experimental testing produced several findings. A summary of the primary findings is presented as follows:

- *Stiffness:* The initial stiffness of Concept D was about 35 kip/in, which was relatively lower than the other three specimens. This stiffness was maintained until approximately 36 kips (equivalent to 120 percent of the HL-93 notional loading) was reached. After that

point, the specimen started to creep and relax after each displacement increment due to cracks developed at the side surface of the precast specimen, causing the specimen to act more non-composite. Section 5.11.5 discussed an in-depth comparison of each concept's stiffness.

- *Match Cast:* Concept D applied the match-cast construction method for joining these two precast units together. The epoxy adhesive was used for the surfaces of the top and bottom shear key portion. Similar to Concept B, the first place that cracks started to appear during the testing was at the adhesive joint between the two precast decks. A crack formed as early as about 50 percent equivalence to the HL-93 loading. The crack was about 0.16 inch wide at the end of ultimate testing, and it was closed when the load was released.
- *Crack Propagation:* For the deck surface part, only one visible crack formed beside the one at the match-cast joint, and it was about 6 ft away from the match-cast joint. For the side surface of the precast concrete drop panel, two cracks formed at each side of the specimen; they were located at the interface of the concrete drop panel. They were also full-depth cracks, meaning they went all the way through the precast panel. The amount of reinforcement used in the precast drop panel was minimal. This insufficient reinforcement is believed to be a significant cause of these observed cracks at the interface.
- *Bar Tensioning:* The through-hole jack is a reliable method to provide adequate tension in the Williams bars, which was also verified by Concepts B and C. For most designs, a 100-ton through-hole jack was the minimum jack size, with some exceptions. The jack weighs more than 100 lb; therefore, the weight must be accounted for when considering the constructability of the setup.
- *Precast Concrete Drop Panel:* Joining two precast concrete drop panels together by using epoxy adhesive was a quick process. The total construction time for putting the precast units together was about 4 hours, which included the epoxy resin application and PT Williams bar process. The contacted bottom shear key part did not provide an effective load transfer mechanism for the compressive forces, as it could significantly bend the interface of the precast drop panel under live load loading. The lower part of the precast drop panel acted as the reinforced beam and resisted a relatively large bending moment

induced by the live load. The top shear key part also provided the essential tensile force in epoxy resin. The previous figures showed the shear key male part was attached to another precast specimen after the ultimate testing, which showed the epoxy resin tensile strength was relatively high when compared to the precast concrete deck's strength. The cracks forming at the interface of the concrete drop panel were an issue for this connection detail since they caused the specimen to creep during the testing. It makes the panel unstable and lead to reinforcement corrosion in the long term.

5.11. CONCEPT COMPARISON

The following sections compare the overall performance of the precast concrete deck slabs between the specimens. Sections 5.11.1.1, 5.11.1.2, 5.11.1.3, and 5.11.1.4 present observations on each of the concepts, while 5.11.1.5 uses the available data taken from the concrete surface strain gauges and rebar strain gauges to determine which deck performed the best.

5.11.1. Precast Concrete Deck

The precast concrete deck was very similar for each concept except for Concept D. The process of constructing the deck was almost the same between all concepts. The only difference was that for Concept A and Concept C, the U-loop bars had to be installed such that they protruded into the closure region. This change was minor and did not adversely affect the constructability of the specimens' decks. The precast concrete decks for all specimens were also constructed quickly, each taking less than a week to erect the formwork, lay all the rebar, and pour the concrete. Concept D construction was relatively complex compared to the other concepts since it included the concrete drop panel. The complex geometry for Concept D may take longer labor time than others. The long-term durability of the deck was also very good. Although Concept A and Concept C had more cracks than Concept B and Concept D, all cracks that formed in the precast concrete deck were relatively small, at under 0.2 inch across. The safety of the concepts is very good too. The assembly of the decks is mainly reliant on the proper construction of the formwork, and if it is properly designed, then no issues should arise when constructing them. Transporting the specimens is also relatively safe. The lifting holes in the precast concrete deck provide an excellent way for a crane to attach to the specimens and allow a way for the specimens to be fastened down on a trailer for transportation to the site. Finally, the ability to do

the entire construction of the precast concrete deck in a factory setting allows the fabrication of this portion of the specimens to be as cost-effective as possible.

5.11.1.1. Concept A

Overall, the precast concrete deck of Concept A performed very well during the entire course of testing. In the static portion of the testing, the deck experienced cracking in only one spot: through the lifting holes on the east end of the specimen nearest the closure pour. This crack can be seen in Figure 5.41. This area was a common place for cracks to form because the lifting holes provided a slightly smaller section, which would cause cracks to form. This crack formed at approximately 35 kips, which is equivalent to 125 percent of the HL-93 loading. Besides the cracks that formed in the interface between the closure pour and the precast concrete deck, no other cracks formed during the static testing.

During the cyclic testing of Concept A, two additional cracks developed in the deck. These cracks formed approximately 7 ft away from the transverse centerline of the specimen at about 130,000 cycles. These cracks can be seen in Figure 5.52. One of these cracks formed through the point at which the rebar instrumentation wires in the slab were coming out. This situation could have caused a weakened section, which may have provided an ideal spot for a crack to form. The lack of a significant amount of cracks that formed during the cyclic testing is indicative of the fact that this specimen has long-term durability.

The ultimate testing of Concept A produced seven more cracks in addition to the static and cyclic testing. The lowest magnitude that produced a crack during the ultimate testing was 53 kips, which is equivalent to 176 percent of the HL-93 loading. The cracking during the ultimate testing was fairly uniform across the entire length of the deck. Four cracks formed on the east side of the specimen, and three cracks formed on the west side of the specimen. These cracks and their magnitudes can be seen in Figure 5.75 and Figure 5.76, respectively. Two ranges of cracks formed during the ultimate testing. The first range of cracks formed in the loading range of 53 and 58 kips, which is equivalent to 176 percent to 190 percent of the HL-93 loading. The second range of cracks formed between 70 and 74 kips, which is equivalent to 224 percent to 235 percent of the HL-93 loading. The high loads at which these cracks formed further reinforce

the fact that this concept has long-term durability and will perform well at the lower load levels that exist during typical service conditions.

5.11.1.2. Concept B

The precast concrete deck for Concept B did not form many cracks during the course of testing. Only three cracks formed outside the closure pour, and these cracks formed during the static testing. All of these cracks formed at the 15-kip load level, which is only equivalent to approximately 69 percent of the HL-93 load level. The crack seen in Figure 5.147 is located on the west side of the specimen. This crack formed about 4 ft 6 inches away from the transverse centerline of the specimen. The cracks shown in Figure 5.148 are on the east end of the specimen and were located 3 ft and 4 ft 6 inches away from the transverse centerline. The cracks that were closest to the transverse centerline formed through the lifting holes, which provided a weaker section for the cracks to travel through. The maximum width of these cracks was about 0.008 inches. After these cracks formed, they did not widen at all. All of the rotation was accounted for with the separation between the closure pour and the precast concrete deck, which is discussed in Section 5.11.2.2.

The cyclic and ultimate portion of the testing did not result in any new cracks forming. The cracks that formed during the static testing formed directly above the extent of the Williams bar brackets under the top flange. Since the brackets for this concept did not include any headed studs in the area, it is likely that as the Williams bars were post-tensioned, they caused the brackets to pry into the top flange, causing local stress concentrations that were then passed into the deck.

The cracks that formed on the deck for Concept B were not necessarily a cause for concern. These cracks formed due to a local stress concentration from the brackets below the slab. The more glaring issue with the slab was around the closure pour, which is explored more in Section 5.11.2.2. Overall, the precast concrete deck for Concept B did not experience many cracks due to the lack of reinforcement through the closure region that tied the two decks together. The active loading side of the specimen going through rigid body motion did not allow the deck to go into significant amounts of tension, which would have caused cracking on the surface.

5.11.1.3. Concept C

Similar to Concept A, the deck for Concept C performed well up to lower load levels. During the static testing, only two cracks formed that were away from the closure pour. These cracks can be seen in Figure 5.168 and Figure 5.169. These cracks started to form at 20 kips, which is equivalent to 83 percent of the HL-93 load level. These cracks also formed through the lifting holes, the weakest section of the specimen. On the second application of the static loading, the crack on the active loading end of the specimen expanded across the slab at 30 kips. Other than these two locations, no other cracks formed on the surface of the deck during static testing.

Likewise, no cracks developed on the deck surface during cyclic loading. Many new cracks developed on the deck during ultimate testing. However, the majority of these developed after approximately 61 kips on the active loading actuator, which is equivalent to almost 200 percent of the HL-93 load level. After this load level, numerous cracks formed across the entire deck. These cracks can be seen in Figure 5.200, Figure 5.201, and Figure 5.202. The width of these cracks at the maximum load level of the testing for Concept C (about 94 kips) was approximately 0.01 inch or smaller. Because of minimal cracking during static testing, no new cracking during cyclic testing or low-level ultimate testing, and the cracks remaining small even at high load levels, this concept maintains a level of long-term durability.

5.11.1.4. Concept D

The precast concrete deck for Concept D did not form many cracks during the course of testing, similar to Concept B. For the deck surface part, only two cracks formed at each side of the precast deck. The maximum width of these two cracks was about 0.004 inch. Figure 5.254 showed the crack was located on the west side of the specimen. This crack formed about 5 ft away from the transverse centerline of the specimen. Another crack formed during the cyclic loading, which was also 5 ft away from the transverse centerline at the east side of the specimen. The cracks on the deck surface did not widen at all, as all of the rotation was accounted for with the separation between the two precast units. For the side surface part, there are two cracks developed at the interface of the precast drop panel at the 8-kip load level, which is only approximately 30 percent of the equivalent HL-83 load level. Figure 5.224 and Figure 5.225 describe the cracks at the side surface. The crack locations were pretty symmetrical for both

sides of the specimen. The crack width was developed with the load increasing during the ultimate testing. The maximum crack width was about 0.08 inch.

The cyclic and ultimate portion of the testing did not result in many new cracks forming. Only one crack formed in the cyclic testing and only one crack formed in the ultimate testing. They were symmetrically located on two sides of the concrete deck surface. The cracks that formed on the deck for Concept D were not necessarily a cause for concern. These cracks formed due to the negative moment induced by the actuator loading. The more glaring issue with the slab was around the adhesive joint, but the crack width was near 0.004 inch when the specimen was back on the support pedestal. The Concept D match-cast joint portion is shown in Section 5.11.2.4. Overall, the precast concrete deck for Concept D did not experience many cracks due to the lack of reinforcement through the adhesive joint between the two precast units. The cracks at the interface of the concrete drop panel may cause the specimen to creep during the loading process.

5.11.1.5. Direct Data Comparison

The average deck stresses on the surface of the precast concrete deck at gridline E1 can be seen in Figure 5.258. The stresses in Concept A started at zero stress and increased in tension as the load was being applied, which is consistent with expectations for a system without PT. The stresses for Concept B and Concept C started in net compression due to the precompression from the Williams bars, and as the load increased, the stress in the deck trended toward zero net stress but never reached net tension. The stresses for Concept D also started in net compression due to the post-tension effect, but the magnitude was about two times the magnitude for Concept B and C since Concept D has four Williams bars instead of two Williams bars. Up to approximately 40 kips, the stresses between Concept B and Concept C are very similar. The stresses for Concept D also increased during the ultimate testing, but it was still in net compression. Past 60 kips, cracking around the area of the strain gauges caused the stresses to be relieved, which is why the Concept C data dropped down in compressive stress.

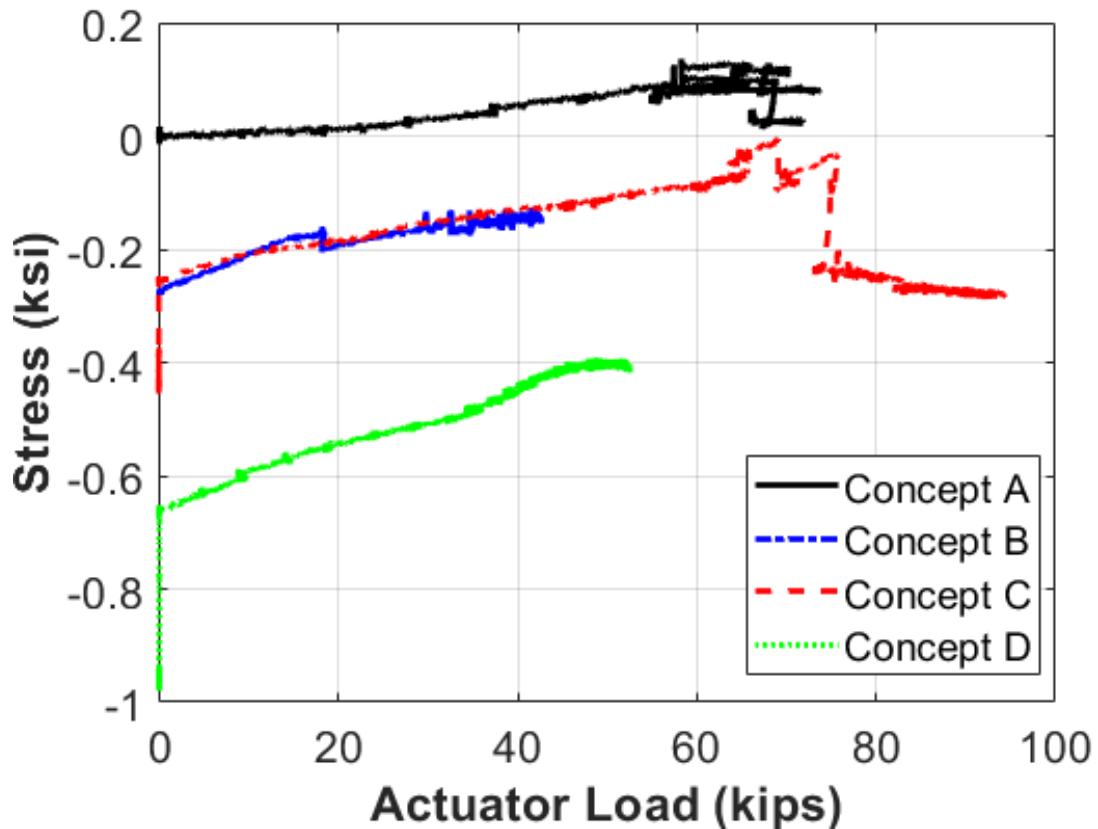


Figure 5.258. All Concepts Ultimate Testing Precast Concrete Deck Stresses at E1.

Similar to gridline E1, the data from gridline E2 can be seen in Figure 5.259. The data from Concept A started at zero net stress (due to the absence of the Williams bars) and increased as the actuator load increased. Concept B, Concept C, and Concept D started in net compression, and the stress trended toward net tension as the load increased but never reached net tension. Again, the data between Concept B and Concept C are very consistent.

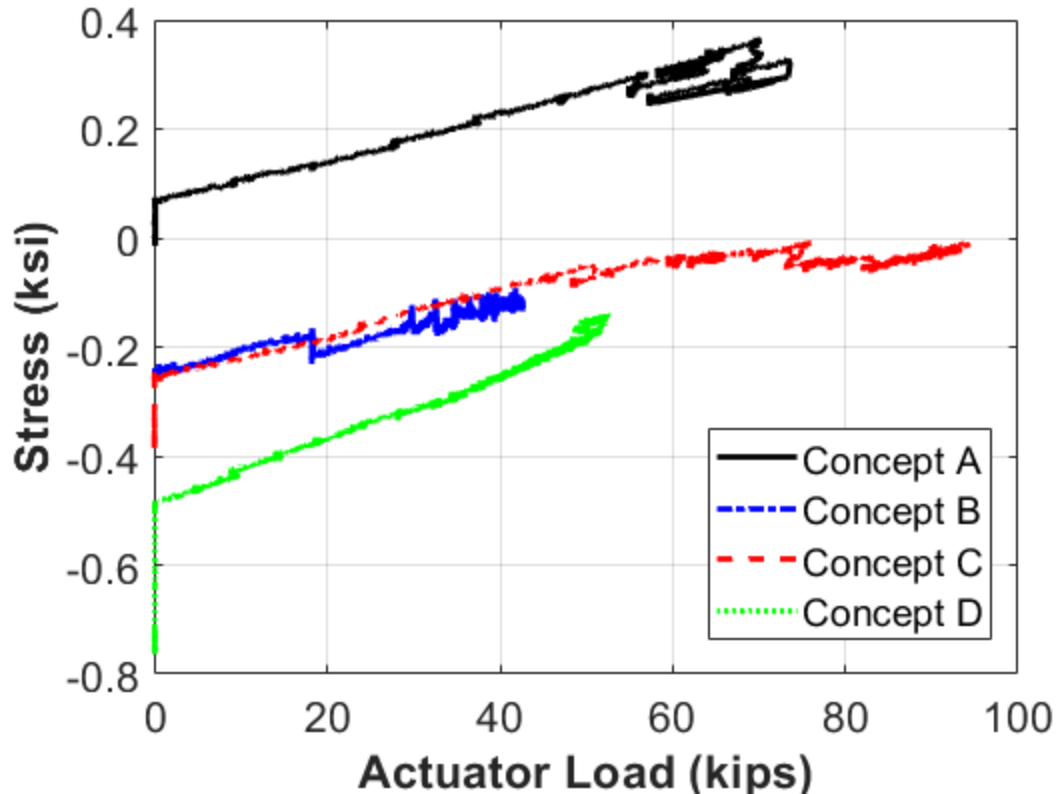


Figure 5.259. All Concepts Ultimate Testing Precast Concrete Deck Stresses at E2.

The average stress in the rebar at gridline E1 for each concept can be seen in Figure 5.260. All three concepts started near zero net stress. Concept A saw several jumps from zero to 50 kips of load, likely due to the lack of a positive connection between the specimen and the active loading end actuator. Up to 50 kips, all the concepts had similar stress in the rebar at E1. Concept A saw a drastic increase in stress in the rebar at approximately 55 kips; past 60 kips, the slipping of the splice plates and the cracking of the concrete caused a notable amount of noise in the data. The testing for Concept B was stopped before 50 kips was reached, so no major increase in stress in the rebar at this location was recorded. The stresses for Concept B and Concept D remained relatively low during ultimate testing in comparison to the other two concepts. The reason may be that the reinforcement was not developed through the closure pour and did not take a relatively large portion of the tensile force during the loading process. Concept C had a small increase in stress up to about 75 kips, and then, similar to Concept A, showed a serious increase in stress. The maximum stresses for Concept A and Concept C were about 23 ksi, which is well below the yield of the rebar.

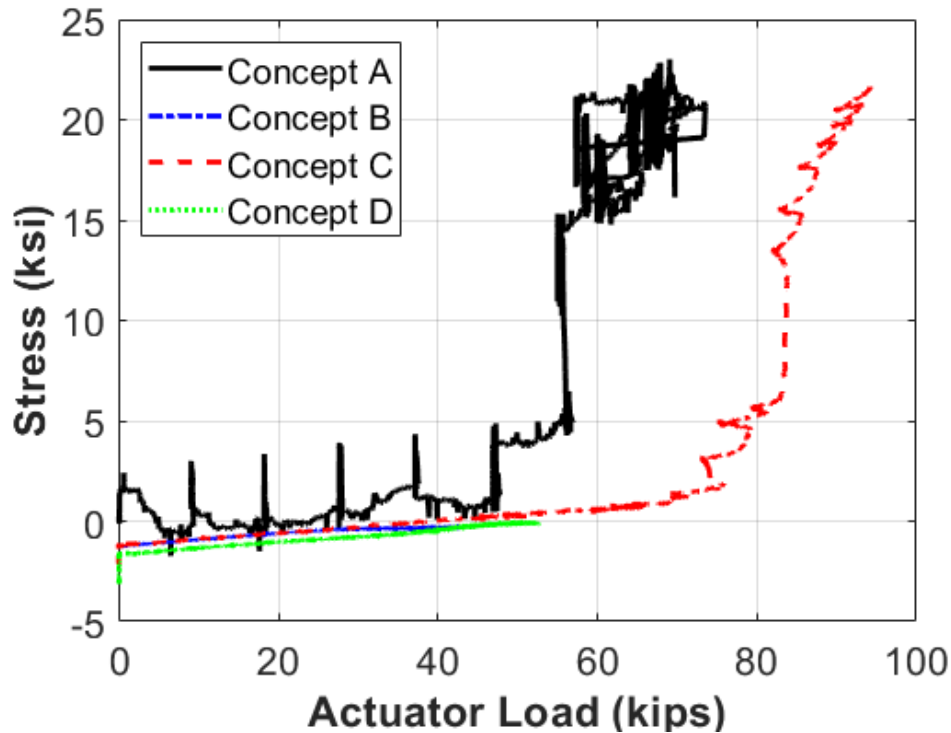


Figure 5.260. All Concepts Ultimate Testing Rebar Stresses at E1.

The average stresses in the rebar at gridline E3 can be seen in Figure 5.261. At this location, the initial stresses for Concept A jumped due to the specimen becoming self-supporting, while Concept B and Concept C recorded very modest initial jumps. Concept A recorded a relatively linear increase in stress in the rebar up to about 55 kips of load. Past that point, cracking in the slab around E3 caused noise in the data. Concept B and Concept C had nearly identical data up to 45 kips, which is when Concept B testing stopped. Concept D also shows a similar tendency for the stresses at E3. The stresses for rebar of Concepts B and D were also kept low during the ultimate testing, which may be the same reason that was explained for testing rebar stresses of Concept B and Concept D at E1. At approximately 55 kips, the stresses in the rebar for Concept C drastically increased. Compared to gridline E1, this jump in stress occurred about 20 kips earlier. The maximum stress recorded between all tests at this location was about 35 ksi, which is just over half of the yield stress.

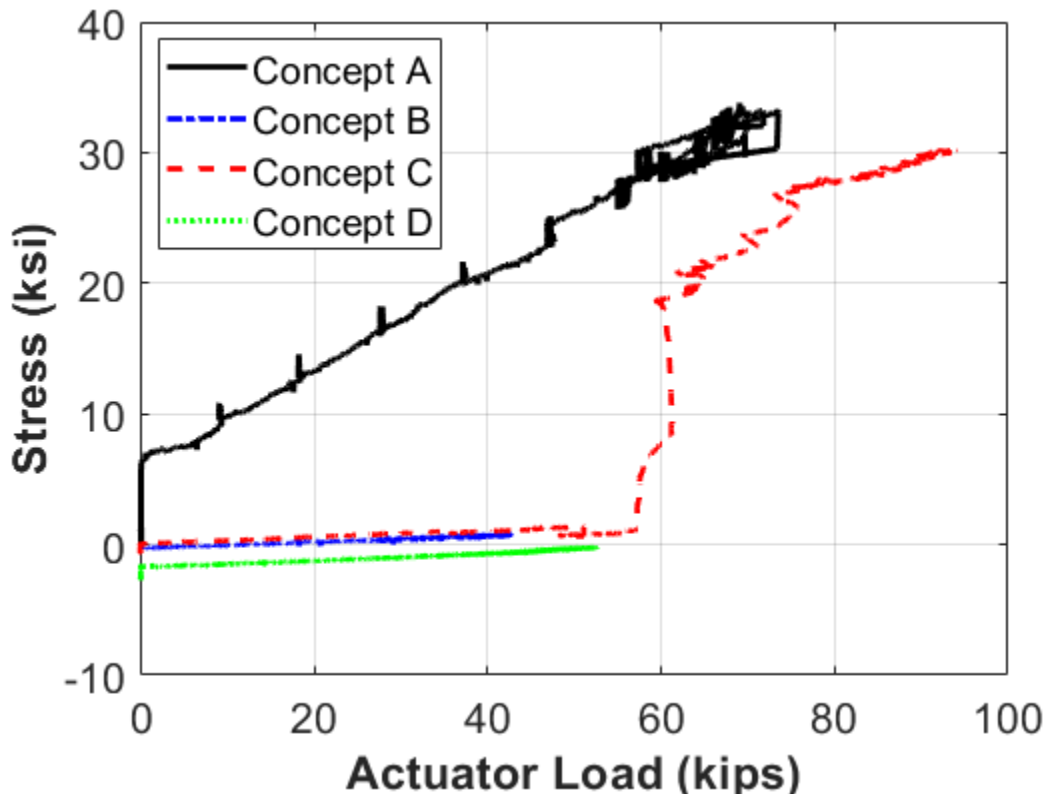


Figure 5.261. All Concepts Ultimate Testing Rebar Stresses at E3.

5.11.2. Closure Pour

The following sections compare the overall performance of the closure pour between the specimens. Sections 5.11.2.1, 5.11.2.2, 5.11.2.3, and 5.11.2.4 describe the observations of each of the concepts, while 5.11.2.5 uses the available data taken from the nearby concrete surface strain gauges and nearby rebar strain gauges (and in the case of Concept A and Concept C, the closure pour reinforcement strain gauges) to determine which closure pour performed the best.

The construction of the closure pour was essentially the same for Concept A and Concept C. They both only took 1 or 2 days to set up all the formwork for the closure pour, lay the rebar, and pour the closure pour. In the case of Concept B, the closure pour went even faster due to not having to lay any rebar. However, that lack of reinforcement in the closure pour for Concept B proved to be its weakness. The long-term durability of the closure pour is the biggest issue that could come from using these specimens. Concept D applied the match-cast construction method to join two precast units together, which is the fastest way among these concepts. As with Concept B, durability in the long term is the issue because of this method. All the concepts had issues with their closure pours, with Concept A and Concept C experiencing some larger

cracking, and Concept B completely separating from the precast concrete deck. The precast units of Concept D were separated at the 10-kip load level during the ultimate testing. Similar to the precast concrete deck, the match-cast joint was safe to make. When the formwork is properly designed, there are no issues with the specimens becoming unstable, having a concrete blowout, or something else detrimental happening. The cost-effectiveness portion of these concepts is not as good as a precast concrete deck. Since this portion needs to be carried out in the field, it will by necessity cost more and possibly delay schedules. However, since it is relatively quick to assemble, lay rebar, and pour, it should not be a disqualifying aspect of these concepts.

5.11.2.1. Concept A

The interface between the closure pour and the precast concrete deck was the first place where cracks formed during testing. During the static testing, the cracking in this area started to develop at 15 kips, which is equivalent to 69 percent of the HL-93 loading. Cracks developed at both intersections of the closure pour and at the precast concrete deck as well. Cracks are expected to form in this area first because it is a cold joint. The cracks that formed during the static testing at the interface were relatively small cracks—less than 0.02 inch across. A view of a section of these cracks can be seen in Figure 5.262.

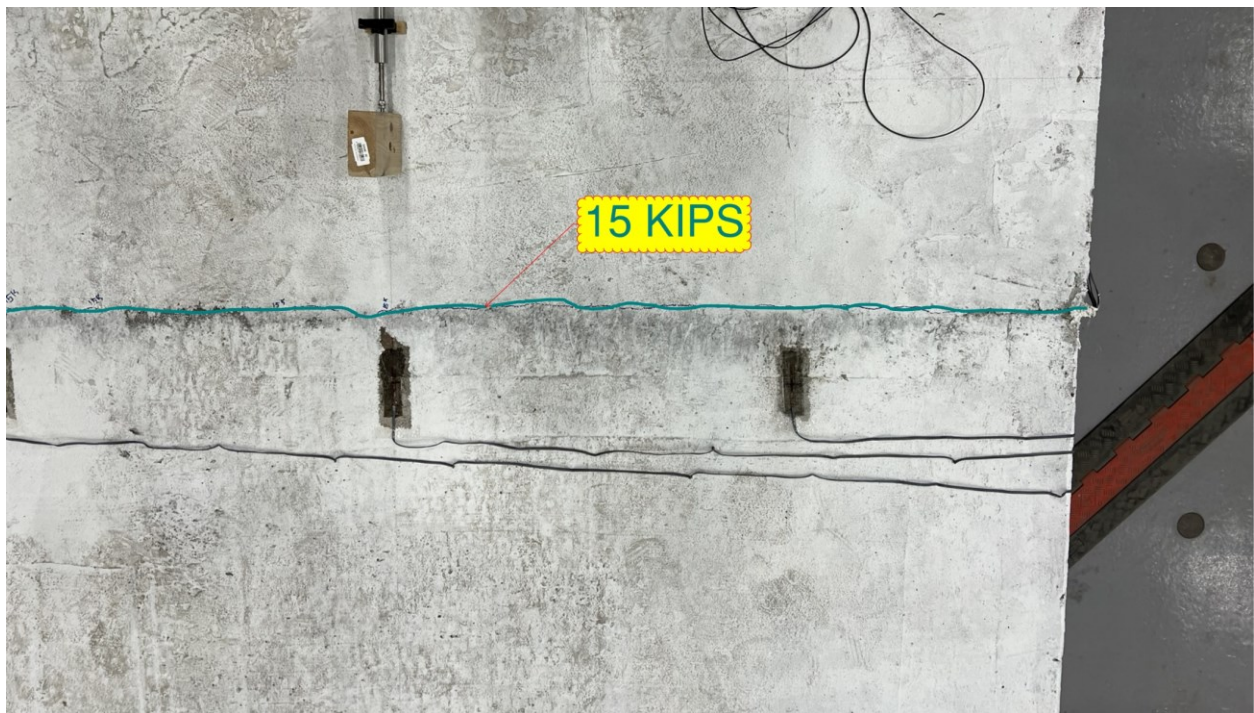


Figure 5.262. Concept A Closure Pour Interface Crack.

During cyclic testing, one crack developed at the transverse centerline of the closure pour at approximately 8,000 cycles. This crack can be seen in Figure 5.51. This crack was full width across the deck and remained smaller than 0.02 inch across. The cracks that formed at the interface of the closure pour and precast concrete deck were also less than 0.02 inch during the cyclic testing for Concept A.

In the ultimate portion of the testing, there was almost no new crack formation in the closure pour. The only cracks that formed were small extensions of the cracks that formed during the cyclic testing. These extensions were less than 6 inches in length and only formed at load levels that were equivalent to over 200 percent of the HL-93 loading. The cracks that formed during cyclic loading were approximately 0.03 inch wide at the maximum actuator load that was reached during ultimate testing. See Figure 5.263 for a view of the north side and Figure 5.264 for a view of the south side of the deck at the maximum load level.

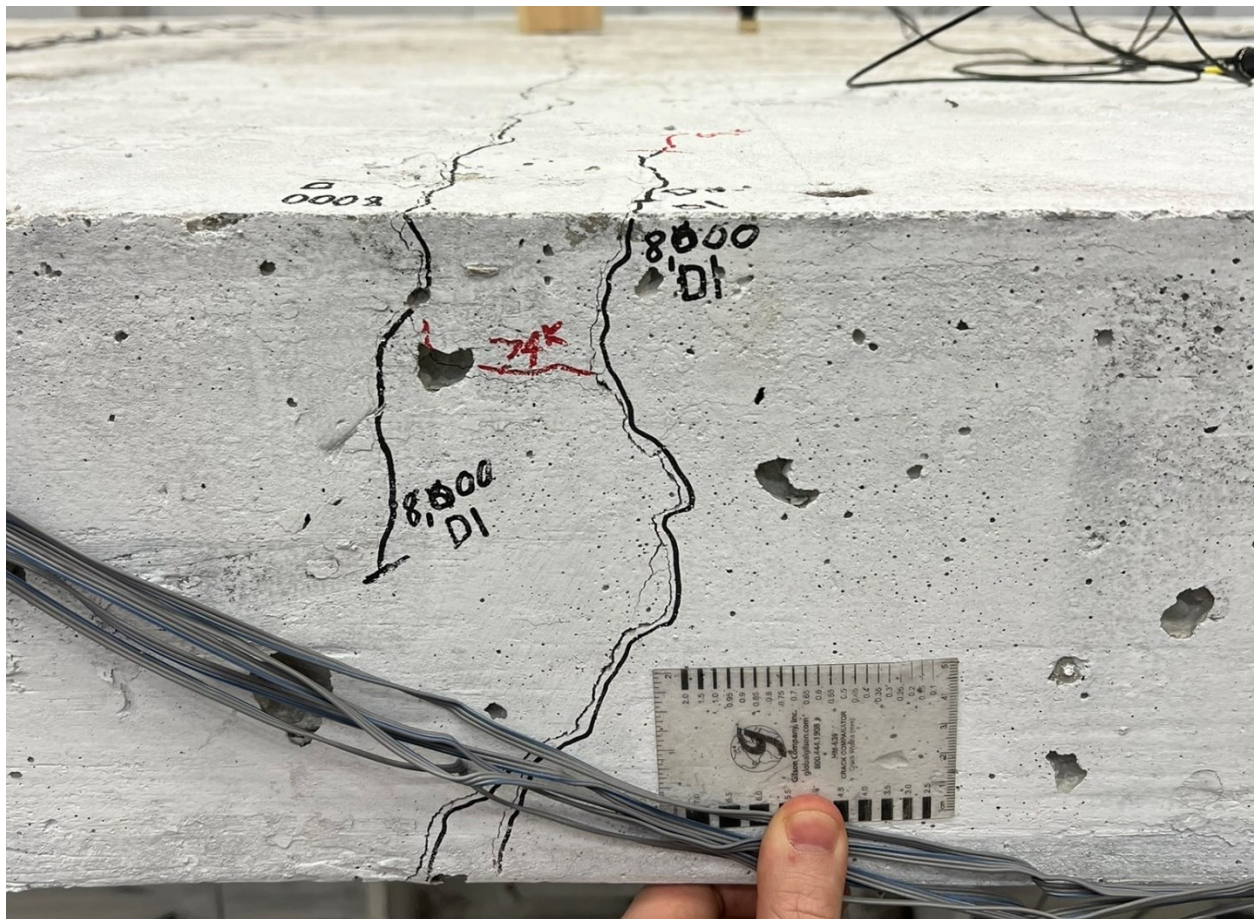


Figure 5.263. Concept A North Side of Closure Pour Cracking.

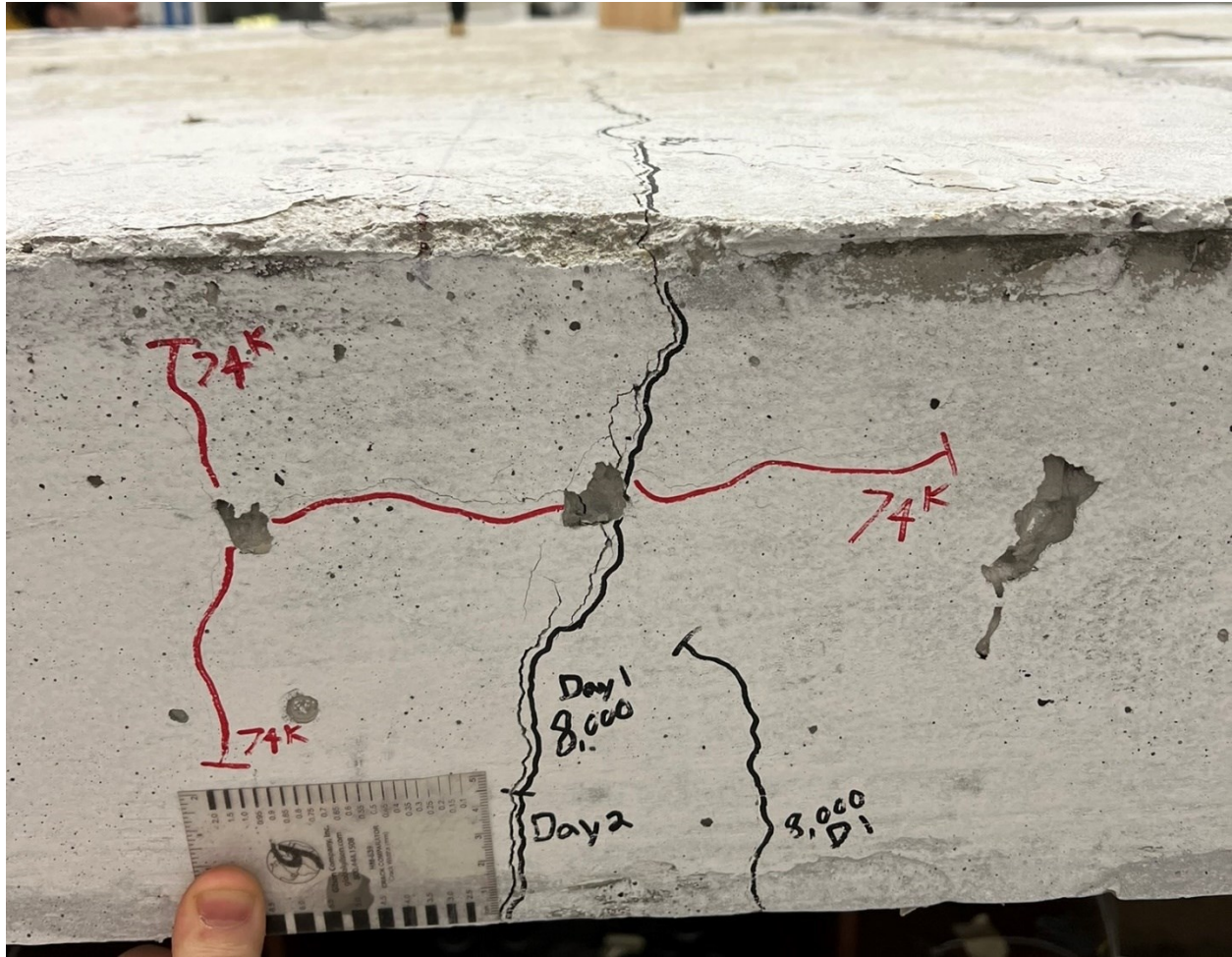


Figure 5.264. Concept A South Side of Closure Pour Cracking.

Overall, the amount of cracking in the closure pour for Concept A remained low. The interface between the closure pour and the precast concrete deck was the site of the first cracks at low load levels; however, during the static portion of the testing, these cracks remained small. The crack that formed during the cyclic testing also remained small during low load levels, only expanding when the load imparted on the specimen exceeded 200 percent of service loading. Based on the amount of cracking that formed in the closure pour and the size of these cracks, this concept performed relatively well and demonstrated that it has the ability to be durable long-term.

5.11.2.2. Concept B

Overall, the closure pour region of Concept B performed the worst of all the concepts. Namely, the interface between the UHPC closure pour and the precast concrete deck opened up once 28 kips was reached, which is about equivalent to the HL-93 load level. The lack of

reinforcement running through the closure pour for this concept allowed the closure pour to completely separate from the rest of the precast concrete deck. Since there was no reinforcement in the closure region, no force was transferred between the slabs. Without this force transfer, no method to develop cracks in the closure pour was present. During the cyclic testing, the interface opened to 0.12 inch across every cycle. See Figure 5.265 for a view of this crack. No other cracks developed in the closure region.

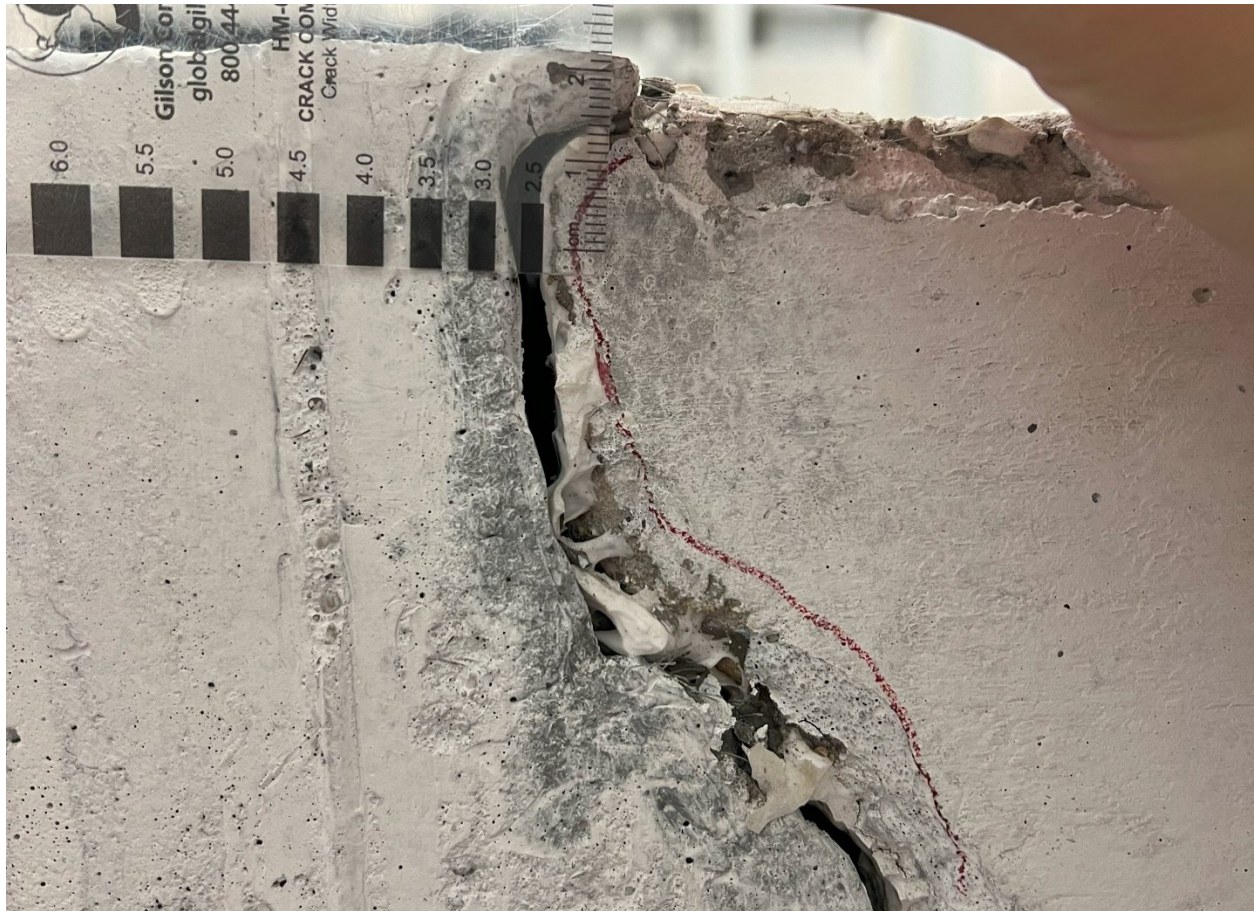


Figure 5.265. Concept B Closure Pour Interface Crack during Cyclic Testing.

At the end of ultimate testing, the gap between the closure pour and the precast concrete deck exceeded 0.24 inch across at its widest. See Figure 5.266 for a view of this crack. Notice how only one side of the interface is separated, which indicates that the specimen was undergoing rigid body motion and was pivoting about the bottom flange channel connection.

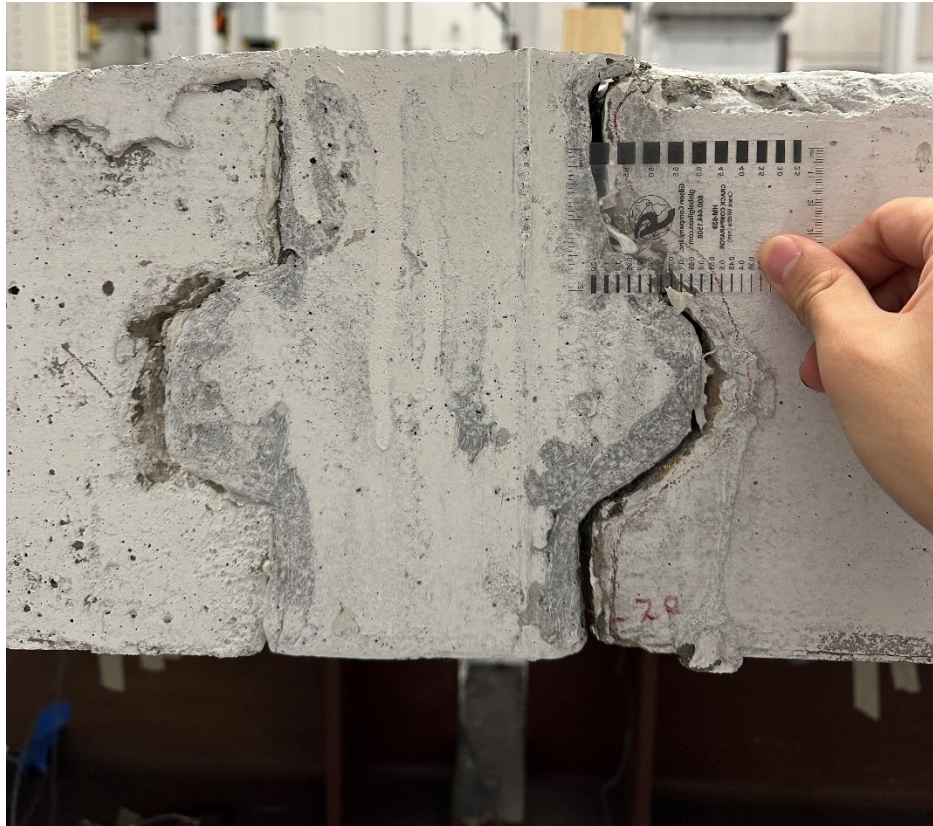


Figure 5.266. Concept B Closure Pour Interface Crack during Ultimate Testing.

Due to the separation between the closure pour and the precast concrete deck, it was determined that out of all the concepts, this concept performed the worst in the closure pour region. The formation of such a large separation is extremely detrimental to the long-term durability of this concept. This issue could be remedied by increasing the post-tension in the Williams bars, but it would require redesigning the brackets and increasing the Williams bar size.

Without any rebar in the closure region, the higher tensile strength of UHPC was not utilized. To take advantage of the higher tensile strength of UHPC, rebar should have been included in the closure pour—similar to Concept A and Concept C. This process would have also provided additional stiffness to the overall specimen.

5.11.2.3. Concept C

The closure pour region for Concept C performed well. Similar to Concept A, the interface between the closure pour and the precast concrete deck was the first place that cracks developed because it was a construction joint. These cracks developed on both sides as early as 10 kips,

which is equivalent to 55 percent of the HL-93 load level. During the static testing, the cracks in the interface were the only ones that formed, and these cracks were small, at about 0.02 inch across. These cracks can be seen in Figure 5.267.

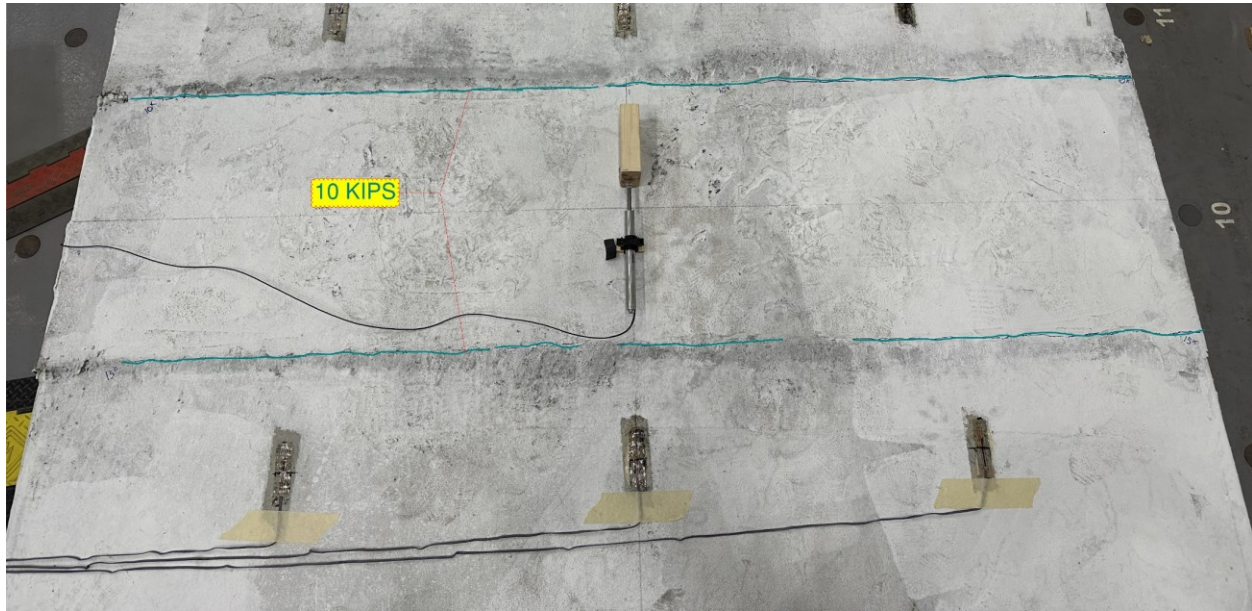


Figure 5.267. Concept C Closure Pour Interface Cracks.

The specimen's closure pour performed very well during the cyclic portion of testing. No new cracks formed during this portion. In the ultimate testing portion, numerous new cracks formed in the closure pour. These cracks can be seen in Figure 5.201. The minimum load level at which cracks started to form in the closure pour was 66 kips, which is equivalent to 213 percent of the HL-93 load level. Most of the cracks in the closure pour formed in the transverse direction across the deck, but as the load level increased, some of the cracks started to form in the longitudinal direction too. Although there were many cracks on the top surface, only one crack extended through the depth of the slab. This crack was directly down the transverse centerline, similar to Concept A. This crack can be seen in Figure 5.268.



Figure 5.268. Concept C Closure Pour Transverse Centerline Crack on Underside of Deck.

At its widest point, this crack was about 0.14 inch across on the north side of the deck. This crack width is seen in Figure 5.269. This crack formed on the south side of the deck as well. However, it formed as one large crack on the bottom of the deck and split into smaller cracks as it traveled toward the top of the deck. See Figure 5.270 for a view of this crack on the south side of the deck.

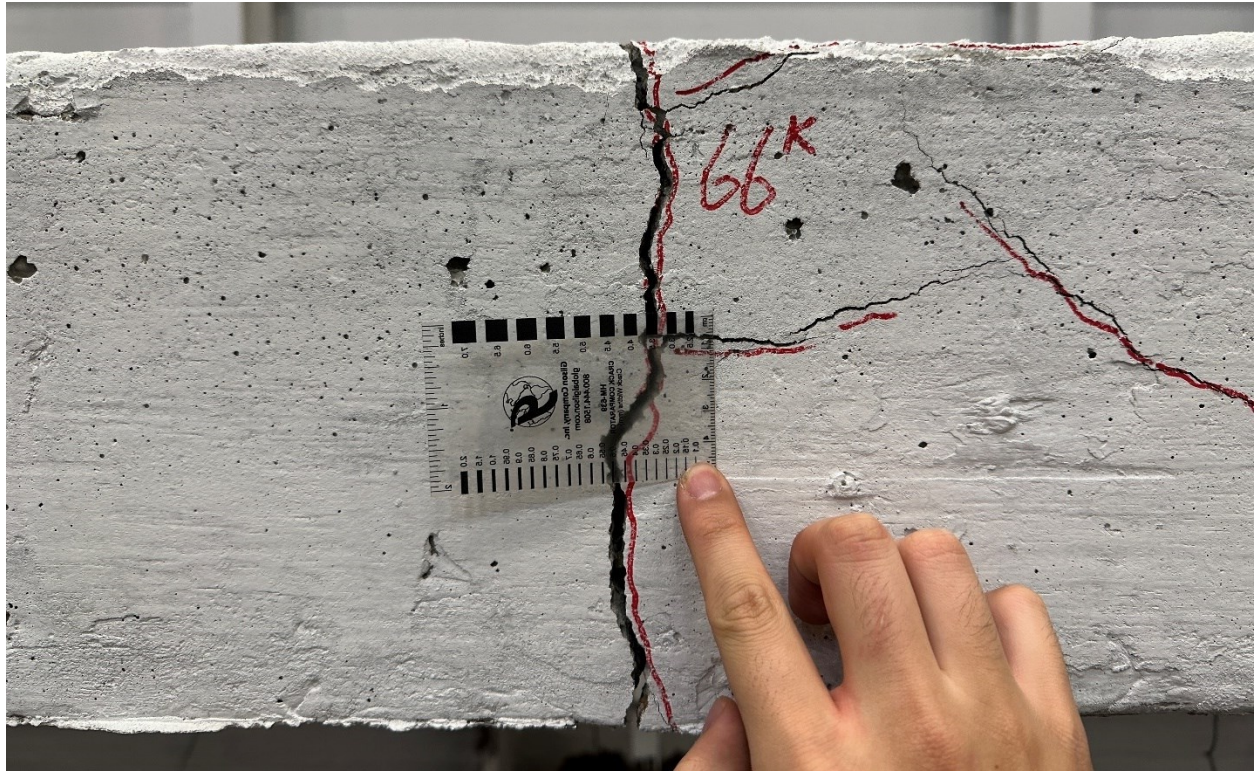


Figure 5.269. Concept C Closure Pour Crack Width North Side.

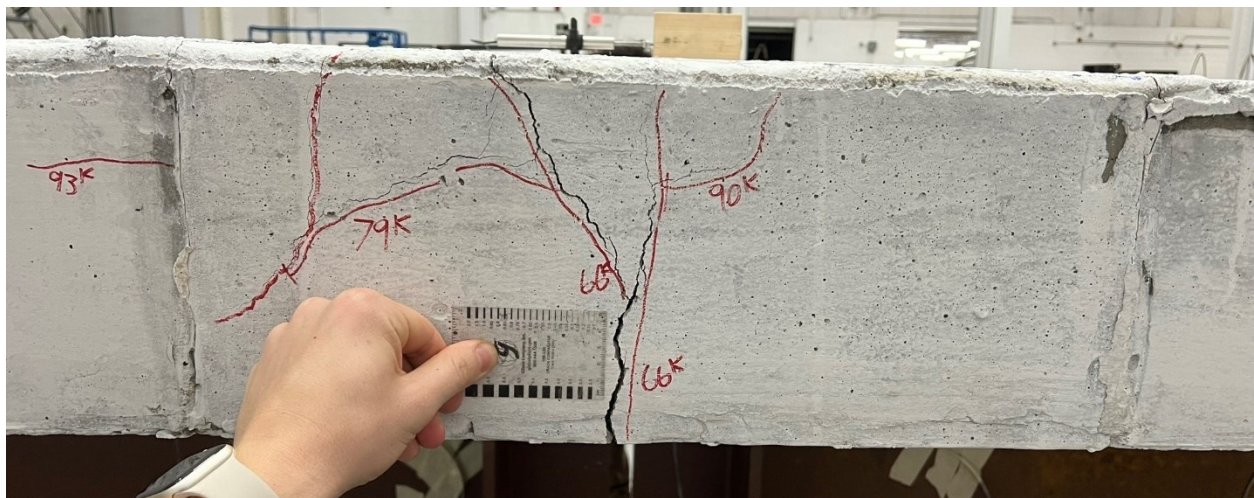


Figure 5.270. Concept C Closure Pour Crack Width South Side.

Overall, due to the number of cracks and the width of the major crack that formed in this concept, Concept C performed very well in the closure pour region. The Concept C behavior was relatively similar to Concept A up to the same load level (74 kips), which is well above HL-93 loading (28 kips). Therefore, the closure pour for Concept C demonstrated that it has the ability to be durable long-term under service-level loading.

5.11.2.4. Concept D

The transverse joint between the two precast units was filled with epoxy adhesive, then these two units were post-tensioned. The adhesive joint was the first place where cracks formed when the load was about 5 kips. Due to the lack of reinforcement running through the match-cast joint for this concept, these two precast units were completely separated from each other when the load was about 45 kips, which is equivalent to 160 percent of the HL-93 load level. During the cyclic loading, the crack width opened up to 0.08 inch across every cycle.

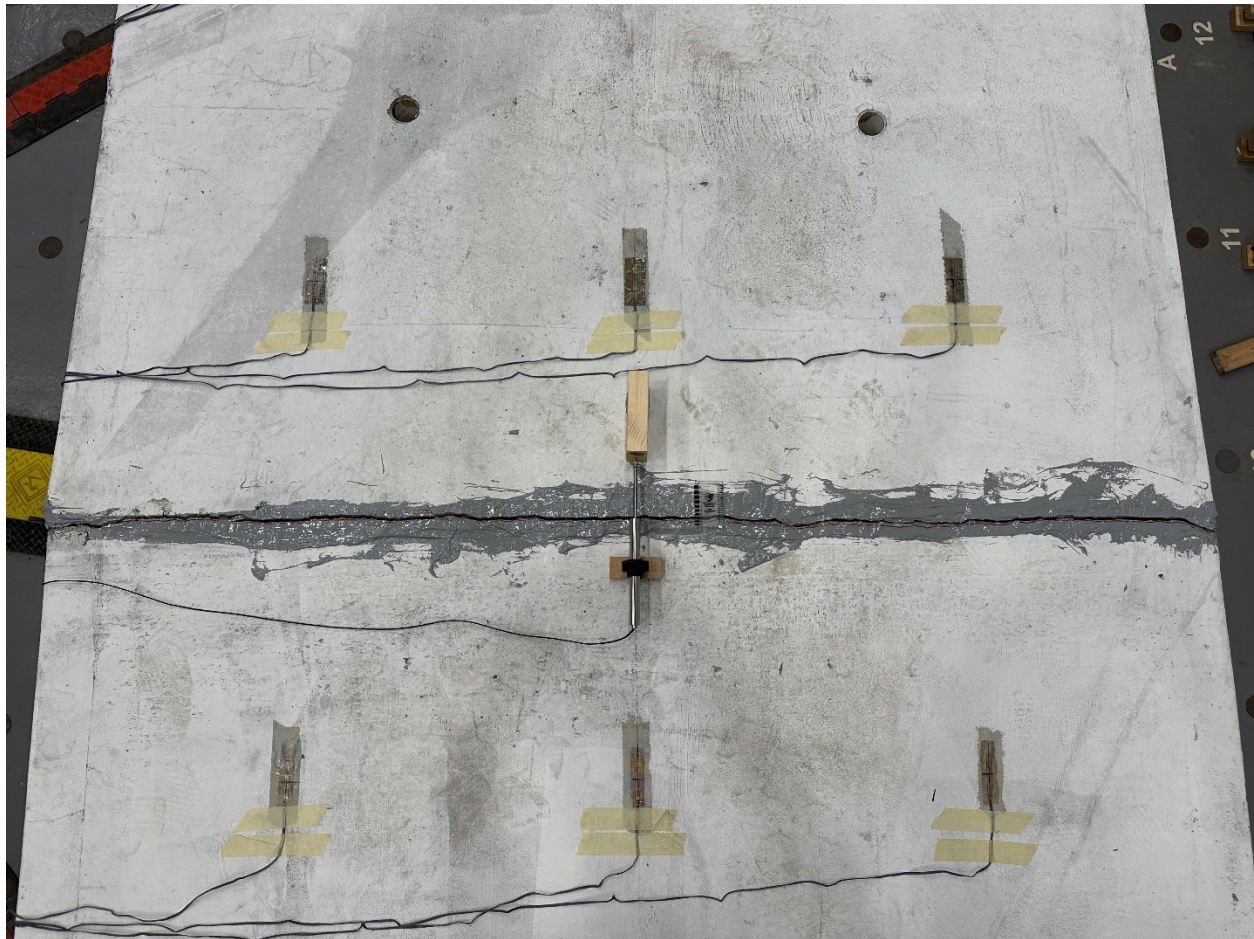


Figure 5.271. Concept D Match-Cast Joint Interface Cracks during Ultimate Testing.

The crack width reached about 0.2 inch at the top deck surface when the load reached 52 kips. Figure 5.271 presents the top view of the crack developed at the adhesive joint at the end of the ultimate testing. No other cracks formed and developed in the transverse joint region. Figure 5.272 describes the southside view of the crack at the adhesive joint. Figure 5.273 shows the northside view of the crack. The crack width at both sides was very close to 0.2 inch. The

separation of the two units shows that it is not relatively durable in the long term since it can trap moisture and other toxic materials in the gap and will be harmful to the connection detail. When the actuator load was released, the crack width was about 0.14 inch at the top deck. Due to the post-tension effect, the compressive force could bring the gap back a little bit.

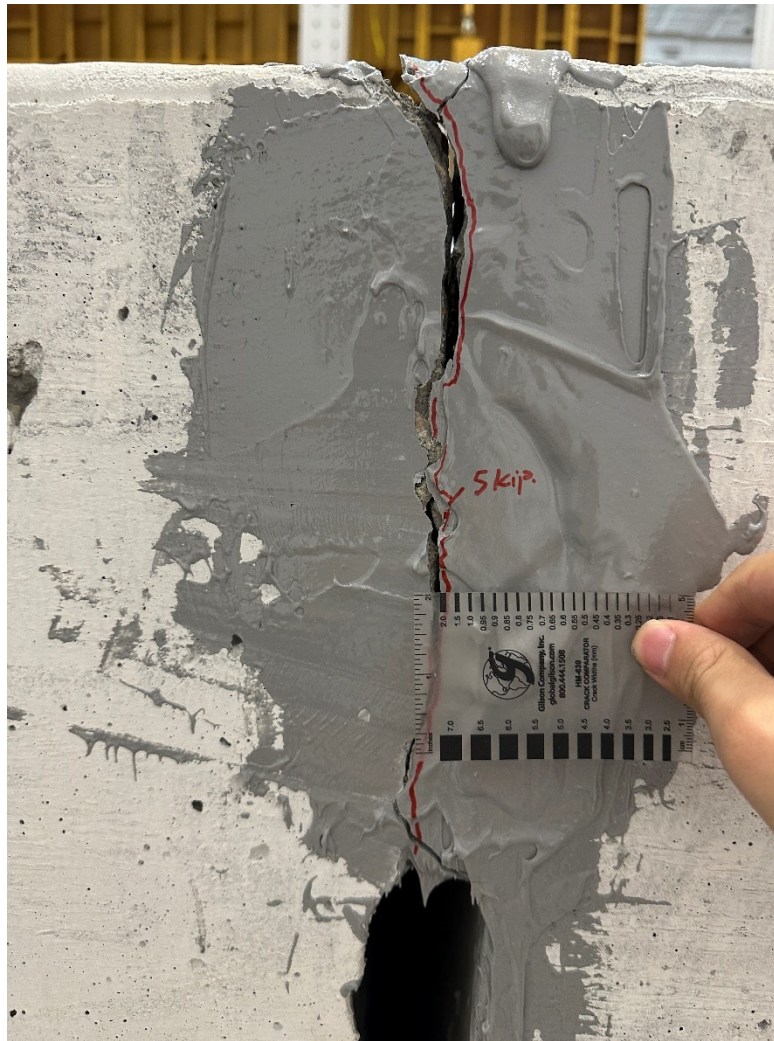


Figure 5.272. Concept D Match-Cast Joint Southside View of Interface Crack.

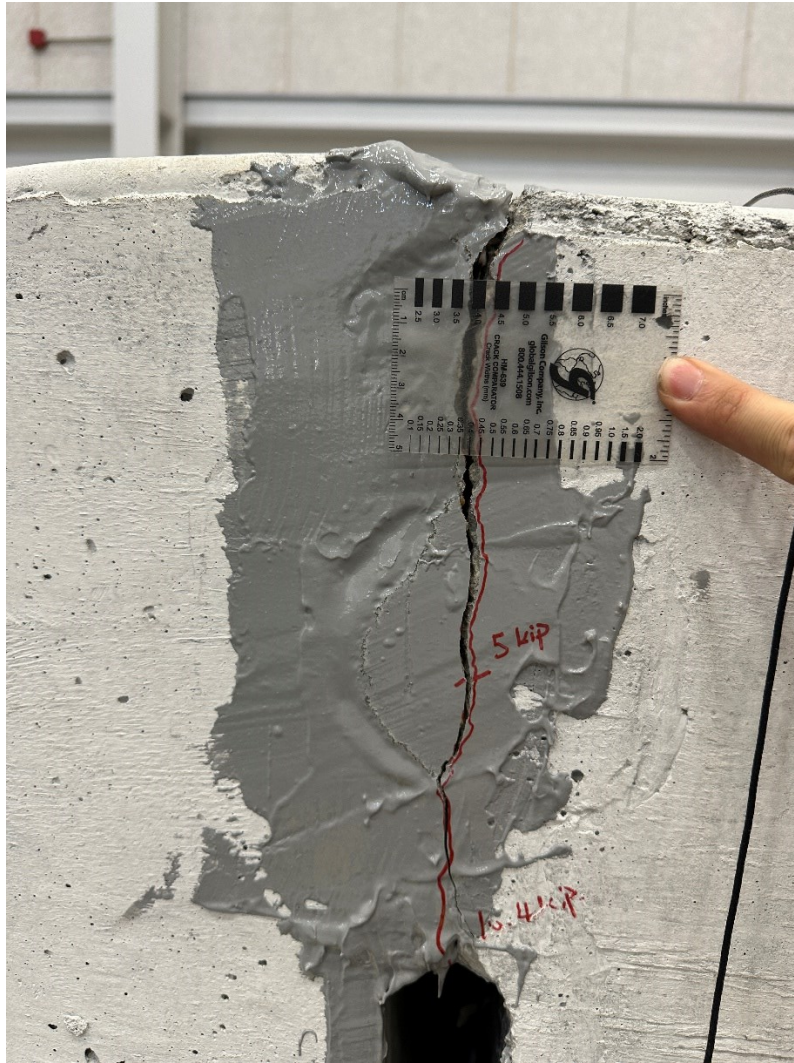
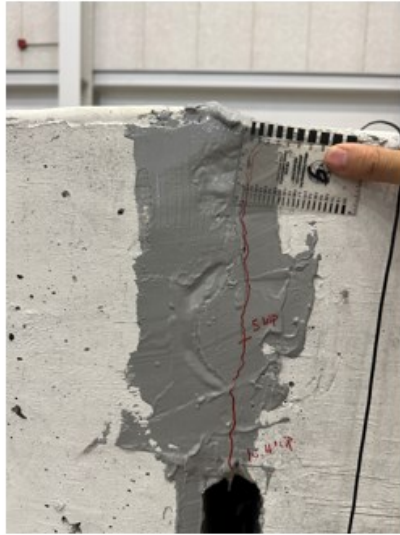
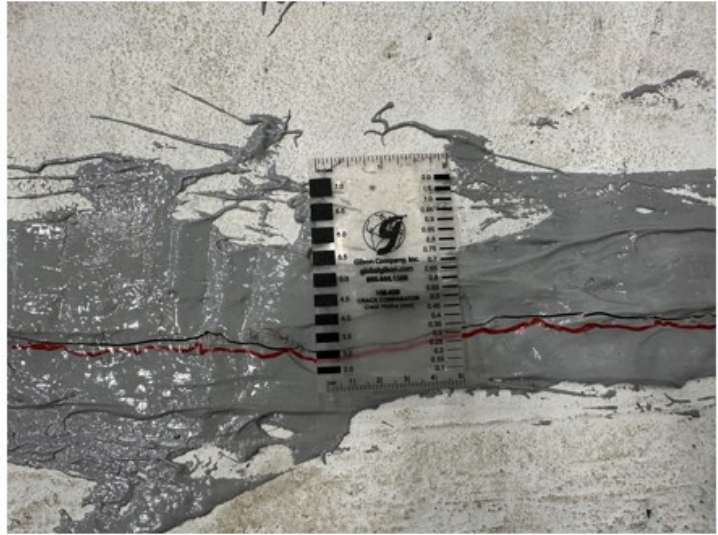


Figure 5.273. Concept D Match-Cast Joint Northside View of Interface Crack.

The crack width measurement after the specimen was put back on the support pedestal was captured. Figure 5.274 reveals the crack width at the adhesive joint was close to 0.004 inch at the top deck surface and side of the adhesive joint, which shows that the crack could close up by itself when all of the live load was released. The match-cast construction method may also be considered a good method to implement if the open gap can be controlled in a very small range.



(a)



(b)

Figure 5.274. Concept D Match-Cast Joint Interface Cracks after Sitting on Support Pedestal: (a) Elevation View and (b) Top View.

5.11.2.5. Direct Data Comparison

The average of the concrete surface stresses at gridline W1 for each concept can be seen in Figure 5.275. Similar to gridline E1, Concept A started at near-zero stress due to the absence of the Williams bar PT, while Concept B and Concept C started in net compression. Concept A saw a modest increase in stress during the testing. Concept B and Concept D remained in net compression during the entirety of the testing. Concept C remained in net compression until approximately 65 kips was reached, which is equivalent to over two times the HL-93 load. Past 65 kips, the cracking around the gauges caused noise to be captured in the data.

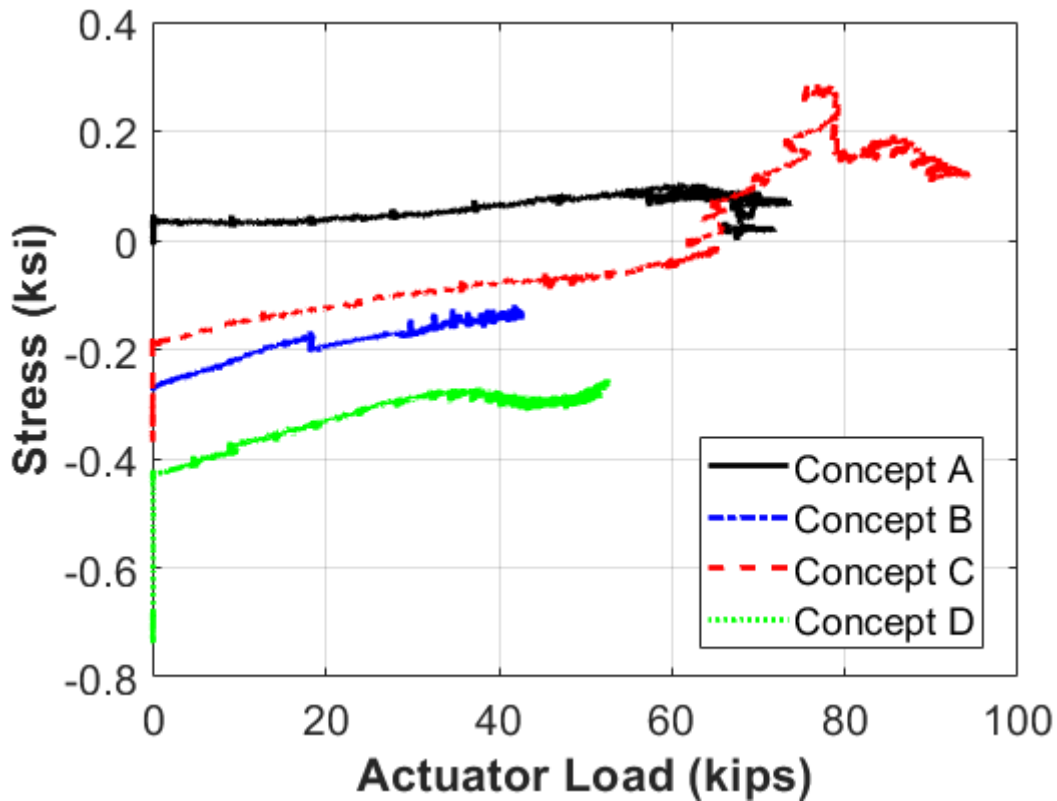


Figure 5.275. All Concepts Ultimate Testing Precast Concrete Deck Stresses at W1.

The average of the rebar stresses for each concept at gridline W1 can be seen in Figure 5.276. All the concepts recorded very similar stresses during the initial portion of the testing. The rebar for Concept A, Concept B, and Concept D remained below 5 ksi during the entirety of the testing, while Concept C remained below 5 ksi until 80 kips was reached on the active loading end, which is equivalent to over 250 percent of the HL-93 loading. Therefore, the rebar was not highly stressed at this location. The reason that the rebar was not highly stressed was that the rebar had not been developed at this location.

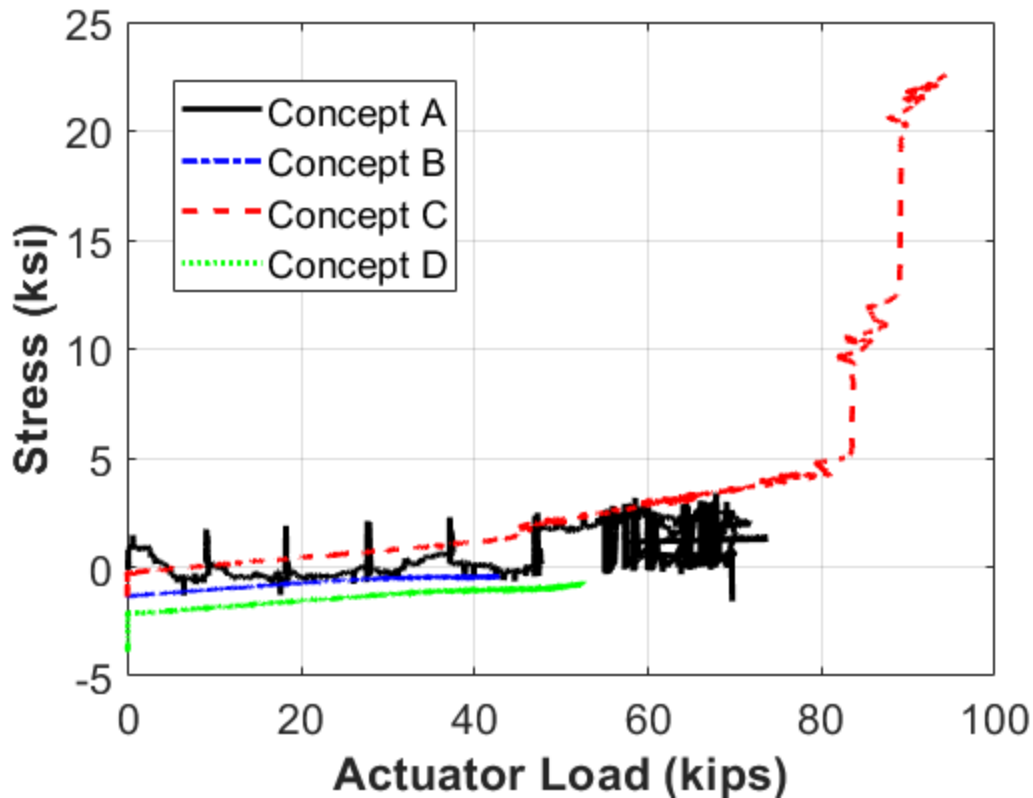


Figure 5.276. All Concepts Ultimate Testing Rebar Stresses at W1.

The stress on the centerline rebar for Concept A and Concept C in the closure region at gridline E0.5 (Concept A) or E0.3 (Concept C) is shown in Figure 5.277. Due to the loss of data at the other gauges on this gridline, only the centerline gauge data are shown. Both concepts show similar data during the testing. The Concept A rebar maxed out just below 20 ksi, which is only a third of yield stress. Concept C, however, maxed out at almost 60 ksi, which is the yield stress of the rebar. The load that it took to get to that point was approximately 85 kips, though, which is equivalent to 266 percent of the HL-93 loading, and therefore is a very high load level that would not be seen in an actual bridge.

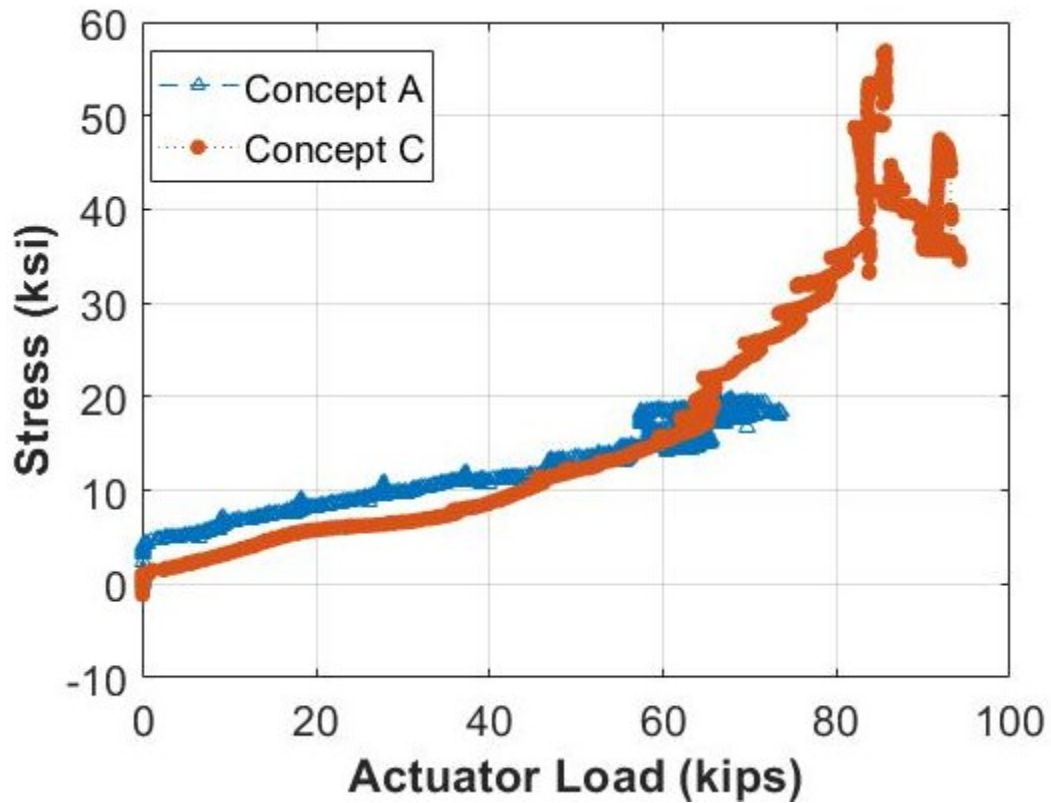


Figure 5.277. Concept A and C Ultimate Testing Rebar Stresses at E0.5 or E0.3.

Similar to the previous plot, the average rebar stresses at gridline W0.5 (Concept A) or W0.3 (Concept C) can be seen in Figure 5.278. Since the data from the other gauges were available at these locations, the average data of three gauges were used instead of only a single gauge. The data are very similar to data from the east side of the closure pour, with Concept A maxing out at just below 20 ksi, and Concept C reaching almost 60 ksi.

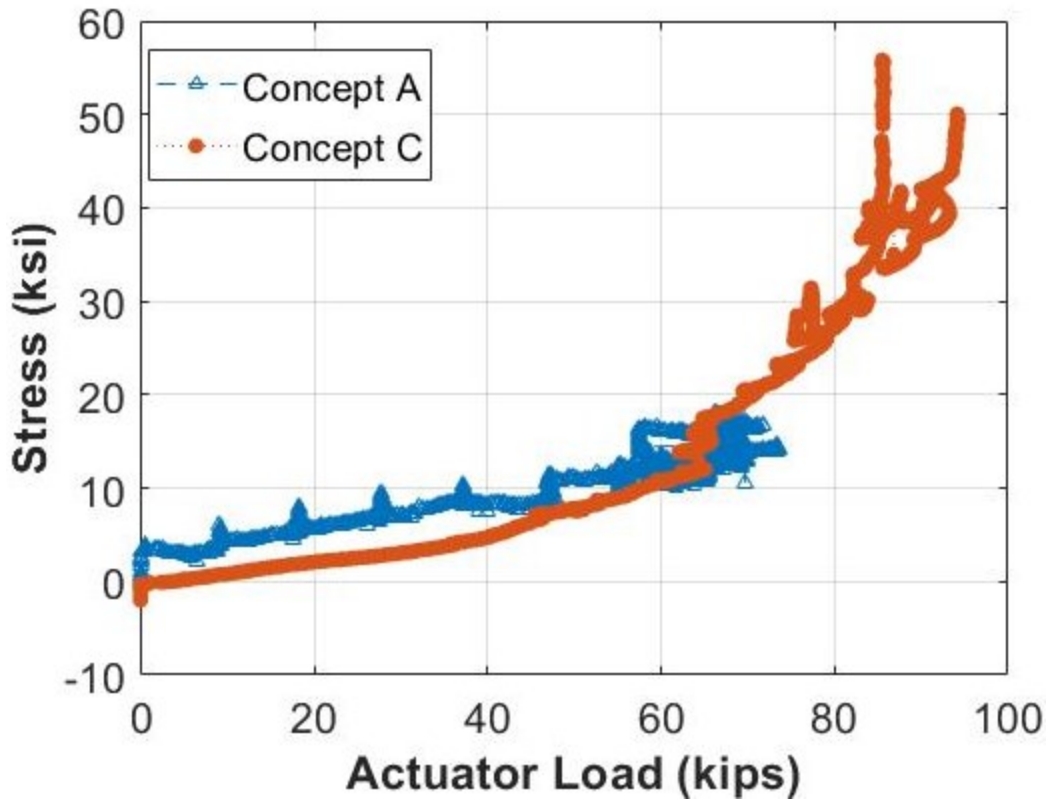


Figure 5.278. Concept A&C Ultimate Testing Rebar Stresses at W0.5 or W0.3.

5.11.3. Tension-Resisting Elements

The following sections compare the overall performance of the tension-resisting elements between the specimens. Sections 5.11.3.1, 5.11.3.2, 5.11.3.3, and 5.11.3.4 describe the observations of each of the concepts, while 5.11.3.5 uses the available data taken from the steel strain gauges on the splice plates in Concept A and the steel strain gauges on the Williams bars in Concept B, Concept C, and Concept D to determine which tension element performed the best.

Overall, the tension-resisting elements for Concept A differed from the other three concepts. The top flange splice plates for Concept A were relatively quickly assembled, only taking 1 or 2 days. The issue with the rate of assembly of the top flange plates comes when the holes do not line up properly. If that situation is the case, then the holes must be modified in the field, or a new plate must be made. The bracket assemblies for Concept B and Concept C took slightly longer to assemble. The brackets should be welded to the bottom of the top flange to allow it to be done off-site; however, the tightening of the Williams bars is a more time- and labor-intensive process. The Williams bars should not be fully tightened before first tightening the adjacent Williams bars

to help preventing uneven compressive stress distribution in the deck. Therefore, it takes more time to switch between the Williams bars than to only tighten the top flange plate, like in Concept A. Concept D took about two times as long as Concept B and Concept C since it had to post-tension four Williams bars instead of two of them.

The long-term durability varied between the specimens. The splice plates for Concept A may need to be replaced if they start to become corroded, which will require the removal of the closure pour area directly above it. The bracket assemblies and Williams bars for Concept B and Concept C, on the other hand, can be replaced without damaging the rest of the specimen in the case of damage. Concept D is relatively easy to check and replace if necessary. The safety of the specimens is highest for Concept A. There is virtually no risk of injury or damage happening from the assembly or use of the top flange splice plates. There are more things to consider for Concept B and Concept C bracket assemblies, such as welding or Williams bar failure during tensioning, which could cause severe injury. Concept D is also relatively safe since the Williams bars are against the concrete block. The PT process for Concept D is similar to that of Concept B and Concept C. However, if all aspects of the bracket and Williams bar are properly designed, this should not present any issues. The cost-effectiveness of Concept A is the highest since the splice plates are relatively cheap to manufacture and install. The bracket assembly for Concept B and Concept C are costlier to manufacture and install, and the Williams bars are expensive to ship if ordered in small quantities. Concept D also requires special labor for the PT process; in addition, the number of Williams bars for Concept D is two times the bars for Concept B and Concept C.

5.11.3.1. Concept A

The tension-resisting elements of Concept A consisted of two parts. The main intended element to resist tension is the top flange splice plates. The secondary part to resist tension is the rebar in the concrete slab/closure pour. The splice plates were easy to assemble. The only difficult portion of the splice plate assembly was getting around the protruding U-loop bars that stuck out of the precast slab. In the case of increased slab rebar, accessing the area of the bolt to pretension them may become problematic.

The top flange splice plates performed very well during the experimental testing. Three physical methods were used to evaluate their performance during testing. The first was to mark the ends of the plates so that if there was any movement during the testing, it could be seen upon inspection. See Figure 5.279 for an example view of these markings.



Figure 5.279. Concept A Splice Plate Markings.

The second method to evaluate the performance of the splice plates was by listening for any sounds of the plates slipping. This approach is not reliable by itself for determining which plate slipped. The third way to evaluate the splice plates was to visually inspect them after testing. The plates were taken off the specimen, and the surfaces were inspected for signs of slippage.

During static testing, the plates performed well. No signs of the plates slipping past their markings were seen upon inspection. No sounds were heard either. Similarly, for the cyclic testing, no signs of slippage were observed. However, during the ultimate portion of testing, signs of slippage were observed. At approximately 74 kips, the first sign of slippage occurred. A

loud bang was heard, accompanied by a drop in actuator load to about 58 kips. The load was increased again to 72 kips, at which point another loud bang was heard, and another drop in load occurred. Upon visual inspection, the plates on the top flange did not appear to have moved from their pretest position, indicating that slippage had occurred on the bottom flange/web plates (these splice plates' performance is evaluated in Section 5.11.4.1). Removing the splice plate under the top flange provided visual proof that no slippage had occurred on the top flange. See Figure 5.280 for a view of the splice plate under the top flange after it had been removed from the specimen. The dark marks on the plate did not move from one side to the other, indicating that the plate remained stationary.



Figure 5.280. Concept A Top Flange Splice Plate.

The top splice plate on the top flange could not be inspected because it was encased in concrete. Since it was encased in concrete and no signs of concrete damage directly above the plate were observed, it can be assumed that the top plate did not slip either.

5.11.3.2. Concept B

The only tension-resisting element in Concept B was the Williams bars. Initially, the Williams bars were tensioned to approximately 73 ksi, which is 49 percent of their theoretical ultimate strength. After running the static portion of the experimental testing, the specimen started to lose stiffness at only 14 kips. It was decided to increase the tension in the bars to approximately 70 percent of their theoretical ultimate strength. This step allowed the slab to remain in compression longer, which was until approximately 28 kips on the active loading end actuator.

During the first static testing, a loud bang was heard, and the strain in the Williams bars dropped significantly. It was determined that the brackets had slipped and that they would need to be modified. The brackets were welded to eliminate the possibility of slip.

Tensioning the Williams bars was a difficult procedure. A special stand had to be fabricated to support the through-hole jack as the PT was completed. In a real-world bridge construction setting, it would be difficult to support this jack when it is high in the air.

Welding the brackets provides a much more consistent way to fasten the brackets to the beams than using slip-critical bolts. The brackets can be welded to the beam in the fabrication shop, eliminating the need for field welding or for construction workers to do any bolt pre-tensioning. Welding is also a much more controllable process than using slip-critical bolts. Eliminating the bolts in this area allows for headed studs to be welded to the top of the beam flange, which much better locally ties the beam flange to the precast concrete deck. Without these headed studs in this area, the flange distorts, which can cause a gap to form between the flange and the haunch, as seen in Figure 5.149.

Using Williams bars alone did not provide the required stiffness to the specimen. The Williams bars should be paired with a reinforced closure pour to provide the greatest continuity across the slab, as was done in Concept C.

5.11.3.3. Concept C

Concept C consisted of two tension-resisting elements. The first was the Williams bars, like Concept B. The second was the rebar in the slab going through the closure pour, like Concept A. The combination of the Williams bars and slab rebar allowed this specimen to have the highest initial stiffness out of all the concepts. The Williams bars provided the initial compression to hold the slab together and to close any cracks that formed at low load levels, while the rebar held the slab together at higher load levels so that the specimen did not start to pivot about the bottom-flange bearing plates.

The same comments about the Concept B brackets and Williams bars apply to this concept as well. The brackets should be welded to the flange to eliminate potential plate slips. The same stand that was used in Concept B to support the through-hole jack was used for this concept.

With the brackets being welded, headed studs can be welded to the top of the flange, which ties the flange to the precast concrete deck. Because headed studs (see Figure 5.158) were added to the brackets for this concept, no air gap was seen between the flange and haunch, and no deck cracking directly above the brackets was observed.

Using Williams bars in conjunction with rebar in the slab provided compression to close any cracks that formed at low load levels, while the rebar held the specimen together at higher load levels. These two elements working together show that this concept has the potential to be durable in the long term.

5.11.3.4. Concept D

Williams bars were the only tension-resisting element for Concept D. The end of the Williams bars was against the precast concrete drop panel, and there was no reinforcement between precast concrete decks. The epoxy adhesive was filled between the precast units. The magnitude of the post-tension force was twice as high as Concept B and Concept C; however, the initial stiffness was only about 35 kips/in, which was the lowest of these four concepts. Creep behavior is an issue for Concept D. The displacement at E7 was about twice as much as the other concepts. Once the load passed about 45 kips, a relatively large portion of the tensile force was taken by the Williams bars.

The PT process was similar to Concept B and Concept C. The special stand was adjusted to adapt the height for Concept D. The same through-hole jack was used to post-tension the Williams bars. The whole process was longer than the previous concept because of the number of Williams bars. Similar to Concept B, using the Williams bar may not provide adequate stiffness to the specimen, but the crack at the transverse joint might close up when the live load is released.

5.11.3.5. Direct Data Comparison

The direct data comparison for each tension-resisting element of each concept is explained in the following paragraphs. The stresses on the top flange plates for Concept A can be seen in Figure 5.281 and the average stresses in the Williams bars for Concept B and Concept C can be seen in Figure 5.282. These data are from the ultimate testing portion of the experimental testing.

The stresses for Concept A start out at zero because there are no Williams bars in this concept to add any compression. The stress in the plates increases without an increase in actuator load because the top flange goes into tension as the specimen is self-supporting as a cantilever. As the load is increased, the tensile stresses in the plate increase as well. The reason there are spikes in the data is that the specimen was not positively connected to the ram, so when the ram stopped pushing down, the specimen kept going down for a moment and then rebounded. This pattern continued until about the 55-kip mark, which is when a lot of noise was read by the gauges. It was after that point that the plates started to experience small amounts of slipping, and the deck started to crack more. Even at the maximum loading, however, the stresses in the flange plates were lower than 15 ksi, indicating that the plates had much more capacity.

In the Williams bars' plot (Figure 5.282), the data start similarly until the active loading end reaches about 28 kips. Past this point, the stress in the Williams bars for Concept B started to drastically increase. The stresses in the Williams bars for Concept C, however, kept going on the same earlier trend, even decreasing some. The stresses in the Williams bars for Concept C did not start to seriously increase until 65 kips was reached. The stress in the Williams bar for Concept D increased when the load was about 47 kips, which was about twice as much as the load magnitude of Concept B since the post-tension stresses were also two times the stress for Concept B and there was also no reinforcement between the two precast decks. The reason that the stresses in Concept B increased earlier was due to the lack of rebar in the closure pour. The rebar in the closure pour of Concept C provided continuity across the slab, allowing the rebar to take some of the tension along with the Williams bars. It also prevented the specimen from splitting apart, as was seen in Concept B. These data, paired with the stiffness of the specimens (which is discussed in Section 5.11.5) show that rebar should be used in the closure region to allow the Williams bars to perform better.

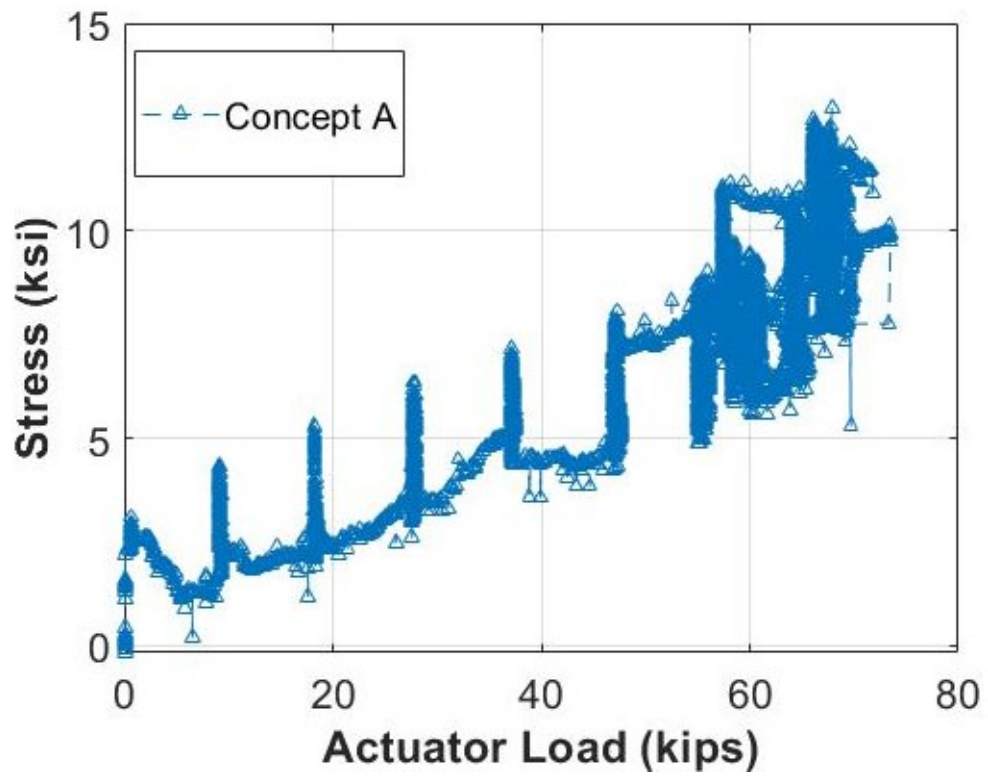


Figure 5.281. Ultimate Testing Concept A Top Flange Splice Plate Stress versus Load.

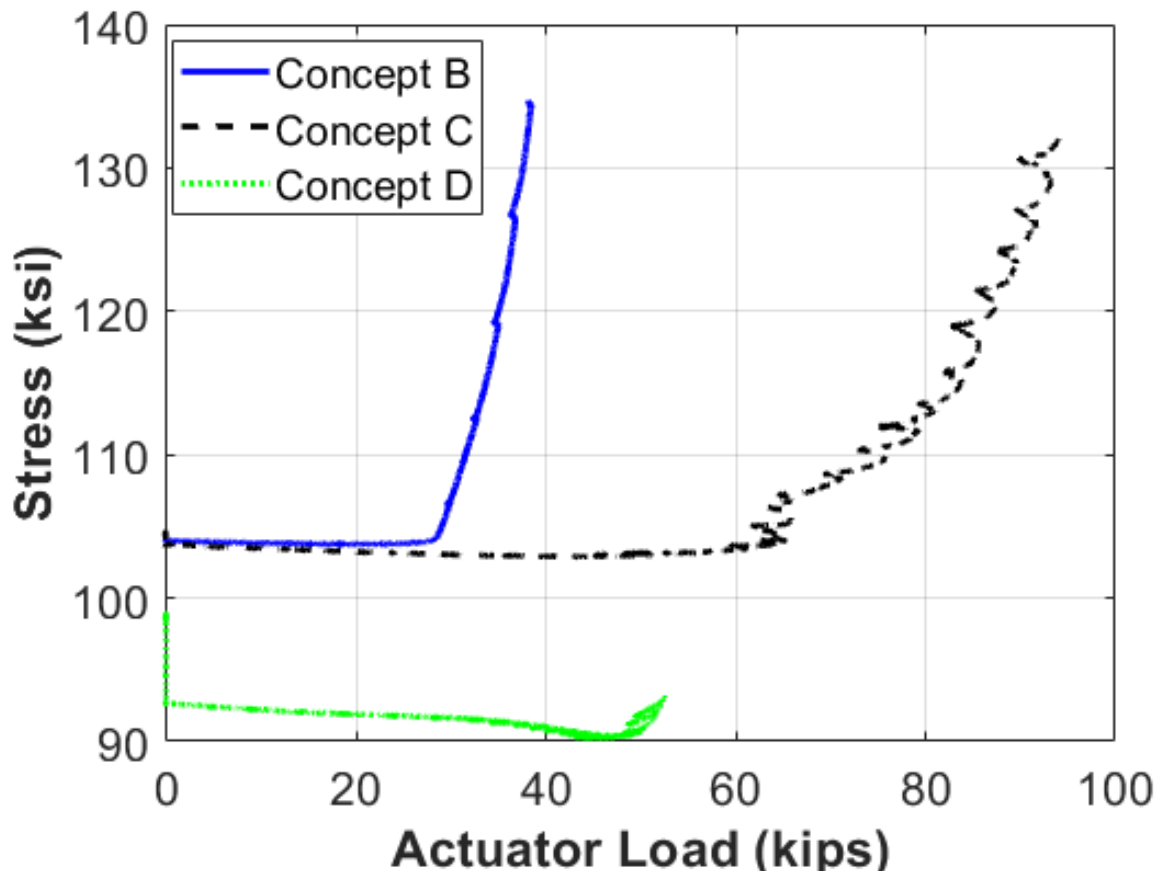


Figure 5.282. Ultimate Testing Concept B, C, and D Williams Bar Stress versus Load.

The average stresses in the beam top flange for each concept at gridline E1 can be seen in Figure 5.283. The stresses for Concept B, Concept C, and Concept D started in compression due to the PT of the Williams bars. Concept B remained in compression during the entire test, while Concept C remained in compression until approximately 50 kips was reached on the active loading end. Concept D remained in compression until about 25 kips of the actuator load. Concept A started in slight compression but moved to tension as the specimen was self-supporting and increased the most rapidly out of all the specimens. The reason that Concept A stresses increased so much is because the top flange was directly connected by the top flange splice plates. The splice plates provided a direct path for the tensile forces to travel as the testing proceeded. Concept B, Concept C, and Concept D were not directly connected across the top flange and therefore saw a much smaller increase in tension. The magnitude of all the specimens' stresses was still relatively low. Only Concept A saw an appreciable amount of stress in the top flange, but it was still less than 10 ksi at its maximum, which is well below yield.

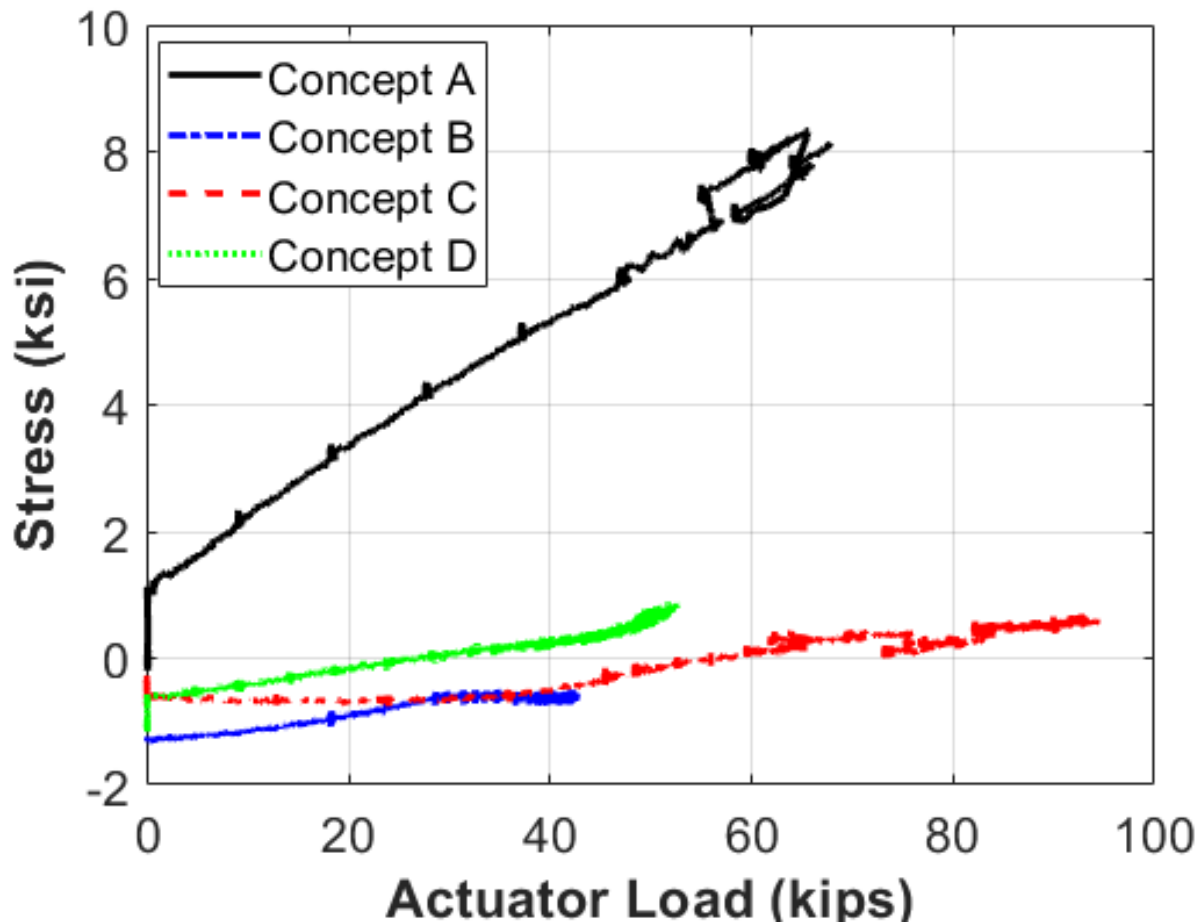


Figure 5.283. All Concepts Ultimate Testing Top Flange Stress at E1.

Similar to the previous figure, Figure 5.284 shows the average stresses in the top flange at gridline W1. Concept A data are very similar to data from gridline E1, while Concept B, Concept C, and Concept D are slightly different. Concept B started out with approximately 2 ksi of compression, and Concept C started out with no stress. Concept D started out with about 1 ksi of compression and went to tension when the load was about 25 kips, which was very close to the stress at E1 for Concept D. Concept B remained in net compression during the entire test, while Concept C saw a small increase in tension to about 1 ksi. The total magnitude of the stresses at W1 on the top flange was very low, like at gridline E1.

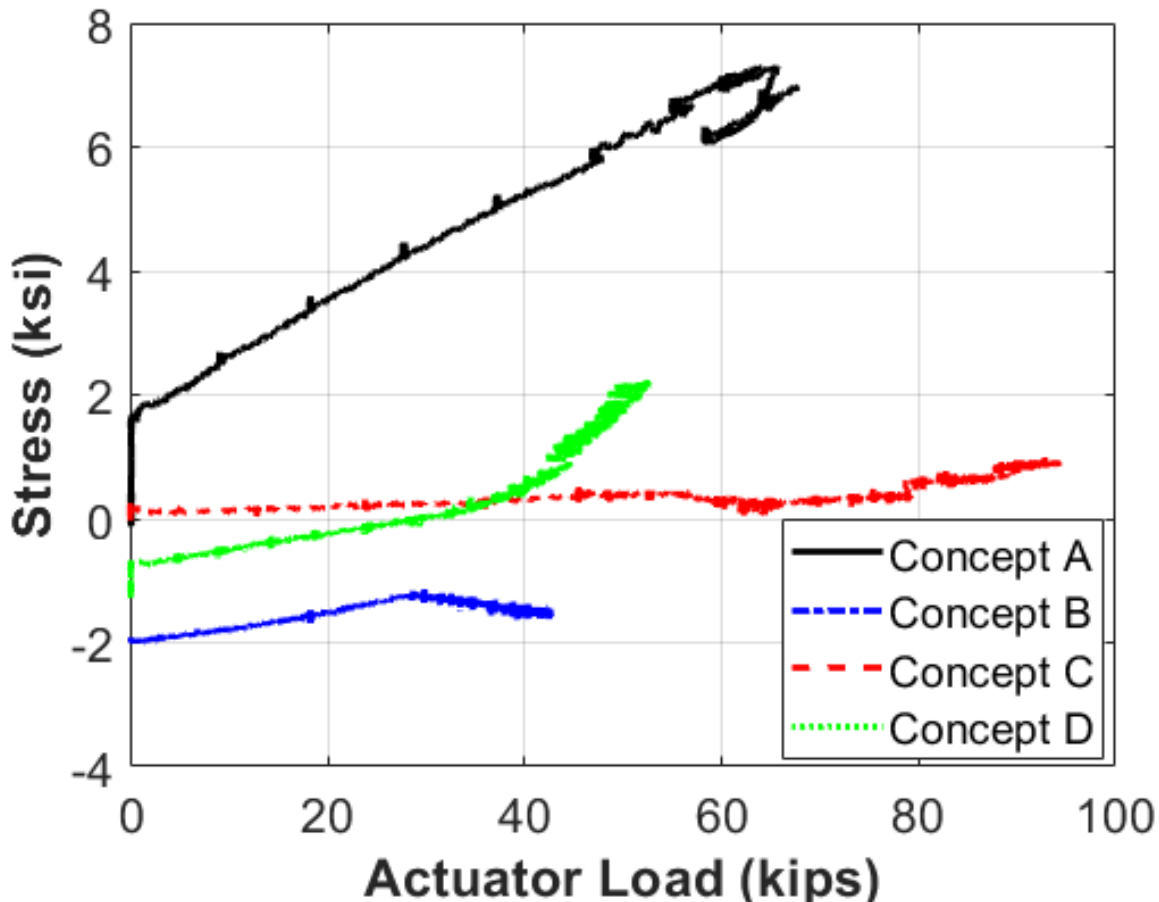


Figure 5.284. All Concepts Ultimate Testing Top Flange Stress at W1.

5.11.4. Compression-Resisting Elements

The following sections compare the overall performance of the compression-resisting elements between the specimens. Sections 5.11.4.1, 5.11.4.2, 5.11.4.3, and 5.11.4.4 describe the observations of each of the concepts, while 5.11.4.5 uses the available data taken from the steel strain gauges on the splice plates in Concept A and the steel strain gauges on the bottom flange nearest the transverse centerline in Concept B, Concept C, and Concept D to determine which compression element performed the best.

The compression-resisting elements' performance varied between the concepts. The fastest and easiest of the elements to assemble was the bearing plates for Concept C because it only required bolts to be inserted into the prefabricated holes to hold the specimen in place during erection. Concept D was the second fastest. Concept B was the third fastest, and Concept A was the slowest. The long-term durability of each concept was relatively similar. In the event of damage, each element for each concept can be replaced with relative ease. The safety of each of these

elements is very good too. None of these elements are at risk of causing major injury or damage as long as proper construction site safety rules are followed. Concept A and Concept C are also cost-effective since plates and bolts are relatively cheap items. The UHPC for Concept B is more costly, but it can possibly be replaced with high-strength concrete. Concept D was fully precast and only needed epoxy adhesive placed on the surface of the bottom shear key part.

5.11.4.1. Concept A

The compression element for Concept A consisted of splice plates on the bottom flange and a web with slip-critical bolts. These splice plates resisted the compressive forces well, maintaining their function until approximately 65 kips, or the equivalent of 210 percent of the HL-93 loading, had been reached. At that point, a small amount of slip was detected, as seen in Figure 5.66. SG47 and SG48—located on the bottom splice plates—maintained a linear relationship between the actuator load and the stress in the plates until the slip happened at 65 kips.

The same physical metrics to evaluate the top flange splice plates were used to evaluate the bottom flange splice plates. The edges of the plates were marked so that it could be seen if they slipped. Unlike with the top flange splice plates, it could be visually determined that the splice plates had moved at the end of the ultimate testing (indicating the bottom splice controlled the design). The location of the splice plates relative to the beam flange before testing can be seen in Figure 5.285, and the location of the splice plate relative to the beam flange after testing can be seen in Figure 5.286. It can be seen that the splice plates had moved between $\frac{1}{16}$ and $\frac{1}{8}$ of an inch.

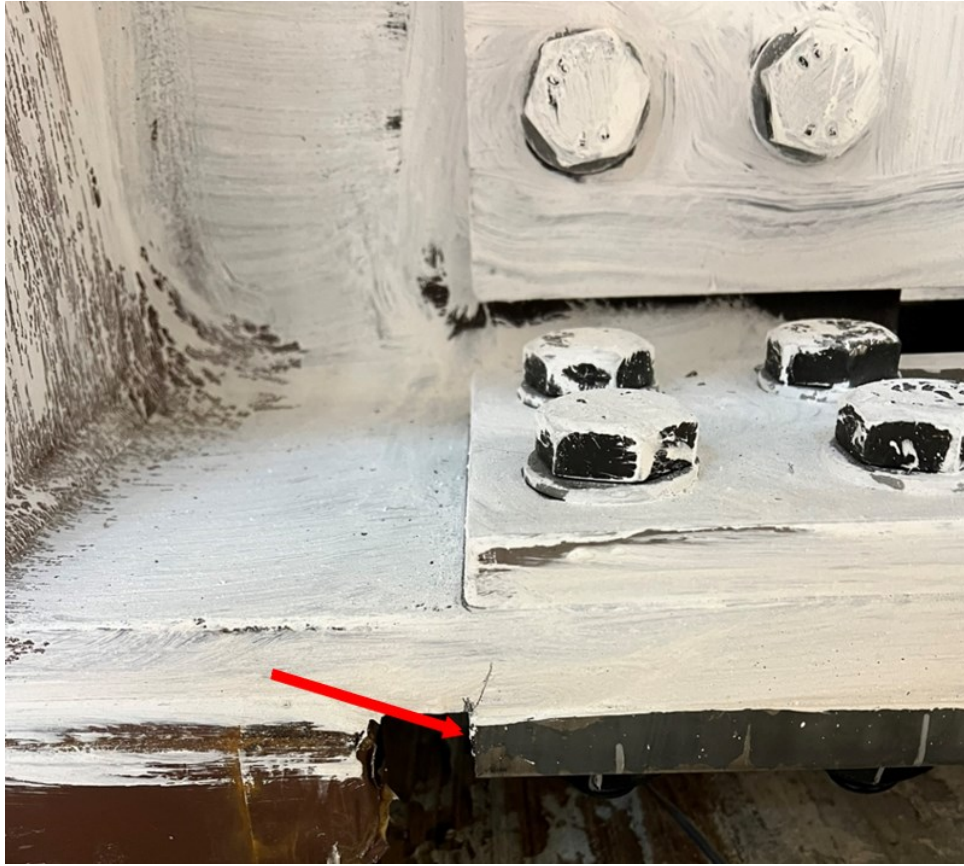


Figure 5.285. Concept A Bottom Flange Splice Plate Markings Pre-slip.



Figure 5.286. Concept A Bottom Flange Splice Plate Markings Post-slip.

A loud bang was also heard when the bottom flange splice plates slipped. Upon inspection of the splice plates after they had been removed, it can be seen from the markings on the surface in contact with the steel beam that movement had occurred. See Figure 5.287 for a view of the splice plate after testing. It can be seen that the markings for this splice plate moved parallel to the direction of the beam, indicating that a slip happened.

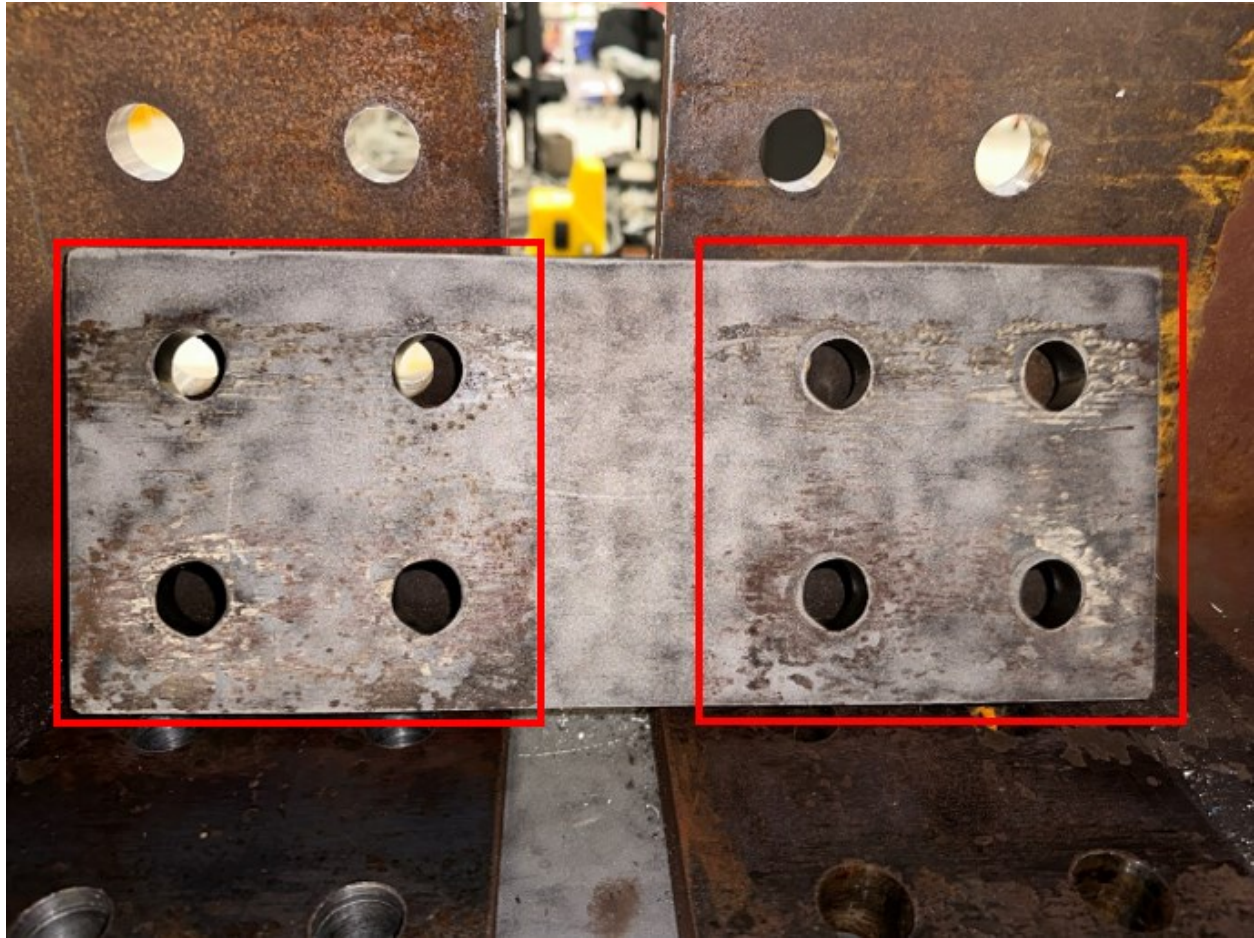


Figure 5.287. Concept A Bottom Flange Splice Plate after Testing.

In Figure 5.288, similar markings can be seen on the splice plates that were on the bottom portion of the web. The markings for those plates do not extend quite as far as the ones for the flange splice plates. Interestingly, the markings appear to be concentrated on only one side, indicating that only one beam moved when the web splice plates slipped, and not both of them, as with the flange splice plates.

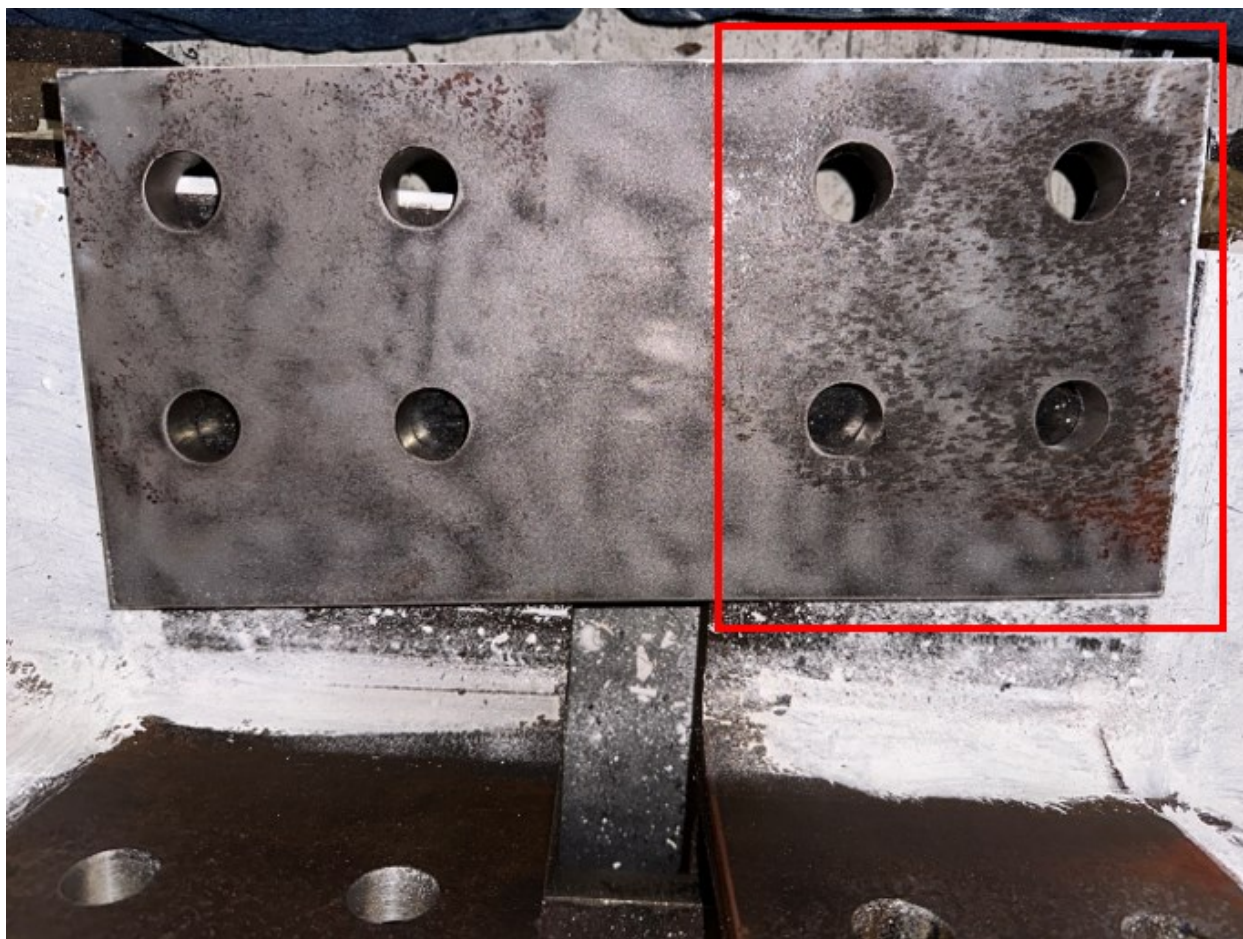


Figure 5.288. Concept A Web Splice Plate after Testing.

Since the bottom flange splice plates maintained their function until at least 65 kips, or 210 percent, of service loading, they can be considered to be durable long-term. Moreover, when the negative moment over the pier is relatively large, it may not be possible to fit enough bolts in the provided space without moving the bearing pads further apart, which will cause the pier bent to have to be expanded.

5.11.4.2. Concept B

The compression-resisting element for Concept B consisted of two channels welded to the bottom portion of the web and the bottom flange that were face-to-face, with the void between the channels filled with UHPC. Because the channels were shop-welded to the beam, the installation for this concept was very quick. The only step that needed to be completed in this area before pouring UHPC into the void was to seal the small gap between the channels with caulk to prevent any UHPC from leaking out of the void. Since it would have been difficult to

ensure that the entire surface of the channels was in contact with each other, a $\frac{1}{16}$ - to $\frac{1}{8}$ -inch gap was left between the channels that could be filled with caulk to close the gap. This gap, after being filled with caulk, can be seen in Figure 5.289.



Figure 5.289. Concept B Channel Void Gap Filled with Caulk.

The UHPC was poured into the void between the channels at the same time as the closure pour. Due to the formwork around the void, it was slightly difficult to access this area, but since it was a small volume, it did not hinder progress much.

No cracks were observed to have formed in this area after testing concluded. The concrete provided a path for the compressive forces to be transferred from one beam to the other. Due to the high cost of acquiring UHPC compared to normal concrete, this portion of the concept could have been replaced with high-strength concrete.

5.11.4.3. *Concept C*

The compression-resisting elements for Concept C consisted of two steel plates that were shop-welded to the bottom flange and bottom portion of the web and placed against each other in bearing. This step provided a very simple yet effective method to transfer the compressive forces from beam to beam. See Figure 5.290 for a view of these bearing plates.



Figure 5.290. Concept C Bottom Flange Bearing Plates.

These bearing plates performed very well during the experimental testing. They were extremely easy to install, only requiring two ½-inch bolts to be installed through the plates to hold the beams in place while placing them on the pedestal. The only issue with installing these plates that arose was when it was observed that both plates were not perfectly parallel to each other when installed. If the beams were placed so that the plates were parallel to each other, the end of the beam on the active loading end was 3–4 inches off of the center, but if the beams were lined up, then the bearing plates had a gap on one side that was approximately ⅛ inch across, which can be seen in the previous image. This issue was rectified by placing the beam in a straight line and then tightening the bolt on the side with the gap to bring the plates together as much as possible, which slightly closed the gap. If the gap between the plates was larger, a shim plate could be inserted into the gap to provide a bearing between the plates.

5.11.4.4. Concept D

The compression-resisting elements for Concept D consisted of two shear key parts of the precast concrete drop panel. All of them are precast concrete parts, which is a very simple and effective way to transfer the compressive forces from beam to beam. Figure 5.291 presents an elevation view of the bottom shear key parts.

The bottom shear key parts performed relatively well during the course of testing. There were no extra steps to connect the bottom parts except for putting the epoxy adhesive on the surface, which only took about 30 minutes. The relatively large contact area also distributes the compression force equally to the beam, which makes the specimen stable at the bottom part.

Out of all the concepts, Concept D and Concept C both provided the greatest combination of ease of installation, cost-effectiveness, long-term durability, and compressive resistance. The UHPC channel enclosure of Concept B takes longer to construct and requires the use of UHPC or high-strength concrete. Although Concept A provides another excellent way to transfer the compressive forces, it takes the longest to assemble. The bottom flange splice plates are also limited by the width of the concrete pier, which could control the design.

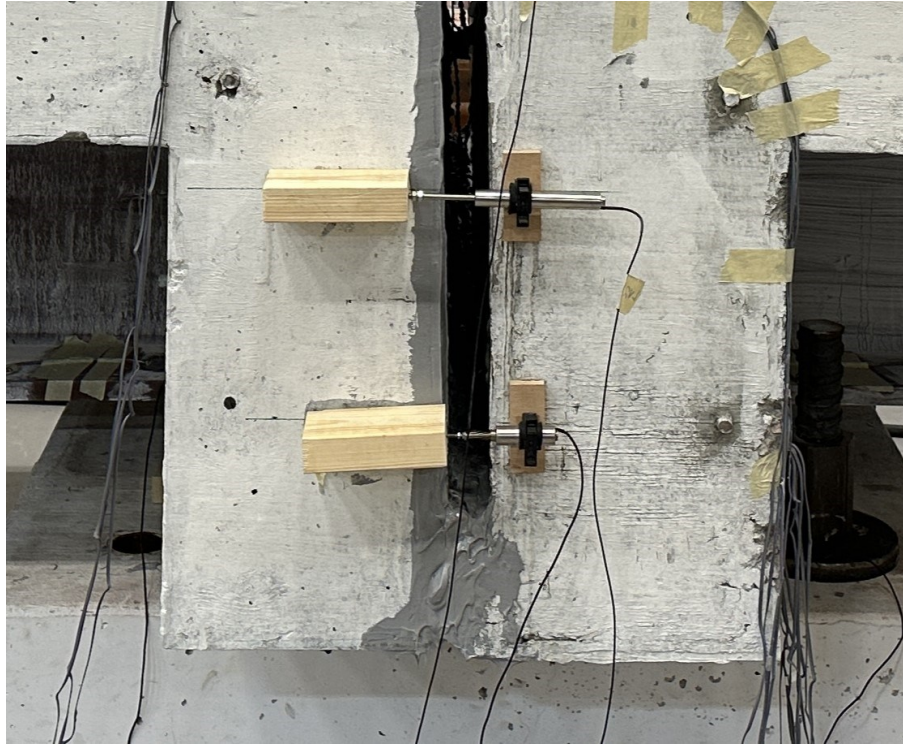


Figure 5.291. Concept D Bottom Shear Key Parts.

5.11.4.5. Direct Data Comparison

The direct data comparison for each compression-resisting element for each concept is explained in the following paragraphs. The average stresses in the bottom flange at gridline E1 for each concept are shown in Figure 5.292. The stresses in Concept A started out at 0 ksi and dropped slightly as the specimen became self-supporting as a cantilever. It continued to increase in compression until the slip in the bottom flange plates occurred at 74 kips. It decreased in compression slightly but followed the same path as testing continued. The data for Concept B and Concept C are nearly identical up to about 28 kips. They both started with net compression in the bottom flange due to the PT from the Williams bars. This compression increased as the specimen became self-supporting as a cantilever. The compression increased linearly for Concept B until 28 kips was reached, which is when the specimen started to exhibit nonlinear behavior. The stresses started to increase at a more rapid rate toward the end of the test. The stresses for Concept C continued to linearly increase in compression, almost reaching 30 ksi by the end of the testing, which is almost 60 percent of the yield. Concept D also started with net compression in the bottom flange, but the stress was less than Concept B and Concept D since the compression-resisting element was a concrete shear key instead of steel plates against each

other. The concrete drop panel also took a small portion of the compressive force during the testing. The stress on the bottom flange for Concept D only reached 10 kips when the load was about 52 kips, which was about 60 percent of the magnitude for Concept C.

The reason that Concept B, Concept C, and Concept D have a higher magnitude of stresses than Concept A is due to the Williams bars. The Williams bars provided initial compression to the entire specimen, while Concept A did not have any precompression.

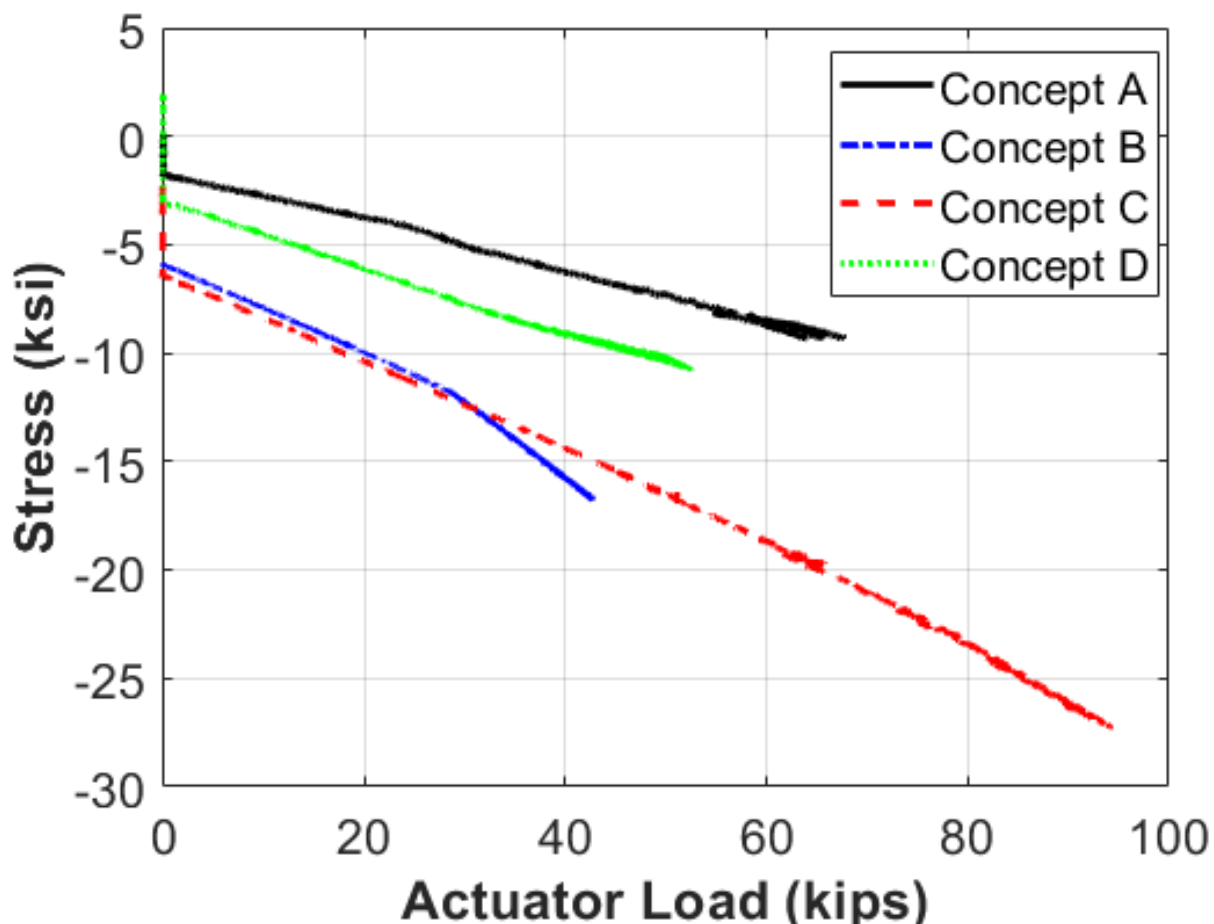


Figure 5.292. All Concepts Ultimate Testing Bottom Flange Stress at E1.

The data at W1, which can be seen in Figure 5.293, on the bottom flange show very similar results to those on gridline E1. The stresses in Concept A maxed out at about 14 ksi, while the stress in the bottom flange of Concept B also maxed out at about 14 ksi but at a much lower load level. The stress for Concept D was quite close to Concept A, which was about 8 kips when the load reached about 50 kips. The stresses for Concept C, however, nearly reached 25 ksi. All concepts' stresses increased at nearly the same rate.

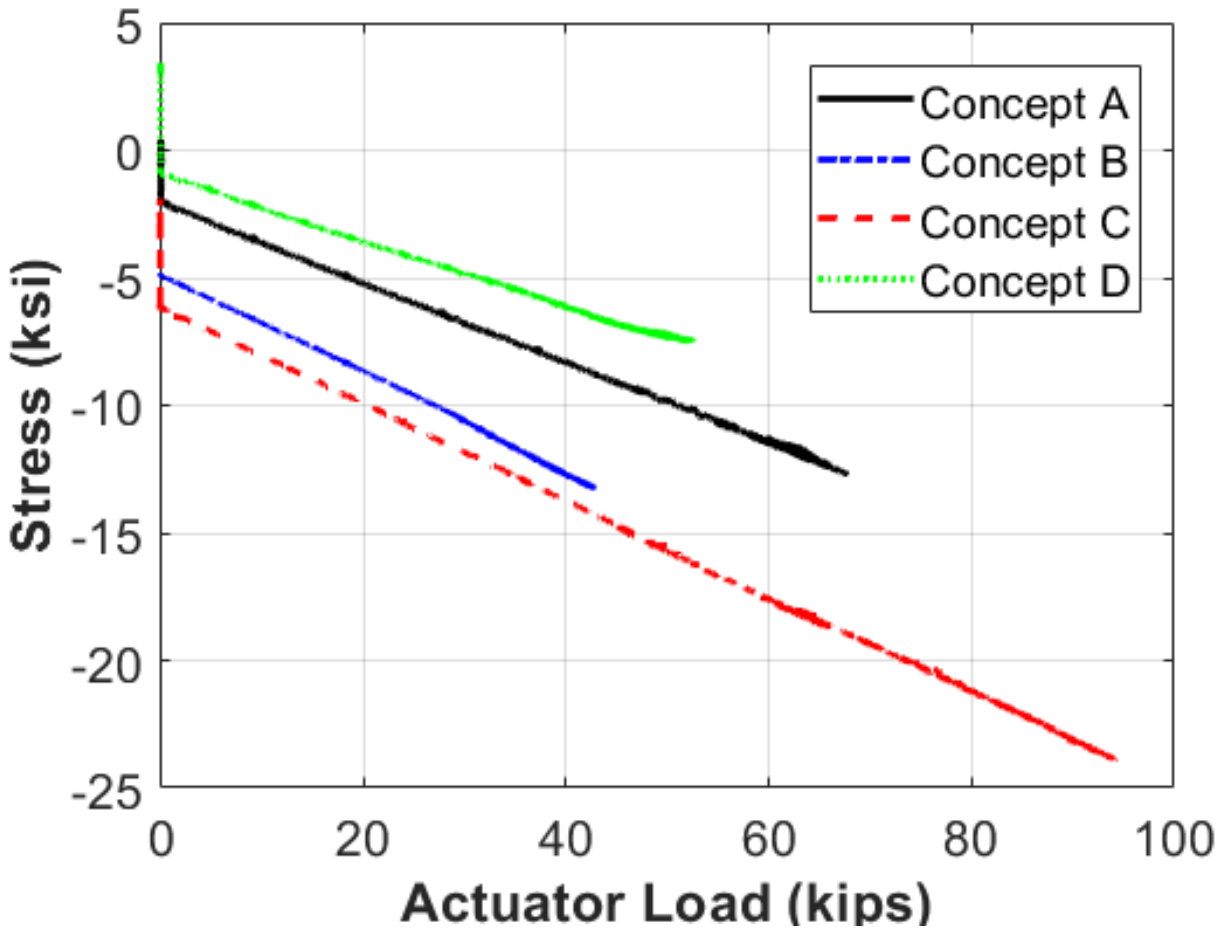


Figure 5.293. All Concepts Ultimate Testing Bottom Flange Stress at W1.

5.11.5. Stiffness

The following sections compare the overall flexural stiffness of the specimens. Sections 5.11.5.1, 5.11.5.2, 5.11.5.3, and 5.11.5.4 describe the observations of each of the concepts, while 5.11.5.5 uses the available data taken from the string pots, load cells, and LVDTs to determine which specimen had the most stiffness and had the smallest loss of stiffness at the end of the ultimate testing.

5.11.5.1. Concept A

Concept A had the second lowest initial stiffness, at approximately 75 kip/in. This stiffness was mostly maintained until the active loading end actuator reached 56 kips, at which point some of the stiffness was lost after each loading application (see Figure 5.60). Each small drop was a crack forming, while the larger drops were from the splice plates on the bottom portion of the

specimen slipping. Interestingly, after each drop in load, the stiffness appeared to be almost identical to the initial stiffness.

When the testing was stopped at the maximum load of 74 kips, the maximum stresses in the steel beam were only 10 ksi. The stresses in the splice plates stayed under 20 ksi, and the rebar in the closure pour was less than 25 ksi. Therefore, the stiffness was controlled by the cracking of the concrete slab and not due to any plastic behavior of the steel.

5.11.5.2. Concept B

Concept B had the second-highest initial stiffness, at approximately 80 kip/in. However, this stiffness was maintained only until about 28 kips, after which point the stiffness dropped significantly to 7 kip/in. This loss in stiffness coincided with the strain in the Williams bars starting to increase, indicating the NA had dropped below the bars. Without the rebar in the closure pour to provide continuity across the slab, the specimen started to rotate. The Williams bars were not able to compress the slab enough to hold the specimen together.

Based on these details, this loss of stiffness would have detrimental effects on the performance of a real-world bridge. Without the rebar holding the slab together, the closure region would open up, allowing water and other materials to penetrate the deck and damage it.

5.11.5.3. Concept C

Concept C had the highest initial stiffness, at approximately 90 kip/in. This stiffness was maintained until 64 kips was reached, at which point the stiffness decreased to about 20 kip/in. The higher stiffness was maintained until a relatively high load level (the equivalent of 207 percent of the HL-93 load level). The combination of the Williams bars to compress the slab as well as the rebar going through the closure pour—thereby providing continuity—allowed this concept to have the highest initial stiffness as well as the highest secondary stiffness.

5.11.5.4. Concept D

Concept D had the lowest initial stiffness, at approximately 35 kip/in. This stiffness was maintained only until about 36 kips, after which point the stiffness dropped significantly to 9 kip/in. The specimen crept too much, and the connection part was relatively soft due to the

cracks at the interface of the concrete drop panel. The strain in the Williams bars also started to increase when the load was about 40 kips, which showed that the NA of the specimen at the connection location had dropped below the bars. The specimen started to pivot at the interface of the precast drop panel since there was no continuous reinforcement between the two precast units. The Williams bar could not compress the concrete deck together when the load reached about 35 kips.

Similar to Concept B, the softening behavior of the connection detail will cause an issue in field applications. The adhesive joint would open up when the truck event happens, which will allow water and other materials to penetrate the transverse joint and cause damage. The cracks at the interface can cause similar issues and may speed the corrosion of reinforcement.

5.11.5.5. Direct Data Comparison

The data shown in Figure 5.294 show the overall displacement of the specimen versus the actuator load on the active loading end. The steeper the slope, the stiffer the behavior. Concept C had the highest initial stiffness out of the concepts, followed by Concept B, Concept A, and Concept D. The initial stiffnesses for all concepts were relatively similar except for Concept D, and all fell within the range that was expected. If only the steel beam and rebar were considered (cracked section analysis), the theoretical stiffness was calculated to be as small as 47 kip/in, while if the uncracked section was analyzed, the stiffness rose to 120 kip/in. During the experimental testing, the specimen went through several stages. At the start of testing, the specimen mostly resembled the fully uncracked composite section, but as testing progressed, the precast concrete deck started to crack, which more resembled the steel beam and rebar section. The stiffnesses of Concept A, Concept B, and Concept C fell within this range. Concept D was slightly below the range.

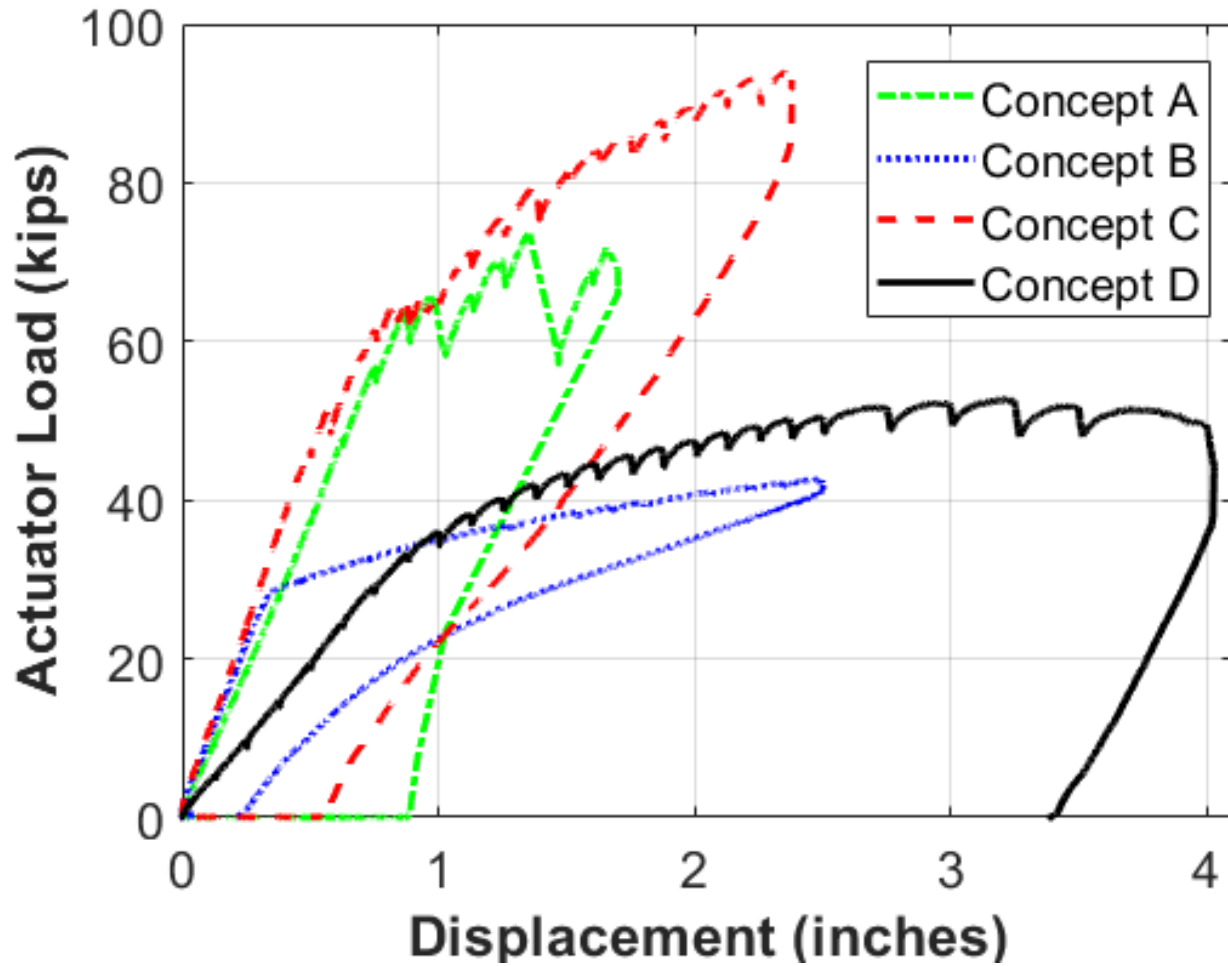


Figure 5.294. Load versus Displacement Concept Comparison.

The stiffnesses for Concept A and Concept C remained very similar until above 60 kips was reached. Past that point, Concept A started to experience plates slipping, and Concept C started to experience more cracking. Concept B had the lowest secondary stiffness due to having a more rigid body motion past 28 kips. The presence of a rebar in the closure pour connecting the two beams is what most contributed to the higher secondary stiffness of Concept A and Concept C.

5.11.6. Speed of Assembly

5.11.6.1. Concept A

Table 5.14 presents the full application and approximate construction time for Concept A based on the construction process implemented in the lab. The total construction time for the superstructure part, which includes girder erections, longitudinal and transverse concrete closure pour, and connection details for Concept A, was about 3 days. This type of connection

construction procedure could eliminate the potential bolt fit-up issues since the splice plates will have shop holes, and the flange holes could be field drilled. Some locations will utilize oversize or slotted holes in order to have more tolerance for the field connection construction, which could reduce construction time in the field.

Table 5.14. Typical Construction Procedures and Time of Concept A.

Construction Procedures	Construction Time of Concept A
Erection precast units	1 day (typically)
Longitudinal closure pour	1 day (typically)
Bolt left side of bottom splice	1 hour
Drill holes/bolt right bottom splice	3 hours
Bolt left side of top splice	1 hour
Drill holes/bolt right bottom splice	3 hours
Transverse closure pour	2 hours
	Total time: 3 days

5.11.6.2. Concept B

Table 5.15 shows the typical construction time for a Concept B connection type. Concept B included post-tensioned Williams bars, 4-inch wide UHPC closure pour and UHPC confined in a bottom channel. The total approximate construction time for Concept B was about 2.5 days, which was also based on the real construction completed in the lab. The narrow UHPC closure pour reduced construction time for Concept B. The post-tension installation was also relatively easy to implement since the number of Williams bars are only two per girder.

Table 5.15. Typical Construction Procedures and Time of Concept B.

Construction Procedure	Construction Time of Concept B
Erection precast units	1 day (typically)
Longitudinal closure pour	1 day (typically)
UHPC closure pour (4-inch wide) and UHPC in the bottom confined channel	2 hours
Install and post-tension threaded rods	2 hours
	Total time: 2.5 days

5.11.6.3. Concept C

Table 5.16 introduces the typical construction time for the Concept C connection type. The total construction time was about 2.5 days, which is based on the actual construction process finished in the lab. The bearing plates on the bottom part were easy to connect to each other by fastening the bolts, which reduced construction time for Concept C. The post-tensioned Williams bars were relatively easy to install because of the limited number of bars per girder.

Table 5.16. Typical Construction Procedures and Time of Concept C.

Construction Procedure	Construction Time of Concept C
Erection precast units	1 day (typically)
Longitudinal closure pour	1 day (typically)
Shim bottom bearing plates (optional)	1 hour
Transverse closure pour	2 hours
Install and post-tension threaded rods	2 hours
	Total time: 2.5 days

5.11.6.4. Concept D

Table 5.17 presents the typical construction time for Concept D connection details. Total construction time was about 2.5 days based on the actual construction process conducted in the lab. The overall procedures were the simplest among these experimental concepts since they are fully precast units. Applying epoxy adhesive on the shear key part and PT Williams bars are the two essential steps.

Table 5.17. Typical Construction Procedures and Time of Concept D.

Construction Procedure	Construction Time of Concept C
Erection precast units	1 day (typically)
Longitudinal closure pour	1 day (typically)
Shim bottom bearing plates (optional)	1 hour
Match cast with epoxy adhesive	1 hour
Install and post-tension threaded rods	4 hours
	Total time: 2.5 days

5.12. SUMMARY

A summary of the concepts based on the metrics of ease of construction, speed of assembly, long-term durability, construction and erection safety, and cost-effectiveness are now presented.

The ease of the precast concrete deck construction for all concepts was similar except for Concept D, with Concept A and Concept C being slightly harder to construct due to the U-loop bars protruding into the closure pour. Concept D was fully precast and used epoxy adhesive to join the precast units together, which was the easiest for the match-cast joint. The top flange splice plates for Concept A were easy to construct compared to the bracket assembly and Williams bars for Concept B and Concept C (somewhat more labor-intensive). Initially, the brackets were attached with slip-critical bolts only, but this step was changed to a welded detail later to eliminate the slip of the brackets. Although the welding could be done in the shop, the amount of overhead welding required makes the bracket slightly more difficult to construct and could be a fatigue concern. The tightening of the Williams bars is also relatively difficult because of the weight of the through-hole jack and the position of the Williams bar. Concept D needed more construction time during the PT process since it required more Williams bars to be done. The bottom flange connections were all relatively easy to construct, with the bearing plates for Concept C being the easiest and the splice plates for Concept A the hardest.

The concepts in terms of speed of assembly ranked similarly to ease of construction. The precast concrete deck was assembled at similar times for each concept. Assembling Concept D was fastest since both units were fully precast. Assembling Concept B's closure pour was second fastest because there was no rebar, but Concept A and Concept C were still relatively easy to construct. The splice plate for Concept A went together quickly, as did the initial installation of the bracket assemblies, which took only about 2–3 hours each. The welding of the assemblies took longer—approximately 6 hours per concept. The tightening of the Williams bars was relatively fast, taking under 2 hours to complete per concept. Concept D needed about 4 hours to complete the PT process since there were four Williams bars total. The bottom flange plates for Concept A took the longest to assemble, with the bearing plates for Concept C requiring the least amount of time. Concept D also required less time since the only requirement was putting the epoxy adhesive on the bottom concrete shear key part for both precast units.

Long-term durability varied by specimen. Although Concept B had the least amount of cracking, it also lost a significant amount of stiffness at the design load. Similar to Concept B, Concept D had a relatively small amount of cracking, but it lost a significant amount of stiffness after about the 35-kip load level. The creep behavior was apparent for Concept D. The lack of any reinforcement throughout the closure pour would also allow water and debris to penetrate into the concrete, accelerating the rate of damage due to the elements. Concept A and Concept C both exhibited a minor amount of cracking prior to the design load and during cyclic testing, but extensive cracking was not documented until two or three times the design load was exceeded; A and C also maintained relatively high stiffnesses during the entirety of the testing. The presence of reinforcement through the closure pour also held the concrete together, which would delay the onset of water and debris from penetrating the slab.

The overall safety of each concept remained relatively constant. The only part of the construction that was deemed somewhat risky was the tightening of the Williams bars. If the brackets or the welds of the brackets to the top flange are not adequate, there is a risk of the brackets breaking during tensioning, which could cause serious injury. Provided the brackets and welds are properly designed and constructed, the risk of injury is mitigated.

The cost-effectiveness of each concept varied. Concept A is likely the most cost-effective specimen to construct in the shop, but installing the splice plates would require the most work in the field. Concept B and Concept C would be the least cost-effective specimens to construct in the shop because the construction and welding of the brackets are relatively time-consuming. Concept D is the second most cost-effective specimen to construct in the shop since it is fully precast. The additional concrete and rebar for the drop panel construction also needed to be considered. Installing PT bars could require the most work in the field. Once the beams are sent to the field, however, the only thing that needs to be done is to install the Williams bars, which is relatively fast. Creating the UHPC channel enclosure for Concept B and the bearing plates for Concept C are extremely fast compared to installing the splice plates of Concept A.

6. ANALYTICAL MODELING OF TESTED SPECIMENS

6.1. OVERVIEW

To further evaluate the structural behavior of the connection experiments, 3D FE models of each concept was constructed. The commercial software package used was Abaqus Version 6.14 [26] with the Abaqus/Explicit method. There were three main phases to this effort: (a) a-priori modeling, (b) model validation, and (c) modeling of refined concepts. Note that a significant FEM parametric study was later performed that evaluated full bridges (see Section 7).

The initial phase of modeling created four a-priori (or preliminary) finite element models. The geometry and the material properties of the test setup models came from the original design assumption. A series of loading conditions (mentioned earlier) were applied to the models, which allowed for service-level deformation and prediction of the failure mechanisms. These conditions were also utilized during the testing for quality control and real-time decision-making concerning the experiments.

The second phase of modeling was more refined finite element analysis (FEA) of each experimental setup. More precise geometry and material properties from the actual test specimens were utilized. The measurements from the experiments were compared to the FEM results. Refinements were made to the FE models as necessary to improve the accuracy. The purpose was to validate the modeling approach. Sections 6.2 to 6.5 describe the FE models and the validation process for Concepts A to D, respectively. In addition, Section 6.6 provides a summary of these finite element models.

The third phase of modeling analyzed refined connection concepts within the same experimental setup configuration. The validated modeling methodology was utilized to ensure reasonably accurate results. This phase was critical to the study because it allowed the research team to explore variations to the connection concepts without having to perform additional experiments. Section 6.7 documents the two main connection options later recommended for future use.

6.2. ANALYTIC MODELING OF CONCEPT A

6.2.1. Test Setup Model Description

As previously discussed in the analytic modeling overview (Section 6.1), Abaqus Version 6.14 was used for the test setup modeling. Abaqus/Implicit was first used to evaluate the steel beam-only model for Concept A. This analysis was conducted to understand the non-composite behavior that is the upper bound for most responses (e.g., displacement, rotations, and strains). This non-composite modeling also allowed for easier comparison with the first principal calculations. The implicit analysis was first applied to the Concept A composite model. The analysis process was not completed because of the convergence error, and the computational time also could not be determined. Various convergence problems happened during the implicit analysis program, like contact simulations, element behavior, constraints, loading materials, etc. [26]. Many potential issues can cause severe convergence errors, like concrete materials degradation and failure, and the complexity of geometry surfaces. Therefore, the Abaqus explicit analysis program was used for the composite model of Concepts A, B, C, and D. The following sections illustrate the details of the model.

The Concept A test setup is explained in Section 5.7.2.1. The modeling process includes geometry, material properties, assembly, contact interaction, load step, boundary conditions, mesh analysis, and data processing. Table 6.1 shows the major geometric information of the Concept A test setup model. The major material properties of the model are shown in Table 6.2. Figure 6.1 presents the main parts of the FEM, which include the regular concrete closure pour, the rebar embedded in the closure pour and precast deck slab, the structural steel girders, splice plates, bolts, and the whole FEM assembly. The mesh element selection is consistent with Concept B and Concept C. A 3D eight-node linear brick (C3D8) element type was used to model a steel girder, precast concrete slab, concrete closure pour, steel splice plates, and bolts. A 3D two-node linear truss (T3D2) element type was used to model the steel rebar portion, which included the longitudinal rebar, extended U-loop rebar, and transverse rebar. The mesh size is different for each part. The closure pour mesh size is 1 inch. The bolt mesh size was 0.2 inches because of its small size. Other mesh sizes ranged from 1 inch to 6 inches. The total number of mesh elements was 74,370, which was greater than the other two concepts since it included many bolts and splice plates.

Table 6.1. Major Geometric Information of Concept A Test Setup Model.

Structure Component	Length	Width	Depth
Steel Girder W33×201	20 ft	15.7 in. (Flange) 0.72 in. (Web)	33.7 in. (Total) 1.15 in. (Flange)
Precast Concrete Deck	19 ft 10 in.	7 ft	8.5 in.
Male-to-Female Key Closure Pour	4 in. (Min.) 5 in. (Max.)	7 ft	8.5 in.

Table 6.2. Major Material Properties of the Model.

Structure Component	Modulus of Elasticity (ksi)	Poisson's Ratio	Unit Weight
Steel Girder W33×201	29,000	0.3	201 lb/ft
Precast Concrete Deck	5,022	0.2	150 pcf
Male-to-Female Key Closure Pour	7,181	0.2	150 pcf

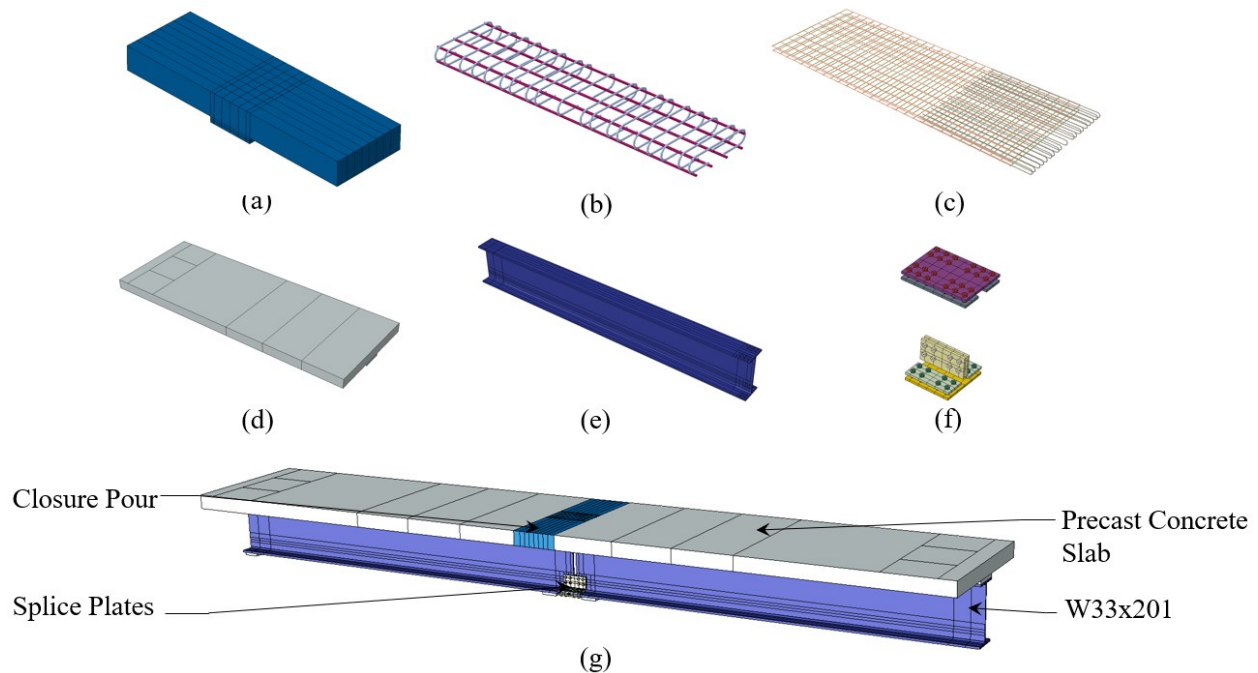


Figure 6.1. (a) Concrete Closure Pour, (b) Rebar in Closure Pour, (c) Rebar in Precast Concrete Slab, (d) Precast Concrete Slab, (e) Steel Girder, (f) Splice Plates with Bolts, and (g) Model Assembly.

For the material properties of the specimen, there were various models to simulate the damage behavior of concrete during experiments, like the concrete damage plasticity (CDP) model, Drucker Prager model, concrete smeared cracking model, etc. The CDP model was selected to represent the tension and compression inelastic behavior with damage parameters of concrete [26]. Lubliner et al. first presented the theoretical constitutive model for both elastic and plastic stiffness degradation [27]. Lee and Fenves developed the plastic-damage model for concrete subjected to cyclic loading based on fracture energy and stiffness degradation in continuum damage mechanics [28]. The main failure mechanism of the CDP model was crushing in compression and cracking in tension. There are many parameters related to the CDP model, like the eccentricity ϵ , the dilation angle φ , the ratio of σ_{b0}/σ_{c0} , the viscosity parameter μ , the ratio of the second stress invariant in the tensile meridian to the compressive meridian K_C , etc. [26]. The default eccentricity value was set as 0.1, and most studies apply this value. The range of dilation angle φ was about 30 degrees to 40 degrees, which is commonly used by most researchers. Aikaterini et al. compared and examined the dilation angle from 20 degrees to 42 degrees and set 40 degrees for the FE analysis of punching shear of concrete slabs [29]. The dilation angle of 30 degrees was applied for the modeling of the nonlinear cyclic load behavior of shear walls of nuclear power plants by Ali et al. [30]. Wosatko et al. evaluated the dilation angle from 5 degrees to 55 degrees for the plasticity-based model, which was used for the punching shear response in a slab-column connection [31]. The value of the dilation angle φ was initially set as 35 degrees for all specimens. The stress ratio σ_{b0}/σ_{c0} of 1.16 was determined. The viscosity parameter μ was set as 0. Some researchers set this value as a sufficiently small value since it can help the Abaqus/Implicit Analysis get rid of the convergence issue caused by material properties, like from 0.0001 to 0.0005. K_C was set as 0.667. Table 6.3 shows each value of CDP model parameters.

Table 6.3. CDP Model Parameters Used for All Concepts.

Dilation Angle φ	Eccentricity ϵ	σ_{b0}/σ_{c0}	K_C	Viscosity Parameter μ
35	0.1	1.16	0.667	0

The concrete compressive and tensile behavior are two main aspects of the CDP model. Figure 6.2 illustrates the required parameters used for the CDP model and shows the general

stress-strain relationship of the CDP model tension stiffening behavior [26]. The cracking strain $\tilde{\epsilon}_t^{ck}$ is defined as the total strain minus the elastic strain of the undamaged material, which is calculated by Equations (7) and (8). The tensile plastic strain $\tilde{\epsilon}_t^{pl}$ in the CDP model should be always positive and increasing with increasing cracking strain to make sure the tensile damage curves are correct. Abaqus obtained the plastic strain values using Equation (9) and (10) [26].

$$\tilde{\epsilon}_t^{ck} = \epsilon_t - \epsilon_{0t}^{el} \quad (7)$$

$$\epsilon_{0t}^{el} = \sigma_t / E_0 \quad (8)$$

$$\tilde{\epsilon}_t^{pl} = \tilde{\epsilon}_t^{ck} - \frac{d_t}{(1 - d_t)} \epsilon_{0t}^{el} \quad (9)$$

$$d_t = 1 - \frac{\sigma_t}{\sigma_{t0}} \quad (10)$$

Where:

ϵ_t = total tensile strain.

ϵ_{0t}^{el} = tensile elastic strain corresponding to the undamaged material.

σ_t = tensile stress (ksi).

σ_{t0} = tensile cracking stress (ksi).

E_0 = modulus of elasticity (ksi).

d_t = tensile damage parameter.

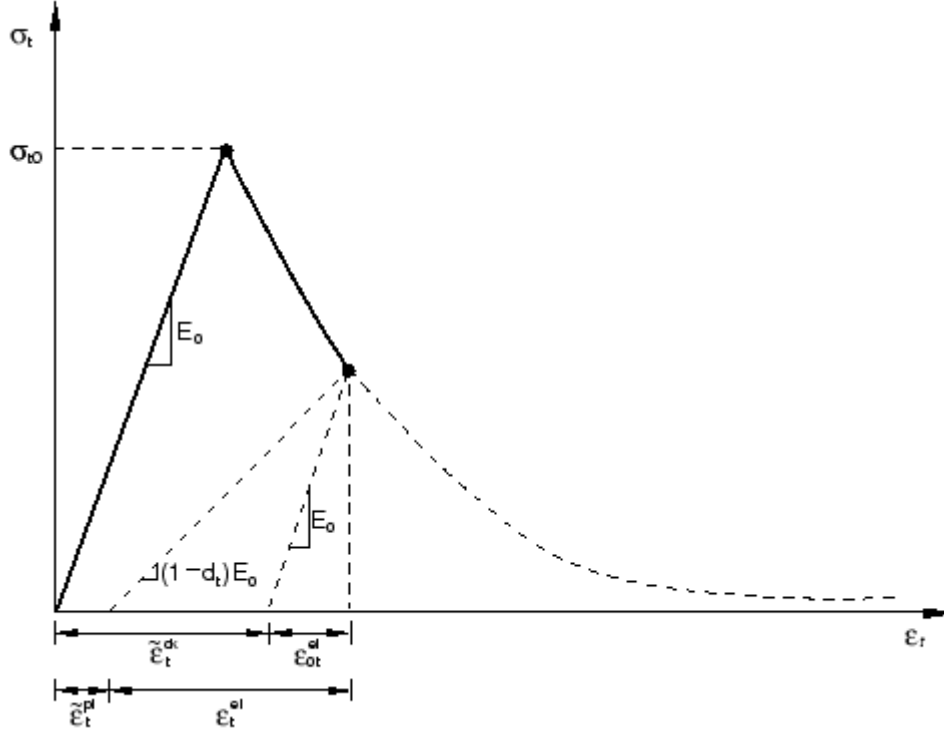


Figure 6.2. Typical Stress-Strain Relationship for CDP Model Tension Stiffening Behavior in Abaqus [26].

The compressive stress-strain relationship used in Abaqus is shown in Figure 6.3. The compressive inelastic (crushing) strain $\tilde{\epsilon}_c^{in}$ is calculated by Equations (11) and (12). The compressive plastic strain $\tilde{\epsilon}_c^{pl}$ also needs to be always positive and increasing with increasing crushing strain to make sure the compressive damage curves are correct. It is calculated by Equations (13) and (14).

$$\tilde{\epsilon}_c^{in} = \epsilon_c - \epsilon_{0c}^{el} \quad (11)$$

$$\epsilon_{0c}^{el} = \sigma_c / E_0 \quad (12)$$

$$\tilde{\epsilon}_c^{pl} = \tilde{\epsilon}_c^{in} - \frac{d_c}{(1-d_c)} * \epsilon_{0c}^{el} \quad (13)$$

$$d_c = 1 - \frac{\sigma_c}{\sigma_{c0}} \quad (14)$$

Where:

ϵ_c = total compressive strain.

ϵ_{0c}^{el} = compressive elastic strain corresponding to the undamaged material.

σ_c = compressive stress (ksi).

σ_{c0} = compressive breaking stress (ksi).

d_c = compressive damage parameter.

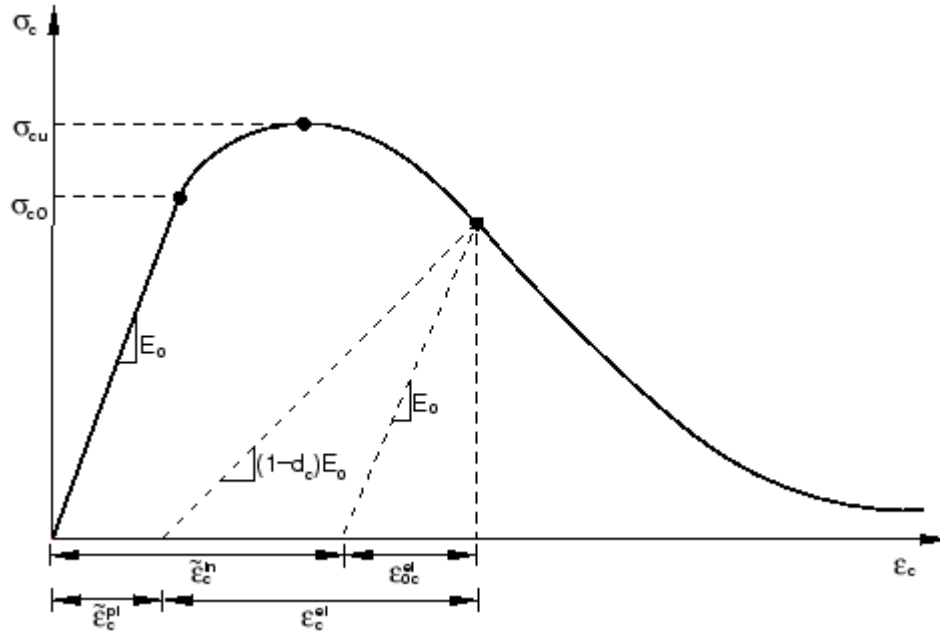


Figure 6.3. Typical Stress-Strain Relationship for CDP Model Compression Hardening Behavior in Abaqus [26].

There are various compressive and tensile stress-strain models created and developed by researchers. The Hognestad stress-strain model is usually used for confined concrete [32]. The Kent and Park model is applied to the CDP compressive behavior, and the stress and strain relationship is shown in Figure 6.4, but the CDP model used the linear elastic compressive behavior before the yield stress. The Kent and Park model includes two types of concrete. The unconfined concrete model is mainly used for the present study. The ascending branch is represented by Equation (15). The post-peak branch is a straight line and is defined by Equations (16), (17), and (18). Based on the compression test done in the High Bay laboratory, the average compressive strength of test cylinders for a precast concrete slab on the test day was 5.85 ksi, which is used for the compressive breaking stress in the CDP model. The simple linear stress-strain relationship is used for concrete tensile behavior, and it is shown in Figure 6.5.

$$f_c = f'_c \left[\frac{2}{\epsilon_{co}} - \left(\frac{\epsilon_c}{\epsilon_{co}} \right)^2 \right] \quad (15)$$

$$f_c = f'_c [1 - Z(\epsilon_c - \epsilon_{co})] \quad (16)$$

$$Z = \frac{0.5}{\epsilon_{50u} - \epsilon_{co}} \quad (17)$$

$$\epsilon_{50u} = \frac{3 + 0.002f'_c}{f'_c - 1000} \quad (f'_c \text{ in psi}) \quad (18)$$

Where:

ϵ_{50u} = the strain corresponding to the stress equal to 50 percent of the maximum concrete strength for unconfined concrete.

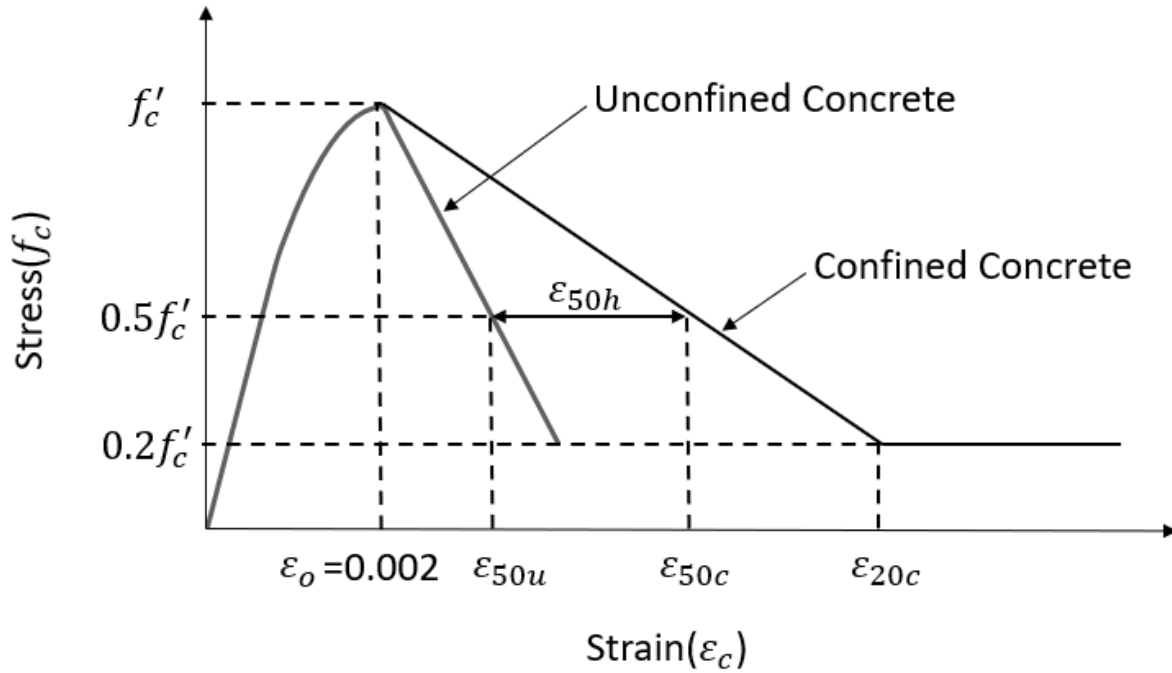


Figure 6.4. Proposed Stress-Strain Model for Unconfined and Confined Concrete-Kent and Park Model.

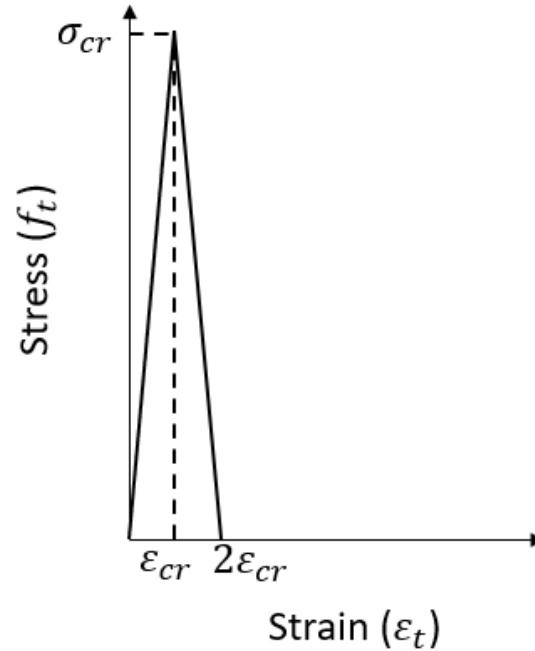


Figure 6.5. Bilinear Stress-Strain Relationship for Concrete Tensile Behavior.

The typical bilinear with hardening branch stress-strain curves of various steel properties are shown in Figure 6.6. For the boundary conditions, a stationary hydraulic actuator was used to hold down one end of the specimen in the experiment. Therefore, the Encastre boundary condition was used to constrain any relative movement at the end of the specimen during the FEM analysis. In order to simulate the behavior of the elastomeric bearings, a Cartesian-type connector connected with the ground with different stiffnesses in three directions was applied for the FEM. The embedded constraint was selected to simulate the interaction between steel rebar and concrete. The tie constraint was used for the interaction between the steel girder and precast concrete slab to simulate the composite behavior of the whole specimen. The general contact type was chosen for the whole specimen, which includes all the contact pairs. It can save a great amount of time since the general contact type can avoid setting the friction coefficient for every contact pair. There are also many reference points to connect to the rigid body to simulate the pedestal location.

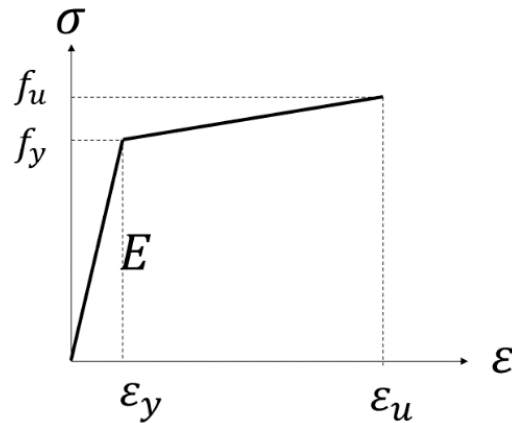


Figure 6.6. Bilinear Stress-Strain Curves of Steel Materials in the FEM.

The loading process is comprised of three steps that include pretension bolts (if present), a gravity load applied to the model, and displacement control at the load end. All three steps were consistent with the experiment. Table 6.4 introduces these steps and their corresponding step time. The step period was shorter than the other two concepts since the displacement is about one-half of the displacement of the other two concepts. Figure 6.7 shows the ratio of kinetic energy over inertial energy through each step. This ratio should not rise above 5–10 percent when using Abaqus/Explicit analysis in a quasi-static simulation [26]. The maximum ratio was about 1.2 percent, which was in Step 1 since the pre-tensioning bolts could increase the internal energy. The ratio in Step 2 and Step 3 were lower than 0.5 percent, which indicates that the process was relatively stable, and the analysis result is reliable.

Table 6.4. Load Step with Step Time for Concept A Test Setup Model.

Step	Step Time (sec)
Prestress bolts at the top, web, and bottom splice plates	0–1
Applied gravity load for the whole model	1–5
Displacement control (1.5 inches)	5–25

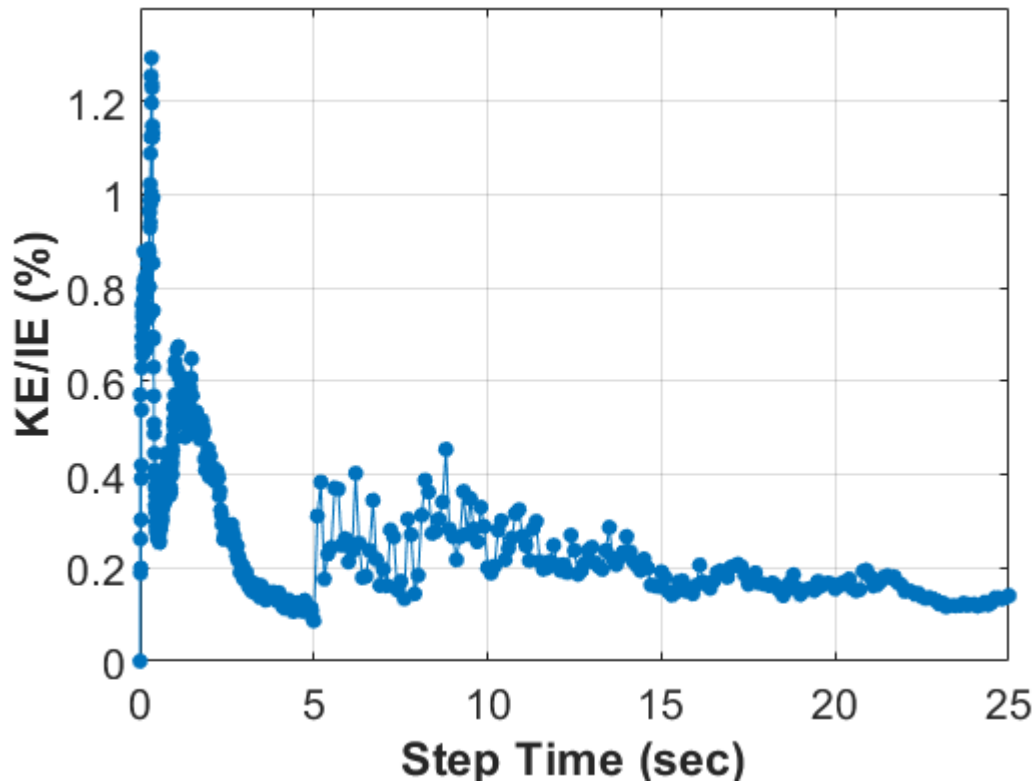


Figure 6.7. Energy Content Ratio of Kinetic Energy over Inertial Energy during Load Steps.

6.2.2. Model Validation with the Experimental Results

The FEM methodology was validated with the experimental results after the testing was performed. The validation of the Concept A test setup model included the load-displacement relationship, the stresses at the deck surface, splice plates comparison, the structural strain profile comparison, the bolt tensile stresses analysis, the precast concrete deck damage pattern comparison, and the bolt tensile stress analysis. All the experimental test data results shown in this section come from the Concept A ultimate test, which was discussed in Section 5.7.2.5.

The load-displacement relationship between the experiment and the FEM was compared. The FEM results, using the displacement control, were relatively close to the experimental results up to an actuator load of 65 kips. The specimen stiffness difference was about 3 percent before the displacement reached 1.0 inch. The stiffness difference was about 8 percent after 65 kips.

Figure 6.8 presents the relationship between these results. The displacement difference was about 0.2 inches between them when the initial bolt slip occurred at the bottom flange splice. However, the corresponding load was roughly the same (73 kips). Both curves show that the load suddenly

dropped from 73 kips to about 60 kips. This difference may be caused by the different loading speeds, pre-tensioning force in bolts, coefficient of friction between splice plates, and the concrete deck creep behavior. The finite element results are also filtered using a moving-average. The window size for each calculated average value was 5, which means 5 data points are in each window. Both curves show the ascending tendency after the load dropped. The difference of the second load drop induced by the bolt slip at the lower web splice was about 6 kips. For the FEM curve, the second load drop happened right after the first one, which was at about 78 kips. For the experimental curve, the second one happened when the load was about 72 kips.

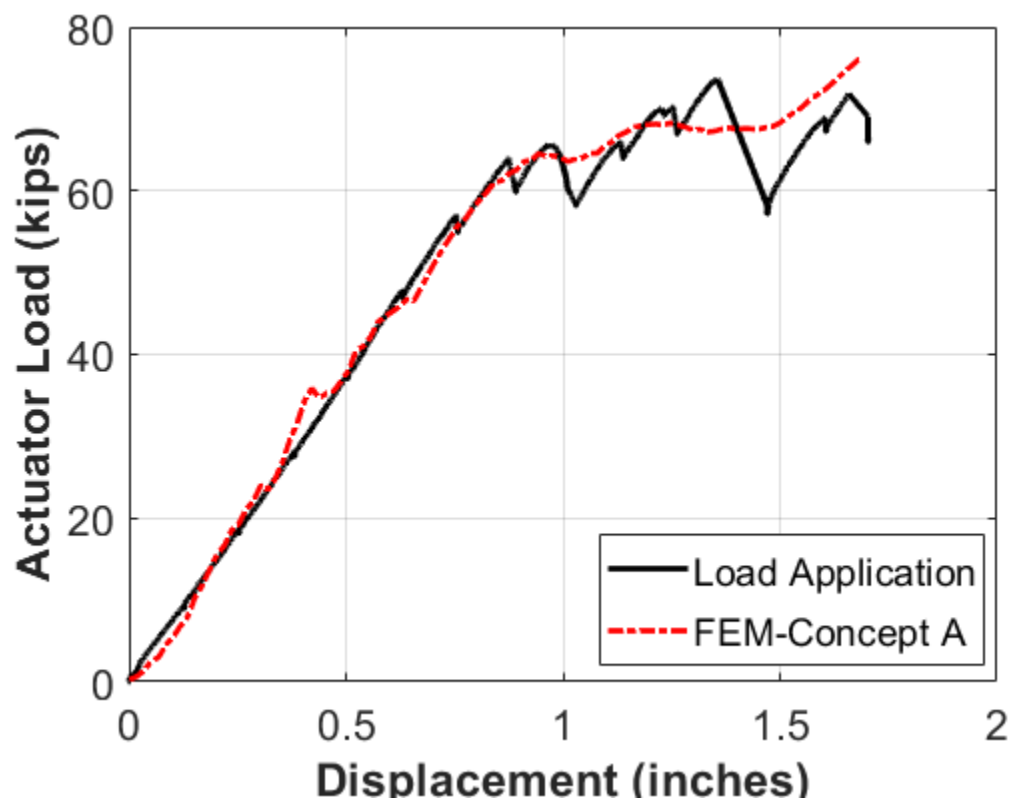


Figure 6.8. Load-Displacement Curve Comparison between the Concept A FEM and Experimental Test.

Figure 6.9 provides the tensile stress in the bolts. The bolt stresses jumped from 92 ksi to 110 ksi when the displacement was about 1.1 inches. The corresponding load is about 73 kips, which indicates that the load dropped from 73 kips because the bolt slipped at 73 kips.

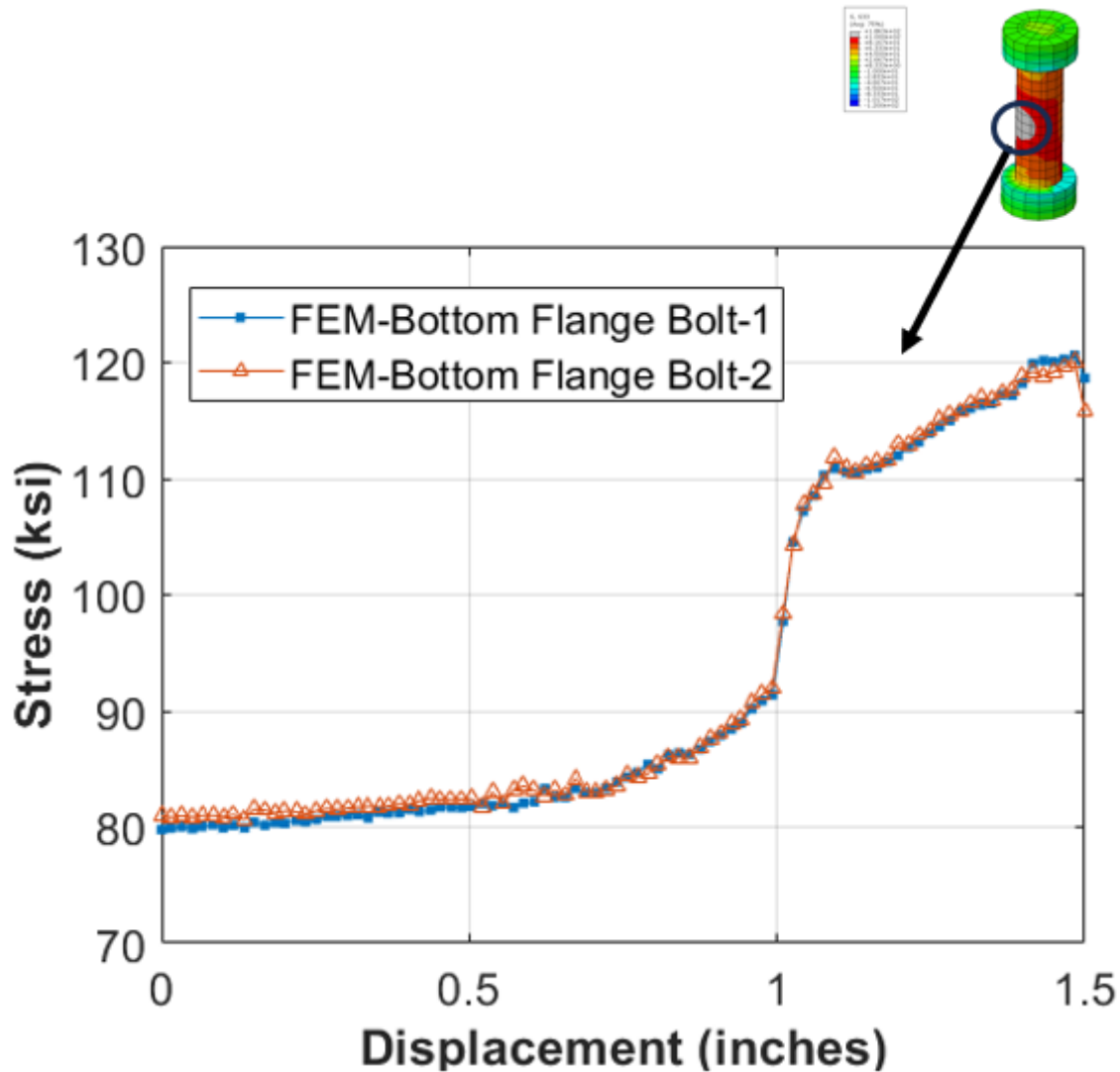


Figure 6.9. Bolt Tensile Stresses at the Bottom Flange Splice Plate in the FEM.

The stresses at the deck surface of E1 between the FEM and the experiment were compared. Figure 6.10 presents the stress value comparison against displacement at E7. Both stresses increased to about 0.25 ksi. The stress in the FEM increased faster than the experimental one, and they dropped when the displacement was about 1.1 inches. Both of them dropped at about the same displacement magnitude. The embedded rebar stresses were compared between the FEM and the experiment. Figure 6.11 shows the comparison between them. The stresses' increasing tendencies were similar, and both jumped from about 6 kips to 24 kips when the displacement was about 0.7 inches. The rebar stress difference was relatively small compared to the deck stress difference.

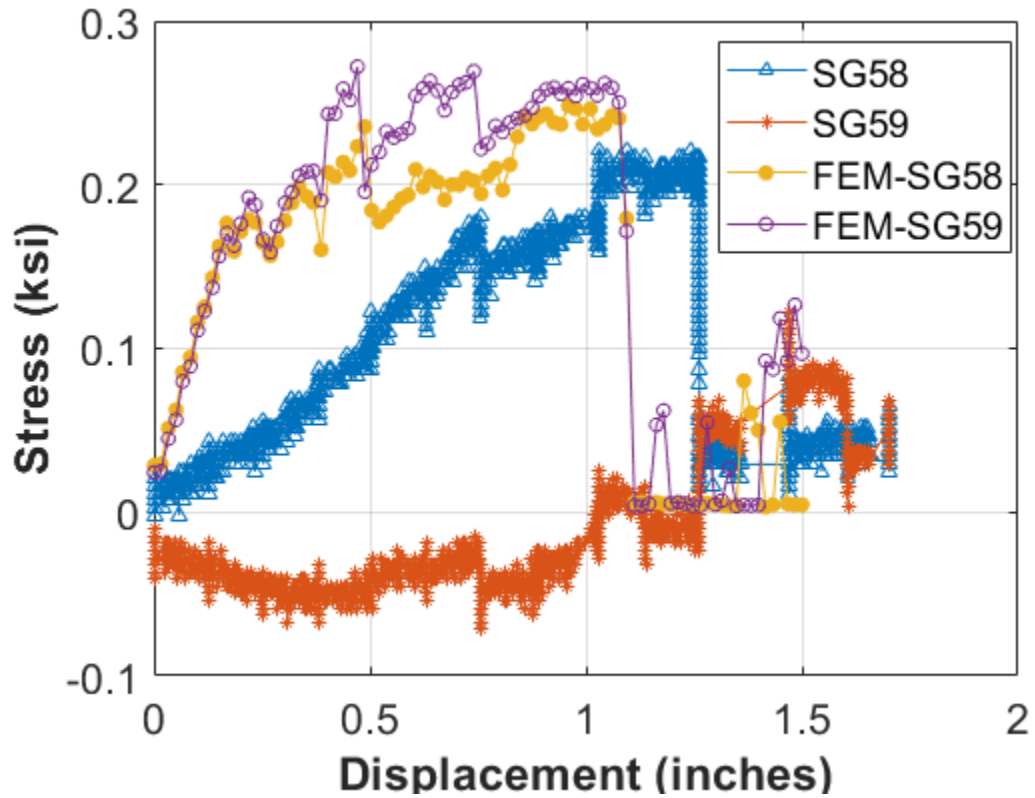


Figure 6.10. Stresses at Deck Surface of E1 Comparison.

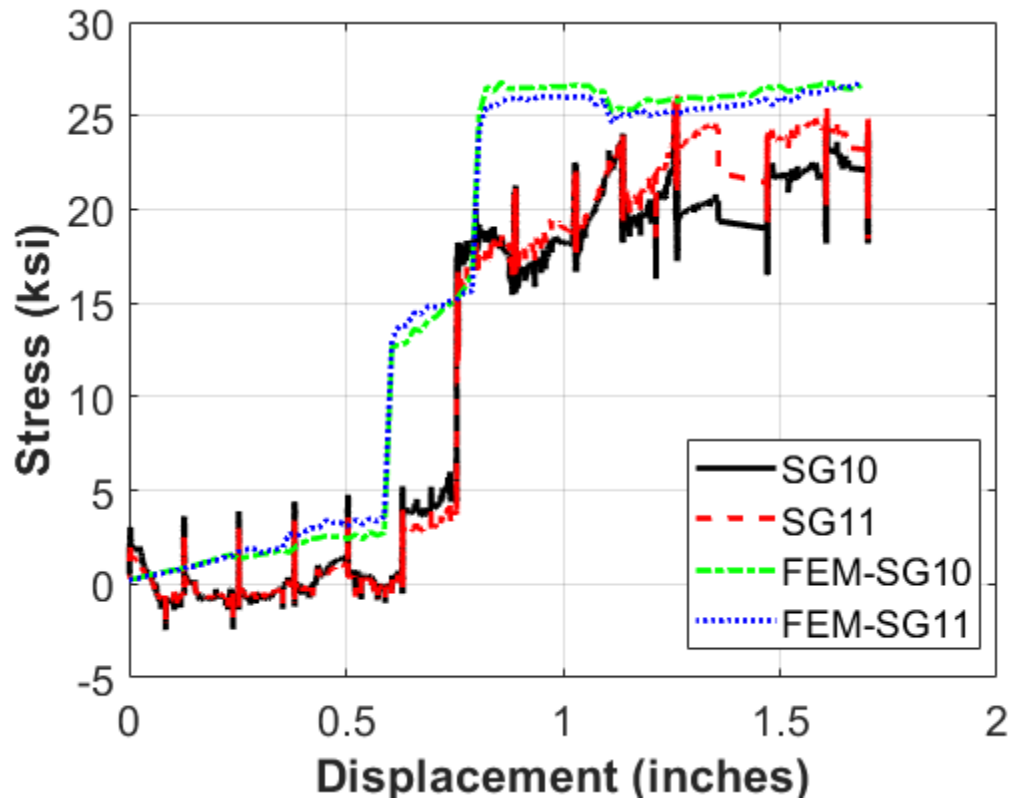


Figure 6.11. Rebar Stresses at E1.4 Comparison.

The stresses at the top splice plates and bottom splice plates were compared between the FEM and the experiment. Figure 6.12 presents the comparison of tensile stresses at the top splice plates. The stiffness difference was relatively small (5 percent) when the displacement was increasing. Both show the increasing tendency of stress. Figure 6.13 shows the comparison of the compressive stresses at the bottom splice plates. The slope difference between FEM results and the experiment was about 4 percent before the load reached 64 kips. The experimental results show a decreasing tendency after 64 kips, while the FEM results keep at the same stress magnitude after 64 kips. The difference may be caused by the applied load at the end of the specimen. The load kept increasing after the bolt slipped in the FEM, but the load did not exceed 74 kips after the bolts slipped.

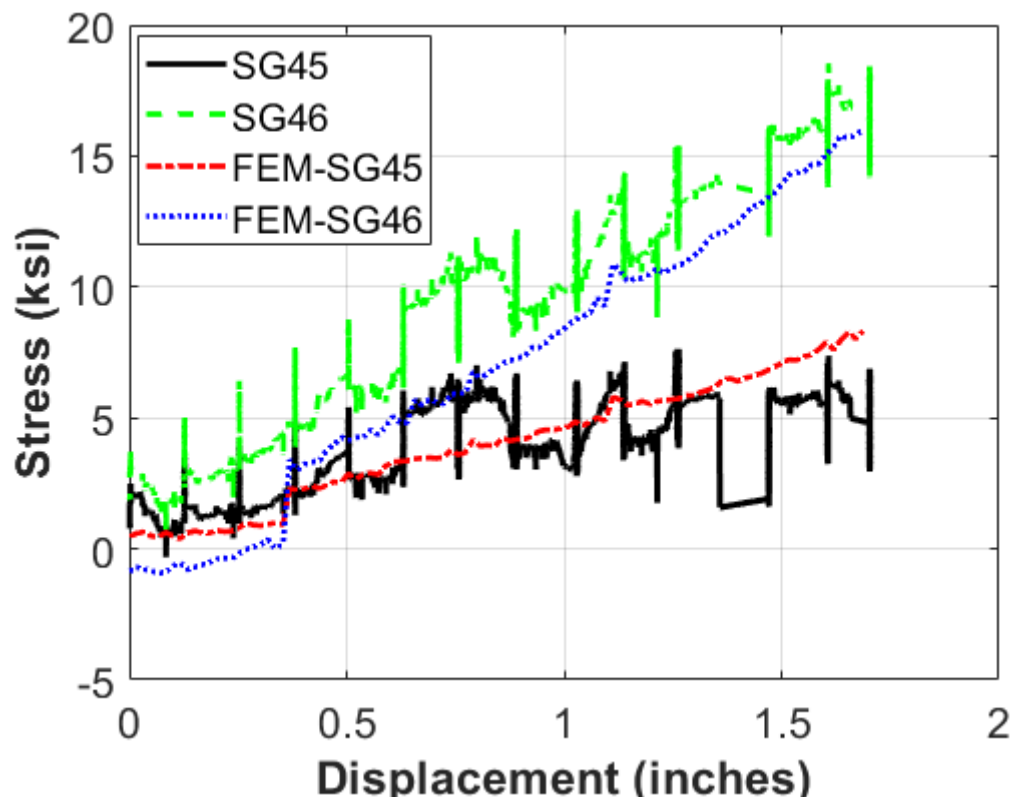


Figure 6.12. Stresses at Top Flange Splice Plate Comparison.

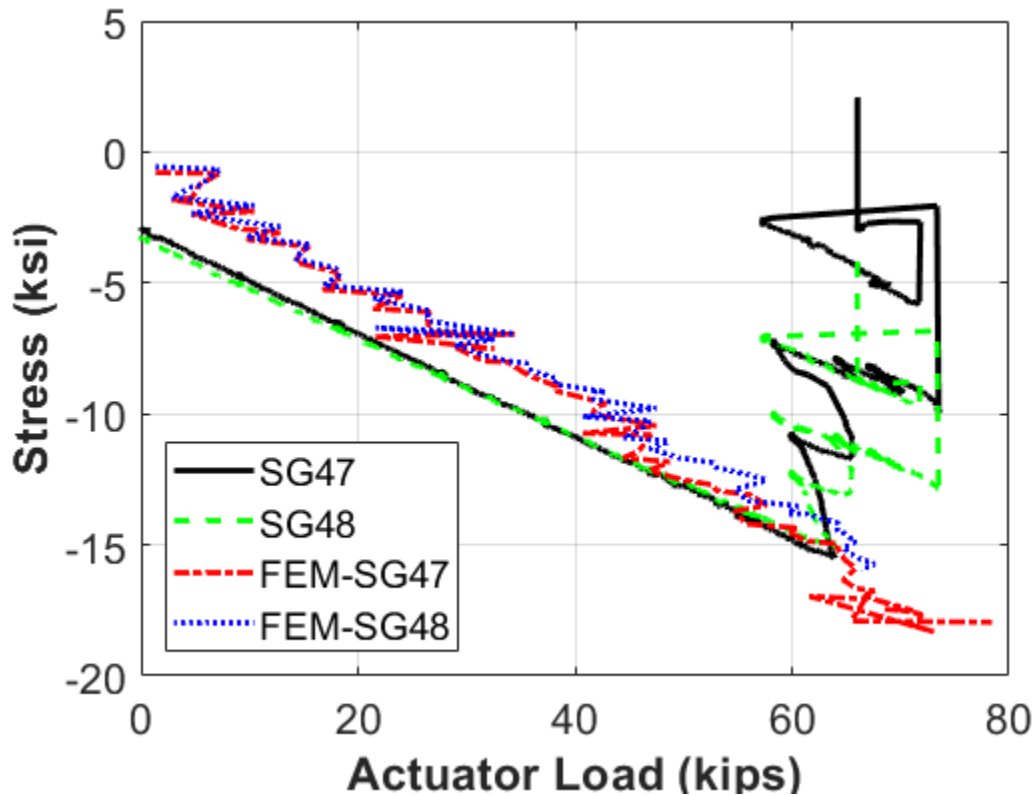
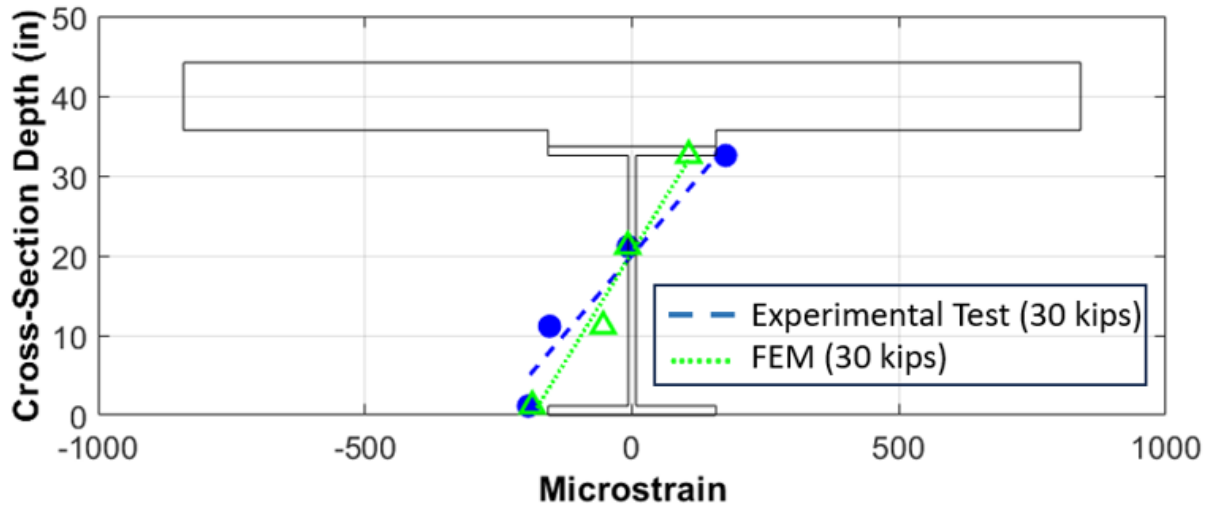


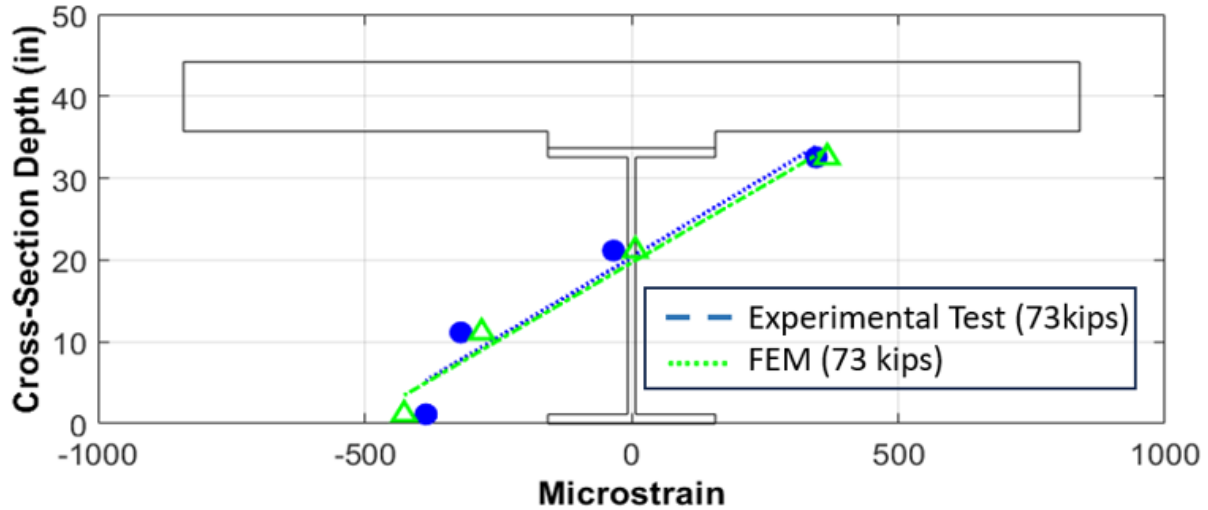
Figure 6.13. Stresses at Bottom Flange Splice Plate Comparison.

The structural strain profile at E1 was compared between the FEM and the experiment.

Figure 6.14 illustrates the comparison of the strain profiles. The slope difference between the FEM and the experiment was 21 percent when the load was 30 kips and 2 percent when the load was 73 kips. The FEM results were close to the experimental results.



(a)



(b)

Figure 6.14. Strain Profile Comparison at E1 for a Load of (a) 30 kips and (b) 73 kips.

The relative displacement between the bolts and the bottom flange splice plates was discussed. Figure 6.15 (a) and (c) provides the relative displacement between them, and it clearly shows relative displacement around the bolt holes was higher than at other locations. Figure 6.15 (b) and (d) provides the scour marks after the ultimate test was done, which was explained in Section 5.7.2.6. The tensile stresses of bolts at the bottom flange splice plate were illustrated.

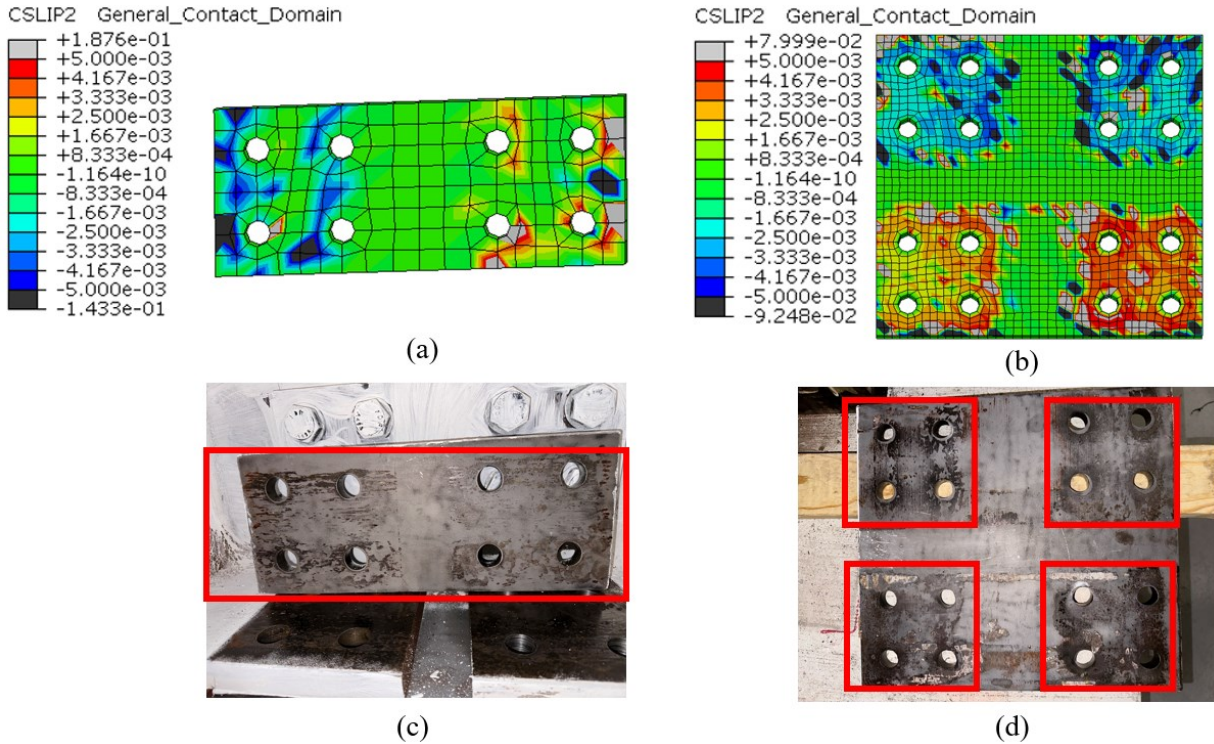
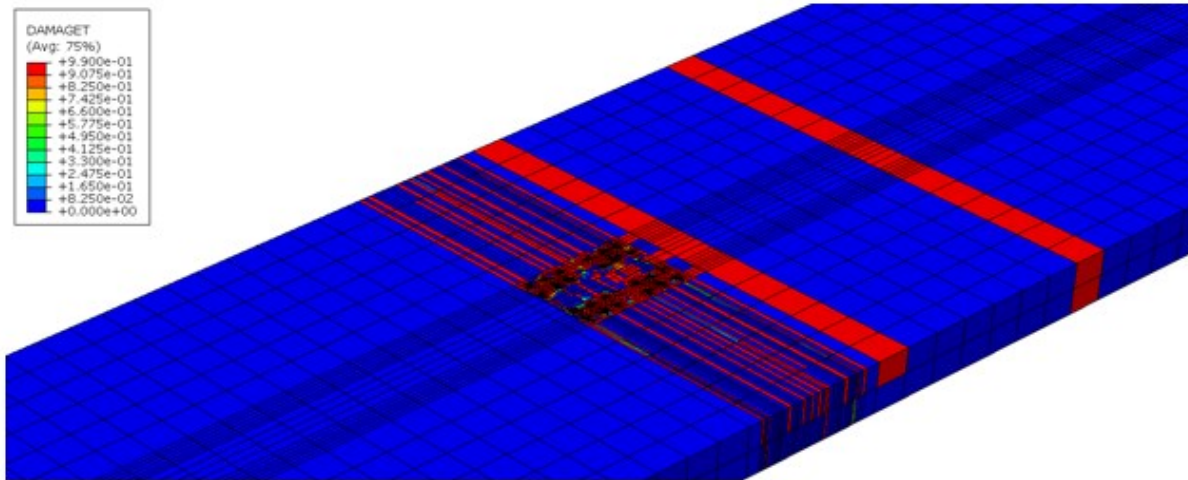
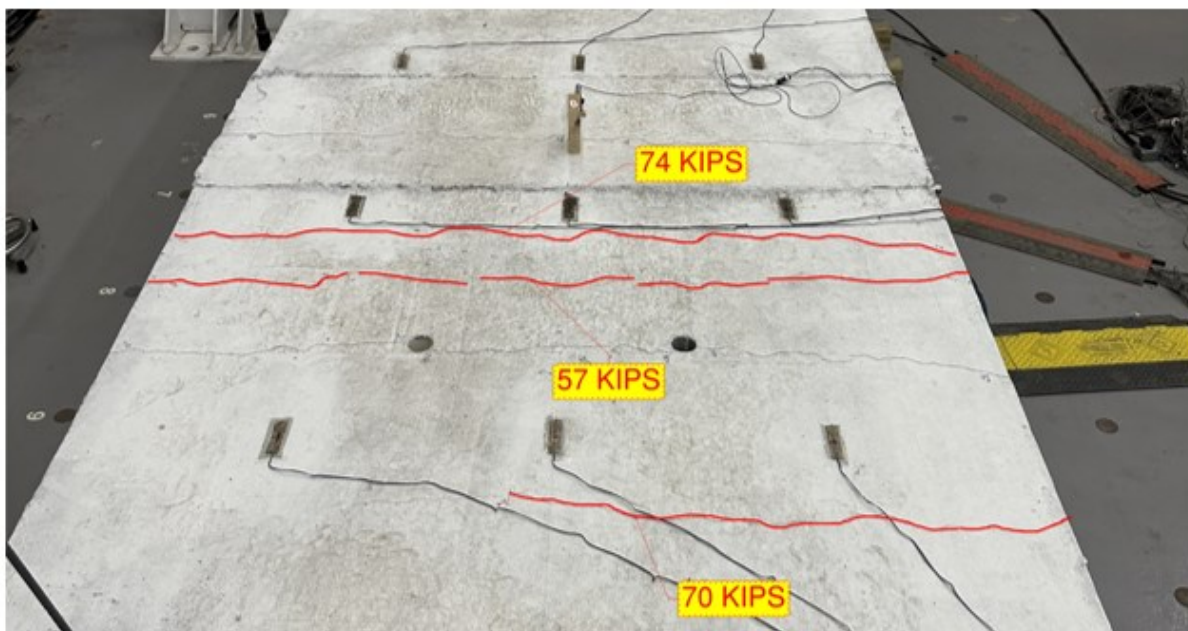


Figure 6.15. Bolts Slipped at Bottom Flange Splice Plate in the FEM: (a) Up Splice Plate, (b) Down Splice Plate and Bottom Flange Splice Plate Scour Marks in the Experiment: (c) Up Splice Plate, (d) Down Splice Plate.

The concrete deck damage pattern was compared between the FEM and the experiment. DAMAGE parameters represent the material's progressive degradation up to failure, and DAMAGET refers to the percentage of material tensile damage. Figure 6.16 (a) shows the damage pattern when the load was 73 kips. Figure 6.16 (b) presents the damage patterns when the load was up to 74 kips. The FEM was relatively consistent with the experimental results. Most concrete cracks happened at the interface of the precast concrete deck and the closure pour. One crack happened about 4 ft away from the edge of the closure pour for both the FEM and the experimental test.



(a)



(b)

Figure 6.16. Concrete Damage Patterns at Closure Pour Comparison: (a) FEM Damage Patterns (73 kips) and (b) Experiment Concrete Crack Patterns.

6.3. ANALYTIC MODELING OF CONCEPT B

6.3.1. Test Setup Model Description

The Concept B experimental test setup is illustrated in Section 5.8.2.1. Abaqus/Explicit Analysis Program was applied with the Double Precision/Explicit Packager for this model. The modeling

process using Abaqus usually includes these procedures: geometry, material properties, assembly, contact interaction, load step, boundary conditions, mesh, analysis, and data processing. The major geometries and material properties were discussed in Section 5.8.2.1.

The models of the steel girder with C-Channel at the bottom flange, the precast concrete deck, rebar, and the entire assembly are shown in Figure 6.17. For the mesh element selection, a C3D8 element type was used to model a steel girder with C-Channel, concrete precast slab, UHPC closure pour, steel brackets, and steel Williams bars. A T3D2 element type was used to model the steel rebar portion, which included the longitudinal rebar and transverse rebar. The mesh size is different for each part. The male-to-female key closure pour mesh size is 1 inch. Other mesh sizes range from 3 inches to 6 inches. The total number of mesh elements is 33,350.

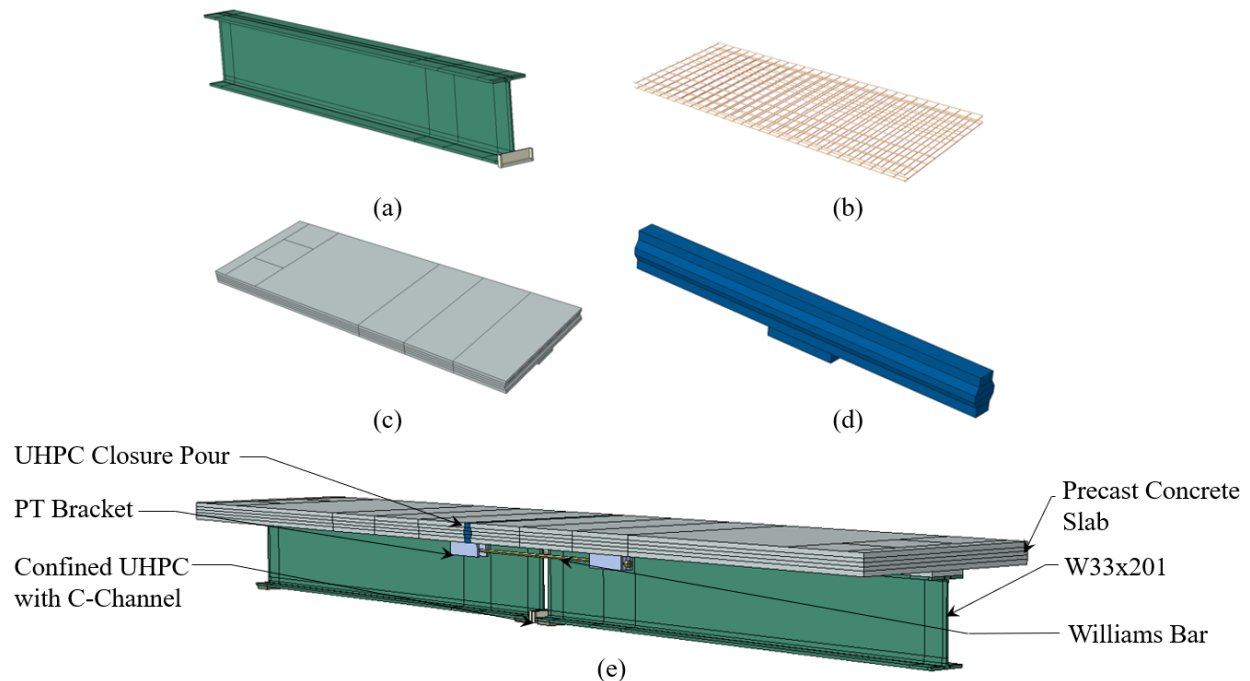


Figure 6.17. Concept B Test Setup Model Components: (a) Steel Girder with C-Channel, (b) Rebar, (c) Precast Concrete Deck, (d) UHPC Closure Pour, and (e) Assembly.

For the boundary conditions, a stationary hydraulic actuator was used to hold down the specimen at one end of the steel girder during the experimental test. The Encastre boundary condition was used to constrain any relative movement at the end of the specimen during loading applications. A Cartesian-type connector with different stiffnesses in three directions connected with the ground was used to simulate the elastomeric bearing pad on the pedestal in the experimental test. The embedded constraint was used for the interaction between steel rebar and concrete. The tie

constraint was applied for the interaction between the steel girder and concrete precast slab to model the composite behavior of the specimen. The tie constraint was used for the interaction between the steel bracket and the steel girder to simulate the weld condition, which helped avoid the relative motion between them. Because the UHPC closure pour was attached to the hold-down side of the precast specimen throughout the ultimate testing, a tie constraint was applied to that side as well. However, an air gap was present between the UHPC closure pour and the loading side of the precast specimen, so no constraint was applied on that side. The general contact type was selected for the interaction of the whole specimen to avoid setting different complex contact pairs. There are many reference points to restrain all of the total nodes on the surface, and it was easier to set boundary conditions at those points instead of the whole rigid body or surface.

The same CDP model for simulating concrete behavior and same steel parts' material properties were applied for the Concept B test setup model, which were illustrated in Section 6.2.1. The corresponding concrete compressive strengths were matched with different concepts' ultimate tests shown in Section 5.6.1 and 5.6.2.

The loading process was comprised of three steps—PT the Williams bars, a gravity load applied to the total model, and displacement control at the load side. All three steps are consistent with the experimental testing. Table 6.5 shows each step procedure and step time. Figure 6.18 presents the ratio of kinetic energy over inertial energy through each step. This ratio should not rise above 5–10 percent when using Abaqus/Explicit analysis in a quasi-static simulation [26]. The ratio is about 1 percent during the first step, which is relatively larger than the following steps because of the PT effect. The total energy also increased in Step 1. The PT effect was induced by temperature change in this present study. The initial applied temperature was calculated from Equation (19) [33]. In Steps 2 and 3, the ratio was below 0.5 percent, which means the load acceleration and the inertial effect were negligible. The dynamic oscillations of the ratio in the load steps were caused by the tensile failure of the precast concrete deck, the load speed, the stretch in the Williams bars, the step time length, etc.

Table 6.5. Load Step with Step Time for Concept B Test Setup Model.

Step	Step Time (sec)
PT Williams bar	0–10
Applied gravity load for the whole model	10–14
Displacement control (2.5 inches)	14–54

$$C = - \frac{P}{c * E * A} \quad (19)$$

Where:

C = coefficient of linear expansion taken as $1.0 * 10^{-5}$ (MPa/Celsius).

E = modulus of elasticity (MPa).

P = force (N).

A = cross-section area of Williams bars (mm²).

c = temperature (Celsius).

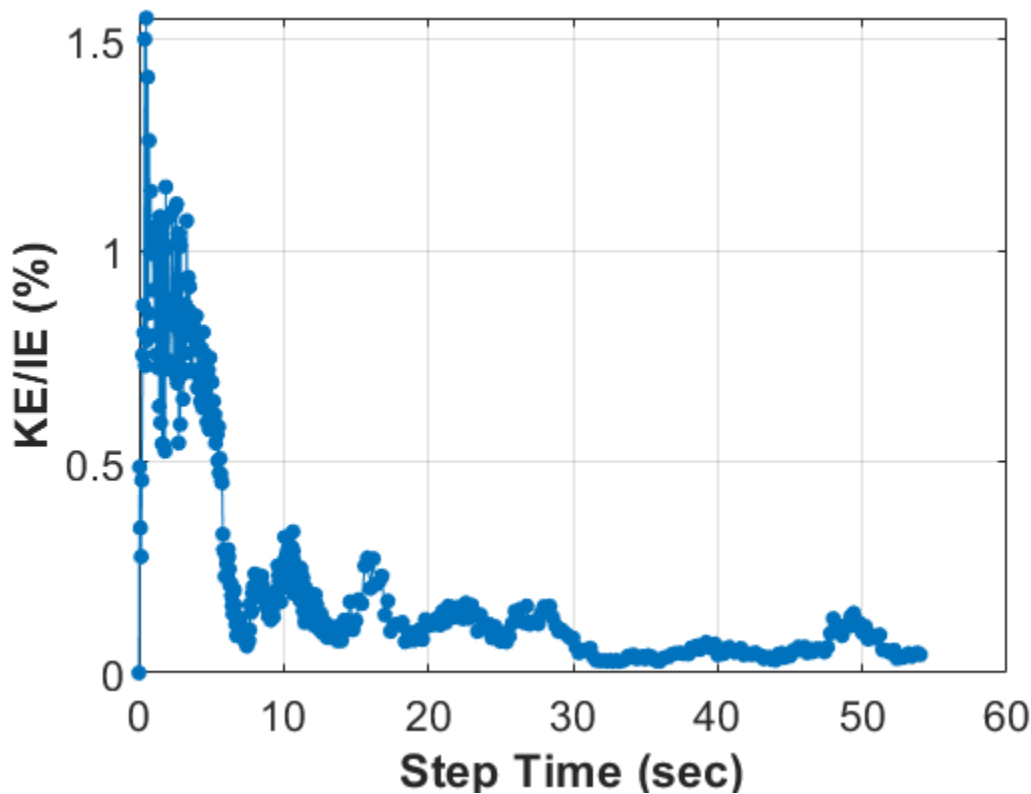


Figure 6.18. Energy Content Ratio of Kinetic Energy over Inertial Energy during Load Steps.

6.3.2. Model Validation with the Experimental Results

The Concept B test setup model was validated from different perspectives, which consists of the load-displacement relationship, stresses (Williams bars, deck surface, rebar, and structural steel), relative displacement at the closure pour, and precast concrete deck damage patterns. All the experimental test results and data shown in this section come from the Concept B ultimate test, which was discussed in Section 5.8.2.6. The comparison of the load-displacement relationship between the FEM and the experimental test is shown in Figure 6.19. The FEM using load control or displacement control predicted relatively close to the experimental test results. The slope difference between the FEM and the experiment was about 5 percent at most when the load reached 28 kips and was 2 percent for higher loads. The load and displacement data directly came from the Abaqus job result for both methods.

The following FEM result data were all extracted from the model using the displacement control method since it simulated the real test circumstance that happened in the lab. For the FEM using the displacement control method, there were some dynamic oscillations during the load steps.

The difference between the FEM and the actual test after the load reaches 30 kips might be caused by the variations of the concrete strength, steel parts strength, and interaction between the concrete slab and steel girder. The tie constraints make the specimen act as a fully composite behavior in the FEM, which is different from the actual test specimen that connected by shear studs welding on the steel girder.

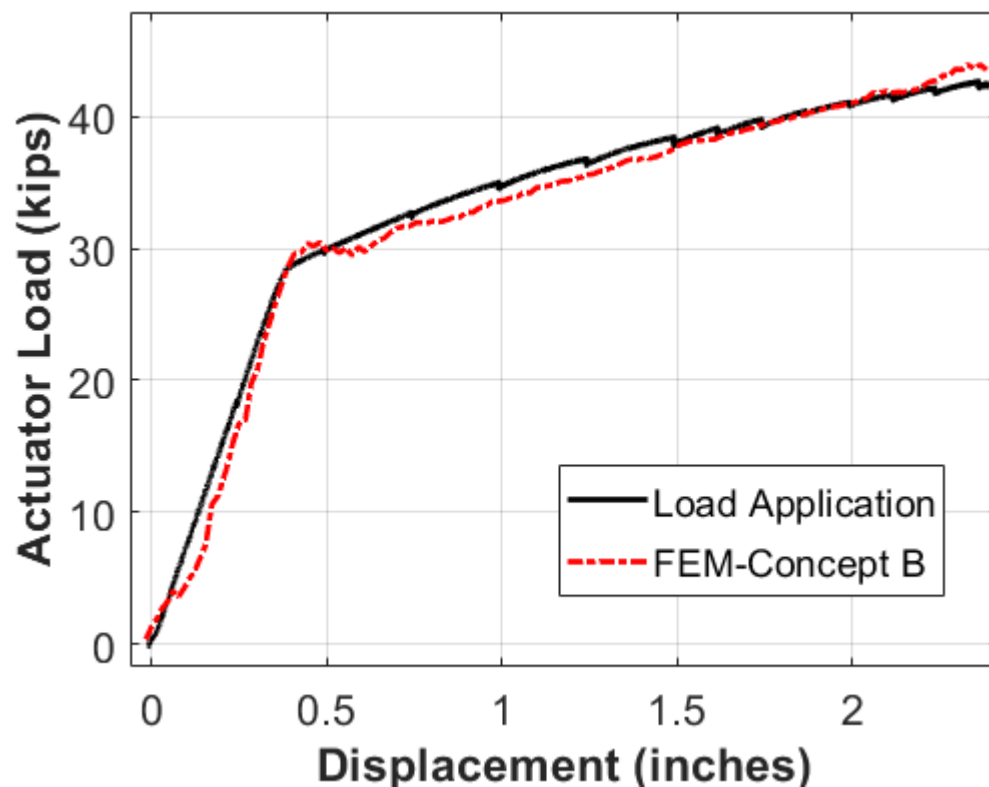


Figure 6.19. Load-Displacement Curve Comparison between the FEM and Experimental Test.

The FEM behavior of the Williams bars was similar to that of the experimental results.

Figure 6.20 presents the Williams bars' stress comparison between the FEM results and the experiment test results. The PT stress in the Williams bars is around 106 ksi, which is 1 percent larger than the experimental test result for SG43 and 3 percent larger than the experimental test result for SG44. The FEM results show a very similar tendency of stress increasing and captures the decreasing change of specimen stiffness when the load is around 30 kips.

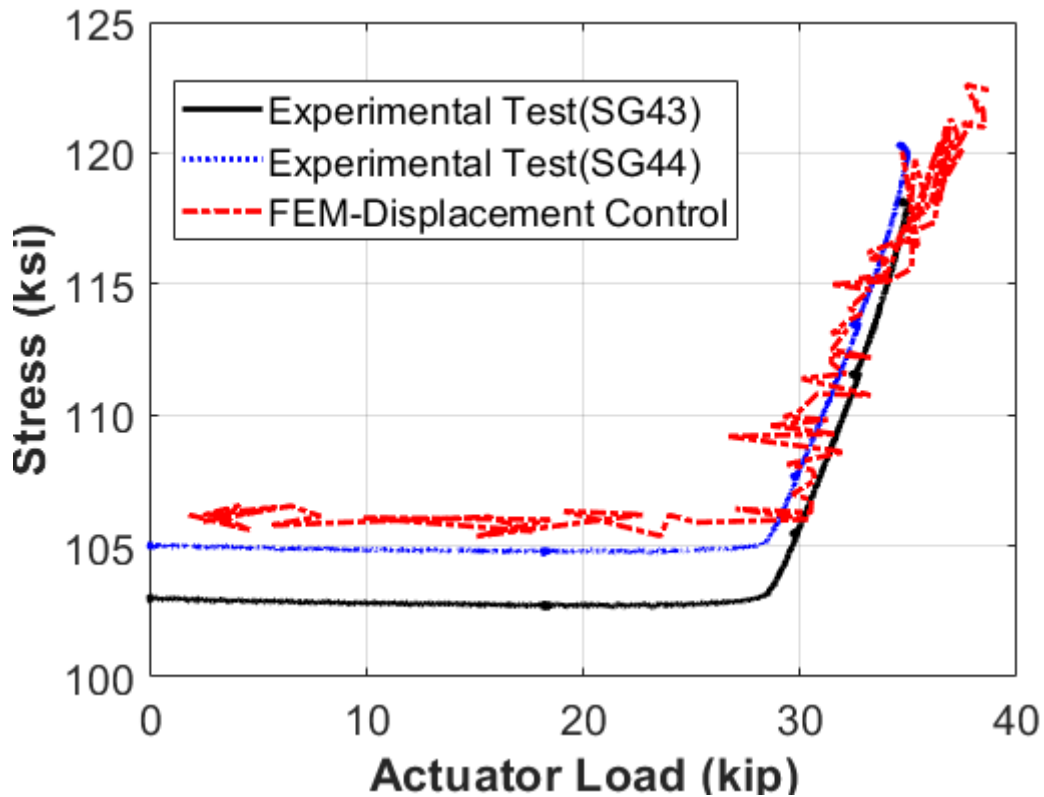


Figure 6.20. Stress on the Williams Bar versus Load Curves Comparison.

The relative longitudinal movement at the UHPC closure was compared with the FEM results. Figure 6.21 compares the relative longitudinal displacement at the closure pour, which was experimentally measured with an LVDT set at the center of the closure pour. The FEM result is chosen from the same instrumentation location. The difference was about 1–5 percent before the load reached 30 kips. In addition, the longitudinal displacement was similar for higher load levels.

The UHPC closure pour separated from the precast portion of the specimen at 43 kips. Figure 6.22 depicts the experimental failure mechanism with the FEM simulation. Note that U3 is the relative displacement along the longitudinal direction. The results match the value presented in Figure 6.21.

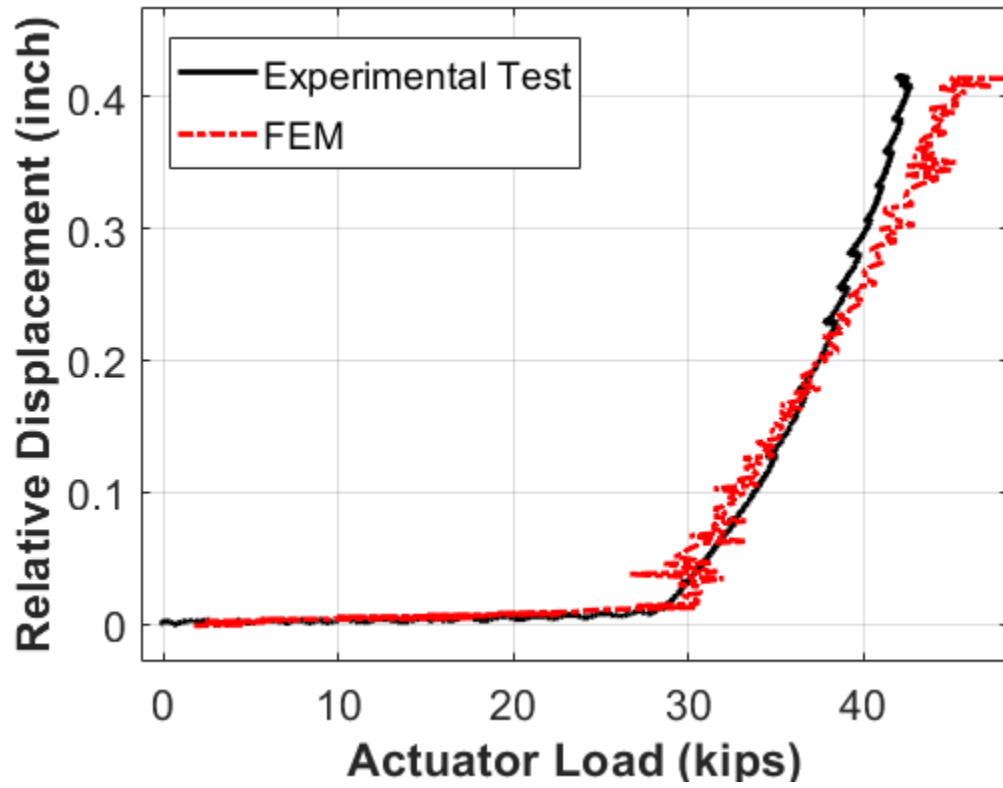
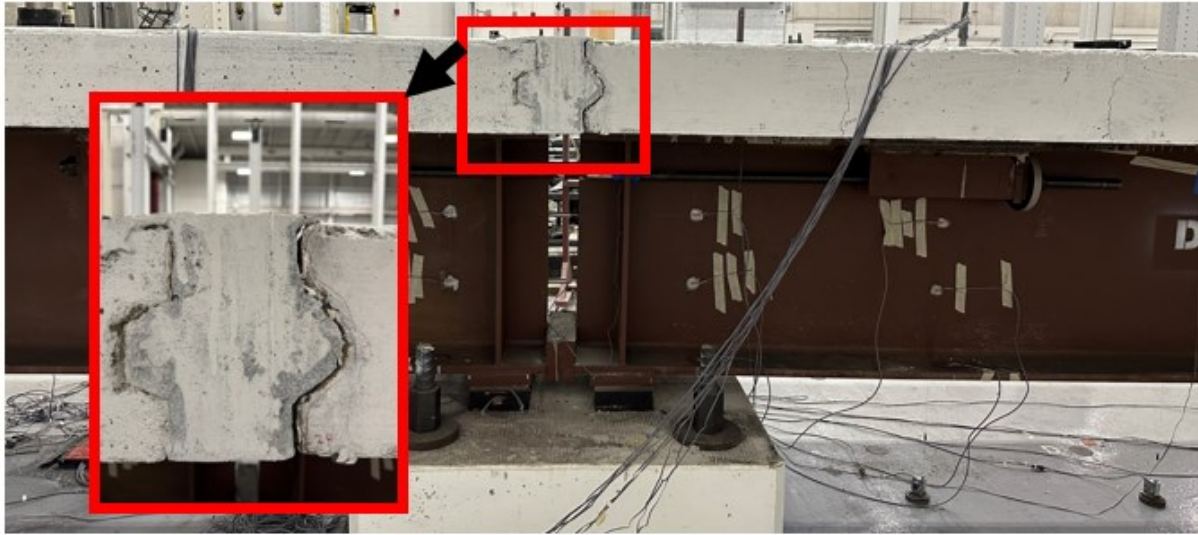
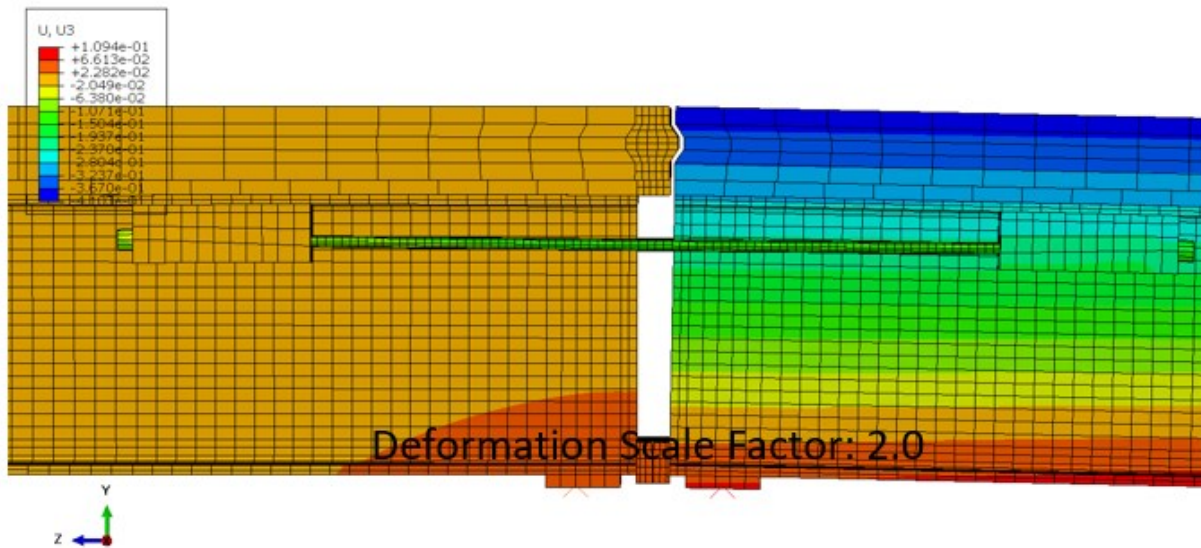


Figure 6.21. Relative Displacement versus Load Comparison.



(a)



(b)

Figure 6.22. Closure Pour Separation at 43 kips in the (a) Ultimate Test and (b) FEM.

The structural steel stresses/strains in the beam were compared between the FEM and the experiment. Figure 6.23(a) illustrates the specific cross-section E1 that was compared. Figure 6.23(b) shows the FEM structural steel stresses at E1 when the load reached 42 kips. The strain values were extracted when the load was 28 kips and 42 kips, which are shown in Figure 6.24. This figure compares the structural strain profile in the FEM and the experimental test. When the load is 28 kips, the slope difference is about 27 percent since the specimen is acting as fully

composite before 30 kips in the FEM. The slope difference is slight (5 percent) when the load is 42 kips since the closure pour has an opening gap. Both the FEM and experimental specimen exhibited non-composite section behavior. The Williams bar takes most of the tension force after 28 kips.

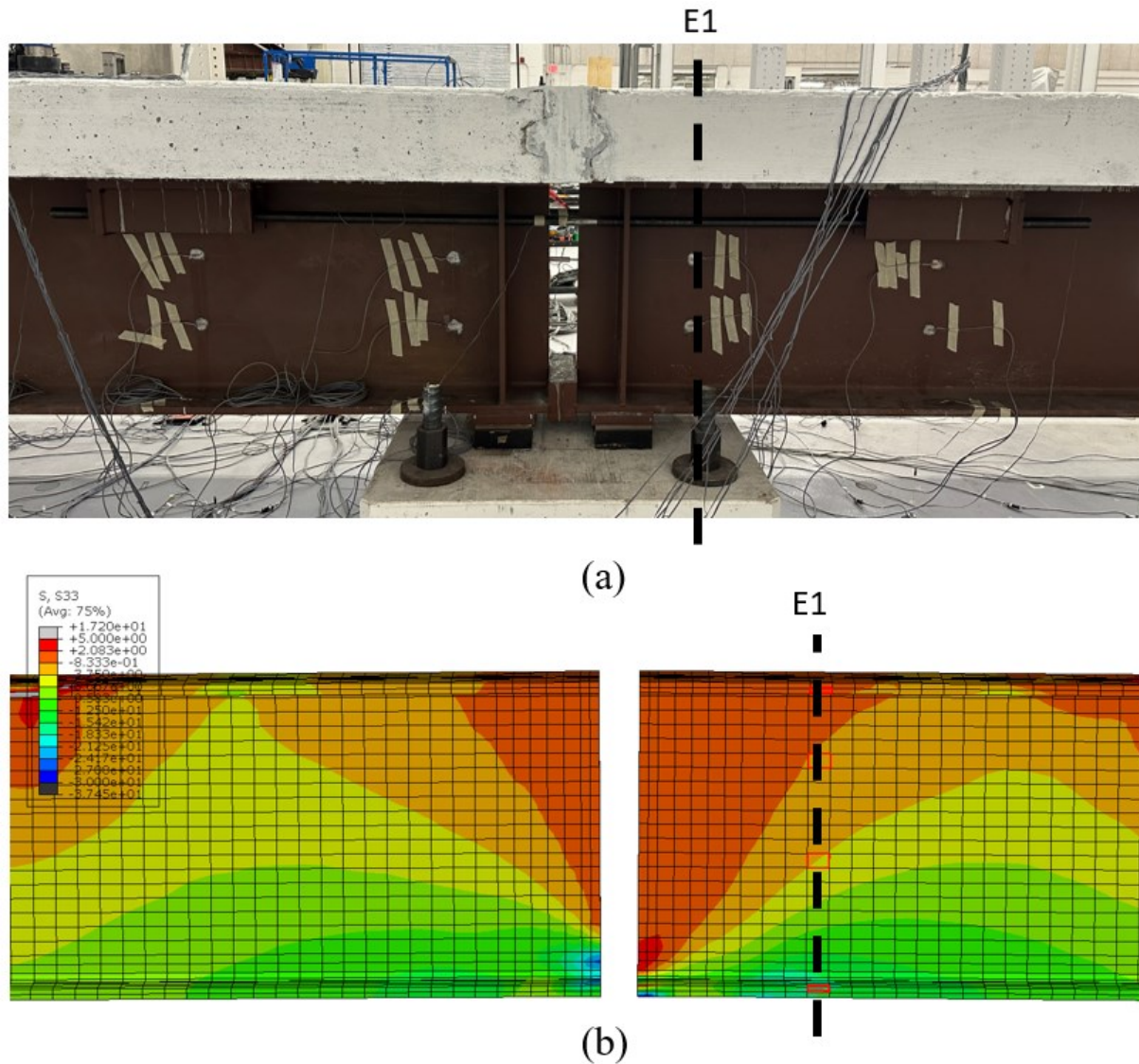
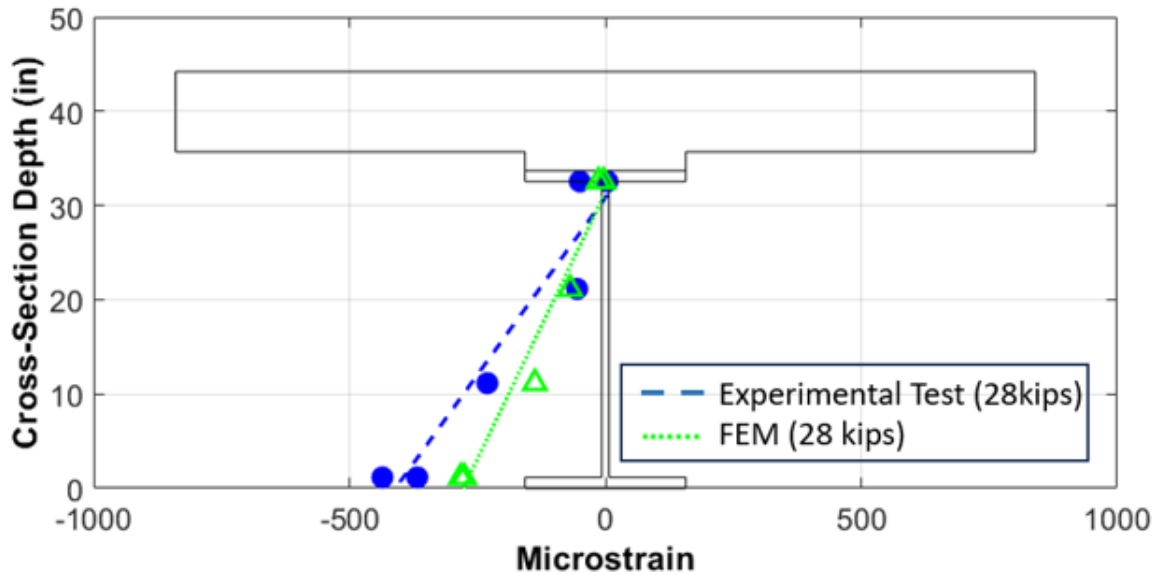
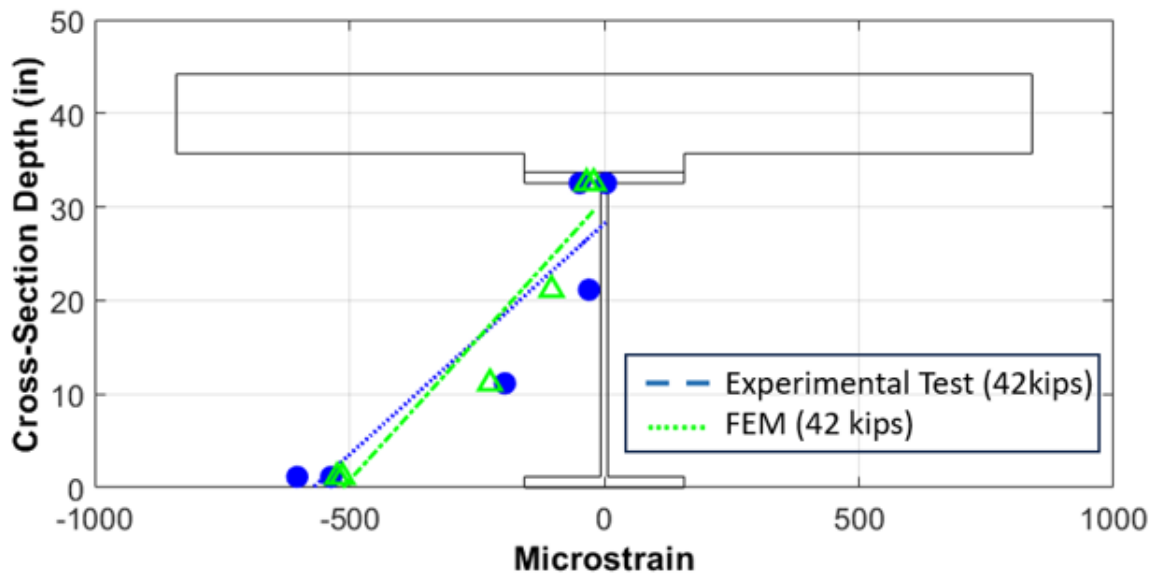


Figure 6.23. Stress at Structural Steel at E1 When Load Reached 42 kips in the (a) Ultimate Test and (b) the FEM.



(a)



(b)

Figure 6.24. Strain Profile Comparison at E1 for a Load of (a) 28 kips and (b) 42 kips.

The stress at the deck surface at E1 was compared between the FEM and the ultimate test.

Figure 6.25 depicts the comparison between the two results. The initial stress differences after PT at the center (SG59) and the sides (SG58 and SG60) were small, which means the simulated PT performed relatively well. The stresses in the experiment and FEM both increased to the

maximum when the displacement was about 0.3 inch. The stresses in the experiment and FEM at the sides were about 0.0 ksi. The center stress had appreciable differences.

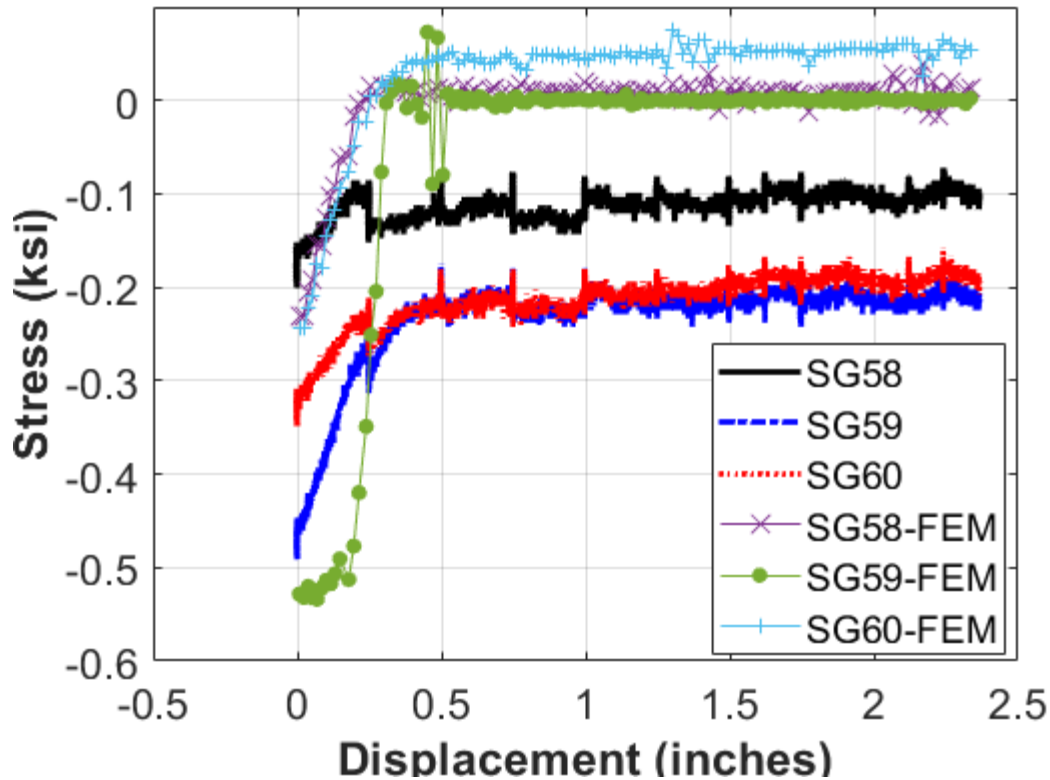


Figure 6.25. Stress at Deck Surface of E1 versus Displacement at E7 Comparison.

6.4. ANALYTIC MODELING OF CONCEPT C

6.4.1. Test Setup Model Description

The Concept C experimental test setup was depicted in Section 5.9.2.1. Like the previous concept test setup models, Abaqus/Explicit Analysis Program was also applied with the Double Precision/Explicit Packager for the Concept C test setup model. This section discusses the following aspects: geometry, material properties, assembly, contact interaction, load step, boundary conditions, mesh, analysis, and data processing.

The geometries of each part—regular concrete closure pour, rebar embedded in the closure pour, rebar in the precast concrete slab, precast concrete slab, steel girder with welded PT bracket and steel bearing plate, Williams bar, and the whole model assembly—are presented in Figure 6.26. The mesh element selection was similar to the previous concept models, and a C3D8 element type was selected to model a steel girder, steel bearing plate, steel brackets, steel Williams bars,

precast concrete slab, and regular concrete closure pour. A T3D2 element type was chosen for modeling the steel rebar, including the longitudinal and transverse rebar, extended U-loop rebar, and drop-in loop rebar. The mesh size varied for each part. The mesh size of the regular concrete closure pour was 3 inches. The precast concrete slab mesh size was 6 inches. Other parts' mesh sizes ranged from 1 inch to 3 inches. The total number of mesh elements was 30,531, which was close to Concept B. The total computation time was also close to the total time of the Concept B FEM.

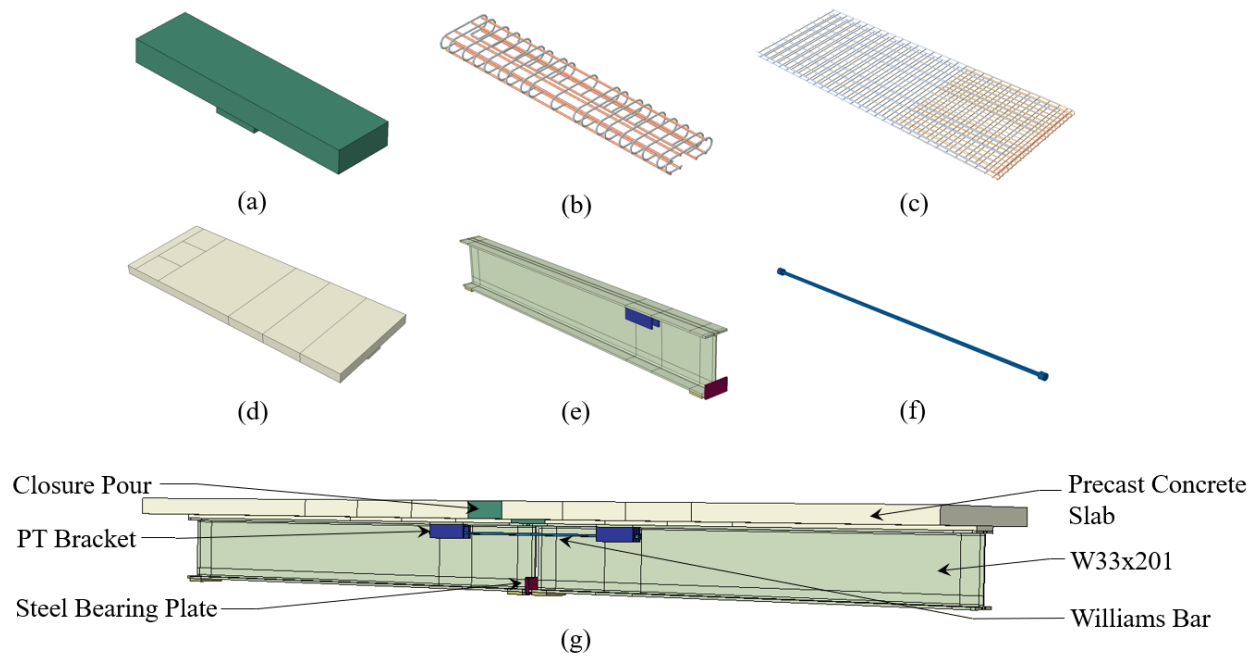


Figure 6.26. (a) Concrete Closure Pour, (b) Rebar in Closure Pour, (c) Rebar in Precast Concrete Slab, (d) Precast Concrete Slab, (e) Steel Girder with PT Bracket and Steel Bearing Plate, (f) Williams Bar, and (g) Model Assembly.

The FEM boundary condition assumptions were similar to Concept B. The Encastre boundary condition was selected for simulating the hold-down end of the specimen. A Cartesian-type connector with different stiffnesses in three directions connected with the ground was used to represent the elastomeric bearing pad on the pedestal. The embedded constraint was applied for the interaction between steel rebar and concrete. The tie constraint was applied for the interaction between the steel girder and concrete precast slab to model the composite behavior of the specimen. The tie constraint was used for the interaction between the steel bracket and the steel girder to simulate the weld condition, which helped avoid the relative displacement between them. The tie constraint was also set for the interaction between the closure pour and the precast

concrete slab. The general contact type was selected for the interaction of the whole specimen to avoid setting different complex contact pairs.

For the material properties' settings, the same CDP model for simulating concrete behavior and the same steel parts' material properties were applied for the Concept C test setup model, which was illustrated earlier in Section 6.2.1. The corresponding concrete compressive strength was matched with different concepts' ultimate tests that are shown in Section 5.6.1.

Similar to Concept B, the loading steps were divided into three parts consistent with the experiment: PT the Williams bars, gravity load applied to the total model, and displacement control at the load side. In order to increase the efficiency of the model analysis, the step time of Step 1 and Step 2 decreased to 1 second and 4 seconds when they were compared with Concept B. Table 6.6 presents each step time.

Table 6.6. Load Step with Step Time for Concept C Test Setup Model.

Step	Step Time (sec)
PT Williams bar	0–1
Applied gravity load for the whole model	1–5
Displacement control (2.5 inches)	5–45

During Step 1, the PT effect was also induced by the temperature change method, which was used in Concept B. A detailed description of this method was discussed in Section 6.3.1. Overall, the ratio of kinetic energy over inertial energy is depicted in Figure 6.27. The maximum ratio was about 1.2 percent, which was lower than 5–10 percent. The whole loading process was relatively stable. The ratio increased from about 0 percent to 0.2 percent when the step time was about 20 seconds because the number of cracks increased at the closure pour. The ratio rapidly increased at 40 seconds since the Williams bar took almost all the tensile force and yielded at that time. The crack width also increased at the closure pour.

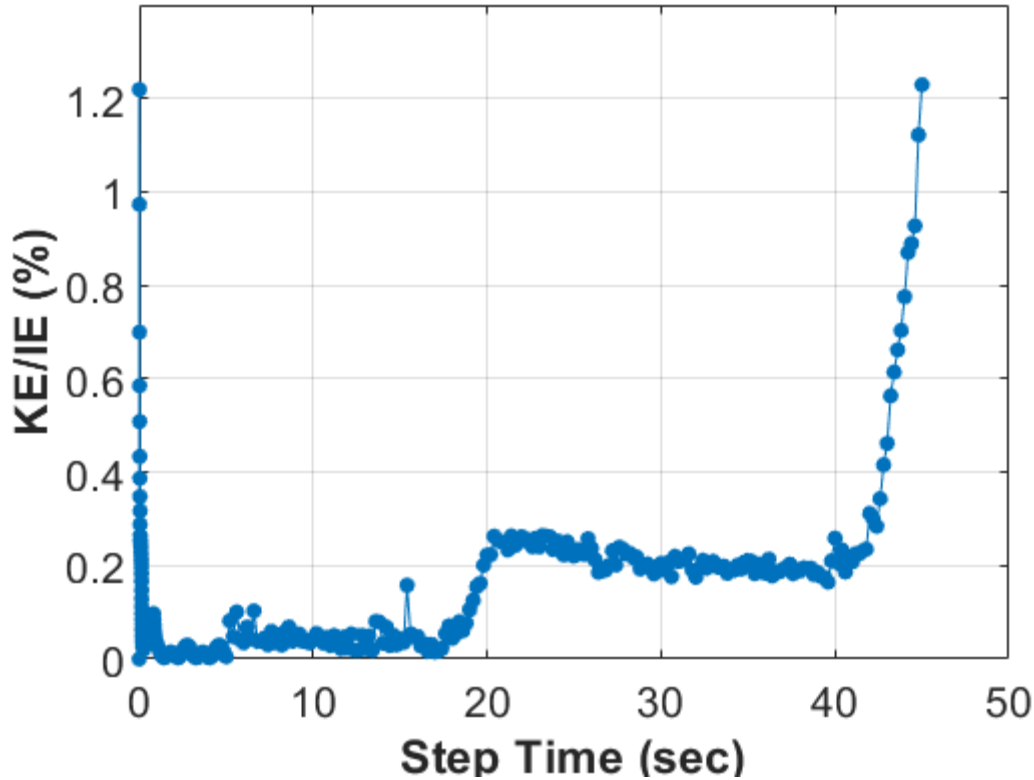


Figure 6.27. Energy Content Ratio of Kinetic Energy over Inertial Energy during Load Steps.

6.4.2. Model Validation with Experimental Results

The Concept C test setup model validation procedures include the load-displacement relationship, stresses (Williams bars, deck surface, rebar, and structural steel), relative displacement at the closure pour, and precast concrete deck damage patterns. All the experimental test results and data shown in this section come from the Concept C ultimate test, which was discussed in Section 5.9.2.4. The load-displacement relationship between the FEM and the experimental test is compared in this section. Figure 6.28 reveals this relationship is similar to the previous concept models. This FEM applied the displacement control method. The load was about 70 kips when the specimen stiffness began to decrease, which is about 7 percent higher than the experiment, which was around 65 kips. The initial FEM stiffness was about 93 kip/in when the load reached before 70 kips, which is about 4 percent greater than the experiment. The specimen stiffness difference was relatively small after 70 kips, which may come from the assumption of material properties or interaction behaviors.

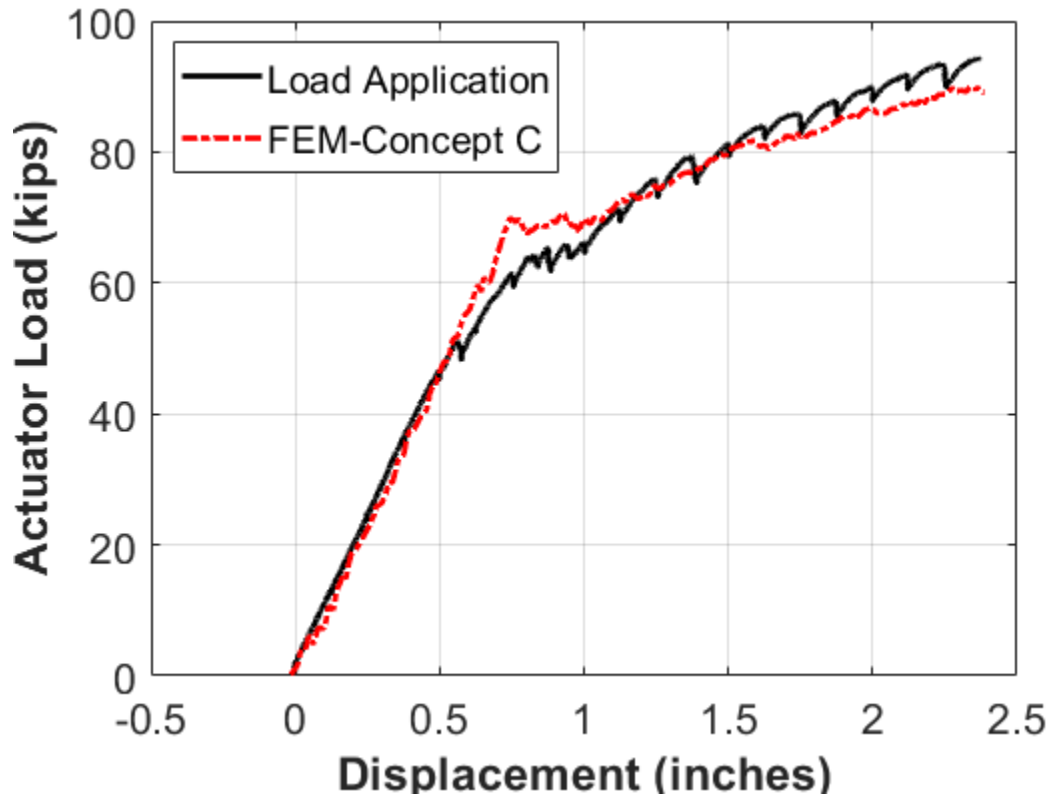


Figure 6.28. Load-Displacement Curve Comparison between the Concept C FEM and Experimental Test.

The stress on the Williams bars was compared with the FEM results. Figure 6.29 depicts the comparison between the FEM and the experiment. The stresses in Williams bars of the FEM were close to the experiment through the whole loading process. The maximum difference between them was about 4 percent when the actuator load was about 72 kips at E7. Both stresses started to decrease before the actuator load was 70 kips since the NA was higher than the Williams bars. Both greatly increased when the load was about 70 kips, which validated the Williams bar behavior in the FEM.

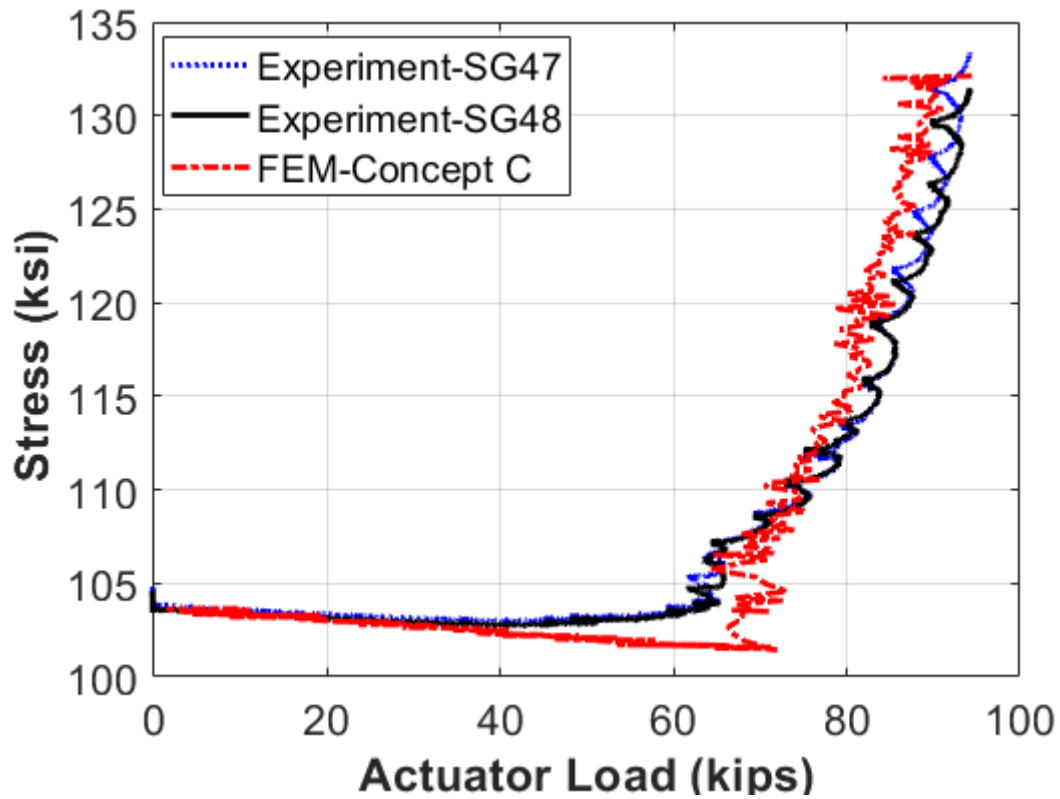
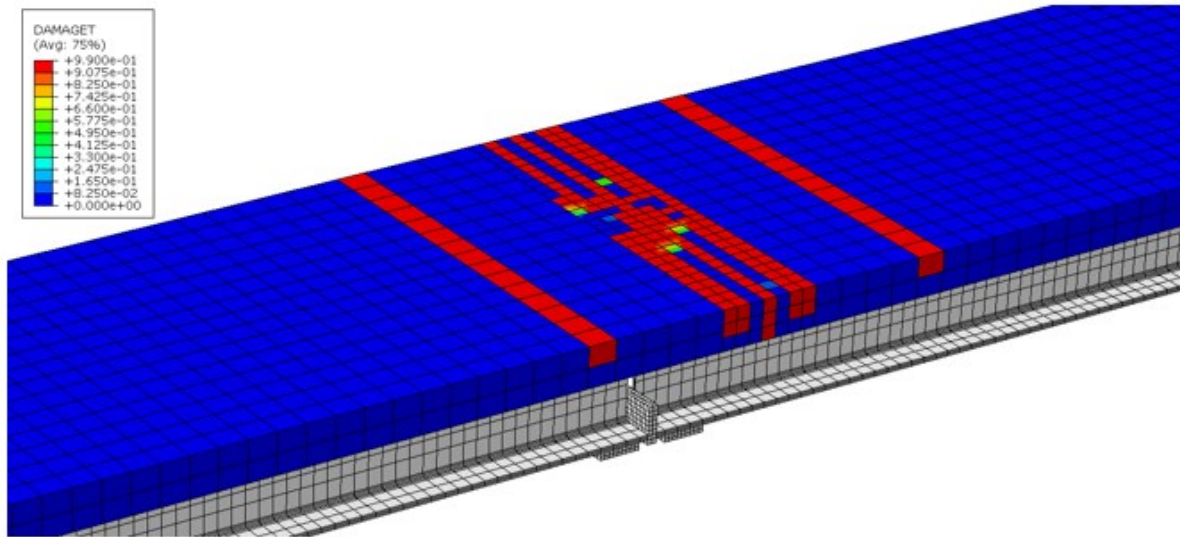
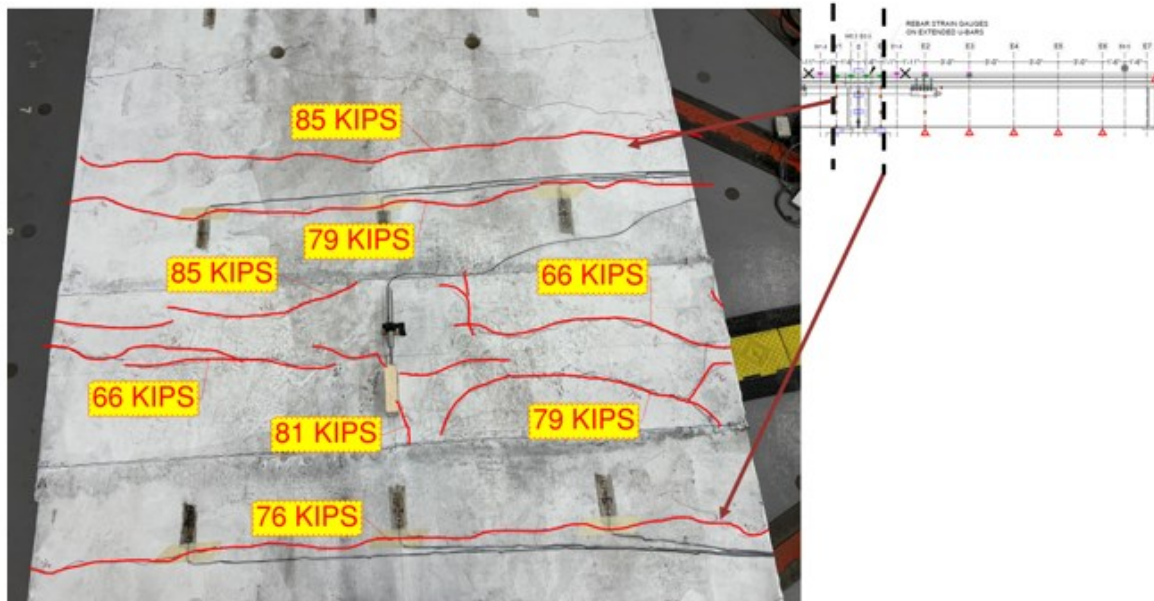


Figure 6.29. Stress on the Williams Bar versus Load at E7 Curves Comparison of Concept C.

The concrete damage patterns of the FEM and experiment were compared. Figure 6.30 shows the cracks at the closure pour region when the load was about 75 kips, and the crack patterns happened in the experimental test when the load was from 66 kips to 85 kips. The crack patterns are similar in this region.



(a)

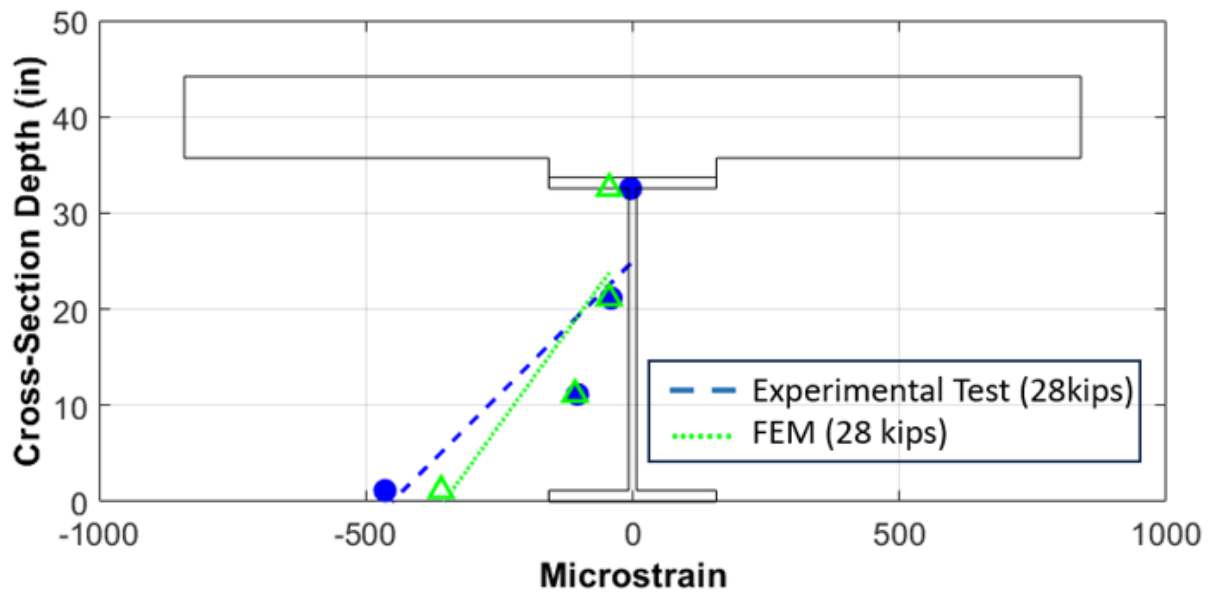


(b)

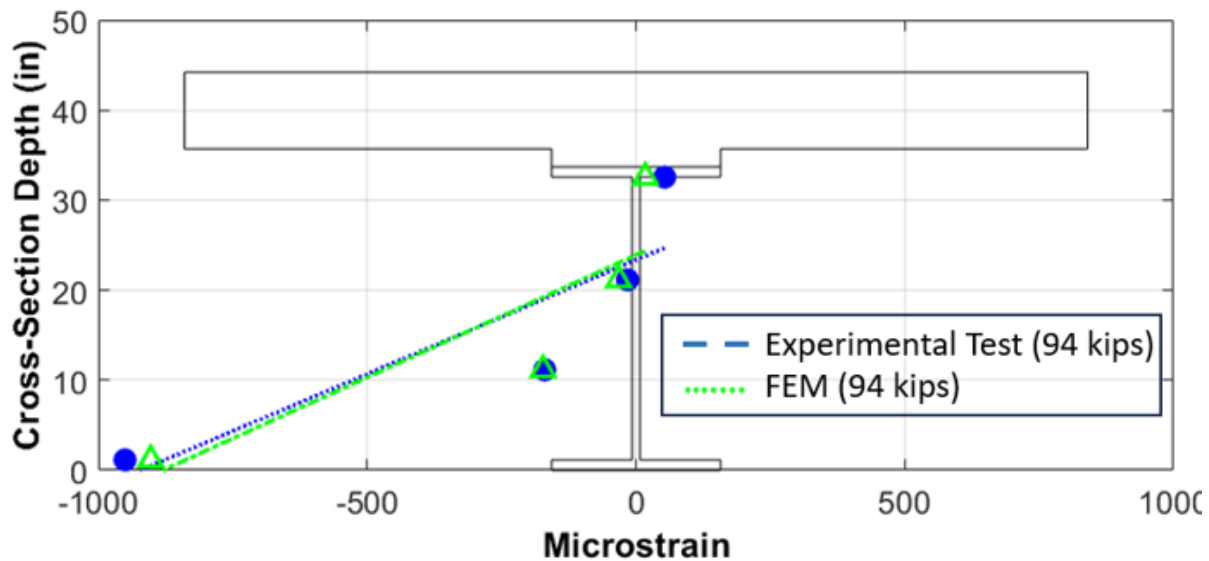
Figure 6.30. Concrete Damage Patterns at Closure Pour Comparison: (a) FEM Damage Patterns (75 kips) and (b) Experiment Concrete Crack Patterns.

The structural stresses/strain in the beam were compared between the FEM and the experiment. Figure 6.31 shows the strain values at E1 when the load was 28 kips and 94 kips. The strain difference is about 8 percent when the load reached 28 kips. The strain in the experiment was larger than the strain in the FEM since the FEM behaved as fully composite at the beginning.

The slope difference was about 3 percent when the load reached 94 kips. The strain in the FEM is very close to the strain in the experiment when the load was 94 kips.



(a)



(b)

Figure 6.31. Strain Profile Comparison at E1 for a Load of (a) 28 kips and (b) 94 kips.

The stress at the deck surface at E1 was compared for the FEM and the ultimate test. Figure 6.32 presents the comparison and the stress difference between them. The initial prestressed stress at the center (SG59) and side (SG58) difference is relatively small, which means the prestressed

effect in the FEM performed well. The stresses in the FEM increased to the maximum when the displacement was about 0.6 inch, while the stresses in the experiment reached the maximum value when the displacement was about 1 inch. The stress difference may be caused by the various concrete crack locations. The stresses in the experiment dropped when the displacement was about 1.1 inches. The stress in the FEM at the center dropped when the displacement was 1 inch, and the side one dropped when the displacement was 1.7 inches. The center one was close to the experiment, while the side one was far from the experiment.

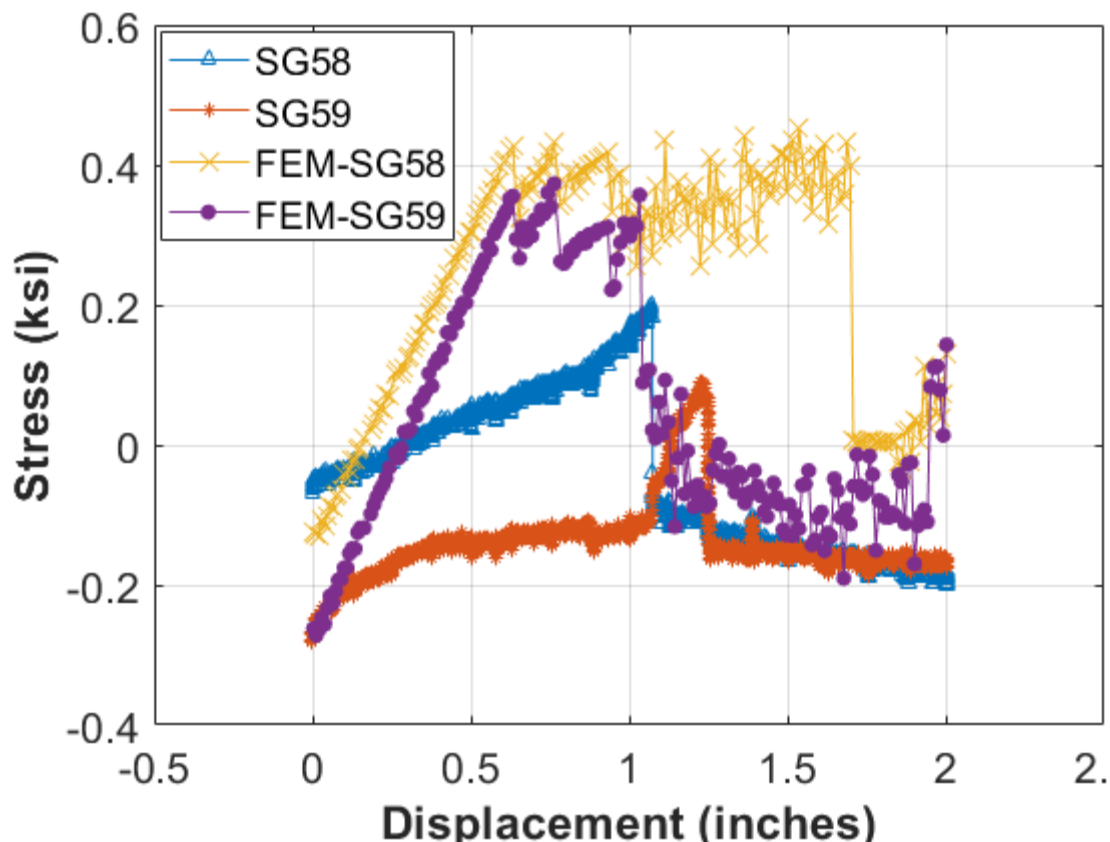


Figure 6.32. Stress at Deck Surfaces of E1 versus Displacement at E7 Comparison.

The relative displacement at closure pour was compared between the FEM and the experiment in Figure 6.33. The LV4 was an LVDT that was set on the center of the concrete closure pour (E0) surface in the longitudinal direction. Overall, both reached almost the same value when the displacement was about 2.4 inches. The experimental one was nearly kept at zero inches before the displacement reached 0.8 inches. The FEM increased as a relatively similar slope overall. The difference may be because of the different concrete crack widths and locations that happened in the FEM and the experiment.

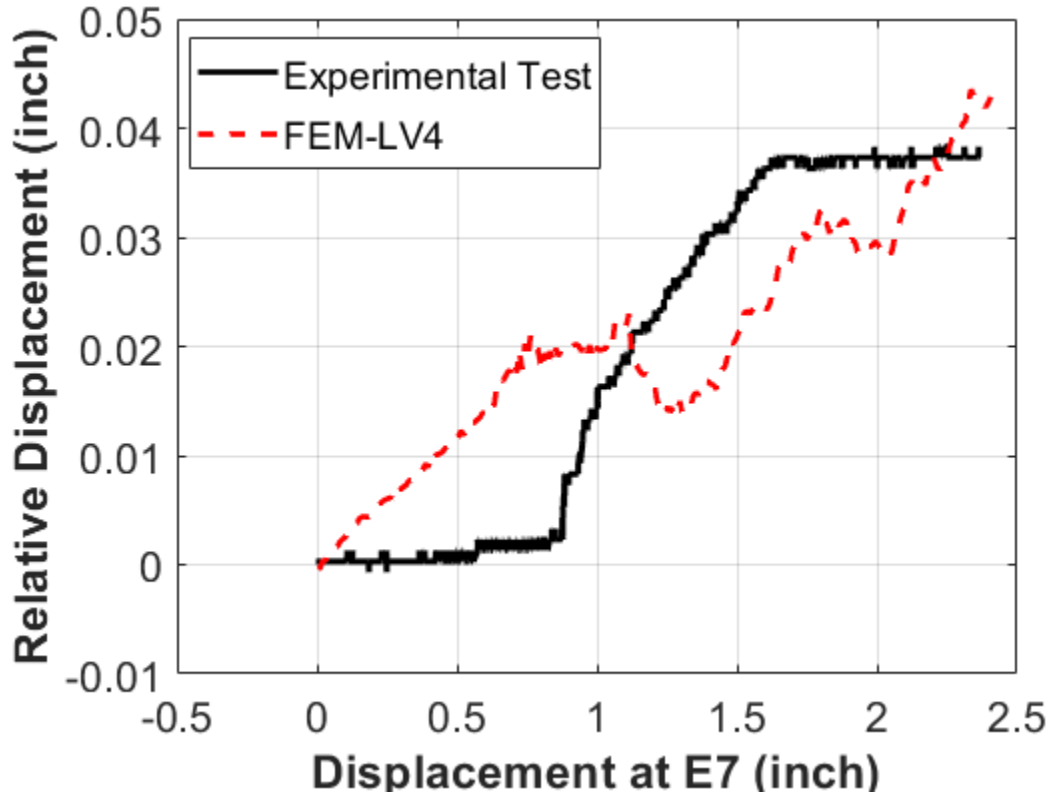


Figure 6.33. Relative Displacement at Closure Pour Comparison.

6.5. ANALYTIC MODELING OF CONCEPT D

6.5.1. Test Setup Model Description

The Concept D experimental test setup is presented in Section 5.10.2.1. The Concept D test setup FEM was set by Abaqus/Explicit Program with the Double Precision/Explicit Packager. The modeling process of Concept D included these procedures: geometry, material properties, assembly, contact interaction, load step, boundary conditions, mesh, analysis, and data processing. The detailed material properties are illustrated in Section 5.6.1. The major geometries are shown in Section 5.10.2.1.

The basic model parts included the steel beam, precast concrete drop panel, rebar mats, and Williams bars, which are shown in Figure 6.34. For the mesh element selection, a C3D8 element type was used to model the steel beam, concrete drop panel, and steel Williams bars. A T3D2 element type was used to model the steel rebar portion, which included the longitudinal rebar, transverse rebar, and loop rebar in the drop panel. The mesh size is different for each part. The mesh size of the male-to-female key at the top and bottom parts is 1 inch. Other mesh sizes range

from 2 inches to 6 inches to save computation time. The total number of mesh elements is 37,522, which is similar to previous concepts. The total computation time is also close to the total time of the Concept C FEM.

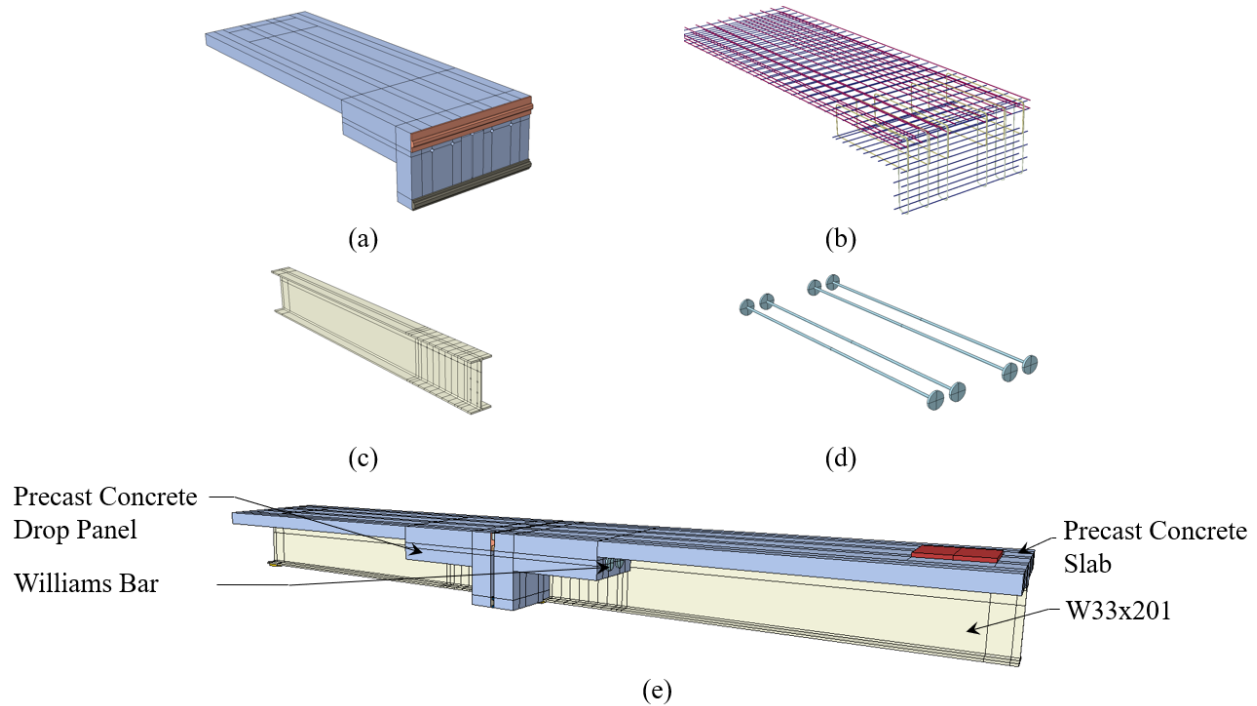


Figure 6.34. (a) Precast Unit, (b) Rebar in Precast Unit, (c) Steel Girder, (d) Williams Bars, and (e) Model Assembly.

The FEM boundary condition assumptions were a little bit different from the previous concepts since Concept D is more complex. The Encastre boundary condition was selected for simulating the hold-down end of the specimen. A Cartesian-type connector with different stiffnesses in three directions connected with the ground was used to represent the elastomeric bearing pad on the pedestal. The embedded constraint was applied for the interaction between steel rebar and concrete. The tie constraint was applied for the interaction between the steel girder and concrete precast slab to model the composite behavior of the specimen. The tie constraint was used for the interaction between the shear key part and the concrete deck to simulate the whole part, which helped avoid the relative displacement between them. The general contact type was selected for the interaction of the whole specimen to avoid setting different complex contact pairs.

For the material properties' settings, the same CDP model for simulating concrete behavior and the same steel parts' material properties were applied for the Concept D Test Setup Model,

which was described previously in Section 5.10.2.1. The corresponding concrete compressive strength was matched with different concepts' ultimate tests shown in Section 5.10.2.4.

Similar to Concept C, the loading steps are divided into five parts consistent with the experiment: PT the Williams bars, gravity load applied to the whole model, static testing process that include push down and pull up, and ultimate testing process at the active loading side. In order to increase the efficiency of the model analysis, the step time of Step 1 and Step 2 decreased to 1 second and 4 seconds when they were compared to Concept B. Table 6.7 presents each step time.

Table 6.7. Load Step with Step Time for Concept D Test Setup Model.

Step	Step Time (sec)
PT Williams bar	0–1
Applied gravity load for the whole model	1–5
Push down (1 inch)	5–25
Pull up (1 inch)	25–45
Push down (4 inches)	45–65

During Step 1, the PT effect was also induced by the temperature change method, which was used in Concept B and Concept C. A detailed description of this method was introduced in Section 6.3.1. Overall, the ratio of kinetic energy over inertial energy is depicted in Figure 6.35. The maximum ratio was about 1.2 percent, which was well below 5 percent. The whole loading process was relatively stable before 45 seconds. The ratio increased from about 0 percent to 0.2 percent when the step time was about 20 to 40 seconds because of the number of cracks formed at the interface of the concrete drop panel. The crack width also increased at the adhesive joint when the specimen was pushed down.

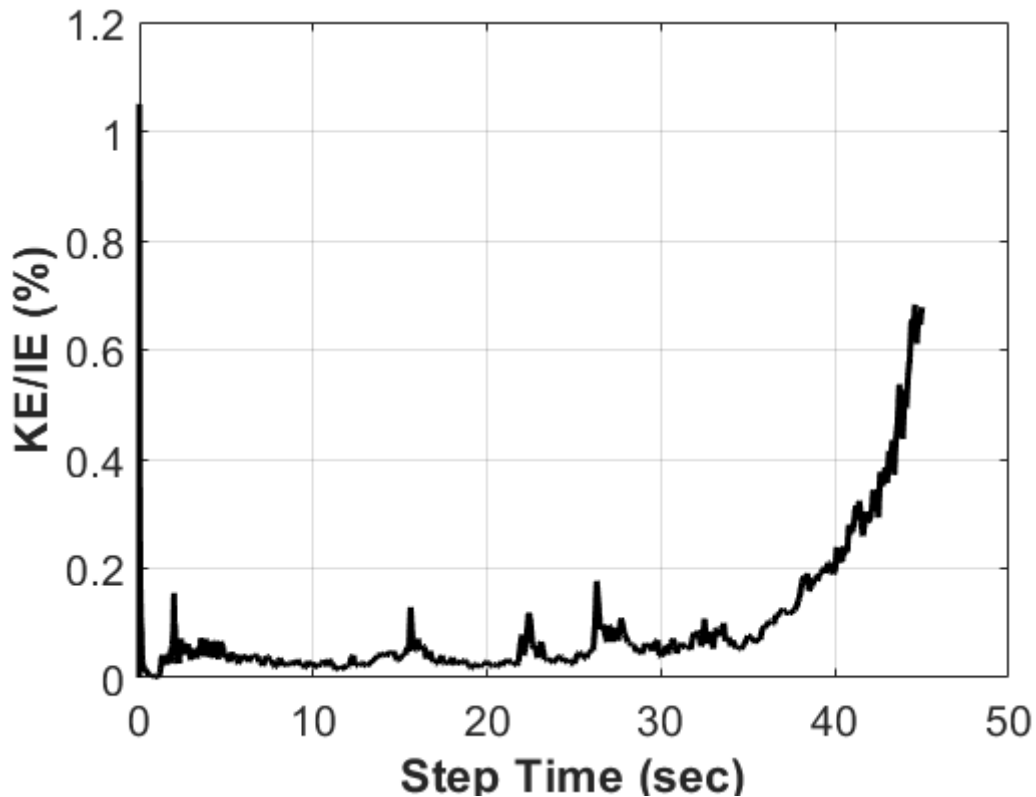


Figure 6.35. Energy Content Ratio of Kinetic Energy over Inertial Energy during Load Steps.

6.5.2. Model Validation with Experimental Results

For Concept D, the FEM validation procedures include the load-displacement relationship, stresses (Williams bars and structural steel beam), steel beam strain profiles, and precast concrete deck damage patterns. All the experimental test results and data in this section come from the Concept D ultimate test discussed in Section 5.10.2.4. The load-displacement relationship between the FEM and the experimental test is compared in this section. Figure 6.36 reveals this relationship is similar to the previous concept models. This FEM applied the displacement control method. The load was about 42 kips when the specimen stiffness began to decrease, which is about 11 percent higher than the experiment which was around 37 kips. The initial FEM stiffness was about 35 kip/in when the load reached 36 kips, about 1 percent greater than the experiment. The specimen stiffness difference was relatively small after 43 kips, which may come from the assumption of material properties or interaction behaviors or from the uneven stresses in the four Williams bars in experiments. The structural stiffness was about 20 percent higher than in the experiment when the load was between 35 and 42 kips.

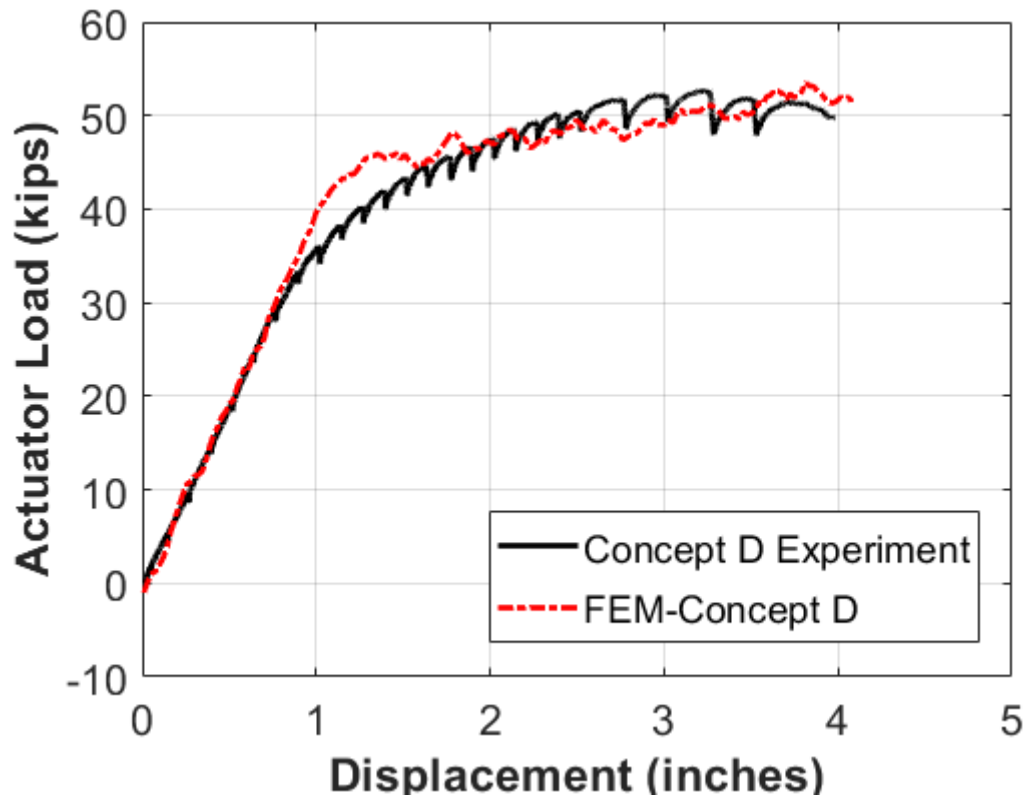


Figure 6.36. Load-Displacement Curve Comparison between FEM and Experiment.

The stress on the Williams bars was compared with the FEM results. Figure 6.37 depicts the comparison between the FEM and the experiment. The average stresses in Williams bars of the FEM were close to the experiment through the whole loading process. The maximum difference between them was about 2 percent when the load was about 45 kips. Both stresses started to decrease when the load was before 45 kips since the NA was higher than the Williams bars. Both greatly increased when the load was about 47 kips, which validated the Williams bar behavior in the FEM. Both of them show very similar stress tendencies when the load increases.

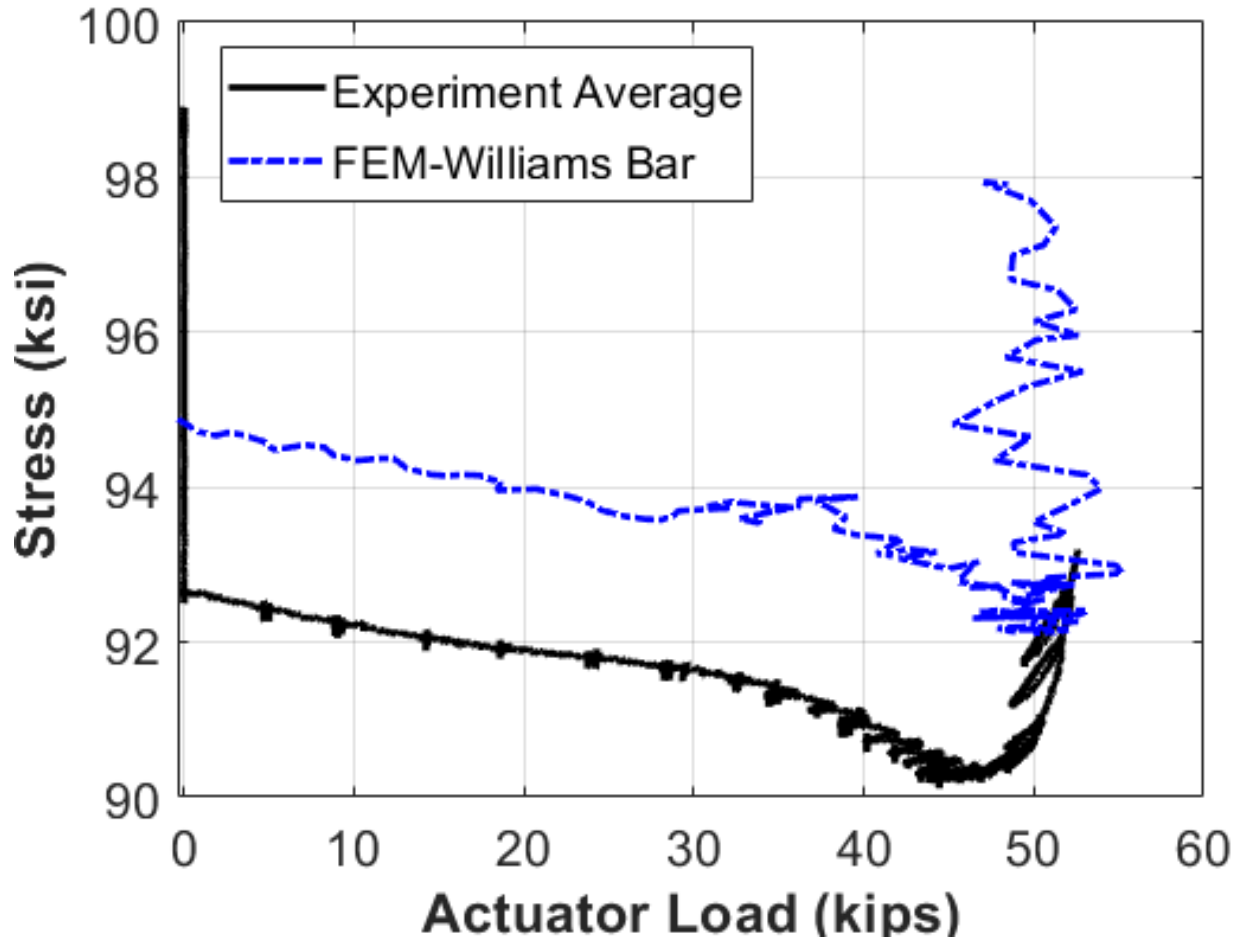


Figure 6.37. Stress on the Williams Bars versus Displacement at E7 Comparison of Concept D.

The concrete damage patterns of the FEM and experiment were compared. Figure 6.38 shows the cracks at the side view of the precast concrete drop panel when the load was about 10 kips, and the crack patterns happened in the experimental test when the load was about 10 kips during the static testing. The crack patterns are similar in this drop panel interface. Figure 6.39 presents the comparison of concrete damage patterns in the front view of the precast unit. They both formed about 10 inches under the Williams bars and the bottom part, which is closed to the steel beam bottom flange.

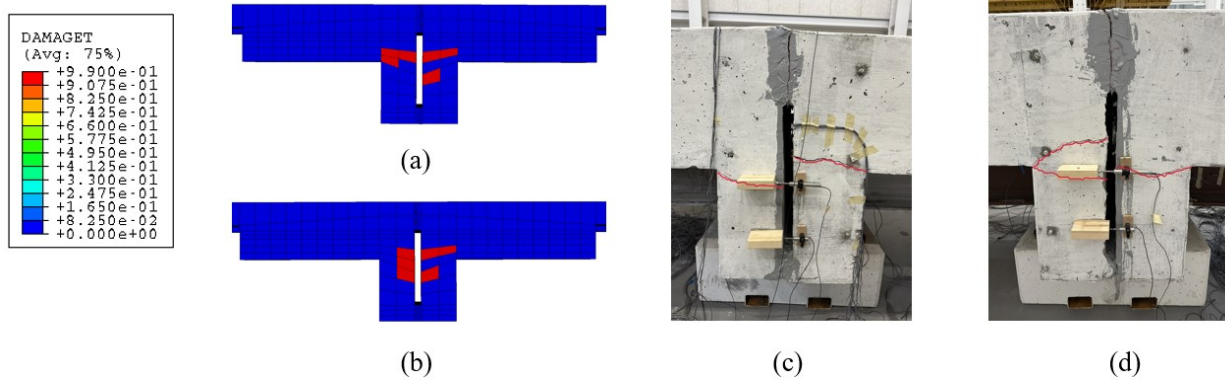


Figure 6.38. Concrete Damage Patterns at the Side Surface of the Precast Drop Panel Comparison: (a) FEM Damage Patterns at North Side (20 kips), (b) FEM Damage Patterns at North Side (20 kips), (c) Experiment Concrete Crack Patterns at North Side, and (d) Experiment Concrete Crack Patterns at South Side.

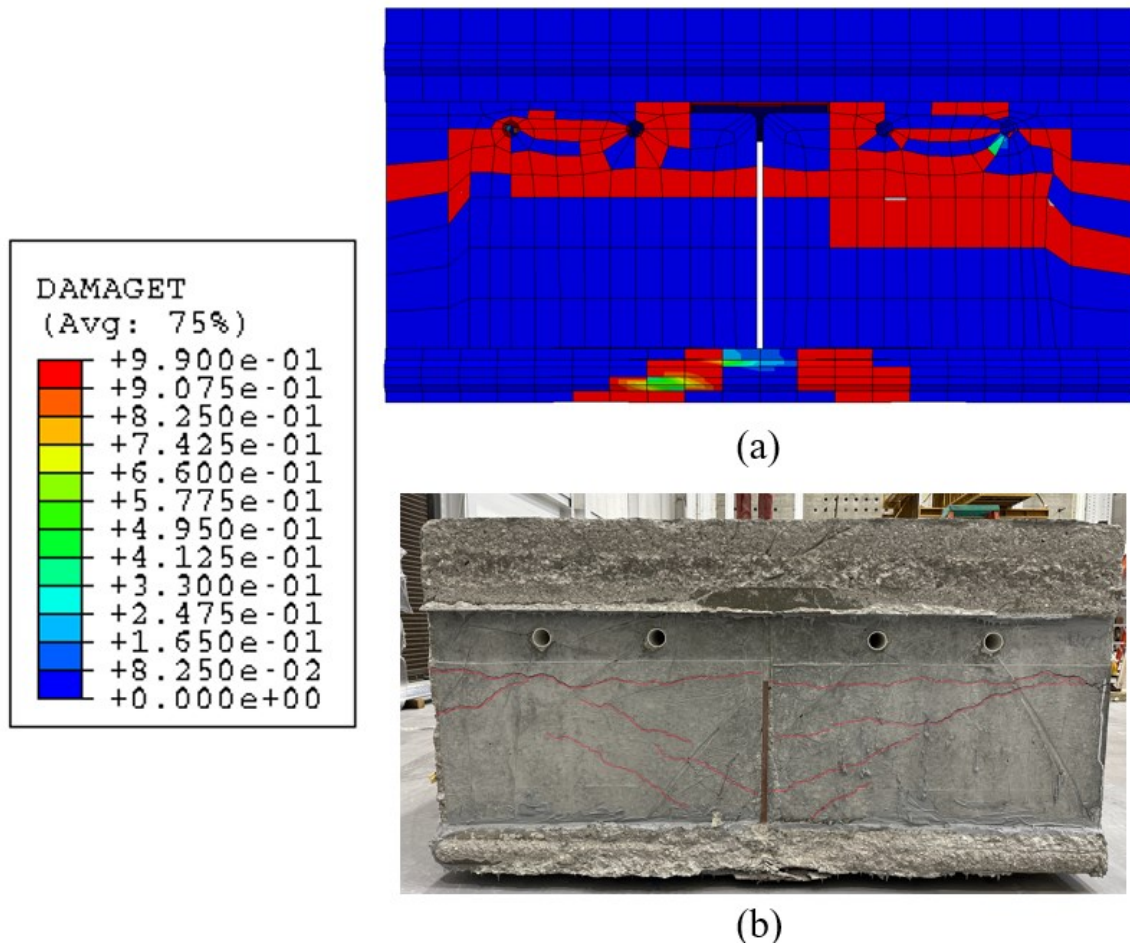
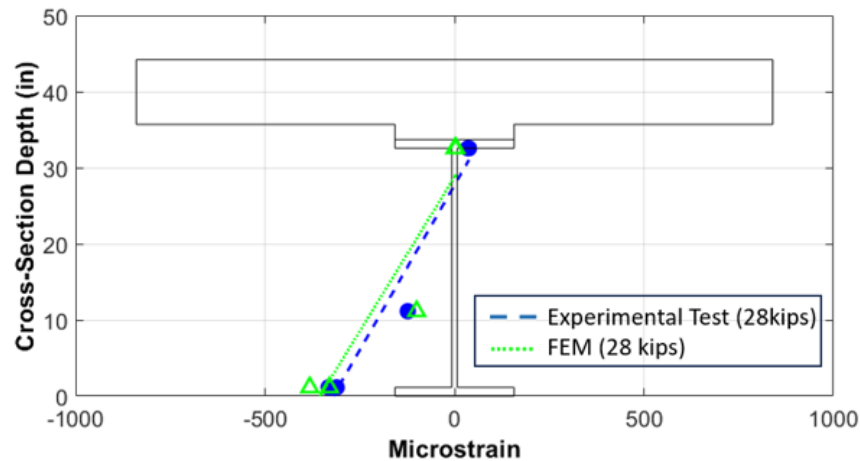
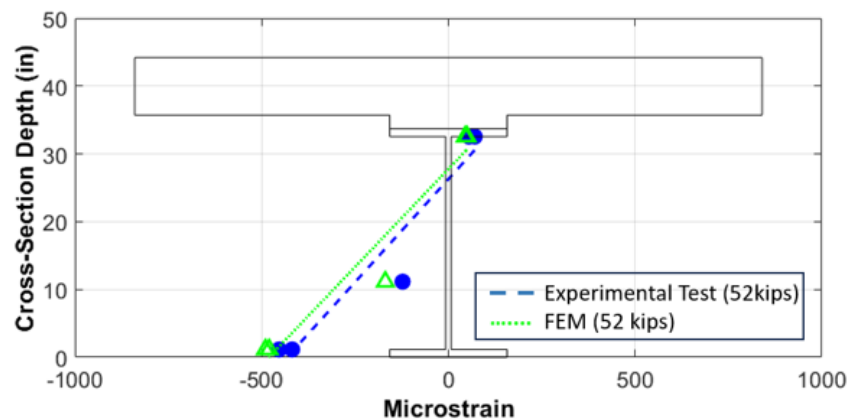


Figure 6.39. Concrete Damage Patterns at the Front Surface of the Precast Drop Panel Comparison: (a) FEM Damage Patterns (20 kips) and (b) Experiment Concrete Crack Patterns.

The structural stresses/strain in the beam between the FEM and the experiment were compared. Figure 6.40 shows the strain values at E1 when the load was 28 kips and 52 kips. The strain difference is about 3 percent when the load reaches 28 kips. The strain in the experiment was larger than the strain in the FEM since the FEM behaves as fully composite at the beginning. The slope difference was about 9 percent when the load reached 52 kips. The strain in the FEM is very close to the strain in the experiment when the load was 28 kips.



(a)



(b)

Figure 6.40. Strain Profile Comparison at E1 When Load at (a) 28 kips and (b) 52 kips.

6.6. ANALYTIC MODELING FOR TESTED SPECIMENS' FINDINGS

A comparison of the FEM for Concepts A to D to the experimental results produced the following general findings:

- For all of the concepts, the difference for the load-displacement plot between finite element models and experiments is relatively small, especially for Concept B. Concept A FEM captured the load peak when the bolts slipped at the bottom flange, which was also very close to the magnitude of the load peak for experiments. Concept C FEM presented the temporary load peak when the number of cracks developed at the closure pour, which happened at almost the same load magnitude for experiments. All of the FEM accurately presented the failure mechanism of each test setup. They were considered valid for further studies and final recommendation modeling.
- The temperature change method was valid and relatively reliable. For the pre-tensioning effect of the bolts in Concept A, the prestressed force was relatively close to the experiments. The PT effect of the Williams bars also applied this method, and the stress-actuator load plots present moderately accurate stress changing along with the actuator load.
- The CDP model was applicable for these concept setups. The difference of deck surface stresses between finite element models and experiments was relatively small. The concrete damage pattern comparison also showed that the cracks happened at very close locations for FEM and experiments. The CDP model predicted the concrete behavior relatively well and can be utilized for the final design approach.
- The FEM provided reasonable estimates of the measured stresses on structural steel girders and concrete deck surfaces, the initial stiffness of the structure, and the basic failure mechanism of the specimens.

FEM for variations to the connection concepts is presented in the following section.

6.7. ANALYTICAL MODELING OF REFINED CONCEPTS

6.7.1. Introduction

The knowledge gained from the experimental testing and analytical modeling allowed the research team to refine the connection concepts. These refinements were evaluated numerically with FEA using the validated approach discussed earlier. The result of this effort were two final system options for steel SDCL bridges using ABC. The primary option (Final System Option 1) is explained in Sections 6.7.2 to 6.7.4. The secondary option (Final System Option 2) is presented in Sections 6.7.5 and 6.7.6. Then a discussion and comparison is provided in Section 6.7.7.

6.7.2. Final System Option 1 Details

The overall purpose for creating the transverse connection is to improve the long-term durability and performance of the structure. Final System Option 1 combines the most effective portions of Concept A and Concept C (which were the most successful concepts tested) based on the five criteria (constructability, speed, quality, long-term durability, safety, and cost). The top splice plate of Concept A is combined with the bottom flange bearing plates of Concept C. The deck slab connection is a conventional concrete closure pour, which was the same for Concepts A and C. Concept C included PT bars (or Williams bars). This adds additional complexity to the connection. However, as was shown in the testing, it is necessary to precompress the deck slab, which reduces cracking. Thus, the Final System Option 1 provides PT bars (mounted to the bottom of the top flange) as an optional item.

The ease of construction for the Final System Option 1 should be better than the experimental concepts. The concrete deck closure should be relatively easy to make using conventional concrete rather than UHPC. The top flange splice plates are easy to construct since the construction method is relatively mature in the field and there is no special labor required. The bottom bearing plates are also relatively easy to attach (and bolt together if needed).

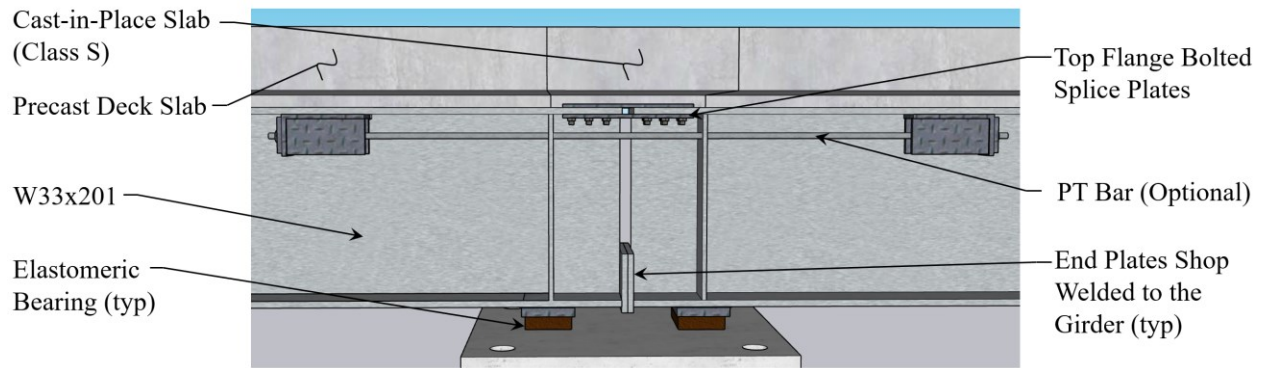
The speed of assembly should be relatively fast since the splice plates and bearing plates are easy to assemble. The CIP closure pour may take a few hours since it needs additional reinforcement in the closure pour. The PT system is optional. If PT is implemented, it will increase the assembly time.

The long-term durability of Final System Option 1 is considered the highest when compared to the experiment concepts. The bearing plates on bottom can avoid the bolt slipping issues that happened with Concept A. The bolted spliced plates on top can restrain the relative displacement between the precast units and eliminate the major cracks that happened on the deck surface. The optional PT system also provides additional precompressive stresses in the deck surface over the pier location if there is a special requirement for the deck surface cracking level.

The cost-effectiveness of the Final System Option 1 is highest when compared to the experiment concepts if there is no PT system installed. The welded bearing plates on the bottom are easy to construct in the shop. The splice plates can be done in a relatively short time in the field when the oversize hole and field-drill hole on one side is applied. There is no UHPC or other special materials used for the closure pour.

The overall safety features for the Final System Option 1 remain relatively high. However, the addition of PT does reduce the level of safety. Nonetheless, PT is very common in the bridge industry and should be able to be implemented with minimal risk.

For the structural performance aspect, the top flange splice plates provide a direct path for the tensile forces to transfer across the beams, while the bottom flange bearing plates provide a direct compression-resisting element; they are also the fastest, easiest, most cost-effective, and best performing of the bottom flange choices. The PT brackets and Williams bars can be implemented if the design requires precompression of the deck slab to mitigate cracking of the slab. A general rendering of the recommended connection is provided in Figure 6.41. The structural behavior is further evaluated (without and with PT) in the following sections.



Bent Elevation

Figure 6.41. Beam Elevation View of the Final System Option 1.

6.7.3. Final System Option 1 FEM—No PT

6.7.3.1. Final System Option 1 FEM Description

Based on the Final System Option 1 details in Section 6.7.2, the corresponding finite element model was built using Abaqus Version 6.14. The Abaqus/Explicit Analysis Program was applied with Double Precision/Explicit Packager for this model. The modeling included the following procedures: geometry, material properties, assembly, contact interaction, load step, boundary conditions, mesh, analysis, and data processing. The major geometries and material properties follow the previous concepts' FEM settings, which were validated with the experimental data.

The models of the steel beam with steel bearing plates at the bottom flange, the precast concrete deck, the rebar, and the entire assembly are shown in Figure 6.42. For the mesh element selection, a C3D8 element type was used to model a steel beam with bearing plates, concrete precast slab, and closure pour. A T3D2 element type was used to model the steel rebar portion, which included the longitudinal rebar and transverse rebar. The mesh size is different for each part. The closure pour mesh size is 1 inch. Other mesh sizes range from 3 inches to 6 inches. The total number of mesh elements is 73,926.

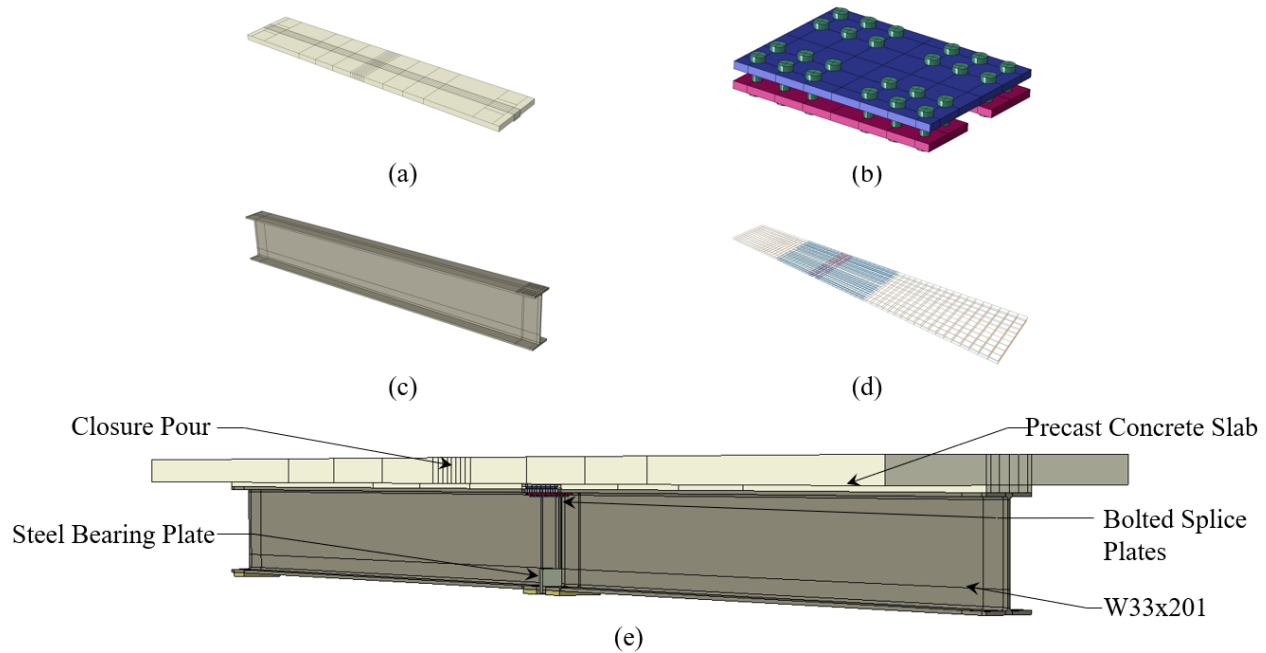


Figure 6.42. (a) Precast Concrete Deck with Closure Pour, (b) Splice Plates with Bolts, (c) Steel Beam, (d) Rebar Mat, and (e) Model Assembly.

The FEM boundary condition assumptions were similar to Concept A. The Encastre boundary condition was selected for simulating the hold-down end of the specimen. A Cartesian-type connector with different stiffnesses in three directions connected with the ground was used to represent the elastomeric bearing pad on the pedestal. The embedded constraint was applied for the interaction between steel rebar and concrete. The tie constraint was applied for the interaction between the steel beam and concrete precast slab to model the composite behavior of the specimen. The tie constraint was used for the interaction between the steel bearing plates and the steel beam to simulate the welding condition, which helped avoid the relative displacement between them. The general contact type was selected for the interaction of the whole specimen to avoid setting different complex contact pairs.

The material properties of this finite element model were similar to Concept A. The same CDP model for simulating concrete behavior and the same steel parts' material properties were applied for this model.

Similar to Concept A, the loading steps were divided into three parts that include pre-tensioning bolts, gravity load applied to the total model, and displacement control at the load side, which is

simulated with the experiment. To increase the efficiency of the model analysis, the step time of Step 1 and Step 2 decreased to 1 second and 4 seconds. Table 6.8 presents each step time.

Table 6.8. Load Step with Step Time for Final System Option 1 FEM.

Step	Step Time (sec)
Pre-tensioning bolts	0–1
Applied gravity load for the whole model	1–5
Displacement control (2.5 inches)	5–25

The first step of pre-tensioning bolts was achieved by the temperature change method, which was used in Concept A. Overall, the ratio of kinetic energy over inertial energy is depicted in Figure 6.43. The maximum ratio was about 0.6 percent, which was lower than 5–10 percent. The ratio increased from about 0 percent to 0.3 percent when the step time was about 1 second because of the pre-tensioning effect. The whole loading process was relatively stable since there was no bolt slippage issue during the process.

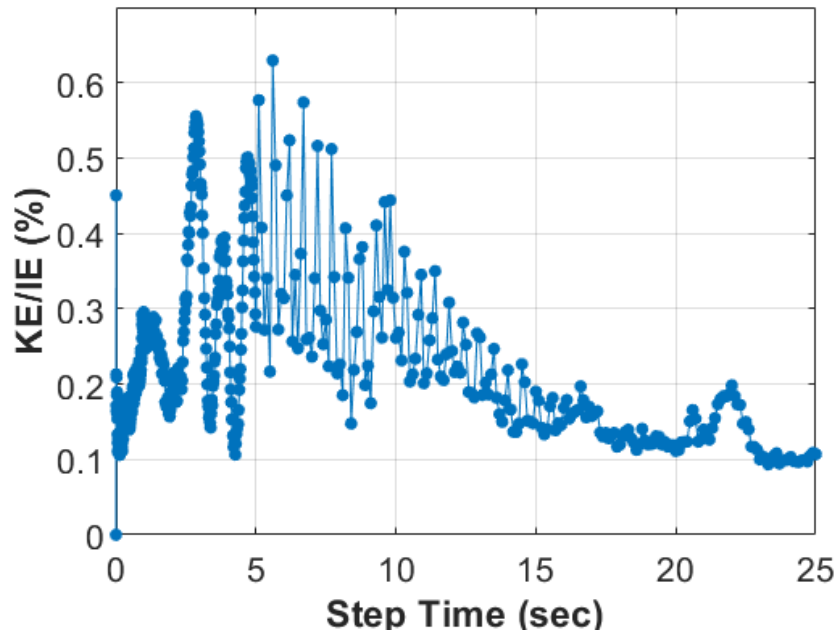


Figure 6.43. Energy Content Ratio of Kinetic Energy over Inertial Energy during Load Steps.

6.7.3.2. Final System Option 1 Model Comparison with Concept A

The load-displacement relationship from the experimental test, the Final System Option 1 FEM, and the Concept A FEM were compared. The Concept A FEM results, using the displacement

control, are relatively close to the experimental results up to an actuator load of 65 kips. This load magnitude is more than double the HL-93 live load response. At 65 kips, the bolts slipped in the bottom flange connection.

A quantitative comparison was performed. The stiffness difference between the Final System Option 1 FEM and the experiment was about 1 percent before 65 kips. The stiffness difference between the Final System Option 1 FEM and the experiment was about 30 percent after 65 kips since there was no bolt slippage issue at the bottom flange part for the Final System Option 1 design. Figure 6.44 presents the relationship between these results. The FEM results are also filtered using a moving-average filter. The window size for each calculated average value was five, which means five data points are in each window.

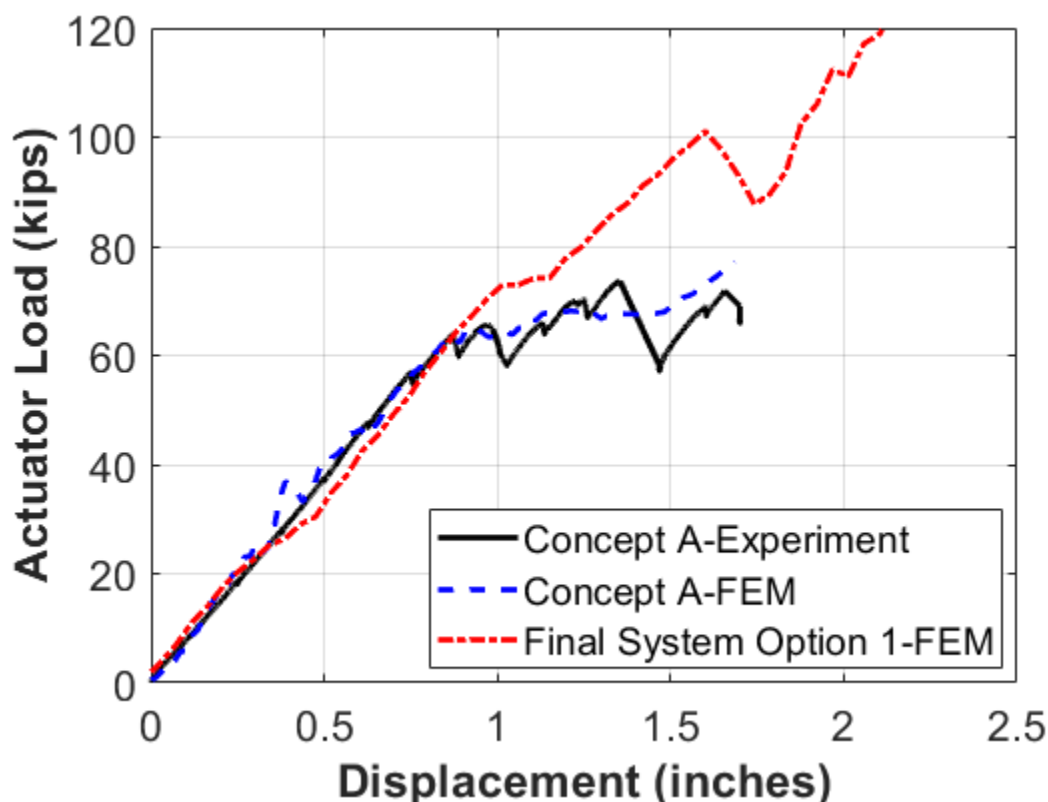


Figure 6.44. Load-Displacement Curve Comparison between the Final System Option 1 Finite Element Model and Concept A.

The beam and bearing plate stresses are shown in Figure 6.45. The maximum compressive stress of one mesh element at the beam was about 45 ksi. The stresses of the majority of the beam end and the bearing plates were about 30 ksi, which was 60 percent of yield stress. This compression

element design performed well in the Final System Option 1 FEM, which was compared to Concept A.

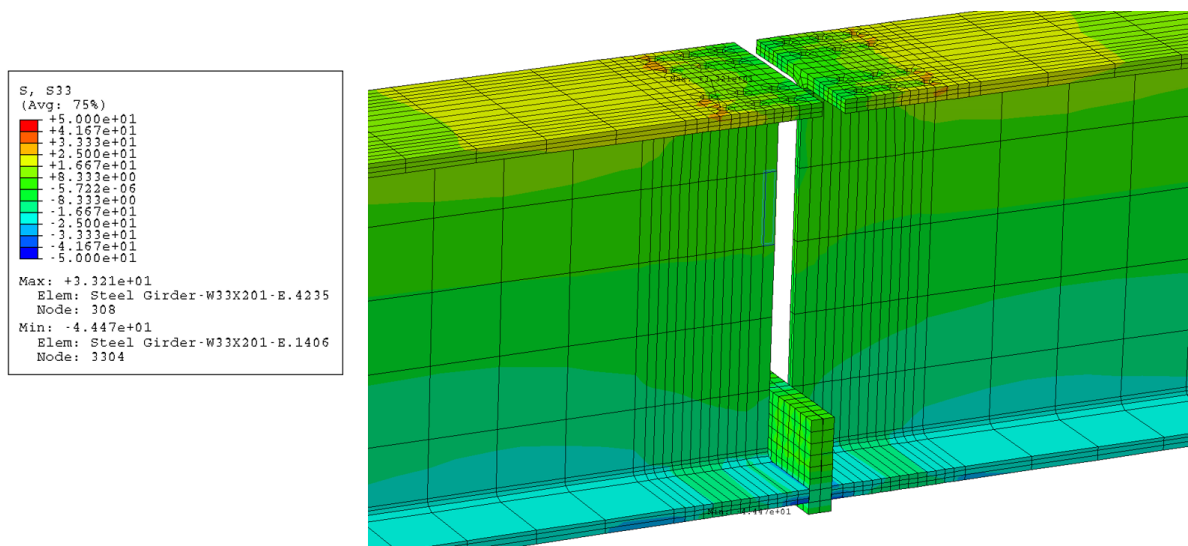


Figure 6.45. Beams and Bearing Plates Stresses at Connection When Load Is 80 kips.

6.7.4. Final System Option 1 FEM with PT (Optional)

6.7.4.1. Final System Option 1 FEM with PT Brackets Description

Based on the Final System Option 1, adding the PT (using Williams bars) on the Final System Option 1 is an optional design for bridge engineers to consider since it can add compressive force on the deck at the transverse joint over the pier, thereby minimizing deck cracking. The geometry, material properties, and boundary conditions are the same as the Final System Option 1 FEM. Figure 6.46 shows the geometry and the assembly for this FEM. The tie constraint was used for the interaction between the steel bracket and the steel beam to simulate the weld condition. The load steps are slightly different since the Williams bars need to be PT. Table 6.9 describes each load step and its time.

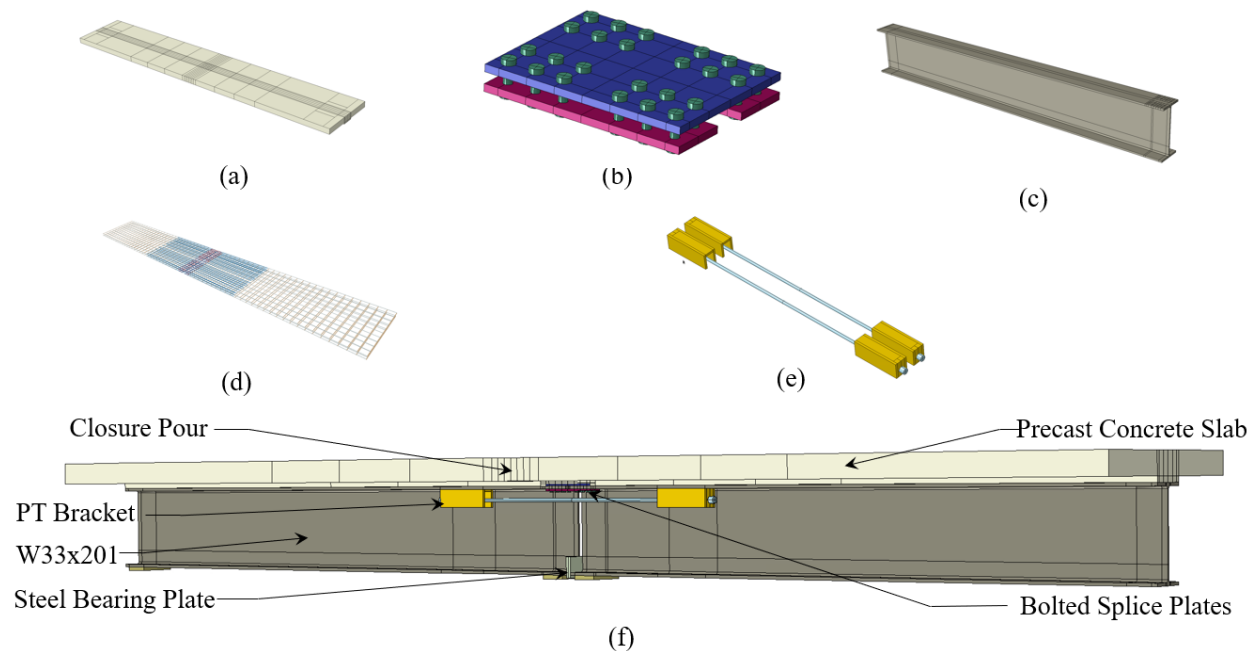


Figure 6.46. (a) Precast Concrete Deck with Closure Pour, (b) Splice Plates with Bolts, (c) Steel Beam, (d) Rebar Mat, (e) PT Brackets with Williams Bars, and (f) Model Assembly.

Table 6.9. Load Step with Step Time for Final System Option 1 with PT Model.

Step	Step Time (sec)
Pre-tensioning bolts	0–1
PT Williams bar	1–2
Applied gravity load for the whole model	2–6
Displacement control (2.5 inches)	6–26

The energy content ratio of kinetic energy over inertial energy during load steps is shown in Figure 6.47. The maximum ratio is 0.4 percent, and most of the ratios are below 0.1 percent, which is relatively stable. The ratio increased in the first 3 seconds because of the pre-tensioning bolts and PT effects.

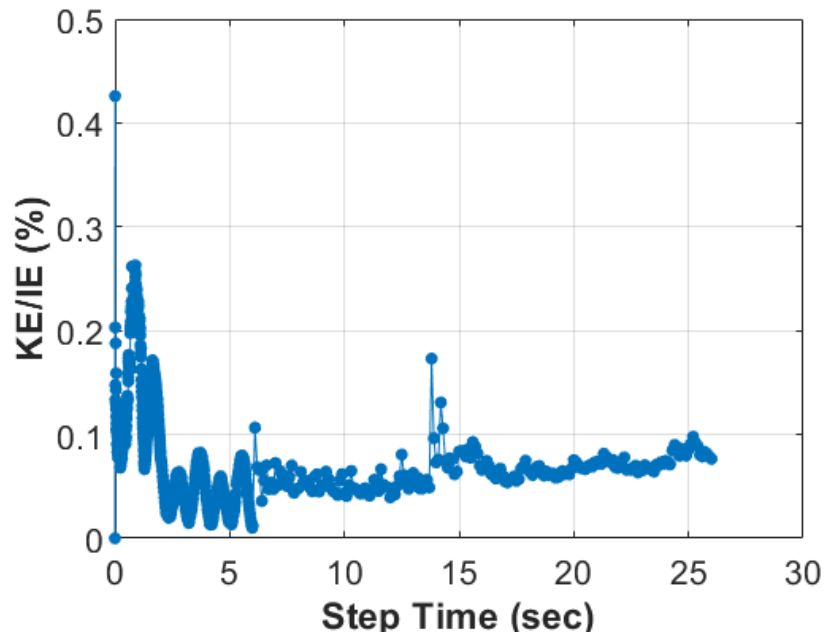


Figure 6.47. Energy Content Ratio of Kinetic Energy over Inertial Energy during Load Steps.

6.7.4.2. Final System Option 1 Model Comparison with Concept A and Concept C

The load-displacement relationship between the Concept C experiment, the Final System Option 1 FEM (with optional PT), and the Concept C FEM was compared. The Concept C FEM used the displacement control to load the specimen. The results are relatively close to the experimental results up to an actuator load of 64 kips (more than double the HL-93 response).

The stiffness difference between the Final System Option 1 FEM and the experiment was about 2 percent before 64 kips. The stiffness difference between the Final System Option 1 FEM (with PT) and the experiment was about 55 percent after 64 kips since the splice plates restrain the relative displacement between the two steel beams. The whole specimen still acts as a partial composite system. The load-displacement curve of the Final System Option 1 with PT shows the benefit of adding splice plates between the steel beams. Figure 6.48 presents the relationship between these results. The FEM results are also filtered using a moving-average filter. The window size for each calculated average value was five, which means five data points are in each window.

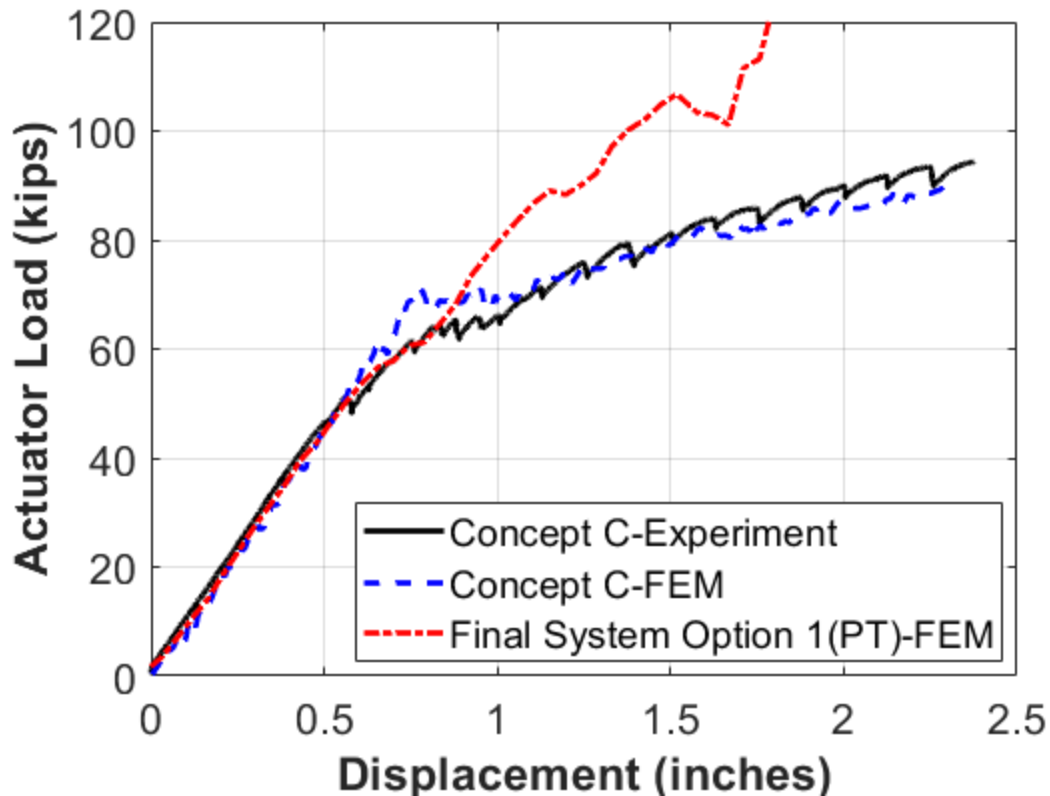


Figure 6.48. Load-Displacement Curve Comparison between the Final System Option 1 FEM with PT and Concept C.

The Williams bar stresses were compared between the Concept C experiment and the Final System Option 1 FEM (with PT). Figure 6.49 shows the stress on the Williams bar of the Final System Option 1 FEM with PT increased by 3 percent along with the load since the top flange splice plates also took a portion of tensile force, which is helpful for this connection. The stress on the Williams bars of the Concept C experiment greatly increased by 30 percent at 64 kips since the Williams bar took most of the tensile force.

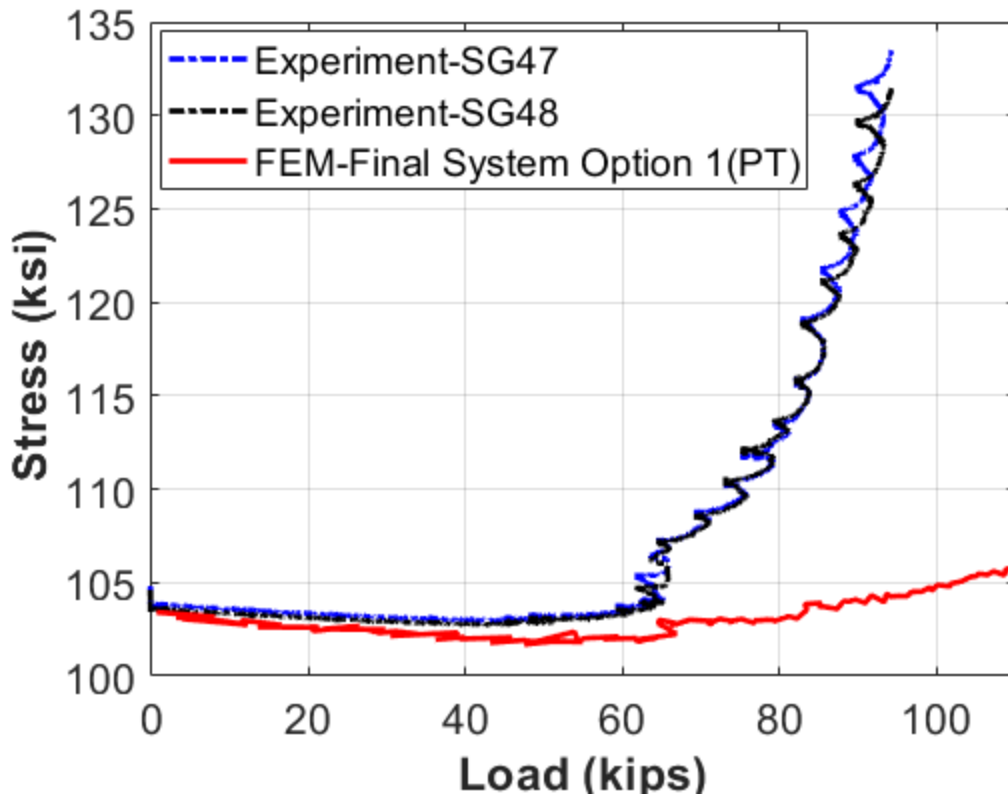


Figure 6.49. Stress on the Williams Bar versus Displacement at E7 Curves Comparison of Concept C and Final System Option 1 FEM with PT.

The stress on the deck after PT the Williams bars was compared between the Concept C FEM and the Final System Option 1 FEM with PT. The main difference for the Final System Option 1 (compared to Concept C) is the top flange splice plates. These plates increase the stiffness and strength of the connection. However, they reduce the precompression in the deck applied by the PT bars.

Figure 6.50 shows the stress comparison between Concept C and the Final System Option 1 FEM with PT (longitudinal section cuts shown). The deck surface stress range of the Concept C FEM was from -0.35 ksi to 0 ksi. The deck surface stress range of the Final System Option 1 FEM with PT was about -0.25 ksi to 0 ksi. The center area shows higher compressive stresses than the edge, as expected. The compressive stress difference between these two models was about 10 percent to 20 percent, which indicates that the bolted top flange splice plates, induced by the PT effect, decrease the compressive stresses at the deck. However, this reduction is relatively minor. Overall, the top flange splice increase in stiffness and strength outweighs the compressive stress loss.

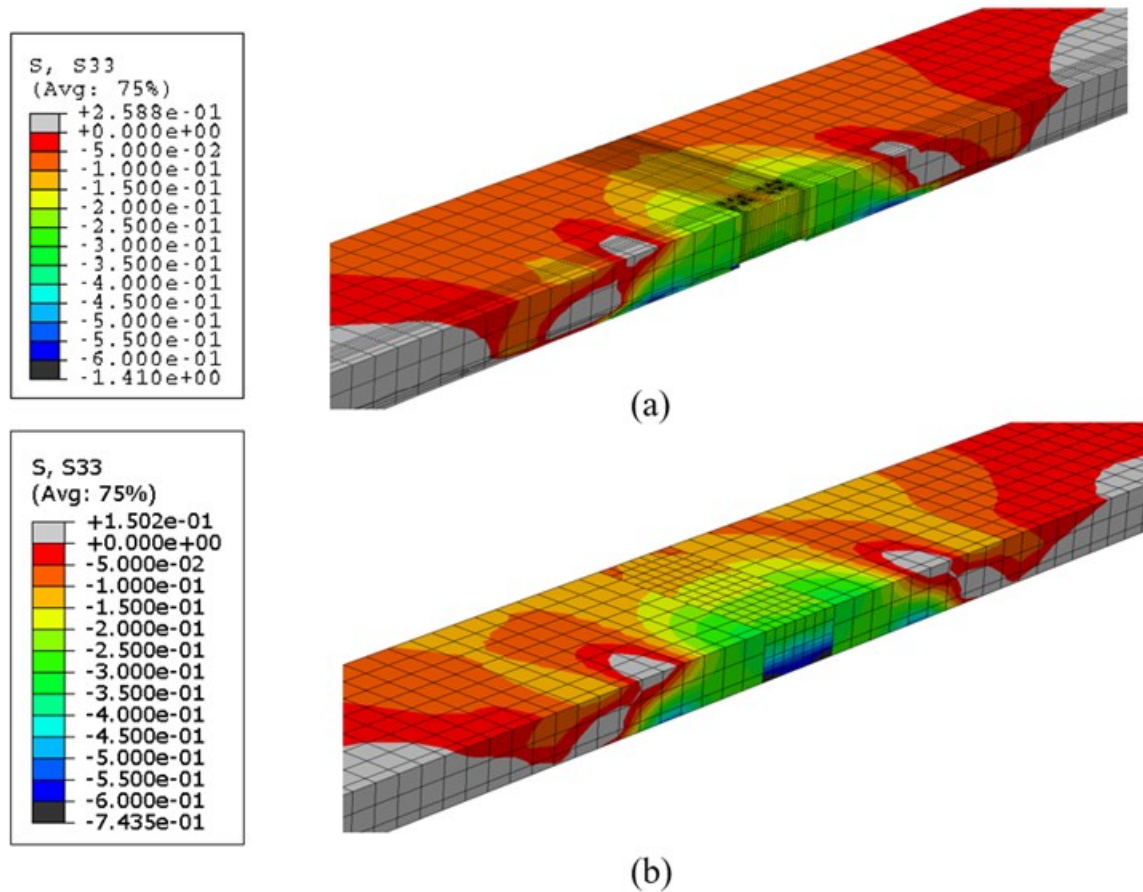


Figure 6.50. Deck Stresses at the Middle Cut in Longitudinal Direction Cut after PT Comparison: (a) Concept C FEM and (b) Final System Option 1 with PT FEM.

The load-displacement curves were compared among the Final System Option 1 FEM, the Final System Option 1 FEM with PT, the Concept A experiment, and the Concept C experiment, which was shown in Figure 6.51. Concept A had the lowest initial stiffness, at approximately 75 kip/in, and Concept C was about 90 kip/in. The stiffness difference between the Final System Option 1 FEM and the Final System Option 1 FEM with PT was about 18 percent. The ultimate capacity for the Final System Option 1 FEM (with and without PT) was more than the experimental testing due to the improvement of the connection.

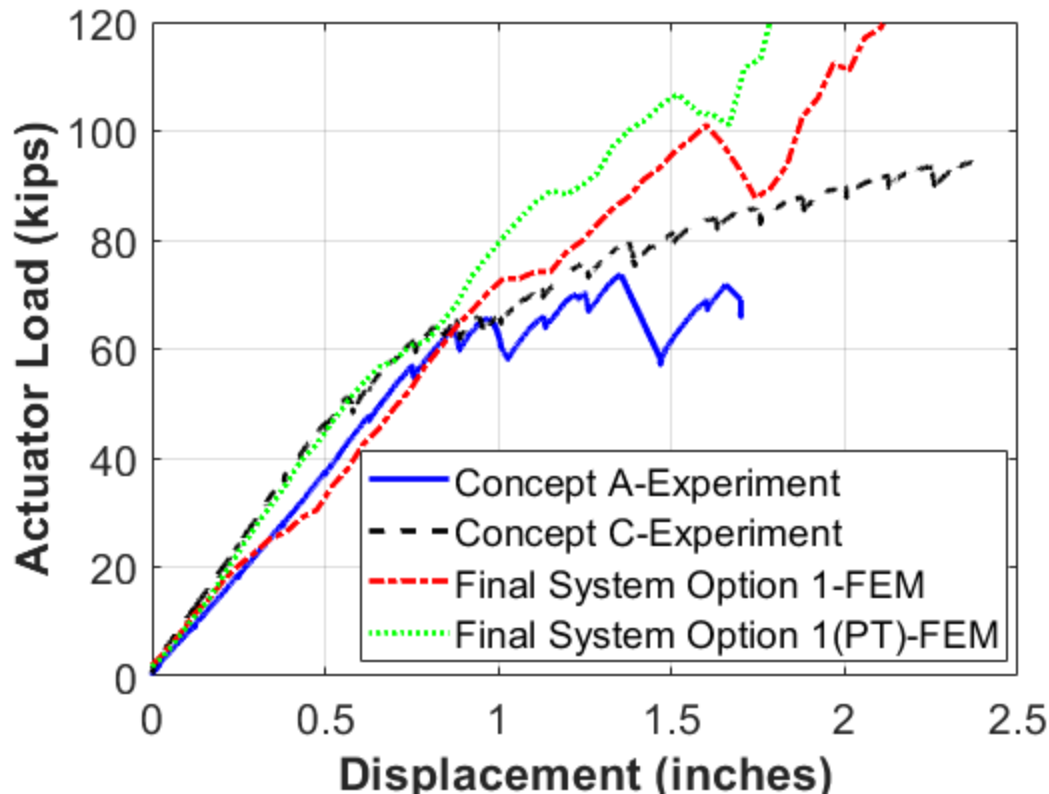


Figure 6.51. Load-Displacement Curve Comparison among the Final System Option 1 FEM, the Final System Option 1 with PT FEM, Concept A, and Concept C.

6.7.5. Final System Option 2 Details

A secondary alternative for making steel SDCL-ABC bridges is now provided. This system is referred to as Final System Option 2. Essentially, this connection is Concept D with refinement to the reinforcement and the addition of steel bottom flange bearing plates similar to the plates found in Concept C. The match-cast construction method is utilized with epoxy adhesive at the interface of the two precast units. The additional reinforcement is to reduce the cracking observed during testing. In addition, the bottom flange bearing plates provide a direct compression-resisting element. The Williams PT bars are implemented to provide adequate precompressive stresses at the precast concrete deck in order to mitigate the cracking of the slab over the pier. The biggest advantage of the Final System Option 2 is the simple construction process and rapid assembly, which is the reason for including a secondary alternative. A general illustration of this connection is shown in Figure 6.52.

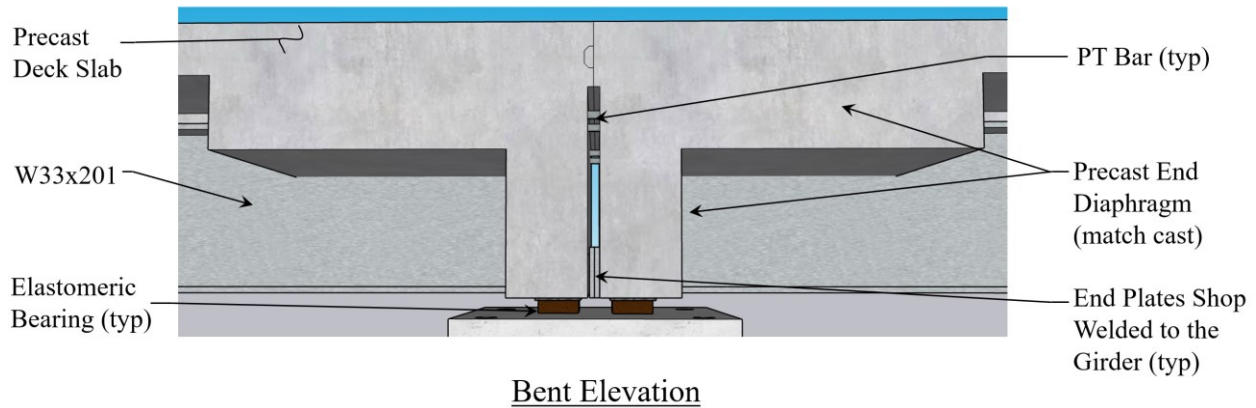


Figure 6.52. Bent Elevation View of Final System Option 2.

6.7.6. Final System Option 2 FEM

6.7.6.1. Final System Option 2 FEM Description

The Final System Option 2 finite element model was built using Abaqus Version 6.14. Similar to the Final System Option 1, the Abaqus/Explicit Analysis Program was applied with the Double Precision/Explicit Packager for this model. The modeling includes the following procedures: geometry, material properties, assembly, contact interaction, load step, boundary conditions, mesh, analysis, and data processing. The major geometries and material properties follow the previous concepts' FEM settings, which were validated with the experimental data.

The models of the steel beam with steel bearing plates at the bottom flange, the precast concrete deck drop panel, the rebar, and the entire assembly are shown in Figure 6.53. For the mesh element selection, a C3D8 element type was used to model a steel beam with bearing plates and the concrete precast deck drop panel. A T3D2 element type was used to model the steel rebar portion, which included the longitudinal rebar, transverse rebar, and loop rebar. The mesh size is different for each part. The match-cast shear key part mesh size is 1 inch. Other mesh sizes range from 2 inches to 6 inches. The total number of mesh elements is 33,166.

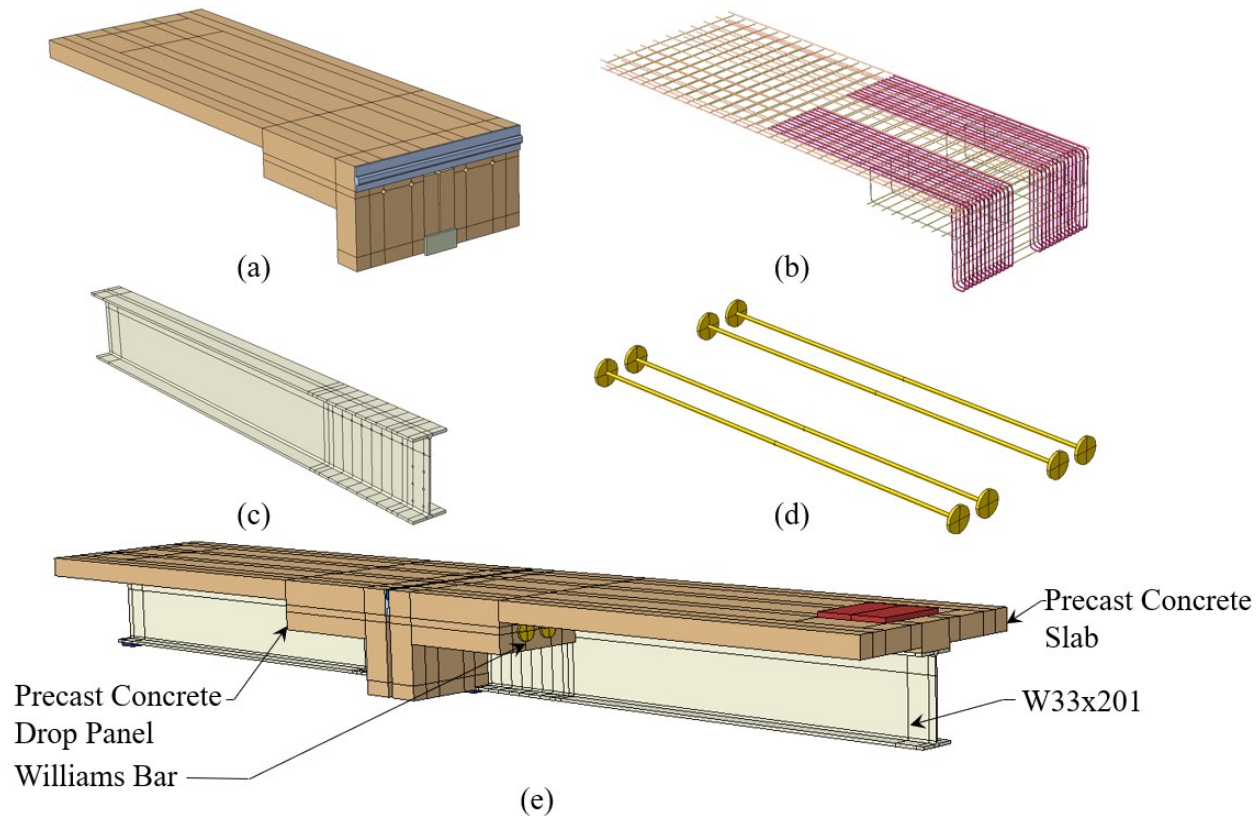


Figure 6.53. (a) Precast Concrete Deck with the Drop Panel, (b) Rebar Mat, (c) Steel Beam, (d) Williams Bars with Steel Plates, and (e) Model Assembly.

The FEM boundary condition assumptions were similar to Concept D. The Encastre boundary condition was selected for simulating the hold-down end of the specimen. A Cartesian-type connector with different stiffnesses in three directions connected with the ground was used to represent the elastomeric bearing pad on the concrete pedestal. The embedded constraint was applied for the interaction between steel rebar and concrete. The tie constraint was applied for the interaction between the steel beam and concrete precast slab to model the composite behavior of the specimen. The tie constraint was used for the interaction between the steel bearing plates and the steel beam to simulate the welding condition, which helped avoid the relative displacement between them. There was no tie constraint between the two precast units to avoid the over-restraint between them. The general contact type was chosen for the interaction of the whole specimen to avoid setting different complex contact pairs, which was the same as in the previous FEM.

The material properties of this FEM were similar to previous concepts. The same CDP model for simulating concrete behavior and the same steel parts' material properties were applied for this model. The compressive strength was the same as the Concept D FEM.

The load steps for the Final System Option 2 were similar to Concept D. They were divided into five parts, which were consistent with the experiment: PT of the Williams bars, gravity load applied to the whole model, static test process that includes push down and pull up procedures, and ultimate testing process at the active loading side. In order to increase the efficiency of the model analysis, the step time of Step 3 and Step 4 decreased to 15 seconds when they were compared with Concept D. Table 6.10 provides each step with their corresponding step time.

Table 6.10. Load Steps with Step Time for Final System.

Step	Step Time (sec)
PT Williams bar	0–1
Applied gravity load for the whole model	1–5
Push down (1 inch)	5–20
Pull up (1 inch)	21–35
Push down (3 inches)	35–55

During Step 1, the PT effect was also induced by the temperature change method, which was used in Concept D. Overall, the ratio of kinetic energy over inertial energy is depicted in Figure 6.54. The maximum ratio was about 3 percent, which was below 5 percent. The whole loading process was relatively stable. The ratio increased from about 0.5 percent to 3 percent when the step time was about 48 to 55 seconds because of the number of cracks formed at the interface of the concrete drop panel. The crack width also increased at the adhesive joint when the specimen was pushed down. The overall internal energy is released due to the concrete cracking. The maximum load was already reached when the step time was about 51 seconds. Then, the whole specimen could not achieve the higher load after that. The energy ratio was going up because of the release of the internal energy.

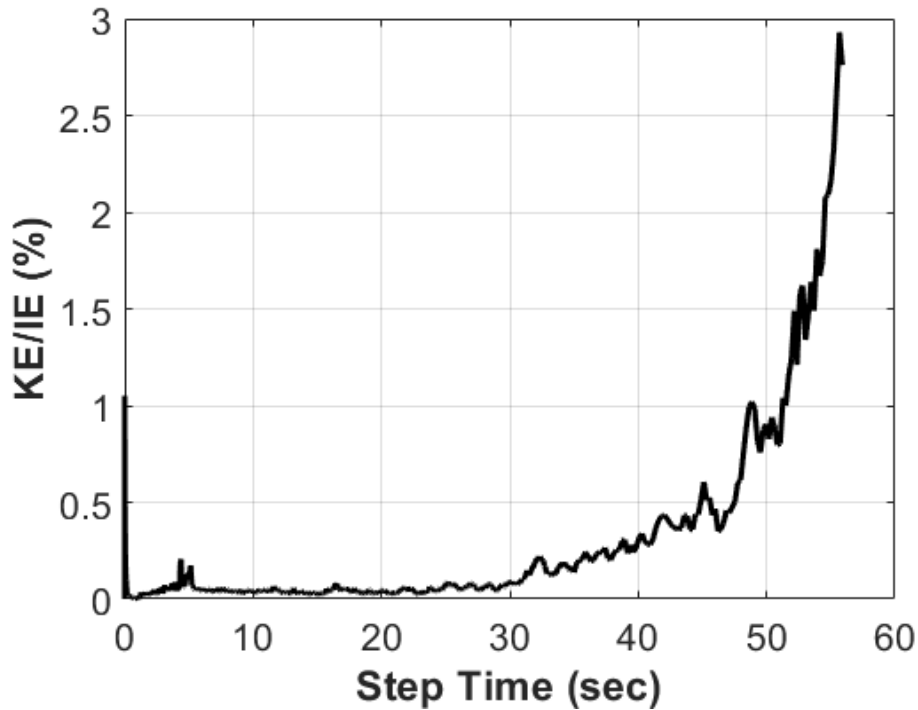


Figure 6.54. Energy Content Ratio of Kinetic Energy over Inertial Energy during Load Steps.

6.7.6.2. Final System Option 2 Model Comparison

The load-displacement relationship from the experimental test, the Final System Option 2 FEM, and the Concept D FEM were compared. The Concept D FEM results, using the displacement control, are very close to the experimental results up to an actuator load of 52 kips. This load magnitude is about 170 percent of the HL-93 live load response. The load was dropped after it passed 52 kips.

A quantitative comparison was performed. The initial stiffness of the Final System Option 2 FEM was about 85 kip/in, and the Concept D experiment was 35 kip/in before 35 kips. The Final System Option 2 was about 240 percent of the Concept D experiment, which means the revised bottom bearing plate and the additional reinforcement did improve the whole structure's performance. The ultimate load also increased from 52 kips to 70 kips, which was about a 40 percent increase in load based on the Final System Option 2 revision. The stiffness dropped quickly after the load was about 60 kips. Figure 6.55 presents the relationship between these results. The FEM results are also filtered using a moving-average filter. The window size for each calculated average value was five, which means five data points are in each window.

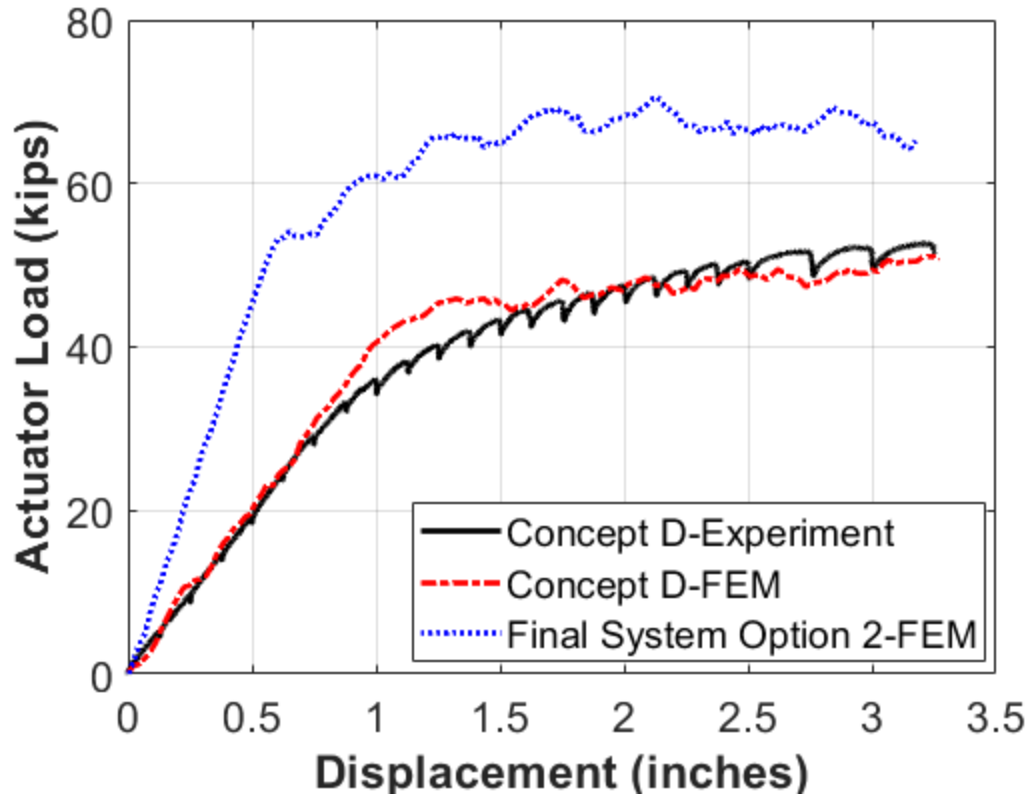


Figure 6.55. Load-Displacement Curve Comparison between the Final System Option 2 FEM and Concept D.

The damage patterns of the concrete drop panels were compared when the load was about 30 kips. Figure 6.56 provides the front surface view of the drop panels and shows the concrete crack patterns. The Final System Option 2 only has slight damage around the through-holes, and there is no damage happening at the bottom shear key part since it has been replaced with a steel bearing plate. The major concrete damage happened below the through-holes and the bottom shear key part for Concept D.

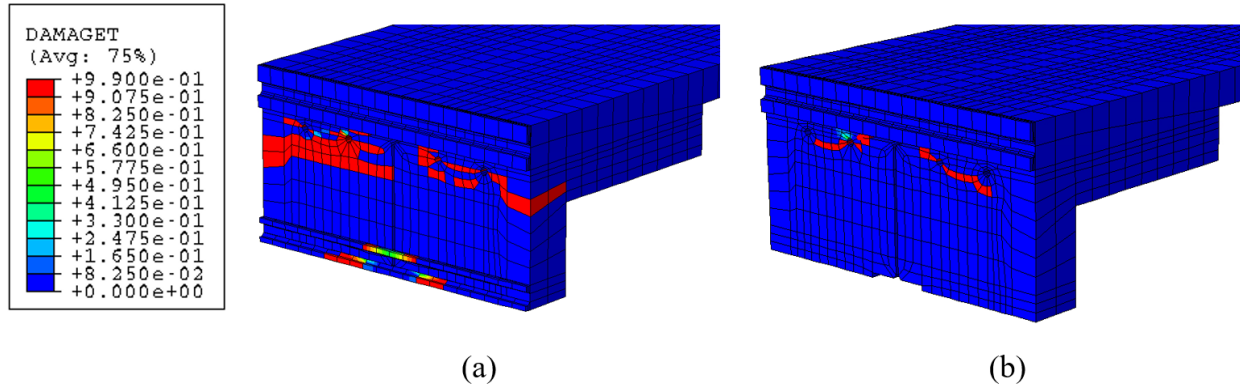


Figure 6.56. Damage Pattern Comparison When Load at 30 kips between (a) Concept D FEM and (b) Final System Option 2 FEM.

6.7.7. Discussion and Comparison

Final System Option 1 is selected as the primary recommended alternative based on the objectives of the study. The performance of this connection proved superior to the other alternative. In addition, Final System Option 2 is recommended as a secondary option for projects that require fully precast elements with minimal on-site construction time.

A general structural performance comparison of Final System Options 1 and 2 were made with the load-displacement curves. Figure 6.57 presents the load-displacement curves for each option. The initial stiffness of Option 1 (PT) is about 90 kip/in, which is the highest among these options. The Option 2 stiffness is about 85 kip/in. Option 1 is about 75 kip/in, which is slightly lower than the other since there is no PT effect for this concept. The stiffness of Option 2 quickly dropped after about 52 kips, which is about 170 percent of the HL-93 notional load, while the stiffness of Option 1 and Option 1 (PT) still kept the relatively same stiffness after 53 kips. The bolts at the top splice plate slipped at about 105 kips for Option 1 and Option 1 (PT), which is about 310 percent of the HL-93 notional load.

To aid future bridge engineers, design guidance has been developed for the recommended Final System Option 1 detail, which includes an annotated design example along with standard drawings. This design guidance is further discussed in Section 8.

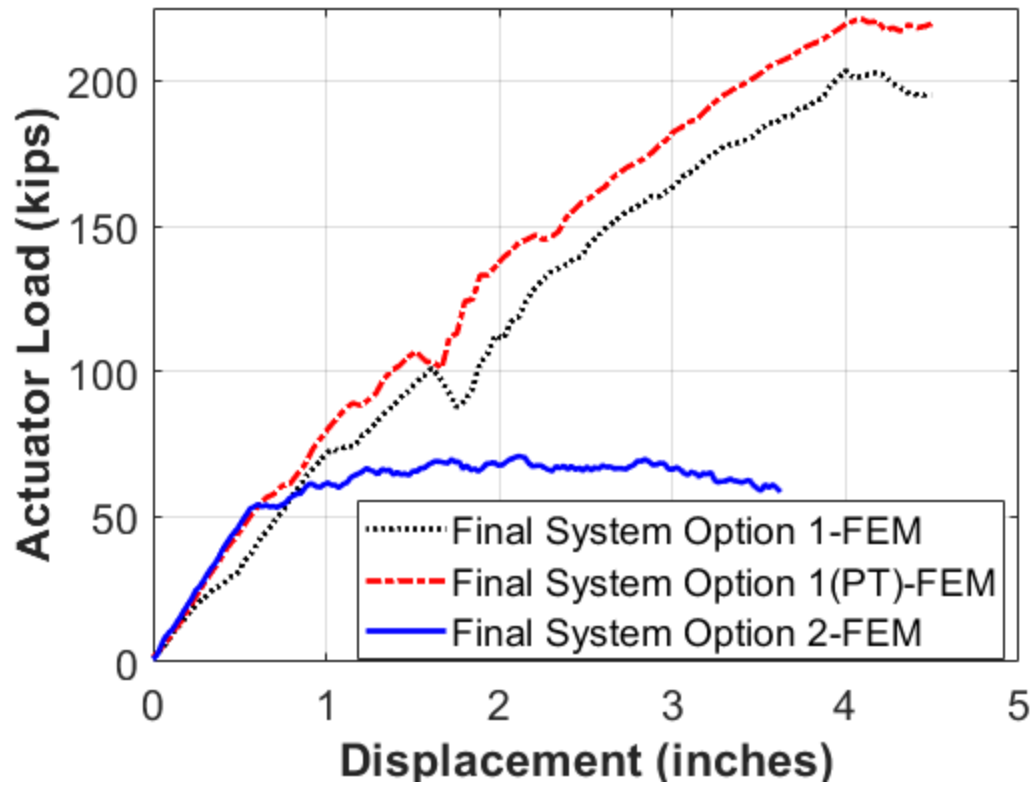


Figure 6.57. Load-Displacement Curves Comparison between Final System Option 1 and Final System Option 2.

7. PARAMETRIC STUDY

7.1. OVERVIEW

The objective of the parametric study is to understand and evaluate the behavior of complete bridge configurations (as opposed to the laboratory setup) with varying materials and parameters. This study permits analysis of a broad range of configurations and their effects on the performance and behavior of the bridge and the proposed details. The study was conducted using the Abaqus v6.14 software package.

The study incorporated the design parameters of bridge configuration, span, length, girder geometry and spacing, skew angle, and concrete strength. These parameters set results in approximately 300 possible model iterations. The number of iterations required highlights the importance of automating the model construction and analysis process. This procedure allows for the exploration of a broader range of scenarios by implementing a script that constructs these models based on simple geometries and material inputs without generating each model by hand.

Simplified constraints are used in model construction when appropriate. These simplified constraints reduce the computational cost. These simplifications were primarily applied to replace components of the proposed connection details. This step differs from the laboratory test model (see Section 6), which includes high-resolution modeling for the connection details. After the validation of the simplifications, the full bridge configuration parametric analysis study was completed. This full modeling sequence is depicted in 6.2.1.

The TxDOT Standard Design Tables provide guidance on typical configurations of steel girder bridges used in Texas. The tables were leveraged as initial information on the common bridge design in order to limit the range of the parameters used in the study. These tables offer standard design guidelines and specifications for various aspects of common 24 ft, 28 ft, and 30 ft span lengths, including girder sizing, spacing, lateral bracing details, deck details, etc.

7.2. FOUNDATION DATA SOURCES

The TxDOT Standard Design Tables present information about general details and specifications for the design and construction of steel beam bridges. This information includes details about

bracing requirements, elastomeric bearing pad placement, and dimensions, control joint details, and drain details. These details lead to consistent designs that can be replicated across multiple projects or products to ensure the same quality and functionality are achieved every time.

For each one of the 24, 28, and 30 ft roadway configurations included in the standard design table, the beam sections, optional girder plates beams, elastomeric bearing pad types, and lateral displacement restriction diaphragm spaces are provided according to the load rating factors and span length. An example portion of these tables is shown in Figure 7.1. Additionally, for each one of the roadway configurations, information and details about the abutment, interior bents, and steel beam framing plan for skew angles of 0, 15, and 30 degrees are included.

TABLE OF REQUIRED BEAM SIZES, DESIGN DATA AND STEEL QUANTITIES													
SPAN (ft)	ROLLED BEAM				OPTIONAL PLATE GIRDER						Diaphragm Spaces "N" (ea)	Stud Spacing "X" (in)	Elastomeric Bearing Type
	Beam Member	Dimension "Y" (in)	Deflection "A" (feet)		Plate Sizes (Inches)			Dimension "Y" (in)	Deflection "A" (feet)				
			Slab DL	Total DL	Top Flange	Bot. Flange	Web		Slab DL	Total DL			
30	W18 x 130	29.750	0.013	0.017	1 x 12	1 ½ x 12	½ x 17	29.750	0.014	0.018	2	5	SB - 1
	W21 x 111	32.000	0.012	0.016	¾ x 12	1 x 12	½ x 19.5	31.750	0.013	0.017	2	6	SB - 1
	W24 x 104	34.500	0.011	0.014	¾ x 12	¾ x 12	½ x 22.5	34.625	0.011	0.013	2	6	SB - 1
	W27 x 146	37.875	0.006	0.008	¾ x 14	1 x 14	½ x 25.5	37.750	0.007	0.009	2	4	SB - 2
	W30 x 173	41.000	0.004	0.006	1 x 15	1 ¼ x 15	½ x 28.5	41.250	0.004	0.005	2	4	SB - 3
	W33 x 118	43.375	0.006	0.007	¾ x 12	¾ x 12	½ x 31.5	43.500	0.005	0.007	2	6	SB - 1
	W36 x 135	46.000	0.004	0.006	¾ x 12	¾ x 12	½ x 34	46.125	0.004	0.006	2	5	SB - 1
	W40 x 149	48.750	0.003	0.005	¾ x 12	1 x 12	½ x 36.5	48.750	0.004	0.005	2	4	SB - 1
35	W18 x 130	29.750	0.025	0.033	1 x 12	1 ¼ x 12	½ x 17	29.750	0.026	0.033	2	6	SB - 1
	W21 x 111	32.000	0.023	0.030	¾ x 12	1 x 12	½ x 19.5	31.750	0.025	0.032	2	5	SB - 1
	W24 x 104	34.500	0.020	0.025	¾ x 12	¾ x 12	½ x 22.5	34.625	0.020	0.025	2	8	SB - 1
	W27 x 146	37.875	0.011	0.015	¾ x 14	1 x 14	½ x 25.5	37.750	0.013	0.017	2	5	SB - 2
	W30 x 173	41.000	0.008	0.011	1 x 15	1 ¼ x 15	½ x 28.5	41.250	0.008	0.010	2	5	SB - 3
	W33 x 118	43.375	0.011	0.014	¾ x 12	¾ x 12	½ x 31.5	43.500	0.010	0.014	2	7	SB - 1
	W36 x 135	46.000	0.008	0.011	¾ x 12	¾ x 12	½ x 34	46.125	0.008	0.011	2	6	SB - 1
	W40 x 149	48.750	0.006	0.009	¾ x 12	1 x 12	½ x 36.5	48.750	0.007	0.009	2	5	SB - 1

Figure 7.1. TxDOT Standard Design Table Example for a 30-ft Roadway Project [25].

The TxDOT Standard Design Tables were augmented with data from the LTBP InfoBridge database, part of the U.S. Department of Transportation FHWA, which includes information about a broad sample of highway bridges nationwide [34]. This information is used mainly to extract the standard bridge span length configurations used in the state to study realistic cases in which the connections developed can be implemented.

7.3. PARAMETER RANGE

The parameters considered in this study, with a short description, are listed as follows:

- Bridge configuration: the number of spans and the roadway width.
- Span length: the length of all spans included in a given configuration.

- Girder geometry: the size of the selected girders for a given bridge configuration.
- Girder spacing: the spacing of the girders of a given size.
- Lateral support spacing: the type and location of lateral supports.
- Skew angle: the angle of skew relative to the line of travel of the bridge.
- Concrete strength: the design strength of concrete.

The discussion of how the range for each parameter was selected is presented, considering the 30 ft roadway width configuration scenarios. The process is similar for all roadway widths.

7.3.1. Bridge Configuration and Span Length

To select the total number of spans for the full bridge configuration analysis, consideration of the computational cost and processing time was important. In Texas, there are numerous configurations of steel multigirder bridges. Given the focus of the study on continuity, the minimum number of spans required is two. A two-span configuration represents the conditions in which the negative bending at the internal support will be highest, a simply supported condition will exist at the ends, and a continuity condition at the mid-support will exist. Because the study's objective is to analyze an extensive range of scenarios, defining the largest response scenario with the least number of spans is essential to reduce the computational cost. A three-span configuration was also considered when determining the span lengths that would be considered, but it was not included in the parametric study.

Another critical aspect of the span configuration is the length of each one of the spans. For this information, a study of the data presented by the InfoBridge database was developed for Texas. There are 68,514 bridges total in Texas, which are constructed with different materials, including concrete and steel. Concrete was included because if a concrete bridge were to be replaced with the proposed ABC details, the geometry of the structure that defined span lengths was unlikely to change. A filter of the bridges with a total span configuration of two and three was applied to limit the study of the information with the range selected for the parametric analysis, leaving a total of 10,341 two- or three-span bridges as potential contenders for future ABC construction.

A study of span length distribution was conducted to determine the most common span configuration used in this type of project. It was discovered that a total of 8,172 bridge span configurations have a difference of 5 ft or less between their longest and shortest spans,

representing 79 percent of the total bridges in the population. Within that group, 3,759 bridges with identical span lengths were found, representing 36 percent of the population.

Table 7.1 shows the bridge's span configuration corresponding to the length scenarios considering the minimum and maximum span lengths for the population of 10,341 two- and three-span bridges in Texas. The tight band in the middle of the table represents the majority of structures that fall within the ranges defined above (i.e., maximum and minimum spans within 5 ft of one another). Considering that the parametric study aims to analyze the behavior and performance of the common bridge configurations in which the proposed ABC connection can be applied, the span length configuration is limited to one scenario in which both sides will have the same length. This configuration is representative of the majority of span configurations in two- and three-span bridges in Texas, and it maximizes negative bending at the support.

Table 7.1. Two- and Three-Span Configuration Bridges, Minimum (Span 1) and Maximum (Span 2) Span Length Configurations in Feet for Texas [34].

Span Length	30	35	40	45	50	55	60	65	70	75	80	85	90	95	100	105	110	115	120	
30	883	0	0	0	0	0	0	0	0	0	0	0	0	0	0	0	0	0	0	
35	1222	441	0	0	0	0	0	0	0	0	0	0	0	0	0	0	0	0	0	
40	54	303	265	0	0	0	0	0	0	0	0	0	0	0	0	0	0	0	0	
45	5	160	1033	533	0	0	0	0	0	0	0	0	0	0	0	0	0	0	0	
50	22	13	163	101	340	0	0	0	0	0	0	0	0	0	0	0	0	0	0	
55	1	2	4	13	189	95	0	0	0	0	0	0	0	0	0	0	0	0	0	
60	5	10	15	72	88	237	130	0	0	0	0	0	0	0	0	0	0	0	0	
65	2	2	9	22	50	70	354	160	0	0	0	0	0	0	0	0	0	0	0	
70	4	2	8	8	17	15	64	60	90	0	0	0	0	0	0	0	0	0	0	
75	1	0	2	17	2	9	17	19	186	78	0	0	0	0	0	0	0	0	0	
80	1	2	2	1	10	9	26	56	35	139	78	0	0	0	0	0	0	0	0	
85	1	3	5	7	10	12	41	56	42	53	110	319	0	0	0	0	0	0	0	
90	0	0	0	1	0	5	12	7	7	79	27	47	55	0	0	0	0	0	0	
95	0	0	0	0	1	0	0	4	1	13	12	7	81	51	0	0	0	0	0	
100	1	1	0	2	5	3	5	9	2	12	20	31	19	84	42	0	0	0	0	
105	0	0	0	0	8	3	6	6	0	14	29	37	31	47	154	78	0	0	0	
110	0	0	0	3	0	2	2	1	0	4	6	21	8	50	19	27	51	0	0	
115	0	0	0	0	1	1	4	5	1	1	3	5	10	18	11	23	59	36	0	
120	0	0	0	1	0	0	3	0	1	2	3	6	28	27	22	18	30	50	34	
Total	2202	939	1506	781	721	461	664	383	365	395	288	473	232	277	248	146	140	86	34	10341

7.3.2. Girder Geometry

The information provided in the TxDOT Standard Design Tables for steel beams is used to provide initial guidance on girder sizing. These standard design tables show a total of approximately 100 bridge configurations, in which, according to the span and load presented, a specific girder size is recommended. These sizes range from a W18×130 for a 30 ft-span length to a W40×324 for a 120 ft-span distance. Although appropriate designs for bridge length are important, many girder sizes recommended in the standard design tables do not have the appropriate dimensions for flange width to accommodate the proposed ABC connection details. The selection of the girder was made according to the dimensions required for the connections studied on the experimental tests from within the population of girders provided in the standard design tables. From this, Table 7.2 shows the selected girder elements for the 30-ft roadway details.

Table 7.2. Girder Elements Selected from the Standard Design Tables of the 30-ft Roadway Configuration [25].

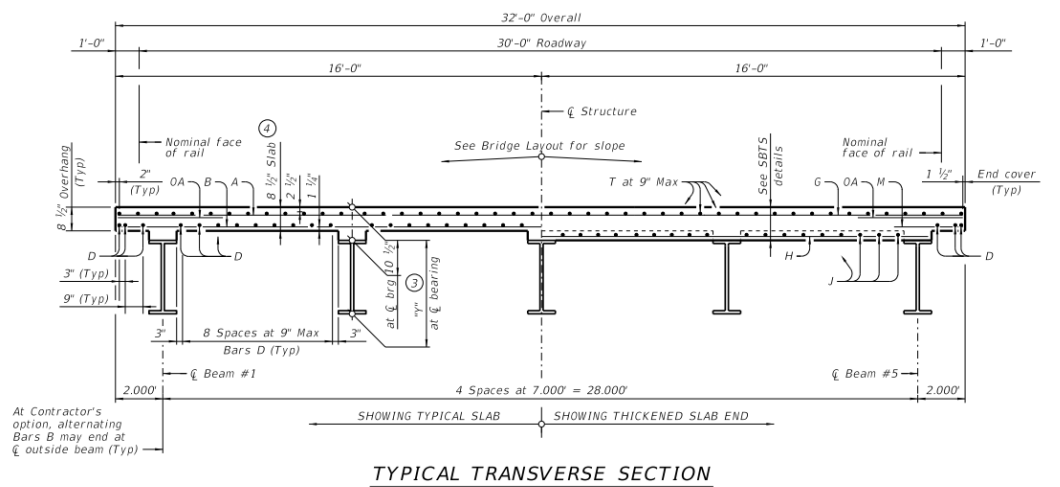
	Span (ft)		Depth (in.)		Weight (lbf/ft)
1	70	W	30	×	173
2	75	W	30	×	173
3	80	W	30	×	191
4	80	W	33	×	201
5	85	W	30	×	211
6	85	W	33	×	201
7	90	W	30	×	235
8	90	W	33	×	221
9	90	W	36	×	231
10	90	W	40	×	199
11	95	W	30	×	235
12	95	W	33	×	221
13	95	W	40	×	199
14	100	W	33	×	291
15	100	W	36	×	262
16	100	W	40	×	249
17	105	W	33	×	291
18	105	W	36	×	262
19	105	W	40	×	249
20	110	W	33	×	318
21	110	W	36	×	302
22	110	W	40	×	277
23	115	W	36	×	330
24	115	W	40	×	297
25	120	W	40	×	324

Note that the W30×173 is the lightest viable section for spans ranging from 30 ft to 75 ft. The span length range for the parametric analysis will be set initially to a span length equal to 70 ft.

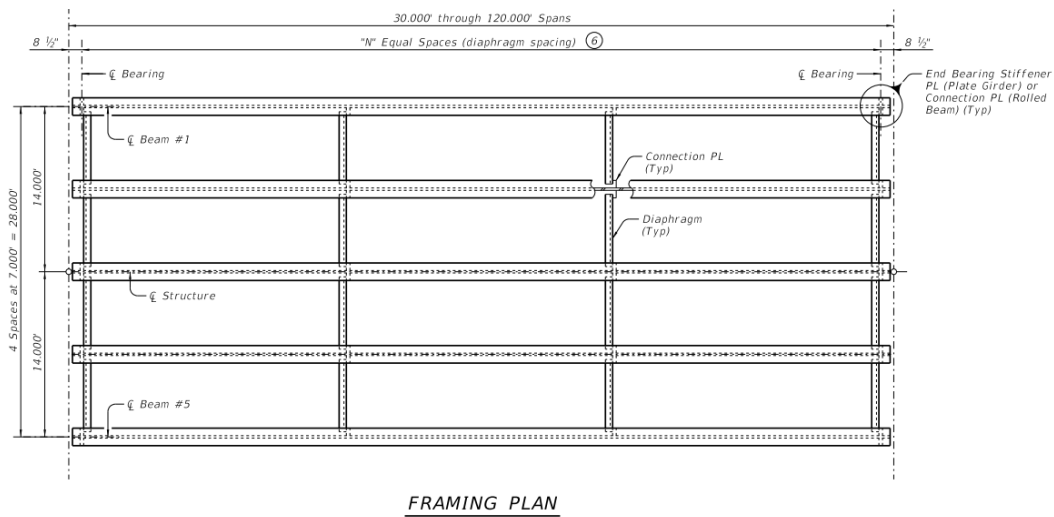
This action will maximize load effects for the connection details while limiting the number of model iterations.

7.3.3. Girder Spacing

Girder spacing refers to the distance between the individual girders in a bridge. It is determined through engineering analysis and by considering the structural requirements, cost, aesthetic goals, and safety. However, the TxDOT Standard Design Tables provide a standard recommendation of four spaces for projects of 30-ft roadway, which was shown in Figure 7.2 (a) and (b). This analysis will use the spacings provided in the standard design tables.



(a)



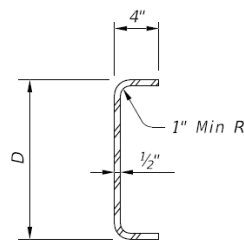
(b)

Figure 7.2. TxDOT Standard Design (a) Typical Transverse Section and (b) Framing Plan for a 30-ft Roadway [25].

7.3.4. Lateral Support Spacing

The TxDOT Standard Design Tables present the option of using C bent plates, which was shown in Figure 7.3. The tables define four different sizes according to the size of the girder used. Additionally, it presents the number of spaces needed according to the girder size and the length of the span. For this study, the parametric analysis will take into consideration this criterion according to the cases analyzed going from a total of three to five spaces.

<i>Beam Size</i>	<i>Diaphragm Member</i>	<i>Optional Bent PL Diaph Depth, D</i>
W18	C12 x 20.7	12"
W21 thru W30	C15 x 33.9	15"
W33 & W36	MC18 x 42.7	18"
W40	W21 x 44 (1)	21"



**OPTIONAL BENT PLATE
DIAPHRAGM SECTION**

Figure 7.3. TxDOT Standard Design Optional Lateral Support Bent Plate [25].

7.3.5. Skew Angle

The skew angle of a bridge refers to the angle of a line through the supports of the bridge measured relative to a line perpendicular to the direction of travel. The TxDOT standard design for a 30-ft roadway with a 30-degree skew angle was shown in Figure 7.4. Varying this parameter is important because of the uneven load distribution in high levels of skew, which can introduce bending moments and shear forces that are not present in a perpendicular (i.e., 0 degree skew) bridge.

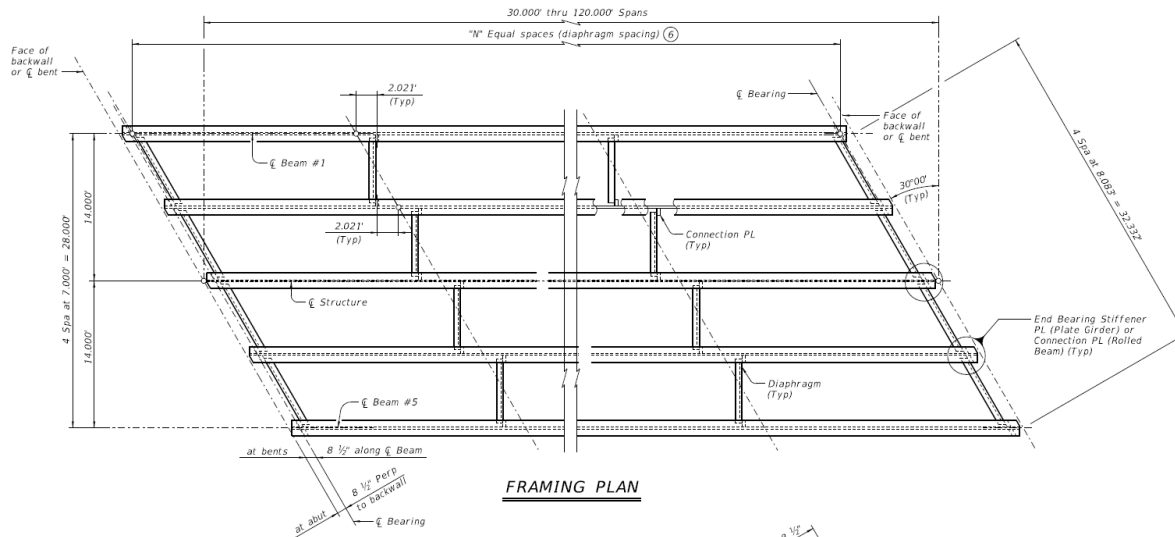


Figure 7.4. TxDOT Standard Design Framing Plan for a 30-ft Roadway with a 30-Degree Skew Angle [25].

7.4. FULL BRIDGE CONFIGURATION STUDY FRAMEWORK

A set of ranges for the parameter of the full bridge configuration parametric is selected to delimit the application of the connections developed to realistic scenarios of bridge configurations in the state. Table 7.3 summarizes the ranges for each parameter.

Table 7.3. Parameters Range Summary.

Parameters	Range of Study	Source
Number of Spans	2-Span Configurations	LTBP Info Bridge Database
Span Length	70 ft to 120 ft	TxDOT Standard Design Tables
Girder Size	Around 28 Configurations	TxDOT Standard Design Tables
Girder Spacing	4 Spaces	TxDOT Standard Design Tables
Skew Angle	0, 15, 30 and 45 Degrees	TxDOT Standard Design Tables
Total Number of Models	100 Bridge Configurations	

With this information, it is possible to define an initial set of around 100 configurations models for each one of the details developed. This study aims to present at the end of the project a set of valid capabilities for each parameter to understand the applicability of the details developed under the TxDOT standard design scenarios. These tolerances provide information to generate the final design guidance recommendations and general design details by determining with which developed connections can be used with the standard configurations.

7.5. PARAMETRIC 3D MODEL DESCRIPTION

The primary output of interest from the parametric modeling study is the stress distribution in the deck in the vicinity of the proposed connection details. It is not possible to explicitly model the connection elements for all bridge configurations because it would require a unique design for each setup. This study presents the implementation of the actual details of the elements without considering the change in the size of the elements that make up the connection system. Taking this into consideration, the size of the elements of the connection detail remains constant over the entire range of analysis cases.

The script developed follows the modeling process described in the test setup model description subsection, which includes geometry, material properties, assembly, contact interaction, load step, boundary conditions, mesh, analysis, and data processing. Additionally, because the parametric analysis is an extension of the experimental test and analytical validation of the experimental test, the same properties of the material are implemented.

7.5.1. Area of Interest

The principal area of interest of the parametric analysis is the stress distribution generated at the top of the deck area in and adjacent to the closure pour, as highlighted in Figure 7.5.

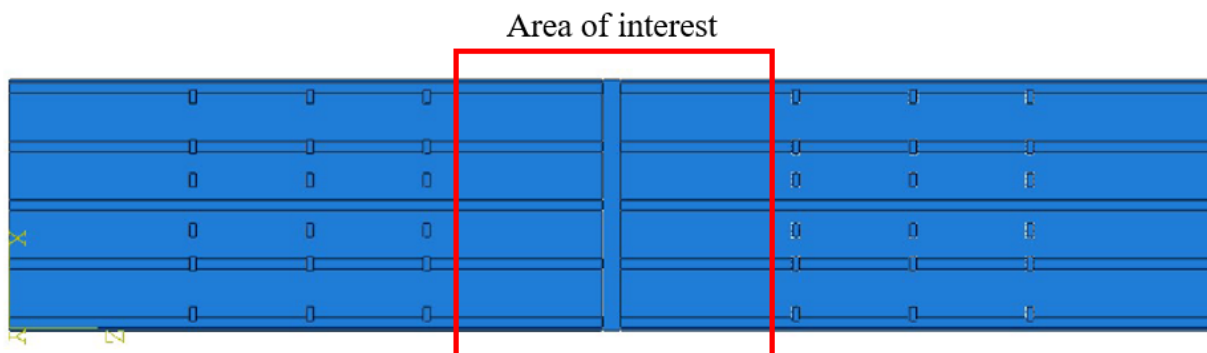


Figure 7.5. Stress Distribution Area of Interest.

7.5.2. Load Case

The number of model iterations and associated model run time precluded the use of multiple load cases and vehicle positions. A modified HL-93 load was applied. This load case was unfactored and was applied in a single static load step. The load included a uniform lane load of 0.64 k/ft in all lanes, as well as pairs of HS-20 trucks positioned in each lane on either side of the proposed

connection detail. The trucks were positioned in order to maximize negative bending at the proposed connection, not specifically at the 50-foot interval specified in the AASHTO LRFD Specification Article 3.6. Based on the geometry of the bridge geometries being modeled, a 3-lane configuration with the HS-20 load was placed at the center of each lane and staggered for the skew angle. The general load position is shown in Figure 7.6.

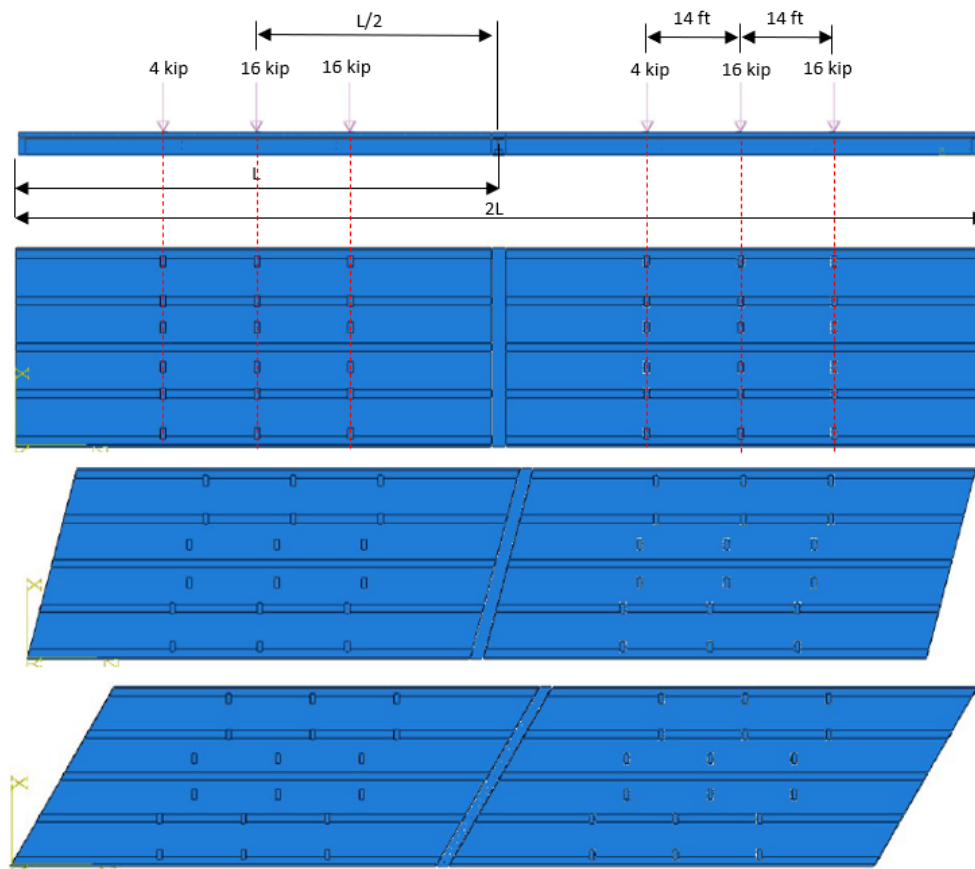


Figure 7.6. Load Case and Area Distribution of the Wheels of the Truck for 0, 15, and 30 Skew.

For this load configuration, the 3D footprint of the wheels of a HS-20 consisted of a steering axle that distributed a total of 8 kips between the two sides of the truck, and two rear axles that distributed a total of 32 kips per rear axle between the two sides of the trucks. As shown in Figure 7.6, the steering and rear axles had a distance between them of 14 ft in the longitudinal direction, and the transversal distance between the two sides of the truck was equal to 6 ft, according to the *AASHTO LRFD Bridge Design Specifications* [3]. The distribution of the surface load of the trucks on deck was applied over an element with thickness of 0.5 inches and a

corresponding surface of 10 inches by 20 inches placed above the deck surface in their corresponding longitudinal distance.

This static load scenario, applied with a linear elastic behavior of the materials, simplified the analysis of the 3D bridge structure and helped to effectively study how stress is distributed across various situations. Additionally, it allowed the team to perform the parametric analysis and be able to change key parameters like material properties, dimensions, and load conditions. This process is important for understanding how different factors affect the bridge's performance, optimizing the design, and ensuring the bridge is safe and reliable under different conditions.

7.5.3. Support

The proposed connection details all utilized an elastomeric bearing pad for support. This element was included in the model as a spring support element. The spring element was assumed to be rigid in the vertical direction and utilized the spring stiffness value leveraged for the experimental modeling in Section 6.2.1. No substructure elements were modeled.

7.5.4. Lateral Support Elements

The lateral support details and spacing were based on the TxDOT standard design tables according to the size of the girder and span length, as shown in Figure 7.7. There were a total of three spaces for spans of 70 and 75 ft; four spaces for 80, 85, 90, 95, and 100 ft; and five spaces for 105, 110, 115, and 120 ft.

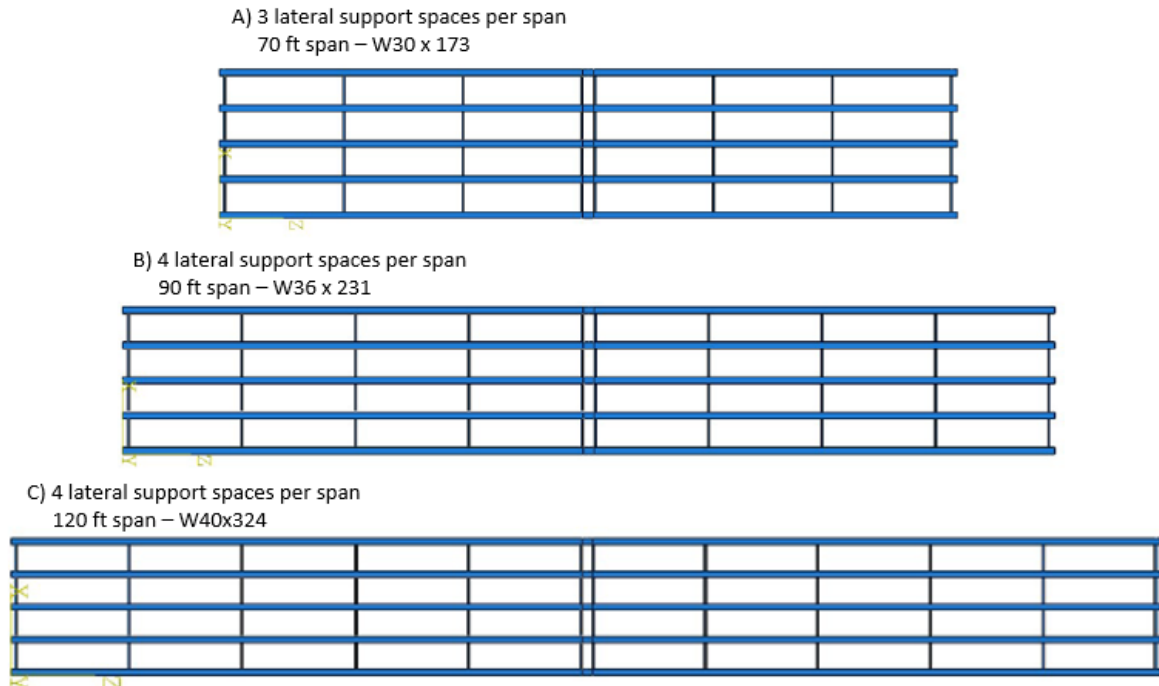


Figure 7.7. Spacing Distribution for Different Full Bridge Configuration Cases According to the Span Length and Girder Size Presented by the TxDOT Standard Design Tables.

7.5.5. Abaqus General Script Description

As mentioned before, a Python script was developed as part of the parametric analysis to automate the generation of models, significantly reducing the time required to build and run each case. This script facilitated the exploration of various design scenarios by automatically adjusting key parameters. The script focused on varying the variables of beam dimensions, length, and skew angle.

7.5.6. Concept A

For Concept A, an explicit 3D modeling approach was used for the development of the parametric analysis, as shown in Figure 7.8.

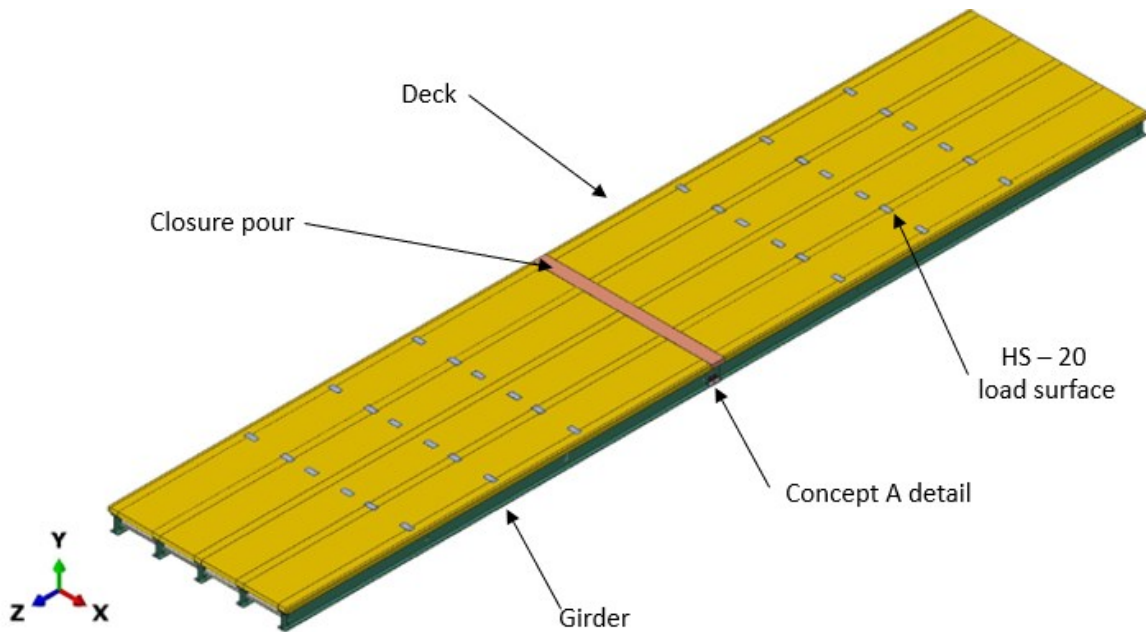


Figure 7.8. General Model Elements.

Based on the test specifications for the experimental test, two different element types were used to model the structure components of the model. A 3D cube element type was chosen for the girders, lateral support beams, deck, closure pour, and plates. This type of element is suitable because it accurately represents the structure's 3D behavior and load distribution.

A linear truss element type was used for the rebar, which is ideal because it effectively models the axial forces and tensions these elements experience. Truss elements simplify the representation of rebar by focusing on their primary function of bearing tensile loads.

By using these specific element types, the model better captures the structure's actual behavior while presenting an efficient computational cost solution.

To ensure uniform application of the boundary conditions to simulate the interaction between the bridge's elements over the experimental and parametric analysis, the conditions were implemented as follows:

1. Embedded constraints: Used for the interaction between the rebar and the concrete sections to represent the composite behavior of the composite concrete elements.
2. General contact: Used for the interaction between the closure pour and the surrounding deck and beam element. This constraint ensures load transfer interaction between the

elements under compression load, and it allows the elements to separate under tension force to accurately represent the cold joint generated between the deck and closure pour.

3. Tie constraint: Used to define the interaction between the deck and girder to ensure composite behavior of the elements, thereby allowing continuity between the mesh of both elements. Additionally, a simplification of the bolted plate connections in Concept A was leveraged for the parametric modeling. Explicit modeling of bolt slip was not required for the parametric study. The plates were modeled with a fully composite surface-to-surface constraint that substantially improved model run time.

Figure 7.9 provides a general overview of Concept A details applied to the model.

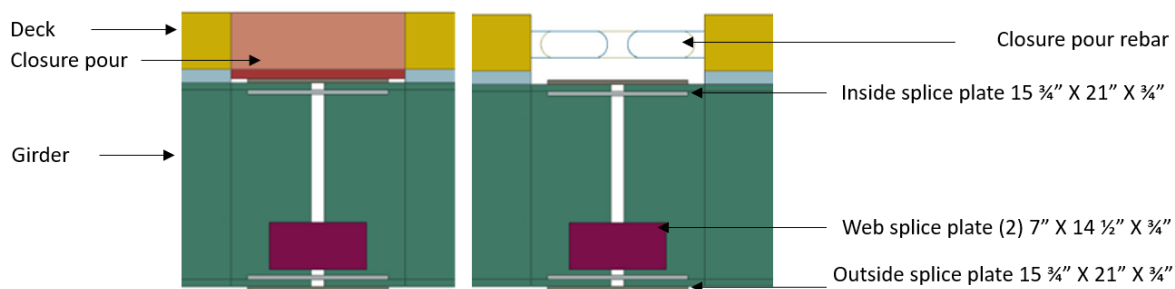


Figure 7.9. General Overview of Concept A Model.

Additionally, the element mesh was set to a uniform size of 4 over all of the elements. This decision provided a good compromise between the overall results of the implementation of the detail connections and the various different parameters of the full bridge configuration.

7.5.7. Concept C

Like Concept A, Concept C consisted of an explicit 3D modeling approach that was used for the development of the parametric analysis, as shown in Figure 7.10.

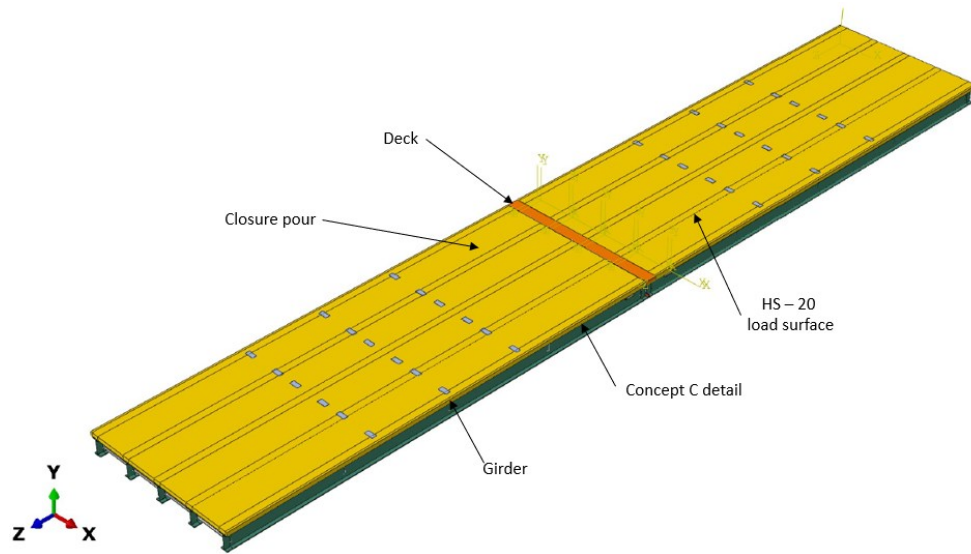


Figure 7.10. Concept C General Model Elements.

Similar to Concept A, two different element types were used to model the structure components of the model—a 3D cube element type for the girders, lateral support beams, deck, closure pour, plates and Williams bars; and a linear truss element type for the rebar in the deck and closure pour.

As for the boundary conditions that simulate the interaction between the bridge elements, the same conditions used for Concept A were applied to the Concept C models:

1. Embedded constraints: Used for the interaction between the rebar and the concrete sections and represented the composite behavior of the composite concrete elements.
2. General contact: Used for the interaction between the closure pour and the surrounding deck and beam element. This constraint ensured load transfer interaction between the elements under compression load, and it allowed the elements to separate under tension force to accurately represent the cold joint generated between the deck and closure pour.
3. Tie constraint: Used to define the interaction between the deck and girder to ensure composite behavior of the elements, thereby allowing continuity between the mesh of both elements. Additionally, similar to Concept A, a simplification of the bolted plate connections in Concept C was leveraged for the parametric modeling with a fully composite surface-to-surface constraint that substantially improved model run time.
4. Williams bars: To simplify the complexity and run time of the model, a simplification of the connection between the bars and the PT bracket plates was implemented, and a

continuity was assumed between the end of these two elements using a tie constraint. Additionally, the temperature change method was used to define the initial prestress on the bars, as applied in the analytic modeling of Concept C section.

Figure 7.11 provides a general overview of Concept C details applied to the model.

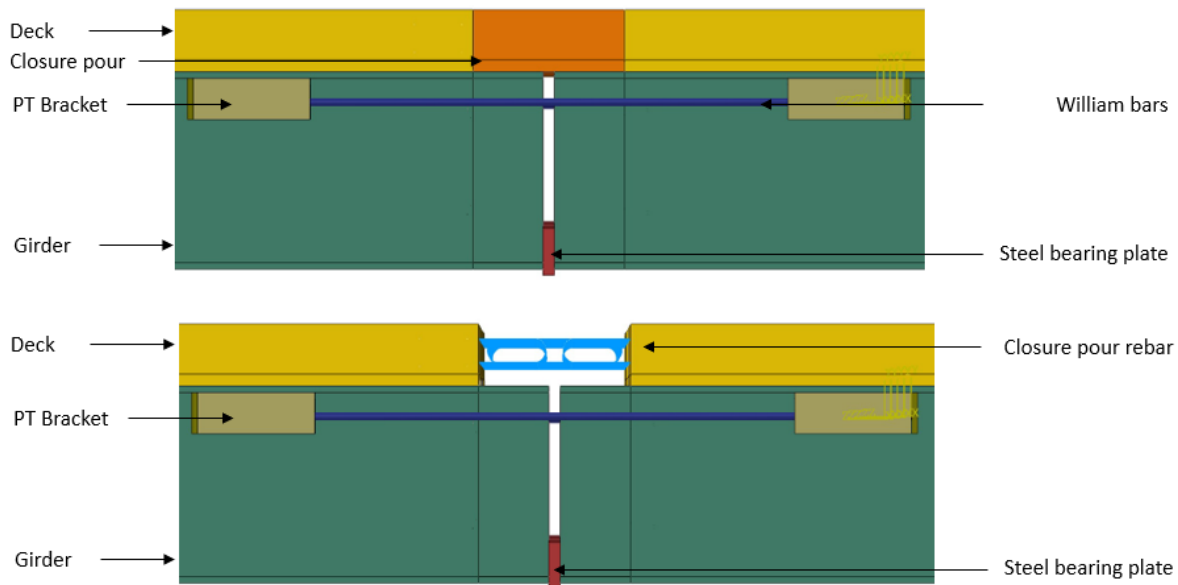


Figure 7.11. General Overview of Concept C Model.

For the element mesh, just as with Concept A, a size of 4 was uniformly set over all of the elements, which provided a good compromise between the overall results of the implementation of the detail connections and the varying different parameters of the full bridge configuration.

7.6. RESULTS OF PARAMETRIC ANALYSIS—CONCEPT A

The results in this section focus on the maximum bending longitudinal stress present in the deck and the closure pour section. A table with the maximum longitudinal stress in the rebar in the closure pour is presented to analyze its overall behavior among the study cases.

7.6.1. Maximum Deck and Closure Pour Stress

To analyze the impact of the implementation of Concept A over different cases, Table 7.4 presents the maximum bending stress experienced by the deck and closure elements using the 30-ft-wide roadway scenario under various conditions. The data consider different spans, depths, weights, and skew angles of the beams chosen for this parametric analysis.

Table 7.4. Maximum Longitudinal Stress on the Deck and Closure Pours for Each Case.

			Max Bending Stress lb/in ²							
			0 Skew Angle		15 Skew Angle		30 Skew Angle		45 Skew Angle	
No.	Span (ft)	Beam Type	Deck	Closure Pour	Deck	Closure Pour	Deck	Closure Pour	Deck	Closure Pour
1	70	W30×173	171.0	147.9	173.5	146.4	180.8	145.1	196.6	142.0
2	75	W30×173	199.1	166.2	204.3	165.6	212.0	163.7	227.8	161.9
3	80	W30×191	218.9	178.5	224.4	178.6	232.3	176.5	246.9	175.2
4	80	W33×201	196.0	161.4	201.1	159.6	208.0	158.8	241.2	194.7
5	85	W30×211	239.7	193.2	245.1	191.6	253.0	189.8	267.5	228.8
6	85	W33×201	222.7	179.5	228.2	177.9	235.7	176.7	251.4	217.3
7	90	W30×235	255.1	205.0	260.6	203.7	268.4	201.8	281.9	240.9
8	90	W33×221	239.9	192.0	245.5	190.6	253.1	189.0	267.9	230.4
9	90	W36×231	215.2	177.0	219.8	174.8	228.9	173.9	243.0	211.7
10	90	W40×199	212.6	175.7	217.4	173.0	225.1	173.2	240.5	213.9
11	95	W30×235	285.5	225.8	291.9	224.6	300.1	222.6	312.5	265.8
12	95	W33×221	268.3	211.5	274.1	210.3	282.6	208.2	296.9	253.8
13	95	W40×199	238.1	193.2	243.5	190.7	251.5	190.4	267.5	235.5
14	100	W33×291	261.0	209.0	266.0	208.3	274.8	205.8	286.4	245.4
15	100	W36×262	252.3	203.9	257.5	201.9	266.3	201.3	280.0	241.3
16	100	W40×249	236.1	194.6	241.5	192.2	248.9	191.4	263.2	231.9
17	105	W33×291	290.0	227.8	295.9	227.8	304.9	225.0	316.5	269.7
18	105	W36×262	280.3	222.1	286.3	220.5	295.6	219.3	310.0	264.5
19	105	W40×249	262.5	211.8	268.4	209.9	276.5	208.4	290.7	254.1
20	110	W33×318	309.7	239.7	311.3	239.2	320.5	236.4	331.8	280.7
21	110	W36×302	293.4	229.9	295.7	228.0	304.6	226.6	318.0	269.8
22	110	W40×277	281.1	222.2	279.3	219.1	287.6	216.8	305.5	263.4
23	115	W36×330	308.6	240.4	306.7	238.1	314.5	236.5	327.3	278.6
24	115	W40×297	303.4	235.4	301.2	232.7	309.4	230.4	323.1	275.6
25	120	W40×324	313.4	243.6	316.3	243.0	324.3	240.3	337.7	239.9

Based on these results, it can be concluded that:

1. The length of the beam influences the stress distribution over the elements.
2. For a given span length, increasing the depth of the beam reduces the stress distribution over the deck.

- The skew angle affects the distribution of the stress in the elements, which is an important consideration for the design of the details, because the stress levels creep up to around 10 percent more for the cases of a 45 degree skew angle compared to the one with 0 degrees skew.

7.6.2. Deck and Closure Pour Localized Stress Distribution

Using a 120-ft span length with the W40×324 beam, the stress distributes differently over different skew angles (see Figure 7.12). While increasing the skew angle of the bridge, the stress distribution on the deck became more localized but had a similar magnitude and did not rise drastically.

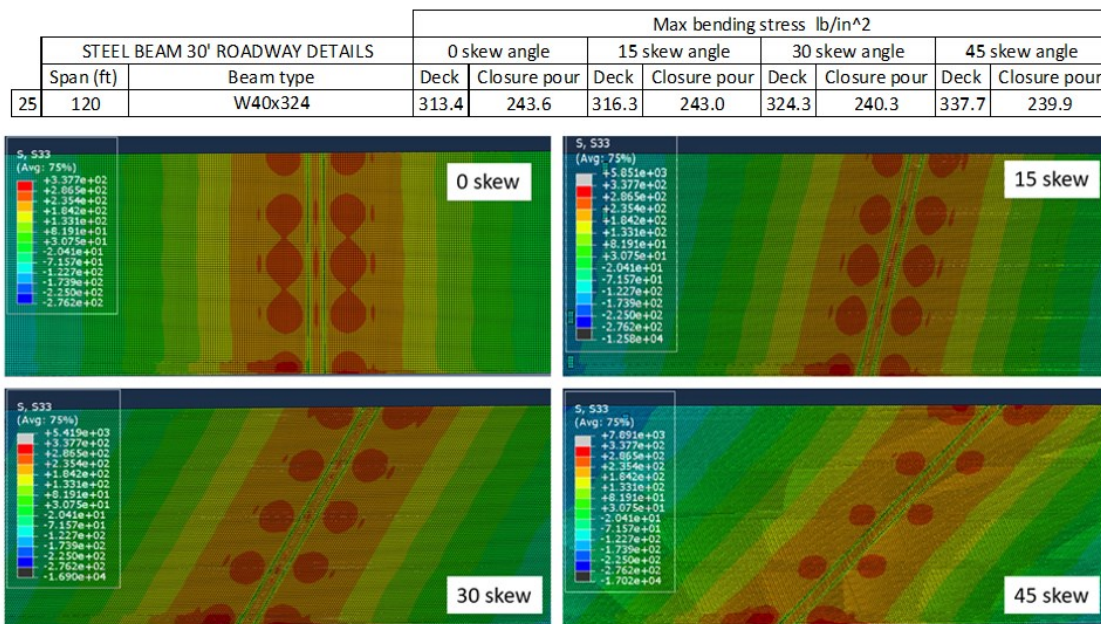


Figure 7.12. Deck and Closure Pour Stress Distribution Example for W40x324 and 120-ft Span Length.

7.6.3. Rebar Localized Stress Distribution

The stress distribution in the rebar used to connect and transfer the tension forces between the deck and closure pour elements shows similar changes in the magnitude of the tensile stress in the rebar increase as the skew angle increases, similar to the stress distribution over the deck.

Table 7.5 presents the magnitude and change of the maximum tensile stress presented in the change of section between the deck and closure pour elements, as shown in Figure 7.13.

Table 7.5. Maximum Rebar Tensile Stress of Concept A.

No.			Max Tensional Stress lb/in²			
	Span (ft)	Beam Type	0 Skew Angle	15 Skew Angle	30 Skew Angle	45 Skew Angle
1	70	W30×173	14,400.0	14,370.0	14,610.0	15,410.0
2	75	W30×173	16,230.0	16,220.0	16,600.0	17,470.0
3	80	W30×191	17,490.0	17,460.0	18,010.0	18,810.0
4	80	W33×201	15,620.0	15,610.0	15,750.0	16,790.0
5	85	W30×211	18,810.0	18,820.0	19,000.0	20,120.0
6	85	W33×201	17,420.0	17,420.0	17,700.0	18,840.0
7	90	W30×235	20,020.0	20,090.0	20,250.0	21,420.0
8	90	W33×221	18,670.0	18,760.0	19,040.0	20,220.0
9	90	W36×231	17,150.0	17,230.0	17,360.0	18,510.0
10	90	W40×199	17,050.0	17,060.0	17,150.0	18,390.0
11	95	W30×235	22,150.0	22,250.0	22,490.0	23,810.0
12	95	W33×221	20,690.0	20,800.0	21,130.0	22,440.0
13	95	W40×199	18,820.0	18,880.0	19,060.0	20,390.0
14	100	W33×291	20,570.0	20,710.0	20,890.0	22,080.0
15	100	W36×262	19,990.0	20,090.0	20,300.0	21,490.0
16	100	W40×249	19,060.0	19,120.0	19,250.0	20,390.0
17	105	W33×291	22,580.0	22,690.0	23,020.0	24,310.0
18	105	W36×262	21,920.0	22,040.0	22,370.0	23,670.0
19	105	W40×249	20,880.0	20,960.0	21,150.0	22,430.0
20	110	W33×318	23,890.0	23,970.0	24,260.0	25,550.0
21	110	W36×302	22,820.0	22,880.0	23,170.0	24,430.0
22	110	W40×277	22,060.0	22,030.0	22,230.0	24,430.0
23	115	W36×330	24,030.0	23,980.0	24,280.0	25,550.0
24	115	W40×297	23,580.0	23,560.0	25,110.0	25,110.0
25	120	W40×324	24,540.0	24,590.0	24,900.0	26,300.0

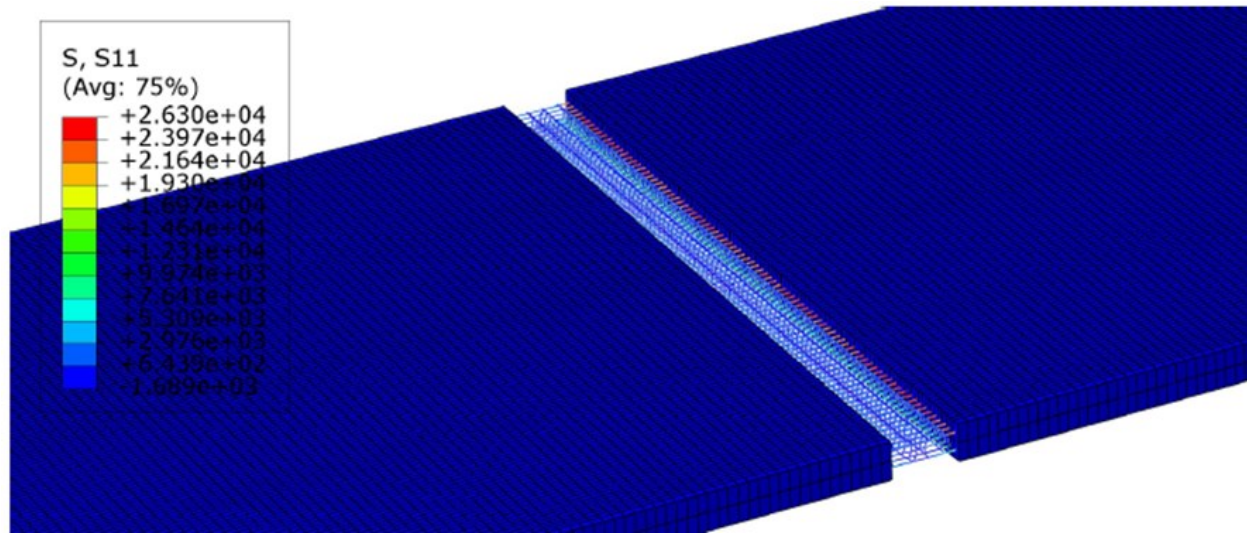


Figure 7.13. Maximum Closure Pour Rebar Tensional Stress.

7.7. RESULTS OF PARAMETRIC ANALYSIS—CONCEPT C

The results in this section focus on the maximum bending longitudinal stress present in the deck and the closure pour section. A table with the maximum longitudinal stress in the rebar in the closure pour is presented to analyze its overall behavior among the study cases.

7.7.1. Maximum Deck and Closure Pour Stress

To analyze the impact of the implementation of Concept C, over different cases, Table 7.6 presents the maximum bending stress experienced by the deck and closure elements using the 30-foot-wide roadway scenario under various conditions. The data consider different spans, depths, weights, and skew angles of the beams chosen for this parametric analysis.

Table 7.6. Maximum Longitudinal Stress on the Deck and Closure Pours for Each Case.

			Max Bending Stress lb/in ²							
			0 Skew Angle		15 Skew Angle		30 Skew Angle		45 Skew Angle	
No.	Span (ft)	Beam Type	Deck	Closure Pour	Deck	Closure Pour	Deck	Closure Pour	Deck	Closure Pour
1	70	W30×173	434.8	39.9	423.6	−9.0	415.6	−13.9	410.6	−1.6
2	75	W30×173	442.4	54.5	430.7	−1.6	448.1	−4.7	441.6	−0.5
3	80	W30×191	420.4	63.5	421.0	1.1	448.6	3.7	447.6	8.4
4	80	W33×201	425.8	45.1	417.2	−5.0	416.8	−9.2	416.0	2.4
5	85	W30×211	420.6	72.6	423.5	3.0	448.3	21.7	452.9	19.6
6	85	W33×201	437.3	59.8	430.1	8.8	447.3	4.0	416.0	2.4
7	90	W30×235	427.1	83.6	428.2	4.6	449.0	39.9	443.3	35.8
8	90	W33×221	415.0	67.8	422.7	2.5	447.8	19.6	444.7	6.7
9	90	W36×231	415.5	55.1	413.3	5.7	430.0	−6.4	428.5	8.4
10	90	W40×199	467.1	52.3	457.4	−1.9	443.3	−4.6	450.9	17.2
11	95	W30×235	462.2	102.1	460.2	68.9	481.2	63.8	476.2	61.1
12	95	W33×221	446.0	84.5	452.7	46.3	477.6	41.8	481.1	36.4
13	95	W40×199	483.2	6.2	474.3	8.7	474.1	8.7	472.4	13.4
14	100	W33×291	412.1	81.6	415.4	56.0	429.4	50.4	436.1	47.4
15	100	W36×262	413.6	74.8	425.7	39.9	451.6	36.7	454.9	30.3
16	100	W40×249	408.1	65.6	413.4	23.1	432.5	18.5	441.8	19.7
17	105	W33×291	446.0	95.5	445.5	77.5	460.5	72.9	468.6	72.2
18	105	W36×262	446.1	90.4	455.3	60.4	484.5	50.7	484.8	53.7
19	105	W40×249	427.1	79.3	438.9	43.0	462.8	61.9	470.2	91.3
20	110	W33×318	448.7	98.4	452.0	91.3	465.1	91.7	473.7	91.3
21	110	W36×302	444.5	93.5	446.3	73.3	470.0	74.2	471.4	72.8
22	110	W40×277	431.7	85.9	422.2	58.7	456.7	57.2	467.9	54.9
23	115	W36×330	454.7	105.1	451.9	90.9	470.8	92.8	476.4	91.3
24	115	W40×297	439.8	88.4	451.2	75.2	464.4	76.8	479.7	76.2

			Max Bending Stress lb/in ²							
			0 Skew Angle		15 Skew Angle		30 Skew Angle		45 Skew Angle	
No.	Span (ft)	Beam Type	Deck	Closure Pour	Deck	Closure Pour	Deck	Closure Pour	Deck	Closure Pour
25	120	W40×324	457.0	106.4	456.8	94.1	466.0	93.6	480.6	94.5

Based on these results, it can be concluded that:

1. Even the length of the beam influences the stress distribution over the elements; the increment between the 70 ft span and the 120 ft span is 4.8 percent.
2. Similar to Concept A, for a given span length, increasing the depth of the beam reduces the stress distribution over the deck.
3. Skew angle affects the distribution of the stress in the elements, which is an important consideration to have for the design of the details; the stress levels inch up to around 2.7 percent more for the cases of the 15 degree skew angle, 7.3 percent for the 30 degree skew angle and 9.1 percent for the 45 degree skew angle, compared to the one with 0 degrees skew.
4. The stress distribution on the deck, over the cases, presents a uniform behavior without a wide variation between the 70 ft span and the 120 ft span, revealing only an increment of 4.8 percent of the stress in the deck. However, the deck stress range is closer to the cracking stress of the deck than the values obtained in Concept A, making it more likely to crack.
5. The stress over the closure pour presents smaller values of tension than Concept A, as expected, due the prestress added to this section.

7.7.2. Deck and Closure Pour Localized Stress Distribution

Using a 120 ft span length with the W40×324 beam, like for Concept A, the stress distributed differently over different skew angles, going from a more uniform distribution to a more localized distribution over the beam elements area (see Figure 7.14). While increasing the skew angle of the bridge, the stress distribution on the deck became more localized but had a similar magnitude and did not rise drastically.

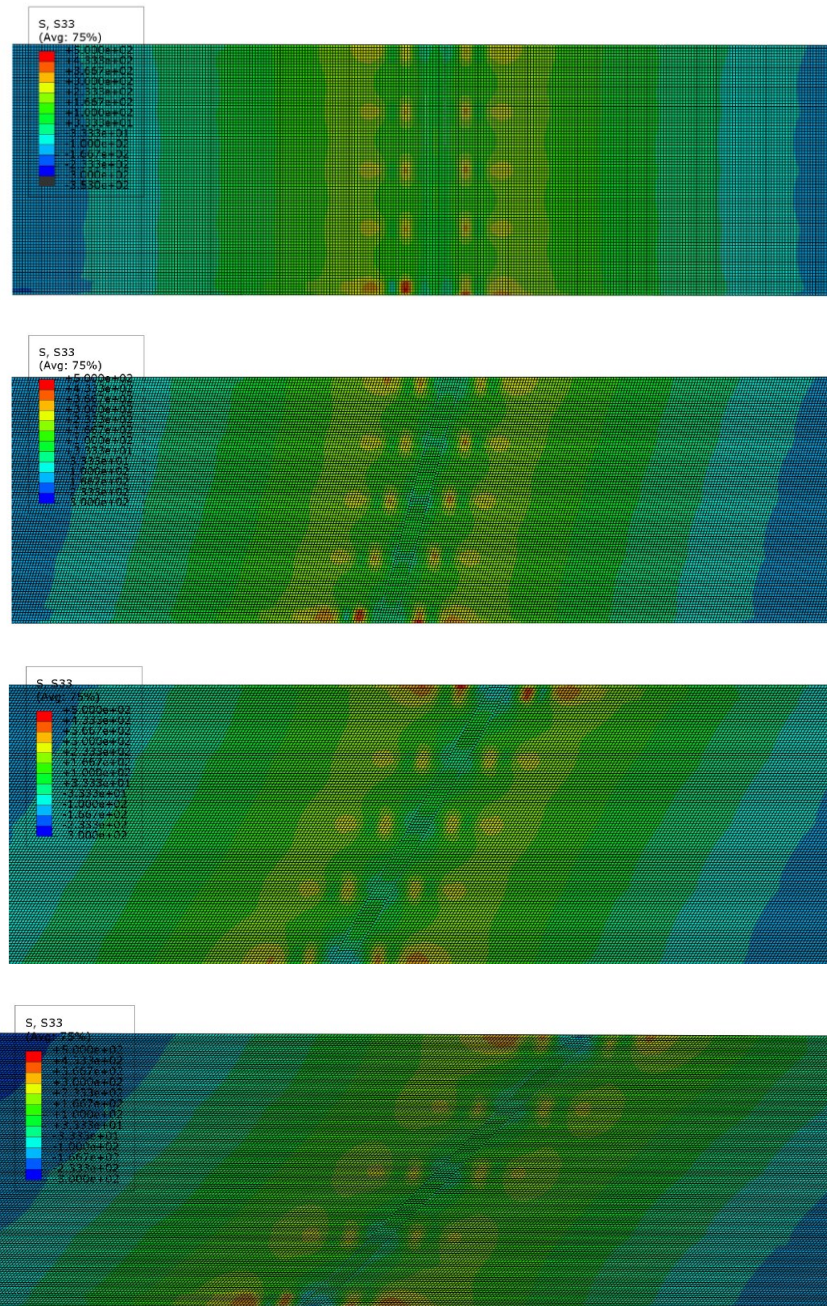


Figure 7.14. Concept C Deck and Closure Pour Stress Distribution for W40×324 and 120 ft Span Length.

However, similar to Concept A, in the 3D model, it was possible to capture a stress concentration on one of the sides of the deck due to the lateral displacement generated, which corresponds to the maximum longitudinal stress presented on the elements.

7.8. CONCEPT A—RESULTS DISCUSSION

The results for Concept A indicate that incorporating a skew angle in a full bridge configuration led to an increase in the tension stress levels within the deck. Despite this increase, the impact on the generation of cracks in the concrete elements is not severe. However, it is important to account for this factor during the design process, particularly when dealing with greater skew angles that can increase stress levels by up to approximately 10 percent in comparison to a zero-skew scenario.

7.9. CONCEPT C—RESULTS DISCUSSION

The results for Concept C indicate that the prestress added to the section helps to maintain a more uniform stress distribution over the different scenarios. However, the stress values obtained in the deck are closer to the cracking stress of the concrete than the ones obtained in Concept A.

Additionally, similar to Concept A, incorporating a skew angle led to an increase in the stress levels of the deck up to approximately 10 percent in comparison to a zero-skew scenario.

7.10. OVERALL DISCUSSION

The parametric study presented in this section focused on the modeling of Concept A and Concept C in a variety of global configurations. It is important to note that Concept B was not explicitly modeled because of the relative similarity of the components of the connection detail to that of Concept C. Given the adoption of simplifications in the connection detail, there was no need to explicitly model Concept B.

The results of Concept A and Concept C indicate similar behavior at the deck under variation of global geometric parameters. As such, modeling of Concept D was not conducted. Similarly, the recommended detail presented in Section 8, which is a combination of other concepts, was not explicitly modeled since the behaviors will be similar. The parametric study indicated that, irrespective of connection details, the effect of global geometric bridge configuration changes on deck stress is minimal, with the largest influence being skew effects resulting in a 10 percent increase.

8. RECOMMENDATIONS AND DESIGN GUIDANCE

The goal of this research was to develop a prefabricated steel ABC connection detail at the pier bent locations that allows the structure to behave SDCL. This connection must be relatively easy to fabricate, fast to assemble, safe, cost-effective, and durable long-term. The connection that accomplishes this the best is the recommended detail illustrated in Figure 8.1 (labeled as Final System Option 1 in Section 6.7). It was developed through extensive research that began with a detailed literature review (Section 2) along with a field assessment on a recent TxDOT steel girder ABC project (Section 3). Next, an array of connection concepts was developed and presented at a workshop to an IRP (Section 4). Four connection concepts were selected for full-scale experimental testing (Section 5). In addition, analytical FEM was performed of the tested specimens (Section 6), along with a finite element parametric study to capture the global bridge behavior (Section 7). Finally, as discussed in this section, a primary and secondary recommended connection was established with design guidance for future engineers.

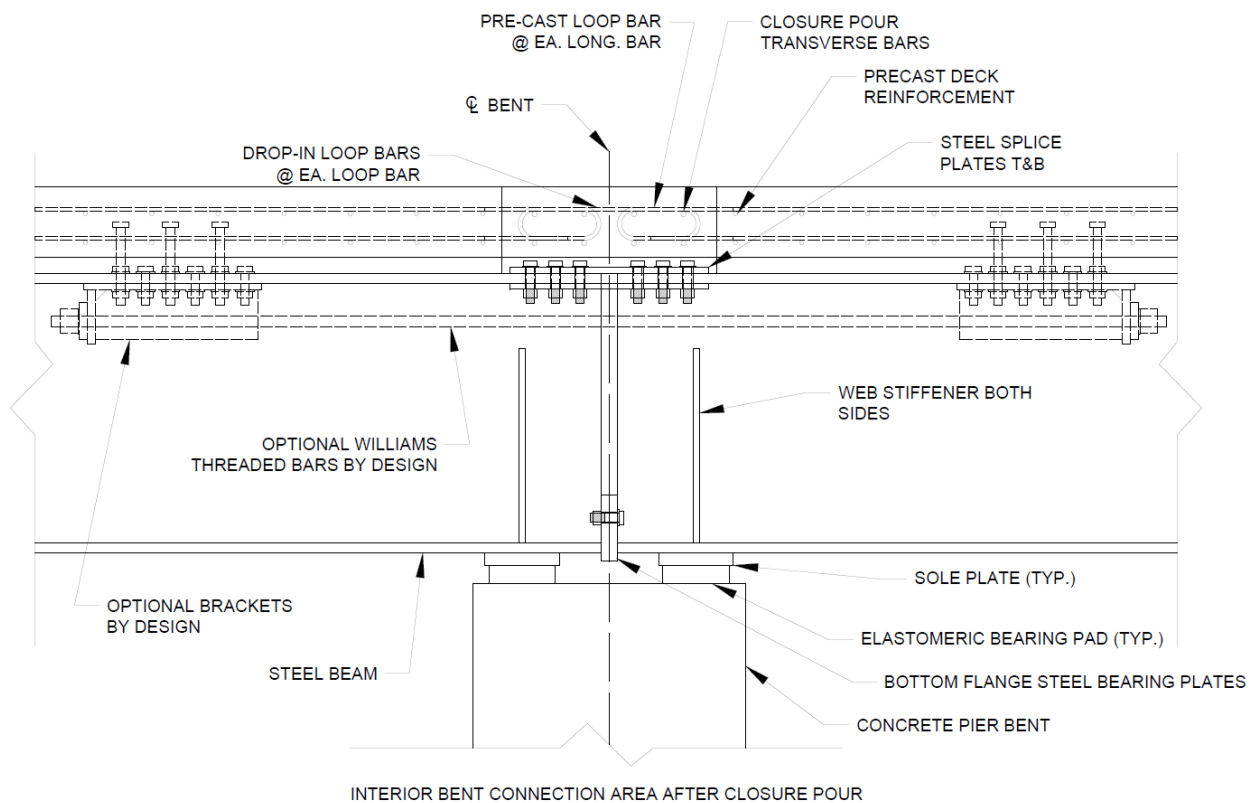


Figure 8.1. Recommended Steel SDCL Connection Using ABC (Final System Option 1).

The recommended connection shown in Figure 8.1 is a combination of Concepts A and C. These concepts each performed well during the full-scale laboratory testing. The concrete closure pour (using conventional concrete) was the same for both concepts. This detail performed well with relative ease, avoiding the need for UHPC. Concept A utilized top flange splice plates, unlike Concept C, which had no positive top flange connection (only PT bars). This positive top flange connection provides a more rigid connection and minimizes deck cracking. In contrast, the bottom flange splice plates for Concept A were more difficult to use than the steel bearing end plates utilized in Concept C. Therefore, steel end plates are part of the recommended alternative. The recommended detail does not require PT bars. However, for situations in which deck stresses are relatively high, PT bars are considered optional to allow for precompression of the slab (minimizing cracking). Note that this recommended detail was also rigorously evaluated using FEA, which validated the decision.

To aid future bridge engineers, design guidance has been developed for the recommended detail shown in Figure 8.1. This design guidance is provided in the form of an annotated design example provided in Appendix D. In addition, standard drawings are provided in Appendix E.

Note another steel SDCL connection using ABC was developed as a secondary option (labeled as Final System Option 2 in Section 6.7). Essentially, this connection is Concept D with refinement to the reinforcement and the addition of steel bottom flange bearing plates, similar to the ones used in Concept C. This option performed adequately, but not as well overall compared to Option 1. The biggest advantage of Final System Option 2 is the simple construction process and rapid assembly. Additionally, this option might minimize the number of cracks on the concrete deck surface over the pier location since the main crack is located at the match-cast joint. The main crack can be closed once there is no live loading on the bridge. These two elements are the reason for including a secondary alternative.

REFERENCES

1. Azizinamini, A., *Simple for Dead Load—Continuous for Live Load Steel Bridge Systems*. Engineering Journal, 2014. **51**: p. 59-82.
2. Freyermuth, C.L., *DESIGN OF CONTINUOUS HIGHWAY BRIDGES WITH PRECAST, PRESTRESSED CONCRETE GIRDERS*. Pci Journal, 1969. **14**: p. 14-39.
3. Lampe, N.M., Nazanin & Yakel, Aaron & Azizinamini, Atorod, *Development and Experimental Testing of Connections for the Simple for Dead Load-Continuous for Live Load Steel Bridge System*. Engineering Journal, 2014. **51**: p. 83-109.
4. Wasserman, E., *Simplified Continuity Details for Short- and Medium-Span Composite Steel Girder Bridges*. Transportation Research Record: Journal of the Transportation Research Board, 2005. **11s**: p. 197-202.
5. John W. van de Lindt, A.J.S., and Suren Chen, *Development of Steel Design Details and Selection Criteria for Cost-Effective and Innovative Steel Bridges in Colorado*. 2008. p. 168.
6. Robert I. Johnson, R.A.A., *Innovative and Economical Steel Bridge Design Alternatives for Colorado*. 2015: Mountain-Plains Consortium.
7. Anthony Ream, W.B., *Continuous for Live Load Steel Girder Construction in the Northern Panhandle of West Virginia*. Engineering Journal, 2014. **SECOND QUARTER**: p. 127.
8. Farimani, R.J., Saeed & Kowalski, Derek & Azizinamini, Atorod, *Numerical Analysis and Design Provision Development for the Simple for Dead Load-Continuous for Live Load Steel Bridge System*. Engineering Journal, 2014. **51**: p. 109-126.
9. Javidi, S.K., Derek & Azizinamini, Atorod, *Numerical Analysis and Design Provision Development for the Simple for Dead Load-Continuous for Live Load Steel Bridge System*. Engineering Journal, 2014. **51**: p. 109-126.
10. Culmo, M.P., *Accelerated Bridge Construction—Experience in Design, Fabrication and Erection of Prefabricated Bridge Elements and Systems* 2011: CME Associates, Inc. & Applied Research Associates, Inc. p. 346.
11. Balkos, K.D., et al., *Static and Fatigue Tests of Steel-Precast Composite Beam Specimens with Through-Bolt Shear Connectors*. Journal of Bridge Engineering, 2019. **24**(5): p. 04019036.
12. Eric Thorkildsen, G.P., Inc. , *Case Study: Eliminating Bridge Joints with Link Slabs— An Overview of State Practices*. 2020. p. 9.
13. Birely, A.C., et al., *Experimental Behavior of Reinforced Concrete and Pretensioned Concrete Bent Caps*. Journal of Bridge Engineering, 2020. **25**(2): p. 04019137.
14. Shoushtari, E., et al., *Design, Construction, and Shake Table Testing of a Steel Girder Bridge System with ABC Connections*. Journal of Bridge Engineering, 2019. **24**(9): p. 04019088.
15. Elmira Shoushtari, M.S.S., Ahmad Itani, Mohamed A. Moustafa, *Seismic performance of a two-span steel girder bridge with ABC connections*. Engineering Structures, 2021. **241**.
16. Attanayake, U. and H. Aktan, *Procedures and Guidelines for Design of Lateral Bridge Slide Activities*. Journal of Bridge Engineering, 2019. **24**(9): p. 04019093.
17. Solae, C., et al., *Investigation of Cracks Observed on a Skewed Bridge Constructed Using Self-Propelled Modular Transporters*. Journal of Performance of Constructed Facilities, 2020. **34**(5): p. 04020098.

18. Saeed Javidi, A.Y., Atorod Azizinamini, *Experimental Investigation, Application and Monitoring of a Simple for Dead Load-Continuous for Live Load Connection for Accelerated Modular Steel Bridge Construction*. Engineering Journal, 2014. **51**: p. 177-198.
19. Corporation, H., *Innovative Bridge Designs for Rapid Renewal*. 2014, Washington, DC: The National Academies Press: National Academies of Sciences, Engineering, and Medicine. 357.
20. Ahmad Abu-Hawash, Y.J.D., Andrew Putz, and Brent Phares, *Accelerated Innovation Deployment (AID) Demonstration Project: Testing, Performance Evaluation, and Documentation of the Little Silver Creek Bridge*. 2018. p. 110.
21. Sadeghnejad, A., R. Taghinezhadbilondy, and A. Azizinamini, *Seismic Performance of a New Connection Detail in an SDCL Steel Bridge System*. Journal of Bridge Engineering, 2019. **24**(10): p. 04019094.
22. District, T.D. *Accelerated bridge construction I-635 over Seagoville Road*. 2021; Available from: <https://www.txdot.gov/projects/projects-studies/dallas/i635-seagoville.html>.
23. Amir Sadeghnejad, S.R., Islam M. Mantawy, Atorod Azizinamini, *Comparative Study of Cyclic and Shake Table Tests for Simple for Dead Load and Continuous for Live Load Steel Bridge System in Seismic Area*. Transportation Research Record: Journal of the Transportation Research Board, 2020. **2674**(7): p. 233–243.
24. *AASHTO LRFD Bridge Design Specifications*. 9 ed. 2020, Washington, D.C.: American Association of State Highway and Transportation Officials.
25. *TxDOT Bridge Standards*. Texas Department of Transportation (State of Texas).
26. Smith, M., *ABAQUS/Standard User's Manual, Version 6.14*. 2014, Dassault Systèmes Simulia Corp.: United States.
27. J. Lubliner, J.O., S. Oller, E. Oñate, *A plastic-damage model for concrete*. International Journal of Solids and Structures, 1989. **25**(3): p. 299-326.
28. Lee, J. and G.L. Fenves, *Plastic-Damage Model for Cyclic Loading of Concrete Structures*. Journal of Engineering Mechanics, 1998. **124**(8): p. 892-900.
29. Aikaterini S. Genikomsou, M.A.P., *Finite element analysis of punching shear of concrete slabs using damaged plasticity model in ABAQUS*. Engineering Structures, 2015. **98**: p. 38-48.
30. Ali, A.K., Doo & Cho, Sung, *Modeling of nonlinear cyclic load behavior of I-shaped composite steel-concrete shear walls of nuclear power plants*. Nuclear Engineering and Technology, 2013. **45**.
31. Adam Wosatko, A.W., Maria Anna Polak, Jerzy Pamin, *Role of dilatancy angle in plasticity-based models of concrete*. Archives of Civil and Mechanical Engineering, 2019. **19**(4): p. 1268-1293.
32. Eivind Hognestad, N.W.H. and M. Douglas, *Concrete Stress Distribution in Ultimate Strength Design*. ACI Journal Proceedings, 1955. **52**(12).
33. Ren, W., et al., *Numerical Simulation of Prestressed Precast Concrete Bridge Deck Panels Using Damage Plasticity Model*. International Journal of Concrete Structures and Materials, 2015. **9**(1): p. 45-54.
34. *LTBP InfoBridge, U.S. Department of Transportation Federal Highway Administration*. Available from: <https://infobridge.fhwa.dot.gov/Data/SelectedBridges>.

35. Transportation, T.D.o., *Low Bid Average for New and Replaced Bridges*. 2013-2023: txdot.gov.
36. *PBES Cost Study: Accelerated Bridge Construction Success Stories*, F.H. Administration, Editor. 2006, FHWA.
37. Duane S. Milligan, M.Z.R., *Value of Delay Time and Road User Costs*, T.D.o. Transportation, Editor. 2021, TxDOT.
38. *TxDOT AADT Annuals 2022*, T.D.o. Transportation, Editor. 2024.
39. Feyijimi Adegbohun, A.v.J., E.B. Agamloh, Alexandre Yokochi, *Geographical Modeling of Charging Infrastructure Requirements for Heavy-Duty Electric Autonomous Truck Operations*. *Energies*, 2023. **16**(10).

APPENDIX A: SECTION PROPERTIES

Section Information:

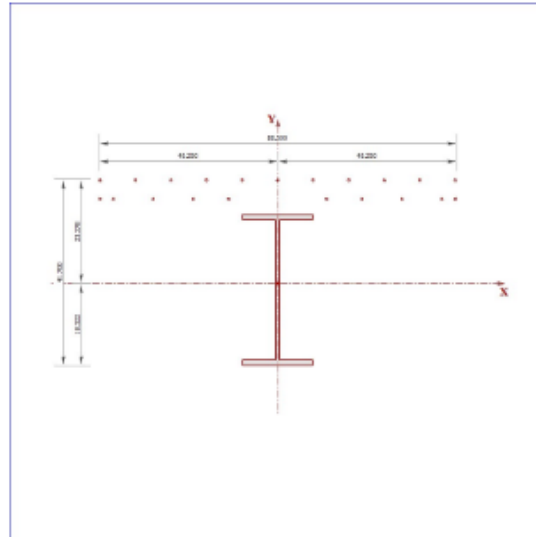
Material Type	=	General
Shape Type	=	Arbitrary
Number of Shapes	=	22

Basic Properties:

Total Width	=	80.500	in
Total Height	=	41.700	in
Centroid, X _o	=	0.000	in
Centroid, Y _o	=	1.472	in
X-Bar (Right)	=	40.250	in
X-Bar (Left)	=	40.250	in
Y-Bar (Top)	=	23.378	in
Y-Bar (Bot)	=	18.322	in
Max Thick	=	1.150	in

Equivalent Properties:

Area, A _x	=	63.223	in ²
Inertia, I _{xx}	=	1.358E+004	in ⁴
Inertia, I _{yy}	=	3794.45	in ⁴
Inertia, I _{xy}	=	0.000	in ⁴
S _x (Top)	=	581.03	in ³
S _x (Bot)	=	741.34	in ³
S _y (Left)	=	94.272	in ³
S _y (Right)	=	94.272	in ³
r _x	=	14.658	in
r _y	=	7.747	in
Plastic Z _x	=	851.08	in ³
Plastic Z _y	=	245.37	in ³
Torsional J	=	20.929	in ⁴
As-xx Def	=	1.000	
As-yy Def	=	1.000	
As-xx Stress	=	1.000	
As-yy Stress	=	1.000	



Section Diagram

Figure A.1. Section Properties of Structural Steel and Rebar (Cracked Section).

Section Information:

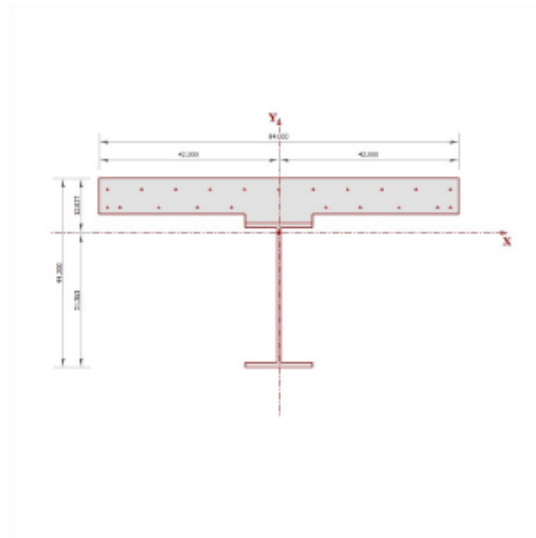
Material Type	=	General
Shape Type	=	Arbitrary
Number of Shapes	=	23

Basic Properties:

Total Width	=	84.000	in
Total Height	=	44.200	in
Centroid, X _o	=	0.000	in
Centroid, Y _o	=	14.513	in
X-Bar (Right)	=	42.000	in
X-Bar (Left)	=	42.000	in
Y-Bar (Top)	=	12.837	in
Y-Bar (Bot)	=	31.363	in
Max Thick	=	84.000	in

Equivalent Properties:

Area, A _x	=	161.77	in ²
Inertia, I _{xx}	=	3.191E+004	in ⁴
Inertia, I _{yy}	=	5.938E+004	in ⁴
Inertia, I _{xy}	=	0.003	in ⁴
S _x (Top)	=	2485.82	in ³
S _x (Bot)	=	1017.48	in ³
S _y (Left)	=	1413.91	in ³
S _y (Right)	=	1413.91	in ³
r _x	=	14.045	in
r _y	=	19.160	in
Plastic Z _x	=	1487.43	in ³
Plastic Z _y	=	2243.98	in ³
Torsional J	=	2445.45	in ⁴
As-xx Def	=	1.000	
As-yy Def	=	1.000	
As-xx Stress	=	1.000	
As-yy Stress	=	1.000	



Section Diagram

Figure A.2. Section Properties of Structural Steel, Concrete, and Rebar (Composite Section).

APPENDIX B: INSTRUMENTATION LIST

Table B.1. Concept A Instrumentation List.

Module	Instrument Type	Number	Designation	Type	HBL Channel
M4	REBAR STRAIN GAUGES	28	A-RSG-W3/0.2D	RSG-1	SG1
M4		29	A-RSG-W3/C	RSG-2	SG2
M4		30	A-RSG-W3/0.8A	RSG-3	SG3
M4		31	A-RSG-W2/0.2D	RSG-4	SG4
M4		32	A-RSG-W2/C	RSG-5	SG5
M4		33	A-RSG-W2/0.8A	RSG-6	SG6
M4		34	A-RSG-W1.4/0.2D	RSG-7	SG7
M4		35	A-RSG-W1.4/C	RSG-8	SG8
M5		36	A-RSG-W1.4/0.8A	RSG-9	SG9
M5		37	A-RSG-E1.4/0.2D	RSG-10	SG10
M5		38	A-RSG-E1.4/C	RSG-11	SG11
M5		39	A-RSG-E1.4/0.8A	RSG-12	SG12
M5		40	A-RSG-E2/0.2D	RSG-13	SG13
M5		41	A-RSG-E2/C	RSG-14	SG14
M5		42	A-RSG-E2/0.8A	RSG-15	SG15
M5		43	A-RSG-E3/0.2D	RSG-16	SG16
M6		44	A-RSG-E3/C	RSG-17	SG17
M6		45	A-RSG-E3/0.8A	RSG-18	SG18
M6		46	A-RSG-W0.5/0.2D	RSG-19	SG19
M6		47	A-RSG-W0.5/C	RSG-20	SG20
M6		48	A-RSG-W0.5/0.8A	RSG-21	SG21
M6		49	A-RSG-E0.5/0.2D	RSG-22	SG22
M6		50	A-RSG-E0.5/C	RSG-23	SG23
M6		51	A-RSG-E0.5/0.8A	RSG-24	SG24
M7	STRUCTURAL STEEL STRAIN GAUGES	52	A-SSG-W2-TF-N	SSG-1	SG25
M7		53	A-SSG-W2-TF-S	SSG-2	SG26
M7		54	A-SSG-W2-BF-N	SSG-3	SG27
M7		55	A-SSG-W2-BF-S	SSG-4	SG28
M7		56	A-SSG-W1-TF-N	SSG-5	SG29
M7		57	A-SSG-W1-TF-S	SSG-6	SG30
M7		58	A-SSG-W1-WB-T	SSG-7	SG31
M7		59	A-SSG-W1-WB-B	SSG-8	SG32
M8		60	A-SSG-W1-BF-N	SSG-9	SG33
M8		61	A-SSG-W1-BF-S	SSG-10	SG34

Module	Instrument Type	Number	Designation	Type	HBL Channel
M8		62	A-SSG-E1-TF-N	SSG-11	SG35
M8		63	A-SSG-E1-TF-S	SSG-12	SG36
M8		64	A-SSG-E1-WB-T	SSG-13	SG37
M8		65	A-SSG-E1-WB-B	SSG-14	SG38
M8		66	A-SSG-E1-BF-N	SSG-15	SG39
M8		67	A-SSG-E1-BF-S	SSG-16	SG40
M9		68	A-SSG-E2-TF-N	SSG-17	SG41
M9		69	A-SSG-E2-TF-S	SSG-18	SG42
M9		70	A-SSG-E2-BF-N	SSG-19	SG43
M9		71	A-SSG-E2-BF-S	SSG-20	SG44
M9		72	A-SSG-0-TPL-N	SSG-21	SG45
M9		73	A-SSG-0-TPL-S	SSG-22	SG46
M9		74	A-SSG-0-BPL-N	SSG-23	SG47
M9		75	A-SSG-0-BPL-S	SSG-24	SG48
M10	CONCRETE SURFACE STRAIN GAUGES	76	A-CSG-W3/0.2D	CSG-1	SG49
M10		77	A-CSG-W3/C	CSG-2	SG50
M10		78	A-CSG-W3/0.8A	CSG-3	SG51
M10		79	A-CSG-W2/0.2D	CSG-4	SG52
M10		80	A-CSG-W2/C	CSG-5	SG53
M10		81	A-CSG-W2/0.8A	CSG-6	SG54
M10		82	A-CSG-W1/0.2D	CSG-7	SG55
M10		83	A-CSG-W1/C	CSG-8	SG56
M11		84	A-CSG-W1/0.8A	CSG-9	SG57
M11		85	A-CSG-E1/0.2D	CSG-10	SG58
M11		86	A-CSG-E1/C	CSG-11	SG59
M11		87	A-CSG-E1/0.8A	CSG-12	SG60
M11		88	A-CSG-E2/0.2D	CSG-13	SG61
M11		89	A-CSG-E2/C	CSG-14	SG62
M11		90	A-CSG-E2/0.8A	CSG-15	SG63
M11		91	A-CSG-E3/0.2D	CSG-16	SG64
M12		92	A-CSG-E3/C	CSG-17	SG65
M12		93	A-CSG-E3/0.8A	CSG-18	SG66
M12		94	VOID	VOID	SG67
M12		95	VOID	VOID	SG68
M12		96	VOID	VOID	SG69
M12		97	VOID	VOID	SG70
M12		98	VOID	VOID	SG71

Module	Instrument Type	Number	Designation	Type	HBL Channel
M12		99	VOID	VOID	SG72
M1	ACTUATOR AND LOAD CELL	1	A-ACT-W6.5/C	L-1	Ram1
M1		2	A-PRES-W6.5/C	P-1	Press1
M1		3	A-ACT-E6.5/C	L-2	void
M1		4	A-PRES-E6.5/C	P-2	void
M2	DISPLACEMENT/STRING POTS	13	A-DISP-E6.5/C	DISP-1	DP1
M2		14			
M2		15	A-SP-W5-C	SP-1	SP1
M2		16	A-SP-W4-C	SP-2	SP2
M2		17	A-SP-W3-C	SP-3	SP3
M2		18	A-SP-W2-C	SP-4	SP4
M2		19	A-SP-E2-C	SP-5	SP5
M2		20	A-SP-E3-C	SP-6	SP6
M3		21	A-SP-E4-C	SP-7	SP7
M3		22	A-SP-E5-C	SP-8	SP8
M3		23	A-SP-E7-N	SP-10	SP9
M3		24	A-SP-E7-S	SP-11	SP10
M3		25	VOID	VOID	SP11
M3		26	VOID	VOID	SP12
M3		27	VOID	VOID	SP13
M13	LVDTs	100	A-LVDT-E1-BF-C	LV-1	LV1
M13		101	A-LVDT-0-WB-B	LV-2	LV2
M13		102	A-LVDT-0-WB-T	LV-3	LV3
M13		103	A-LVDT-0-CONC	LV-4	LV4
M13		104	A-LVDT-W1-BF-C	LV-5	LV5
M13		105	A-LVDT-W6-BF-C	LV-6	LV6
M13		106	A-LVDT-W7-BF-C	LV-7	LV7
M13		107	VOID	VOID	LV8

Table B.2. Concept B Instrumentation List.

Module	Instrument Type	Number	Designation	Type	HBL Channel
M4	REBAR STRAIN GAUGES	28	B-RSG-W3/0.2D	RSG-1	SG1
M4		29	B-RSG-W3/C	RSG-2	SG2
M4		30	B-RSG-W3/0.8A	RSG-3	SG3
M4		31	B-RSG-W2/0.2D	RSG-4	SG4
M4		32	B-RSG-W2/C	RSG-5	SG5
M4		33	B-RSG-W2/0.8A	RSG-6	SG6
M4		34	B-RSG-W1/0.2D	RSG-7	SG7
M4		35	B-RSG-W1/C	RSG-8	SG8
M5		36	B-RSG-W1/0.8A	RSG-9	SG9
M5		37	B-RSG-E1/0.2D	RSG-10	SG10
M5		38	B-RSG-E1/C	RSG-11	SG11
M5		39	B-RSG-E1/0.8A	RSG-12	SG12
M5		40	B-RSG-E2/0.2D	RSG-13	SG13
M5		41	B-RSG-E2/C	RSG-14	SG14
M5		42	B-RSG-E2/0.8A	RSG-15	SG15
M5		43	B-RSG-E3/0.2D	RSG-16	SG16
M6		44	B-RSG-E3/C	RSG-17	SG17
M6		45	B-RSG-E3/0.8A	RSG-18	SG18
M6	STRUCTURAL STEEL STRAIN GAUGES	46	B-SSG-W2-TF-N	SSG-1	SG19
M6		47	B-SSG-W2-TF-S	SSG-2	SG20
M6		48	B-SSG-W2-WB-T	SSG-3	SG21
M6		49	B-SSG-W2-WB-B	SSG-4	SG22
M6		50	B-SSG-W2-BF-N	SSG-5	SG23
M6		51	B-SSG-W2-BF-S	SSG-6	SG24
M7		52	B-SSG-W1-TF-N	SSG-7	SG25
M7		53	B-SSG-W1-TF-S	SSG-8	SG26
M7		54	B-SSG-W1-WB-T	SSG-9	SG27
M7		55	B-SSG-W1-WB-B	SSG-10	SG28
M7		56	B-SSG-W1-BF-N	SSG-11	SG29
M7		57	B-SSG-W1-BF-S	SSG-12	SG30
M7		58	B-SSG-E1-TF-N	SSG-13	SG31
M7		59	B-SSG-E1-TF-S	SSG-14	SG32
M8		60	B-SSG-E1-WB-T	SSG-15	SG33
M8		61	B-SSG-E1-WB-B	SSG-16	SG34
M8		62	B-SSG-E1-BF-N	SSG-17	SG35
M8		63	B-SSG-E1-BF-S	SSG-18	SG36

Module	Instrument Type	Number	Designation	Type	HBL Channel
M8		64	B-SSG-E2-TF-N	SSG-19	SG37
M8		65	B-SSG-E2-TF-S	SSG-20	SG38
M8		66	B-SSG-E2-WB-T	SSG-21	SG39
M8		67	B-SSG-E2-WB-B	SSG-22	SG40
M9		68	B-SSG-E2-BF-N	SSG-23	SG41
M9		69	B-SSG-E2-BF-S	SSG-24	SG42
M9		70	B-SSG-0-TR-N	SSG-25	SG43
M9		71	B-SSG-0-TR-S	SSG-26	SG44
M9		72	VOID	SSG-27	SG45
M9		73	VOID	SSG-28	SG46
M9		74	VOID	VOID	SG47
M9		75	VOID	VOID	SG48
M10	CONCRETE SURFACE STRAIN GAUGES	76	B-CSG-W3/0.2D	CSG-1	SG49
M10		77	B-CSG-W3/C	CSG-2	SG50
M10		78	B-CSG-W3/0.8A	CSG-3	SG51
M10		79	B-CSG-W2/0.2D	CSG-4	SG52
M10		80	B-CSG-W2/C	CSG-5	SG53
M10		81	B-CSG-W2/0.8A	CSG-6	SG54
M10		82	B-CSG-W1/0.2D	CSG-7	SG55
M10		83	B-CSG-W1/C	CSG-8	SG56
M11		84	B-CSG-W1/0.8A	CSG-9	SG57
M11		85	B-CSG-E1/0.2D	CSG-10	SG58
M11		86	B-CSG-E1/C	CSG-11	SG59
M11		87	B-CSG-E1/0.8A	CSG-12	SG60
M11		88	B-CSG-E2/0.2D	CSG-13	SG61
M11		89	B-CSG-E2/C	CSG-14	SG62
M11		90	B-CSG-E2/0.8A	CSG-15	SG63
M11		91	B-CSG-E3/0.2D	CSG-16	SG64
M12		92	B-CSG-E3/C	CSG-17	SG65
M12		93	B-CSG-E3/0.8A	CSG-18	SG66
M12		94	VOID	VOID	SG67
M12		95	VOID	VOID	SG68
M12		96	VOID	VOID	SG69
M12		97	VOID	VOID	SG70
M12		98	VOID	VOID	SG71
M12		99	VOID	VOID	SG72
M1	ACTUATOR AND LOAD CELL	1	B-ACT-W6.5/C	L-1	Ram1

Module	Instrument Type	Number	Designation	Type	HBL Channel
M1		2	B-PRES-W6.5/C	P-1	Press1
M1		3	B-ACT-E6.5/C	L-2	void
M1		4	B-PRES-E6.5/C	P-2	void
M2	DISPLACEMENT/STRING POTS	13	B-DISP-E6.5/C	DISP-1	DP1
M2		14	-----		
M2		15	B-SP-W5-C	SP-1	SP1
M2		16	B-SP-W4-C	SP-2	SP2
M2		17	B-SP-W3-C	SP-3	SP3
M2		18	B-SP-W2-C	SP-4	SP4
M2		19	B-SP-E2-C	SP-5	SP5
M2		20	B-SP-E3-C	SP-6	SP6
M3		21	B-SP-E4-C	SP-7	SP7
M3		22	B-SP-E5-C	SP-8	SP8
M3		23	B-SP-E7-N	SP-10	SP9
M3		24	B-SP-E7-S	SP-11	SP10
M3		25	VOID	VOID	SP11
M3		26	VOID	VOID	SP12
M3		27	VOID	VOID	SP13
M13	LVDTs	100	B-LVDT-E1-BF-C	LV-1	LV1
M13		101	B-LVDT-0-WB-B	LV-2	LV2
M13		102	B-LVDT-0-WB-T	LV-3	LV3
M13		103	B-LVDT-0-CONC	LV-4	LV4
M13		104	B-LVDT-W1-BF-C	LV-5	LV5
M13		105	B-LVDT-W6-BF-C	LV-6	LV6
M13		106	B-LVDT-W7-BF-C	LV-7	LV7
M13		107	VOID	VOID	LV8

Table B.3. Concept C Instrumentation List.

Module	Instrument Type	Number	Designation	Type	HBL Channel
M4	REBAR STRAIN GAUGES	28	C-RSG-W3/0.2D	RSG-1	SG1
M4		29	C-RSG-W3/C	RSG-2	SG2
M4		30	C-RSG-W3/0.8A	RSG-3	SG3
M4		31	C-RSG-W2/0.2D	RSG-4	SG4
M4		32	C-RSG-W2/C	RSG-5	SG5
M4		33	C-RSG-W2/0.8A	RSG-6	SG6
M4		34	C-RSG-W1.4/0.2D	RSG-7	SG7
M4		35	C-RSG-W1.4/C	RSG-8	SG8
M5		36	C-RSG-W1.4/0.8A	RSG-9	SG9
M5		37	C-RSG-E1.4/0.2D	RSG-10	SG10
M5		38	C-RSG-E1.4/C	RSG-11	SG11
M5		39	C-RSG-E1.4/0.8A	RSG-12	SG12
M5		40	C-RSG-E2/0.2D	RSG-13	SG13
M5		41	C-RSG-E2/C	RSG-14	SG14
M5		42	C-RSG-E2/0.8A	RSG-15	SG15
M5		43	C-RSG-E3/0.2D	RSG-16	SG16
M6		44	C-RSG-E3/C	RSG-17	SG17
M6		45	C-RSG-E3/0.8A	RSG-18	SG18
M6		46	C-RSG-W0.3/0.2D	RSG-19	SG19
M6		47	C-RSG-W0.3/C	RSG-20	SG20
M6		48	C-RSG-W0.3/0.8A	RSG-21	SG21
M6		49	C-RSG-E0.3/0.2D	RSG-22	SG22
M6		50	C-RSG-E0.3/C	RSG-23	SG23
M6		51	C-RSG-E0.3/0.8A	RSG-24	SG24
M7	STRUCTURAL STEEL STRAIN GAUGES	52	C-SSG-W2-TF-N	SSG-1	SG25
M7		53	C-SSG-W2-TF-S	SSG-2	SG26
M7		54	C-SSG-W2-BF-N	SSG-3	SG27
M7		55	C-SSG-W2-BF-S	SSG-4	SG28
M7		56	C-SSG-W1-TF-N	SSG-5	SG29
M7		57	C-SSG-W1-TF-S	SSG-6	SG30
M7		58	C-SSG-W1-WB-T	SSG-7	SG31
M7		59	C-SSG-W1-WB-B	SSG-8	SG32
M8		60	C-SSG-W1-BF-N	SSG-9	SG33
M8		61	C-SSG-W1-BF-S	SSG-10	SG34
M8		62	C-SSG-E1-TF-N	SSG-11	SG35
M8		63	C-SSG-E1-TF-S	SSG-12	SG36

Module	Instrument Type	Number	Designation	Type	HBL Channel
M8		64	C-SSG-E1-WB-T	SSG-13	SG37
M8		65	C-SSG-E1-WB-B	SSG-14	SG38
M8		66	C-SSG-E1-BF-N	SSG-15	SG39
M8		67	C-SSG-E1-BF-S	SSG-16	SG40
M9		68	C-SSG-E2-TF-N	SSG-17	SG41
M9		69	C-SSG-E2-TF-S	SSG-18	SG42
M9		70	C-SSG-E2-WB-T	SSG-19	SG43
M9		71	C-SSG-E2-WB-B	SSG-20	SG44
M9		72	C-SSG-E2-BF-N	SSG-21	SG45
M9		73	C-SSG-E2-BF-S	SSG-22	SG46
M9		74	C-SSG-0-TR-N	SSG-23	SG47
M9		75	C-SSG-0-TR-S	SSG-24	SG48
M10	CONCRETE SURFACE STRAIN GAUGES	76	C-CSG-W3/0.2D	CSG-1	SG49
M10		77	C-CSG-W3/C	CSG-2	SG50
M10		78	C-CSG-W3/0.8A	CSG-3	SG51
M10		79	C-CSG-W2/0.2D	CSG-4	SG52
M10		80	C-CSG-W2/C	CSG-5	SG53
M10		81	C-CSG-W2/0.8A	CSG-6	SG54
M10		82	C-CSG-W1/0.2D	CSG-7	SG55
M10		83	C-CSG-W1/C	CSG-8	SG56
M11		84	C-CSG-W1/0.8A	CSG-9	SG57
M11		85	C-CSG-E1/0.2D	CSG-10	SG58
M11		86	C-CSG-E1/C	CSG-11	SG59
M11		87	C-CSG-E1/0.8A	CSG-12	SG60
M11		88	C-CSG-E2/0.2D	CSG-13	SG61
M11		89	C-CSG-E2/C	CSG-14	SG62
M11		90	C-CSG-E2/0.8A	CSG-15	SG63
M11		91	C-CSG-E3/0.2D	CSG-16	SG64
M12		92	C-CSG-E3/C	CSG-17	SG65
M12		93	C-CSG-E3/0.8A	CSG-18	SG66
M12		94	VOID	VOID	SG67
M12		95	VOID	VOID	SG68
M12		96	VOID	VOID	SG69
M12		97	VOID	VOID	SG70
M12		98	VOID	VOID	SG71
M12		99	VOID	VOID	SG72
M1	ACTUATOR AND LOAD CELL	1	C-ACT-W6.5/C	L-1	Ram1

Module	Instrument Type	Number	Designation	Type	HBL Channel
M1		2	C-PRES-W6.5/C	P-1	Press1
M1		3	C-ACT-E6.5/C	L-2	void
M1		4	C-PRES-E6.5/C	P-2	void
M2	DISPLACEMENT/STRING POTS	13	C-DISP-E6.5/C	DISP-1	DP1
M2		14			
M2		15	C-SP-W5-C	SP-1	SP1
M2		16	C-SP-W4-C	SP-2	SP2
M2		17	C-SP-W3-C	SP-3	SP3
M2		18	C-SP-W2-C	SP-4	SP4
M2		19	C-SP-E2-C	SP-5	SP5
M2		20	C-SP-E3-C	SP-6	SP6
M3		21	C-SP-E4-C	SP-7	SP7
M3		22	C-SP-E5-C	SP-8	SP8
M3		23	C-SP-E7-N	SP-10	SP9
M3		24	C-SP-E7-S	SP-11	SP10
M3		25	VOID	VOID	SP11
M3		26	VOID	VOID	SP12
M3		27	VOID	VOID	SP13
M13	LVDTs	100	C-LVDT-E1-BF-C	LV-1	LV1
M13		101	C-LVDT-0-WB-B	LV-2	LV2
M13		102	C-LVDT-0-WB-T	LV-3	LV3
M13		103	C-LVDT-0-CONC	LV-4	zz
M13		104	C-LVDT-W1-BF-C	LV-5	LV5
M13		105	C-LVDT-W6-BF-C	LV-6	LV6
M13		106	C-LVDT-W7-BF-C	LV-7	LV7
M13		107	VOID	VOID	LV8

Table B.4. Concept D Instrumentation List.

Module	Instrument Type	Number	Designation	Type	HBL Channel
M4	REBAR STRAIN GAUGES	28	D	RSG-1	SG1
M4		29	D	RSG-2	SG2
M4		30	D	RSG-3	SG3
M4		31	D	RSG-4	SG9
M4		32	D	RSG-5	SG5
M4		33	D	RSG-6	SG6
M4		34	D	RSG-7	SG7
M4		35	D	RSG-8	SG8
M5		36	D	RSG-9	SG4
M5		37	D	RSG-10	SG10
M5		38	D	RSG-11	SG11
M5		39	D	RSG-12	SG12
M5		40	D	RSG-13	SG13
M5		41	D	RSG-14	SG14
M5		42	D	RSG-15	SG15
M5		43	D	RSG-16	SG16
M6		44	D	RSG-17	SG17
M6		45	D	RSG-18	SG18
M6	STRUCTURAL STEEL STRAIN GAUGES	46	D	RSG-19	SG19
M6		47	D	RSG-20	SG20
M6		48	D	RSG-21	SG21
M6		49	D	RSG-22	SG22
M6		50	D	RSG-23	SG23
M6		51	D	RSG-24	SG24
M7		52	D	SSG-1	SG25
M7		53	D	SSG-2	SG26
M7		54	D	SSG-3	SG27
M7		55	D	SSG-4	SG28
M7		56	D	SSG-5	SG29
M7		57	D	SSG-6	SG30
M7		58	D	SSG-7	SG31
M7		59	D	SSG-8	SG32
M8		60	D	SSG-9	SG33
M8		61	D	SSG-10	SG34
M8		62	D	SSG-11	SG35
M8		63	D	SSG-12	SG36

Module	Instrument Type	Number	Designation	Type	HBL Channel
M8		64	D	SSG-13	SG37
M8		65	D	SSG-14	SG38
M8		66	D	SSG-15	SG39
M8		67	D	SSG-16	SG40
M9		68	D	SSG-17	SG41
M9		69	D	SSG-18	SG42
M9		70	D	SSG-19	SG43
M9		71	D	SSG-20	SG44
M9		72	D	SSG-21	SG45
M9		73	D	SSG-22	SG46
M9		74	VOID	SSG-23	SG47
M9		75	VOID	SSG-24	SG48
M10	CONCRETE SURFACE STRAIN GAUGES	76	D	CSG-1	SG49
M10		77	D	CSG-2	SG50
M10		78	D	CSG-3	SG51
M10		79	D	CSG-4	SG52
M10		80	D	CSG-5	SG53
M10		81	D	CSG-6	SG54
M10		82	D	CSG-7	SG55
M10		83	D	CSG-8	SG56
M11		84	D	CSG-9	SG57
M11		85	D	CSG-10	SG58
M11		86	D	CSG-11	SG59
M11		87	D	CSG-12	SG60
M11		88	D	CSG-13	SG61
M11		89	D	CSG-14	SG62
M11		90	D	CSG-15	SG63
M11		91	D	CSG-16	SG64
M12		92	D	CSG-17	SG65
M12		93	D	CSG-18	SG66
M12		94	VOID	VOID	SG67
M12		95	VOID	VOID	SG68
M12		96	VOID	VOID	SG69
M12		97	VOID	VOID	SG70
M12		98	VOID	VOID	SG71
M12		99	VOID	VOID	SG72
M1	ACTUATOR AND LOAD CELL	1	D	L-1	Ram1

Module	Instrument Type	Number	Designation	Type	HBL Channel
M1		2	D	P-1	Press1
M1		3	D	L-2	void
M1		4	D	P-2	void
	FT Voltage Inputs	5	50B Load		L1
		6	50B Stroke		S1
		7	220B Load		L2
		8	220B Stroke		S2
		9			
		10			
		11			
		12			
M2	DISPLACEMENT/STRING POTS	13	D	DISP-1	DP1
M2		14			
M2		15	D	SP-1	SP1
M2		16	D	SP-2	SP2
M2		17	D	SP-3	SP3
M2		18	D	SP-4	SP4
M2		19	D	SP-5	SP5
M2		20	D	SP-6	SP6
M3		21	D	SP-7	SP7
M3		22	D	SP-8	SP8
M3		23	D	SP-10	SP9
M3		24	D	SP-11	SP10
M3		25	VOID	VOID	SP11
M3		26	VOID	VOID	SP12
M3		27	VOID	VOID	SP13
M13	LVDTs	100	D	LV-1	LV1
M13		101	D	LV-2	LV2
M13		102	D	LV-3	LV3
M13		103	D	LV-4	LV4
M13		104	D	LV-5	LV5
M13		105	D	LV-6	LV6
M13		106	D	LV-7	LV7
M13		107	D	LV-8	LV8

APPENDIX C: VALUE OF RESEARCH

C.1. MOTIVATION AND SIGNIFICANCE

This research study developed and quantitatively evaluated the concept of a continuous for live load prefabricated steel accelerated bridge construction (ABC) unit for Texas bridges. The primary objective of this project was to develop connection details that allow a prefabricated steel ABC unit to perform continuous for live load. The system must be easily constructible, fast to assemble, durable long-term, safe, and cost-effective.

Compared to conventional bridge construction, ABC using prefabricated steel units leads to less traffic disruptions, faster construction times, increased worker safety, and better cost-effectiveness. This project realized these advantages through the development of prefabricated ABC units subjected to extensive experimental testing. The chosen details were able to minimize cracking in the deck while also providing continuity for live load over the pier.

Several functional areas of focus were selected for this project. These areas are shown in Table C..

Table C.1. Functional Areas of Project 0-7112.

Benefit Area	Qualitative	Economic	Both	TxDOT	State	Both
Level of Knowledge	X			X		
System Reliability	X					X
Increased Service Life			X			X
Improved Productivity and Work Efficiency			X	X		
Expedited Project Delivery		X		X		
Reduced Construction, Operations, and Maintenance Cost		X		X		
Infrastructure Condition		X				X
Engineering Design Improvement			X			X

C.2. QUALITATIVE BENEFITS

Qualitative benefits are nonmonetary, intangible, and subjective benefits that cannot be measured and can influence business and legislative decisions. The project identified two functional areas that contain qualitative benefits:

- Level of knowledge.
- System reliability.

The qualitative benefits related to the performance of this project are summarized as follows.

C.2.1. Level of Knowledge

This project increased the knowledge related to the construction of bridges using accelerated construction methods. The methods and practices learned during the experimental testing of these prefabricated units provide excellent knowledge to implement these concepts. These construction methods will provide TxDOT with increased ways to design and construct bridges.

C.2.2. System Reliability

ABC methods will provide TxDOT with more reliable systems for bridge construction. Reliability is of paramount importance when constructing bridges that are designed to last for decades. This increased reliability will further extend the life of bridges while also maintaining a high standard of performance.

C.3. ECONOMIC BENEFITS

Economic benefits are relatively easier to identify than qualitative benefits because of their measurable costs and savings. The project identified three functional areas that contain economic benefits:

- Expedited project delivery.
- Reduced construction, operations, and maintenance cost.
- Infrastructure condition.

The economic benefits related to the performance of this project are summarized as follows.

C.3.1. Expedited Project Delivery

Expedited project delivery is a key component of ABC. The prefabricated bridge units are constructed off-site, allowing rapid assembly once brought to the construction site. The combination of prefabricated units and rapid assembly allows for a significant reduction in construction site manual labor costs, erection costs, construction time, and traffic impacts.

C.3.2. Reduced Construction, Operations, and Maintenance Cost

Reducing construction, operations, and maintenance costs for Texas bridges is a core goal for this project. By developing connection concepts that provide the opportunity for rapid assembly, the overall construction costs for bridges will be dramatically reduced. Operation and maintenance costs will also be reduced by providing a durable and safe connection, thereby reducing the need for future repairs or retrofits.

C.3.3. Infrastructure Condition

ABC methods will provide a straightforward way to assess existing infrastructure conditions. By developing standard connection details that can be used over a wide array of bridge arrangements, the assessment of the connection area for signs of fatigue, corrosion, and damage can be streamlined. This process will allow for more inspections to be done in the same amount of time, further reducing the costs of existing bridge evaluations.

C.4. QUALITATIVE AND ECONOMIC BENEFITS

Three benefits that fall under both qualitative and economic areas are:

- Increased service life.
- Improved productivity and work efficiency.
- Engineering design improvement.

These benefits related to the performance of this project are summarized as follows.

C.4.1. Increased Service Life

Increasing the service life of Texas bridges is an important metric that ABC can meet. The extensive cyclic testing that was done showed that these connection details are durable in the

long term for service-level loading. These connection details will increase the service life of bridges in Texas, thereby reducing the need for future replacements.

C.4.2. Improved Productivity and Work Efficiency

ABC will improve the productivity and work efficiency of bridge construction projects that utilize ABC methods. The reduction in construction time needed for bridges that use ABC methods will drastically improve productivity and efficiency both on the construction site and in the office doing the design work.

C.4.3. Engineering Design Improvement

Engineering design will be greatly improved by using ABC methods. The design process for ABC bridges is relatively straightforward, with only slight modifications needed based on the configuration of the bridge. These concepts will provide a more streamlined process for design engineers to follow, which will considerably reduce engineering time.

C.5. QUANTITATIVE ANALYSIS OF ECONOMIC BENEFITS

Two general areas were evaluated when calculating the economic value of research for this project. These two areas were construction cost savings and time cost savings.

Using TxDOT data on the number of bridges constructed per year, it was determined that approximately nine bridges per year were constructed using steel I-beams [35]. Using the average cost per square foot of this type of bridge, and assuming an average bridge length of 500 LF and bridge width of 32 ft, the total cost of building these bridges was estimated at \$21 million per year.

To estimate the construction savings per year, several projects over the last 15 to 20 years that used ABC methods were evaluated, and their percentage savings were averaged [36]. This average was found to be approximately 17 percent. This average was multiplied by the total cost of building the bridges, for a construction savings of \$3.6 million per year.

To estimate the time cost savings, it was assumed that a project that would take 8 months with traditional bridge construction could be completed in 2 months using ABC methods, leading to a 6-month reduction in construction time. The traffic delay costs of passenger vehicles and

commercial vehicles were estimated by the University of Texas at Austin Center for Transportation Research as approximately \$30 and \$41 per hour, respectively [37]. The average annual daily traffic of Texas bridges was calculated at approximately 9,600 vehicles per day [38]. Assuming that 98 percent of vehicles that use the bridges per day are passenger vehicles [39], and that road users spend an average of an extra 15 minutes per day in traffic due to road construction, the average yearly cost savings were calculated at approximately \$26 million.

C.6. SUMMARY

In conclusion, in terms of both qualitative and economic benefits, there is excellent value in using prefabricated ABC unit methods in Texas bridges. For the scenario described above, assuming half of new steel bridge construction is done using these ABC methods, the **annual estimated value is \$14.5 million** for a research project that costs \$571,000. Over a future 20-year period, the net present value (NPV) is roughly \$107 million (calculated using the TxDOT Value of Research template). This is graphically shown in Figure C..

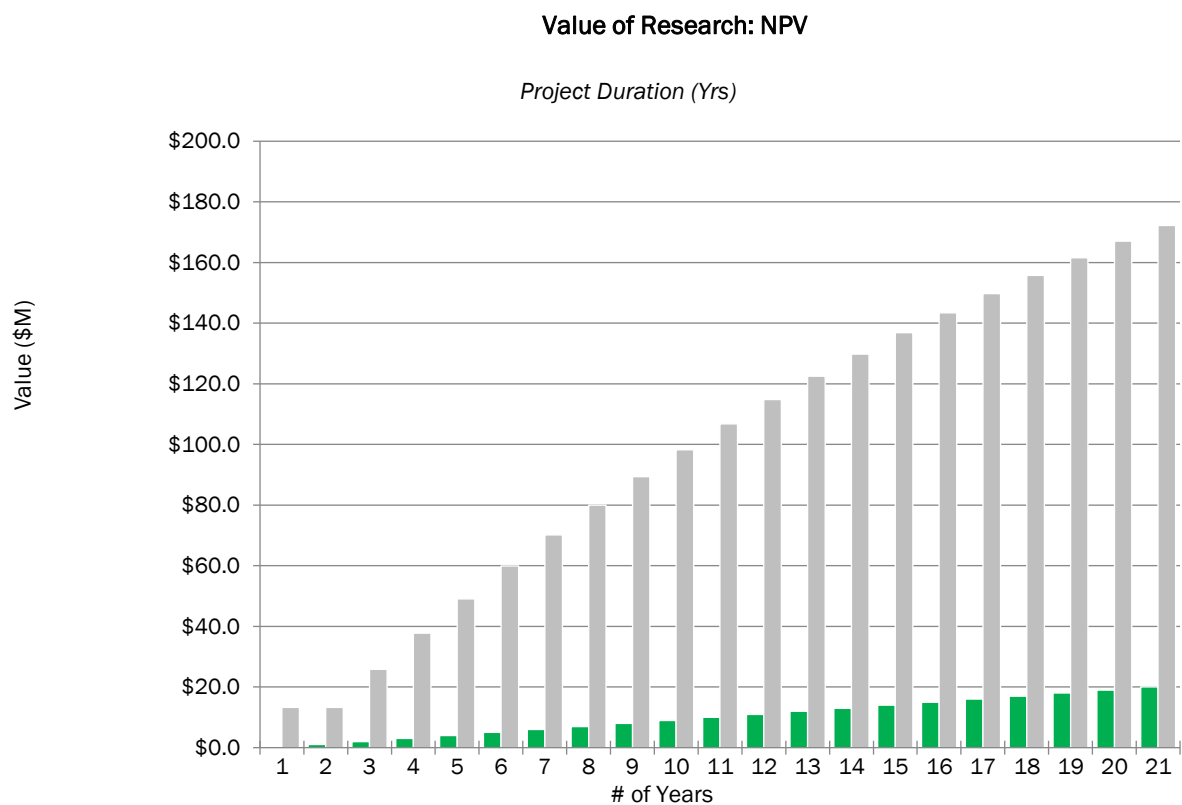


Figure C.1. Value of Research per Year.

APPENDIX D: DESIGN EXAMPLE

Design Guidance Document

Annotated Design Example

<u>Table of Contents</u>	Page No.
Introduction	2
Design Step 1: General Information / Introduction	5
-Design Step 1.1 Introduction	
-Design Step 1.2 Design Philosophy	
-Design Step 1.3 Design Criteria	
-Design Step 1.4 Compute Live Load Effects	
-Design Step 1.5 Compute Live Load Distribution Factor	
-Design Step 1.6 Moment per Beam	
-Design Step 1.7 Minimum Negative Flexure Concrete Deck Reinforcement	
-Design Step 1.8 Flexural Steel Stresses	
-Design Step 1.9 Flexural Capacity	
Design Step 2: Recommended Connection Design	21
-Design Step 2.1 Flexural Resistance by Flange	
-Design Step 2.2 Top Flange Splice Plates	
-Design Step 2.3 Top Flange Bolts	
-Design Step 2.4 Bottom Flange Bearing Plate	
-Design Step 2.5 Flexural Capacity at the Connection	
-Design Step 2.6 Draw Schematic of Final Bolted Field Splice Design	
-Design Step 2.7 Post-Tensioning Rods and Bracket Design (Optional)	
Design Step 3: Summary	36

Introduction

This guidance document provides the design procedure for a steel beam bridge employing Accelerated Bridge Construction (ABC). The ABC technique uses prefabricate bridge units, which are comprised of two beams and a concrete deck slab (see Figure 1). These prefabricated bridge units are connected at the pier bents as illustrated in Figure 2. The primary focus of the example herein is to clearly convey the recommended design for this connection at interior beams. Exterior beams can be designed in a similar manner using a modified cross-section (due to the overhand) and load distribution.

In the following example, Design Step 1 illustrates the general design information and calculations for the interior beams. Design Step 2 shows the detailed connection design that includes the top flange splice plates, bottom bearing plates, and post-tensioning brackets with Williams bars (optional).

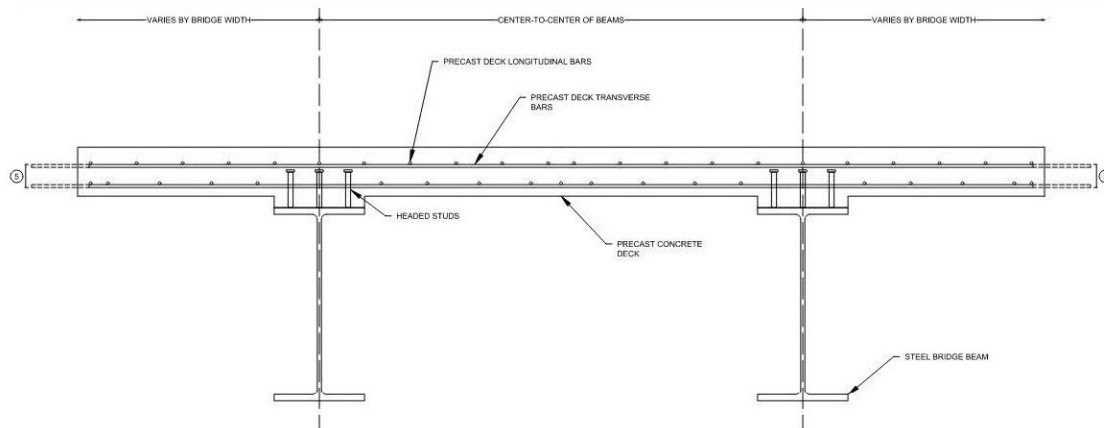


FIGURE 1: Precast Beam Unit Cross Section View

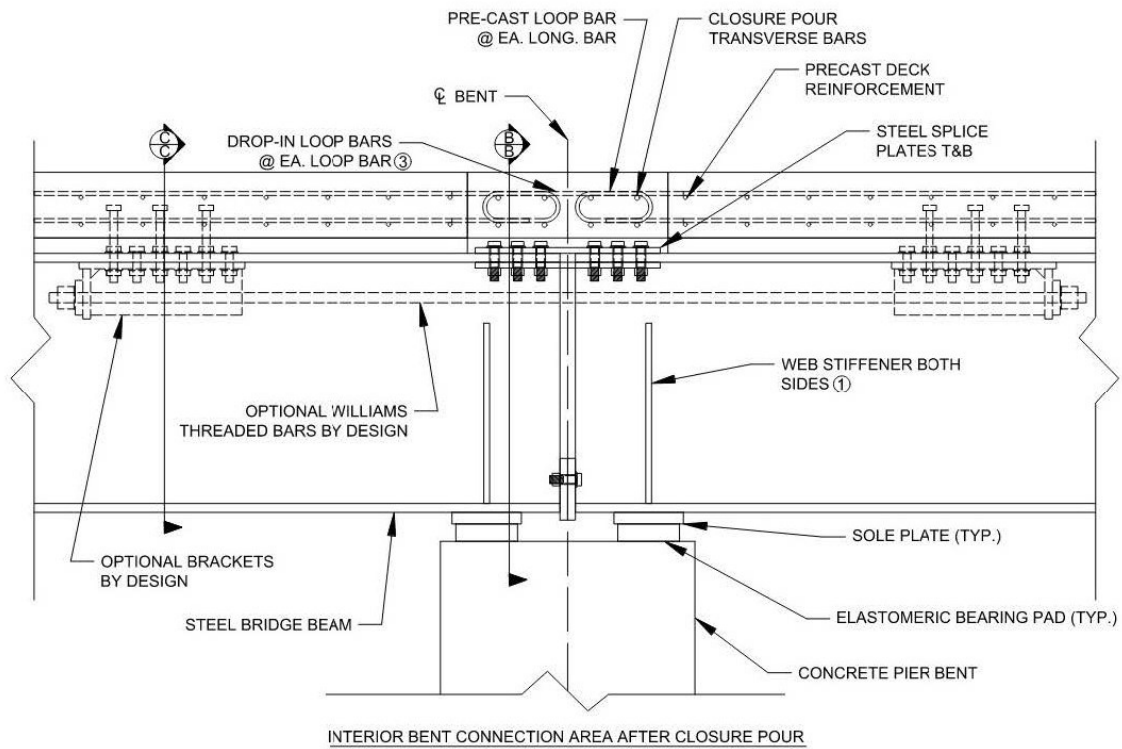


FIGURE 2: Connection Elevation View

Purpose

The purpose of this design example is to allow entry-level bridge engineers (and higher) to accurately design the necessary components to make prefabricated steel ABC beam units continuous for live load.

AASHTO References

For uniformity and simplicity, the design example is based on the *AASHTO LRFD Bridge Design Specifications (Ninth Edition, 2020)*. References to *AASHTO LRFD Bridge Design Specifications* are included throughout the design example. AASHTO references are adjacent to the corresponding design procedure. The following abbreviations are used in the AASHTO references:

S designates specifications

*S**Table* designates a table within the specification

*S**Figure* designates a figure within the specification

*S**Equation* designates an equation within the specification

*S**Appendix* designates an appendix within the specification

C designates commentary

*C**Table* designates a table within the commentary

*C**Figure* designates a figure within the commentary

*C**Equation* designates an equation within the commentary

Design Methodology

This design example is based on Load and Resistance Factor Design (LRFD), as presented in the *AASHTO LRFD Bridge Design Specification (Ninth Edition, 2020)*.

Software

An analysis of the superstructure was performed using RISA-3D software. The design moments, shears, and reactions used in the design example are taken from the RISA-3D output, the moment envelope is shown but the computation process is not shown in the design example.

Design Step 1: General Information / Introduction

Design Step 1.1 Introduction

The design of this superstructure system follows AASHTO LRFD and is based on a three-span (60 feet - 80 feet - 60 feet) bridge with no skew. Based on these dimensions, TxDOT bridge design standards were utilized to select the steel beam sizes and the concrete deck parameters. A roadway width of 30 feet was chosen and the beams were spaced at 7'-0" center-to-center. The bridge deck is precast reinforced concrete with overhangs at the outermost beams. The longitudinal beams are erected as simply supported units and made continuous for live load by connection plates, cast-in-place deck joints, and post tensioning (optional). The following procedure focuses on the ABC connection at the pier bents for interior beams.

An typical transverse section from TxDOT bridge design standards is shown in Figure 3. An elevation view of the benchmark bridge used in this example is shown in Figure 4 and a section view is shown in Figure 5.

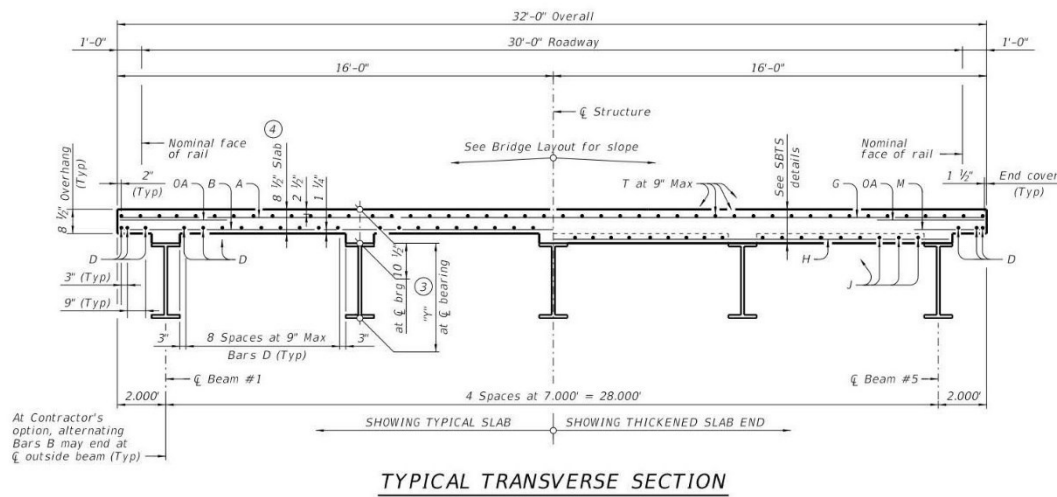


Figure 3: Typical Transverse Section (30' Roadway) from TxDOT Bridge Design Standard

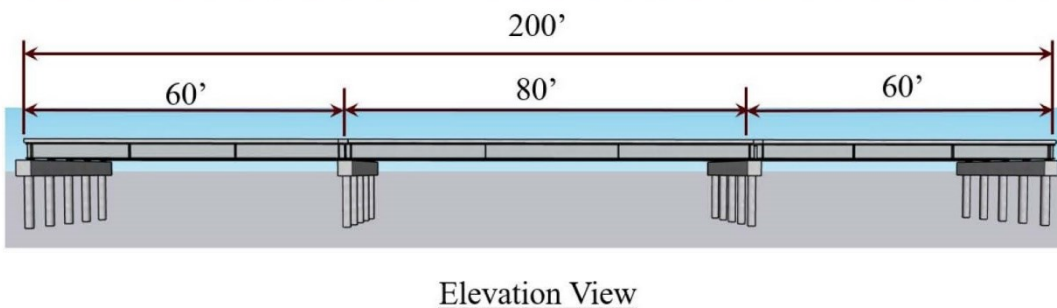


Figure 4: Rendering of the Three-Span Benchmark Bridge

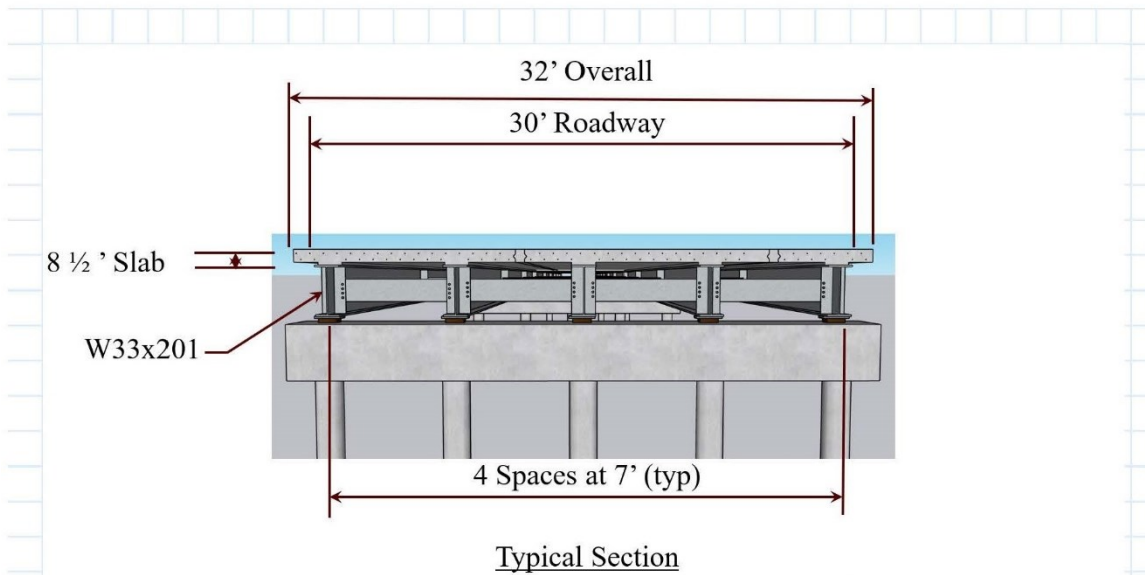


Figure 5: Rendering of the Transverse Bridge Section

Design Step 1.2 Design Philosophy

The geometry of this superstructure consists of five rolled steel beams with a reinforced concrete deck slab. It is assumed that the initial condition for these beams is simply supported under the weight of the precast concrete deck pour (off site). Each steel beam is assumed to carry the weight of the precast deck. After the deck and beams (typically two cast together) are made composite (forming a prefabricated unit), the unit is assumed to be simply supported when erected. It is assumed that 28-day concrete strength has been reached in the precast deck and it is fully composite with the beams.

The continuous for live load span configuration is analyzed for bending and shear at the pier bent locations. The negative bending moment over the pier is used for connection design.

Design Step 1.3 Design Criteria

Governing specifications: *AASHTO LRFD Bridge Design Specifications (Ninth Edition, 2020)*

Design methodology: Load and Resistance Factor Design (LRFD)

Live Load Requirements: HL-93 and Fatigue Loading

Material Properties:

The structural steel for rolled sections is Grade A709, Grade 50. Plate steel is A709, Grade 50. All concrete is TxDOT Class S.

Structural Steel Yield Strength: $F_y := 50 \text{ ksi}$ STable 6.4.1-1

Structural Steel Ultimate Tensile Strength: $F_u := 65 \text{ ksi}$ STable 6.4.1-1

Rebar Yield Strength: $F_{y_rebar} := 60 \text{ ksi}$ S5.4.3

Concrete 28-Day Compressive Strength: $f'_c := 4000 \text{ psi}$ STable 5.4.2.1

Concrete Density: $w_c := 150 \text{ pcf}$ STable 3.5.1-1

Steel Density: $w_s := 490 \text{ pcf}$ STable 3.5.1-1

Modulus of Elasticity - Steel: $E_{steel} := 29000 \text{ ksi}$

Modulus of Elasticity - Concrete: $E_{concrete} := \left(\left(\left(\frac{w_c}{\text{pcf}} \right)^{1.5} \cdot 33 \cdot \sqrt{\frac{f'_c}{\text{psi}}} \right) \right) \cdot 1 \text{ ksi}$
 $E_{concrete} = 3834.3 \text{ ksi}$ CEquation5.4.2.4-2

Modular Ratio (Steel to Concrete): $n := \frac{E_{steel}}{E_{concrete}} = 7.6$

Beam Section Properties (W33x201):

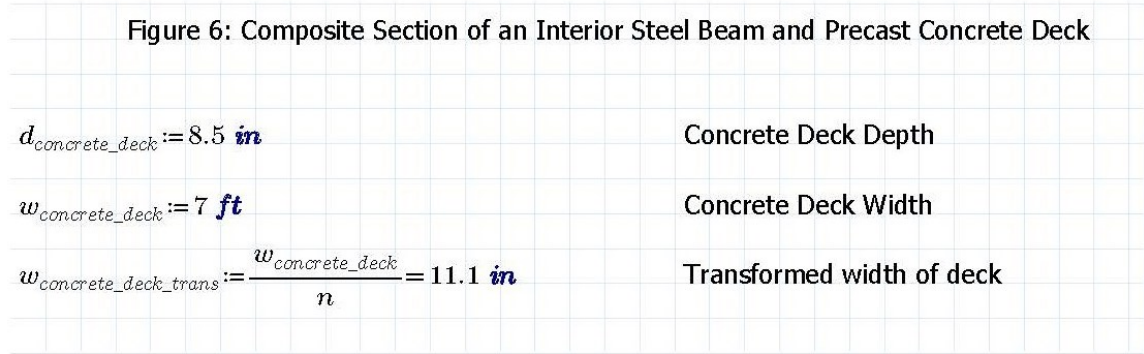
Top Flange: $t_f := 1.15 \text{ in}$ $b_f := 15.7 \text{ in}$

Bottom Flange: $t_f = 1.2 \text{ in}$ $b_f = 15.7 \text{ in}$

Beam Depth: $d_{beam} := 33.7 \text{ in}$ $h := d_{beam} - 2 \cdot t_f = 31.4 \text{ in}$

Web: $t_w := 0.715 \text{ in}$

	$h := d_{beam} - 2 \cdot t_f = 31.4 \text{ in}$	
Moment of Interia (MOI):	$I_{x_steel_beam} := 11600 \text{ in}^4$	
Elastic Section Modulus of x-axis	$S_{x_steel_beam} := 686 \text{ in}^3$	
Plastic Section Modulus of x-axis	$Z_{x_steel_beam} := 773 \text{ in}^3$	
Cross Section Area:	$A_{steel_beam} := 59.1 \text{ in}^2$	
Workable Gage for Inner Flange Holes:	$gage := 5.5 \text{ in}$	
Bolt Information:		
A325 high strength bolts chosen		
$d_b := 1.0 \text{ in}$	Bolt Diameter, STable 6.13.2.4.2-1	
$d_h := d_b + \frac{1}{4} \text{ in} = 1.250 \text{ in}$	Oversize hole diameter, STable 6.13.2.4.2-1	
$F_{ub} := 120 \text{ ksi}$	STable 6.4.3.1.1-1	
Connection Plate Information:		
A709, Grade 50 Steel		
$F_{yp} := 50 \cdot \text{ksi}$		
$F_{up} := 65 \cdot \text{ksi}$		
Longitudinal Reinforcement: (within the effective width)		
$d_{rebar} := 0.625 \text{ in}$	#5 rebar diameter	
$A_{rebar} := 0.31 \text{ in}^2$	Area of each #5 rebar	
$n_{barTop} := 15$	Number of top longitudinal bars	
$n_{barBot} := 10$	Number of bottom longitudinal bars	



$A_{concrete_deck} := d_{concrete_deck} \cdot w_{concrete_deck} = 714.0 \text{ in}^2$	Concrete Deck Area
$d_{haunch} := 2.0 \text{ in}$	Haunch Depth
$w_{haunch} := b_f$	Haunch width
$w_{haunch_trans} := \frac{w_{haunch}}{n} = 2.1 \text{ in}$	Transformed width of haunch
Composite Section Properties (Pier Bent Location):	
Two sections are analyzed:	
<ul style="list-style-type: none"> - Full composite section including the concrete deck slab - Steel composite section including the rebar (no concrete) 	
Neutral Axis of Composite Section	
$ybar_{steel_beam} := \frac{d_{beam}}{2} = 16.9 \text{ in}$	Neutral axis of steel beam
$A_{rebar_top} := A_{rebar} \cdot n_{barTop} = 4.7 \text{ in}^2$	Area of top mat of rebar
$A_{rebar_bottom} := A_{rebar} \cdot n_{barBot} = 3.1 \text{ in}^2$	Area of bottom mat of rebar
$ybar_{rebar_top} := 41.7 \text{ in}$	Neutral axis of top rebar
$ybar_{rebar_bottom} := 36.1 \text{ in}$	Neutral axis of bottom rebar
$A_{haunch_trans} := w_{haunch_trans} \cdot d_{haunch} = 4.2 \text{ in}^2$	Area of transformed haunch
$A_{conc_deck_trans} := w_{concrete_deck_trans} \cdot d_{concrete_deck} = 94.4 \text{ in}^2$	Area of transformed deck
$ybar_{haunch} := d_{beam} + \frac{d_{haunch}}{2} = 34.7 \text{ in}$	Neutral axis of haunch
$ybar_{concrete_deck} := d_{beam} + d_{haunch} + \frac{d_{concrete_deck}}{2} = 40.0 \text{ in}$	Neutral axis of deck
$ybar_{Full} := \frac{A_{steel_beam} \cdot ybar_{steel_beam} + A_{rebar_top} \cdot ybar_{rebar_top} + A_{rebar_bottom} \cdot ybar_{rebar_bottom} + A_{haunch_trans} \cdot ybar_{haunch} + A_{conc_deck_trans} \cdot ybar_{concrete_deck}}{A_{steel_beam} + A_{rebar_top} + A_{rebar_bottom} + A_{haunch_trans} + A_{conc_deck_trans}}$	
$ybar_{Full} = 31.5 \text{ in}$	Full composite neutral axis (from bottom of beam)
$ybar_{SO} := \frac{A_{steel_beam} \cdot ybar_{steel_beam} + A_{rebar_top} \cdot ybar_{rebar_top} + A_{rebar_bottom} \cdot ybar_{rebar_bottom}}{A_{steel_beam} + A_{rebar_top} + A_{rebar_bottom}}$	
$ybar_{SO} = 19.5 \text{ in}$	Steel only composite neutral axis (from bottom of beam)

Moment of Inertia (MOI) of Each Beam Section

$I_{x_steel_beam} = 11600.0 \text{ in}^4$	MOI of Steel Beam
$I_{rebar_top} := \frac{\pi \cdot (d_{rebar})^4}{4} \cdot n_{barTop} = 1.8 \text{ in}^4$	MOI of top rebar
$I_{rebar_bottom} := \frac{\pi \cdot (d_{rebar})^4}{4} \cdot n_{barBot} = 1.2 \text{ in}^4$	MOI of bottom rebar
$I_{haunch} := \frac{w_{haunch_trans} \cdot d_{haunch}^3}{12} = 1.4 \text{ in}^4$	MOI of haunch
$I_{concrete_deck} := \frac{w_{concrete_deck_trans} \cdot d_{concrete_deck}^3}{12} = 568.4 \text{ in}^4$	MOI of deck

Distances from overall neutral axis to each individual neutral axis

Full Composite Section

$$dist_{steel_beam_F} := |ybar_{steel_beam} - ybar_{Full}| = 14.7 \text{ in}$$

$$dist_{top_rebar_F} := |ybar_{rebar_top} - ybar_{Full}| = 10.2 \text{ in}$$

$$dist_{bottom_rebar_F} := |ybar_{rebar_bottom} - ybar_{Full}| = 4.6 \text{ in}$$

$$dist_{haunch_F} := |ybar_{haunch} - ybar_{Full}| = 3.2 \text{ in}$$

$$dist_{concrete_deck_F} := |ybar_{concrete_deck} - ybar_{Full}| = 8.4 \text{ in}$$

Steel Only Composite Section

$$dist_{steel_beam_S} := |ybar_{steel_beam} - ybar_{SO}| = 2.6 \text{ in}$$

$$dist_{top_rebar_S} := |ybar_{rebar_top} - ybar_{SO}| = 22.2 \text{ in}$$

$$dist_{bottom_rebar_S} := |ybar_{rebar_bottom} - ybar_{SO}| = 16.6 \text{ in}$$

MOI using the parallel axis theorem

Full Composite Section

$$I_{steel_beam_pat_F} := I_{x_steel_beam} + A_{steel_beam} \cdot dist_{steel_beam_F}^2 = 24356.1 \text{ in}^4$$

$$I_{rebar_top_pat_F} := I_{rebar_top} + A_{rebar_top} \cdot dist_{top_rebar_F}^2 = 481.7 \text{ in}^4$$

$$I_{rebar_bottom_pat_F} := I_{rebar_bottom} + A_{rebar_bottom} \cdot dist_{bottom_rebar_F}^2 = 65.6 \text{ in}^4$$

$$I_{haunch_pat_F} := I_{haunch} + A_{haunch_trans} \cdot dist_{haunch_F}^2 = 42.8 \text{ in}^4$$

$$I_{concrete_deck_pat_F} := I_{concrete_deck} + A_{conc_deck_trans} \cdot dist_{concrete_deck_F}^2 = 7242.9 \text{ in}^4$$

$$I_{Full} := I_{steel_beam_pat_F} + I_{rebar_top_pat_F} + I_{rebar_bottom_pat_F} + I_{haunch_pat_F} + I_{concrete_deck_pat_F}$$

$$I_{Full} = 32189 \text{ in}^4$$

Full Composite Section Moment of Inertia

Steel Only Composite Section

$$I_{steel_beam_pat_S} := I_{x_steel_beam} + A_{steel_beam} \cdot dist_{steel_beam_S}^2 = 12006.1 \text{ in}^4$$

$$I_{rebar_top_pat_S} := I_{rebar_top} + A_{rebar_top} \cdot dist_{top_rebar_S}^2 = 2299.5 \text{ in}^4$$

$$I_{rebar_bottom_pat_S} := I_{rebar_bottom} + A_{rebar_bottom} \cdot dist_{bottom_rebar_S}^2 = 858.4 \text{ in}^4$$

$$I_{SO} := I_{steel_beam_pat_S} + I_{rebar_top_pat_S} + I_{rebar_bottom_pat_S}$$

$$I_{SO} = 15164 \text{ in}^4$$

Steel Only Composite Section Moment of Inertia

Neutral axis from bottom and top

Full Composite Section

$$ybar_{b_Full} := ybar_{Full} = 31.5 \text{ in} \quad \text{bottom of steel}$$

$$ybar_{t_Full} := d_{beam} + d_{haunch} + d_{concrete_deck} - ybar_{b_Full} = 12.7 \text{ in} \quad \text{top of deck}$$

Steel Only Composite Section

$$ybar_{b_SO} := ybar_{SO} = 19.5 \text{ in} \quad \text{bottom of steel}$$

$$ybar_{t_SO} := d_{beam} - ybar_{b_SO} = 14.2 \text{ in} \quad \text{top of steel beam}$$

Section Modulus from bottom and top

Full Composite Section

$$S_{wb_Full} := \frac{I_{Full}}{ybar_{b_Full}} = 1020.5 \text{ in}^3 \quad \text{bottom of steel}$$

$$S_{wt_Full} := \frac{I_{Full}}{ybar_{t_Full}} = 2542.9 \text{ in}^3 \quad \text{top of deck}$$

Steel Only Composite Section

$$S_{wb_SO} := \frac{I_{SO}}{ybar_{b_SO}} = 778.8 \text{ in}^3 \quad \text{bottom of steel}$$

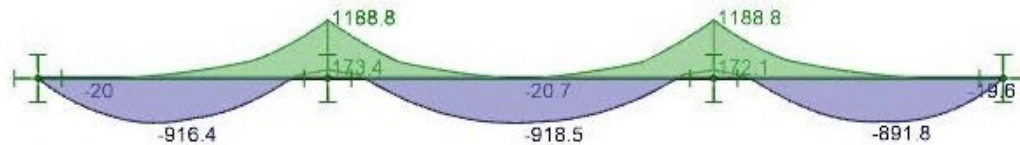
$$S_{wt_SO} := \frac{I_{SO}}{ybar_{t_SO}} = 1065.7 \text{ in}^3 \quad \text{top of steel beam}$$

Design Step 1.4 Compute Live Load Effects

LL + IM (IM=1.33)

S3.6.1.3.1

Below is an envelope of HL-93 loading controlling case. Note RISA software used.

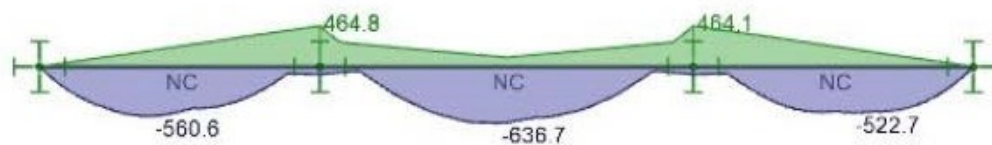


$M_{LL_{max_neg}} := -1189 \text{ kip} \cdot \text{ft}$ HL93 back-to-back trucks with lane load

No positive bending moment at the pier bent locations

FATIGUE LL + IM (IM=1.15)

The fatigue truck was analyzed. Below is the controlling positive and negative bending moment at the pier bent locations.



$M_{fat_{max_pos}} := 84 \text{ kip} \cdot \text{ft}$

$M_{fat_{max_neg}} := -465 \text{ kip} \cdot \text{ft}$

Design Step 1.5 Compute Live Load Distribution Factor

These calculations are only for the interior beams.

$$S := 7 \quad \text{beam spacing}$$

$$t_s := d_{\text{concrete_deck}} = 8.5 \text{ in} \quad \text{deck slab thickness}$$

$$L_1 := 60 \text{ ft} \quad L_2 := 80 \text{ ft} \quad L_3 := 60 \text{ ft} \quad \text{span lengths}$$

$$\bar{y}_{\text{concrete_deck}} := d_{\text{beam}} + d_{\text{haunch}} + \frac{d_{\text{concrete_deck}}}{2} = 40.0 \text{ in} \quad \text{Neutral axis of deck}$$

$$e_g := \bar{y}_{\text{concrete_deck}} - \bar{y}_{\text{steel_beam}} = 23.1 \text{ in}$$

$$K_g := n \cdot \left(\frac{I_{x_{\text{steel_beam}}}}{\text{in}^4} + \frac{A_{\text{steel_beam}}}{\text{in}^2} \cdot \left(\frac{e_g}{\text{in}} \right)^2 \right) = 326257.6 \quad \text{SEq. 4.6.2.2.1-1}$$

The shortest span length was used because that will give the higher g value (worst case)

$$L_{\min} := \min(L_1, L_2, L_3) = 60.0 \text{ ft}$$

One design lane loaded (STable 4.6.2.2.2b-1)

$$g_{m1} := 0.06 + \left(\frac{S}{14} \right)^{0.4} \cdot \left(\frac{S}{\left(\frac{L_{\min}}{\text{ft}} \right)} \right)^{0.3} \cdot \left(\frac{K_g}{12 \cdot \left(\frac{L_{\min}}{\text{ft}} \right) \cdot \left(\frac{t_s^3}{\text{in}^3} \right)} \right)^{0.1} = 0.45$$

Two or more design lanes loaded (STable 4.6.2.2.2b-1)

$$g_{m2} := 0.075 + \left(\frac{S}{9.5} \right)^{0.6} \cdot \left(\frac{S}{\left(\frac{L_{\min}}{\text{ft}} \right)} \right)^{0.2} \cdot \left(\frac{K_g}{12 \cdot \left(\frac{L_{\min}}{\text{ft}} \right) \cdot \left(\frac{t_s^3}{\text{in}^3} \right)} \right)^{0.1} = 0.60$$

$$g_m := \max(g_{m1}, g_{m2}) = 0.60 \quad \text{controlling distribution factor (lanes/beam)}$$

Design Step 1.6 Moment per Beam

The following is only for interior beams.

LL + IM (IM=1.33)

$$M_{LL_pos} := 0 \text{ kip} \cdot \text{ft} \quad \text{positive moment over pier due to service live load}$$

$$M_{LL_neg} := M_{LL_max_neg} \cdot g_m = -714.0 \text{ kip} \cdot \text{ft} \quad \text{Negative Moment due to service live load}$$

FATIGUE LL + IM (IM=1.15)

$$M_{fat_pos} := M_{fat_max_pos} \cdot g_m = 50.4 \text{ kip} \cdot \text{ft} \quad \text{Positive Moment due to Fatigue Load}$$

$$M_{fat_neg} := M_{fat_max_neg} \cdot g_m = -279.3 \text{ kip} \cdot \text{ft} \quad \text{Negative Moment due to Fatigue Load}$$

Strength I

$$M_{LL_neg_StrI} := 1.75 \cdot M_{LL_neg} = -1249.6 \text{ kip} \cdot \text{ft} \quad \text{Negative Moment due to live load}$$

Service II

$$M_{LL_neg_ServII} := 1.3 \cdot M_{LL_neg} = -928.3 \text{ kip} \cdot \text{ft} \quad \text{Negative Moment due to live load}$$

Fatigue I

$$M_{fat_pos_FatI} := 1.75 \cdot M_{fat_pos} = 88.3 \text{ kip} \cdot \text{ft} \quad \text{Positive Moment due to Fatigue Load}$$

$$M_{fat_neg_FatI} := 1.75 \cdot M_{fat_neg} = -488.7 \text{ kip} \cdot \text{ft} \quad \text{Negative Moment due to Fatigue Load}$$

Design Step 1.7 Minimum Negative Flexure Concrete Deck Reinforcement

The area of the longitudinal reinforcement must be at least 1% of the cross-sectional area of the deck slab (S6.10.1.7)

$$A_{rebar_Total} := A_{rebar_top} + A_{rebar_bottom} = 7.8 \text{ in}^2 > 1\% \cdot A_{concrete_deck} = 7.1 \text{ in}^2$$

Service II stress check

$$\phi := 0.9 \quad \text{S6.10.1.7}$$

$$f_r := 0.24 \cdot \sqrt{\frac{f'_c}{1 \text{ ksi}}} \text{ ksi} = 0.48 \text{ ksi} \quad \text{modulus of rupture (S6.10.1.7)}$$

$$\phi \cdot f_r = 0.432 \text{ ksi} \quad \text{tensile stress limit (S6.10.1.7)}$$

$$f_{min_rein_check} := \frac{-M_{LL_neg_ServII}}{S_{xt_Full} \cdot n} = 0.58 \text{ ksi} > \phi \cdot f_r = 0.432 \text{ ksi} \quad \text{No Good}$$

The tensile stresses at the top of the deck exceed the limit. To reduce the tensile stress in the deck (and meet the specification), external post-tensioning is applied, which precompresses the section (calculated later).

To avoid post-tensioning, the section modulus may be increased. Increasing the longitudinal reinforcement will only have a minor impact and may not be sufficient. In most cases the steel section will need to be increased if the check above is not sufficient.

Note the deck stresses should be checked outside the limits of the post-tensioning. This step is not included in this design example.

Design Step 1.8 Flexural Steel Stresses

Strength I Limit State:

At the strength limit state, the section stresses must be checked for tension flanges with holes (S6.10.1.8).

$$f_b := \frac{M_{LL_neg_StrI}}{S_{xb_SO}} = -19.3 \text{ ksi} \quad \text{bottom flange stresses (Strength I limit state)}$$

$$f_t := \frac{-M_{LL_neg_StrI}}{S_{xt_SO}} = 14.1 \text{ ksi} \quad \text{top flange stresses (Strength I limit state)}$$

$$A_n := t_f \cdot (b_f - 2 \cdot d_h) = 15.2 \text{ in}^2 \quad \text{net tension flange area}$$

$$A_g := t_f \cdot b_f = 18.1 \text{ in}^2 \quad \text{gross tension flange area}$$

$$f_{tLimit} := \min \left(\left(0.84 \cdot \frac{A_n}{A_g} \cdot F_u \right), F_y \right) = 45.9 \text{ ksi} \quad \text{SEq. 6.10.1.8-1}$$

$$f_t = 14.1 \text{ ksi} < f_{tLimit} \quad \text{OK}$$

Service II Limit State:

At the service state, the section stresses must be checked for permanent deformation (S6.10.4.2.2)

$$R_h := 1.0 \quad \text{S6.10.1.10.1}$$

$$f_{top_serviceII} := \frac{-M_{LL_neg_ServII}}{S_{xt_SO}} = 10.5 \text{ ksi} \quad \text{Service II top flange stress}$$

$$f_{f_top} := f_{top_serviceII} = 10.5 \text{ ksi} < 0.95 \cdot R_h \cdot F_y = 47.5 \text{ ksi} \quad \text{OK} \quad \text{SEq. 6.10.4.2.2-1}$$

$$f_{bot_serviceII} := \frac{M_{LL_neg_ServII}}{S_{xb_SO}} = -14.3 \text{ ksi} \quad \text{Service II bottom flange stress}$$

$$f_{f_bot} := f_{bot_serviceII} = -14.3 \text{ ksi}$$

$$f_l := 0 \text{ ksi} \quad \text{flange lateral bending (S6.10.4.2)}$$

$$\left| f_{f_bot} + \frac{f_l}{2} \right| = 14.3 \text{ ksi} < 0.95 \cdot R_h \cdot F_y = 47.5 \text{ ksi} \quad \text{OK} \quad \text{SEq. 6.10.4.2.2-2}$$

Design Step 1.9 Flexural Capacity (SAppendix A6)

Calculate of Ybar and Mp for the cross-section in Negative Flexure:

Web Length: $D := h = 31.4 \text{ in}$

Web Cross-Area: $A_w := t_w \cdot D = 22.5 \text{ in}^2$

Plastic Force in the Compression Flange: $P_c := F_y \cdot t_f \cdot b_f = 902.8 \text{ kip}$

Plastic Force in the web: $P_w := F_y \cdot A_w = 1122.6 \text{ kip}$

Plastic Force in the Tension Flange: $P_t := F_y \cdot t_f \cdot b_f = 902.8 \text{ kip}$

Plastic Force in the Top Rebar Mat: $P_{rt} := F_{y_rebar} \cdot A_{rebar_top} = 279.0 \text{ kip}$

Plastic Force in the Bottom Rebar Mat: $P_{rb} := F_{y_rebar} \cdot A_{rebar_bottom} = 186.0 \text{ kip}$

$$P_c + P_w = 2025.3 \text{ kip} \geq P_t + P_{rt} + P_{rb} = 1367.8 \text{ kip} \quad \text{STable D6.1-2}$$

Case 1: PNA in the Web

$$Y_{p_bar} := \left(\frac{D}{2} \right) \cdot \left(\frac{P_c - P_t - P_{rt} - P_{rb}}{P_w} + 1 \right) = 9.2 \text{ in} \quad \text{STable D6.1-2}$$

Distance from top rebar mat to Ybar: $d_{rt} := |ybar_{rebar_top} - Y_{p_bar}| = 32.5 \text{ in}$

Distance from bottom rebar mat to Ybar: $d_{rb} := |ybar_{rebar_bottom} - Y_{p_bar}| = 26.9 \text{ in}$

Distance from the midthickness of top flange to Ybar: $d_t := \left| D + \frac{t_f}{2} - Y_{p_bar} \right| = 22.8 \text{ in}$

Distance from the midthickness of bottom flange to Ybar: $d_c := \left| \frac{t_f}{2} - Y_{p_bar} \right| = 8.6 \text{ in}$

Plastic Moment:

$$M_p := \frac{P_w}{2 \cdot D} \cdot \left(Y_{p_bar}^2 + (D - Y_{p_bar})^2 \right) + (P_{rt} \cdot d_{rt} + P_{rb} \cdot d_{rb} + P_t \cdot d_t + P_c \cdot d_c) = 4395.2 \text{ kip} \cdot \text{ft}$$

Depth of the Web in Compression at the plastic moment:

$$D_{cp} := \frac{D}{2 \cdot F_y \cdot A_w} \cdot (P_t + P_w + P_{rt} + P_{rb} - P_c) = 22.2 \text{ in} \quad \text{SEq. D6.3.2-2}$$

$$F_y = \frac{M_{D1}}{S_{NC}} + \frac{M_{D2}}{S_{LT}} + \frac{M_{AD}}{S_{ST}} \quad \text{SEq. D6.2.2-1}$$

Therefore,

$$M_{ADT} := F_y \cdot S_{xt_SO} = 4440.5 \text{ kip} \cdot \text{ft}$$

$$M_{ADC} := F_y \cdot S_{xb_SO} = 3244.9 \text{ kip} \cdot \text{ft}$$

$$M_y = M_{D1} + M_{D2} + M_{AD} \quad \text{SEq. D6.2.2-2}$$

Therefore,

$$M_{yc} := M_{ADC} = 3244.9 \text{ kip} \cdot \text{ft}$$

$$M_{yt} := M_{ADT} = 4440.5 \text{ kip} \cdot \text{ft}$$

$$M_y := \min(M_{yc}, M_{yt}) = 3244.9 \text{ kip} \cdot \text{ft} \quad \text{Yield moment in negative flexure}$$

$$\text{Web Slenderness: } \frac{2 \cdot D_{cp}}{t_w} = 62.1 \leq 3.76 \cdot \sqrt{\frac{E_{steel}}{F_y}} = 90.6 \quad \text{OK} \quad \text{SEq. 6.10.6.2.2-1}$$

Therefore, Compact web;

$$\text{The Web Plastification Factor: } R_{pc} := \frac{M_p}{M_{yc}} = 1.4 \quad (\text{SA6.2.1-5})$$

$$R_{pt} := \frac{M_p}{M_{yt}} = 1.0 \quad (\text{SA6.2.1-6})$$

$$\phi_f := 1.0 \quad \text{For flexure (S6.5.4.2)}$$

Section with Continuously Braced Compression Flanges:

$$M_u := -M_{LL_neg_StrI} = 1249.6 \text{ kip} \cdot \text{ft} \quad (\text{SA6.1.3-1})$$

$$M_u < \phi_f \cdot R_{pc} \cdot M_{yc} = 4395.2 \text{ kip} \cdot \text{ft} \quad \text{OK}$$

Section with Continuously Braced Tension Flanges:

$$M_u < \phi_f \cdot R_{pt} \cdot M_{yt} = 4395.2 \text{ kip} \cdot \text{ft} \quad \text{OK} \quad (\text{SA6.1.4-1})$$

Design Step 2: Recommended Connection Design

Design Step 2.1 Flexural Resistance by the Flange

Flange Gross, Net, and Effective Areas

$$F_{yf} := F_y = 50.0 \text{ ksi} \quad \text{A709 GR.50 Steel Yield Strength}$$

$$\phi_u := 0.8 \quad \text{S6.5.4.2}$$

$$\phi_y := 0.95 \quad \text{S6.5.4.2}$$

$$A_g := b_f \cdot t_f = 18.1 \text{ in}^2 \quad \text{gross area of flange}$$

$$A_n := A_g - 4 \cdot (d_h \cdot t_f) = 12.3 \text{ in}^2 \quad \text{net area of flange}$$

Strength Limit State:

Determine the minimum design forces for the controlling flange of the negative moment over the pier case.

Maximum flexural stress due to the factored loads at the midthickness of the controlling flange at the point of splice:

$$A_e := A_n \cdot \left(\frac{\phi_u \cdot F_u}{\phi_y \cdot F_{yf}} \right) = 13.5 \text{ in}^2 < A_g, \text{ OK} \quad \text{SEq. 6.13.6.1.3b-2}$$

$$P_{fy} := F_{yf} \cdot A_e = 673.5 \text{ kip} \quad \text{Design yield resistance of each flange (S6.13.6.1.3b-1)}$$

Design Step 2.2 Top Flange Splice Plates

Top Plate Dimension Parameters:

$$\text{Plate Thickness:} \quad t_{plate} := \frac{15}{16} \text{ in}$$

$$\text{Number of Bolts:} \quad n_{bolts} := 12$$

$$\text{Bolt Diameter:} \quad d_b = 1.0 \text{ in}$$

$$\text{Bolt Shank Area:} \quad A_b := \frac{\pi \cdot d_b^2}{4} = 0.785 \text{ in}^2$$

$$\text{Bolt Tensile Strength:} \quad F_{ub} = 120 \text{ ksi}$$

$$\text{Bolt Hole Diameter:} \quad d_h = 1.25 \text{ in}$$

Tensile Resistance of Top Flange Top Plate: Strength Limit State (S6.8.2)

Plate Yielding (S6.8.2.1-1)

$$F_{yp} = 50.0 \text{ ksi} \quad \text{connection plate yield stress}$$

$$w_{top_plate} := 15.75 \text{ in} \quad \text{width of top plate}$$

$$A_{g_top_plate} := w_{top_plate} \cdot t_{plate} = 14.8 \text{ in}^2 \quad \text{gross area of top plate}$$

$$\phi_y := 0.95$$

$$\phi P_{r_yield_top_plate} := \phi_y \cdot A_{g_top_plate} \cdot F_{yp} = 701 \text{ kip} > \frac{P_{fy}}{2} = 337 \text{ kip}, \text{ OK}$$

Flange Plate Fracture (S6.8.2.1-2)

$$A_{n_top} := t_{plate} \cdot w_{top_plate} - 4 \cdot t_{plate} \cdot d_h = 10.1 \text{ in}^2 \quad \text{net area of the top plate}$$

$$R_p := 1.0$$

$$U := 1.0$$

$$\phi P_{r_ult_top_plate} := \phi_u \cdot A_{n_top} \cdot F_{up} \cdot R_p \cdot U = 524 \text{ kip} > \frac{P_{fy}}{2} = 337 \text{ kip}, \text{ OK}$$

Block Shear (S6.13.4)

$$\phi_{bs} := 0.80$$

$$R_p := 1.0$$

$$A_{tn} := (w_{top_plate} \cdot t_{plate}) - t_{plate} \cdot (2 \cdot 1.5 \text{ in} + 3 \cdot d_h) = 8.4 \text{ in}^2 \quad \text{Net tension area}$$

$$A_{vg} := 2 \cdot (2 \cdot 3 \text{ in} + 2.5 \text{ in}) \cdot t_{plate} = 15.9 \text{ in}^2 \quad \text{Gross Shear Area}$$

$$A_{vn} := A_{vg} - 2 \cdot (t_{plate} \cdot d_h \cdot 2.5) = 10.1 \text{ in}^2 \quad \text{Net Shear Area}$$

$$U_{bs} := 1.0 \quad \text{Reduction Factor}$$

$$R_{r_top_plate_blockshear} := \phi_{bs} \cdot R_p \cdot \min(0.58 \cdot F_{up} \cdot A_{vn} + U_{bs} \cdot F_{up} \cdot A_{tn}, 0.58 \cdot F_{yp} \cdot A_{vg} + U_{bs} \cdot F_{yp} \cdot A_{tn})$$

$$R_{r_top_plate_blockshear} = 743 \text{ kip} > \frac{P_{fy}}{2} = 337 \text{ kip}, \text{ OK}$$

Tensile Resistance of Top Flange Bottom Plates: Strength Limit State (S6.8.2)

Plate Yielding (S6.8.2.1-1)

$$w_{bot_plate} := 6 \text{ in}$$

width of bottom plates

$$n_{bp} := 2$$

number of top flange bottom plates

$$A_{g_bot_plate} := n_{bp} \cdot w_{bot_plate} \cdot t_{plate} = 11.3 \text{ in}^2$$

gross area of the bottom plates

$$\phi_y := 0.95$$

$$\phi P_{r_yield_bot_plate} := \phi_y \cdot A_{g_bot_plate} \cdot F_{yp} = 534 \text{ kip} > \frac{P_{fy}}{2} = 337 \text{ kip}, \text{ OK}$$

Flange Plate Fracture (S6.8.2.1-2)

$$A_{n_bot} := t_{plate} \cdot 2 \cdot w_{bot_plate} - 4 \cdot t_{plate} \cdot d_h = 6.6 \text{ in}^2$$

net area of the bottom plates

$$R_p := 1.0$$

$$U := 1.0$$

$$\phi P_{r_ult_bot_plate} := \phi_u \cdot A_{n_bot} \cdot F_{up} \cdot R_p \cdot U = 341 \text{ kip} > \frac{P_{fy}}{2} = 337 \text{ kip}, \text{ OK}$$

Block Shear (S6.13.4)

$$R_p := 1.0$$

$$A_{tn} := (2 \cdot w_{bot_plate} \cdot t_{plate}) - t_{plate} \cdot (4 \cdot 1.5 \text{ in} + 2 \cdot d_h) = 3.3 \text{ in}^2 \quad \text{Net tension area}$$

$$A_{vg} := 4 \cdot (2 \cdot 3 \text{ in} + 2.5 \text{ in}) \cdot t_{plate} = 31.9 \text{ in}^2 \quad \text{Gross Shear Area}$$

$$A_{vn} := A_{vg} - 4 \cdot (t_{plate} \cdot d_h \cdot 2.5) = 20.2 \text{ in}^2 \quad \text{Net Shear Area}$$

$$U_{bs} := 1.0 \quad \text{Reduction Factor}$$

$$R_{r_bot_plate_blockshear} := \phi_{bs} \cdot R_p \cdot \min(0.58 \cdot F_{up} \cdot A_{vn} + U_{bs} \cdot F_{up} \cdot A_{tn}, 0.58 \cdot F_{yp} \cdot A_{vg} + U_{bs} \cdot F_{up} \cdot A_{tn})$$

$$R_{r_bot_plate_blockshear} = 779 \text{ kip} > \frac{P_{fy}}{2} = 337 \text{ kip}, \text{ OK}$$

Design Step 2.3 Top Flange Bolts

Slip Resistance: Permanent Deflection Service Limit State (S6.13.2.8)

$$A_g = 18.1 \text{ in}^2$$

$$P_s := f_{top_serviceII} \cdot A_g = 189 \text{ kip}$$

Service II top flange design force

$$N_s := 2$$

Number of slip planes

$$P_t := 51 \text{ kip}$$

Minimum bolt tension (A325), STable 6.13.2.8-1

$$K_h := 0.85$$

Hole size factor (oversize), STable 6.13.2.8-2

$$K_s := 0.5$$

Surface condition factor (Class B), STable 6.13.2.8-3

$$R_{n_boltslip} := K_s \cdot K_h \cdot P_t \cdot N_s \cdot n_{bolts} = 520 \text{ kip} > P_s = 189 \text{ kip}, \text{ SEq. 6.13.2.8-1}$$

Tip: Friction Coefficient Selection

Class A surface has a friction coefficient of 0.3. This example uses Class B surface conditions, which allows for a coefficient of 0.5. If Class A surface conditions are needed, then additional bolt tension may be required. This can be achieved using larger diameter bolts or higher grade (e.g., A490). Using standard holes improved the hole size factor (increases the slip resistance). However, this is not recommended due to potential fit-up issues in the field.

Shear Resistance: Strength Limit State (S6.13.2.7)

$$N_s := 2$$

number of shear planes

$$\phi_s := 0.8$$

S6.5.4.2

$$R_{n_boltshear} := \phi_s \cdot 0.45 \cdot A_b \cdot F_{ub} \cdot N_s \cdot n_{bolts} = 814 \text{ kip}$$

SEq. 6.13.2.7-2

Flange Bolt Bearing and Tearout (S6.13.2.9)

$$\phi_{bb} := 0.8$$

$$t := \min(t_{plate}, t_f) = 0.9 \text{ in} \quad \text{min thickness of plate or flange}$$

$$R_{n_boltbearing} := \phi_{bb} \cdot 2.4 \cdot d_b \cdot t \cdot F_u = 117 \text{ kip} \quad \text{SEq. 6.13.2.9-1, per bolt}$$

$$s := 3 \cdot d_b = 3.0 \text{ in} \quad \text{bolt spacing}$$

$$d_{edge} := 1.25 \text{ in} \quad \text{minimum edge distance STable 6.13.2.6.6-1}$$

$$L_{c_end} := d_{edge} - \frac{d_h}{2} = 0.6 \text{ in} \quad \text{end clear distance}$$

$$L_{c_int} := s - d_h = 1.8 \text{ in} \quad \text{Interior clear distance}$$

$$R_{n_tearout_int} := \phi_{bb} \cdot 1.2 \cdot L_{c_int} \cdot t \cdot F_u = 102 \text{ kip} \quad \text{SEq. 6.13.2.9-2, interior bolt tearout}$$

$$R_{n_tearout_end} := \phi_{bb} \cdot 1.2 \cdot L_{c_end} \cdot t \cdot F_u = 37 \text{ kip} \quad \text{SEq. 6.13.2.9-2, exterior bolt tearout}$$

$$R_{n_end} := \min(R_{n_boltbearing}, R_{n_tearout_end}) = 37 \text{ kip}$$

$$R_{n_int} := \min(R_{n_boltbearing}, R_{n_tearout_int}) = 102 \text{ kip}$$

$$R_{n_bblto} := 8 \cdot R_{n_int} + 4 \cdot R_{n_end} = 965 \text{ kip} \quad > P_{fy} = 674 \text{ kip}, \text{ OK}$$

Flange Bolts - Minimum spacing (S6.13.2.6)

$$d_b = 1.0 \text{ in}$$

$$s_{min} := 3 \cdot d_b = 3.0 \text{ in} \quad \text{Take } s=3 \text{ in} \quad \text{minumum spacing between center of bolts}$$

$$s := 3.0 \text{ in} \quad \text{spacing between center of bolts}$$

Flange Bolts - Edge and End Distance (S6.13.2.6.6)

Minimum:

Edge distance : 1 1/2 in > 1 1/8 in

Maximum:

Edge distance : 1 1/2 in < 5.00 in or $8 \cdot t_{plate} = 7.5 \text{ in}$

Fatigue Resistance of Splice Plate: Fatigue I Limit State (S6.6.1.2.2)

$$M_{fat_neg} = -279 \text{ kip} \cdot \text{ft}$$

$$M_{fat_pos} = 50.4 \text{ kip} \cdot \text{ft}$$

$$f_{top_pos_fatI} := \frac{M_{fat_pos_FatI}}{S_{xt_SO}} = 1.0 \text{ ksi}$$

$$f_{top_neg_fatI} := \frac{M_{fat_neg_FatI}}{S_{xt_SO}} = -5.5 \text{ ksi}$$

$$\gamma \Delta f := |f_{top_neg_fatI}| + f_{top_pos_fatI} = 6.5 \text{ ksi} \quad \text{SEq. 6.6.1.2.2-1}$$

$$\Delta F_{th} := 16 \text{ ksi} \quad \text{STable 6.6.1.2.5-3, Cat B}$$

$$\Delta F_n := \Delta F_{th} \quad \text{SEq. 6.6.1.2.5-1}$$

$$\Delta P := \gamma \Delta f \cdot b_f \cdot t_f = 117.3 \text{ kip}$$

$$P := \frac{\Delta P}{2} = 58.6 \text{ kip}$$

Top Flange Top Plate:

$$\Delta f_{outer_plate} := \frac{P}{t_{plate} \cdot w_{top_plate}} = 4 \text{ ksi} \quad < \Delta F_n = 16.0 \text{ ksi}, \text{ OK}$$

Top Flange Bottom Plates:

$$\Delta f_{inner_plate} := \frac{P}{2 \cdot t_{plate} \cdot w_{bot_plate}} = 5.2 \text{ ksi} \quad < \Delta F_n = 16.0 \text{ ksi}, \text{ OK}$$

Design Step 2.4 Bottom Flange Bearing Plate

$f_b = -19.3 \text{ ksi}$ Compression stress at bottom steel beam

Select the steel bearing plate dimensions:

$h_{bp} := 8 \text{ in}$ height

$w_{bp} := b_f = 15.7 \text{ in}$ width

$A_{bp} := h_{bp} \cdot w_{bp} = 125.6 \text{ in}^2$ bearing area

Using 5/16" weld all around as minimum weld size (Table 6.13.3.4-1). Plate is in compression only.

The bearing plate stress is considered adequate when the beam bottom flange stresses are sufficient for strength and service limit states (determined earlier).

Tip:

A welded bearing plate design at the bottom flange eliminates many issues when compared with bolted splice plates. It can avoid the narrow space issue between bearing pads over the pier (especially for the long span beams). It is relatively easy and fast to assemble, which is required for ABC applications. It can also avoid the bottom bolt slip issues.

It is recommended to use a relatively thick bearing plate (minimum 1/2").

Design Step 2.5 Flexural Capacity at the Connection

Calculate Mp for the cross-section in Negative Flexure:

Plastic Force in the Bearing Plate: $P_{bp} := F_y \cdot A_{bp} = 6280.0 \text{ kip}$

Plastic Force in the Top Splice Plates: $P_{top} := F_y \cdot (A_{n_top}) = 503.9 \text{ kip}$

Plastic Force in the Bottom Splice Plates: $P_{bot} := F_y \cdot (A_{n_bot}) = 328.1 \text{ kip}$

Plastic Force in the Top Rebar Mat: $P_{rt} := F_{y_rebar} \cdot A_{rebar_top} = 279.0 \text{ kip}$

Plastic Force in the Bottom Rebar Mat: $P_{rb} := F_{y_rebar} \cdot A_{rebar_bottom} = 186.0 \text{ kip}$

Distance from top rebar mat to CG of the bearing plate: $d_{rt} := \left| ybar_{rebar_top} - \left(\frac{h_{bp}}{2} - 1 \text{ in} \right) \right| = 38.7 \text{ in}$

Distance from bottom rebar mat to CG of the bearing plate: $d_{rb} := \left| ybar_{rebar_bottom} - \left(\frac{h_{bp}}{2} - 1 \text{ in} \right) \right| = 33.1 \text{ in}$

Distance from the top splice plate to CG of the bearing plate: $d_{top} := \left| d_{beam} + \frac{t_{plate}}{2} - \left(\frac{h_{bp}}{2} - 1 \text{ in} \right) \right| = 31.2 \text{ in}$

Distance from the bottom splice plate to CG of the bearing plate: $d_{bot} := \left| d_{beam} - \frac{t_{plate}}{2} - \left(\frac{h_{bp}}{2} - 1 \text{ in} \right) \right| = 30.2 \text{ in}$

Plastic Moment:

$$M_p := P_{top} \cdot d_{top} + P_{bot} \cdot d_{bot} + P_{rt} \cdot d_{rt} + P_{rb} \cdot d_{rb} = 3548.3 \text{ kip} \cdot \text{ft}$$

$$\phi_f := 1.0 \quad \text{flexure (S6.5.4.2)}$$

$$M_u := -M_{LL_neg_StrI} = 1249.6 \text{ kip} \cdot \text{ft}$$

$$M_u < \phi_f \cdot M_p = 3548.3 \text{ kip} \cdot \text{ft} \quad \text{OK}$$

Design Step 2.6 Draw Schematic of Final Bolted Field Splice Design

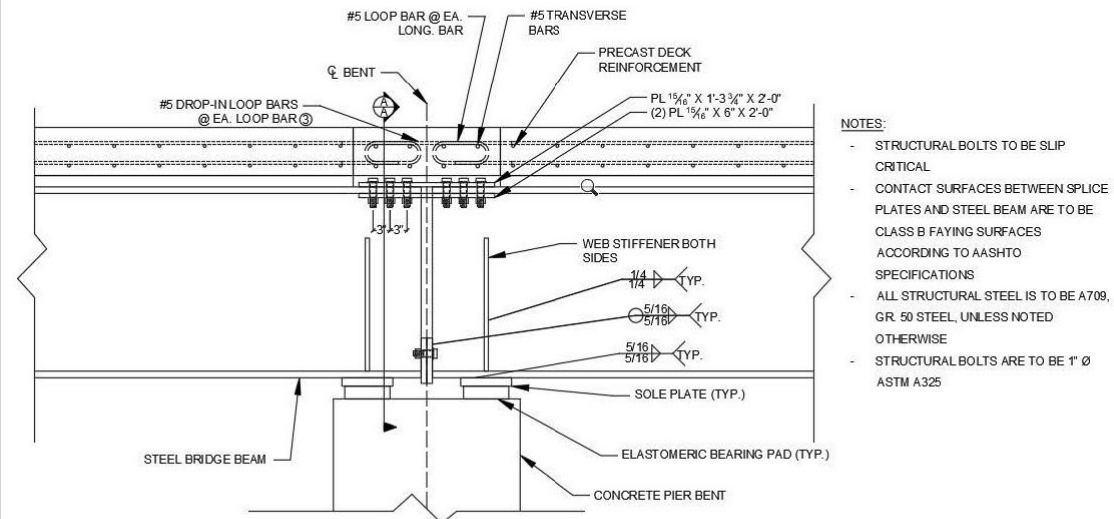


Figure 7: Recommended Connection Design

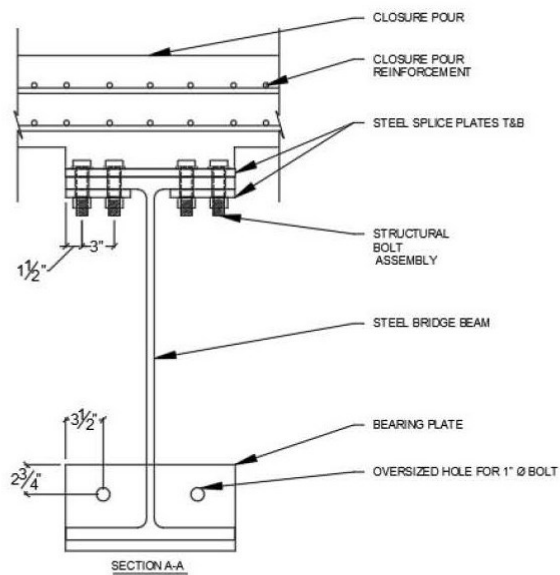


Figure 8: Splice Connection Section

Design Step 2.7 Post-Tensioning Rods and Bracket Design (Optional)

Post-tensioning (PT) rods can be included to minimize deck cracking through precompression of the slab. This is only required if tensile stresses in the slab do not meet the criteria shown earlier in Step 1.7. For this design, the PT rods are required. Note that a larger steel beam section could be utilized to eliminate the need for the PT rods.

PT Rod Diameter Selection: $d_{rod} := 1.375 \text{ in}$

PT Rod Ultimate Stress: $F_{uPT} := 150 \text{ ksi}$

Number of PT Rods $n_r := 2$

Distance from Top Flange to Center of Rod: $d_{rod_to_tf} := 4 \text{ in} + t_f = 5.2 \text{ in}$

This distance depends on the bracket design. It is recommended to connect the bracket to the flange and not the web. Full details of the bracket design are provided later.

Determine New Composite Section Properties (PT Rods and Concrete included):

$A_{rod} := \frac{\pi}{4} \cdot d_{rod}^2 = 1.485 \text{ in}^2$ Area of each PT Rod

$ybar_{rod} := d_{beam} - d_{rod_to_tf} = 28.6 \text{ in}$ Neutral axis of Rods

$$ybar_{PT} := \frac{A_{steel_beam} \cdot ybar_{steel_beam} + A_{haunch_trans} \cdot ybar_{haunch} + A_{conc_deck_trans} \cdot ybar_{concrete_deck} + A_{rebar_top} \cdot ybar_{rebar_top} + A_{rebar_bottom} \cdot ybar_{rebar_bottom} + 2 \cdot A_{rod} \cdot ybar_{rod}}{A_{steel_beam} + A_{haunch_trans} + A_{conc_deck_trans} + A_{rebar_top} + A_{rebar_bottom} + 2 \cdot A_{rod}}$$

$ybar_{PT} = 31.5 \text{ in}$ Composite neutral axis (from bottom of beam) including the PT bars and concrete

$I_{rod} := \frac{\pi \cdot (d_{rod})^4}{64} = 0.2 \text{ in}^4$ MOI of PT Rod

$dist_{rod} := |ybar_{rod} - ybar_{PT}| = 2.9 \text{ in}$ distance to the rod

$I_{rod_pat} := I_{rod} + A_{rod} \cdot dist_{rod}^2 = 13.0 \text{ in}^4$

$I_{PT} := I_{Full} + n_r \cdot I_{rod_pat}$

$I_{PT} = 32215 \text{ in}^4$ composite section MOI with PT bars

$$ybar_{bPT} := ybar_{PT} = 31.5 \text{ in} \quad \text{neutral axis from bottom of the beam}$$

$$ybar_{tPT} := d_{beam} + d_{haunch} + d_{concrete_deck} - ybar_{bPT} = 12.7 \text{ in} \quad \text{neutral axis from the top of the deck}$$

$$S_{xtPT} := \frac{I_{PT}}{ybar_{tPT}} = 2534 \text{ in}^3 \quad \text{section modulus to top of deck}$$

Determine Desired Post Tension Force in Rods

PT Percentage of Ultimate Stress Level: $PT := 0.70$

$$\bar{P} := PT \cdot F_{uPT} \cdot A_{rod} = 155.9 \text{ kip} \quad \text{PT force per rod}$$

Redo the Service II stress check with PT

$$\phi \cdot f_r = 0.432 \text{ ksi} \quad \text{tensile stress limit (S6.10.1.7)}$$

$$y_{bracket} := ybar_{tPT} - d_{concrete_deck} - t_f = 3.1 \text{ in} \quad \text{Distance from N.A. to Bottom of Top flange}$$

$$A_{total} := A_{concrete_deck} + n \cdot (A_{bp} + A_{g_top_plate} + A_{g_bot_plate}) = 1860.7 \text{ in}^2 \quad \text{total area at the connection}$$

$$\sigma_c := \frac{-P \cdot n_r}{A_{total}} + \frac{(-P \cdot n_r) \cdot (ybar_{bPT} - ybar_{rod})}{S_{xtPT} \cdot n} = -0.22 \text{ ksi}$$

Tip:

The PT stress level can be set to achieve no tensile stress in the slab (zero stress). However, losses may occur in the field and loads higher than expected may occur. Therefore, it is recommended to apply higher PT forces producing net compressive deck stresses.

Bolted Bracket to Flange

$$t_p := 1.0 \text{ in} \quad \text{the thickness of the plate vertical to the flange}$$

$$w := 6 \text{ in} \quad \text{the width of the plate vertical to the flange}$$

$$d_{bolt} := 1 \text{ in} \quad \text{Bolt diameter}$$

$$n_{bolts} := 6 \quad \text{number of bolts per bracket}$$

Use A490 Bolts

$s := 3 \text{ in}$ spacing between center of bolts

$s_{end} := 2 \text{ in}$ end edge spacing

Shear Resistance: Strength Limit State (S6.13.2.7)

$A_b := \frac{\pi \cdot d_{bolt}^2}{4} = 0.8 \text{ in}^2$ bolt shank area

$F_{ub} := 150 \text{ ksi}$ (STable 6.4.3.1.1-1)

$N_s := 1$ number of shear plane per bolt

$\phi_s := 0.80$ (S6.5.4.2)

$$R_t := \phi_s \cdot 0.45 \cdot A_b \cdot F_{ub} \cdot N_s \cdot n_{bolts} = 254.5 \text{ kip} > P = 155.9 \text{ kip} \quad \text{SEq.6.13.2.7-2}$$

Slip Resistance: Permanent Deflection Service Limit State (S6.13.2.8)

$K_f := 1.0$ (STable 6.13.2.8-2)

$P_t := 64 \text{ kip}$ (STable 6.13.2.8-1)

$K_s := 0.5$ Surface condition factor (Class B), STable 6.13.2.8-3

$$R_{n_boltslip_bracket} := K_s \cdot K_f \cdot P_t \cdot N_s \cdot n_{bolts} = 192 \text{ kip} > P = 155.9 \text{ kip} \quad \text{SEq. 6.13.2.8-1}$$

Tensile Resistance: (S6.13.2.10)

$$R_{n_nominal_bolttensile} := 0.76 \cdot A_b \cdot F_{ub} \cdot n_{bolts} = 537.2 \text{ kip} > P = 155.9 \text{ kip} \quad \text{SEq.6.13.2.10.2-1}$$

$d_m := 2 \cdot s + 0.5 \cdot 2 \cdot s = 9.0 \text{ in}$ distance from plate edge to center of bolt

$e := 3.75 \text{ in} + \frac{1 \text{ in}}{2} = 4.3 \text{ in}$ distance from center of plate edge to center of rod

$M_{u_rod} := P \cdot e = 662.6 \text{ kip} \cdot \text{in}$ moment due to the rod

$n' := \frac{n_{bolts}}{2}$ one half of the bolts total

neutral axis at center of gravity

$$T_u := \frac{M_{u_rod}}{n' \cdot d_m} = 24.5 \text{ kip} \quad \text{tensile force per bolt due to the rod}$$

Combined Tension and Shear Check : (S6.13.2.11)

$$P_u := \frac{P}{n_{bolts}} = 26.0 \text{ kip}$$

$$R_n := 0.45 \cdot A_b \cdot F_{ub} \cdot N_s = 53.0 \text{ kip} \quad (\text{SEq.6.13.2.7-2})$$

$$\frac{P_u}{R_n} = 0.5 > 0.33$$

$$T_m := n_{bolts} \cdot 0.76 \cdot A_b \cdot F_{ub} \cdot \sqrt{1 - \left(\frac{P_u}{\phi_s \cdot R_n} \right)^2} = 424.6 \text{ kip} > P = 155.9 \text{ kip} \quad \text{OK} \\ (\text{SEq.6.13.2.11-2})$$

Prying Action Check: (S6.13.2.10.4)

$b := 3 \text{ in}$ distance from center of bolt to the toe of fillet of connected part

$a := 3 \text{ in}$ distance from center of bolt to the edge of plate

$t := 1 \text{ in}$ thickness of thinnest connected part

$$Q_u := \left(\frac{3 \cdot b}{8 \cdot a} - \frac{t^3}{20} \right) \cdot P_u = 8.4 \text{ kip} \quad (\text{Eq.6.13.2.10.4-1})$$

$$P_u + Q_u = 34.4 \text{ kip} < T_n := 0.76 \cdot A_b \cdot F_{ub} = 89.5 \text{ kip} \quad \text{OK}$$

Bracket Plates Design

Determine required length of plate: $L_{req} := s \cdot (n - 1) + s_{end} + s = 24.7 \text{ in} \quad L := L_{req} = 24.7 \text{ in}$

$t_{base_plate} := 1 \text{ in}$ thickness of the base plate

$d_h := 1.125 \text{ in}$ bolt standard hole diameter STable 6.13.2.4.2-1

Tensile Resistance of the base plate: Strength Limit State (S6.8.2)

Plate Yielding (S6.8.2.1-1)

$$F_{yp} = 50.0 \text{ ksi} \quad \text{connection plate yield stress}$$

$$w_{base_plate} := 6 \text{ in} \quad \text{width of the base plate}$$

$$A_{g_base_plate} := w_{base_plate} \cdot t_{base_plate} = 6.0 \text{ in}^2 \quad \text{gross area of the baseplate}$$

$$\phi_y := 0.95$$

$$\phi P_{r_yield_base_plate} := \phi_y \cdot A_{g_base_plate} \cdot F_{yp} = 285 \text{ kip} > P = 156 \text{ kip}, \text{ OK}$$

Flange Plate Fracture (S6.8.2.1-2)

$$A_{n_base} := t_{base_plate} \cdot w_{base_plate} - 1 \cdot t_{base_plate} \cdot d_h = 4.9 \text{ in}^2 \quad \text{net area of the top plate}$$

$$R_p := 1.0$$

$$U := 1.0$$

$$\phi P_{r_ult_base_plate} := \phi_u \cdot A_{n_base} \cdot F_{up} \cdot R_p \cdot U = 254 \text{ kip} > P = 156 \text{ kip}, \text{ OK}$$

Fatigue Resistance of Splice Plate: Fatigue I Limit State (S6.6.1.2.2)

$$M_{fat_neg} = -279 \text{ kip} \cdot \text{ft}$$

$$M_{fat_pos} = 50.4 \text{ kip} \cdot \text{ft}$$

$$f_{top_pos_fatI} := \frac{M_{fat_pos_FatI}}{S_{xt_SO}} = 1.0 \text{ ksi}$$

$$f_{top_neg_fatI} := \frac{M_{fat_neg_FatI}}{S_{xt_SO}} = -5.5 \text{ ksi}$$

$$\gamma \Delta f := |f_{top_neg_fatI}| + f_{top_pos_fatI} = 6.5 \text{ ksi} \quad \text{SEq. 6.6.1.2.2-1}$$

$$\Delta F_{th} := 16 \text{ ksi} \quad \text{STable 6.6.1.2.5-3, Cat B}$$

$$\Delta F_n := \Delta F_{th} \quad \text{SEq. 6.6.1.2.5-1}$$

$$\Delta P := \gamma \Delta f \cdot b_f \cdot t_f = 117.3 \text{ kip}$$

$$\bar{P} := \frac{\Delta P}{2} = 58.6 \text{ kip}$$

Bracket base plate:

$$\Delta f_{base_plate} := \frac{P}{A_{g_base_plate}} = 9.8 \text{ ksi} < \Delta F_n = 16.0 \text{ ksi}, \text{ OK}$$

Welded Post-Tension Bracket Assembly Welds (S6.13.3)

The PT brackets are designed for the ultimate load of the threaded rod.

$$P_{rodUlt} := F_{uPT} \cdot A_{rod} = 223 \text{ kip} \quad \text{ultimate strength of each rod}$$

$$\phi_{e2} := 0.80 \quad \text{S6.5.4.2}$$

$$F_{e70} := 70 \text{ ksi} \quad \text{S6.13.3.2.1}$$

$$R_{r_bracket_weld} := 0.6 \cdot \phi_{e2} \cdot F_{e70} = 33.6 \text{ ksi} \quad \text{SEq. 6.13.3.2.3b-1}$$

$$L_1 := 20 \text{ in} \quad \text{Bracket Longitudinal Length}$$

$$L_2 := 6 \text{ in} \quad \text{Bracket End Edge Length}$$

$$L_{eff} := (L_1 - 2 \text{ in}) \cdot 4 = 72.0 \text{ in} \quad \text{effective weld length}$$

$$d_{thickness_weld} := \frac{5}{16} \text{ in} \quad \text{weld depth}$$

$$L_{throat_eff} := \frac{d_{thickness_weld}}{\sqrt{2}} = 0.2 \text{ in} \quad \text{effective throat}$$

$$A_{eff} := L_{eff} \cdot L_{throat_eff} = 15.9 \text{ in}^2 \quad \text{effective area}$$

$$R_{resistance} := R_{r_bracket_weld} \cdot A_{eff} = 534.6 \text{ kip} > P_{rodUlt} = 223 \text{ kip} \quad \text{O.K.}$$

Using 5/16" weld at outside edge and end edge (STable 6.13.3.4-1).

Tips:

Welded PT bracket-to-flange design could eliminate many issues when compared with the bolted PT bracket attachment. All of the welding can be done in shop, which is helpful for ABC applications. It can also avoid any bolt slip issues. The cost is lower than a bolted bracket design. However, fatigue may be a concern and should be checked.

Design Step 3: Summary

Performance Ratios

The following is a summary of all the limit states for this design. Values equal to or greater than 1.0 are required for a sufficient design.

Beam Design:

$PR_1 := \frac{f_{tLimit}}{f_t} = 3.26$	Tension flange stresses (step 1.8, strength I)
$PR_2 := \frac{A_{rebar_Total}}{1\% \cdot A_{concrete_deck}} = 1.09$	Minimum deck reinforcement (step 1.7)
$PR_3 := \frac{0.95 \cdot R_h \cdot F_y}{\left f_{f_bot} + \frac{f_t}{2} \right } = 3.32$	Tension flange permanent deformation (step 1.8, service II)
$PR_4 := \frac{\phi_f \cdot R_{pc} \cdot M_{yc}}{M_u} = 3.52$	Plastic moment checks (step 1.9, compression flange)
$PR_5 := \frac{\phi_f \cdot R_{pt} \cdot M_{yt}}{M_u} = 3.52$	Plastic moment checks (step 1.9, tension flange)
$PR_6 := \frac{A_g}{A_e} = 1.34$	Flange area check (step 2.1)

Connection Design:

$PR_7 := \frac{\phi P_{r_yield_top_plate}}{\frac{P_{fy}}{2}} = 2.08$	Top flange top plate yielding (step 2.2)
$PR_8 := \frac{\phi P_{r_ult_top_plate}}{\frac{P_{fy}}{2}} = 1.56$	Top flange top plate fracture (step 2.2)
$PR_9 := \frac{R_{r_top_plate_blockshear}}{\frac{P_{fy}}{2}} = 2.21$	Top flange top plate block shear (step 2.2)
$PR_{10} := \frac{\phi P_{r_yield_bot_plate}}{\frac{P_{fy}}{2}} = 1.59$	Top flange bottom plate yielding (step 2.2)
$PR_{11} := \frac{\phi P_{r_ult_bot_plate}}{\frac{P_{fy}}{2}} = 1.01$	Top flange bottom plate fracture (step 2.2)
$PR_{12} := \frac{R_{r_bot_plate_blockshear}}{\frac{P_{fy}}{2}} = 2.31$	Top flange bottom plate block shear (step 2.2)
$PR_{13} := \frac{R_{n_boltslip}}{P_s} = 2.76$	Top flange bolt slip (step 2.3)
$PR_{14} := \frac{R_{n_boltshear}}{P_s} = 4.31$	Top flange bolt shear (step 2.3)
$PR_{15} := \frac{R_{n_bb\&to}}{P_{fy}} = 1.43$	Top flange bolt bearing and tearout (step 2.3)
$PR_{16} := \frac{\Delta F_n}{\Delta f_{outer_plate}} = 4.03$	Top flange top plate fatigue resistance (step 2.3)
$PR_{17} := \frac{\Delta F_n}{\Delta f_{inner_plate}} = 3.07$	Top flange bottom plate fatigue resistance (step 2.3)
$PR_{18} := \frac{\phi_f \cdot M_p}{M_u} = 2.84$	Flexural capacity at the connection (step 2.5)

PT Bracket to Flange Design:

$PR_{19} := \frac{R_r}{P} = 4.34$	Bracket bolt shear resistance (step 2.7)
$PR_{20} := \frac{R_{n_boltslip_bracket}}{P} = 3.27$	Bracket bolt slip resistance (step 2.7)
$PR_{21} := \frac{R_{n_nominal_bolttensile}}{P} = 9.16$	Bracket bolt tensile resistance (step 2.7)
$PR_{22} := \frac{T_r}{P} = 7.24$	Bracket bolt combined tension and shear resistance (step 2.7)
$PR_{23} := \frac{T_n}{P_u + Q_u} = 2.60$	Bracket bolt prying check (step 2.7)
$PR_{24} := \frac{\phi P_{r_yield_base_plate}}{P} = 4.86$	Tensile resistance of bracket base plate (step 2.7)
$PR_{25} := \frac{\phi P_{r_ult_base_plate}}{P} = 4.32$	Tensile fracture of bracket base plate (step 2.7)
$PR_{26} := \frac{\Delta F_n}{\Delta f_{base_plate}} = 1.64$	Fatigue resistance of bracket base plate (step 2.7)

Schematic of Final Bolted Field Splice Design (PT Included)

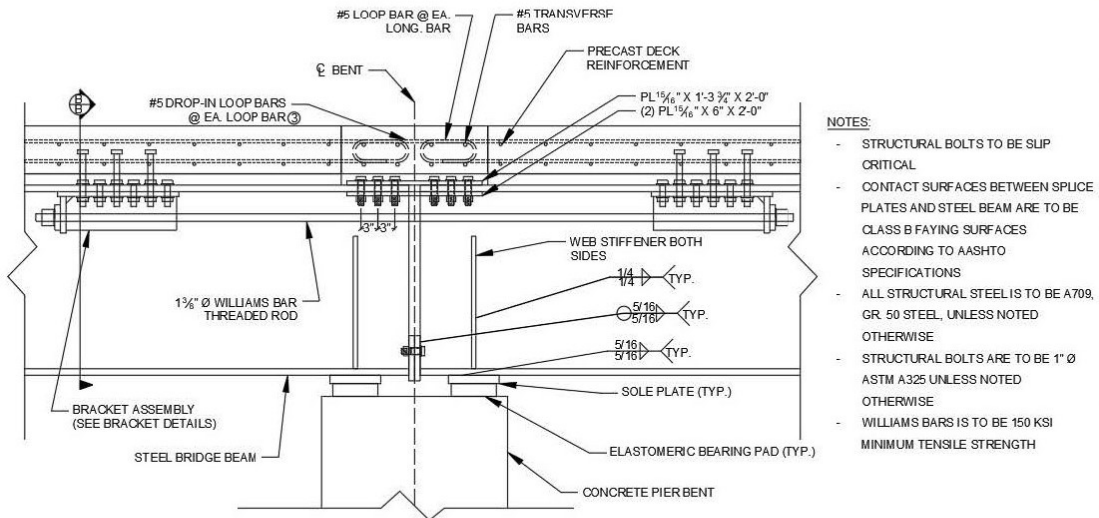


Figure 9: Recommended Connection Design with PT Rods/Brackets

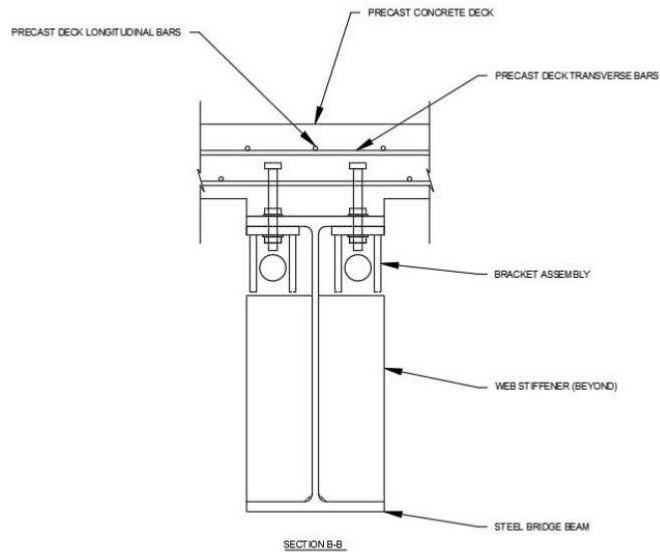


Figure 10: Section Through PT Brackets

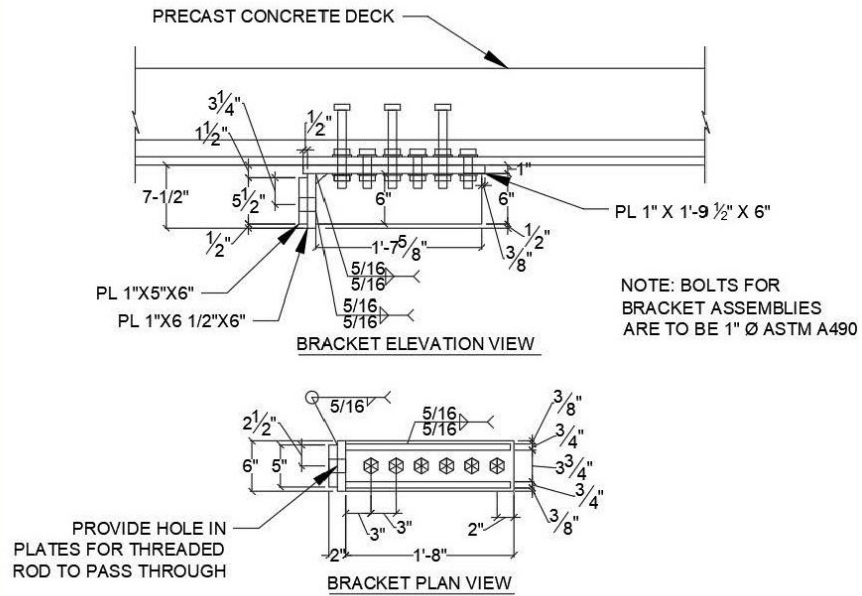


Figure 11: PT Bracket Assembly

APPENDIX E: STANDARD DRAWING

